SECOND INTERNATIONAL SYMPOSIUM ON
SPACE TERAHERTZ TECHNOLOGY

February 26-28, 1991

Jet Propulsion Laboratory
California Institute of Technology
Pasadena, California

Proceedings

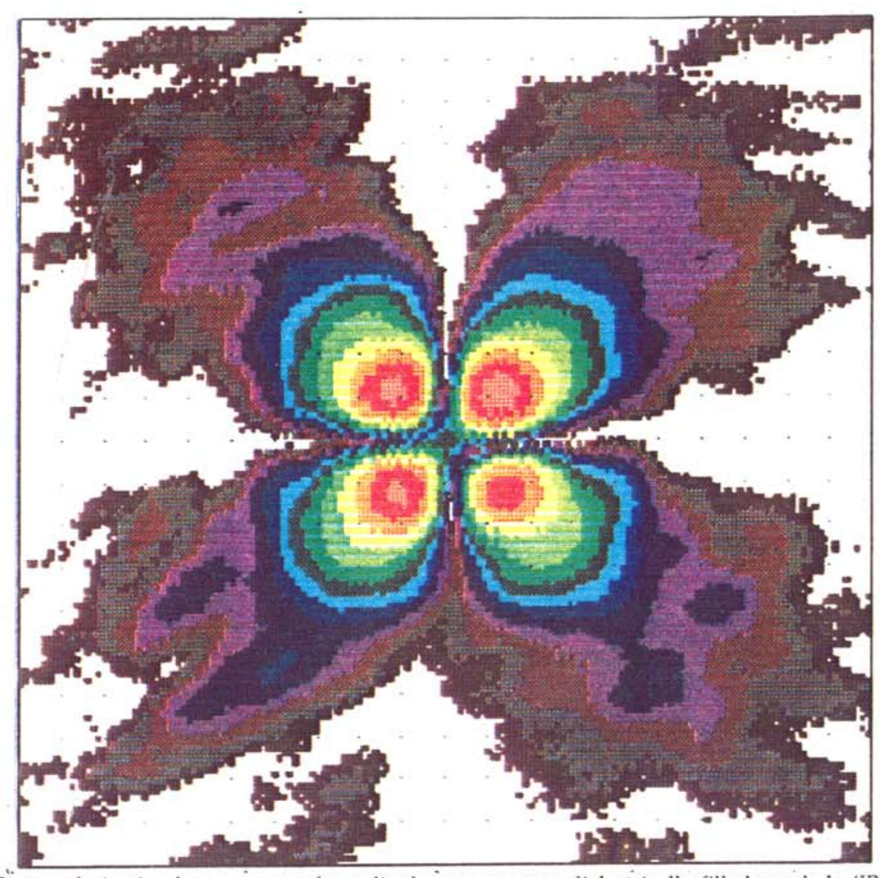

Cross-polarization beam pattern for a dipole antenna on a dielectrically filled parabola (JPL).

Sponsored by University Space Engineering Research Centers Program of NASA's Office of Aeronautics, Exploration and Technology (OAET); andStrategic Defense Initiative Organization, Innovative Science and Technology Office (SDIO/IST)

Cooperative Sponsorship by: IEEE Microwave Theory and Techniques Society

Organized Jointly by: NASA Center for Space Terahertz Technology, University of Michigan; and Center for Space Microelectronics Technology, Jet Propulsion Laboratory

Proceedings of the SECOND INTERNATIONAL SYMPOSIUM ON SPACE TERAHERTZ TECHNOLOGY

February 26-28, 1991

Jet Propulsion Laboratory
California Institute of Technology
Pasadena, California

Organizing Committee

Symposium Co-chairs:	Fawwaz T. Ulaby, University of Michigan Carl A. Kukkonen, Jet Propulsion Laboratory
Technical Co-chairs:	Margaret A. Frerking, Jet Propulsion Laboratory Gabriel M. Rebeiz, University of Michigan
Treasurer:	Virendra Sarohia, Jet Propulsion Laboratory
Local Arrangements:	Pat McLane, Jet Propulsion Laboratory
Symposium Proceedings:	Valerie Franklin, University of Michigan

Smiling faces at the 1991 Symposium on February 26, JPL.

Preface

The Second International Symposium on Space Terahertz Technology was held at the Jet Propulsion laboratory, California Institute of Technology, Pasadena, California, on February 26-28, 1991. The Symposium, which was attended by approximately 150 scientists and engineers from the U.S., Europe, and Japan, featured papers relevant to the generation, detection, and use of the terahertz spectral region for space astronomy and remote sensing of the Earth's upper atmosphere. The program included ten sessions covering a wide variety of topics including solid-state oscillators, power-combining techniques, mixers, harmonic multipliers, antennas and antenna arrays, submillimeter receivers, and measurement techniques.

The Symposium was sponsored by the University Space Engineering Research Centers Program of NASA's Office of Aeronautics, Exploration, and Technology (OAET), and by the Strategic Defense Initiative Organization, Innovative Science and Technology Office (SDIO/IST). The Microwave Theory and Techniques Society of IEEE served as a cooperative sponsor of the Symposium, as well as a medium for publication of some of the papers that were presented at the Symposium in the form of a mini-special issue (March 1992) of the *IEEE-MTT Transactions*.

The Third International Symposium on Space Terahertz Technology will be held at the University of Michigan in Ann Arbor, Michigan, on March 24-26, 1992.

Fawwaz T. Ulaby
Carl A. Kukkonen

Session 9: Circuits and More — Chair: H. Fetterman

Sliding Backshorts for Planar Circuits 536
V. M. Lubecke, W. R. McGrath, D. B. Rutledge

Low-loss Guiding Structures for THz Frequency Applications 545
A. G. Engel, Jr.; T. E. van Deventer; L. P. B. Katehi

Improved Superconductive Mixer Coupling: Sub-millimeter Performance without Sub-micron Lithography 558
J. A. Carpenter, E. R. Arambula, E. B. Guillory, A. D. Smith

D-band Vector Network Analyzer 573
J. Steimel, Jr.; J. East

Tunable High-frequency Radiation Source Utilizing a Relativistically Propagating Ionization Front 585
R. L. Savage, Jr.; C. Joshi; W. B. Mori

Session 10: Receivers and More — Chair: G. I. Haddad

Submillimeter InP-based High Electron Mobility Transistors 597
L. D. Nguyen, A. S. Brown, L. E. Larson

Wave-coupled $LiNbO_3$ Electro-optic Modulator for Microwave and Millimeter-wave Modulation 606
W. B. Bridges, F. T. Sheehy, J. H. Schaffner

A Planar Wideband Subharmonic Millimete-wave Receiver 616
B. K. Kormanyos, C. C. Ling, G. M. Rebeiz, P. H. Ostdiek, W. L. Bishop, T. W. Crowe

380 GHz Receiver Front-end for the Balloon-borne Radioastronomical Experiment - Pronaos 622
O. Perrin, C. Robert, P. Feautrier, P. Febvre, G. Beaudin, P. Encrenaz, M. Gheudin, J. Lacroix, G. Montignac

Submillimeter Receiver Development at the University of Cologne 641
J. Hernichel, F. Lewen, K. Matthes, M. Klumb, T. Rose, G. Winnewisser, P. Zimmermann

A Water Vapour and Temperature Atmospheric Vertical Sounder Between 110 and 190 GHz: Observing Campaigns in Prospect 648
P. Abba, G. Beaudin, A. Deschamp, P. Encrenaz, M. Gheudin, J. R. Jégou, C. Prigent, G. Ruffié, G. Thomas

Session 6: Mixers 1 Chair: G. M. Rebeiz

GaAs Schottky Diodes for Mixing Applications Beyond 1 THz....323
T. W. Crowe, W. C. B. Peatman

Millimeter Wave Planar Doped Barrier Detector Diodes....340
Y. Anand, J. Hillson, A. Torabi, J. East

Two-dimensional Electron Gas Hot-electron ("2DEG") Mixers for Millimeter Waves and Submillimeter Waves....353
J.-X. Yang, W. Grammer, F. Agahi, K. M. Lau, K. S. Yngvesson

InGaAs Schottky Barrier Mixer Diodes for Minimum Conversion Loss and Low LO Power Requirements at Terahertz Frequencies....371
U. V. Bhapkar, T. A. Brennan, R. J. Mattauch

High Gain and Noise in SIS Mixers at Submillimeter Wavelengths....389
M. J. Wengler, N. Dubash, G. Pance, R. E. Miller

Terahertz Detectors Based on Superconducting Kinetic Inductance....407
E. N. Grossman, D. G. McDonald, J. E. Sauvageau

Session 7: Mixers 2 Chair: R. J. Mattauch

Low-noise 205 GHz SIS Mixers Using High Current Density Nb and NbN Tunnel Junctions....423
W. R. McGrath, H. H. S. Javadi, S. R. Cypher, B. Bumble, B. D. Hunt, H. G. LeDuc

Nb Based Mixer Elements for Millimeter and Submillimeter Wavelengths....439
A. W. Lichtenberger, D. M. Lea, A. C. Hicks, J. D. Prince, R. Densing, D. Peterson, B. S. Deaver

A Low Noise 230 GHz Heterodyne Receiver Employing .25μm^2 Nb/Al-AlO_x/Nb Tunnel Junctions459
J. W. Kooi, M. Chan, T. G. Phillips, B. Bumble, H. G. LeDuc

SIS Mixing at 345 GHz with Arrays of NB-Al_2O_3-Nb Junctions....473
C. E. Honingh, H. H. Schaeffer, Th. de Graauw, M. M. T. M. Dierichs, T. M. Klapwijk

Session 8: Antennas 2 and More Chair: T. Itoh

Quasi-optical Slot Antenna SIS Mixers....481
Jonas Zmuidzinas

Millimeter-wave Double-dipole Antennas for High Efficiency....491
D. F. Filipovic, W. Y. Ali-Ahmad, G. M. Rebeiz

Update of the LeRC Submillimeter Backward-wave Oscillator Program....497
Stankiewicz, Barnett, Dayton

Millimeter Wave Radiation Generated by Optical Mixing in FETs Integrated with Printed Circuit Antennas....523
D. V. Plant, H. R. Fetterman, D. C. Scott, D. C. Ni

Session 3: Power Combining Chair: F. T. Ulaby

Josephson Junction Oscillator Arrays....163
M. J. Lewis, D. Durand, A. D. Smith, P. Hadley

Terahertz Power-combining with Coupled Oscillator Arrays....179
R. A. York, R. C. Compton

Millimeter and Submillimeter Wave Quasi-optical Oscillator with Multi-elements....187
M. Nakayama, M. Hieda, T. Tanaka, H. Kondo, K. Osakabe, K. Mizuno

Network Analysis of Planar Spatial Power Combining....191
T. Itoh

Session 4: Multipliers 1 Chair: M. A. Frerking

Theoretical Efficiency of Multiplier Devices....197
T. J. Tolmunen, M. A. Frerking

Multipliers for THz Heterodyne Systems....212
B. L. A. Rydberg, B. N. Lyons, U. S. Lidholm

Quantum Well Diode Frequency Multiplier Study....226
R. J. Hwu; N. C. Luhmann, Jr.

90 to 180 GHz Heterostructure Monolithic Integrated Doubler....238
Y. Kwon, D. Pavlidis, P. Marsh, M. Tutt, G. I. Ng, T. Brock

Session 5: Multipliers 2 Chair: T. W. Crowe

Recent Development of Barrier-intrinsic-N+ Diode (BIN) Frequency Tripler....255
R J. Hwu; N. C. Luhmann, Jr.

Design of Planar Varactor Frequency Multiplier Devices with Blocking Barriers....270
U. Lieneweg, T. Tolmunen, M. Frerking, J. Maserjian

Monolithic Metal-insulator-semiconductor (MIS) Varactor Frequency Multipliers in the Millimeter and Submillimeter Wave Region....285
R. J. Hwu, L. P. Sadwick, G. B. Stringfellow

Millimeter-wave Monolithic Solid State Device Arrays....293
H-X. King; N. C. Luhmann, Jr.; X. Qin; L. B. Sjogren; W. Wu

Current Saturation in Submillimeter-wave Varactors....306
E. Kollberg, T. Tolmunen, M. Frerking, J. East

Contents

Opening Session — Chair: C. A. Kukkonen

NASA's OAET Sensors Program .... *
M. Sokoloski

NASA Program Plans for Submillimeter-wave Astrophysics Program 1
M. Kaplan

The Submillimeter Mission (SMMM) Heterodyne Instrument 17
M. A. Frerking

EOS MLS: A View from the Front 32
P. Siegel

Session 1: Antennas 1 — Chair: J. W. Mink

Integrated Terahertz Corner-cube Antennas and Receivers 57
S. S. Gearhart, C. C. Ling, G. M. Rebeiz, G. Chin, H. Davé

Antennas for Submillimeter Wave Recievers 63
J. F. Johansson, N. D. Whyborn, P. R. Acharya, H. Ekström, S. W. Jacobsson, E. L. Kollberg

Progress in 94 GHz Integrated Horn Antennas 82
W. Ali-Ahmad, G. Eleftheriades, L. P. B. Katehi, G. M. Rebeiz

Imaging Arrays for the Millimeter- and Submillimeter-wave Region 91
K. Uehara, K. Miyashita, K. Natsume, K. Hatakeyama, K. Mizuno

Session 2: Oscillators — Chair: E. L. Kollberg

Fundamental Mode Operation of Gunn Devices above 100 GHz 98
R. Kamoua, J. R. East, G. I Haddad

Design and Evaluation of W- and D-band TUNNETT Devices 114
C. Kidner, G. I. Haddad, J. R. East, H. Eisele

Recent Advances in Resonant-tunneling-diode Oscillators 133
E. R. Brown, C. D. Parker, K. M. Molvar, M. K. Conners

GaAs IMPATT Diodes for Frequencies above 100 GHz: Technology and Performance 145
H. Eisele, R. K. Mains, G. I. Haddad, C. C. Chen

Lossy-line Stabilization of Negative-resistance Diodes for Integrated-circuit Oscillators 154
K. D. Stephan, S. C. Wong, E. R. Brown

*Presentation only.

Preface

The Second International Symposium on Space Terahertz Technology was held at the Jet Propulsion laboratory, California Institute of Technology, Pasadena, California, on February 26-28, 1991. The Symposium, which was attended by approximately 150 scientists and engineers from the U.S., Europe, and Japan, featured papers relevant to the generation, detection, and use of the terahertz spectral region for space astronomy and remote sensing of the Earth's upper atmosphere. The program included ten sessions covering a wide variety of topics including solid-state oscillators, power-combining techniques, mixers, harmonic multipliers, antennas and antenna arrays, submillimeter receivers, and measurement techniques.

The Symposium was sponsored by the University Space Engineering Research Centers Program of NASA's Office of Aeronautics, Exploration, and Technology (OAET), and by the Strategic Defense Initiative Organization, Innovative Science and Technology Office (SDIO/IST). The Microwave Theory and Techniques Society of IEEE served as a cooperative sponsor of the Symposium, as well as a medium for publication of some of the papers that were presented at the Symposium in the form of a mini-special issue (March 1992) of the *IEEE-MTT Transactions*.

The Third International Symposium on Space Terahertz Technology will be held at the University of Michigan in Ann Arbor, Michigan, on March 24-26, 1992.

Fawwaz T. Ulaby
Carl A. Kukkonen

NASA Program Plans for Sub-millimeter Wave Astronomy

Mike Kaplan

Chief, Advanced Programs Branch
Astrophysics Division
Office of Space Science and Applications
NASA Headquarters

February 26, 1991

Presentation to the Second International Symposium on Space Terrahertz Technology, Jet Propulsion Laboratory, Pasadena, CA

NASA

Outline of Presentation

Astrophysics Division

- NASA's Astrophysics Program
- Planned Missions
- Technology Requirements for Future Missions
- Comments and Summary

NASA

Program Goal

Astrophysics Division

Conduct a comprehensive exploration of the universe

Themes:

- Astronomy: What is the nature of planets, stars and galaxies?
- Cosmology: What is the origin and fate of the universe?
- Physics: What are the laws of physics in the extreme conditions of astrophysical objects?

NASA

Program Strategy

Astrophysics Division

- Contemporaneous observations across the electromagnetic spectrum with high sensitivity, high angular resolution and high spectral resolution

  - *Implemented through the Great Observatories*

- Fill in crucial gaps in "wavelength" or "spectroscopy" space

  - *Implemented through Explorers and moderate missions*

- Maintain National science and technology capability

  - *Implemented through grants, sub-orbital program and technology development*

- Analyze and publish results

  - *Implemented through Mission Operations and Data Analysis program*

NASA

Science Planning Process

Astrophysics Division

- Strong grass roots community involvement in our program
  - Four Management Operations Working Groups (MOWGs) plus "Astrophysics Council"
- National Academy of Sciences
  - Committee on "Space Astronomy and Astrophysics"
  - 10 year strategy from "Bahcall report" to be released March 19, 1991
  - Prioritizes all National astronomy programs
- Integrate astrophysics initiatives into OSSA program plan

NASA

Great Observatories

Astrophysics Division

- Hubble Space Telescope (HST)
- Gamma Ray Observatory (GRO)
- Advanced X-ray Astrophysics Facility (AXAF)
- Space Infrared Telescope Facility (SIRTF)

NASA

Sub-millimeter Astronomy Missions

Astrophysics Division

- Kuiper Airborne Observatory (KAO)
- Sub-millimeter Wave Astronomy Satellite (SWAS)
- Stratospheric Observatory for Infrared Astronomy (SOFIA)
- Sub-millimeter Moderate Mission (SMMM)
- Large Deployable Reflector (LDR)
- Sub-millimeter Interferometer

NASA

Sub-millimeter Astronomy Program Plans

Astrophysics Division

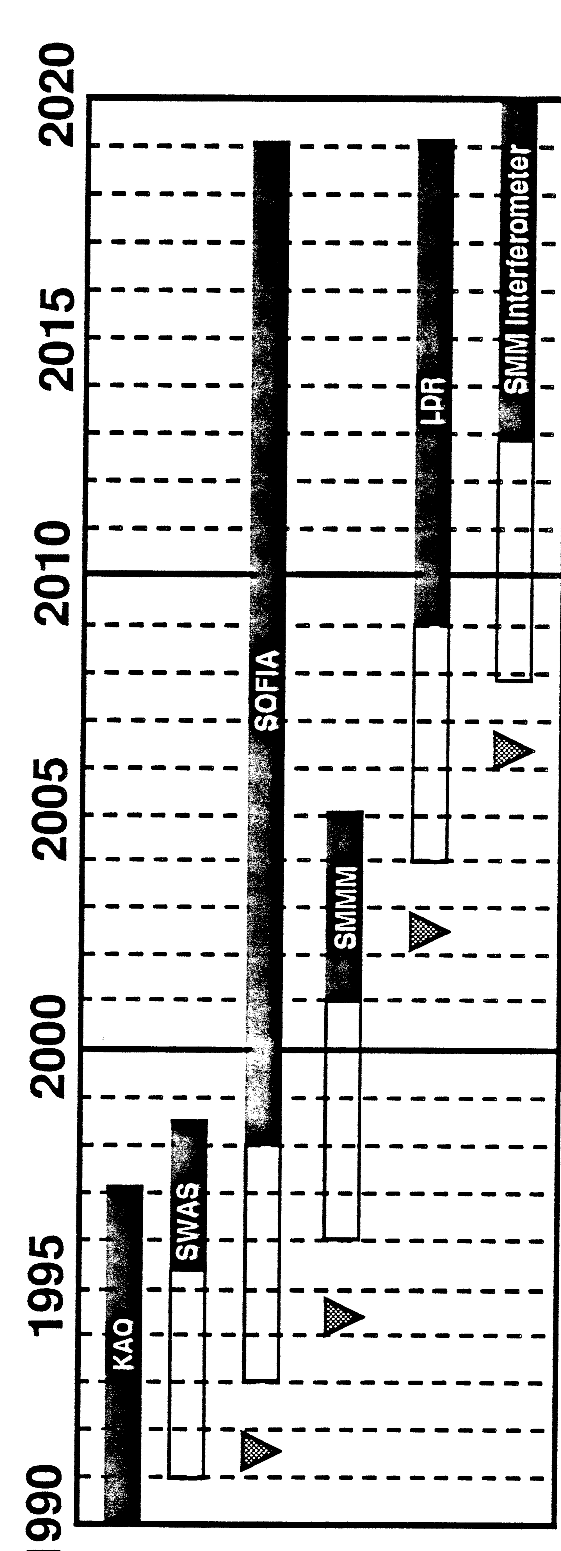

NASA

Sub-millimeter Wave Astronomy Satellite (SWAS)

Astrophysics Division

- Science Strategy: SWAS will perform both pointed and survey observations in 4 lines crucial to the study of interstellar cloud chemistry, energy balance and structure: 487, 557, 492 and 551 GHz
- Description:
  - 3 axis stabilized, stellar-pointing "Small Explorer" spacecraft (Scout-class)
  - 530 km altitude, 3 degree inclination angle orbit
  - 55 cm off-axis Cassegrain antenna, passively cooled heterodyne receivers and acousto-optical spectrometer
- Launch Date: 1995
- Principal Investigator/ Payload List:
  - PI -- Dr. Gary Melnick, SAO
  - Antenna, Star Tracker, Instrument Integration -- Ball Aerospace
  - Sub-millimeter Heterodyne Receiver -- Millitech
  - Acousto-optical Spectrometer -- University of Cologne
- NASA Program Manager: Dr. David Gilman, NASA HQ

NASA

Stratospheric Observatory for Infrared Astronomy (SOFIA)

Astrophysics Division

- Science Strategy: SOFIA will provide frequent, high-quality access to the IR/sub-mm spectral region
- Description:
  - 2.5 m Nasmyth IR telescope housed in a modified Boeing 747 SP aircraft
  - Operates from 0.3 to 1600 microns
  - Sensitivity ~ 10^{-19} W/cm^2 /SR
  - Angular Resolution: 2 arcsec in near IR and diffraction limited at wavelengths > 30 microns
  - 120 flights/year with 30 - 40 research teams/year
- Launch Date: 1998
- Technology Development Requirements:
  - Lightweight f/1 primary mirror (Zeiss)
  - Shear layer control
  - Large air bearing
- NASA Program/Project Manager: Mike Kaplan, NASA-HQ / Dr. Gary Thorley, NASA-ARC

NASA

Sub-millimeter Moderate Mission (SMMM)

Astrophysics Division

- Science Strategy: SMMM will be a spectral survey of selected objects from 100 - 750 microns and imaging in the 100 - 300 micron range
- Description:
  - 2.5 to 4 m segmented, ambient temperature aperture
  - High orbit, 2 year lifetime
  - Liquid He-cooled focal plane
    - Fabry-Perot spectrometer with 0.1 deg K bolometers
    - IR camera with 0.3 deg K bolometers
    - Ten-band heterodyne radiometer operating at 2 deg K
- Mission Options: Explorer-class (2.5 m aperture, spectroscopy only), CNES and/or ESA collaboration
- Launch Date: 2001 ?
- Technology Development Requirements:
  - SIS mixers, heterodyne receivers with sensitivities within a factor of 5 of the quantum limit and local oscillators with increased conversion efficiency
  - Far IR integrating arrays (impurity band conduction technology)
  - Bolometers
  - Lightweight precision aperture
- Science Working Group Chairman: Dr. Tom Phillips, Caltech

NASA

Large Deployable Reflector (LDR)

Astrophysics Division

- Science Strategy: LDR will view sources in the wavelength region between 30 and 3000 microns
- Description:
  - 20 m - class diameter antenna for imaging spectroscopy and photometry composed of 90 lightweight, hexagonal panels, 4 mirror, two-stage optical system
  - Diffraction limit < 50 microns
  - Spectral resolving limit from 10 to 10^5
  - Angular resolution of 1 arcsec at 100 microns
  - Sensitivity > 2×10^{-14} W/cm^2/SR
- Launch Date: 2009 ??
- Technology Development Requirements:
  - Lightweight mirror segments
  - Active figure control
  - Heterodyne receivers with SIS mixers
  - Long lifetime cryogenics
- NASA POC: Dr. Larry Caroff, NASA-HQ

NASA

Sub-millimeter Interferometer (SMMI)

Astrophysics Division

- Science Strategy: SMMI will view sources in the wavelength region between 30 and 1000 microns with 100x better resolution than any other existing or proposed instrument. Based at lunar outpost
- Description:
  - Two-dimensional array of 5 - meter antennas distributed on baselines from 50 m to several km
  - Actively-cooled, superheterodyne receivers
  - Spectral resolving limit from 10 to 10^6 over the entire spectrum 10 GHz BW
  - Angular resolution of 10 milliarcsec at 100 microns
- Launch Date: 2013 ??
- Technology Development Requirements:
  - High throughput correlators
  - Lightweight materials that operate at 100 deg K and cycle to 385 deg K
  - Fiber-optics
  - Telerobotic operation
- NASA POC: Mike Kaplan, NASA-HQ

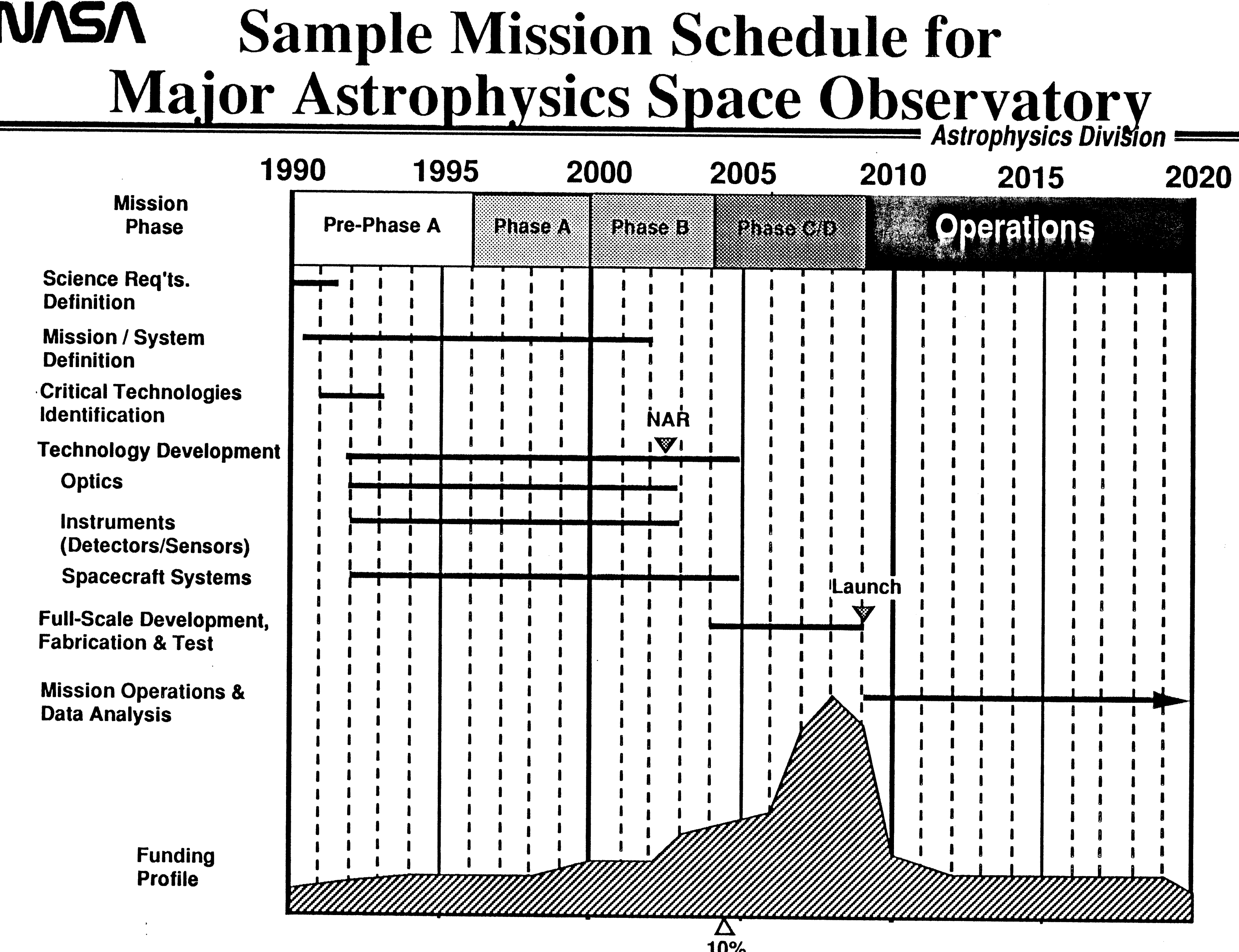
NASA
Sample Mission Schedule for
Major Astrophysics Space Observatory
Astrophysics Division
1990
1995
2000
2005
2010
2015
2020
Mission Phase
Pre-Phase A
Phase A
Phase B
Phase C/D
Operations
Science Req'ts. Definition
Mission / System Definition
Critical Technologies Identification
Technology Development
Optics
Instruments (Detectors/Sensors)
Spacecraft Systems
Full-Scale Development, Fabrication & Test
Mission Operations & Data Analysis
Funding Profile
NAR
Launch
10%

NASA

Technology Requirements for Sub-millimeter Astronomy Missions

Astrophysics Division

- **Sub-millimeter Heterodyne Receivers**: Develop robust, space-qualifiable heterodyne technology for extension into the terraherhz regime, increased sensitivity and array applications
  - Local oscillator power of 50 microwatts to 20 mW for 200 GHz to 1 THz
  - Mixers with noise performance < 10 x quantum limit @ > 600 GHz to 3 THz
  - Low power, smaller size, larger bandwidth spectrometer concepts for space
  - Focal plane arrays covering 100 GHz to 2 THz
- **Sub-millimeter Apertures**: Develop large, precise lightweight segmented apertures up to 30 m in diameter with excellent thermal characteristics - NASA OAET Precision Segmented Reflector (PSR) program
- **Others**:
  - Space cooler and cryogenic technology - to support long duration missions

NASA

Comments & Summary

Astrophysics Division

- Release of Augustine report has caused new emphasis on space science within NASA

- We will see a revolution in space astronomy over the next decade

- NASA has ambitious plans to explore the universe in sub-millimeter portion of the electromagnetic spectrum

- These missions are **enabled** with the development of new sub-millimeter wave technology

- Exciting times for sub-millimeter wave astronomy are around the corner!!

The Submillimeter Mission (SMMM) Heterodyne Instrument

Margaret A. Frerking

Presented at the
Second International Symposium
on Space Terahertz Technology

February 26, 1991

SUBMILLIMETER MISSION HETERODYNE INSTRUMENT

SMMM Science Objectives

Complete submillimeter high resolution spectral line survey of 100 sources
- 40 molecular clouds in the Milky Way
- 30 galaxies
- 30 sources of opportunity

Sensitivity: Spectral line confusion limit ~2mK

Molecular Clouds
- Identify composition
- Study chemistry
- Determine physical conditions: temperature, density, mass
- Study dynamics: velocity structure, thermal mechanisms
- Detailed study of stellar evolution

Galaxies
- Spectroscopy of galaxies to z=2
  - Well known visible and IR lines red shifted into submm by Hubble expansion

MAF 2-26-91

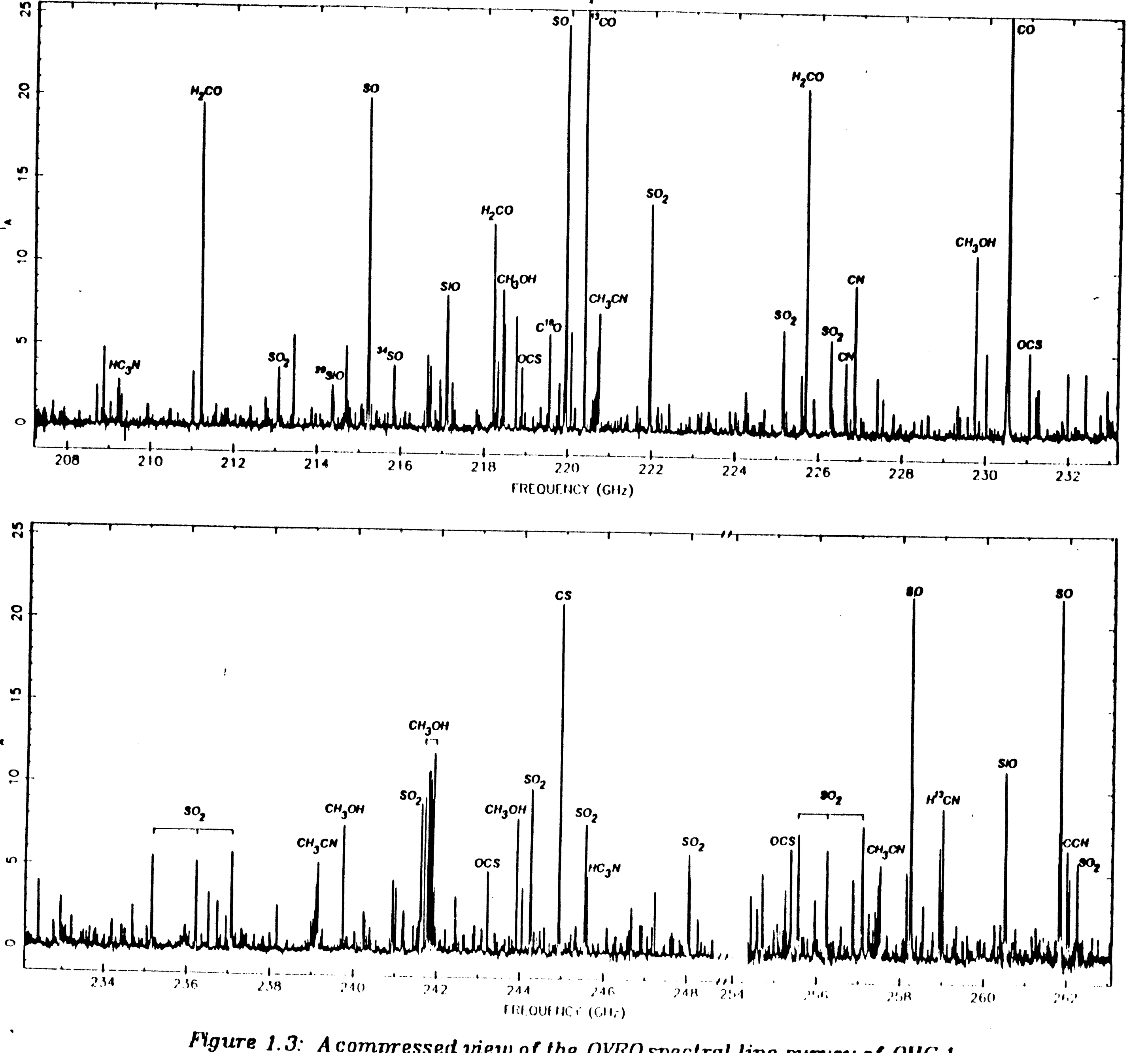

Figure 1.3: ***A compressed view of the OVRO spectral line survey of OMC-1.***

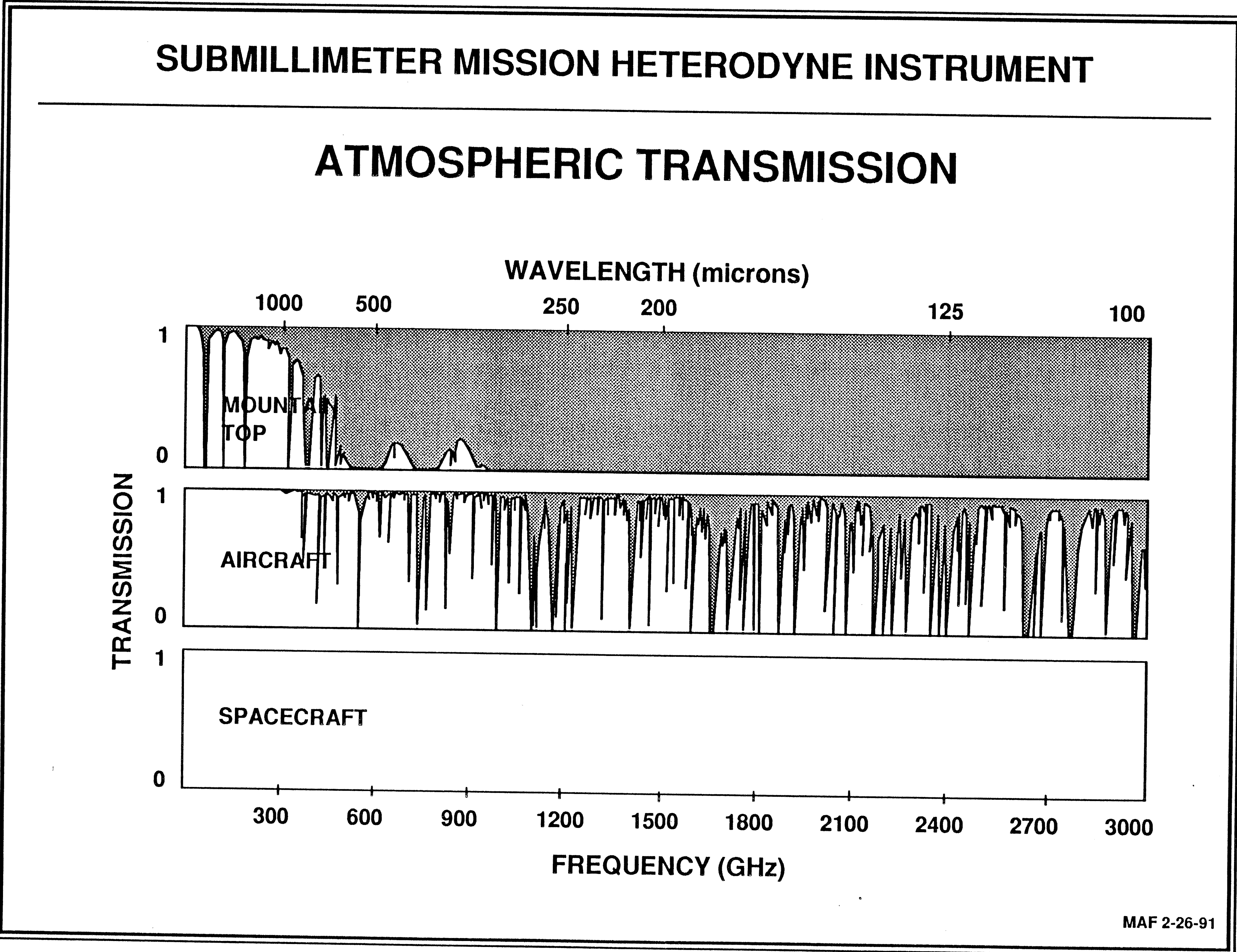
SUBMILLIMETER MISSION HETERODYNE INSTRUMENT
ATMOSPHERIC TRANSMISSION
WAVELENGTH (microns)
1000
500
250
200
125
100
MOUNTAIN TOP
AIRCRAFT
SPACECRAFT
TRANSMISSION
1
0
1
0
1
0
300
600
900
1200
1500
1800
2100
2400
2700
3000
FREQUENCY (GHz)
MAF 2-26-91

SUBMILLIMETER MISSION HETERODYNE INSTRUMENT

SMMM Description

Two Concepts:
Submm Explorer (SMME) and Submillimeter Imaging Line Survey (SMILS)
2.5 or 3.7 m diameter ambient temperature telescope

Liquid Helium cooled focal plane

SIS heterodyne receivers from 400 to 1200 GHz (SMILS)
500 to 1000 GHz and 1145 GHz (SMME)

100 - 300 μ (1000 - 3000 GHz) scanning Fabry-Perot spectrometer

Bolometer camera from 100 to 800 μ (SMILS only)

High elliptical orbit (900 to 70,000 km)

Two year lifetime

MAF 2-26-91

SUBMILLIMETER MODERATE MISSION (SMMM)

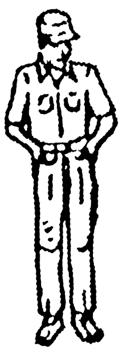

SUBMM EXPLORER (SMME)

SUBMILLIMETER - IMAGING LINE SURVEY (SMILS)

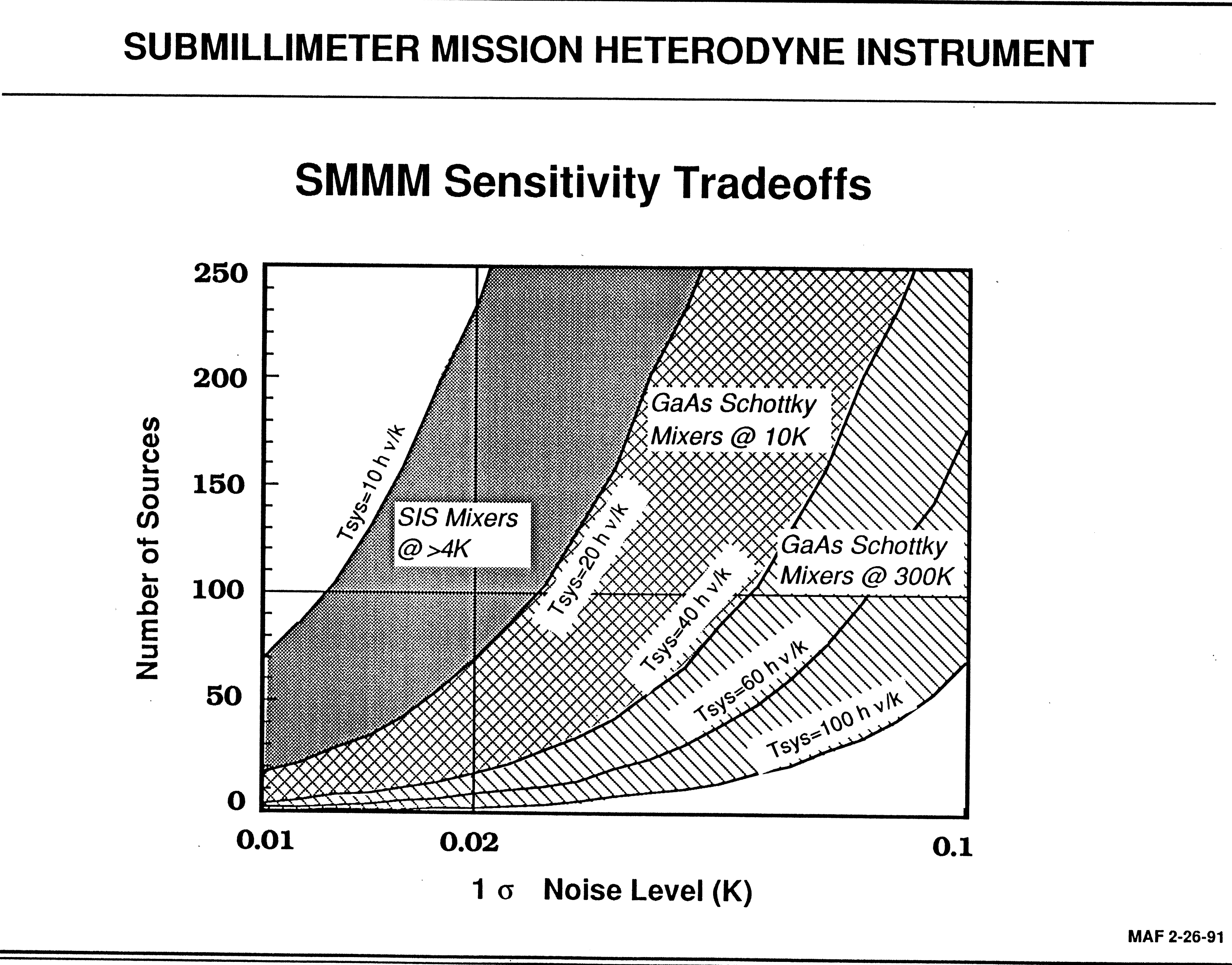

SUBMILLIMETER MISSION HETERODYNE INSTRUMENT
SMMM Sensitivity Tradeoffs
Number of Sources
250
200
150
100
50
0
0.01
0.02
0.1
1 σ Noise Level (K)
SIS Mixers @>4K
GaAs Schottky Mixers @ 10K
GaAs Schottky Mixers @ 300K
Tsys=10 h ν/k
Tsys=20 h ν/k
Tsys=40 h ν/k
Tsys=60 h ν/k
Tsys=100 h ν/k
MAF 2-26-91

SUBMILLIMETER MISSION HETERODYNE INSTRUMENT

Asumptions for SMMM Sensitivty Trades

For each source observe complete frequency range: 400 -1200 GHz
with 2 MHz frequency resolution

400,000 channels/source
Multiplex: 8000 channels simultaneously

Observing mode: position switching on and off source

Integration time blocks: 120 s

Sensitivity determined by DIcke Radiometer Equation

1 σ noise level = $\Delta T = \sqrt{2}\, T_{sys} / \sqrt{B\, \tau}$
Tsys = n hν/k
B = 2 MHz
τ = integration time at a given frequency

Included overhead for aquiring source, calibration, etc.

MAF 2-26-91

SUBMILLIMETER MISSION HETERODYNE INSTRUMENT

SMILS Heterodyne Instrument Concept

Multiplex to increase signal through put - 16 GHz instantaneous RF bandwidth

Accomplished by:
- 2 receivers operate simultaneously
- Double sideband receiver
- 8 - 12 GHz IF bandwidth

Constained by:
- heat load on He bath
- power for local oscillators
- power for spectrometer

Reliability - no cold moving parts; minimize amb. temp. moving parts

Mixers and multipliers fixed tuned - 10% operating bandwith
Electrically tuned pump oscillators - 10% operating bandwidth
10 receivers to cover 400-1200 GHz band

Use frequency diplexers rather than switching mirrors

MAF 2-26-91

SUBMILLIMETER MISSION HETERODYNE INSTRUMENT

Mixer Performance Requirements

Tsys(K)	20 hv/k
Double sideband operation	
Fixed tuned Operational bandwidth	10%
IF Band	8-12 GHz
Operating temperature	Liquid He

10 Mixers to cover frequency range 400 - 1200 GHz

400-450 GHz	710-790 GHz
450-510 GHz	790 -870 GHz
510-570 GHz	870-970 GHz
570-640 GHz	970-1080 GHz
640-710 GHz	1080-1200 GHz

MAF 2-26-91

SUBMILLIMETER MISSION HETERODYNE INSTRUMENT

State of the Art for SIS Mixer Based Heterodyne Receivers

from AT&T Bell Labs, Caltech, Ecole Normale, Iram, JPL, Koln, NRAO, Nobeyama, Onsala

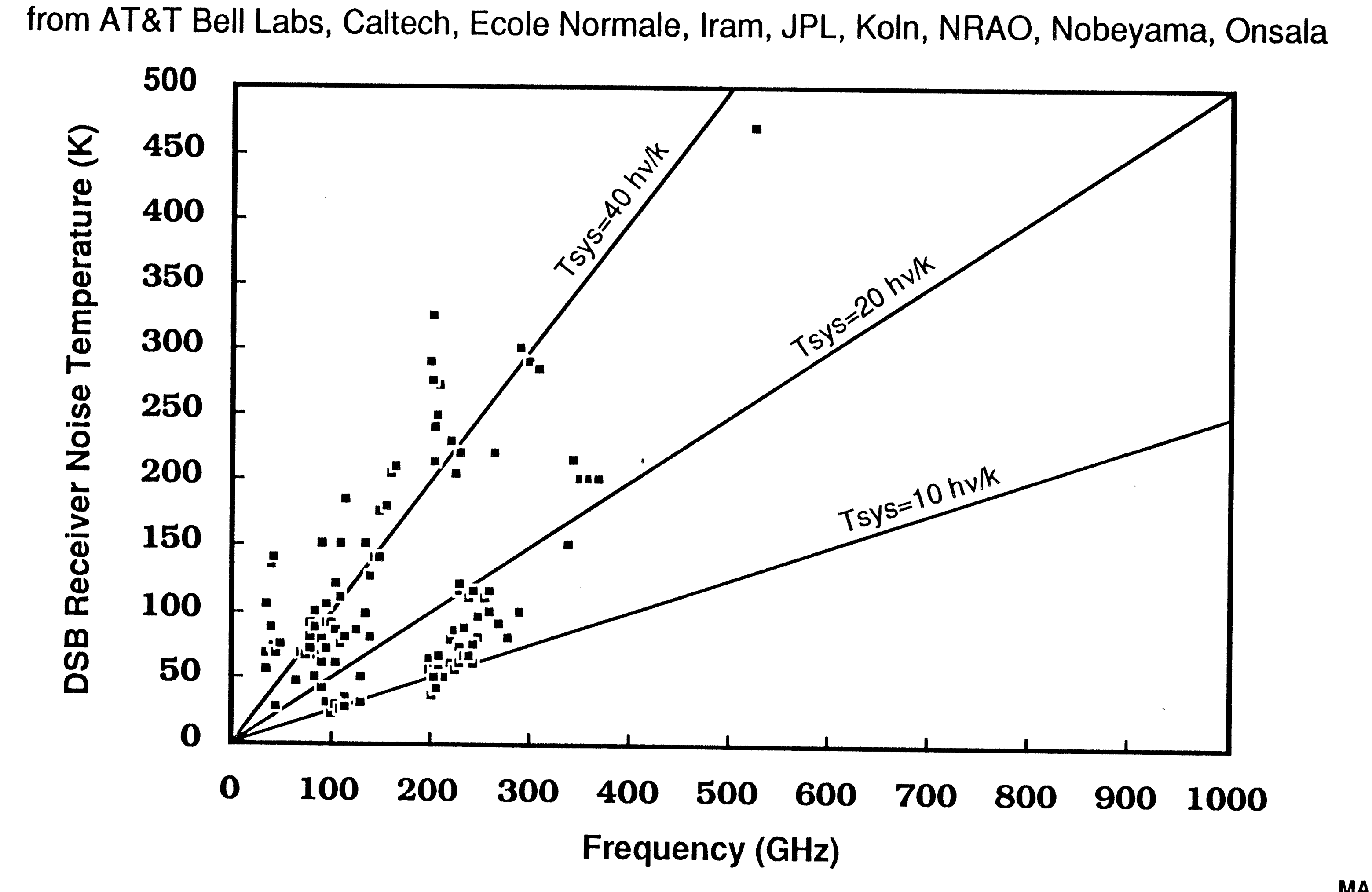

MAF 2-26-91

SUBMILLIMETER MISSION HETERODYNE INSTRUMENT

Local Oscillator Performance Requirements

Operational Bandwidth with electrical tuning	10%
Output power at 1000 GHz	50 μW
Electrical tuning step size	2 GHz
Frequency stability	$1{:}10^7$
Frequency Knowledge	$1{:}10^8$
DC power per LO source	<10 W

10 Local oscillator sources to cover frequency range from 400 - 1200 GHz

MAF 2-26-91

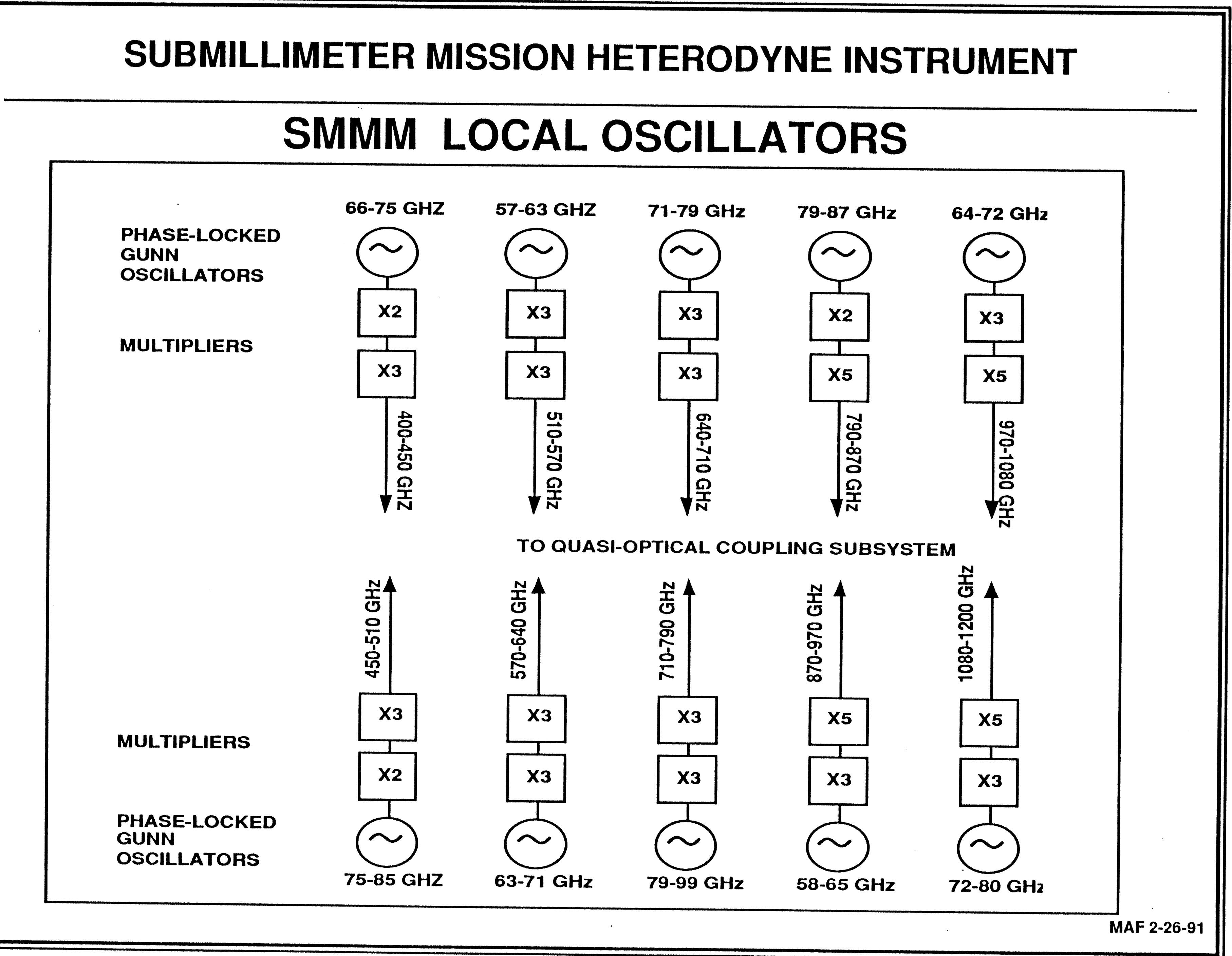
SUBMILLIMETER MISSION HETERODYNE INSTRUMENT
SMMM LOCAL OSCILLATORS
PHASE-LOCKED GUNN OSCILLATORS
MULTIPLIERS
66-75 GHZ
X2
X3
400-450 GHZ
57-63 GHZ
X3
X3
510-570 GHz
71-79 GHz
X3
X3
640-710 GHz
79-87 GHz
X2
X5
790-870 GHz
64-72 GHz
X3
X5
970-1080 GHz
TO QUASI-OPTICAL COUPLING SUBSYSTEM
450-510 GHz
X3
X2
75-85 GHZ
570-640 GHz
X3
X3
63-71 GHz
710-790 GHz
X3
X3
79-99 GHz
870-970 GHz
X5
X3
58-65 GHz
1080-1200 GHz
X5
X3
72-80 GHz
MULTIPLIERS
PHASE-LOCKED GUNN OSCILLATORS
MAF 2-26-91

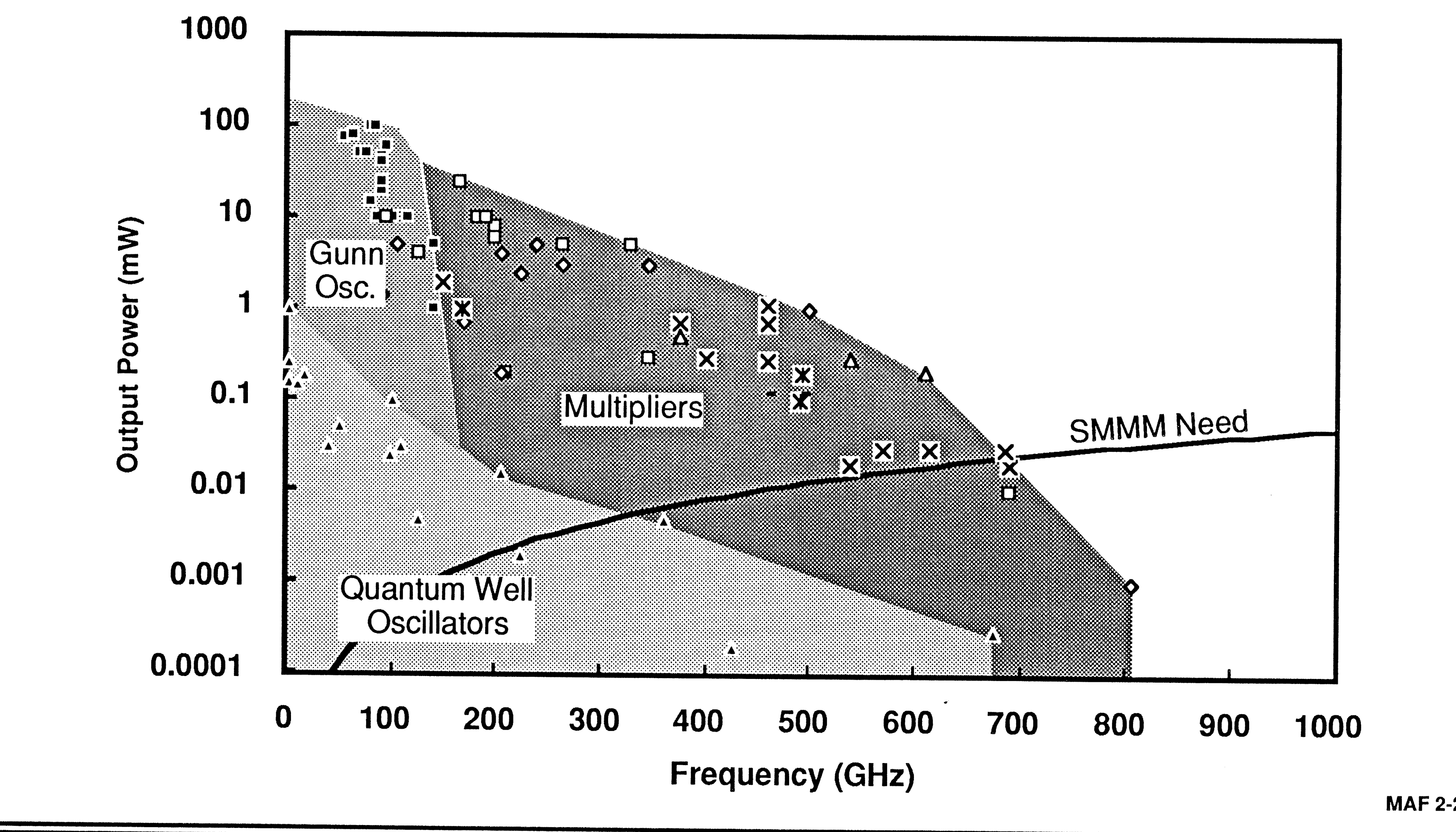
SUBMILLIMETER MISSION HETERODYNE INSTRUMENT
State of the Art
for Solid State Local Oscillators
from Caltech, Chalmers, Helsinki, JPL, Koln, Lincoln Lab, Millitech,UCLA, U. Mass., Zimmermann
Output Power (mW)
1000
100
10
1
0.1
0.01
0.001
0.0001
0
100
200
300
400
500
600
700
800
900
1000
Frequency (GHz)
Gunn Osc.
Multipliers
Quantum Well Oscillators
SMMM Need
MAF 2-26-91

SUBMILLIMETER MISSION HETERODYNE INSTRUMENT

Summary

SMMM Will provide a new view of the submillimeter wave universe

Give a complete, high resolution spectrum of
star forming regions in the Milky Way
galaxies

Poses technology challenges

SIS tunnel junction mixers
Solid state local oscillator sources

Extend frequency of operation to 1200 GHz with excellent performance

Broad band operation with no moving parts

MAF 2-26-91

EARTH OBSERVING SYSTEM MICROWAVE LIMB SOUNDER:

A VIEW FROM THE FRONT

PRESENTED AT THE

SECOND INTERNATIONAL CONFERENCE ON SPACE THZ TECHNOLOGY

CALIFORNIA INSTITUTE OF TECHNOLOGY
JET PROPULSION LABORATORY
PASADENA, CALIFORNIA

FEBRUARY 26, 1991

BY

PETER H. SIEGEL

Earth **O**bserving **S**ystem

Microwave **L**imb **S**ounder

United States
Global Change
Research Program

EOS GOALS

1. LONG TERM RELIABLE MEASUREMENTS OF GEOPHYSICAL & BIOLOGICAL VARIABLES SO THAT GLOBAL, REGIONAL & LOCAL CHANGES CAN BE DOCUMENTED OVER A 15 YEAR PERIOD

2. IDENTIFICATION OF THE MOST IMPORTANT PROCESSES IN EARTH SYSTEM SCIENCE

3. IMPROVEMENTS IN PREDICTIVE MODELS OF THE EARTH'S DYNAMIC PROCESSES

EOS INVESTIGATIONS

1. INTERDISCIPLINARY INVESTIGATIONS
Climatology, Earth Resources, Biological Monitors

2. SPECIFIC SCIENCE INSTRUMENTS
Imaging, Atmospheric Chemistry, Radiance

3. FACILITY INSTRUMENTS
Wind speed & direction, temperature, humidity, cloud cover, IR imaging

EOS INSTRUMENTS ORGANIZED BY TYPE

SURFACE IMAGERS
- CERES
- EOSP
- HIMSS
- HIRIS
- ITIR
- MISR
- MODIS

TROPOSPHERIC SOUNDERS
- AIRS
- HIMSS
- MODIS

STRATOSPHERIC CHEMISTRY
- MLS
- HIRDLS
- SAFIRE
- SAGE
- SWIRLS

RADAR/LIDAR
- ALT
- GGI
- GLRS
- LAWS
- STIK SCAT
- EOS SAR

TROPOSPHERIC CHEMISTRY
- LIS
- MOPITT
- TRACER
- TES

SOLAR IRRADIANCE
- ACRIM
- SOLSTICE

SOLAR-TERRESTRIAL INTERACTIONS
- GOS
- IPEI
- XIE

CURRENT EOS PLATFORM STATISTICS AS OF 2/91

LAUNCH DATES: EOS-A 12/98 EOS-B 6/01
12/03 6/06
12/08 6/11

LAUNCH VEHICLE: TITAN IV

ORBIT: SUN SYNCHRONOUS-705KM 98.2 DEG INCL.

MASS=3500kg • POWER=3200W • DATA RATE=30 Mb/sec
2,600 Gb/day

PAYLOADS: EOS-A 11 INSTRUMENTS
AIRS/AMSU-ASTER-CERES-EOSP-HIRDLS-LIS
MIMR-MISR-MODIS-MOPITT-STIK SCAT

EOS-B 14 INSTRUMENTS PLUS EOS-SAR
SOLSTICE-HIRDLS-MLS-SAFIRE-SAGE-SWIRLS
TES-LAWS-ALT-GLRS-GGI-GOS-IPEI-XIE

TOTAL COST: 30 BILLION OVER 20 YEARS
2-3 BILLION/PLATFORM (6 TOTAL) PLUS SCIENCE

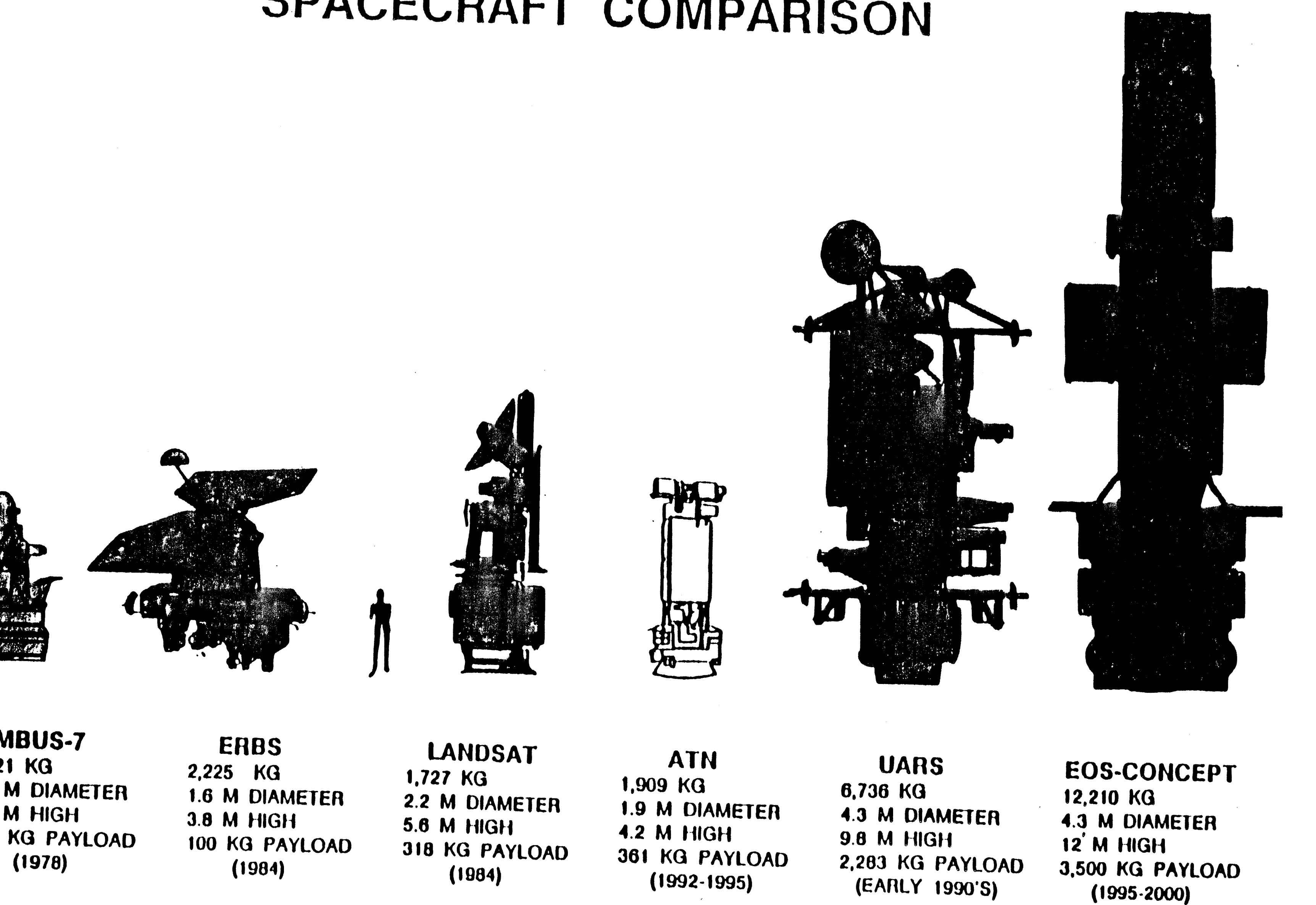
APPROXIMATE
SPACECRAFT COMPARISON
NIMBUS-7
1,021 KG
1.6 M DIAMETER
3.6 M HIGH
303 KG PAYLOAD
(1978)
ERBS
2,225 KG
1.6 M DIAMETER
3.8 M HIGH
100 KG PAYLOAD
(1984)
LANDSAT
1,727 KG
2.2 M DIAMETER
5.6 M HIGH
318 KG PAYLOAD
(1984)
ATN
1,909 KG
1.9 M DIAMETER
4.2 M HIGH
361 KG PAYLOAD
(1992-1995)
UARS
6,736 KG
4.3 M DIAMETER
9.8 M HIGH
2,283 KG PAYLOAD
(EARLY 1990'S)
EOS-CONCEPT
12,210 KG
4.3 M DIAMETER
12 M HIGH
3,500 KG PAYLOAD
(1995-2000)

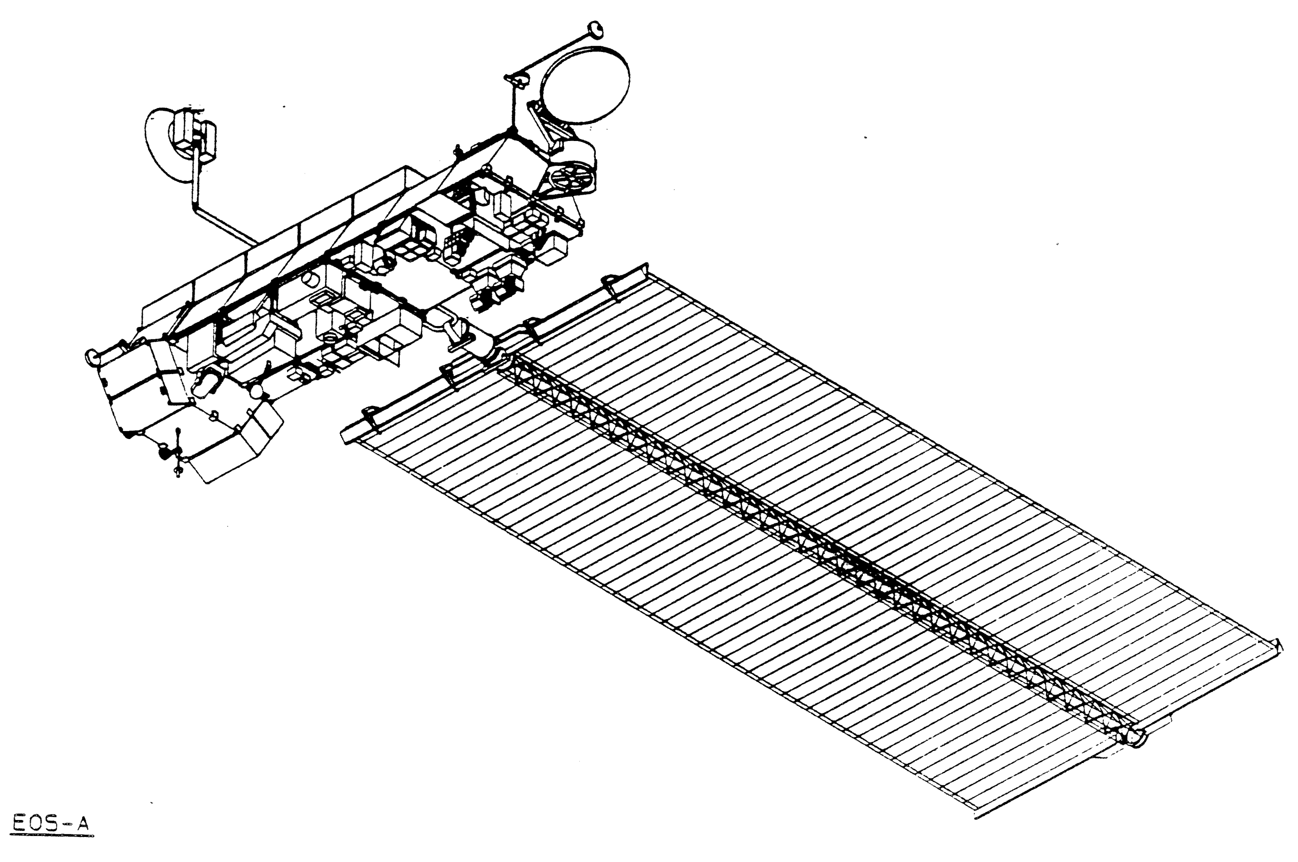

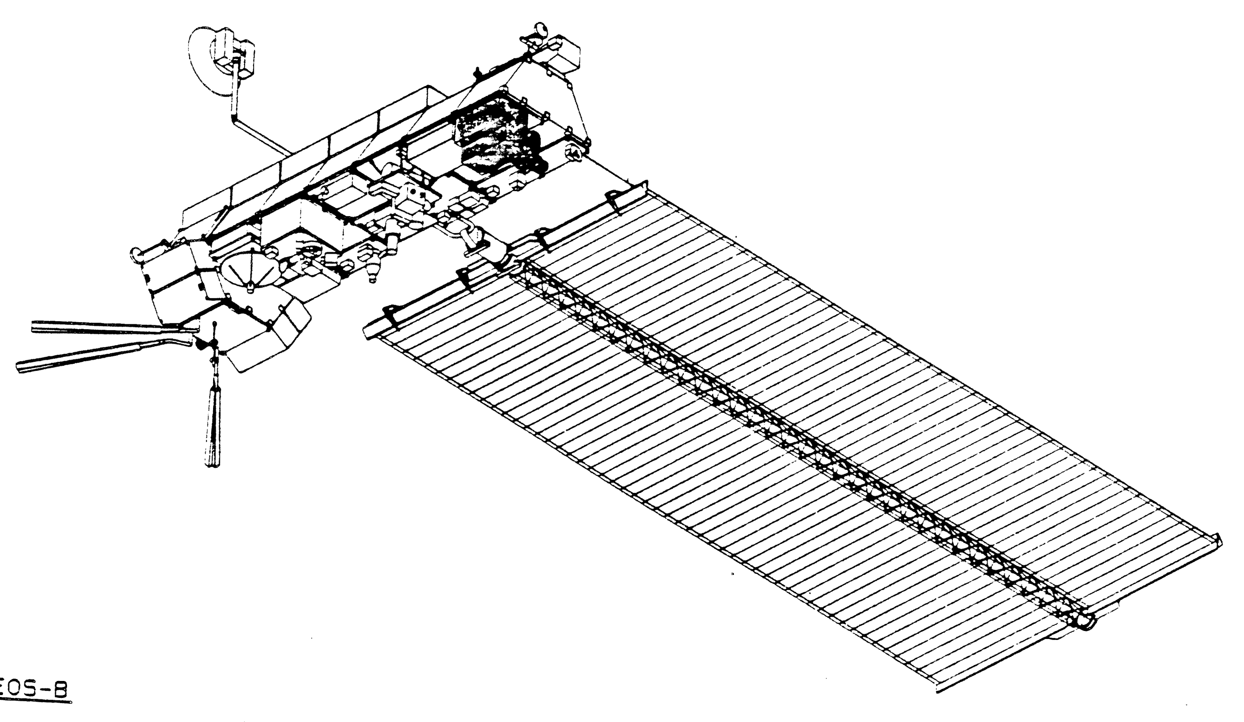

Figure 5. EOS-A and EOS-B Platforms

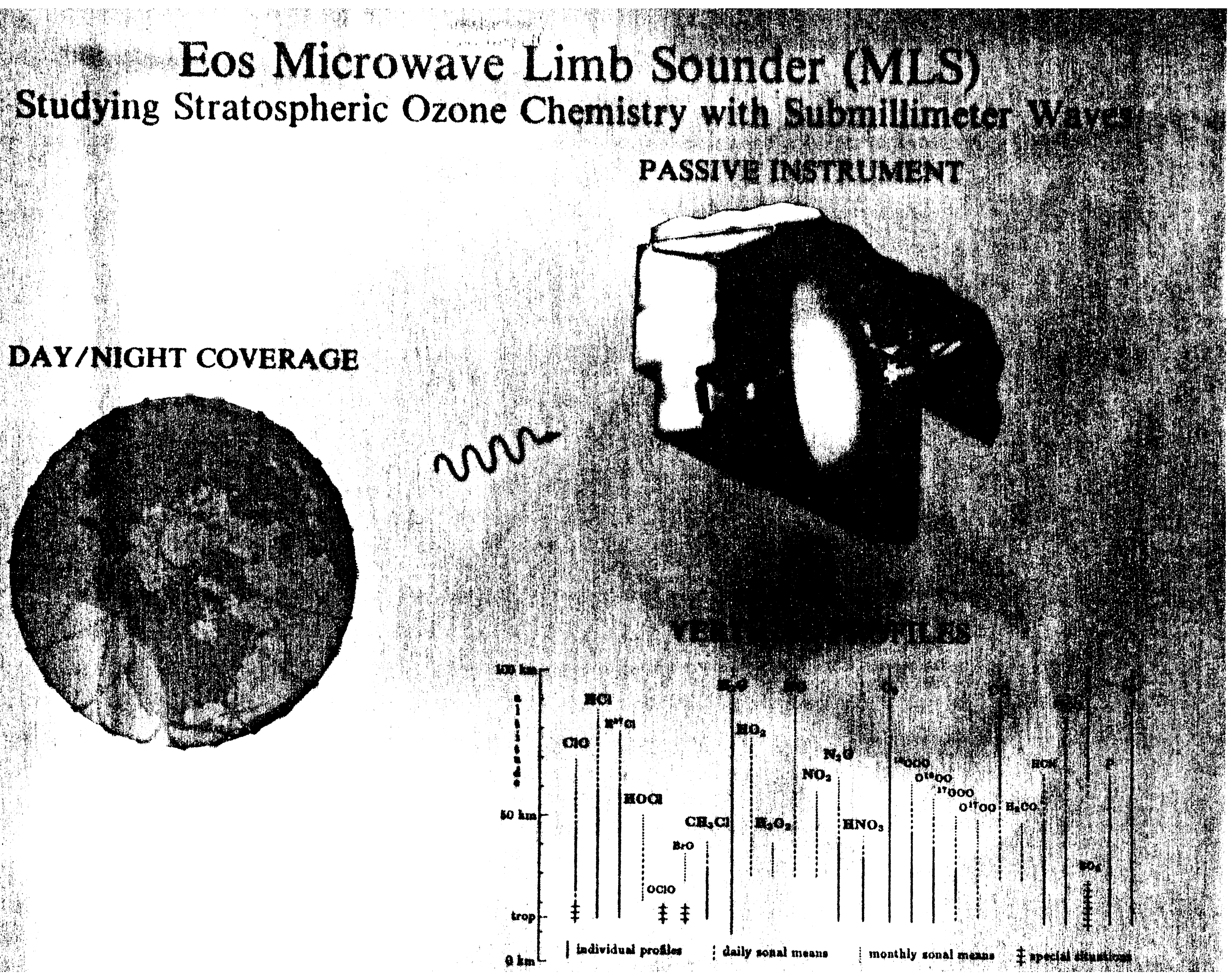
Eos Microwave Limb Sounder (MLS)
Studying Stratospheric Ozone Chemistry with Submillimeter Waves
PASSIVE INSTRUMENT
DAY/NIGHT COVERAGE
100 km
50 km
trop
0 km
ClO
HCl
HOCl
OClO
BrO
CH_3Cl
HO_2
H_2O_2
N_2O
NO_2
HNO_3
H_2CO
individual profiles
daily zonal means
monthly zonal means
special situations

EOS-MLS PRIMARY OBJECTIVES

MONITOR/STUDY GLOBAL CHANGE IN STRATOSPHERE/MESOSPHERE

CRITICAL GLOBAL MONITORING OF OZONE CHEMISTRY

MONITORING OF HETEROGENEOUS CHEMISTRY PERTURBATIONS

INSTRUMENT FEATURES

HIGH SENSITIVITY, HIGH SPECTRAL RESOLUTION HETERODYNE RADIOMETERS IN MILLIMETER & SUBMILLIMETER WAVE BANDS

RADIATIVE COOLING OF DETECTORS TO 90K

COMPLETE SPECTRUM EVERY 0.6 SEC

MODULAR PACKAGING

HERITAGE FROM PRIOR & ON-GOING MLS EXPERIMENTS
BALLOON, AIRCRAFT, UARS

EOS-MLS Vital Stats

Mass=450 kG
Power=650W
Cost (NAR)=320M

Data Rate=15Gb/day

Optics: Off-axis Cass. Eff. f/D=3.75
Ellipsoidal Reflector 1.6x.8m 2.5um RMS

Spectra: 48/scan, 0.64 sec int. time
Vertical Scan Rate=42 sec
Ver. FOV=1.5 arcmin=1.2Km @640GHz

Hor. FOV=2.5 deg along orbit

Front End Radiometers: 640 (2)
540 (2)
440 (2)
220 (1)
63 (1)

LIMB SOUNDING GEOMETRY

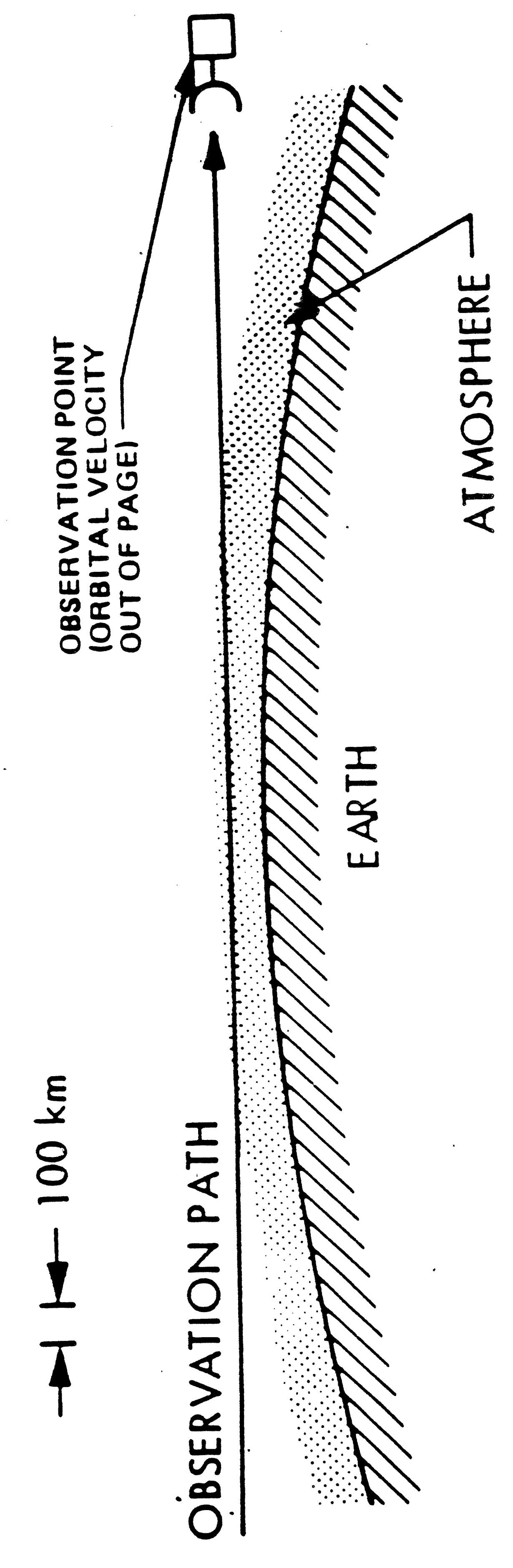

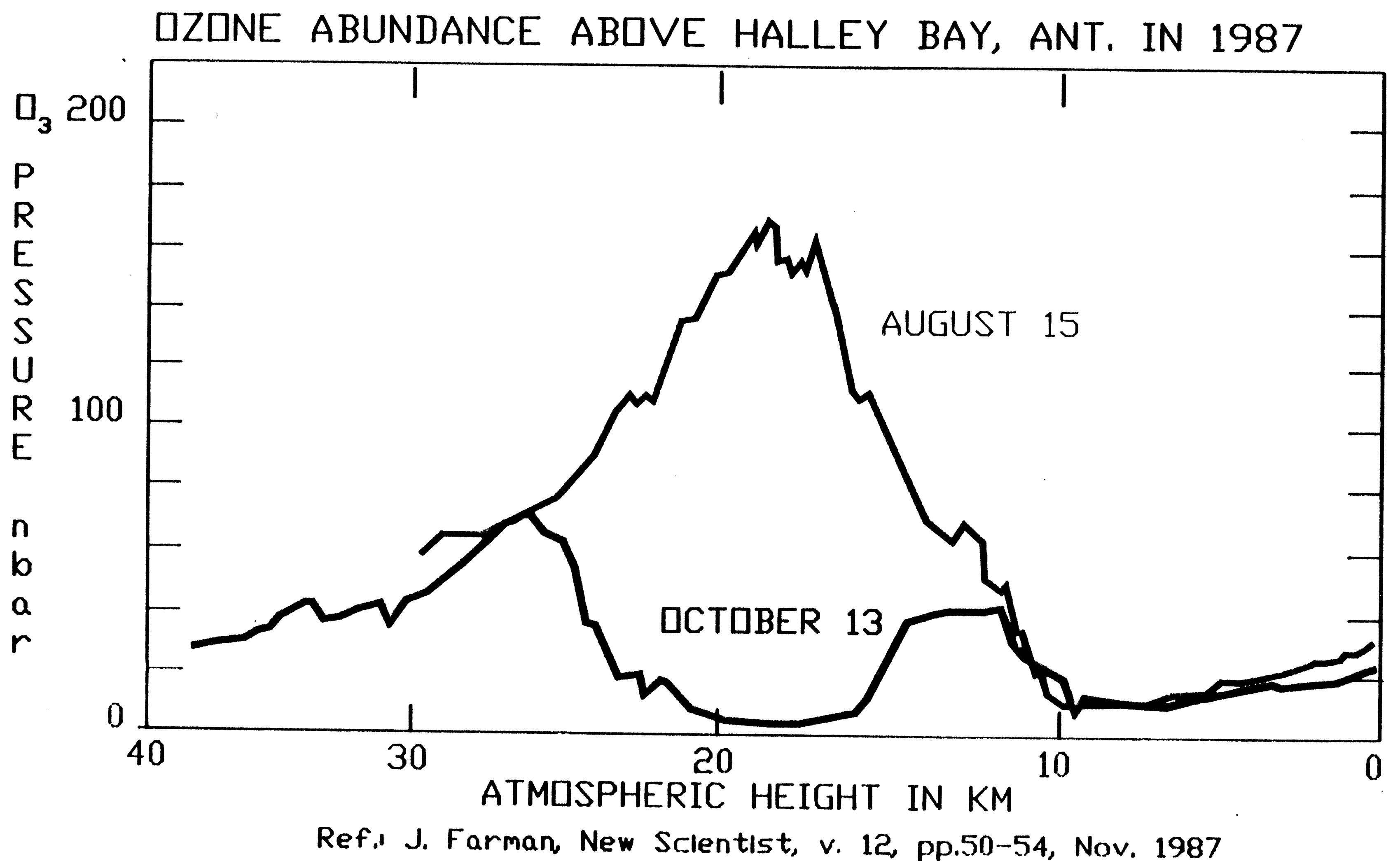
OZONE ABUNDANCE ABOVE HALLEY BAY, ANT. IN 1987
O3 PRESSURE nbar
200
100
0
AUGUST 15
OCTOBER 13
40
30
20
10
0
ATMOSPHERIC HEIGHT IN KM
Ref.: J. Farman, New Scientist, v. 12, pp.50-54, Nov. 1987

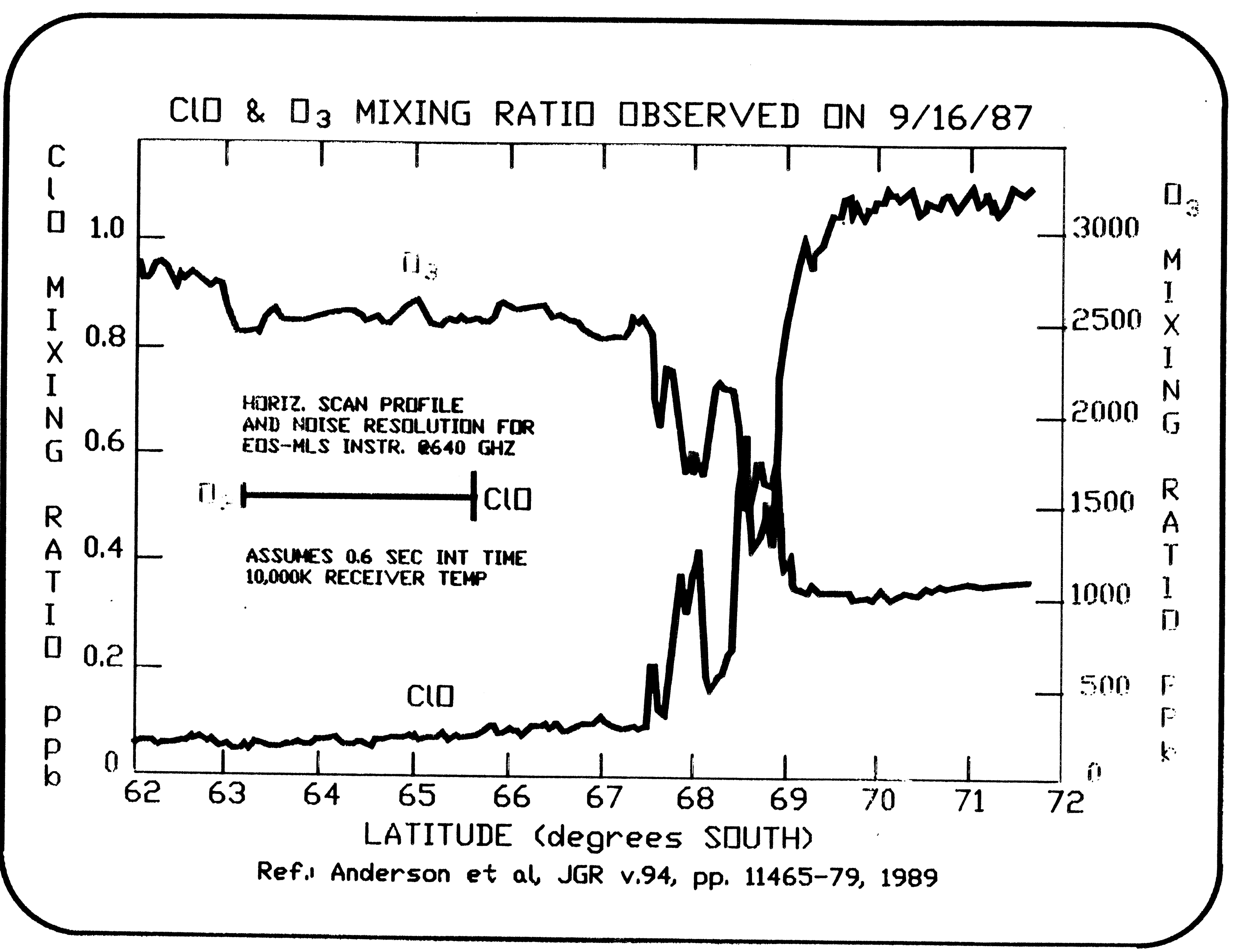
ClO & O3 MIXING RATIO OBSERVED ON 9/16/87
ClO MIXING RATIO ppb
1.0
0.8
0.6
0.4
0.2
0
O3 MIXING RATIO PPB
3000
2500
2000
1500
1000
500
0
O3
HORIZ. SCAN PROFILE
AND NOISE RESOLUTION FOR
EOS-MLS INSTR. @640 GHZ
ClO
ASSUMES 0.6 SEC INT TIME
10,000K RECEIVER TEMP
ClO
62
63
64
65
66
67
68
69
70
71
72
LATITUDE (degrees SOUTH)
Ref.: Anderson et al, JGR v.94, pp. 11465-79, 1989

Eos MLS Measurement Capability

HORIZONTAL COVERAGE

- Figure shows one day's coverage
  - Each cross, except at pole, is independent vertical profile measurement

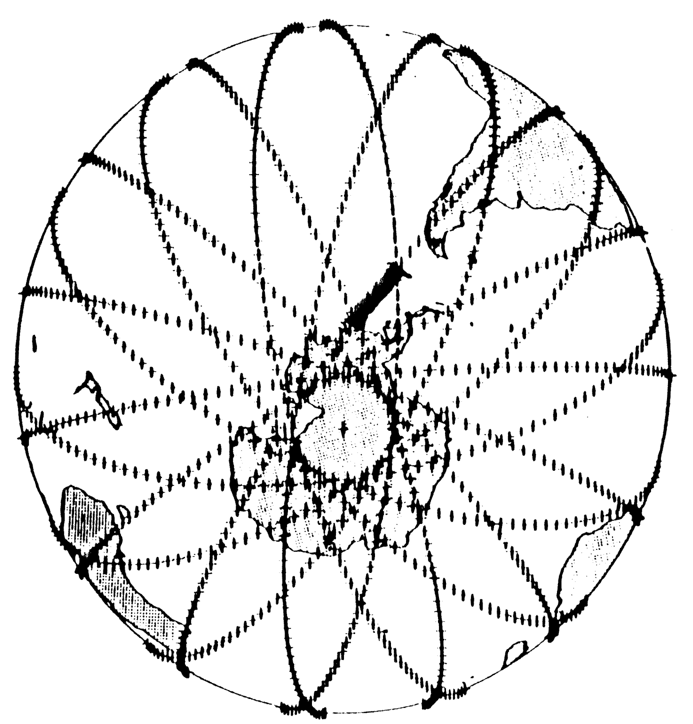

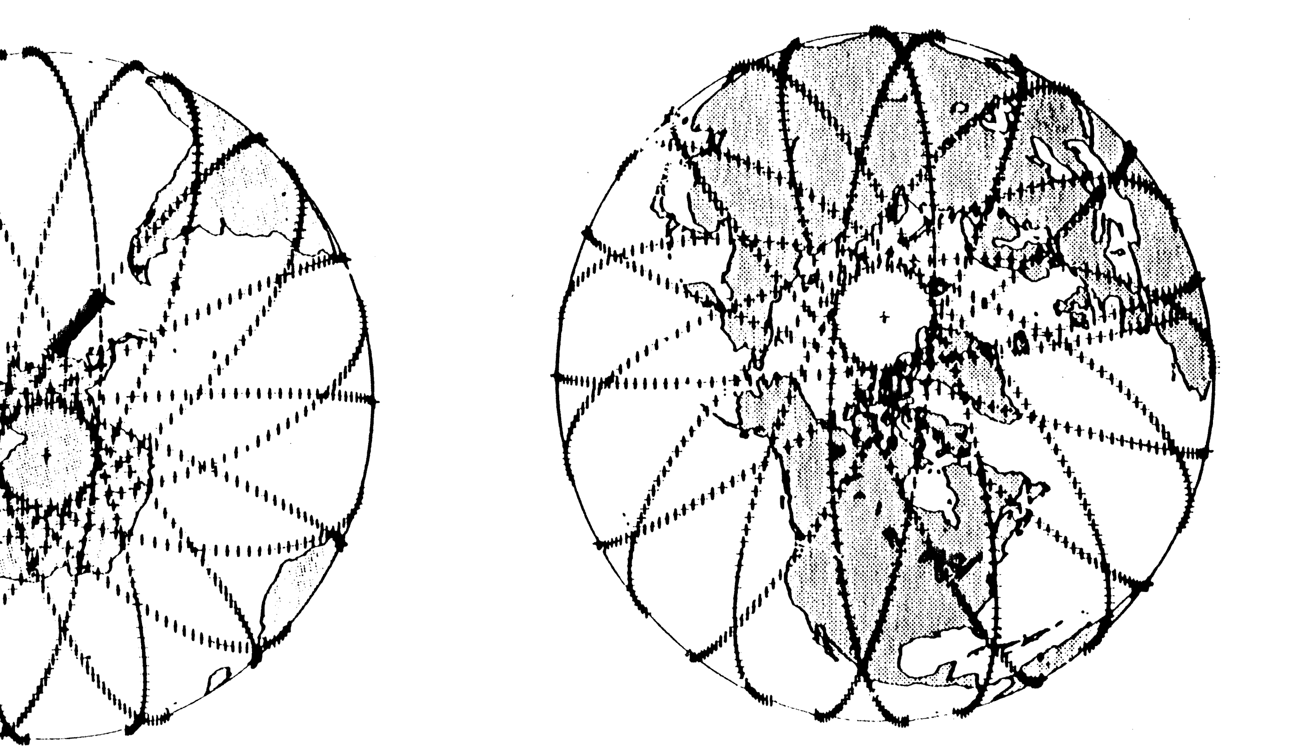

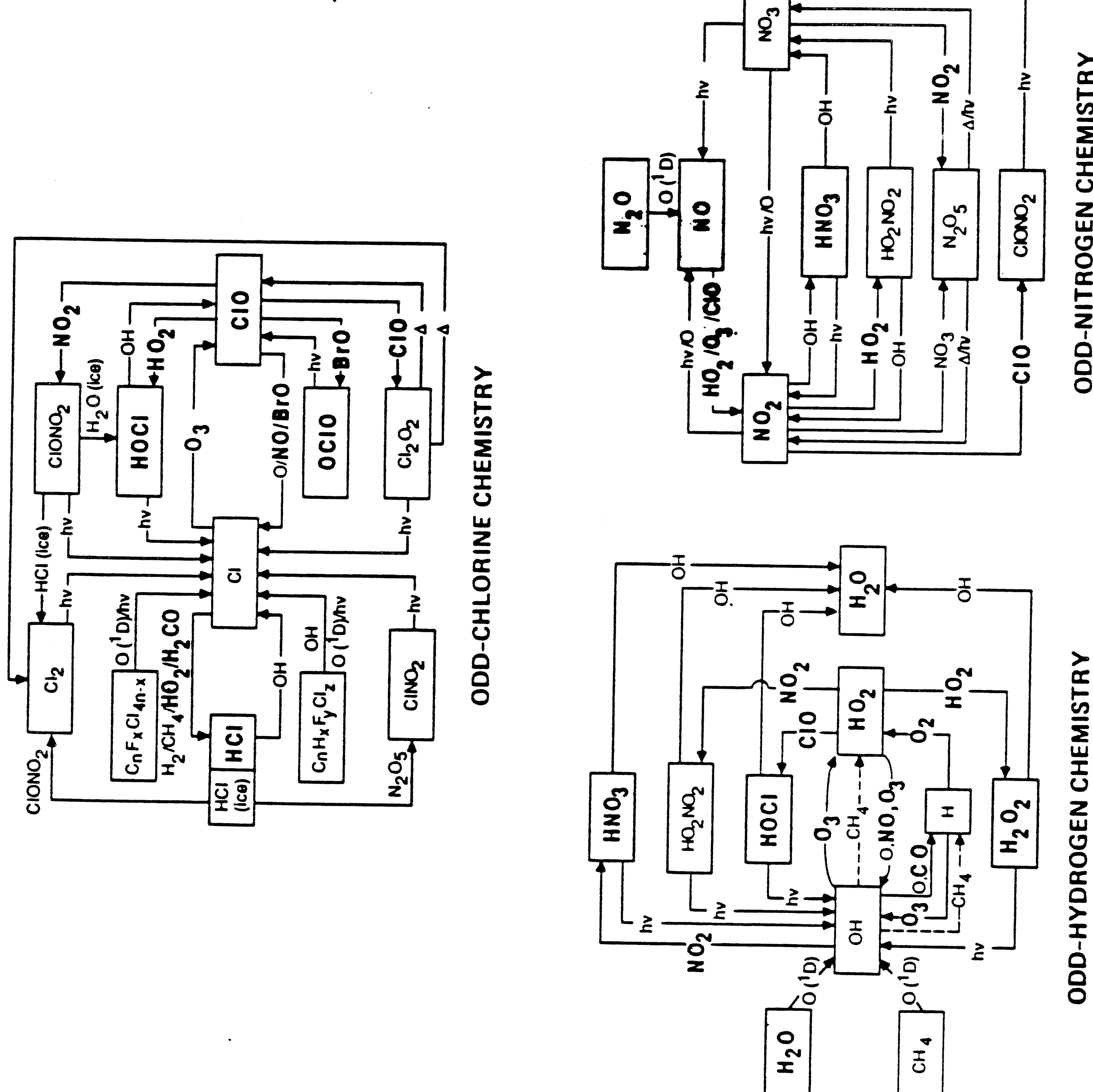

Figure 2. Stratospheric ozone chemistry schematics. MLS measurements in larger type.

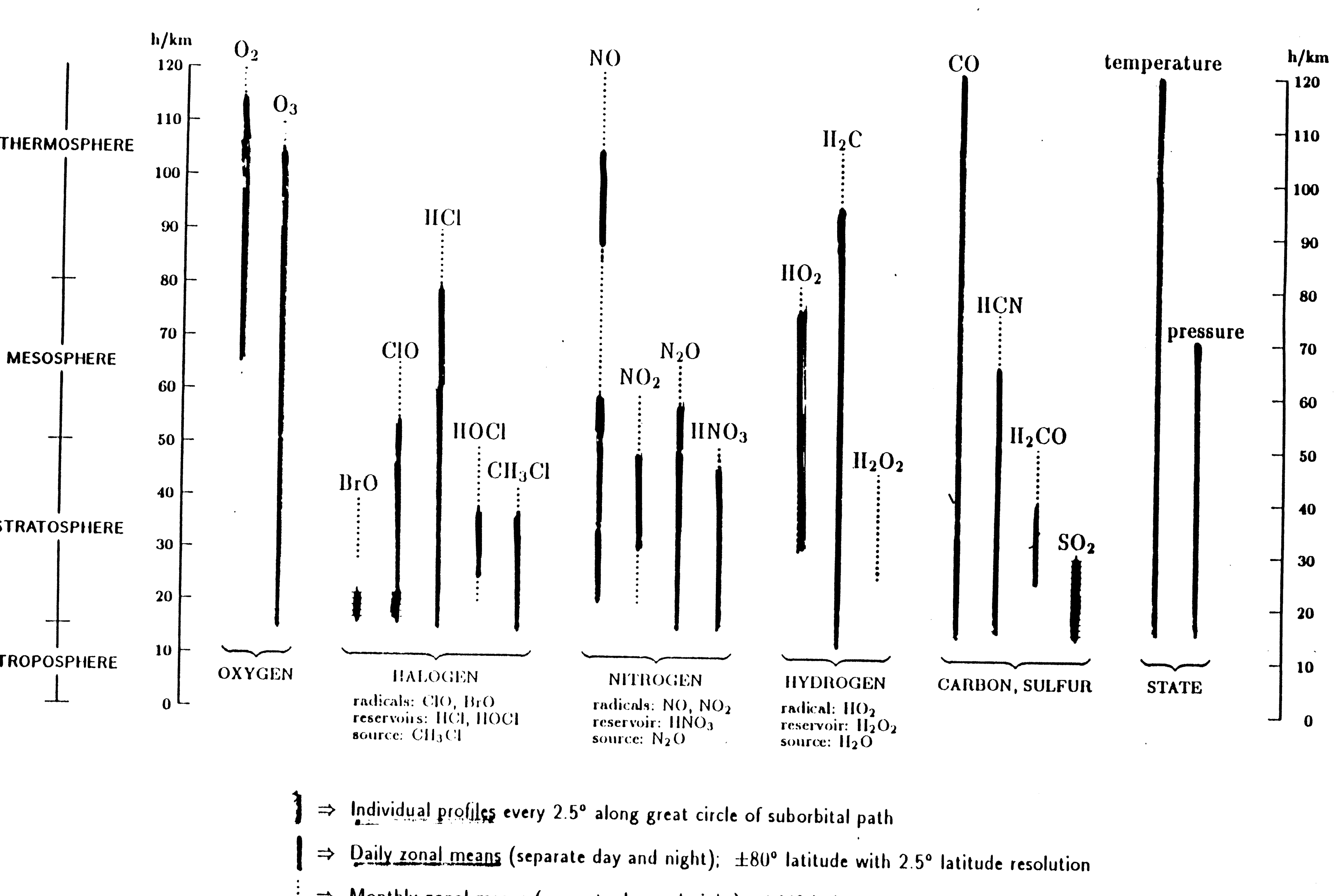

Eos MLS: Primary Measurement Objectives
h/km
THERMOSPHERE
MESOSPHERE
STRATOSPHERE
TROPOSPHERE
O2
O3
OXYGEN
BrO
ClO
HCl
HOCl
CH3Cl
HALOGEN
radicals: ClO, BrO
reservoirs: HCl, HOCl
source: CH3Cl
NO
NO2
N2O
HNO3
NITROGEN
radicals: NO, NO2
reservoir: HNO3
source: N2O
HO2
H2C
H2O2
HYDROGEN
radical: HO2
reservoir: H2O2
source: H2O
CO
HCN
H2CO
SO2
CARBON, SULFUR
temperature
pressure
STATE
⇒ Individual profiles every 2.5° along great circle of suborbital path
⇒ Daily zonal means (separate day and night); ±80° latitude with 2.5° latitude resolution
⇒ Monthly zonal means (separate day and night); ±80° latitude with 2.5° latitude resolution
⇒ Heterogeneous chemistry enhancements for ClO and BrO; volcanic enhancements for SO2

Eos MLS: Additional Measurement Objectives

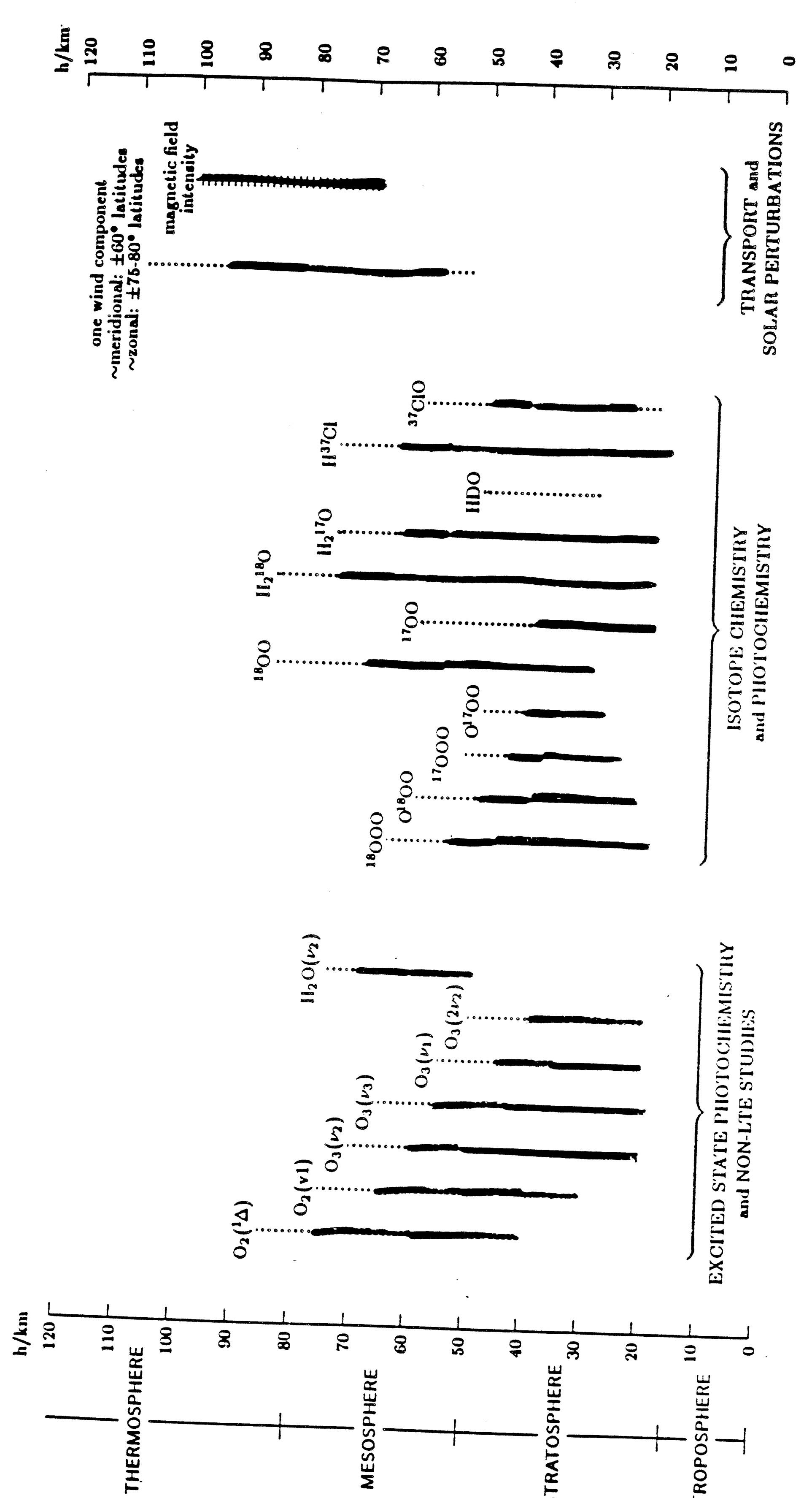

- ⇒ Individual profiles every 2.5° along great circle of suborbital path
- ⇒ Daily zonal means (separate day and night); ±80° latitude with 2.5° latitude resolution
- ⇒ Monthly zonal means (separate day and night); ±80° latitude with 2.5° latitude resolution
- ⇒ During solar storms (magnetic variations identify areas of solar interaction where resulting chemical perturbations will be studied)

COLLABORATORS ON EOS-MLS RECEIVERS

JPL: P.H. SIEGEL, I. MEHDI, R.J. DENGLER, J. OSWALD
ALL ASPECTS

RAL: B. MADDISON, B. ELLISON, D. MATHESON, M. OLDFIELD
440 & 63 GHZ RADIOMETERS

UVA: T. CROWE, W. BISHOP
SCHOTTKY BARRIER MIXER & MULTIPLIER DIODES

MARTIN MARIETTA: S. WEINREB
BROAD BAND AMPLIFIERS & INTEGRATED MIXERS

UNIV. OF MASS.: N. ERICKSON
HIGH POWER FREQUENCY MULTIPLIERS

ADDITIONAL UNCOMMITTED COLLABORATORS

JPL: J. BAUTISTA AMPLIFIERS
B.A. WILSON PLANAR SCHOTTKY DIODES

NRAO: M. POSPIESZALSKI
AMPLIFIERS

UMICH: J. EAST
SOLID STATE DEVICES: MIXER/MULTIPLIER/OSCILLATOR DIODES

EOS-MLS HETERODYNE INSTRUMENT DEPLOYMENT

RADIOMETER FREQUENCY PHYS. TEMP	MIXER TYPE NOISE(SSB) LOSS(SSB)	LOCAL OSC. FREQ(GHz) MULTIPLE GUNN(GHz)	IF AMP BAND(GHz)	IF AMP TIF(K)	TRCVR (SSB)
640 GHz 90K	SHP 5000K 11.5dB	642.85/2 4X 80.356	5.0-10.0 14.0-21.5	40 100	5600 6400
540 GHz 90K	SHP 5000K 11.0dB	535.69/2 4X 66.96	2.0-4.5 6.0-12.0 15.0-22.0	30 50 100	5400 5700 6300
440 GHz 90K	SHP 4500K 10.0dB	442.99/2 3X 73.83	3.0-5.5 7.5-12.0 15.0-21.5	35 50 100	4900 5000 5500
220 GHz AMBIENT	SHP 2000K 8.0dB	216.29/2 1X 108.15	9.5-18.5	180	3100
63 GHz AMBIENT	BAL.MXR 1000K	63.283	.09-.54	50	1200

BACKEND: 32 ACOUSTO-OPTIC SPECTROMETERS: BANDWIDTH=1 GHZ, RES.=1 MHZ
14 DIGITAL AUTOCORRELATORS BANDWIDTH=4 MHZ, RES.=100 KHZ

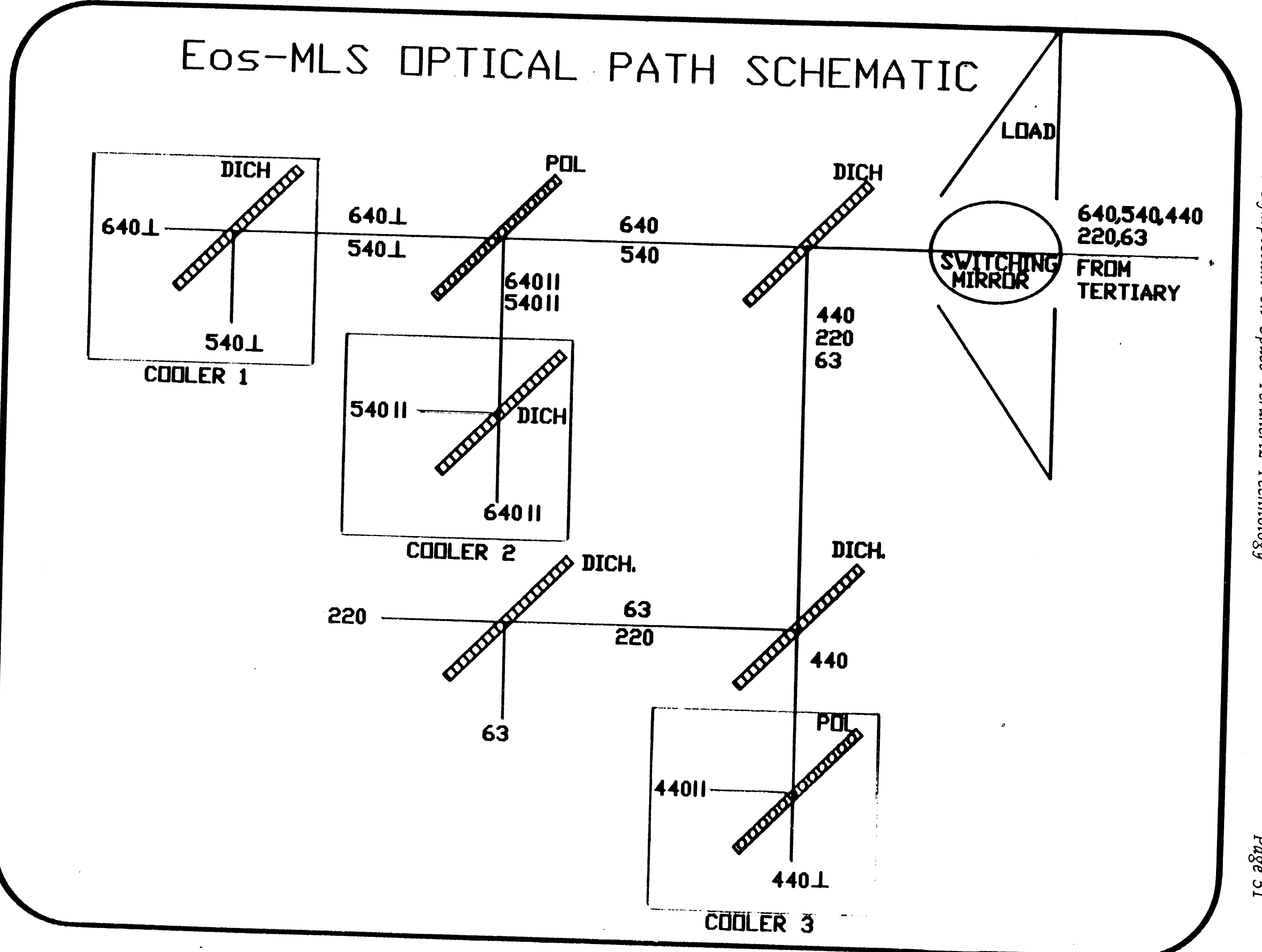

Eos-MLS OPTICAL PATH SCHEMATIC
LOAD
DICH
640⊥
540⊥
COOLER 1
POL
640⊥
540⊥
640∥
540∥
640
540
DICH
640,540,440
220,63
SWITCHING
MIRROR
FROM
TERTIARY
440
220
63
540∥
DICH
640∥
COOLER 2
DICH.
220
63
220
63
DICH.
440
POL
440∥
440⊥
COOLER 3

Challenges for Eos-MLS Submillimeter-Wave Radiometry

1. Elimination of the whisker-contacted diode in both the mixer and LO source to improve reliability & ease fabrication
2. Design of a state-of-the-art coolable broadband fixed tuned subharmonically pumped mixer mount using planar diodes to simplify LO generation & injection
3. Design of a high power fix tuned waveguide multiplier using a series array of planar diodes to produce 5-10mW of power at 320 GHz
4. Design of multi-octave bandwidth low noise coolable HEMT amplifiers which can be matched to the SHP mixers over the full IF band

Eos-MLS RADIOMETER PLANS & PROGRESS I.

1. MIXER DEVELOPMENT

- SHP MIXER MOUNT DESIGNED, MODELLED & CHARACTERIZED AT 8 GHZ
- 200 GHZ BLOCKS COMPLETED. MEASUREMENTS TO BEGIN 3/91
- 640 GHZ MOUNT IN CONSTRUCTION

2. MIXER ANALYSIS

- OBTAIN A BETTER UNDERSTANDING OF MIXER PERFORMANCE AT CRYOGENIC TEMPERATURES THROUGH IMPROVED DIODE EQUIV. CIRCUIT
- PERFORM TWO DIODE MIXER ANALYSIS USING MEASURED EMBEDDING IMPEDANCES AND IMPROVED DIODE EQUIV. CIRCUIT
- COMPARE SINGLE & TWO-DIODE SHP MIXER PERFORMANCE

3. PLANAR DIODE DEVELOPMENT

- EXPLORE PLANARIZATION & SUBSTRATE REMOVAL TECHNIQUES ON UVA AIR BRIDGE DIODES TO REDUCE PARASITICS DECREASE MICROSTRIP LOSS & INCREASE MICROSTRIP BANDWIDTH
- 'LIFT-OFF' & 'ETCH BACK' TECHNIQUES TO REPLACE GaAs SUBSTARTE WITH QUARTZ BOTH SUCCESSFUL WITH INDIVIDUAL DEVICES. INTEG. WITH REMAINING MIXER CIRCUITRY EXPECTED 6/91
- EFFECT OF COMPOSITE GaAs/QUARTZ SUBSTRATE ON MIXER FILTER STRUCTURES STUDIED & CHARACTERIZED
- NEW DIODE STRUCTURES & MATERIALS BEING STUDIED AT UMICH & UVA
- FULLY INTEGRATED MIXER BEING DEVELOPED AT MARTIN MARIETTA

Eos-MLS RADIOMETER PLANS & PROGRESS II.

4. HIGH POWER PLANAR MULTIPLIER DEVELOPMENT

UVA PLANAR VARACTOR DIODE DEVELOPMENT UNDERWAY
MULTI-DIODE MULTIPLIER BLOCK DESIGN TO BEGIN 6/91 AT UMASS

5. AMPLIFIER DEVELOPMENT

BROADBAND INTEGRATED AMP UNDER DEVELOPMENT AT MARTIN MARIETTA
OCTAVE BAND HEMT AMPLIFIERS UNDER DEVELOPMENT AT JPL/NRAO
UNDER SEPARATE IN HOUSE PROGRAMS

6. RADIATIONAL COOLER DEVELOPMENT

80K RADIATIONAL COOLERS BEING DEVELOPED AT SBRC
JPL COOLER DEVELOPMENT EFFORT TO BEGIN IN 92

MIXER PERFORMANCE VS. TYPE AND FREQUENCY

	Whisker Contact							Planar				
freq GHz	FM		HM		SHPM			FM		SHPM		
	Tm	Ldb	Tm	Ldb	Tm	Ldb	P_{LO}	Tm	Ldb	Tm	Ldb	P_{LO}
100	450[1]	6.0			400[5]	7.4	6	560[9] 750[10]	5.9 6.5	1750[10]	9.5	
200	800[2]	6.6			1800[6] 3450[7] 2400[8]	8 Trec 10.5	10 15 6.5			2750[11] 3000[12]	Trec	10
650	5200[3]	12.0	4300[4]	13								

All results are for waveguide mounts at T=300K and f_{IF}<2 GHz

Tm and Ldb are SSB noise and loss, P is required LO in mW

References: (1) Cong,Kerr,Mattauch, MTT-27, Mar. 1979, pp.245-8
(2) Archer, MTT-30, Aug. 1982, pp.1247-52
(3) Erickson, private comm. April 1990
(4) Erickson, 1st Int. Conf. on Space THz Tech, U.Mich, Mar.5,1990
(5) Carlson,Schneider,McMaster, MTT-26, Oct. 1978, p.712
(6) Carlson,Schneider, Int.Conf. on IR&MM Waves, 1979, pp.82-3
(7) Galin, IR&MM Waves, v.8, 1987, p.123
(8) Mann,Matheson,Jones, IR&MM Waves, v.10, 1989, pp.1043-49
(9) Garfield, private comm. UVa, April 1990
(10) Archer, MTT-38, Jan 1990, pp.15-22
(11) Ostdiek,Crowe,Galin, 15th Int.Conf.IR&MM Waves, Dec. 1990
(12) B. Maddison, B. Ellison, private comm, Jan 1991.

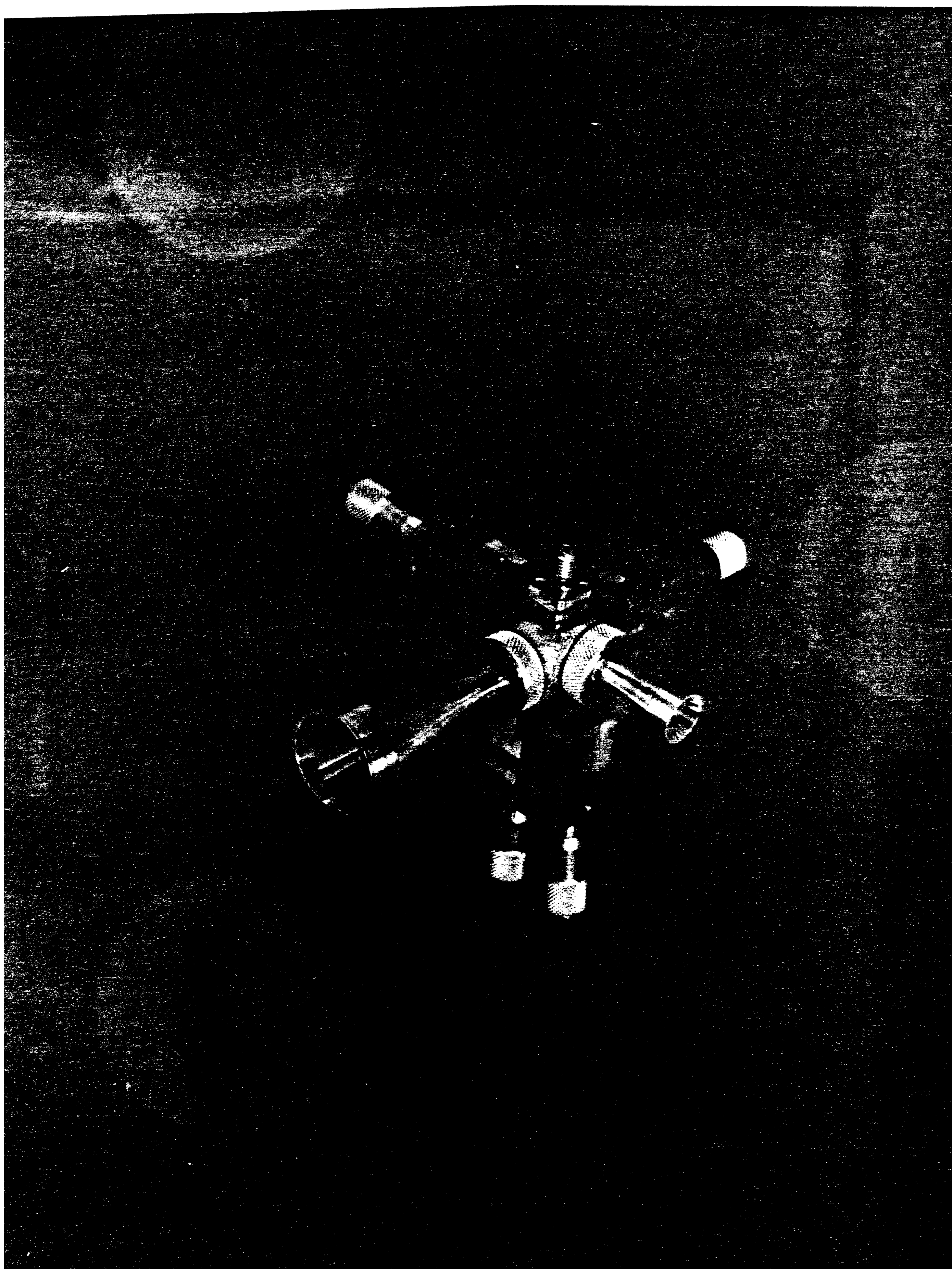

INTEGRATED TERAHERTZ CORNER-CUBE ANTENNAS AND RECEIVERS

Steven S. Gearhart, Curtis C. Ling and Gabriel M. Rebeiz

NASA/Center for Space Terahertz Technology
Electrical Engineering and Computer Science Department
University of Michigan
Ann Arbor, MI 48109-2122

Gordon Chin and Hemant Davé

Planetary Systems Branch
NASA/Goddard Space Flight Center
Greenbelt, MD 20771

SUMMARY

This paper summarizes work completed and under progress on integrated corner-cube antennas and receivers at the University of Michigan. An integrated corner-cube antenna has been developed for use at millimeter-wave and terahertz frequencies. The antenna is high gain and has low cross-polarization levels (<-17dB at 222GHz and <-15dB at 119μm) in the principal planes. The monolithic approach allows the integration of a matching network and a Schottky diode at the base of the antenna to yield a low-noise monolithic 600GHz receiver.

The standard corner-cube antenna, which consists of a traveling-wave antenna backed by a 90° corner reflector, has been a favorite antenna for submillimeter-wave receivers. The standard design is a 4λ-long traveling-wave antenna placed 1.2λ from the apex of the machined corner reflector. The antenna also acts as a whisker contact to a Schottky diode mounted at its base.

The integrated corner-cube antenna consists of a traveling-wave antenna suspended on a 1μm dielectric membrane in a longitudinal pyramidal cavity (Fig. 1). The membrane electrical thickness is 0.02λ at 3THz, so the traveling-wave antenna effectively radiates in free space at 119μm. The cavity is etched in silicon wafers, and the reflector flare angle is fixed by the orientation of the crystal planes at 70.6° [4]. The integrated antenna has a number of advantages over the standard machined corner-cube antenna. The integrated antenna is fully monolithic and easily reproducible for array applications. An RF matching network can be included between the antenna and Schottky diode, thus increasing coupling efficiency and reducing the receiver noise temperature. Also, the integrated antenna is fabricated using standard photolithographic processes, so the antenna can be produced with great precision.

A millimeter-wave linear corner-cube array was fabricated for use at 222GHz. The traveling-wave antenna is 1560μm long (1.15λ at 222GHz) and is 60μm wide with a 20μm bend portion. These dimensions were optimized using microwave scale model measurements. A 6μm-square microbolometer was integrated at the bottom tip of the traveling-wave antenna. This is the same position that one would integrate a matching network and a Schottky diode or SIS detector in a receiver application. The far-field patterns were measured at from 180GHz to 270GHz using millimeter-wave doublers and triplers fed by appropriate Gunn sources. Over the 180-270GHz bandwidth, the patterns are well-behaved with a narrow mainbeam and no off-axis sidelobes. At 222GHz, an increase in the extention of the ground planes was shown to narrow the quasi-H plane resulting in a rotationally symmetric mainbeam with a 10dB beamwidth of approximately 40° (Fig. 2) and cross-polarization levels of less than -17dB in the E and quasi-H planes. A co-polarized directivity of 19dB at 222GHz was calculated from the full two-dimensional patterns [1,2].

A 16-element 119μm array was built at the University of Michigan and tested at NASA Goddard. The traveling-wave antenna is 137μm long (1.15λ at 119μm), and is 8μm wide with a 5μm bend portion. A 4μm-square microbolometer was integrated at the bottom tip of the traveling-wave antenna. The far-field patterns of a single integrated corner-cube antenna in a linear array were measured using a far-infrared laser tuned at 119μm (Fig 2). The mainbeam is circularly symmetric with a 10dB beamwidth of approximately 40°. The higher sidelobes in the E-plane may be due to scattering from the test mount. This will be examined in detail later. A directivity of 18±0.5dB was calculated from measured 119μm E- and quasi-H plane patterns, and the cross-polarization in the E- and quasi-H planes was lower than the noise level of -15dB [3].

600GHz INTEGRATED CORNER-CUBE RECEIVER DESIGN

A 600GHz integrated corner-cube receiver is currently under development at the University of Michigan (Fig. 3). A University of Virginia membrane-type diode with a 1μm anode diameter will be mounted in hybrid fashion to the silicon wafer containing the antenna, RF matching network, and low-pass IF filter. The estimated diode parameters are R_s=20Ω,C_{jo}=1fF, C_p=2fF, n=1.2, and ϕ_{bi}=0.8V. These parameters yield a figure of merit cutoff frequency of $f_T=1/(2\pi C_T R_s)$=2.7THz. The RF and LO signals will be injected quasi-optically through the antenna which is matched to the diode through a simple RF matching network. The RF matching newtork is a single 0.38λ length of 40Ω CPW transmission yielding an RF imbedding impedance of 52+j29Ω at the diode. Using the harmonic balance technique of Held and Kerr [5] with the above diode and RF matching network, the RF diode impedance is 51-j53Ω, and the conversion loss is 7.6dB.

ACKOWLEDGEMENTS

This work was supported by the NASA/Center for Space Terahertz Technology at the University of Michigan.

REFERENCES

[1] S.S. Gearhart, C.C. Ling and G.M. Rebeiz, "Integrated 222GHz Corner-Reflector Antennas," *Microwave and Optical Technology Letters*, vol.4, No.1, pp.12-15, Jan. 5, 1991.

[2] S.S. Gearhart, C.C. Ling and G.M. Rebeiz, "Integrated Millimeter-Wave Corner-Cube Antennas," To be published by *IEEE Transactions on Antennas and Propagation*, July, 1991.

[3] S.S. Gearhart, C.C. Ling, G.M. Rebeiz, G. Chin and H. Davé "Integrated 119μm Linear Corner-Cube Array," Accepted for publication by *IEEE Microwave and Guided Wave Letters*, Mar. 1991.

[4] K.E. Peterson, "Silicon as a mechanical material," *Proc. IEEE*, vol.70, pp.420-457, 1982.

[5] A.R. Kerr, "A technique for determining the local oscillator waveforms in a microwave mixer," *IEEE Transactions on Microwave Theory and Techniques*, vol. MTT-23, pp.828-831, Oct. 1975.

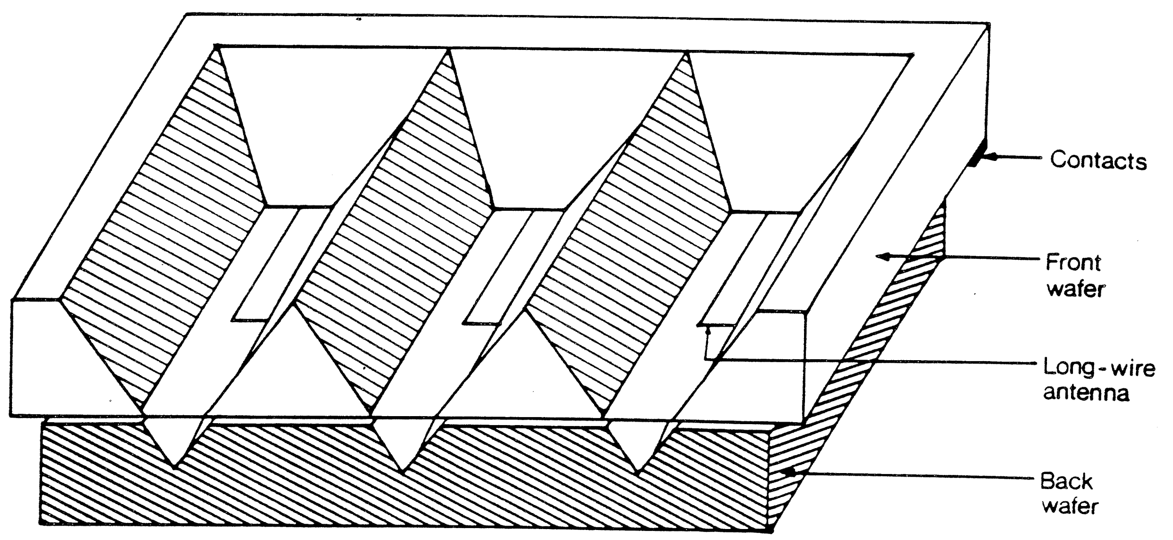

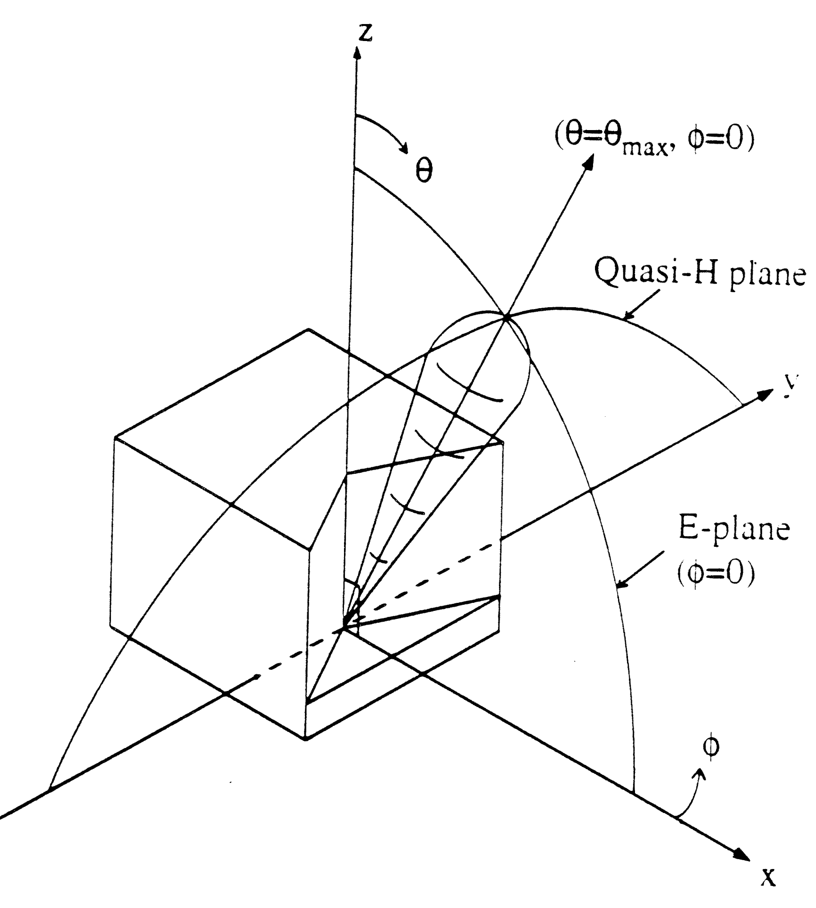

Figure 1: A monolithic corner-reflector imaging array: (a) perspective view. (b) the coordinate system used.

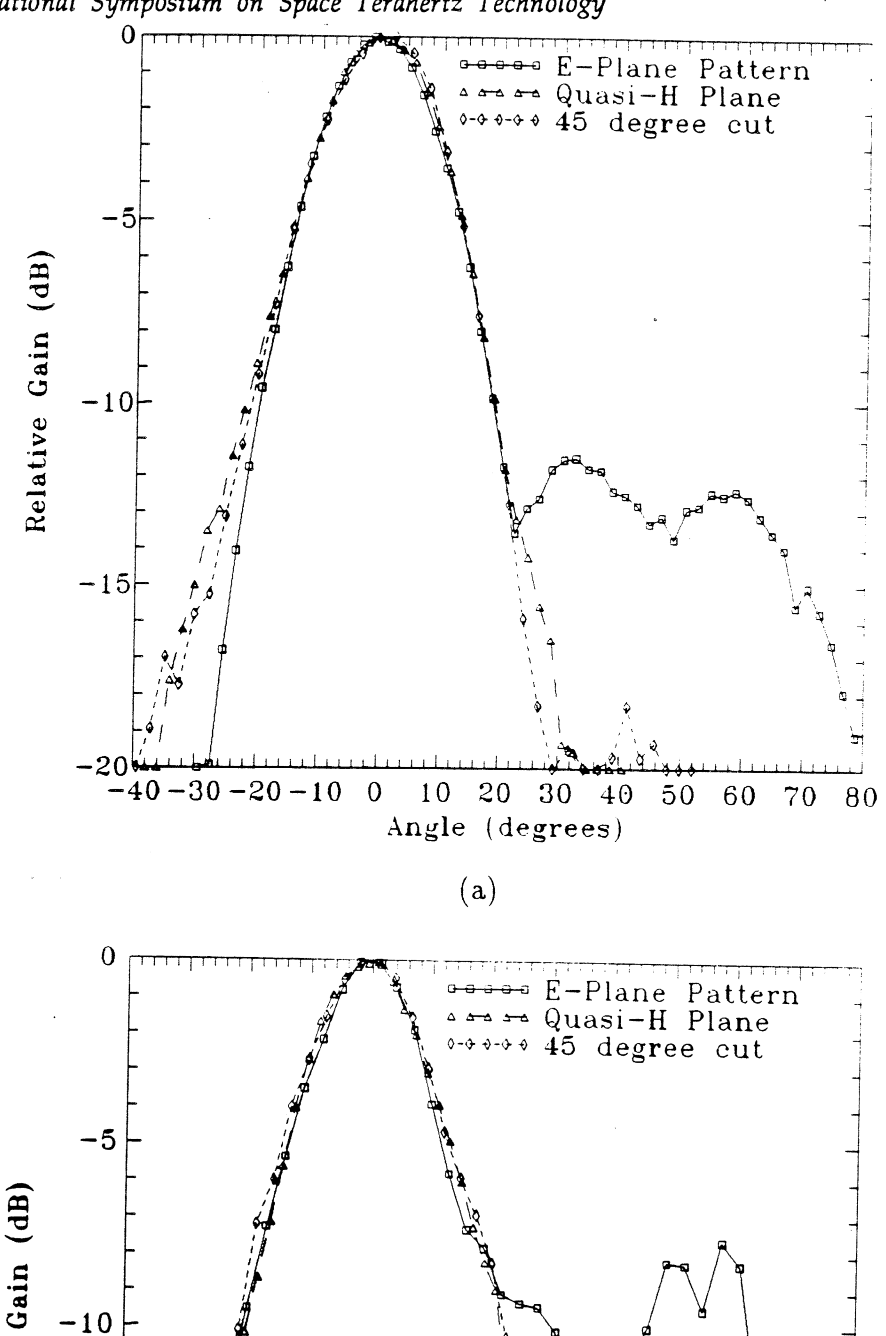

(a)

E-Plane Pattern
Quasi-H Plane
45 degree cut
Relative Gain (dB)
0
-5
-10
-15
-20
-40 -30 -20 -10 0 10 20 30 40 50 60 70 80
Angle (degrees)

(b)

Figure 2: Measured patterns with (L,d)=(1.15λ,0.92λ): (a) 222GHz. (b) 119μm.

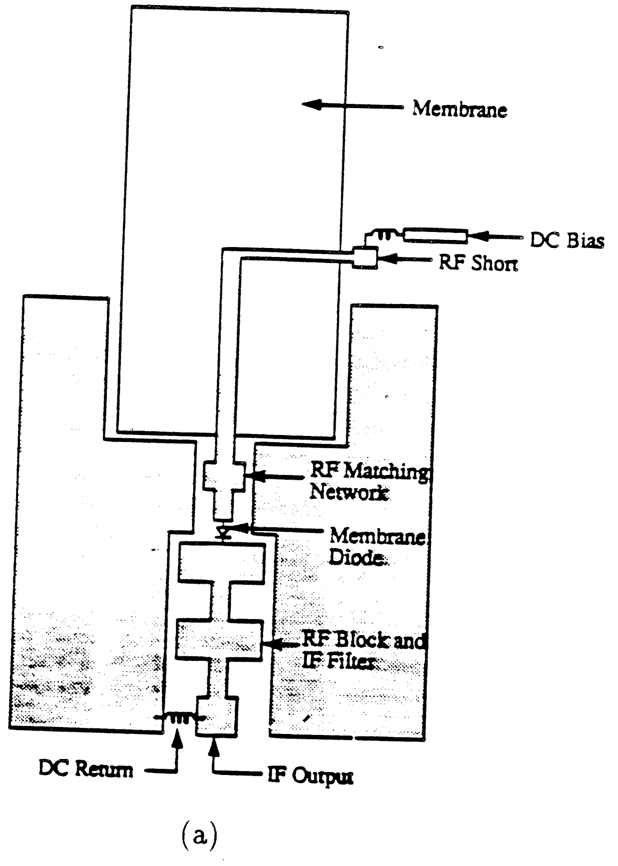

(a)

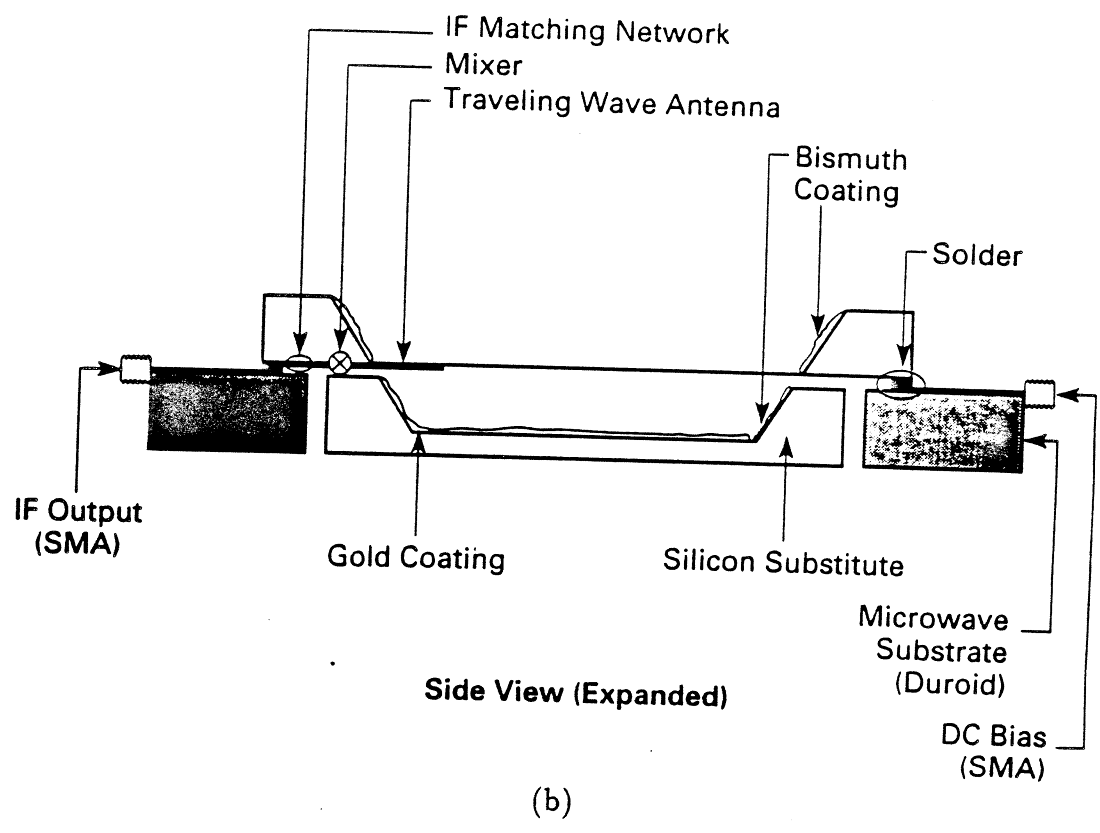

(b)

Figure 3: 600GHz integrated corner-cube receiver: (a) back of membrane wafer. (b) side view.

ANTENNAS FOR SUB-MILLIMETRE WAVE RECEIVERS

Joakim F. Johansson and **Nicholas D. Whyborn**

Department of Radio & Space Science
with Onsala Space Observatory

Pranay Raj Acharya, **Hans Ekström**, **Stellan W. Jacobsson**, and **Erik L. Kollberg**

Department of Applied Electron Physics

Chalmers University of Technology
S-412 96 Gothenburg
Sweden

ABSTRACT

This paper reports on investigations of two antenna types which are suitable for implementation at sub-millimetre wavelengths: the diagonal horn and the sandwiched tapered slot antenna.

The diagonal horn is studied theoretically by expanding the aperture electric field into Gauss-Hermite modes. A few of these modes are then used to model the radiation pattern. The results indicate that the fraction of the power radiated into the fundamental Gaussian mode is about 84 %. About 10 % of the power is radiated in the cross-polarised component. Radiation patterns for a 4 x 4 diagonal horn array, measured at 100 GHz, show good agreement with the theoretical predictions.

The sandwiched tapered slot antenna consists of a slotline antenna which is sandwiched between thick quartz super- and substrates. An elliptical lens is used to collimate the beam. Model experiments have been performed at 30 and 350 GHz. The radiation patterns are worse at the higher frequency, probably due to alignment problems.

1. INTRODUCTION

Commonly used millimetre wave feed antennas, *e.g.* corrugated horns, become very difficult to realize at sub-millimetre wavelengths. The corrugated horns radiate an almost perfect Gaussian beam [1], but the tolerances needed are at the limit of what can be achieved using normal fabrication methods. Some feed types are easier to make, but, as always, there is no such thing as a free lunch. Pyramidal and conical horns exhibit a lack of symmetry in the cardinal planes of the radiation pattern which makes them unsuitable for launching Gaussian beams. The pyramidal horn has the added inconvenience of astigmatism, *i.e.* the phase centres for the E- and H-planes do not generally coincide (*cf.* [2]). The need for an alternative to these horns at sub-millimetre wavelengths is evident.

We have investigated the so-called diagonal horn (*cf.* [2,3]), and it seems to be an interesting candidate for sub-millimetre feeds. The diagonal horn antenna is shown in the following sections to be quite an efficient Gaussian beam launcher. One marked advantage with this horn type is the ease with which it can be machined. When using waveguide technology at millimetre and sub-millimetre wavelengths it is quite common that the mixer is made in the so-called split-block technique. The component is machined in two halves, and when joined together the extra losses are relatively small. The diagonal horn lends itself to this technique (see Figure 0).

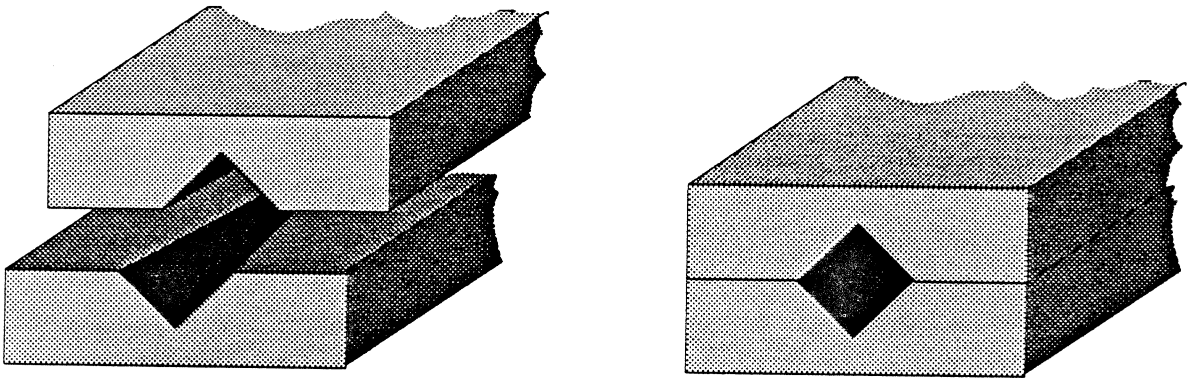

Figure 0. A diagonal horn made in the split-block technique.

The tapered slot antenna is an open structure antenna which radiates a beam in the endfire direction (along the substrate). Classical tapered slot antennas require thin substrates (of the order of <≈ 10 μm at 350 GHz).

One way to solve the substrate problem is to sandwich the antenna between a ***thick*** substrate and superstrate, and then use an elliptical lens to decrease the beamwidth. Results from model experiments at 30 and 350 GHz are presented in the third section of this paper. The results show that it is difficult to achieve good agreement between these two experiments, which is probably due to the stringent tolerance requirements at the sub-millimetre frequency.

2. THE DIAGONAL HORN

The diagonal horn has the following electrical field distribution in the aperture [2, 3] (see Fig. 1 for reference):

$$E_{ap} = E_o\left[\hat{x}\cos\frac{\pi y}{2a} + \hat{y}\cos\frac{\pi x}{2a}\right]e^{jk\delta} \qquad |x|<a \quad |y|<a$$
$$k\delta = \frac{2\pi}{\lambda}\left[\frac{2a^2 - x^2 - y^2}{2L}\right] \tag{1}$$

This means that the field consists of two orthogonal TE_{10} modes, the power evenly distributed between them. This set of modes must be excited somehow. Love [3] used a circular transition from TE_{10}, but the transition seems rather uncritical, and a direct transition from the rectangular waveguide is good enough for most purposes. The aperture equi-phase surface can be assumed to be a sphere centred at the horn apex, and is here approximated by a paraboloid. These assumptions are probably not too wrong, at least not for long horns.

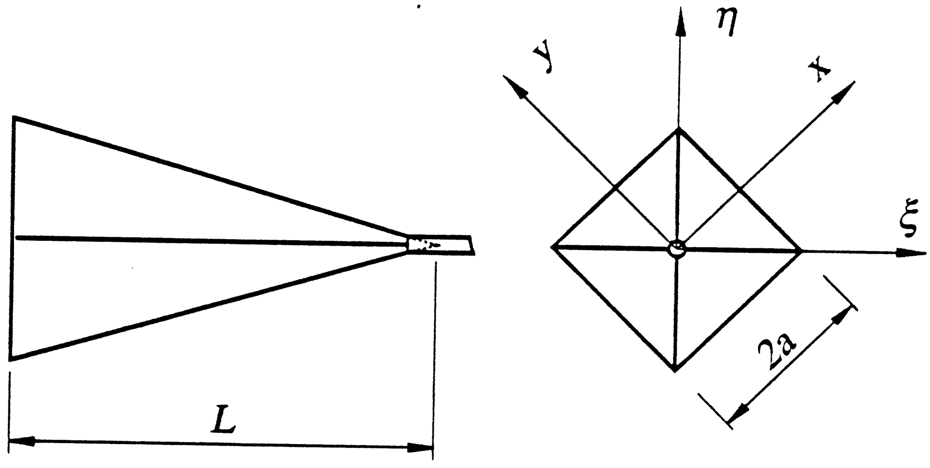

Figure 1. The geometry of the diagonal horn.

The aperture field is seen to have the desired symmetry properties by introducing the following auxiliary coordinate system:

$$\xi = \frac{x-y}{\sqrt{2}} \qquad \eta = \frac{x+y}{\sqrt{2}} \tag{2}$$

Combining Eqns. 1 and 2 yields the following:

$$E_\eta = \hat{\eta}\cdot E_{ap} = \sqrt{2}\, E_o \cos\frac{\pi\xi}{2\sqrt{2}a}\cos\frac{\pi\eta}{2\sqrt{2}a}\, e^{jk\delta} = \frac{E_o}{\sqrt{2}}\left[\cos\frac{\pi y}{2a} + \cos\frac{\pi x}{2a}\right] e^{jk\delta}$$
$$E_\xi = \hat{\xi}\cdot E_{ap} = \sqrt{2}\, E_o \sin\frac{\pi\xi}{2\sqrt{2}a}\sin\frac{\pi\eta}{2\sqrt{2}a}\, e^{jk\delta} = \frac{E_o}{\sqrt{2}}\left[\cos\frac{\pi y}{2a} - \cos\frac{\pi x}{2a}\right] e^{jk\delta} \quad (3)$$

The co-polarised aperture field (η-directed) is thus symmetric with respect to the $\xi\eta$ coordinate system. The cross-polarised aperture field component (ξ-directed) is anti-symmetric, and the feed thus has no boresight cross-polarisation (note that we here use the so-called Ludwig's 1st definition [4] for the polarisation). The aperture field components are shown in Fig. 2.

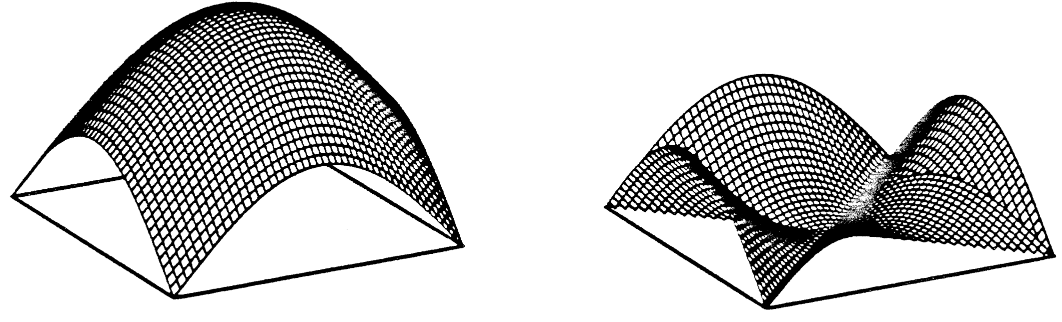

Figure 2. The magnitude of the co- (left) and cross-polarised (right) electric field at the aperture of the horn.

The fraction of the power in the respective components can be found by solving the integrals

$$P_{co} = \int_{-a}^{a}\int_{-a}^{a} |E_\eta|^2\, dxdy \qquad P_{cr} = \int_{-a}^{a}\int_{-a}^{a} |E_\xi|^2\, dxdy \quad (4)$$

where the electric field components are given by Eqn. 3. The numerical results are given by

$$\frac{P_{co}}{P_{co}+P_{cr}} = \frac{1+\frac{8}{\pi^2}}{2} \approx 0{,}9052847$$
$$\frac{P_{cr}}{P_{co}+P_{cr}} = \frac{1-\frac{8}{\pi^2}}{2} \approx 0{,}0947153 \quad (5)$$

It is seen that the cross-polarised part is quite large (≈ 10 %), and this might be excessive for some applications. However, in many cases, this cross-polarised components could be dumped in a termination through the use of a polarising grid. The loss one would encounter by dropping the cross-polarised part is then ≈ 0,43 dB.

2.1. GAUSSIAN MODE EXPANSION

A powerful technique to study the radiation pattern of an aperture antenna is to expand the aperture field into Gauss-Hermite or Gauss-Laguerre functions (*cf.* [1, 5, 6]).

The electric field for a well-collimated beam can be written as

$$E(x,y,z) = \frac{w_A}{w(z)} e^{-jk[z-z_A]} e^{j[\Phi(z)-\Phi_A]} e^{-jk[x^2+y^2]/2R(z)}$$
$$\cdot \sum_{m=-\infty}^{\infty} \sum_{n=-\infty}^{\infty} \mathcal{K}_{mn} e^{j(m+n)[\Phi(z)-\Phi_A]} \widetilde{H}_m\left[\frac{\sqrt{2}x}{w(z)}\right] \widetilde{H}_n\left[\frac{\sqrt{2}y}{w(z)}\right] \qquad (6)$$

where a modified Hermite function, defined by

$$\widetilde{H}_m(x) \triangleq \frac{e^{-x^2/2}}{\sqrt{2^m m!}} H_m(x) \qquad (7)$$

is used to get a compact notation.
The beam parameters in Eqn. 6 are given by (*cf.* [6])

$$w(z) = w_o\sqrt{1+[z/z_c]^2}$$
$$R(z) = z\left[1+[z_c/z]^2\right] \qquad z_c = \frac{\pi w_o^2}{\lambda} \qquad (8)$$
$$\Phi(z) = \arctan\frac{z}{z_c}$$

where w denotes the beam waist radius, R the phase radius of curvature, z_c the confocal distance, and Φ the so-called phase slip. Returning to Eqn. 6, one observes that w and R are common to all modes, whereas the phase slip Φ gets progressively multiplied for higher order modes.

If one now has an aperture field E_A where most of the phase variation can be contained in a spherical phase factor, *viz.*

$$E_A(x,y) = E(x,y,z_A) = g(x,y)\, e^{-jk[x^2+y^2]/2R_A} \qquad (9)$$

then Eqn. 6 collapses into a very convenient form.

Using the orthogonality properties of Hermite polynomials [7], and some algebraic manipulations, the coefficients $\mathcal{K}_{mn}$ are given by

$$\mathcal{K}_{mn} = \frac{2}{\pi w_A^2} \iint_{-\infty}^{\infty} g(x,y)\, \tilde{H}_m\left[\frac{\sqrt{2}x}{w_A}\right] \tilde{H}_n\left[\frac{\sqrt{2}y}{w_A}\right] dxdy \qquad (10)$$

If now the $g(x,y)$ function is real-valued, one avoids all numerical problems due to rapid phase variations in the integrand.

The diagonal horn has no phase variation over the aperture except for the spherical part. It thus lends itself to this Gauss-Hermite analysis. The $g(x,y)$ functions for the co- and cross-pol parts are given by Eqn. 3.

The mode power content is given by

$$\frac{P_{mn}}{P_{tot}} = \frac{\pi w_A^2}{2} \frac{|\mathcal{K}_{mn}|^2}{\iint_{-\infty}^{\infty} |g(x,y)|^2\, dxdy} \qquad (11)$$

and the results for the diagonal horn are the following expressions

$$\frac{P_{mn}^{co}}{P_{tot}} = \frac{64}{\pi}\frac{a^2}{w_A^2}\left|\int_0^1 \int_0^{1-u} \cos\frac{\pi u}{2} \cos\frac{\pi v}{2}\, \tilde{H}_m\left[\frac{2a}{w_A}u\right] \tilde{H}_n\left[\frac{2a}{w_A}v\right] dudv\right|^2 \quad \textit{Even } m, n \qquad (12a)$$

$$\frac{P_{mn}^{cr}}{P_{tot}} = \frac{64}{\pi}\frac{a^2}{w_A^2}\left|\int_0^1 \int_0^{1-u} \sin\frac{\pi u}{2} \sin\frac{\pi v}{2}\, \tilde{H}_m\left[\frac{2a}{w_A}u\right] \tilde{H}_n\left[\frac{2a}{w_A}v\right] dudv\right|^2 \quad \textit{Odd } m, n \qquad (12b)$$

The expressions in Eqns. 12a and 12b can be simplified for a few simple cases by breaking down the double integrals into single integrals. The result for the fundamental Gaussian is

$$\frac{P_{00}^{co}}{P_{tot}} = \frac{16}{\pi}\frac{a^2}{w_A^2}\left|\int_0^1 \cos\frac{\pi t}{2}\, e^{-\left[at/w_A\right]^2} dt \int_0^1 e^{-\left[at/w_A\right]^2} dt\right|^2 \qquad (13)$$

The choice of the ratio w_A/a is in principle arbitrary, but Occam's Razor‡ tells us that the most natural choice is to maximise the fundamental mode coupling [8], *i.e.*

$$\frac{\partial}{\partial \frac{w_A}{a}}\left[\frac{P_{00}^{co}}{P_{tot}}\right] = 0 \tag{14}$$

The coupling has a maximum at $w_A/a \approx 0{,}86$. An optimisation program gave the following results (correct to six decimal places):

$$\begin{cases} \kappa \stackrel{\Delta}{=} \left.\frac{w_A}{a}\right|_{opt} \approx 0{,}863191 \\ \left.\frac{P_{00}^{co}}{P_{tot}}\right|_{opt} \approx 0{,}843025 \end{cases} \tag{15}$$

The diagonal horn thus has quite a high fundamental Gaussian mode content. The mode content for the higher order co-polar and cross-polar components is shown in Table I.

	n = 0	n = 2	n = 4	n = 6	n = 8
m = 0	0,8430	$3{,}655\cdot10^{-18}$	0,005405	0,0009189	$5{,}110\cdot10^{-6}$
m = 2	☆	0,01620	0,003339	$6{,}859\cdot10^{-6}$	0,0003185
m = 4	☆	☆	$1{,}562\cdot10^{-5}$	0,001012	0,0009922
m = 6	☆	☆	☆	0,001356	0,0005954
m = 8	☆	☆	☆	☆	$7{,}364\cdot10^{-5}$

	n = 1	n = 3	n = 5	n = 7	n = 9
m = 1	0,04848	0,007725	0,0004141	$1{,}117\cdot10^{-5}$	$4{,}800\cdot10^{-5}$
m = 3	☆	$6{,}037\cdot10^{-5}$	0,001545	0,001380	0,0006026
m = 5	☆	☆	0,002060	0,0008870	0,0001456
m = 7	☆	☆	☆	0,0001112	$2{,}909\cdot10^{-5}$
m = 9	☆	☆	☆	☆	0,0002786

Table I *The power fraction for the mn^th co- (top) and cross-pol modes (bottom). The stars denote redundant information.*

‡ "Entia non sunt multiplicanda præter necessitatem" — A philosophical principle devised by William of Occam (c. 1290 – 1349)

Now when we know the optimum waist radius, it is easy to find the equivalent Gaussian beam parameters. If one assumes the following (see Figure 3 for reference)

$$
\begin{aligned}
w_A &= w_o\sqrt{1+[z_A/z_c]^2} = \kappa a \\
R_A &= z_A\left[1+[z_c/z_A]^2\right] = L \qquad z_c = \frac{\pi w_o^2}{\lambda} \\
\Phi_A &= \arctan\frac{z_A}{z_c} = \arctan\frac{\pi\kappa^2 a^2}{\lambda L}
\end{aligned}
\tag{16}
$$

then some algebraic manipulations will yield the results

$$
\begin{aligned}
w_o &= \frac{\kappa a}{\sqrt{1+\left[\dfrac{\pi\kappa^2 a^2}{\lambda L}\right]^2}} = \frac{\kappa a}{\sqrt{1+\tan^2\Phi_A}} \\
z_A &= \frac{L}{1+\left[\dfrac{\lambda L}{\pi\kappa^2 a^2}\right]^2} = \frac{L}{1+\cot^2\Phi_A}
\end{aligned}
\tag{17}
$$

The phase slip Φ_A is again seen to be an important parameter in this analysis.

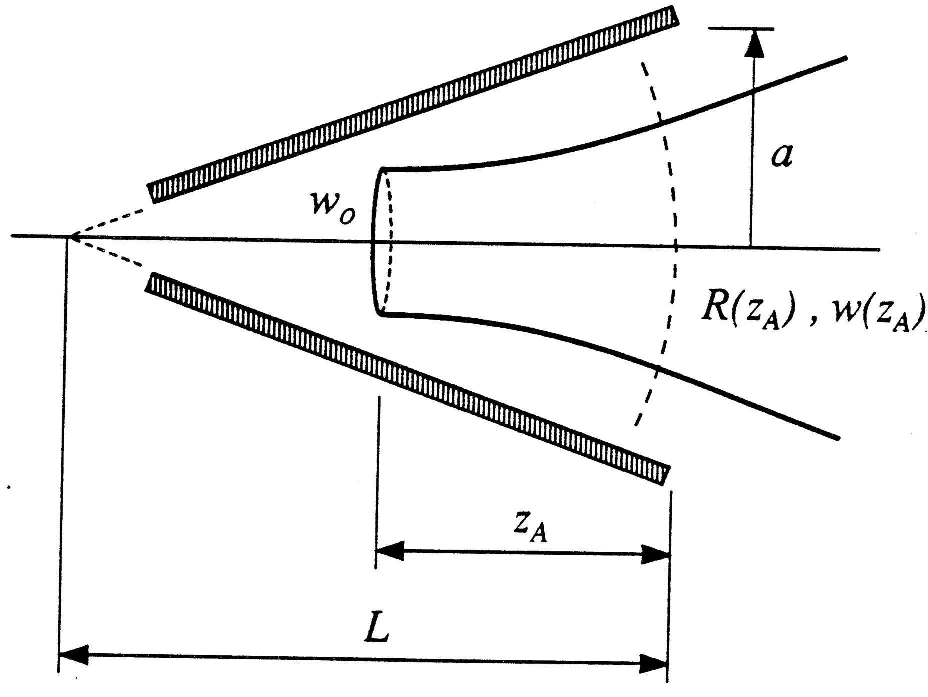

Figure 3. The geometry of the equivalent Gaussian beam

Table I showed that there are just a few terms that contain a significant part of the power, namely the 00, 11, and 22 terms. It is hence possible to devise a simple model for the radiation pattern of the diagonal horn. The far-field radiation pattern is given by (except for an unimportant constant):

$$F_{co}(\theta,\varphi) \approx e^{-2\rho^2}\left|\mathcal{K}_{00} + \frac{1}{2}\mathcal{K}_{22}\, e^{-j4\Phi_A}\left[4\rho^2\cos^2\varphi - 1\right]\left[4\rho^2\sin^2\varphi - 1\right]\right|^2$$

$$F_{cr}(\theta,\varphi) \approx e^{-2\rho^2}\left|\mathcal{K}_{11}\, 4\rho^2\sin\varphi\cos\varphi\right|^2 \qquad (18)$$

$$\rho = \frac{\pi w_o}{\lambda}\tan\theta$$

The coefficients for the optimum waist size (Eqn. 15) are found by numerically evaluating the integral in Eqn. 10, and the coefficients for the model in Eqn. 18 are

$$\frac{\mathcal{K}_{22}}{\mathcal{K}_{00}} \approx -0{,}138628$$

$$\frac{\mathcal{K}_{11}}{\mathcal{K}_{00}} \approx 0{,}239816 \qquad (19)$$

Combining Eqns. 18 and 19 one can draw the conclusion that the far-field radiation pattern is quite rotationally symmetric. The cross-pol level is approximately

$$\frac{e^{-2}\left|2\mathcal{K}_{11}\right|^2}{\left|\mathcal{K}_{00}\right|^2} \approx -15{,}1 \text{ dB} \qquad (20)$$

If the phase slip factor is zero, the radiation pattern will exhibit deep nulls, whereas a non-zero value will yield a more 'smeared' pattern.

It will be shown in the following section that this simplified model is quite accurate.

2.2. MEASUREMENTS

In order to test the theoretical predictions, an array of diagonal horns was manufactured and the radiation patterns were measured. The array is shown in Figure 4. The respective horns are fed by standard waveguide (IEC R-900) and the back side hole patterns match "standard" flanges. A waveguide detector is bolted to the back side. The patterns were measured in an anechoic chamber using a computerised antenna measurement system.

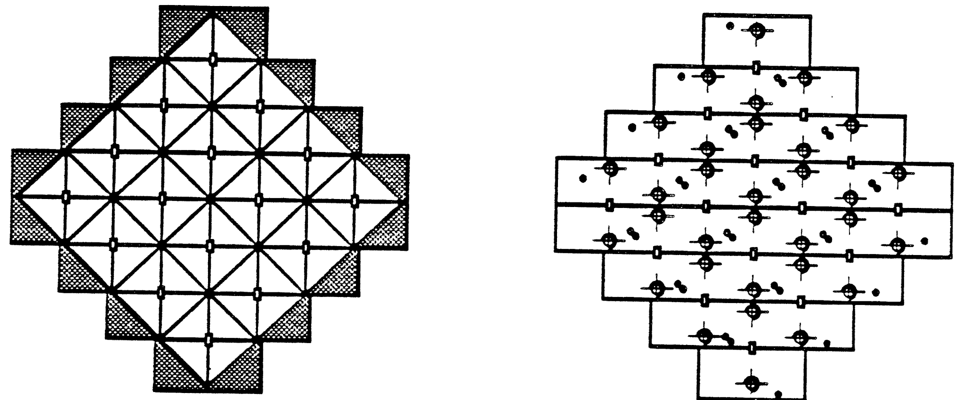

Figure 4 *The diagonal horn array.*

The horns in the array had the following dimensions:

- $2a$ = 14,0 mm
- L = 55,0 mm

The horns were measured at 99 GHz ($\lambda \approx 3{,}03$ mm) and the Gaussian parameters are thus given by (see Eqns. 15, 16, and 17)

- $w_o \approx$ 4,98 mm
- $z_A \approx$ 17,7 mm
- $\kappa a \approx$ 6,04 mm
- $\Phi_A \approx$ 34,54°

The E-, H-, and D-plane co-pol patterns, as well as the D-plane cross-pol patterns were measured for four of the sixteen horns in the array (see Fig. 5 for reference)

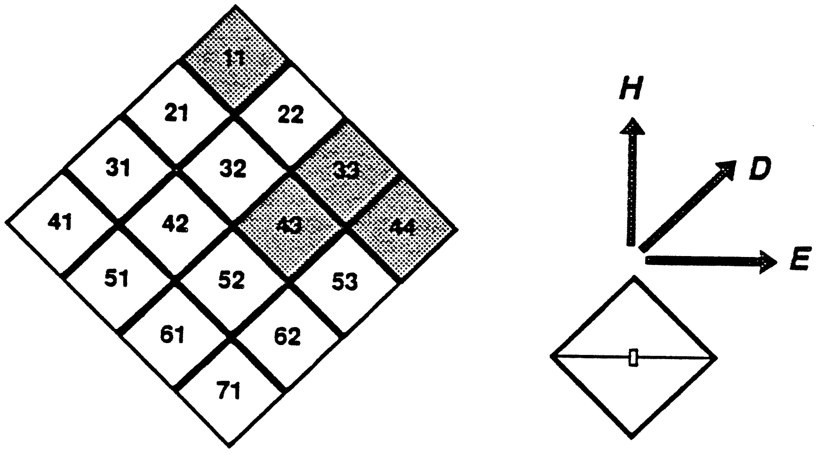

Figure 5. *The enumeration of the array elements and the plane definitions. The measured horns are shaded.*

Figure 6 shows that the measured radiation pattern is rotationally symmetric down to about −17 dB. The D-plane pattern has a 'shoulder', but except for that the pattern looks nice. The E- and H-plane sidelobes are probably hidden by noise below the −30 dB region. The D-plane cross-pol component is shown in Figure 7. The pattern is a little bit asymmetrical, end shows on-axis cross-polarisation. The reasons for these non-idealities are probably found in the difficulty to accurately set up the antennas at 100 GHz. A small error in feed angle will 'leak' co-pol power into the cross-pol measurement. Any lack of polarisation purity of the transmitting horn might influence the accuracy as well.

The horns do not seem to be especially influenced by being embedded in an array. Figure 8 shows a comparison between four H-plane element patterns. The uniformity is excellent, and one can thus safely use the horns in such an array, without deteriorating the radiation patterns.

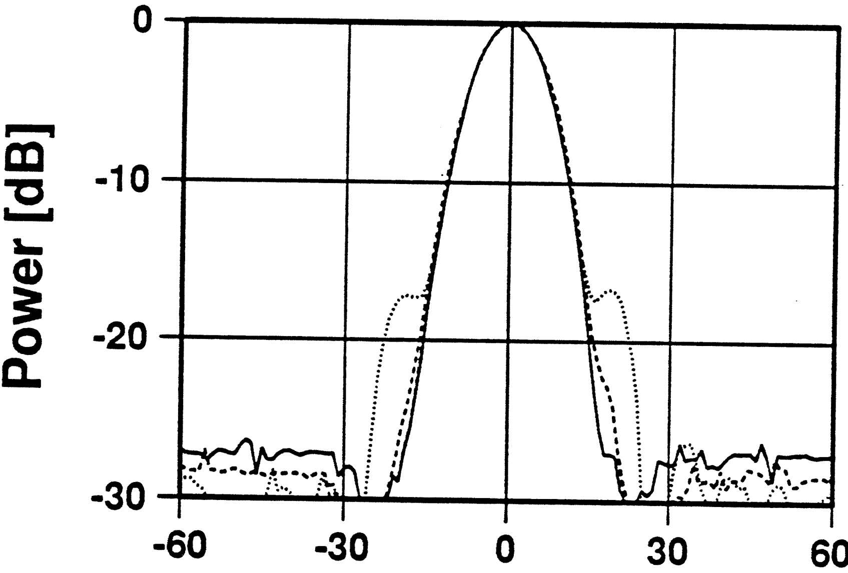

Figure 6. ***Measured radiation patterns for the H- (solid), E- (dashed), and D-planes (dotted) of a diagonal horn in the array (#33 in Fig. 5).***

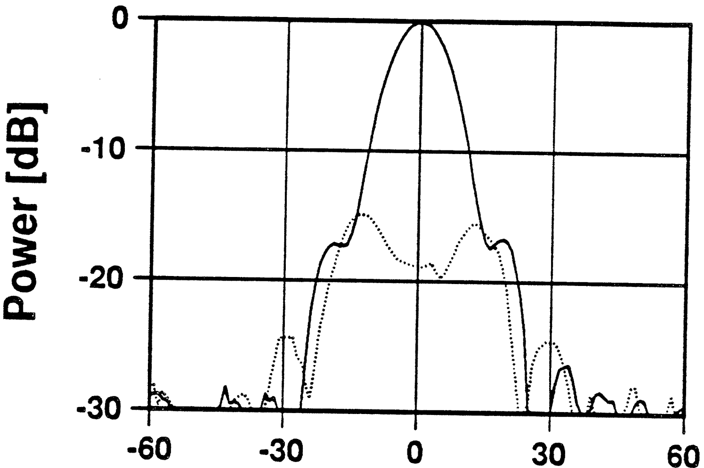

Figure 7. *Measured radiation patterns for the D-plane co-pol (solid) and cross-pol (dotted) components of a diagonal horn in the array (#33 in Fig. 5).*

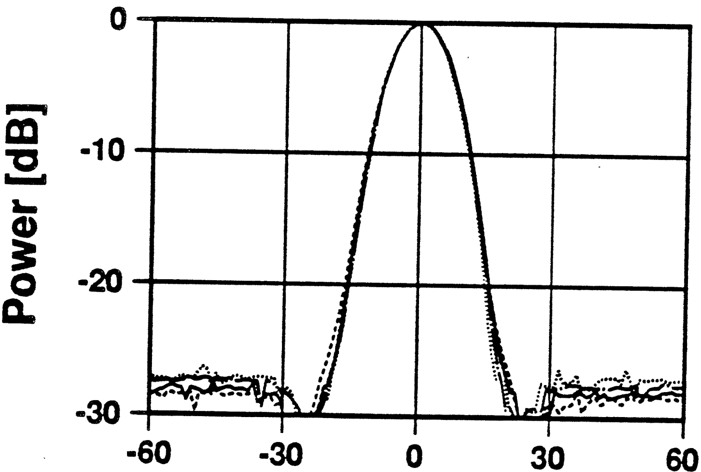

Figure 8. *Comparison between measured H-plane radiation patterns for four different diagonal horn array elements (#11, #33, #43, and #44 in Fig. 5).*

It is quite interesting to compare the measured patterns with the ones predicted by the theoretical model, introduced in Eqn. 18. Figures 9 through 11 show this comparison. The H-plane pattern shows excellent agreement, whereas the theoretical model fails to show the characteristic shoulders in the D-plane (Fig. 10). The cross-pol level (Fig. 11) is predicted to within 1 dB, and the pattern form is qualitatively correct. The simplistic model can hence yield quite a good agreement with measurements.

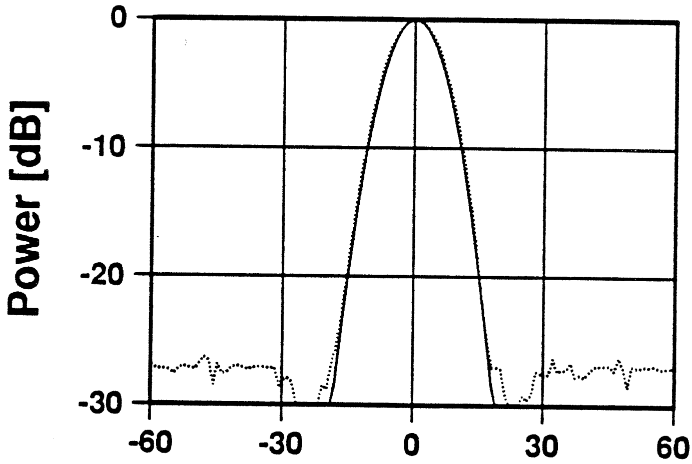

Figure 9. *Comparison between measured (dotted) and theoretical (solid) H-plane radiation patterns.*

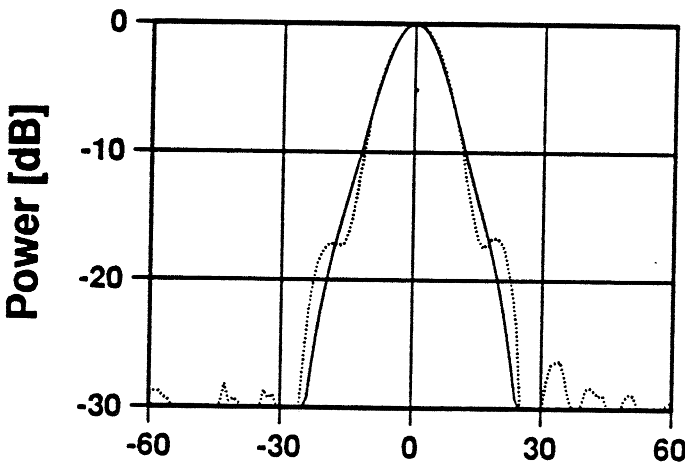

Figure 10. *Comparison between measured (dotted) and theoretical (solid) co-pol D-plane radiation patterns.*

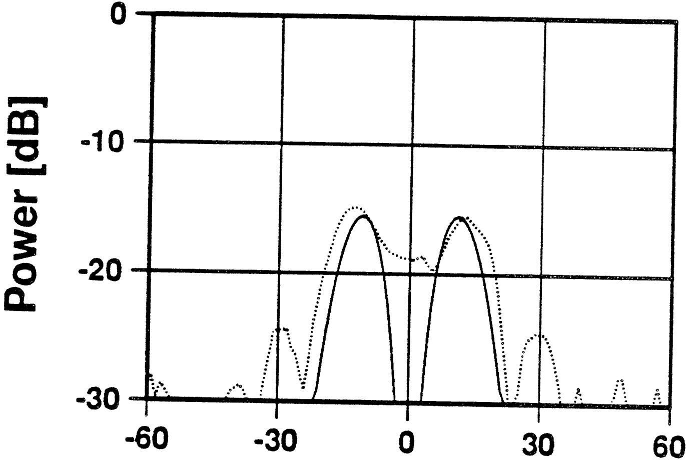

Figure 11. *Comparison between measured (dotted) and theoretical (solid) cross-pol D-plane radiation patterns.*

3. SANDWICHED TAPERED SLOT ANTENNAS

Various forms of slotline components are attractive, topologically and electrically, for integration with *e.g.* sub-millimetre wave SIS mixers. The thickness of the slotline substrate should be small, so that no surface waves are excited. For a slotline antenna the requirement is even more stringent, and the thickness should, as a rule of thumb, be less than ~ 0.03 $\lambda/(\sqrt{\varepsilon_r}-1)$ (*cf.* [9]). Hence, the required thickness of a quartz substrate at 350 GHz is of the order of < 20 μm. Such thin substrates are difficult to handle as well as to fabricate. In order to avoid these problems, we developed a sandwiched slotline antenna, *i.e.* a slotline antenna sandwiched between two thick dielectric sub-/superstrates. The surrounding of the antenna will then have the same dielectric constant, which is equivalent to a free antenna without any supporting substrate, see Figure 12. It should be noted that sandwich type antennas have also been developed elsewhere (see *e.g.* [10, 11]).

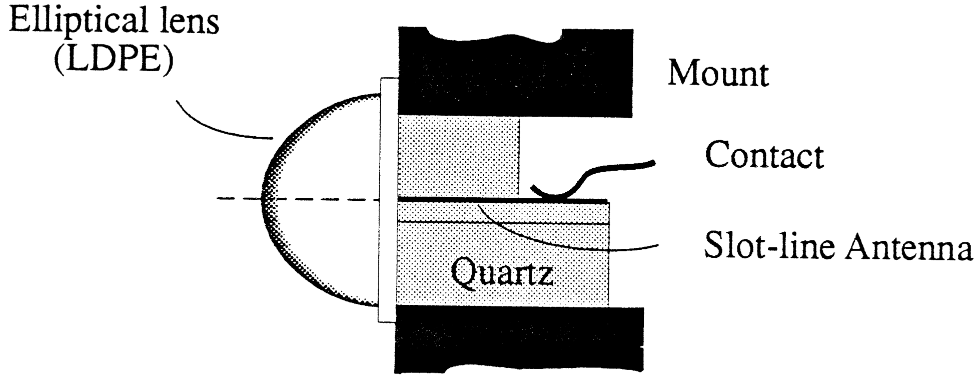

Figure 12. "Artist's view" of the sandwiched slotline antenna, including a beamshaping lens. (side view)

Several 30 GHz scale models were built to evaluate the sandwich concept, see Figure 13. The best antenna found was a slotline antenna of the BLTSA (Broken Linearly Tapered Slotline Antenna) type [12], with an elliptical lens made of low density polyethylene ($\varepsilon_r \approx 2{,}3$), mounted in front of the sandwich. The sidelobe level is typically below -20 dB, and the cross-polarisation in the D-plane is less than -10 dB. Representative E-, H-, and D-plane patterns of this scale model antenna are shown in Figure 14. This scale model antenna was chosen to empirically find suitable dimensions for the sandwiched BLTSA antennas for integration with SIS mixers at 350 GHz.

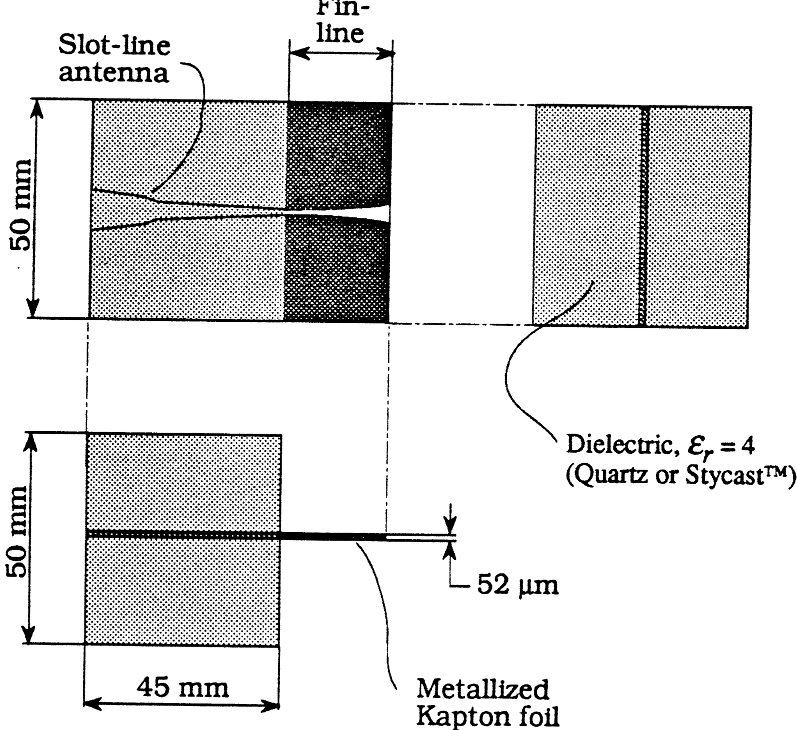

Figure 13. Dimensions of the 30 GHz scale model. Lens not shown.

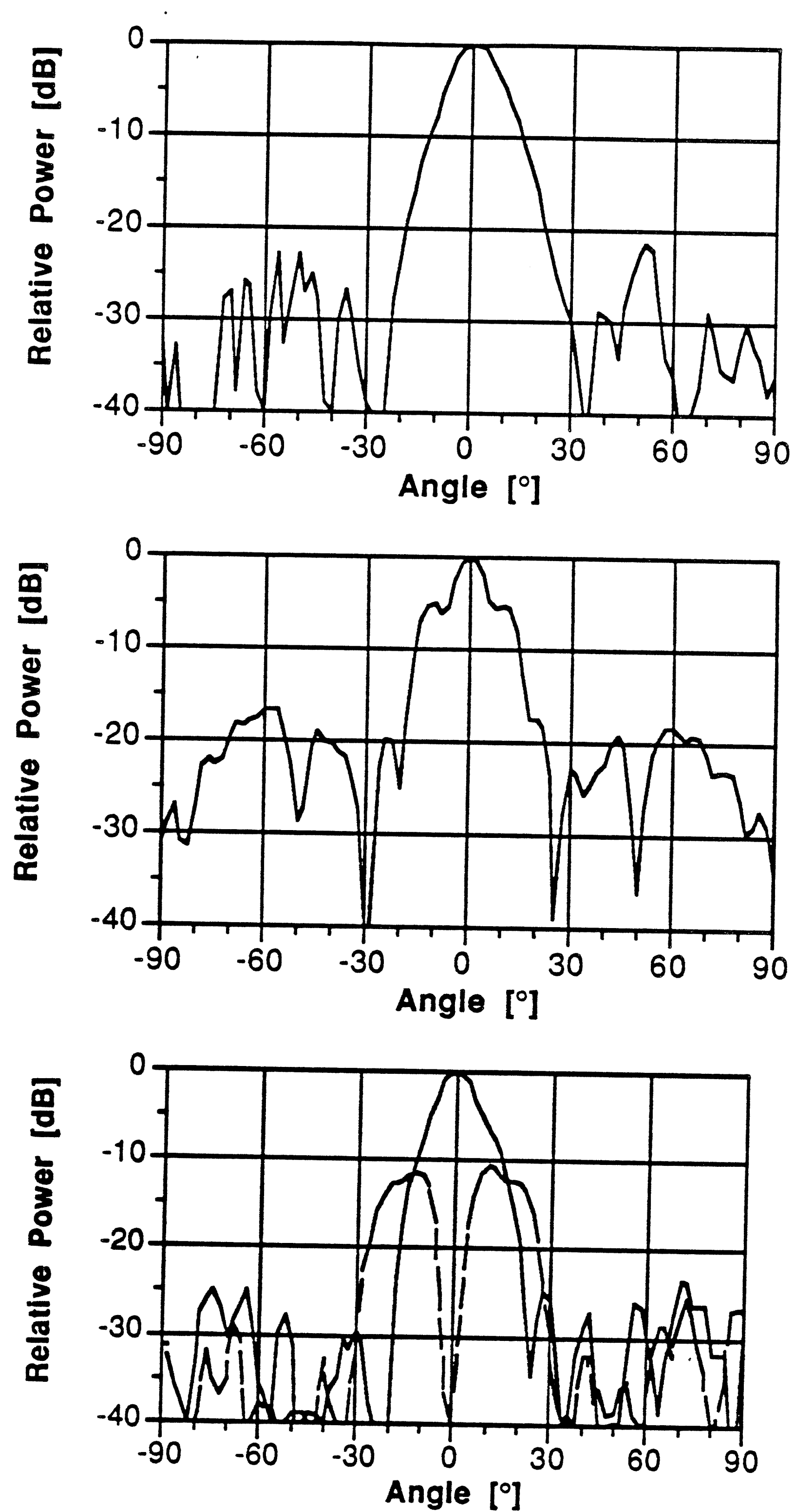

Figure 14. Antenna diagrams measured at 30 GHz (scale model). The panels show the radiation patterns in the E- (top), H- (middle), and D-plane (bottom), respectively. The D-plane plot shows both co- (solid line) and cross-pol (dashed line) data.

In order to test the antenna properties at 350 GHz, a slotline antenna and a bismuth bolometer detector (see Figure 15) were integrated on a 0,5 mm thick crystalline quartz substrate and sandwiched between two ~2 mm thick pieces of crystalline quartz.

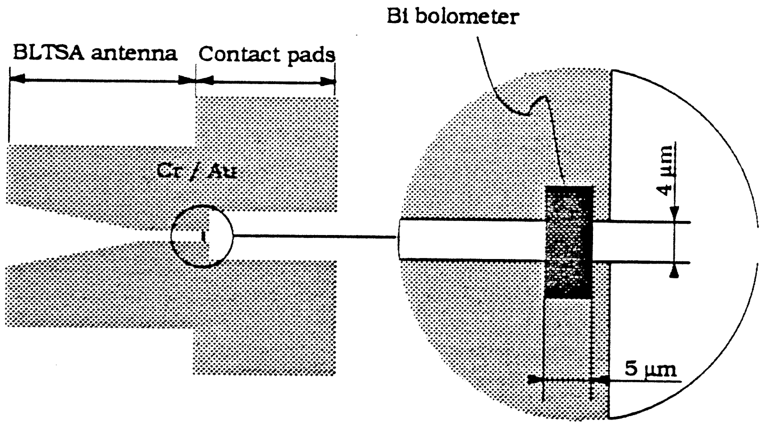

Figure 15. *Schematic of a slotline antenna for 350 GHz with an integrated bismuth bolometer. The resistance of the bolometer should match the impedance of the slot-line, ~ 50 Ω.*

The fabrication of the antenna and the bolometer is straightforward: The antenna (Cr/Au) and the bismuth bolometer are both manufactured by lift-off. The lift-off process gives a smooth gold edge, which is essential for good electrical contact between the bolometer and the antenna. To obtain a uniform bismuth layer the substrate is cooled to approximately –60 °C during the evaporation. The resistance of the bolometer is continuously monitored during evaporation. The evaporation of bismuth is stopped when the bolometer has reached the desired resistance to match the impedance of the antenna.

The measured E- and H- plane antenna patterns for the sandwich slotline antenna at 350 GHz are shown in Figure 16.

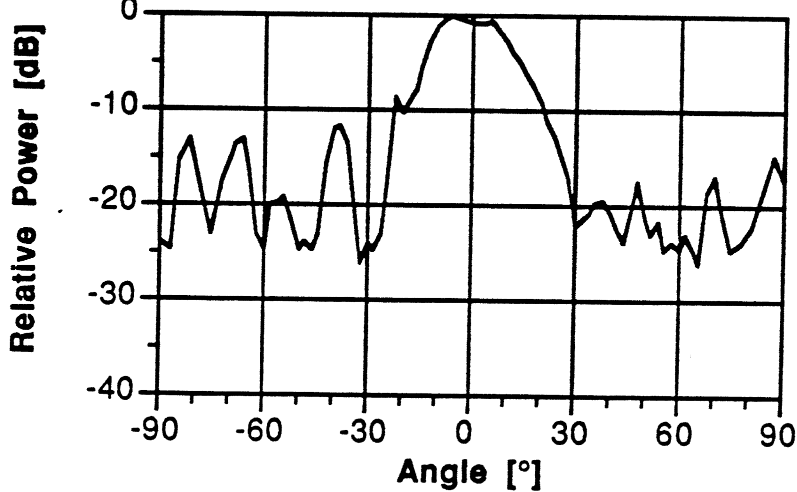

Figure 16a. *Measured E- plane antenna pattern for a sandwiched BLTSA antenna at 350 GHz*

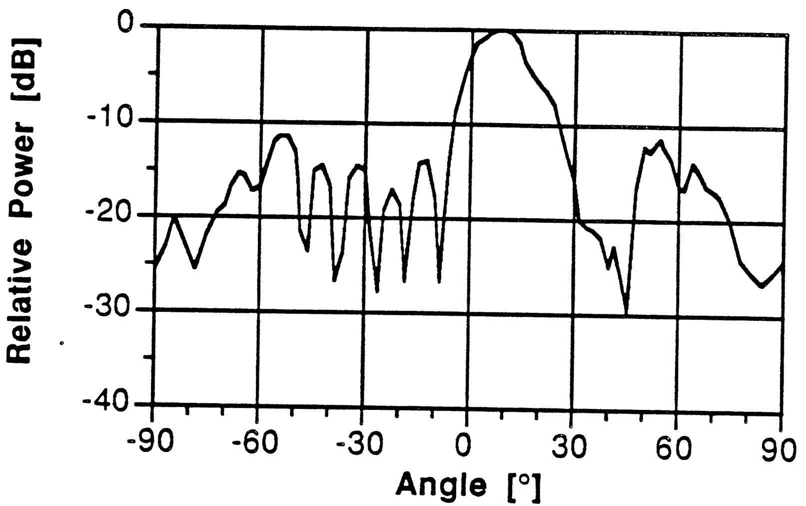

Figure 16b. Measured H- plane antenna pattern for a sandwiched BLTSA antenna at 350 GHz.

At 350 GHz, the sidelobe level in the E-plane is almost 10 dB higher compared to the 30 GHz scale model measurements. In the H-plane the pattern shows more asymmetries, in addition to a 5 dB increase in sidelobe level.

The deteriorated quality of the antenna patterns recorded at 350 GHz, particularly in the H-plane, is most probably due to alignment problems. For instance, the lens has to be accurately aligned (within 50 μm), and it is essential to avoid any air gaps between the quartz pieces.

4. CONCLUSIONS

The diagonal horn antenna has been theoretically investigated. The model using the Gauss-Hermite expansion yields an agreement with measured data which ranges from good to excellent. The horn has a high fundamental Gaussian mode content (≈ 84 %). The design lends itself to conventional millimetre and sub-millimetre construction methods, such as the split-block technique. The small interactions that were seen in the array measurements indicate that the diagonal horn antenna is a strong candidate for focal plane imaging arrays.

The sandwiched tapered slot antenna is a planar feed which can be easily integrated with *e.g.* SIS mixers. The model experiments made at 30 GHz show discrepancies with 350 GHz measurements. The stringent tolerance requirements at sub-millimetre frequencies could at least partly explain these discrepancies.

REFERENCES

[1] R. Wylde, "Optics and Corrugated Feedhorns", IEE Proc.,Vol. 131, Pt. H, No. 4, pp. 258-262, Aug. 1984.

[2] E.I. Muehldorf, "The Phase Center of Horn Antennas", IEEE Trans. Antennas Propagat., Vol. AP-18, No. 6, pp. 753-760, Nov. 1970.

[3] A.W. Love, "The Diagonal Horn Antenna", Microwave J., Vol. V, pp. 117-122, Mar. 1962.

[4] A.C. Ludwig, "The Definition of Cross Polarization", IEEE Trans. Antennas Propagat., Vol. AP-21, No. 1, pp. 116-119, Jan. 1973.

[5] J.A. Murphy and R. Padman, "Phase Centers of Horn Antennas Using Gaussian Beam Mode Analysis", IEEE Trans. Antennas Propagat., Vol. AP-38, No. 8, pp. 1306-1310, Aug. 1990.

[6] P.F. Goldsmith, "Quasi-Optical Techniques at Millimeter and Submillimeter Wavelengths", Ch. 5 in ***Infrared and Millimeter Waves***, Vol. 6, K. Button, Ed., pp. 277-343, Academic Press, 1982.

[7] M. Abramowitz and I.A. Stegun, ***Handbook of Mathematical Functions***, 9th printing, ISBN 0-486-61272-4, Dover Publications, New York.

[8] D.H. Martin, *et al.*, ***Millimetre-Wave Optics*** (Compendium), Queen Mary College, London, UK, 1988.

[9] K.S. Yngvesson, D.H. Schaubert, T.L. Korzeniowski, E.L. Kollberg, T. Thungren, and J.F. Johansson, IEEE Trans. Antennas Propagat., Vol. AP-33, No. 12, pp. 1392-1400, Dec. 1985.

[10] T. L. Hwang, D. B. Rutledge, and S. E. Schwarz, "Planar Sandwiched Antennas for Submillimeter Applications", Appl. Phys. Lett. 34(1), 1 January 1979.

[11] A. Eckart, A.I. Harris and R. Wohlleben, "Scaled Model Measurements of the Sandwiched V-Antenna", Int. J. IR and MM Waves 9, 6 (1988).

[12] P.R. Acharya, J.F. Johansson, and E.L. Kollberg, "Slotline Antennas for Millimeter and Submillimeter Waves", Proc. 20th European Microwave Conf., Budapest, Hungary, Sept. 10-13, 1990, Vol. 1, pp. 353-358.

Integrated Horn Antennas for Terahertz Applications

George V. Eleftheriades, Walid Y. Ali-Ahmad,
Linda P. Katehi and Gabriel M. Rebeiz

NASA/Center for Space Terahertz Technology
Electrical Engineering and Computer Science Department
University of Michigan
Ann Arbor, MI 48109-2122

SUMMARY

We are developing integrated and receivers antennas for terahertz applications. As the remote-sensing/radio-astronomical frequencies are pushed higher into the millimeter and submillimeter- wave regions, integrated antennas and receivers become competitive with standard waveguide receivers. The integrated receivers consist of an antenna integrated directly with a matching network/mixer. Integrated antennas and receivers are easier to manufacture, more reliable and much less expensive than waveguide receivers. The integration also allows the use of linear or two-dimensional arrays without a dramatic increase in cost.

The heart of an integrated receiver is the planar antenna and the antenna/mixer matching network. We have concentrated our efforts into the development and optimization of the high-efficiency integrated horn antenna (Fig. 1). The antenna consists of a dipole suspended in a pyramidal cavity etched in Silicon.The horn antennas are typically between 1λ and 1.5λ-square, and show excellent patterns at 93 GHz with a directivity around 10-12 dB. In the past year, we have achieved significant advance in the analysis and optimization of integrated horn antennas and the projects are summarized below:

1- Full-Wave Analysis of Dipole-Fed Horn Antennas. A rigorous procedure for evaluating the Green's function and input impedance of a dipole-fed horn antenna has been recently developed at the University of Michigan. The geometry of the horn structure is approximated by a cascade of rectangular waveguide sections, and the boundary conditions are matched at each of the waveguide sections and at the aperture of the horn. For the case of a single horn surrounded by an infinite metallic wall, the fields in space are given by a continuous spectrum of plane waves. The input impedance is calculated by solving the Pocklington's integral equation using the method of moments on the source interface.

The patterns for a 1.35λ-square horn in a ground-plane, and in a two-dimensional array are shown in Figure 2. The theoretical patterns agree very well with measured patterns at 92 GHz, and on microwave scale models at 3 GHz. The H-planes are smooth and similar

in both cases, due to the TE_{10} tapering of the electric field across the aperture. The E-plane patterns are much more interesting. The dipole couples to the TM_{12} and the TE_{12} waveguide modes, and their effect is to increase the vertical component at the center and to reduce it at the E-plane edges. The resultant pattern shows a near H- plane behavior near broadside, and levels off at -11dB for larger angles. In the case of the E-plane in a two-dimensional array, the horn sees the array and the spikes and nulls in the patterns are due to specific Floquet- modes. Impedance measurements were done on a microwave scale model at 1-2 GHz for a 1.35λ dipole-fed horn. The input impedance and resonant length are a strong function of the dipole position inside the cavity (Fig. 3), and vary from 40Ω to 170Ω and 0.37λ to 0.45λ, respectively. The dipole impedance for a feed position of 0.39λ is quite suitable for Schottky-diode receivers (Fig. 4). The horn has about 8% and 20% bandwidth for feed positions of 0.39λ and 0.6λ respectively. These bandwidths are adequate for most millimeter-wave applications.

2- Double-Polarized Antennas. A two-dimensional dual-polarized monolithic horn-antenna array has been designed for 92 GHz (Fig. 5). The antenna consists of two perpendicular dipoles suspended on the same membrane inside the horn cavity. The dipoles couple to an orthogonal set of waveguide modes, and therefore are effectively isolated from each other. The measured mutual coupling between the antennas on a microwave scale model was less than -30 dB. A design with an aperture of 1.35λ-square, and a feed position of 0.39λ was fabricated. The antennas are linearly polarized and a polarization isolation better than -23 dB was measured at 92 GHz (Fig. 6). The measured E & H-plane patterns agree well with theory and are virtually identical for both polarizations. Detailed analysis and experimental results are presented in the references.

3- 802 GHz Imaging Array. A 256-element imaging array has been fabricated and tested at 802 GHz (Fig. 7). The patterns agree very well with theory (Fig. 8), and the associated directivity for a 1.4λ horn aperture calculated from the measured E and H-plane patterns is $12.3 \pm 0.2dB$. The patterns show a main-beam efficiency of 88% in a 100°- beamwidth and are suitable for f/0.9 reflector systems. We would like to note that this result presents one of the best patterns measured on a planar antenna at frequencies higher than 500 GHz.

4- Step-Profiled Diagonal Horn Antennas. The main limitations of integrated horn antenna stem from their large flare angle of 70.6° which does not allow us to fabricate apertures greater than 1.5λ before the phase-errors becomes too large. This results in gains around 13 dB and 10-dB beamwidth of $90 - 95°$. We have investigated a new step-profiled horn which reduces the effective flare-angle of the horn to $30 - 40°$ and allows us to achieve gains between 17 and 20 dB (Fig. 9). The circular symmetry is also enhanced by positioning the exciting dipole along the diagonal of the horn. A specific step-profiled horn has been designed for millimeter-wave applications. The horn geometry has an effective flare-angle of 30° and an aperture size of 2.92λ. It is synthesized using 12 wafers each of thickness of 0.4λ. The step-size for each wafer discontinuity is 0.17λ. The calculated

E and H-plane patterns show a 10-dB beamwidth of 40° and a side-lobe level of -17 dB, with a directivity of 17.5 dB (Fig. 10). The 45° plane is effectively wider than either the E and H-planes, but matches them quite well up to the -10 dB points (Fig. 11). The step-profiled horn was also compared to a horn with a cavity defined by its smooth outer envelope and has the same aperture size. It is seen that the patterns match well up to -17 dB but then the step-profiled horn widens and develops a side-lobe (Fig. 12). Similar effects have been observed at the 45° planes. The measured patterns on a 12 GHz model of the smooth dipole-fed horn agree very well with theory. The calculated coupling efficiency of the step-profiled horn to a gaussian beam is around 75% and is approximately the same as a waveguide-fed pyramidal horn antenna.

We are now designing a hybrid Potter horn with a dipole-fed integrated horn cavity and a long machined phasing section. Preliminary results show a 20 dB gain hybrid-horn with a gaussian-beam coupling efficiency of 94%. Additional results and measurements will be presented in the coming CSTT symposium.

For additional information, the reader is referred to the following articles:

[1] G.M. Rebeiz, D P. Kasilingam, P.A. Stimson, Y. Guo and D.B. Rutledge, "Monolithic millimeter-wave two-dimensional horn imaging arrays," *IEEE Trans. Antennas Propag.*, vol. AP-28, Sept 1990.

[2] Y. Guo, K. Lee, P.A. Stimson, K. Potter and D.B. Rutledge, "Aperture Efficiency of Integrated-Circuit Horn antennas," *IEEE AP-S Intl. Symp.*, Dallas, Texas, May 7- 11, 1990.

[3] W.Y. Ali-Ahmad and G.M.Rebeiz, "92 GHz dual-polarized integrated horn antennas," To appear in the June 1991 Issue of the *IEEE Trans. Antennas Propag.*.

[4] W.Y. Ali-Ahmad and G.M. Rebeiz, H. Davee and G. Chin, "802 GHz integrated horn antennas imaging array," To appear in the May 1991 Issue of the *Intl. Journal Infrared and Millimeter Waves.*

[5] G.V. Eleftheriades, L.P. Katehi and G.M. Rebeiz, " High-gain step-profiled integrated horn antennas," To be presented at the *IEEE AP-S Symp.*, Ontario, Canada, June 24-27, 1991.

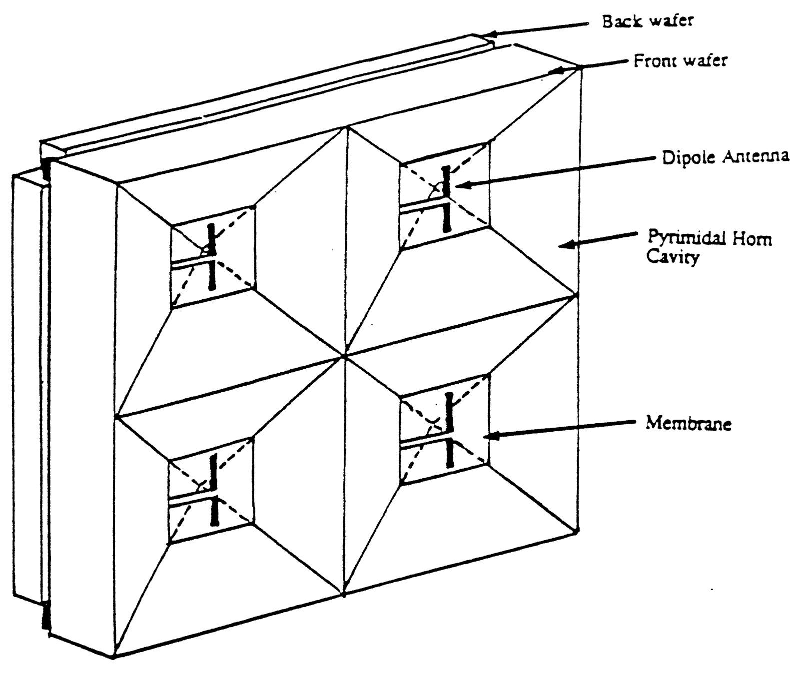

Figure 1: An integrated horn antenna with single polarization.

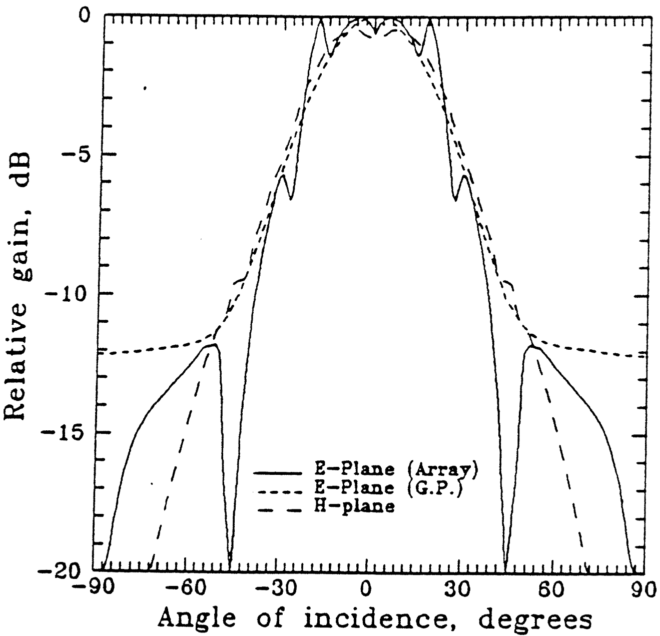

Figure 2: The E- and H-plane patterns of a 1.35λ horn antenna in a ground-plane and in a two-dimensional array. The theoretical agree very well with experiments at 3 GHz and 92 GHz.

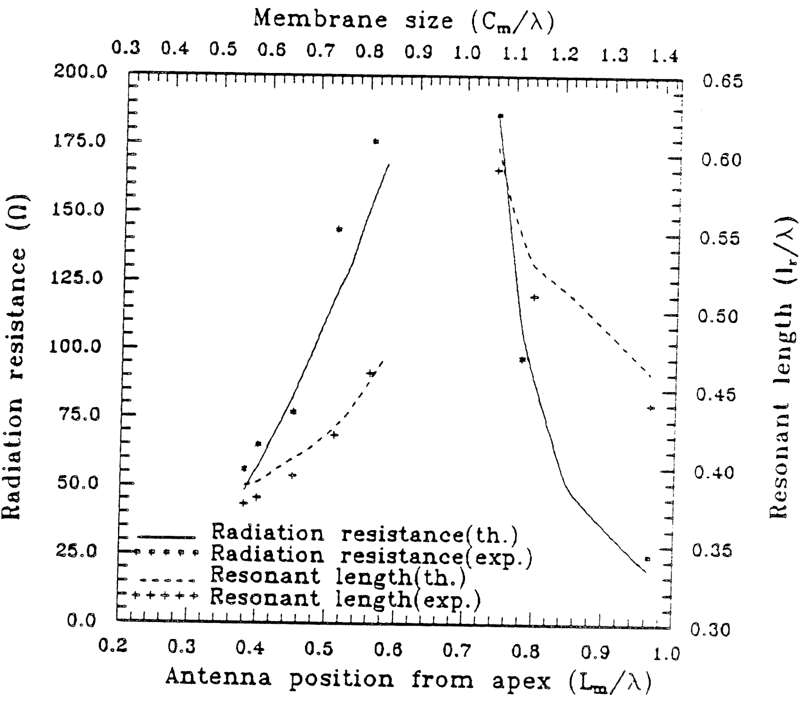

Figure 3: Measured and predicted dipole resonant resistance and resonant length vs. dipole position from the apex. Notice the region of no resonance in the center of the horn.

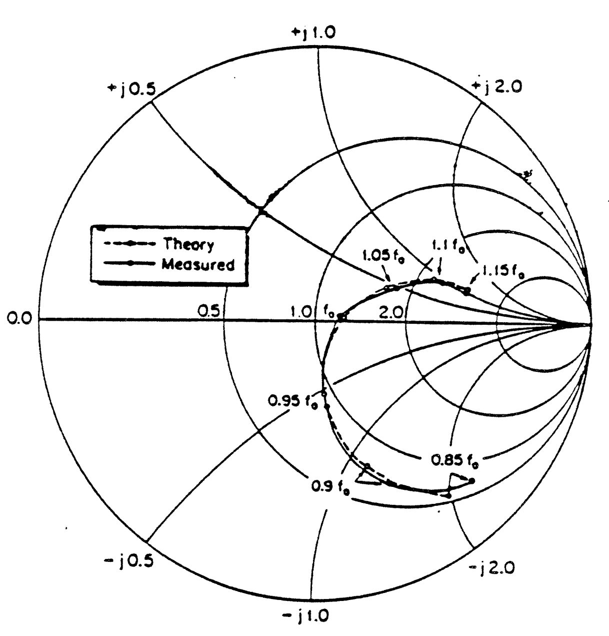

Figure 4: Predicted and measured dipole input impedance vs. frequency for a feed position of 0.41λ.

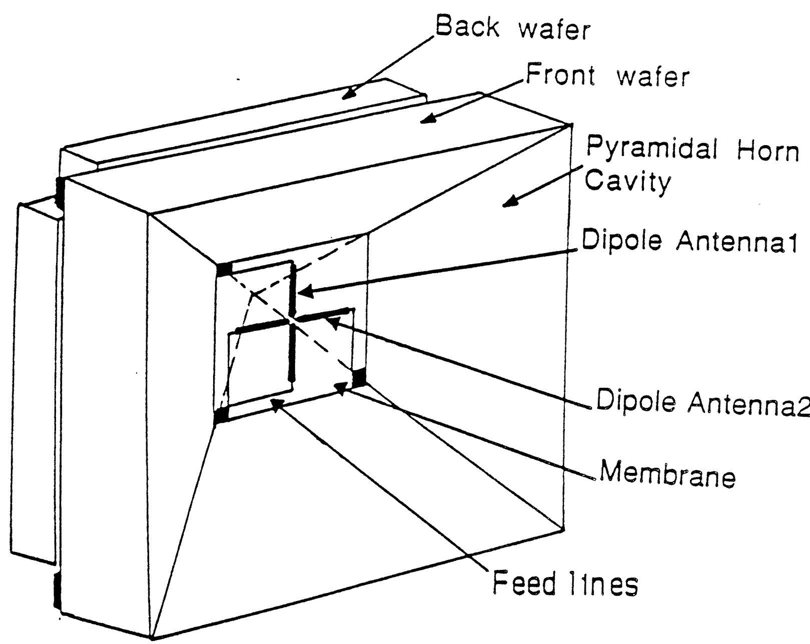

Figure 5: Monolithic dual-polarized horn antenna element with a novel bias and feeding structure.

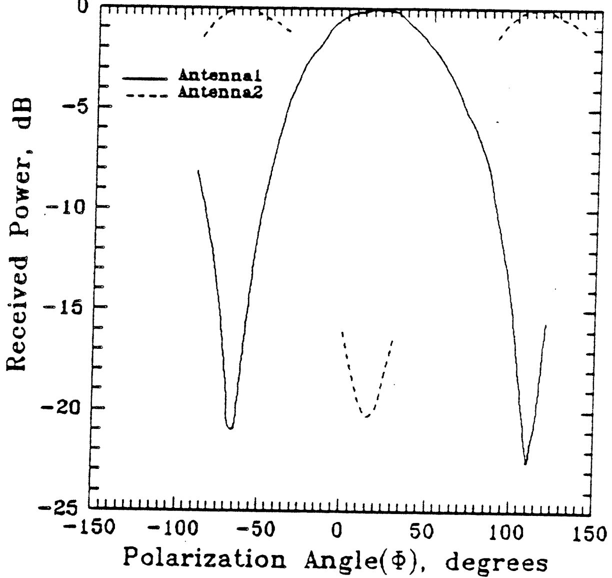

Figure 6: The measured polarization response of the orthogonal antennas at 92 GHz. The polarization isolation is better than -23dB.

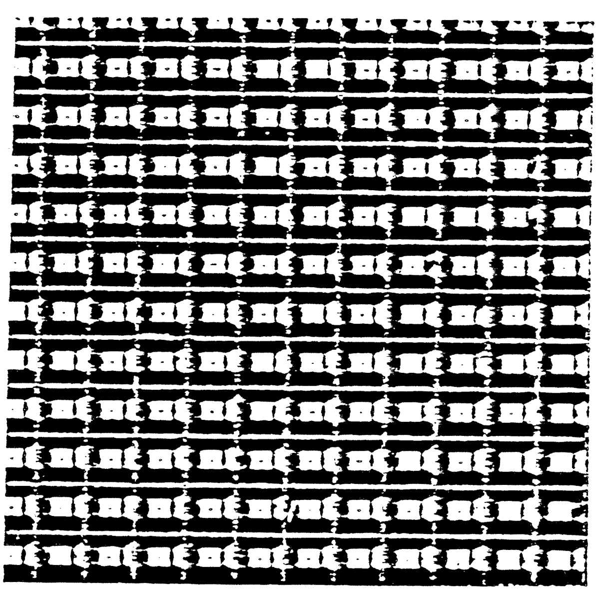

Figure 7: A 256-element two-dimensional horn imaging array at 802 GHz. The period of the array is 525μm and the horn aperture is 1.40λ.

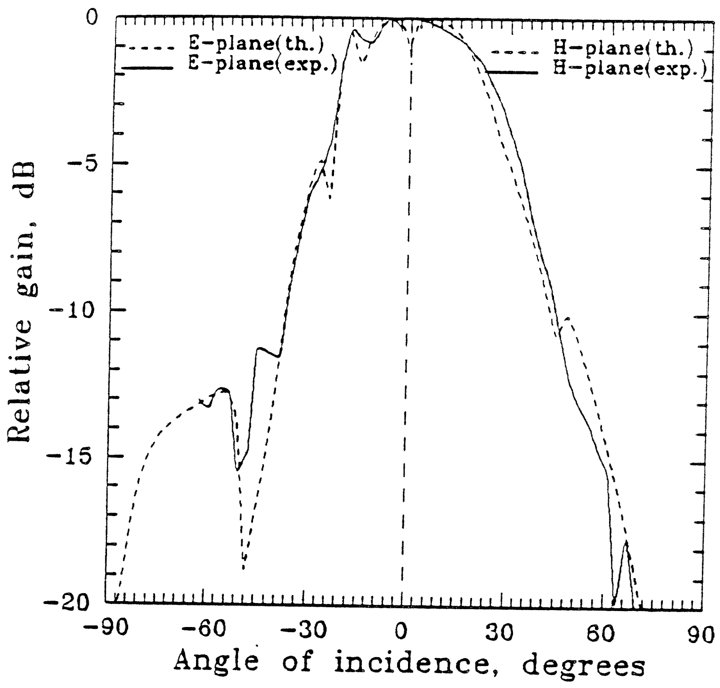

Figure 8: The measured theoretical and experimental E and H-plane patterns at 802 GHz.

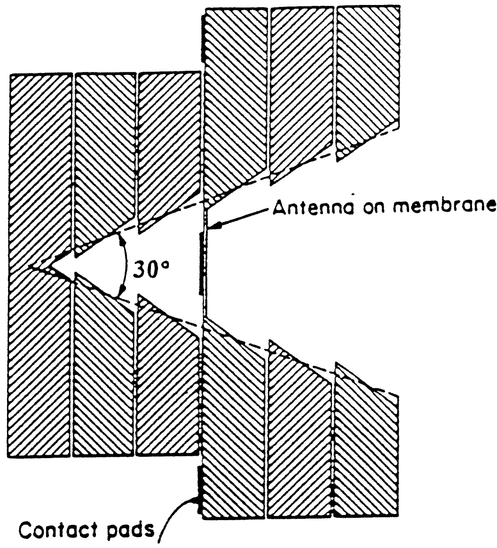

Figure 9: The step-profiled horn geometry (see text).

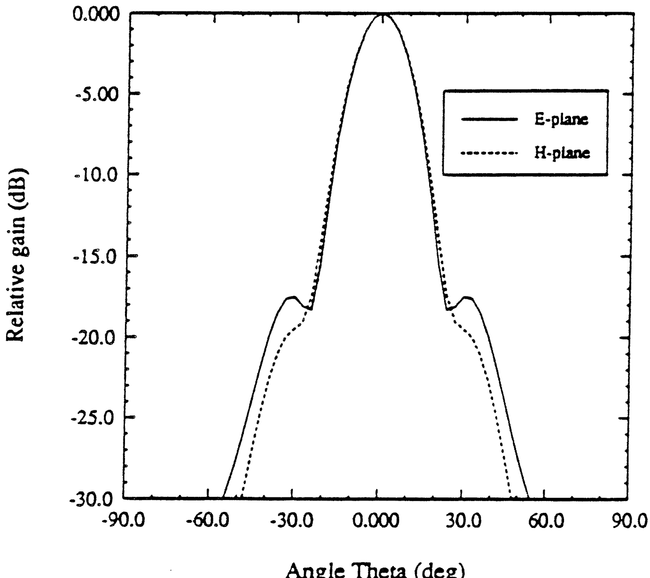

Figure 10: The calculated E and H-plane patterns for a step-profiled horn with an effective flare-angle of 30° and an aperture size of 2.92λ. The feeding dipole is positioned along the diagonal of the horn antenna.

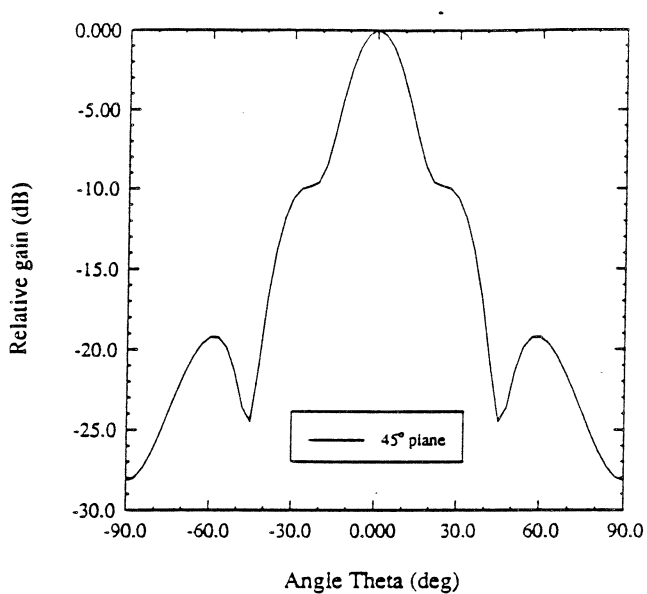

Figure 11: The calculated 45°-plane pattern for a step-profiled horn of figure 10.

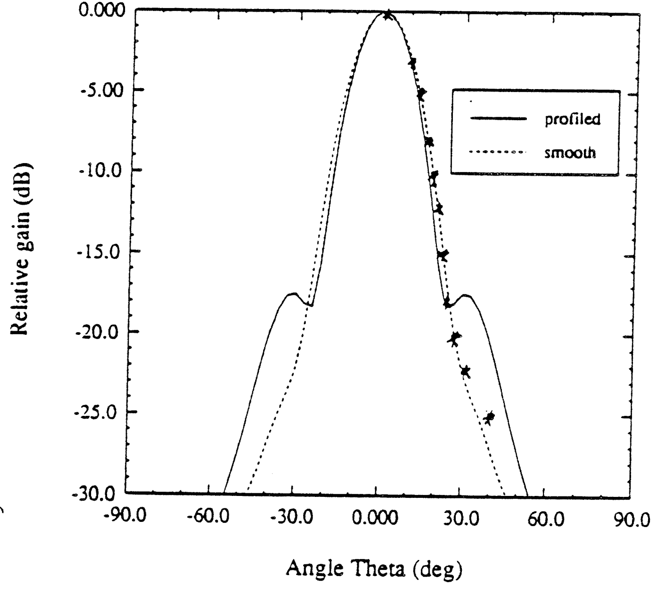

Figure 12: Comparison of the E-plane patterns between a step-profiled horn and its smooth counterpart. The crosses are measured points on a 12.1 GHz model.

Imaging Arrays for the Millimeter- and Submillimeter-Wave Region

K. Uehara, K. Miyashita, K. Natsume, K. Hatakeyama, and K. Mizuno

Research Institute of Electrical Communication, Tohoku University
2-1-1 Katahira, Aoba-ku, Sendai, 980 Japan

Abstract—We have been developing several kinds of lens-coupled antenna imaging arrays for operation at millimeter- and submillimeter-wave frequencies. The comparison of dipoles, Yagi-Uda's, trap-loaded antennas, and microstrip patches will be discussed from the viewpoint of the matching with detectors and optics. The radiation patterns and input impedance of each antenna have been calculated and measured at the model experiment. The arrays have been successfully applied to plasma diagnostics at the Tsukuba GAMMA 10 plasma machine.

I. INTRODUCTION

Millimeter and submillimeter wavelength imaging has recently become increasingly important in plasma diagnostics, remote sensing, and environmental measurements. Accordingly the high-performance multi-element quasi-optical imaging systems have been developing. Those systems require sensitive antennas and detectors, and high resolution optical systems. Planar antenna arrays with integrated detectors have led to improved sensitivity and scanning speed. We have been currently investigating several kinds of printed antennas [1,2,3], which are integrated with detectors and are combined with a low-loss dielectric substrate lens [4], which structure can eliminate RF feed cable-losses or substrate modes and can also offer mechanical stability and facility for cooling. On the other hand, those antennas require careful matching to the detectors and optics. In this paper, we will discuss the comparison of the lens-coupled printed antennas: dipoles, Yagi-Uda's, trap-loaded antennas and microstrip patches, all of which are integrated with beam-lead schottky diodes. Also the measurement of plasma density profile with an imaging array at the Tsukuba GAMMA 10 plasma machine will be shown as a practical application.

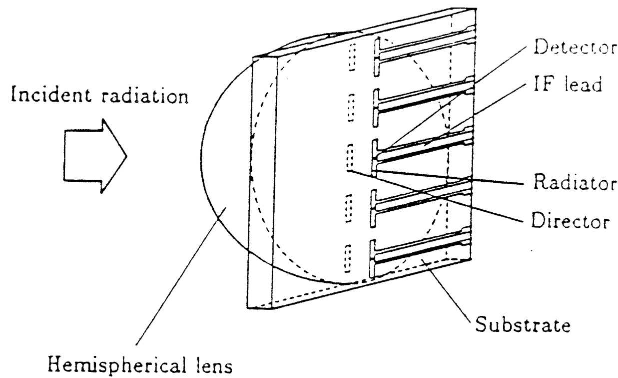

Fig. 1. Yagi-Uda antenna imaging array.

II. YAGI-UAD ANTENNA IMAGING ARRAYS

The fundamental array consists of half-wave dipoles integrated with diodes on a dielectric-air interface [1]. The input impedance of the dipole is generally much larger than that of diodes or SIS junctions, which causes large mismatch loss, because of difficulty to fabricate small-size matching circuits on the each array element. In addition, the dipole radiation pattern shows big sidelobes and large central dip in the H-plane (Fig. 2 (a)). To improve these disadvantages, we have proposed and fabricated Yagi-Uda antenna configuration [3] shown in Fig. 1. The radiator elements are photolithographically fabricated half-wave dipoles on a substrate of glass/PTFE (ϵ_r=2.17), and the SBD's are integrated at the feed point of each radiator. The director elements are on the other side of the substrate to which a hyperhemispherical lens of 60mm diameter made of TPX (ϵ_r=2.13) is attached. The spacing between the radiator and the director can be controlled by choosing the substrate with proper thickness. For optimization of the antenna, the element dimensions

are determined by two conditions: one is impedance matching with the detectors, and the other is beam pattern matching with the optics. The radiation pattern can be adjusted by changing the director length and the element spacing.

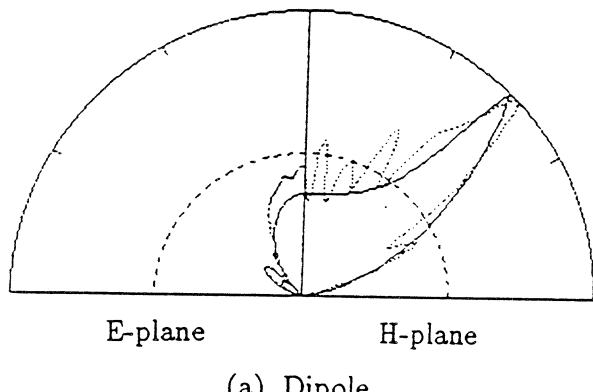

(a) Dipole

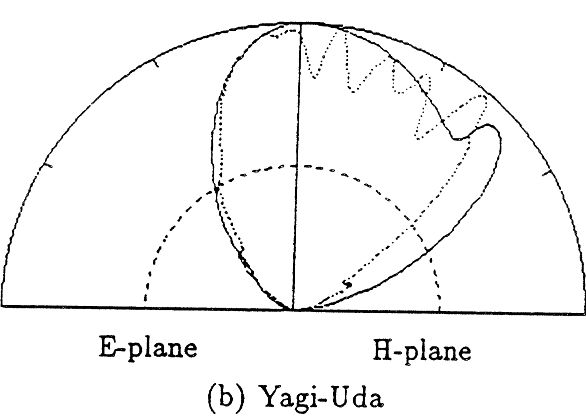

(b) Yagi-Uda

Fig. 2. The calculated and measured radiation patterns of an antenna on a dielectric hemisphere (ϵ_r=2.13) of 100mm diameter. (a) Dipole, (b) Yagi-Uda ($2\ell_1=0.5\lambda_e$, $2\ell_2=0.462\lambda_d$, $d=0.093\lambda_d$). The scale is linear in power; —theory, - - -experiment at 50GHz.

Fig. 2 shows optimized Yagi-Uda patterns, comparing with the dipole's. The radiator length $2\ell_1$ is $0.5\lambda_e$, the director length $2\ell_2$ is $0.462\lambda_d$, and the spacing d is $0.093\lambda_d$. λ_e and λ_d are the effective wavelength at the air-dielectric interface and the wavelength in the dielectric, respectively, being defined by

$$\lambda_e = \frac{\lambda_0}{\sqrt{(1+\epsilon_r)/2)}}, \quad (1)$$

$$\lambda_d = \frac{\lambda_0}{\sqrt{\epsilon_r}}. \quad (2)$$

The improved pattern is almost symmetrical and the directivity G_d becomes 5.5dB. The directivity is defined by

$$G_d = \frac{|D(0,0)|^2}{\frac{1}{4\pi}\int |D(\theta,\phi)|^2 d\Omega}, \quad (3)$$

where $D(\theta,\phi)$ is the directivity function. Because the diameter of the hyperhemispherical lens is electrically enough large and the surface-wave mode can be neglected, we have applied the moment method to the dielectric half spaces to calculate current distributions on the radiator and the director. The theoretical patterns have been calculated from these current distributions. The experimental patterns were measured in a shield room at 50GHz band with a TPX hemispherical lens of 100mm diameter, being fed by the horn located at the focal point of the lens. The results agree well with the theory although many ripples are obtained in the H-planes. These ripples will be due to the effects of the radiation from the orthogonal low-frequency leads.

Also the input impedance can be tuned over a broad range by adjusting the element dimensions (Fig. 3). This method allows improved matching to low impedance detectors.

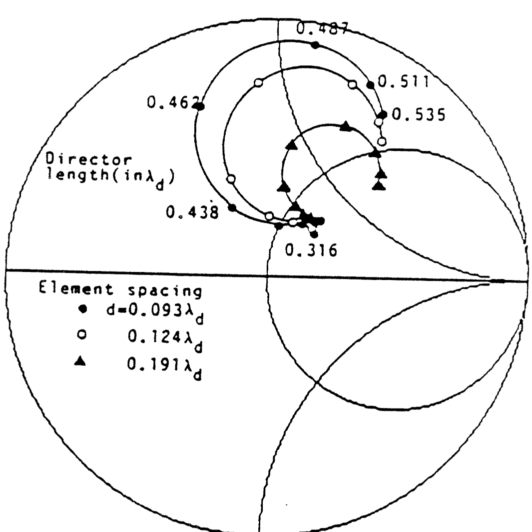

Fig. 3. The calculated input impedance of a Yagi-Uda antenna on a dielectric hemisphere (ϵ_r=2.13).

Consequently good matching conditions are available without complex matching circuits. As detectors, we are using the beam-lead Schottky diode (Sanyo Electric Co. Ltd. , SBL-221) with typical R_s of 5Ω, $C_j(0)$ of 0.02pF and C_p of 0.05pF, whose cutoff frequency runs into 400GHz. With an RF equivalent circuit, we have calculated the 50GHz small signal impedance of 3-j30Ω at the condition of 50μA bias current. The SBD's are useful for imaging applications because they can be applicable for both video detectors and heterodyne mixers at room temperature. Fig. 4 shows calculated directivity and mismatch loss versus the director length. Considering both the impedance mismatch and directivity, we can estimate total efficiency of the individual receptor. Fig. 5 shows calculated and measured total sensitivity of the receptor. For the optimized Yagi-Uda, the receiving power from a incident plane wave is theoretically 8dB improved in comparison with the dipole, and experimentally the 6dB increased power has been measured . In the collinear Yagi-Uda array, crosstalk levels of less than 30dB down between adjacent antennas have been measured when the element interval is $0.7\lambda_d$ in 5GHz model experiments.

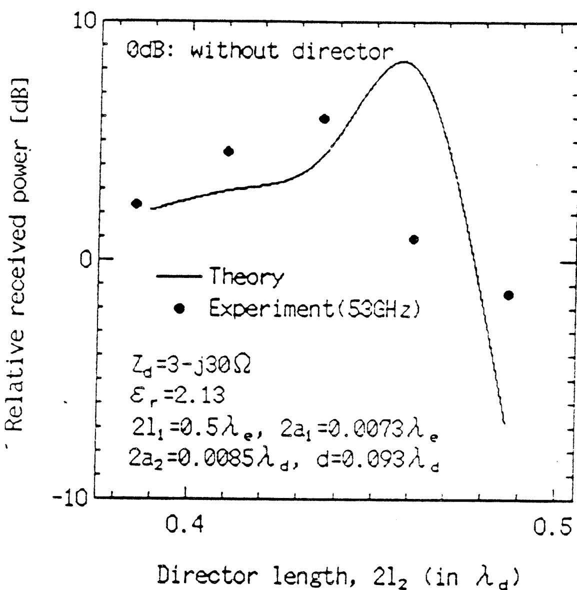

Fig. 5. Total sensitivity of a Yagi-Uda receptor versus director length $2\ell_2$. The 0dB line shows the sensitivity of the dipole; —theory, • experiment at 53GHz.

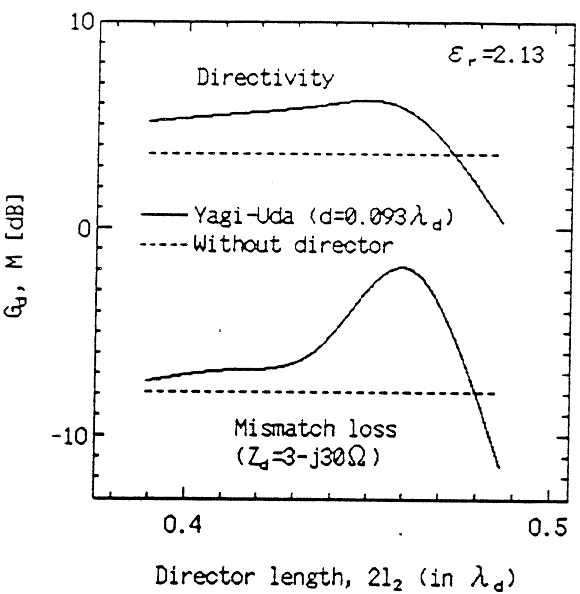

Fig. 4. The calculated directivity and mismatch loss of a Yagi-Uda antenna ($2\ell_1$=0.5λ_e, d=0.093λ_d) versus director length $2\ell_2$. The diode impedance is 3-j30Ω.

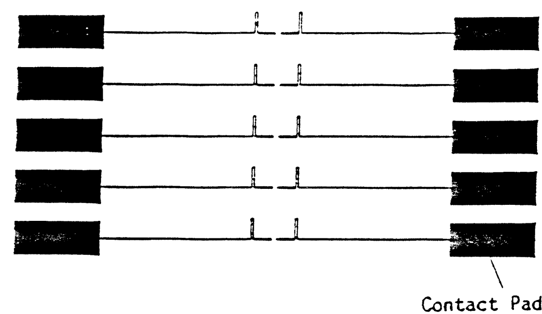

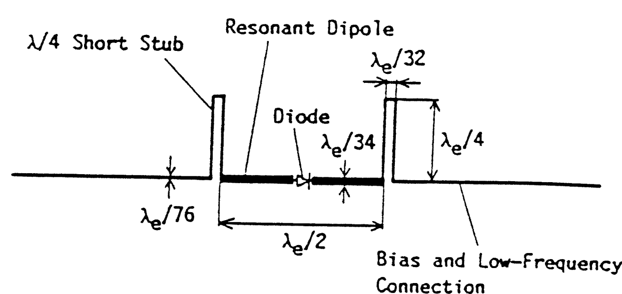

Fig. 6. The configuration of a trap-loaded dipole imaging array.

III. Trap-Loaded Antenna Imagign Arrays

The dipole configuration shown in Fig. 1 offers some difficulties to fabricate parallel array because of the obstruction of the bias and low-frequency leads. In order to avoid any complex circuit designs which may degrade radiation patterns or crosstalks, we have designed trap-loaded antenna configuration [5] shown in Fig. 6. In this structure, the leads are taken from the edges of the dipole through high impedance traps. Each trap consists of a quarter-wavelength long short-stub which offers high Q-value.

Fig. 7 shows measured radiation patterns for the trap-loaded dipole (a) and the Yagi-Uda configuration (b) with $2\ell_2$ of $0.418\lambda_d$ and d of $0.124\lambda_d$. Fig. 7 (a) also shows dipole patterns calculated by assuming sinusoidal standing waves which have large amplitude on the dipole, and small one on the $3\lambda_e$ long outer sections. Undesirable radiations from the waves on the outer sections degrade radiation patterns and cause larger sidelobes in the E-plane. The directivity of 3.7dB for the dipole and 5.9dB for the optimized Yagi-Uda have been measured at 50GHz experiment. The cross polarization level of the trap-loaded dipole have been measured less than 20dB down at ϕ=45°, which indicates the troublesome radiation from the traps can be neglected. The antenna input impedances become higher than those in the previous structure due to effects of the outer sections. The impedance of the dipole with $2\lambda_e$ long traps have been measured about 200Ω in the 5GHz model experiment. Hence these antennas may be useful for heterodyne detection because the RF impedance of the pumped diode is much larger than the small signal impedance. The total receptor 3dB bandwidth of 10% for the dipole and 8% for the Yagi-Uda have been measured at 50GHz band. The results show narrower bandwidths than the previous structure because of the additional of the high Q-value traps.

IV. Monolithic Patch Antenna Imaging Arrays

Although the Yagi-Uda configurations have offered good performance and simple structure to fabricate, lack of efficient space is one of the disadvantage for constructing additional integrated circuits. This disturbs particularly fabricating two-dimensional array. Then we have proposed the lens-coupled patch antenna imaging array configuration which is very suitable for fabricating two-dimensional arrays using MMIC technique (Fig. 8).

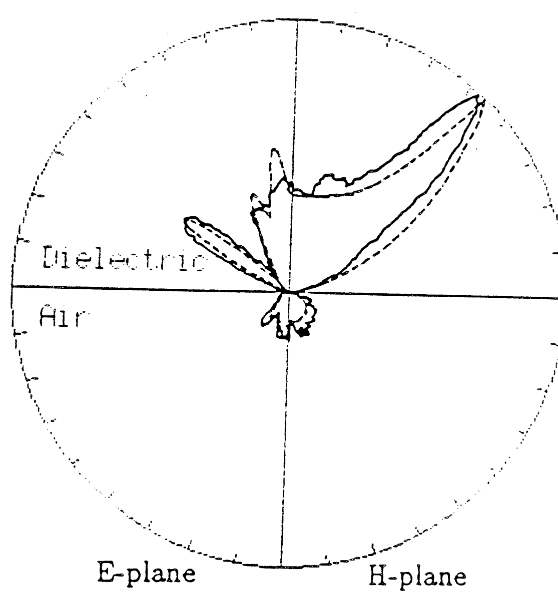

(a) Dipole

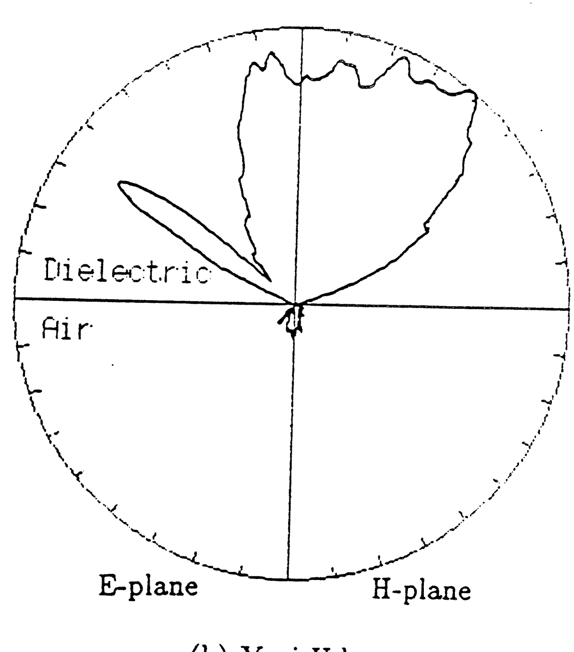

(b) Yagi-Uda

Fig. 7. The calculated and measured radiation patterns of a trap-loaded antenna on a dielectric hemisphere (ϵ_r=2.13) of 100mm diameter. (a) Dipole, (b) Yagi-Uda ($2\ell_1=0.5\lambda_e$, $2\ell_2=0.418\lambda_d$, $d=0.124\lambda_d$). The scale is linear in power; —theory, - - -experiment at 50GHz.

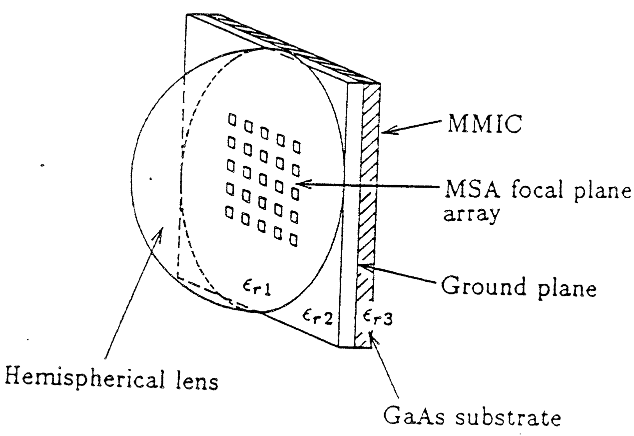

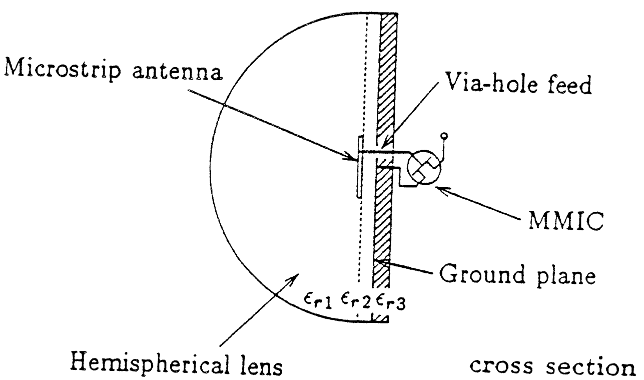

Fig. 8. The configuration of a two-dimensional microstrip patch antenna imaging array.

This array consists of two individual microstrip substrates separated by a common metal ground plane. The antennas are printed on the first substrate (ϵ_{r2}) covered with the low-loss dielectric lens (ϵ_{r1}). Each antenna is fed with a via-hole or coupling slot from the MMIC constructed on the second substrate (ϵ_{r3}). This second substrate offers the efficient space for fabricating additional integrated circuits: such as matching circuits, mixers, amplifiers, and leads. The antennas are ideally isolated from these circuits by the ground plane. Both the patch length a and patch width b are $0.5\lambda_d$, and the feed point (x_1,y_1) is $(0.25a,0.5b)$.

Fig. 9 (a) shows calculated radiation patterns of the individual antenna versus ϵ_r which is defined by the ratio of the effective dielectric constant of the first substrate to the dielectric constant of the lens,

$$\epsilon_r \equiv \frac{\epsilon_{r2eff}}{\epsilon_{r1}}. \tag{4}$$

If ϵ_{r1} equals ϵ_{r2} then the ratio ϵ_r becomes one, and then an ideal radiation pattern can be realized. This pattern is almost symmetrical and has neither any sidelobes nor troublesome radiations at the horizontal directions, which may offer low crosstalk and high beam coupling efficiencies to the incident beam. We have measured the radiation patterns at 50GHz band (Fig. 9 (b)). The results agree well with the theory: the calculated directivity is 9.8dB and the 3dB beam widths are 60° in the E-plane and 71° in the H-plane.

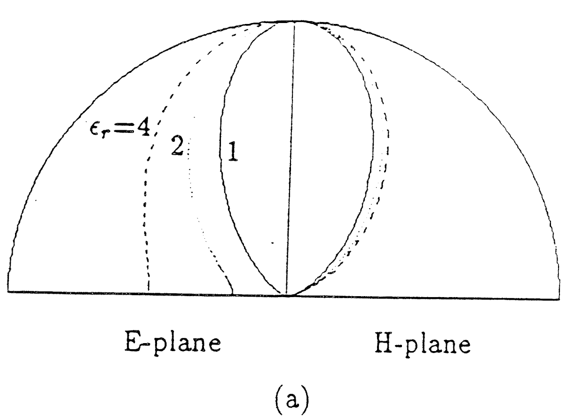

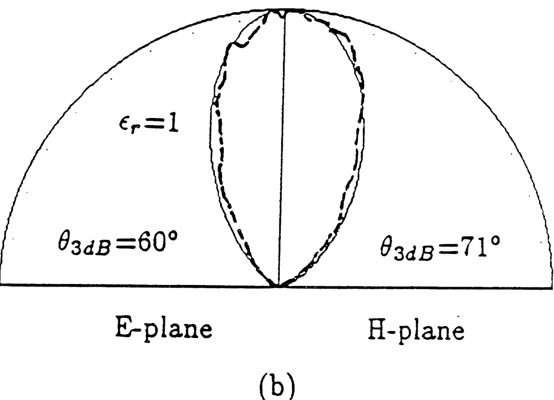

Fig. 9. The calculated and measured radiation patterns of a microstrip patch antenna on a dielectric hemisphere (ϵ_{r1}=2.13) of 100mm diameter. (a) Theory for various ϵ_r, where ϵ_r is the ratio of the effective dielectric constant of the substrate (ϵ_{r2eff}) to the lens (ϵ_{r1}). (b) ϵ_r=1; —theory, - - -experiment at 50GHz. The scale is linear in power.

The antenna input impedance of 85+j25Ω has been calculated with a magnetic-wall model. The crosstalk

level of less than 20dB down in both E and H-plane when the element spacing is $0.7\lambda_d$ has been measured at the 6GHz model experiment. Fig. 10 shows the configuration of 3×3 element integrated patch array. The squares of dot-line show the patch antennas arrayed by the spacing of $0.7\lambda_d$. Matching circuits and low-pass filters are successfully constructed in each resolution unit. Since we can construct matching circuits in the second microstrip substrate, the mismatch loss between the antenna and a detector can be eliminated. Consequently this configuration is suitable for various kinds of detectors. The total 3dB bandwidth of 6% have been measured at 50GHz band experiment.

other lenses are made with low-density polyethylene (ϵ_r=2.28), giving a total magnification of 4.3. The system *f-number* of 1.0 determines the diffraction-limited sampling interval of 2.14mm ($1.0\lambda_d$) and cut-off frequency of 233m^{-1}, corresponding to a plasma dimension of 37mm. Fig. 11 shows the time evolutions of the line-density (a) and line-density profile (b) at the plug cell. The initial plasma produced by a plasma gun cannot be measured since the density is above the cut-off. The results are very close to those obtained by a millimeter-wave interferometer with scanning horn antennas, which is used for the cross-calibration.

Low-pass filter
IF and bias lead
Matching circuit
Feed point
Diode
Patch antenna

Fig. 10. The configuration of 3×3 monolithic microstrip patch antenna imaging array (bottom view).

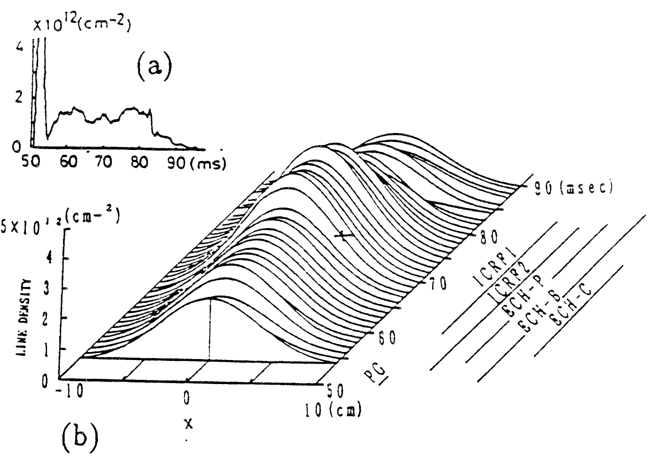

Fig. 11. The measurement of the time evolutions of the line-density (a) and line-density profile (b) at the plug cell in the Tsukuba GAMMA 10 plasma with a 10 element trap-loaded Yagi-Uda antenna imaging array at 70GHz. The time sequence is as follows: following the gun-produced plasma injection (PG), the plasma is heated with ion cyclotron range of frequency (ICRF) powers and electron cyclotron heating (ECH) powers.

V. Applications

As a practical application, we have applied the 10 element trap-loaded parallel Yagi-Uda array to the Tsukuba GAMMA 10 plasma machine in order to measure the plasma density profile [5], for which we have constructed a 70GHz heterodyne phase imaging system. The IF frequency is 2MHz, the diode bias current is 400μA, and the substrate lens is made of fused quartz (ϵ_r=4) with a magnification of 4.0, and

VI. Conclusion

We have designed and investigated several kinds of lens-coupled antennas for operation at millimeter and submillimeter wavelength. The Yagi-Uda antennas have been successfully improved radiation patterns as well as impedance mismatch loss for small impedance detectors. Trap-loaded antennas have been designed in parallel arrays and successfully applied for plasma diagnostics. The lens-coupled patch antennas have been shown ideal radiation patterns and the stacked microstrip configuration has made possible to fabricate multi function arrays monolithically.

ACKNOWLEDGMENT

The authors wish to thank Prof. D. B. Rutledge and Dr. T. Suzuki for their valuable discussion and suggestions and also thank Sanyo Electric Co. Ltd. for kindly providing Schottky diodes. The authors also acknowledge Prof. A. Mase and Dr. K. Hattori of University of Tsukuba for collaborative research on the plasma diagnostics.

REFERENCES

[1] K. Mizuno, Y. Daiku, and S. Ono, "Design of printed resonant antennas for monolithic-diode detectors," *IEEE Trans. Microwave Theory Tech.* , vol. MTT-25, pp. 470-472, Jun. 1977.

[2] Y. Daiku, K. Mizuno, and S. Ono, "Dielectric plate antenna for monolithic Schottky-diode detectors," *Infrared Physics*, vol. 18, pp. 697-682, 1978.

[3] K. Mizuno, K. Uehara, H. Nishimura, T. Yonekura, and T. Suzuki, "Yagi-Uda array for millimeter-wave imaging," *Electronics Letters*, vol. 27, No. 2, pp. 108-109, Jan. 1991.

[4] D. B. Rutledge and M. S. Muha, "Imaging array," *IEEE Trans. Antennas Propagat.* , vol. AP-30, pp. 535-540, Jul. 1982.

[5] K. Uehara, T. Yonekura, H. Nishimura, K. Miyashita, and K. Mizuno, "Millimeter-wave Yagi-Uda antenna imaging arrays," *The 3rd Asia-Pacific Microwave Conference Proceedings*, pp. 365-368, 1990.

Fundamental Mode Operation of Gunn Devices Above 100 GHz[1]

R. Kamoua, J. R. East, and G. I. Haddad
Center for High Frequency Microelectronics
Solid State Electronics Laboratory
Department of Electrical Engineering and Computer Science
The University of Michigan, Ann Arbor, MI 48109-2122

Abstract

An Ensemble Monte Carlo model capable of predicting the high frequency performance of Gunn devices has been developed. Conventional structures (ohmic cathode) with a linearly graded doping in the active region are predicted to generate rf power at frequencies up to 220 GHz. We have also compared Gunn devices with three types of heterojunction injectors at the cathode : a forward biased triangular barrier, a reverse biased triangular barrier, and a rectangular barrier. In general the optimum frequency for power generation decreases as the injector becomes more efficient in reducing the dead zone. InP Gunn devices resulted in a slightly higher oscillation frequency and output power, however the temperature increase is much larger than GaAs devices.

I INTRODUCTION

The high frequency limit of GaAs Gunn devices in the fundamental mode is generally estimated to be less than 100GHz [1]. This limit is due to intrinsic and extrinsic sources. The intrinsic limitations are related to the physics of the semiconductor and the processes responsible for the Gunn effect. The dominant aspect of Gunn operation at very high frequencies is the fact that the transit time becomes comparable to the nucleation time or the collection time of the accumulation layer. Eventually as the frequency increases, the oscillation period becomes less than the time necessary to nucleate and collect an accumulation layer and the Gunn effect disappears. The short transit time requires a short transit region. At frequencies above 100GHz, the device length should be in the submicron range assuming transit time mode of operation. The susceptance of the Gunn diode increases as the transit region becomes shorter and the frequency is higher. As a

[1]This work was supported by the Center for Space Terahertz Technology under Contract No. NAGW-1334

result, the area required to match to a given load becomes smaller and the output power decreases. A smaller area will also result in a higher series resistance which reduces the circuit efficiency and the power delivered to the load. Independent of the frequency of oscillation, an inactive region required by cold electrons streaming from the cathode to gain enough energy and transfer to the upper valleys exists. As the frequency increases, this inactive region represents a larger fraction of the total transit region. For example in a 1 micron device, the inactive region occupies more than half of the device length. Another important aspect of Gunn device operation is the heat dissipation since most of the input power is not converted to rf power. As the operating temperature increases, the average velocity and the differential negative resistance decrease. This results in a lower oscillation frequency and less output power.

The extrinsic limitations are related to the material growth, fabrication process, mounting and packaging of the device, and the design of a resonant circuit. In order to reduce the series resistance, we need to remove the substrate and optimize the specific contact resistance of the cathode and anode contacts. The mounting and packaging of the Gunn diode are very critical steps because they introduce parasitic resistors, stray capacitors, and lead inductors that can reduce the negative resistance and the output power. The design of a resonant waveguide cavity is difficult at high frequencies because the dimensions of the waveguide are very small. The waveguide is also required to present the diode with a low impedance in order to get useful power.

In this paper, we investigate in more detail the high frequency limitations of GaAs and InP Gunn devices operating in the fundamental mode. We present simulation results using a self consistent Ensemble Monte Carlo model on 1 μm devices with n^+ ohmic contacts as well as heterostructure injectors at the cathode. We consider the effects of the series resistance and the temperature rise on the output power and efficiency versus frequency. We also present simulations on InP devices with n^+ contacts having the same structure as GaAs devices.

II GUNN STRUCTURE

The simulated Gunn structure is shown in Fig. 1. It consists of a $0.1\mu m$ cathode region doped at $2 \times 10^{17} cm^{-3}$, a $0.1\mu m$ heterostructure injector, a $1\mu m$ active region with a linearly graded doping increasing from the cathode toward the anode, and finally a $0.2\mu m$ anode region doped at $2 \times 10^{17} cm^{-3}$. In the case of GaAs diodes, the injector region consists of an AlGaAs layer with an aluminum composition varying from x = x_1 to x = x_2. Three types of injectors are considered: the first 'forward injector' has $x_1 = 0$ and $x_2 = 0.05$, the second 'reverse injector' has $x_1 = 0.05$ and $x_2 = 0$, and the

N^+	Injector	Linearly graded	N^+
$2 \times 10^{17} cm^{-3}$	N_B	$1 \times 10^{16} - 3 \times 10^{16} cm^{-3}$	$2 \times 10^{17} cm^{-3}$
GaAs	$Al_xGa_{1-x}As$	GaAs	GaAs

$x = x_1$ $x = x_2$

$0.1\mu m$ $0.1\mu m$ $1\mu m$ $0.2\mu m$

Figure 1: Doping profile of the simulated Gunn structure.

third 'rectangular injector' has $x_1 = 0.05$ and $x_2 = 0.05$. Only n^+ ohmic contacts are considered for the case of InP devices.

III SIMULATION MODEL

The results described in this paper are obtained by using an Ensemble Monte Carlo model which includes three nonparabolic valleys Γ, L, and X. The following scattering mechanisms are included: acoustic, ionized impurity, polar optical phonon, alloy, intervalley, and intravalley scattering. The material parameters are very critical, however values found in the literature vary among different sources. In our simulations, most of the parameters are taken from[2], and [3]. In the case of the heterostructure barrier injector in the cathode region, the material parameters and the effective mass have values that vary with position.

Since the electric field in Gunn structures is nonuniform, the model should be self consistent. In order to update the electric field along the structure, Poisson's equation is solved every 10fs. A more detailed description of the model can be found elsewhere [4]. The device response to an applied voltage is obtained through simulation over many periods (about ten). The resulting particle current density is Fourier analyzed and the fundamental component is used to determine the conductance and susceptance per unit area which are averaged over the last eight r.f. periods. The dc current density is given by:

$$J_{dc} = \frac{1}{2\pi} \int_0^{2\pi} J(\omega t) d(\omega t) \tag{1}$$

The fundamental component of the current density is expressed as:

$$J_{Fun} = (a_1)cos(\omega t) + (b_1)sin(\omega t) \tag{2}$$

where,

$$a_1 = \frac{2}{T}\int_0^T J(t)cos(\omega t)dt \tag{3}$$

$$b_1 = \frac{2}{T}\int_0^T J(t)sin(\omega t)dt \tag{4}$$

The applied voltage consists of a dc and rf components:

$$V(t) = V_{dc} + V_{rf}sin(\omega t) \tag{5}$$

The device admittance per unit area is :

$$Y_D = J_{Fun}(t)/V(t) = -G_D + jB_D \tag{6}$$

where,

$$G_D = \frac{-b_1}{V_{rf}} \tag{7}$$

$$B_D = \frac{a_1}{V_{rf}} + \frac{\omega\epsilon}{W} \tag{8}$$

In the expression for B_D, the cold capacitance has been added since the displacement current was not taken into account in $J(\omega t)$. The generated rf power is given by:

$$P_{rf}(Gen.) = \frac{1}{2}V_{rf}^2 AG_D, \tag{9}$$

where A is the device area. The rf power across the load R_L is :

$$P_{rf}(R_L) = P_{rf}(Gen)\frac{R_L}{R_L + R_s} \tag{10}$$

where R_s is the series resistance and is expressed as : [5]

$$R_s(f) = \frac{\rho_c + \rho_e L_e}{A} + \frac{\rho_s}{\pi\sigma}[0.5ln(\frac{b}{d}) + \frac{h}{b} + 0.5] \tag{11}$$

where,

ρ_c = specific contact resistance $\Omega.cm^2$ (1×10^7),
ρ_e = epilayer resistivity in $\Omega.cm$ (ρ_n = 3.7 $\times 10^{-4}$),
ρ_s = heat sink resistivity in $\Omega.cm$ (for Gold ρ_s = 2.35 $\times 10^{-6}$),
L_e = length of the contact regions,
σ = skin depth in cm given by : $\sqrt{(\frac{2\rho_s}{\mu\omega})}$,
b = heat sink diameter (0.02 cm),
h = height of the heat sink (0.005 cm),
d = diode diameter in cm.

In order to obtain the output rf power we need to evaluate the device area. The area is determined by satisfying the oscillation condition which is expressed as:

$$X_d + X_L = 0 \quad (12)$$

$$R_d + R_s + R_L = 0 \quad (13)$$

where, $Z_d = R_d + jX_d$ is the total device impedance which can be expressed as :

$$Z_d = \frac{1}{AY_D} = \frac{1}{A}[\frac{-G_D}{G_D^2 + B_D^2} - j\frac{B_D}{G_D^2 + B_D^2}], \quad (14)$$

and $Z_L = R_L + jX_L$ is the load impedance.

From equations (13), (11), and (14), the area can be expressed as:

$$A = [\frac{G_D}{G_D^2 + B_D^2} - \rho_c - \rho_e L_e]/[R_{hs} + R_L] \quad (15)$$

Since the area has to be larger than zero, the specific contact resistance ρ_c has to satisfy the following condition :

$$\rho_c \leq \frac{G_D}{G_D^2 + B_D^2} - \rho_e L_e \quad (16)$$

Substituting the expression for the area in (10), we obtain the rf power delivered to the load R_L :

$$P_{rf}(R_L) = \frac{V_{rf}^2}{2}\frac{[G_D - (\rho_c + \rho_e L_e)(G_D^2 + B_D^2)]^2}{G_D^2 + B_D^2}\frac{R_L}{(R_{hs} + R_L)^2} \quad (17)$$

where,

$$R_{hs} = \frac{\rho_s}{\pi\sigma}[0.5ln(\frac{b}{d}) + \frac{h}{b} + 0.5] \quad (18)$$

III-A THERMAL EFFECTS

Gunn devices at millimeter wave frequencies have very low efficiencies and most of the input power is dissipated as heat. As the device temperature increases, the following may occur [6] :

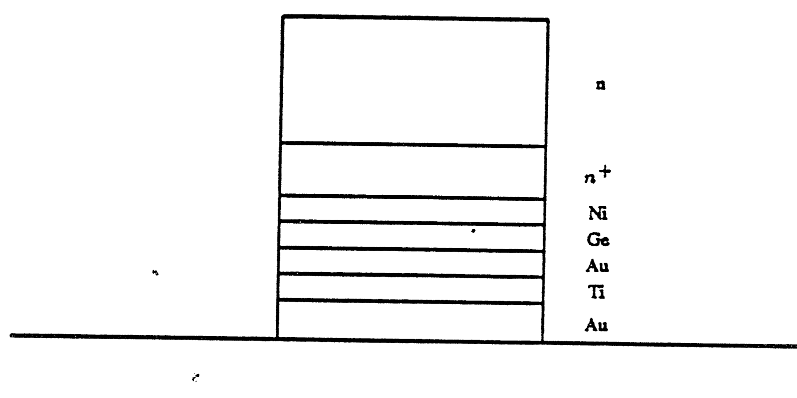

Figure 2: Gunn device mesa structure mounted on a heat sink

- The Arsenic starts to evaporate at 620 $^\circ C$,
- The material becomes intrinsic around 450 $^\circ C$,
- The alloy contacts melt at 350 $^\circ C$,
- The average electron velocity decreases.

From the above considerations it is important to provide a suitable heat sink which should be placed near the anode region where the electric field is highest. The maximum tolerable temperature increase is set to 225 $^\circ C$.
Assuming the heat flows toward the heat sink, the maximum temperature occurs at the top of the active region (Fig. 2). In order to determine the maximum temperature in the device, the heat flow equation in each region has to be solved.

$$\frac{d}{dz}(\kappa \frac{dT}{dz}) = -q(z) \tag{19}$$

where,
q = heat generated per unit volume,
κ = thermal conductivity.
Taking into account the temperature dependence of the thermal conductivity, the maximum temperature is expressed as:[7]

$$T_{max} = [T_A + \frac{P}{A}(\frac{d_c}{\kappa_{eff}} + \frac{\sqrt{(\frac{A}{\pi}}}{\kappa_{hs}})]exp[\frac{P}{A}(\frac{W}{4a_1} + \frac{\epsilon}{a_2})] \tag{20}$$

where,
T_A = ambient temperature
P = total dissipated power
A = device area
κ_{eff} = effective thermal conductivity of the contact
κ_{hs} = heat sink thermal conductivity (3.8 $\frac{W}{cm.^{\circ}K}$ for copper)
W = active area thickness
ϵ = thickness of the n^+ region
a_1, a_2 defined as :

$$\kappa_a = \frac{a_1}{T} \tag{21}$$

$$\kappa_{n^+} = \frac{a_2}{T} \tag{22}$$

where,
κ_a = active region thermal conductivity (150 $\frac{W}{cm.^{\circ}K}$ in GaAs),
κ_{n^+} = n^+ region thermal conductivity (120 $\frac{W}{cm.^{\circ}K}$ in GaAs).

$$d_c = d_{Ni} + d_{Ge} + d_{Au} + d_{Ti} \tag{23}$$

d_{Ni} = thickness of Nickel layer (250 Å),
d_{Ge} = thickness of germanium layer (325 Å),
d_{Au} = thickness of Gold layers (2650 Å),
d_{Ti} = thickness of Titanium layer (100 Å),

$$\kappa_{eff} = \frac{d_c}{(\frac{d_{Ni}}{\kappa_{Ni}} + \frac{d_{Ge}}{\kappa_{Ge}} + \frac{d_{Au}}{\kappa_{Au}} + \frac{d_{Ti}}{\kappa_{Ti}})} \tag{24}$$

κ_{Ni} = Nickel thermal conductivity (0.9 $\frac{W}{cm^{\circ}C}$ at 300 $^{\circ}K$),
κ_{Ge} = Germanium thermal conductivity (0.6 $\frac{W}{cm^{\circ}C}$ at 300 $^{\circ}K$),
κ_{Au} = Gold thermal conductivity (3.18 $\frac{W}{cm^{\circ}C}$ at 300 $^{\circ}K$),
κ_{Ti} = Titanium thermal conductivity (0.219 $\frac{W}{cm^{\circ}C}$ at 300 $^{\circ}K$).
The total thermal resistance is defined as:

$$R_{Th} = \frac{T_{max} - T_A}{P_{dc}} \tag{25}$$

IV SIMULATION RESULTS

All the results presented below correspond to a Gunn device operated at 300 $^{\circ}K$. The power is obtained by matching the device to a 10 Ω load.

IV-A GAAS DEVICES

IV-A.1 OHMIC INJECTOR CATHODE

In this structure, the cathode region consists of an n^+ layer and no heterojunction barrier is present. Fig. 3a shows the output power and efficiency as a function of frequency for Vdc = 2V and Vrf = 0.4V. The oscillations occur over a wide range of frequencies from 120 to 240 GHz. The efficiency has a peak of 1.5 % at 220 GHz and the power reaches a maximum of 5.3 mW at 180 GHz. The power peaks at a lower frequency than the efficiency because the power is proportional to the efficiency and the area which decreases with frequency.

The maximum power possible at 180 GHz is obtained by varying the rf voltage. Fig. 3b shows the efficiency and power as a function of the rf voltage for Vdc = 2V. A maximum power of 10.5 mW occurs when Vrf = 0.7V with an efficiency of 2.77 % and temperature rise of 68 $^{\circ}K$. A higher output power may be obtained by matching to a smaller load which results in a larger device area and requires more dc power. However the much higher operating temperature results in a lower oscillation frequency and smaller output power because the the 'dead zone' and the carrier velocity are reduced.

The evolution of an accumulation layer is conveyed by plotting the electric field (Fig. 4) across the device at equally spaced time intervals of $\frac{T}{8}$, where T is the period. The variation of the electric field is small in a region near the cathode and is larger toward the anode. Nearly half of the transit region corresponds to a 'dead zone' where most of the electrons did not gain enough energy to transfer to the upper valleys.

The oscillation frequency is frequently estimated from the transit time requirements assuming a drift velocity between 8×10^6 and $1 \times 10^7 \frac{cm}{s}$. For devices in the micron range this is not valid because the transit time is no longer the dominant process in a given cycle. The accumulation layer formation and collection times are comparable to the transit time. A 1 μm device is expected to generate fundamental oscillation at a frequency between 80 GHz and 100 GHz. However, taking into account the overlap in time between the three phases of an accumulation layer (or dipole domain): nucleation,

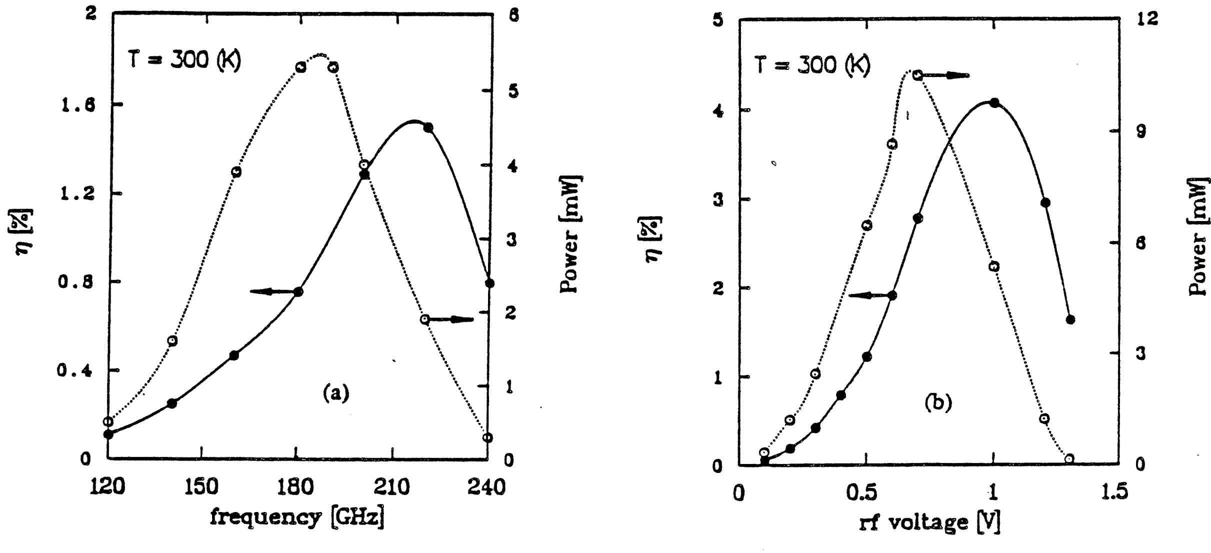

Figure 3: Output power and efficiency for a GaAs diode with ohmic injection, Vdc = 2.0 V: a) versus frequency for Vrf = 0.4 V. b) versus rf voltage for f = 180 GHz.

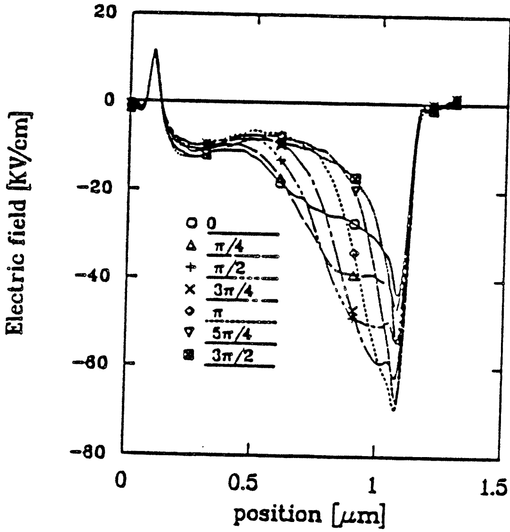

Figure 4: Electric field across the ohmic injector GaAs diode.

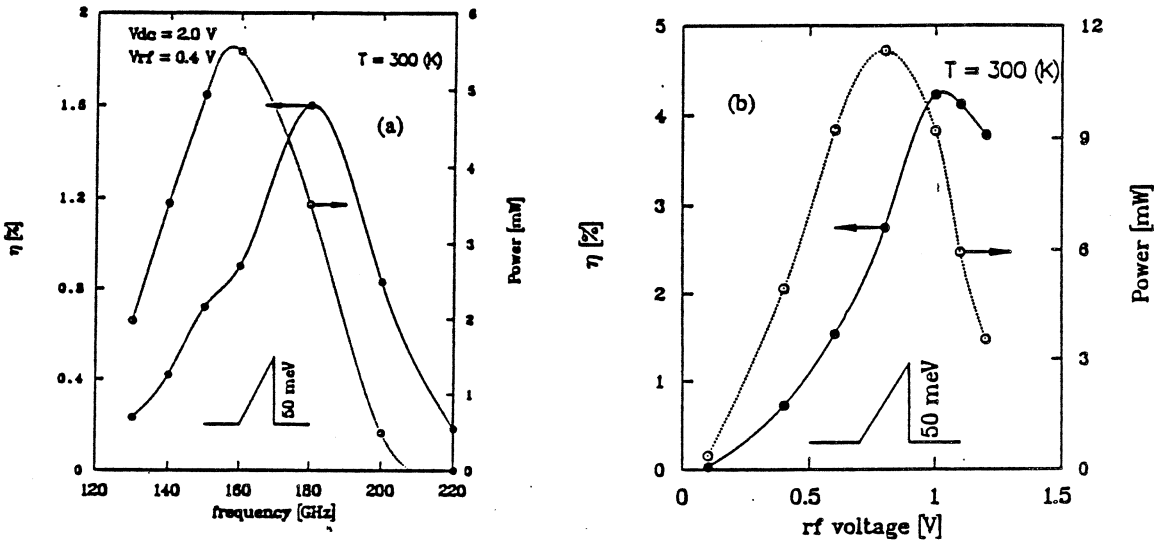

Figure 5: Output power and efficiency for a GaAs diode with a 'forward barrier' injector, Vdc = 2.0 V: a) versus frequency for Vrf = 0.4 V. b) versus rf voltage for f = 150 GHz.

transit, collection and the reduction of the effective transit length due to the dead zone explains the oscillations at frequencies around 180 GHz.

At 180 GHz a 20 μm diameter diode is needed in order to be matched to 10 Ω load. At higher frequencies smaller diodes are required which complicates the bonding process. Increasing the area results in a higher output power but requires matching to a smaller load and mounting the device on a better heat sink.

IV-A.2 'FORWARD INJECTOR' HETEROJUNCTION CATHODE

This structure is similar to the previous one, except a heterojunction triangular barrier injector is added at the end of the n^+ cathode region. Fig. 5a shows the efficiency and output power as a function of frequency for a 50 meV barrier, 0.1 μm wide. The efficiency has a maximum of 1.6 % which occurs at 180 GHz and the power reaches a maximum of 5.5 mW at 160 GHz. In fig. 5b, the effect of changing the rf voltage on the efficiency and power is shown for a frequency of 150 GHz and Vdc = 2 V. When Vrf = 0.8 V, the power reaches a maximum of 11.3 mW with an efficiency of 2.75 %, a temperature rise of 57 $^\circ K$, and a diode diameter of 23 μm. The lower oscillation frequency compared with the previous structure is a result of the 'dead zone' reduction as can be seen in fig. 6 which shows the electric field along the structure. The electric field has a maximum of 45 $\frac{kV}{cm}$ compared with 70 $\frac{kV}{cm}$ in the conventional structure. The lower peak electric field is due to the voltage drop inside the injector region. The addition of

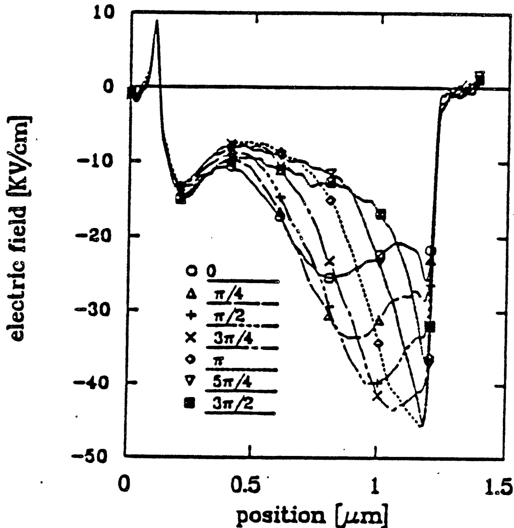

Figure 6: Electric field across the 'forward' barrier injector GaAs diode.

the 'forward injector' has resulted in a shorter 'dead zone' region, smaller temperature rise, lower oscillation frequency, and more power at this frequency.

IV-A.3 'REVERSE INJECTOR' HETEROJUNCTION CATHODE

The barrier injector is similar to the 'forward injector' except that the abrupt side is toward the cathode. Fig. 7a shows the efficiency and output power as a function of frequency. The maximum power is 4 mW and occurs at 150 GHz while the maximum efficiency is 1.2 % at 160 GHz. At 150 GHz and Vdc = 2 V, the maximum power is 5.3 mW when Vrf = 0.6 V (fig. 7b). At this operating point the temperature rise is 41 $^{\circ}K$.

The further reduction in the oscillation frequency compared with the 'forward injector' suggests that the 'reverse barrier' is more effective in reducing the 'dead zone'. This is confirmed by observing the electric field across the structure (fig. 8) which shows clearly a smaller inactive region. We notice also that a domain is formed instead of accumulation layer.

IV-A.4 'RECTANGULAR INJECTOR' HETEROJUNCTION CATHODE

The last cathode injector considered for GaAs Gunn devices is a rectangular barrier 50 meV high. The efficiency and output power as a function of frequency are shown in fig. 9a. The maximum output power is 3 mW at 140 GHz and the maximum efficiency is 0.9 % at 160 GHz. At 140 GHz, the maximum output power possible is 6.7 mW

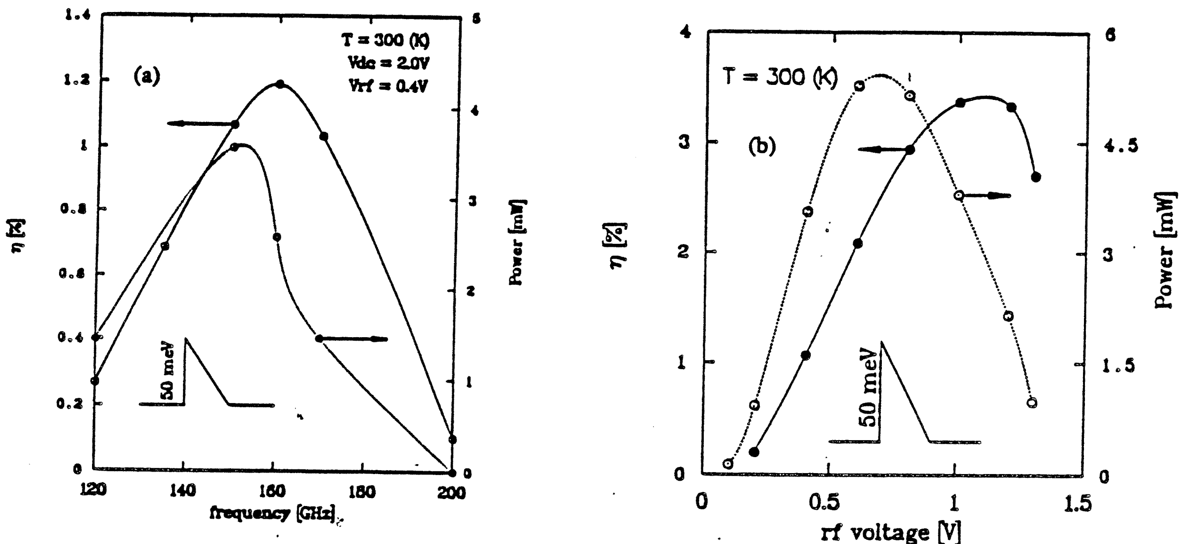

Figure 7: Output power and efficiency for a GaAs diode with a 'reverse' barrier injector, Vdc = 2.0 V: a) versus frequency for Vrf = 0.4 V. b) versus rf voltage for f = 150 GHz.

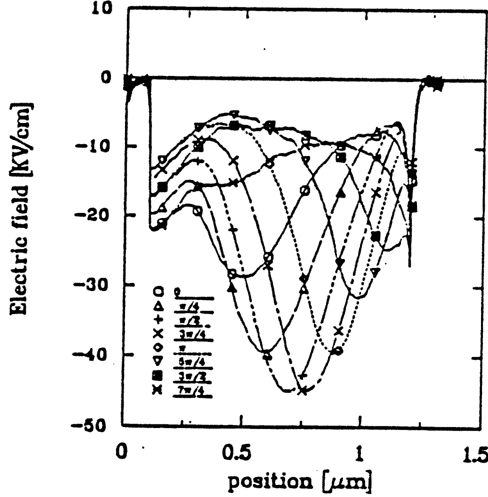

Figure 8: Electric field across the 'reverse' barrier injector GaAs diode.

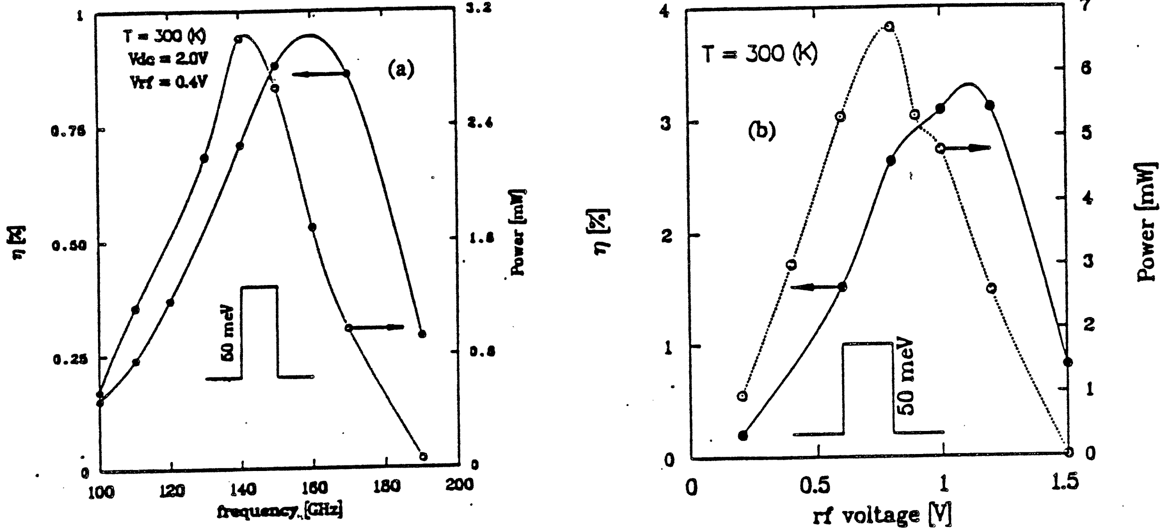

Figure 9: Output power and efficiency for a GaAs diode with a 'rectangular' barrier injector, Vdc = 2.0 V: a) versus frequency for Vrf = 0.4 V. b) versus rf voltage for f = 150 GHz.

for Vrf = 0.8 V with an efficiency of 2.6 %, a temperature rise of 40 $^{\circ}K$, and a diode diameter of 21 μm (fig. 9b). The electric field is not shown since it is similar to the previous structure except that the variation in the field near the cathode is smaller in the 'rectangular barrier' case.

IV-B InP Gunn DEVICES

InP Gunn devices with a similar structure and doping profile to the ohmic injector GaAs devices are also simulated. Compared with GaAs, InP has a higher energy separation between the Γ and L valley, stronger intervalley scattering mechanisms, and higher electron velocity. As a result a higher dc voltage is needed to observe the Gunn effect. A dc voltage of 6 V is found to result in the best performance. Fig. 10a plots the efficiency and output power as a function of frequency for Vrf = 1.2 . We notice that oscillations extend from 120 GHz to 270 GHz which is slightly higher than in GaAs devices. The maximum efficiency is 1.2 % which occurs at 220 GHz and the maximum output power is 11.2 mW at 200 GHz. Fig. 10b is a plot of the efficiency and power as a function of the rf voltage at 200 GHz. The maximum output power is 15.2 mW at Vrf = 1.5V. At this operating point the diode diameter is 18 μm, the efficiency is 1.35 %, and the temperature rises by 200 $^{\circ}K$. The electric field is plotted in fig. 11 which shows a smaller 'dead zone' region compared with the similar GaAs structure. The peak electric

field of 170 $\frac{KV}{cm}$ near the anode is much larger than inside the GaAs device which may lead to electronic failures.

It has been reported [8] that InP devices with a current limiting contact such as a Schottky barrier result in a better performance than n^+ ohmic cathode devices. This can be explained by the fact that a current limiting contact will result in a smaller dc power, peak electric field, and maximum temperature rise. Although the dc power is reduced, the actual output rf power is increased because Gunn devices operate much better at low temperatures.

V CONCLUSIONS

We have performed computer simulations on GaAs and InP Gunn devices. Structures with the conventional n^+ ohmic injector resulted in the highest oscillation frequency. Three types of injectors in the cathode region have been considered. The 'reverse barrier' and the 'rectangular barrier' are more effective in reducing the dead zone than the 'forward injector' but generate less power. It is possible to decrease the 'dead zone' even further by increasing the barrier height. However a point is reached where the fraction of electrons in the upper valleys is large in most of the device. This results in a smaller variation of the current density during one cycle and degrades the performance.

The 'dead zone' is considered to be a parasitic positive series resistance and as such its reduction is advantageous. However according to the results presented in this paper this inactive region is not necessarily undesirable. In order to reduce the dead zone, we need to use a cathode injector different from the ohmic injector. This non-ohmic injector, while reducing the 'dead zone', introduces itself an additional series resistance. Furthermore if we assume that the dead zone can be eliminated, then to achieve oscillations around 200 GHz requires a half micron device which has a larger cold capacitance than the $1\mu m$ structure considered above.

InP devices are capable of generating more power and oscillating at higher frequencies than GaAs devices. However as a result of the larger dc power requirements, the temperature rise is much larger than inside GaAs devices. This requires the use of better heat sinks such as diamond or reducing the device area wich results in smaller output power.

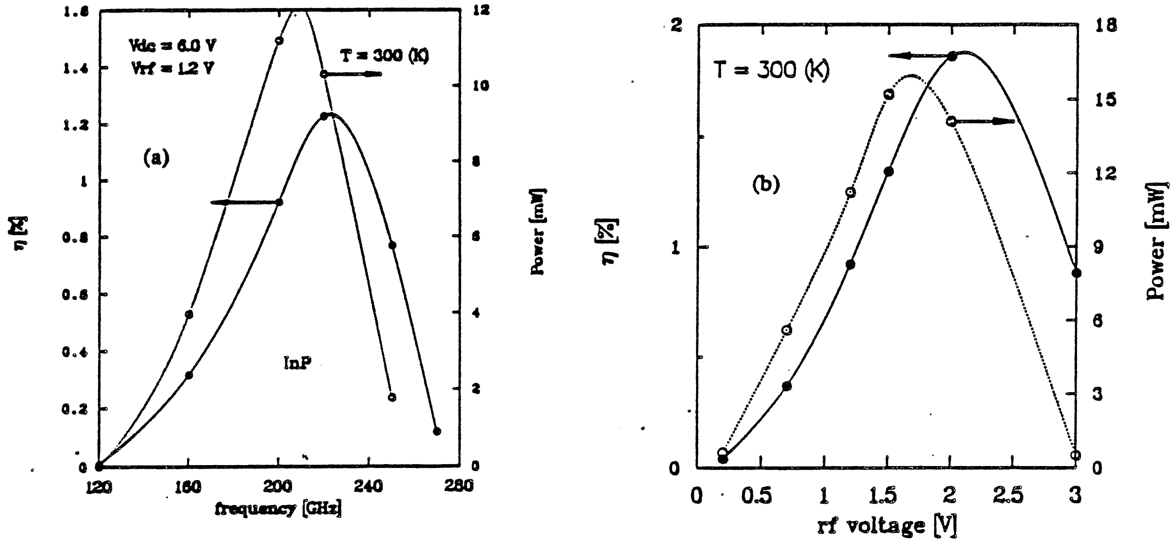

Figure 10: Output power and efficiency for an InP diode with ohmic cathode, Vdc = 6.0 V: a) versus frequency for Vrf = 1.2 V. b) versus rf voltage for f = 200 GHz.

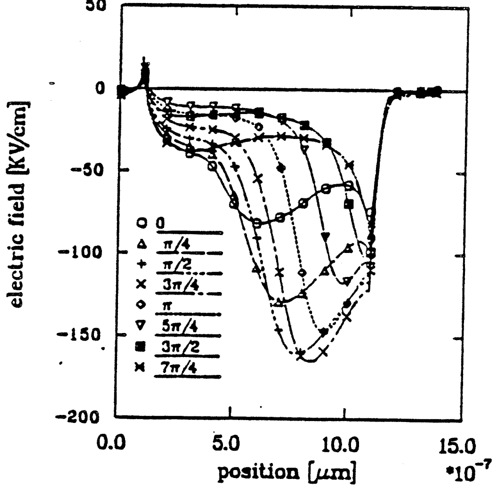

Figure 11: Electric field across the InP Gunn diode.

References

[1] M. J. Lazarus, F. R. Pantoja, S. Novak, and M. G. Somekh, Electron. lett., **17**, No. 20, pp. 739 (1981).

[2] S. Adachi, J. Appl. Phys., **58**(3), pp. 3825 (1987).

[3] M. A. Littlejohn, J. Appl. Phys., **48**, No. 11, pp. 4587 (1977).

[4] R. Kamoua, J. R. East, and G. I. Haddad, J. Appl. Phys., **68**(3), pp. 1114 (1990).

[5] L. E. Dickens, IEEE trans. on M.T.T., Vol. MTT-15, No. 2, pp. 101-109, February. 1967.

[6] B. G. Bosch, R. W. H. Engelmann, Gunn Effect Electronics, (Wiley & Sons, New York, 1974).

[7] A. S. Clorfeine, The Microwave Journal, March 1968, pp. 93.

[8] J. D. Crowley, J. J. Sowers, B. A. Janis, and F. B. Fank, Electron. lett., **16**, No. 18, pp. 705 (1980).

Design and Evaluation of W and D Band TUNNETT Devices [1]

C. Kidner, G. I. Haddad, J. R. East and H. Eisele
Solid-State Electronics Laboratory
Department of Electrical Engineering and Computer Science
University of Michigan
Ann Arbor, Michigan, 48109-2122

Abstract

Preliminary estimates of the power generation capability of Tunnel Transit Time (TUNNETT) devices in the 100-1000 GHz range are promising. A straight forward TUNNETT design procedure based on experimental characterization of the tunnel injector is outlined. A GaAs tunnel injector has been characterized and a nominal 100 GHz design is given. Preliminary results for tunnel injectors using InGaAs lattice matched to InP are described. The Gilden and Hines small signal analysis of transit time devices is modified and applied to TUNNETT devices. The RC time constant of the tunnel injector is shown to be an important figure of merit.

[1] This work was supported by the Center for Space Terahertz Technology under contract No. NAGW-1334

1. Introduction

Two terminal transit time devices are strong candidates for high frequency power generation. IMPATT devices have demonstrated high power capabilities for frequencies up to 100 GHz. The technology at higher frequencies is not as mature, but preliminary work is promising [1–4]. At very high frequencies IMPATTTs are expected to give way to MITATTs and TUNNETTs as fundamental sources. Transit time devices are also attractive due to their relatively simple biasing requirements. Since they do not have intrinsic negative resistance at low frequencies it is relatively simple to suppress bias circuit oscillations.

While IMPATTs are useful devices, they do have limitations. Due to the avalanche multiplication, shot noise in IMPATTs may be relatively high. Devices based on the avalanche process also suffer a significant decrease in efficiency at extremely high frequencies. IMPATTs are also limited because at higher frequencies the narrow active region and high doping level required lead to tunneling mechanisms becoming dominant.

TUNNETTs and MITATTs take advantage of the very fast and relatively quiet tunneling process. These devices are expected to produce significant power at extremely high frequencies. Such devices have been considered previously [5–8] and preliminary experimental results have been obtained in the 100-300 GHz range. Recent advances in material growth and processing technology will greatly improve the performance attainable from these devices.

This paper discusses the basic design and evaluation of TUNNETT devices. First order estimates of the power generation capabilities of TUNNETTs are presented using simple large signal techniques. We then discuss a procedure for designing TUNNETT structures. The design is based on the experimental characterization of the tunnel injector. Characteristics of GaAs and InGaAs injectors are presented and a 94 GHz TUNNETT design based on the GaAs injector is presented. A small signal analysis of TUNNETT structures is carried out by modifying the analysis Gilden and Hines performed on IMPATT diodes [9]. Simple expressions for the real and imaginary parts of

the device impedance are derived. The small signal results show the importance of the tunneling injector in the device operation.

2. Estimation of Expected Power Output From Conventional Single-Drift TUNNETT Devices

The TUNNETT structure we consider is shown schematically in Fig. 1. The devices of interest here will be punched through at the bias voltage and the device is designed to maintain a high field in the drift region. Under these conditions we can assume that the length of the depletion region, x_D is constant and the injected charge travels at v_s, where v_s = the saturated velocity.

The analysis is a simplified first order theory meant to give order of magnitude estimates. Details of the analysis are given in [10]. The effects of the series resistance associated with a realistic device were included and limitations due to power dissipation were also considered. The results of the analysis are given in Tables I–III for 100 GHz, 500 GHz and 1000 GHz, respectively. The analysis predicts useful power can be generated using TUNNETT devices. It can be seen from these tables that for all the cases considered except for one, the temperature rise does not exceed 225 K and therefore CW operation is feasible for these cases.

3. Design of Single-Drift TUNNETT Devices

We have developed a first order TUNNETT design prodedure which will result in a working device so that experimental studies may be carried out. The design is based on an experimental characterization of the tunnel injector. The design procedure ignores some second order effects which will be important for more optimal designs. We conclude the section with the design of a nominal 100 GHz TUNNETT using MBE grown GaAs layers.

For TUNNETT devices the optimum transit angle is $\omega\tau_D = \frac{3\pi}{2}$ and thus the drift

region length (see Fig. 1) is

$$x_D = \frac{3v_s}{4f} \quad . \tag{1}$$

It is important to keep carrier generation in the drift region low. Since the drift region is relatively long carrier generation through impact ionization can be significant. We will therefore require that

$$\int_0^{x_D} \alpha \, dx = 0.1 \tag{2}$$

where α = ionization rate = $Ae^{-(b/E)^m}$. A and b are material parameters.
For a given frequency of operation x_D is known. The magnitude of the electric field at x_D for dc bias is chosen to give saturated velocity and to keep the diffusion coefficient low. The ionization multiplication factor is found numerically for different doping levels in the drift region given an assumed $E(x_D)$. Values for a 100 GHz GaAs design are presented later.

It is difficult to accurately characterize the tunnel injector from simple theory. The basic form of the current generation as a function of the electric field is well known [11] and is expressed as

$$G_T(E) = A_T E^2 \exp\left(\frac{-B_T}{E}\right) \quad . \tag{3}$$

The constants can be found using a highly idealized analysis to be

$$A_T = \frac{1}{2\pi^2}\left[\frac{E_g}{2\pi\hbar}\right]\left[\frac{q}{E_g}\right]^2\left[\frac{2M_r^* E_g}{\hbar^2}\right]^{1/2} \tag{4}$$

and

$$B_T = \frac{\pi}{4}\left[\frac{E_g}{2\pi\hbar}\right]\left[\frac{2M_r^* E_g}{\hbar^2}\right]^{1/2} \tag{5}$$

where E_g is the semiconductor bandgap energy and M_r^* is the effective tunneling mass given by

$$M_r^* = \frac{M_c^* M_v^*}{M_c^* + M_v^*} \quad . \tag{6}$$

In eq. 6 M_c^* is the conduction band effective mass and M_v^* is the valance band effective mass. For accurate characterization of a real semiconductor material, however, the parameters A_T and B_T will require measurements.

For a first order design of a GaAs TUNNETT injector accurate knowledge of A_T and B_T is not required. In GaAs the bandgap energy is large enough that for the desired tunnel current the highest doping levels available are required. With current MBE technology this results in a one sided p^+n junction: $N_A = 5.0 \times 10^{19}/\text{cm}^3$ and $N_D = 5.0 \times 10^{18}/\text{cm}^3$. The only parameter to be calculated is the width of the highly doped n-type region, x_A. The desired dc current density is known from the large signal analysis. By measuring the zero bias capacitance and the bias required to give the correct current density in a p^+n junction without the drift region the magnitude of the field at the p^+n junction necessary to produce this current density is calculated using

$$E_{max} = \frac{qN_D}{A} C_0 \left[\frac{V_{bi} - V_A}{V_{bi}}\right]^2 \tag{7}$$

where N_D is the doping concentration, V_{bi} is the built in voltage (estimated from the forward biased IV characteristic), V_A is the applied voltage, A is the area of the diode and C_0 is the zero bias capacitance of the diode. The magnitude of the electric field at the beginning of the drift region is determined from the doping level and the length of the drift region. Thus the length of the highly doped n-type region is

$$x_A = (E_{max} - E_{drift}) \frac{\epsilon_r \epsilon_0}{qN_D} \quad . \tag{8}$$

For an InGaAs injector the situation is more complex. Due to the smaller bandgap energy the tunnel breakdown voltage of the injector can be made extremely small with doping levels using current MBE technology. In order to determine the optimum doping level available InGaAs (lattice matched to InP) p^+n^+ junctions with various nominal n^+ doping levels are being studied using MBE and gas source MBE grown material. Both growth technologies are available at our laboratory. MBE grown material with nominal doping levels of $p^+ : N_A = 1 \times 10^{19}/\text{cm}^3$ and $n^+ : N_D = \{3 \times 10^{18}/\text{cm}^3, 1 \times 10^{18}/\text{cm}^3, 3 \times 10^{17}/\text{cm}^3, 1 \times 10^{17}/\text{cm}^3\}$ have been processed into diodes. The IV curves of 90μm diameter diodes are given in Fig. 2. Higher doping levels are available with this system than those used for this study. The IV curve of a gas source MBE grown sample with nominal doping levels of $N_A = 1 \times 10^{19}/\text{cm}^3$ and

$N_D = 1\times10^{19}/\text{cm}^3$ is shown in Fig. 3. The InGaAs samples will require careful evaluation in order to give accurate estimates of the tunneling parameters A_T and B_T. A comparison of the growth techniques is under way to determine which technique is more suitable for growing TUNNETT structures.

This design procedure has been used to specify a 100 GHz (nominal) TUNNETT structure in GaAs. The electrons travel at the saturated velocity of $v_s = 10^7$ cm/s in the drift region so

$$x_D = \frac{3v_s}{4f} = 0.75\mu\text{m} \quad . \tag{9}$$

The desired field strength at the end of the drift region $(E(x_D))$ is estimated to be 100kV/cm from large signal analysis and experience with similar devices. The doping level in the drift region should be as large as possible to minimize distortions of the field profile due to the injected charge. The upper limit to the doping level is the level determined by imposing an upper limit on the impact ionization multiplication factor. For GaAs $A_i = 3.85 \times 10^5$/cm, $b = 6.85 \times 10^5$ V/cm and $m = 2$ was used. Numerically integrating eq. 2 gives a maximum doping of $N_D = 3.0\times10^{16}/\text{cm}^3$. Since the magnitude of the field at the end of the drift region (100 kV/cm), the length of the drift region (0.75μm), and the charge density in the drift region (qN_D) are known, Poisson's equation can be used to estimate the magnitude of the electric field at the beginning of the drift region to be E(0)=400k V/cm. The required current density is known from the large signal analysis to be 30 kA/cm^2. We estimate that the maximum field at the junction to be 3.23 MV/cm by characterizing the tunnel injector without a drift region and using eq. 7. The desired width of the n^+ side of the tunnel injector is calculated to be 403Å using eq. 8. If the doping level in the injector is lower than the nominal the field in the drift region will cause excessive impact ionization. To avoid this we specified the injector to be slightly longer; 420Å. This structure was grown by a source outside the University of Michigan. The doping levels of the resulting structure measured using SIMS are shown in Fig. 4. Note the Si (n-type) doping profile, particularly in the injector region, is excellent. The cause of the failure of the Be (p-type) doping is thought to be understood. A new sample has been grown and is currently being tested using SIMS analysis.

4. Small Signal Analysis of TUNNETTs

The small signal analysis of the TUNNETT follows the analysis performed by Gilden and Hines for IMPATT devices. The most important difference is that the tunnel injector is modeled as a parallel R–C circuit rather than a parallel L–C circuit, see Fig. 5. The impedance of the tunnel injector is (compare to eq. (14) in [9])

$$Z_a = \frac{R}{1 + j\omega RC_a} \tag{10}$$

while the impedance of the drift region is (compare with eq. (18) in [9])

$$Z_d = \frac{1}{j\omega C_d}\left\{1 - \frac{1}{1 + j\omega RC_a}\left(\frac{\sin\Theta}{\Theta} - j\frac{1-\cos\Theta}{\Theta}\right)\right\} \quad . \tag{11}$$

Where $R = 1/G$ = dc small signal resistance ($\Delta V/\Delta I$) of the tunnel injector. C_a = junction capacitance of the injector ($\epsilon A/x_A$). C_d = drift region capacitance ($\epsilon A/x_D$). Θ = transit angle of the drift region ($\omega x_D/v_s$). Following the analysis through for the TUNNETT case results in the small signal impedance of the device being (Z_T=R_T+jX_T)

$$R_T = \frac{\omega RC_a \sin\Theta + 1 - \cos\Theta + \omega C_d \Theta R}{\Theta\omega C_d(1 + \omega^2 R^2 C_a^2)} \tag{12}$$

$$X_T = \frac{\sin\Theta - \Theta - R\omega C_a(1-\cos\Theta) - \Theta\omega^2 R^2 C_a(C_a + C_d)}{\omega\Theta C_d(1 + \omega^2 R^2 C_a^2)} \quad . \tag{13}$$

The denominator of both terms contains the term $1 + \omega^2 R^2 C_a^2$ which implies that the RC time constant of the tunnel injector is an important figure of merit when considering a design for high frequency oscillations.

For a TUNNETT device operating at its optimum frequency ($\Theta = \frac{3}{2}\pi$),the equation for the real part of the impedance becomes

$$R_T = \frac{-\omega RC_a + 1 + \omega C_d R\Theta}{\omega C_d \Theta\,(1 + \omega^2 R^2 C_a^2)} \quad . \tag{14}$$

For very high frequencies

$$\lim_{\omega\to\infty}(R_T) = -\frac{1}{\omega^2 C_d RC_a} \quad . \tag{15}$$

Note that since C_d is proportional to the desired operating frequency the negative resistance will drop off as the cube of the frequency. The resistance of the diode is positive

for $\omega < 1/RC_a$, so a TUNNETT will not begin oscillations below the cutoff frequency of the injector. Fortunately, the small signal resistance of the injector increases as the current density is decreased. So injectors with very high cutoff frequencies can be made to operate simply by reducing the current density.

There is some ambiguity to the separate values of R and C_a since the length of the tunnel injection region is not well defined. The RC product, however, is easily obtained from low frequency measurements performed on a simple pn junction. The rate of tunnel injection varies exponentially with the electric field so it is a very close approximation to assume that the tunnel injection region is very short. Also, if space charge effects in the injector are ignored the small signal electric field is constant across the injector region. Then the small signal voltage across the injector is directly proportional to the assumed length of the injector region. Thus if the assumed length of the injector is longer than the real length of the injector (so that the current density appears independent of the length of the injector) the small signal resistance ($\frac{\partial V}{\partial I}$) is directly proportional to the assumed length. Since the capacitance is inversely proportional to the length, the RC time constant is independent of the assumed length of the injection region. So the small signal RC time constant measured using the pn junction alone is the same as that of the injector. The ambiguity in the value of R will have little effect since the $\omega C_d R \Theta$ term is small compared to the other terms for the frequencies considered here.

For the GaAs tunnel injector studied biased to give a current density of 30 kA/cm^2 the measured values were $R = 1.5\Omega$, $C_a = 5.0\,pF$, $RC_a = 7.67\,pS$. Since the resistance value is small and had to be measured at a high current value it could not be measured precisely. The measured value includes a series resistance associated with the measurement system which is of the order of half an ohm. It also includes the contact resistance, which is small, since the diodes are large. The above value is in the range expected from the standard tunneling theory. The measured value is thought to overestimate the RC time constant and should only be considered as a first order estimate. The measured value implies the 3 dB frequency for this injector is 21 GHz. The small signal impedance of the nominal 100 GHz GaAs TUNNETT design given in section 3 as a function of frequency

is shown in Fig. 6. The small signal impedance of a TUNNETT structure designed for 500 GHz is given in Fig. 7.

5. Conclusions

Preliminary estimates of the power generation capability of TUNNETT devices in the 100-1000 GHz range are promising. A straight forward TUNNETT design procedure based on experimental characterization of the tunnel injector has been outlined. A GaAs tunnel injector has been characterized and a nominal 100 GHz design has been given. Preliminary results for tunnel injectors using InGaAs lattice matched to InP has been carried out and the results are promising. The Gilden and Hines small signal analysis of transit time devices has been modified for TUNNETT devices. The RC time constant of the tunnel injector was shown to be an important figure of merit, though the injector is useful far above its cutoff frequency. It is believed that useful power at one terahertz is feasible using TUNNETT structures.

Acknowledgments The authors are grateful to Dr. W. Q. Li and Prof. P. Bhattacharya of the University of Michigan for providing the MBE InGaAs material. They are also grateful to M. Sherwin and G. Munns, both at the University of Michigan, for the gas source MBE InGaAs material.

REFERENCES

[1] W. T. Read, "A Proposed High-Frequency Negative Resistance Diode," *Bell Syst. Tech. J.*, vol. 37, (1958), p. 401.

[2] R. K. Mains and G. I. Haddad, "Properties and Capabilities of Millimeter-Wave IMPATT Diodes," *Infrared and Millimeter-Waves*, K. J. Button (Ed.), vol. 10, Part III, Chap. 3, Academic Press, Inc., New York, 1983.

[3] R. K. Mains, G. I. Haddad and P. A. Blakey, "Simulation of GaAs IMPATT Diodes Including Energy and Velocity Transport Equations," *IEEE Trans. on Electron Devices,* vol. Ed-30, No. 10, October 1983, pp. 1327–1338.

[4] H. Eisele and H. Grothe, "GaAs W-band IMPATT diodes made by MBE", *Proc. MIOP '89*, Sindelfingen, FRG, Feb. 28–March 3rd 1989, Session 3 A.6.

[5] J. Nishizawa, K. Mofoya and Y. Okuno, "GaAs TUNNETT Diodes," *IEEE Trans. on Microwave Theory and Techniques*, vol. MTT-20, No. 12, December 1978, pp. 1029–1035.

[6] M. Elta and G. I. Haddad, "High-Frequency Limitations of IMPATT, MITATT, and TUNNETT Mode Devices," (invited paper) *IEEE Trans. on Microwave Theory and Techniques*, vol. MTT-27, No. 5, May 1979, pp. 442–449.

[7] M. E. Elta, H. R. Fetterman, W. V. Macropoulas and J. J. Lambert, "150 GHz GaAs MITATT Source," *IEEE Electron Device Letters,* vol. EDL-1, No. 6, June 1980, pp. 115–116.

[8] N. S. Dogan, J. R. East, M. E. Elta and G. I. Haddad, "Millimeter-Wave Heterojunction MITATT Diodes," *IEEE Trans. on Microwave Theory and Techniques*, vol. MTT-35, No. 12, December 1987, pp. 1308–1317.

[9] M. Gilden and M. E. Hines, "Electronic Tuning Effects in the Read Microwave Avalanche Diode," *IEEE Trans. on Electron Devices*, vol. ED-13, No. 1, January 1966, pp. 169–175.

[10] G. I. Haddad, J. R. East and C. Kidner, "Tunnel Transit-Time (TUNNETT) Devices for Terahertz Sources," *Microwave and Optical Technology Letters*, vol. 4, no. 1, January 1991, pp. 23–29.

[11] E. O. Kane, "Zener Tunneling in Semiconductors," *J. Phys. Chem. Solids*, vol. 12, pp. 181-188, 1959.

Table I. Estimated Power Output Including R_s

$f = 100$ GHz

$J_{dc} = 3.1 \times 10^4$ A/cm^2 $V_{dc} = 23.2$ V

Diode Diam. (μm)	Area (cm^{-2})	$R_s(\Omega)$	$-R_d(\Omega)$	$R_L(\Omega)$	V_{RF}(V)	I_{dc}(mA)	P_{dc}(W)	P_{RF} (Gen.) (mW)	P_{RF} (R_L) (mW)	η(%)
20	3.1×10^{-6}	0.63	2.84	2.21	21.6	96	2.23	440	342	15
25	4.9×10^{-6}	0.58	1.82	1.24	21.6	150	3.48	688	468	13
30	7.1×10^{-6}	0.55	1.55	1.0	18.1	216	5.01	830	538	10.7
30	7.1×10^{-6}	1	2	1	14.6	216	5.01	667	333	6.7

Table II. Estimated Power Output Including R_s

$f = 500$ GHz

$J_{dc} = 1.8 \times 10^5$ A/cm^2; $V_{dc} = 6.7$ V

Diode Diam. (μm)	Area (cm^{-2})	$R_s(\Omega)$	$R_L(\Omega)$	$-R_d(\Omega)$	V_{RF}(V)	I_{dc} (mA)	P_{dc} (mW)	P_{RF} (Gen.) (mW)	P_{RF} (R_L) (mW)	η(%)
4	1.26×10^{-7}	2.94	2.9	5.9	3.03	22.7	150	14.6	7.3	4.8
5	1.96×10^{-7}	2.5	2.5	5.0	2.44	35.5	240	18.3	9.2	3.9
7	3.85×10^{-7}	2.0	2.0	4.1	1.71	69.5	470	25.2	12.6	2.7
10	7.85×10^{-7}	1.7	1.7	3.5	1.15	141.9	950	34.6	17.3	1.8

Table III. Estimated Power Output Including R_s
$f = 1000$ GHz
$J_{dc} = 4 \times 10^5$ A/cm^2 $V_{dc} = 4.4$ V

Diode Diam. (μm)	Area (cm^{-2})	$R_s(\Omega)$	$R_L(\Omega)$	$-R_d(\Omega)$	V_{RF}(V)	I_{dc} (mA)	P_{dc} (mW)	P_{RF} (Gen.) (mW)	P_{RF} (R_L) (mW)	η(%)
2	0.31×10^{-7}	7.24	7.24	14.48	0.930	12.47	50	2.5	1.2	2.2
3	0.71×10^{-7}	4.68	4.68	9.36	0.712	28.05	120	4.2	2.1	1.7
4	1.26×10^{-7}	3.7	3.7	7.4	0.556	49.9	220	5.9	2.9	1.3
5	1.96×10^{-7}	3.2	3.2	6.4	0.431	77.9	340	7.1	3.6	1.0

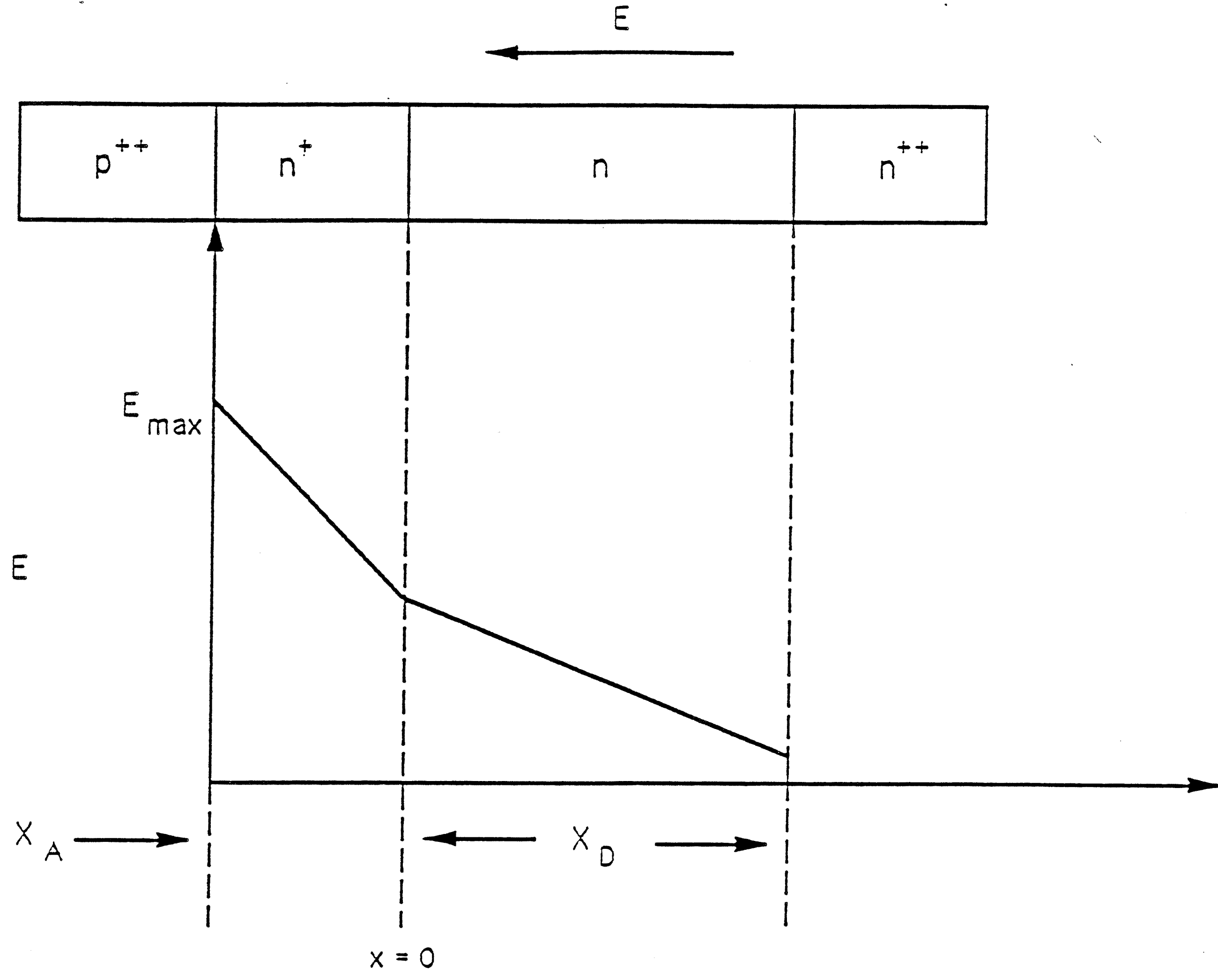

Figure 1. TUNNETT Device Structure and Electric Field Profile.

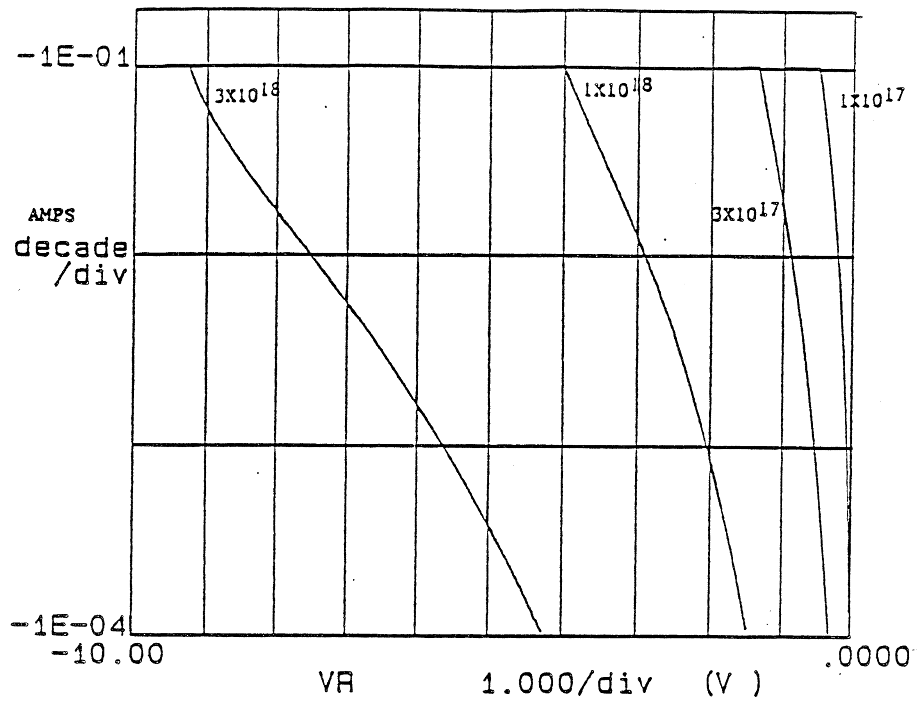

Figure 2. IV Characteristics of MBE Grown p^+n^+ Junctions under Tunnel Breakdown. $p^+ : N_A = 1 \times 10^{19}/cm^3$. From left to right $n^+ : N_D = 3 \times 10^{18}/cm^3$, $1 \times 10^{18}/cm^3$, $3 \times 10^{17}/cm^3$, $1 \times 10^{17}/cm^3$.

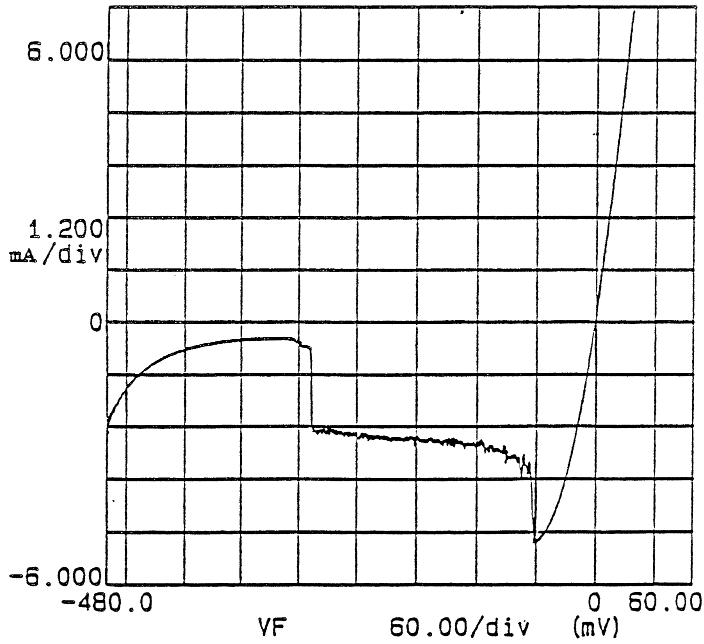

Figure 3. IV Characteristics of Gas Source MBE Grown p^+n^+ Junctions. $p^+ : N_A = 1 \times 10^{19}/cm^3$, $n^+ : N_D = 1 \times 10^{19}/cm^3$.

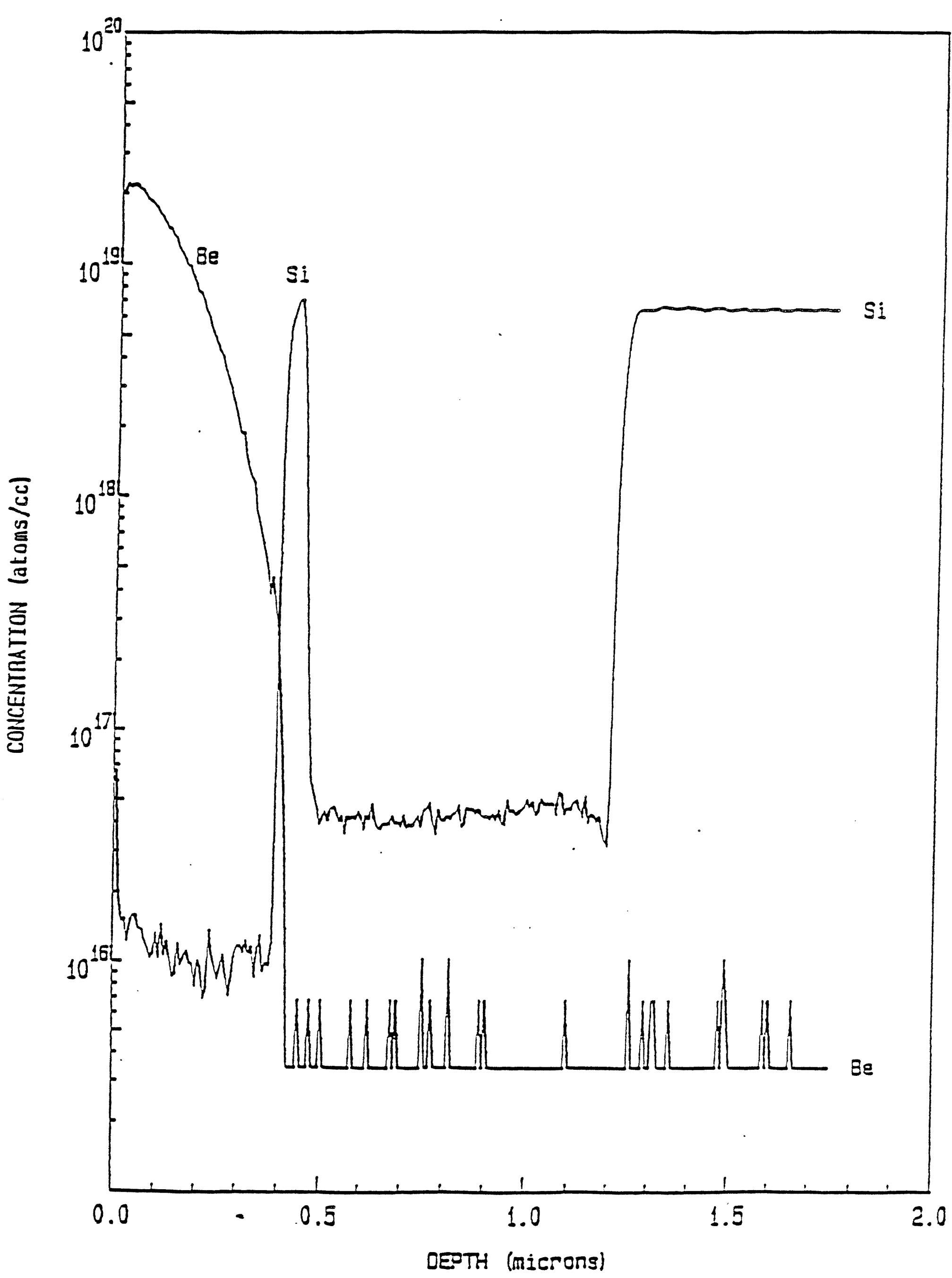

Figure 4. Doping Profile of Nominal TUNNETT Structure Measured using SIMS Analysis (note the excellent Si (n-type) doping profile).

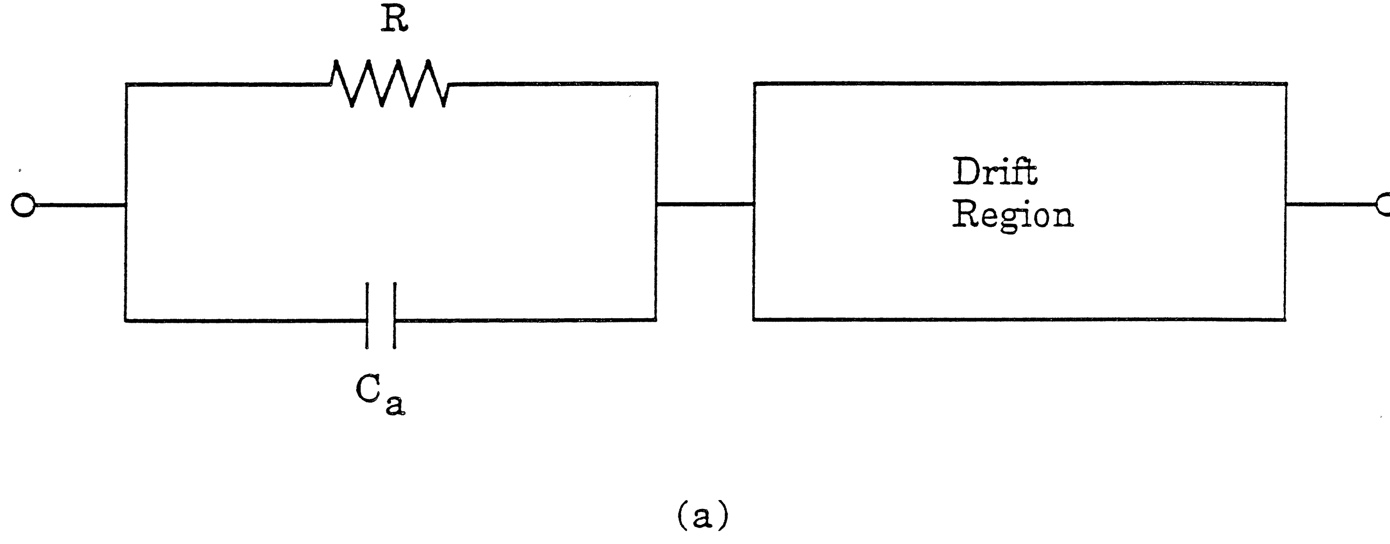

(a)

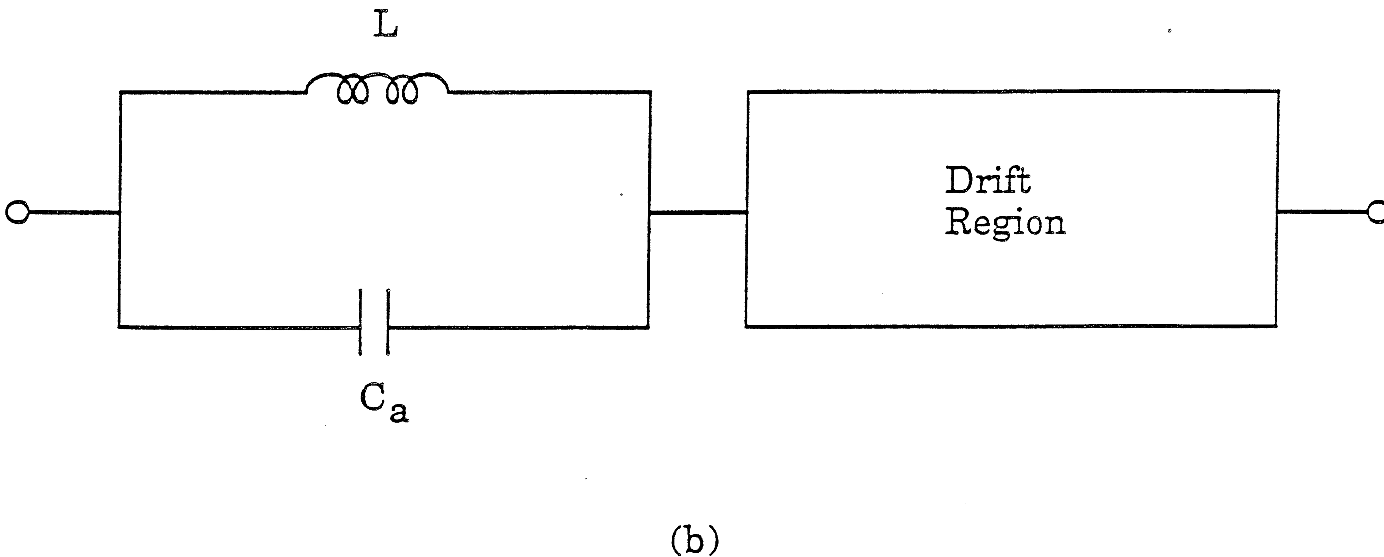

(b)

Figure 5. Small Signal Equivalent Circuit of (a) TUNNETT and (b) IMPATT diodes.

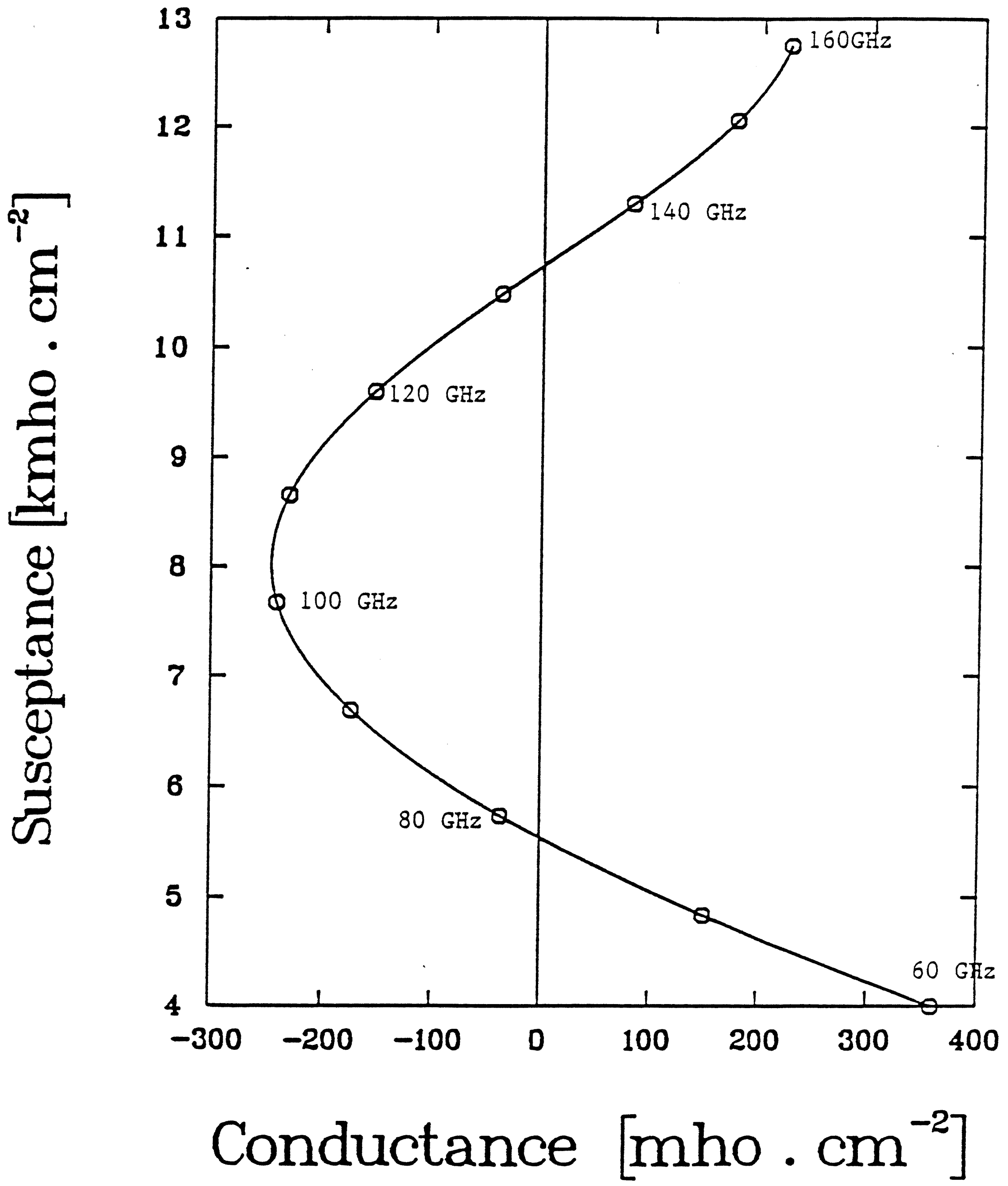

Figure 6. Small Signal Admittance per Square centimeter for a Nominal 100 GHz GaAs TUNNETT Diode using the Injector Described in the Paper (J_{DC}=30kA/cm^2).

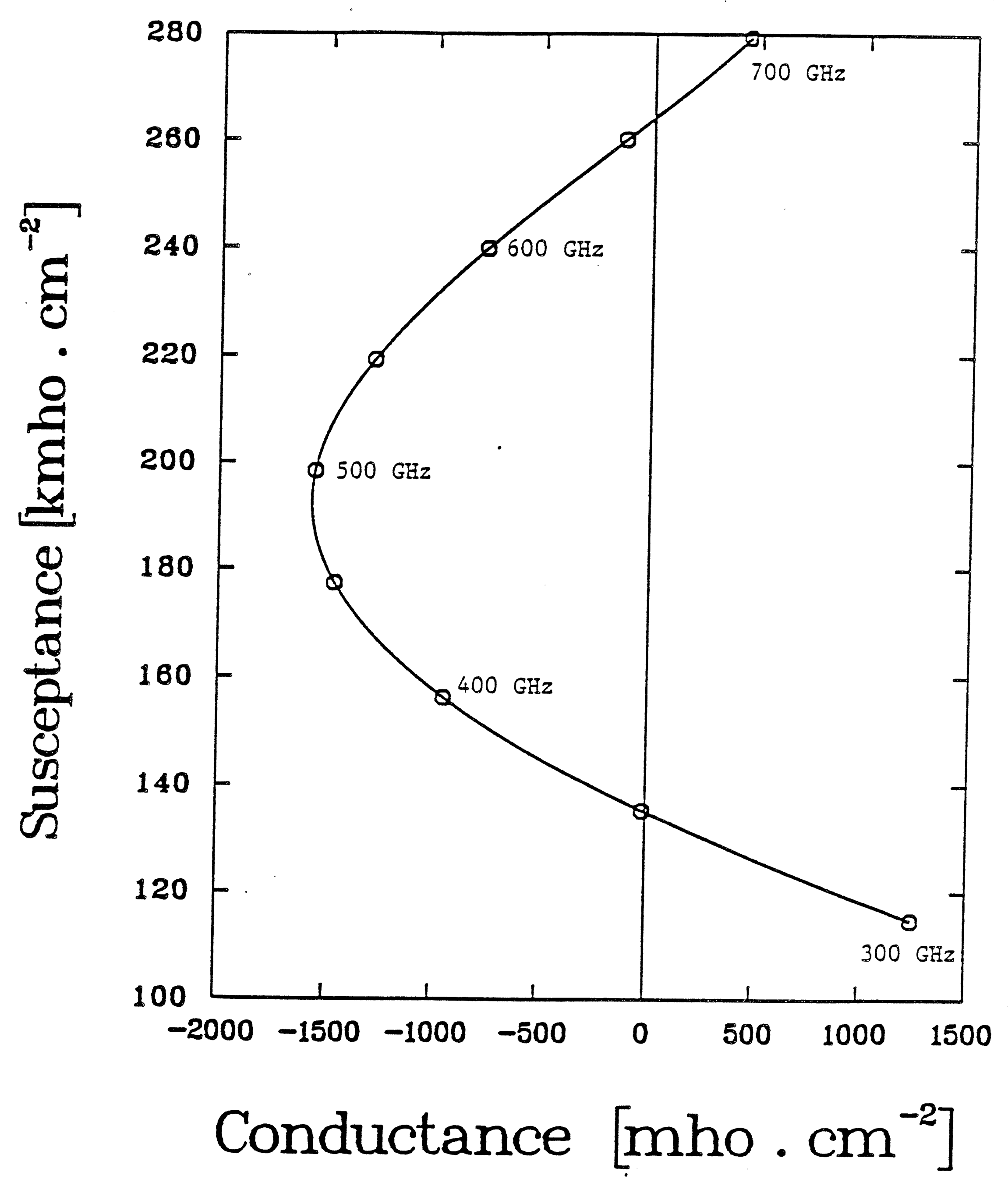

Figure 7. Small Signal Admittance per Square centimeter for a Nominal 500 GHz GaAs TUNNETT Diode using the Injector Described in the Paper (J_{DC}=30kA/cm^2).

Recent advances in resonant-tunneling-diode oscillators

E.R. Brown, C.D. Parker, K.M. Molvar, and M.K. Connors
Lincoln Laboratory, Massachusetts Institute of Technology
Lexington, MA 02173-9108

K.D. Stephan
Department of Electrical and Computer Engineering, University of Massachusetts
Amherst, MA 01003

Abstract

Oscillation frequencies between 100 and 712 GHz have been obtained in InAs/AlSb double-barrier resonant-tunneling diodes (RTDs). The power density obtained at 360 GHz was 90 W cm^{-2}, which is 50 times that obtained from GaAs/AlAs diodes at essentially the same frequency. Oscillation at 712 GHz with a power of 0.3 μW was observed, representing the highest oscillation frequency reported to date from a solid-state electronic oscillator at room temperature. A high-Q semiconfocal resonator has been used to lock a waveguide-resonator-based RTD oscillator operating at a frequency of 103 GHz. The locked-oscillator linewidth was 40 kHz, which is about 250 times narrower than the linewidth of the oscillator without the high-Q resonator.

Introduction

The double-barrier resonant-tunneling diode (RTD) has demonstrated promising high-speed characteristics as an oscillator and a switch. Until recently, most of the high-speed experiments have been conducted with RTDs made from the GaAs/AlAs material system (GaAs quantum well and cladding layers, AlAs barriers). Oscillators made from such diodes have operated at room temperature up to 420 GHz.[1] It has been shown that the maximum oscillation frequency of GaAs/AlAs RTDs, f_{max}, is limited by a high series resistance R_S and a low magnitude of differential conductance G in the negative differential conductance (NDC) region.

These shortcomings are alleviated in RTDs made from the indium-bearing material systems, $In_{0.53}Ga_{0.47}As/AlAs$[2] and InAs/AlSb.[3] The indium-bearing RTDs provide a lower R_S primarily because ohmic contacts on $In_{0.53}Ga_{0.47}As$ and InAs have lower resistance than on GaAs. In addition, indium-bearing RTDs provide a higher magnitude of G because of the larger available current density ΔJ in the NDC region, where $\Delta J = J_P - J_V$, and J_P and J_V are the peak and valley current densities, respectively. The indium-bearing materials also increase f_{max} by reducing the transit-time delay per unit depletion length on the anode side of the double-barrier structure.

Our indium-bearing RTDs are all grown by molecular-beam epitaxy. The $In_{0.53}Ga_{0.47}As/AlAs$ RTDs were grown on InP substrates, and the InAs/AlSb RTDs were grown on GaAs and InAs substrates. The current-voltage (I-V) curve of our fastest InAs/AlSb RTD tested to date is shown in Fig. 1. It has a peak-to-valley current ratio of about 3.4 at room temperature, and a peak current density of 2.8×10^5 A cm^{-2}, corresponding to $\Delta J \cong 2.0\times10^5$ A cm^{-2}. It consists of two 1.5-nm-thick undoped AlSb barriers separated by a 6.4-nm-thick undoped InAs quantum well. Below the double-barrier structure are a 75-nm-thick InAs layer doped to $N_D \cong 2\times10^{17}$ cm^{-3}, a 0.2-µm InAs layer doped to $N_D = 2\times10^{18}$ cm^{-3}, and a 0.5-µm layer doped to $N_D = 5\times10^{18}$ cm^{-3}. The former layer is designed to be fully depleted under bias. Above the double-barrier structure is a 10-nm-thick undoped InAs buffer layer, a 100-nm-thick InAs layer doped to $N_D = 2\times10^{18}$ cm^{-3} , a 100-nm-thick InAs layer doped to $N_D = 5\times10^{18}$ cm^{-3}, and a 20-nm-thick indium layer. The indium layer forms an *in situ* nonalloyed ohmic contact, as shown in the cross-sectional view in Fig. 2. The procedures used to fabricate the diode mesas are described in Ref. 3.

High-frequency chips

With RTDs intended for high-frequency oscillators, it is important to achieve a low-resistance current path from the active region of the device to the ground plane. For diodes to be tested in waveguide circuits, the low resistance is achieved in the manner shown in Fig. 2. The diode mesas are isolated by chemically etching to the top of an n^+ epilayer that is doped to a concentration of $N_D \geq 5\times10^{18}$ cm^{-3}. The wafer is then diced into small (100 × 100 µm) chips, and the sidewalls are metallized with a thin layer of electroless palladium and a thicker layer of electroplated gold. This yields a typical series resistance from the double-barrier structure to the bottom of the chip of 0.5 Ω at dc, increasing to about 1.0 Ω at 600 GHz.

It is also important with high-frequency chips to make low-resistance and stable whisker contacts. This was accomplished by fabricating the surface of the wafer into a honeycomb structure, as shown in Fig. 3. The honeycomb topology is produced by first plasma depositing approximately 1 µm of Si_3N_4 at a temperature of 200 °C. The Si_3N_4 is patterned with photoresist, and via holes extending down to the top of the mesas are opened by reactive-ion etching. In addition, the Si_3N_4 is a passivation layer for InGaAs alloys,[4] so the RTDs should operate under a number of adverse conditions.

Oscillator measurements

After fabrication the chips are mounted in one of four full-height rectangular waveguide resonators operating in frequency bands around 100, 200, 400, and 650 GHz, respectively. The design of these resonators is shown in Fig. 4. In each case, the RTD chip is mounted below a post that extends roughly halfway into the waveguide. The combination of the capacitance of the gap below the post and the inductance of the whisker create an LC resonance that is the basis for the oscillation in these waveguide structures. The highest frequency resonator constructed to date consists of a 0.015×0.030-cm (WR-1) full-height rectangular

waveguide with a contacting backshort.

Up to 400 GHz, the power of the oscillations is measured by waveguide-mounted Schottky-diode detectors. The frequency is measured by wavemeters or by down-conversion techniques. Above 600 GHz, the power is measured by coupling the radiation out of the waveguide with a pyramidal feedhorn and focusing it onto a composite bolometer. This bolometer consists of a silicon thermistor element bonded to a 377-Ω/□ absorber. The absorber is mounted in a hemispherical integrating cavity. The oscillation frequency is measured by placing a scanning Fabry-Perot spectrometer into the path between the waveguide oscillator and the bolometer. By varying the separation of mirrors of the spectrometer over a distance of about 5 cm, we were able to determine the wavelength to an accuracy of about 0.1%.

The highest power density obtained with GaAs/AlAs and InAs/AlSb RTDs in each of these resonators is shown in Fig. 5. At 360 GHz, the InAs/AlSb RTD produced a power density of about 90 W cm^{-2} and an absolute power of 3 μW. This is 50 times the power density obtained from GaAs/AlAs diodes at 370 GHz. In the WR-1 resonator, the highest power was 0.3 μW, which was obtained from a 1.8×1.8-μm InAs/AlSb RTD oscillating at 712 GHz. This corresponds to a power density of 15 W cm^{-2}. Our uncertainty in these values is about 75%, reflecting the great difficulty in calibrating power measurements in this frequency region. To determine whether the 712-GHz signal resulted from a fundamental oscillation or a harmonic of a lower frequency oscillation, we used the Fabry-Perot spectrometer to look for changes in the oscillation frequency with variations in position of the backshort. We found that the backshort tuned the output frequency by about 2 GHz. This tuning would probably not be observed if the oscillation were a harmonic, since propagation at the fundamental frequency could not occur in the waveguide, and thus the oscillation frequency would not depend on the backshort position. However, harmonic-tuning effects cannot be completely ruled out, and better techniques are needed for this determination.

Quasioptical resonator performance

A major challenge in operating solid-state oscillators at frequencies above 100 GHz is the design of the resonator. Conventional resonators, such as those based on closed cavities or radial transmission lines, exhibit an unloaded quality factor Q_u that decreases with increasing frequency because of increases in the ohmic and scattering losses of metallic surfaces. Open resonators, such as those used in lasers, provide a much higher Q_u but are difficult to integrate with lumped-element, solid-state oscillators. We have combined a waveguide RTD oscillator and a high-Q_u semiconfocal cavity to form a quasioptical oscillator operating at frequencies near 100 GHz. With no electromagnetic coupling between the waveguide and the semiconfocal cavity, the oscillator power was approximately 10 μW and the 10-dB-down linewidth was 10 MHz. With coupling to the cavity, the oscillator power decreased by about 3 dB and the linewidth decreased to roughly 40 kHz. Accompanying this reduction in linewidth was a locking of the oscillator output onto a semiconfocal-cavity mode. Our

technique provides a sufficiently narrow linewidth for local-oscillator applications in radiometers.

The schematic diagram of our quasioptical oscillator designed for the 100-GHz region is shown in Fig. 6. The RTD is mounted in a standard-height rectangular waveguide in the manner used in all of our waveguide RTD oscillators operating above 100 GHz. The diode is dc biased by a coaxial circuit that suppresses spurious oscillations by means of a very lossy section of transmission line placed in close proximity to the top wall of the waveguide. The waveguide section opens abruptly within the middle of a flat metallic wall that forms one reflector of a semiconfocal open resonator. The TEM_{00N} modes of this resonator are assumed to have a Gaussian transverse intensity profile with 1/e-point loci as shown in Fig. 6. The spot diameter of these modes at the flat reflector are designed to be about 10 times the height of the rectangular waveguide. This large spot diameter (the radiation pattern from the end of the waveguide is actually more divergent than a Gaussian mode) makes the coupling between the waveguide and the open cavity fairly weak. Weak coupling is necessary to realize a large Q_u for the open resonator. The output radiation of the oscillator is taken from the opposite end of the waveguide section. The power of the oscillator is measured by a Schottky-diode detector and the spectrum is resolved by down-converting the oscillator output to the frequency range of a microwave spectrum analyzer.

Experimental power spectra of the RTD oscillator are shown in Fig. 7. The broad spectrum in Fig. 7(a) results from the insertion of an absorbing element into the open resonator that spoils the Q_u. In this case, the oscillation is based on the waveguide LC resonance discussed previously. The width of the spectrum is roughly 10 MHz, which is unsuitable for local-oscillator applications. Upon removing the absorber, the spectrum shifts and becomes much narrower. The expansion of this spectrum, shown in Fig. 7(b), yields a linewidth of about 40 kHz. The shift in frequency is a result of the RTD oscillation being locked onto the open-cavity resonance. The narrowing is a further indication that locking has occurred and is consistent with the high Q_u of the open resonator compared to that of the waveguide resonance. The center frequency of the cavity resonance is determined, as in all Fabry-Perot resonators, by the spatial separation of the reflectors. By varying this separation, we were able to tune the locked power spectrum over a range of about 0.3 GHz at a fixed RTD bias voltage. We are presently determining the effect of the open cavity for different RTD bias voltages. For the waveguide oscillator, the center frequency could be tuned by roughly 10 GHz with variation of RTD bias voltage.

The power of the cavity-locked oscillation in Fig. 7(a) (the integral under the power spectrum) was found to be about 3 dB less than the unlocked power of approximately 10 μW. One could obtain significantly more power and maintain the advantage of quasioptical locking by implementing an array of RTD oscillators rather than the single-element oscillation demonstrated here. In principle, such an array could consist of a parallel combination of waveguide-mounted RTD structures like that shown in Fig. 6. However, a more practical approach for very high frequencies is a planar RTD array based on microstrip-circuit

techniques. The key point in either approach is that the oscillators all lie in an equiphase plane of the open-cavity mode and are thus synchronized by the high-Q_u resonance. This method of power combination has been used to obtain cw power levels up to 20 W from both planar-MESFET oscillator arrays and Gunn-diode oscillator arrays operating near 10 GHz.[5] It should be a useful technique for obtaining milliwatt levels of power from RTD oscillators in the submillimeter-wave region.

Summary

InAs/AlSb RTDs have oscillated up to 712 GHz at room temperature. The power density generated at lower frequencies is 50 times that obtained from the best GaAs/AlAs RTD at the same frequency. The superiority of the InAs/AlSb RTD stems from its superior ohmic contact and from its higher available current density. A semiconfocal resonator has been used to lock a waveguide-based RTD oscillator at a frequency of 103 GHz. The locked oscillator linewidth was 40 kHz, which is about 250 times narrower than the linewidth of the waveguide oscillator alone. The quasioptical RTD oscillator should be suitable as a local oscillator for superconducting tunnel-junction mixers up to frequencies of at least 400 GHz.

Acknowledgments

The authors are grateful to A.R. Calawa and M.J. Manfra for providing the $In_{0.53}Ga_{0.47}As$/AlAs materials, to J.R. Söderström, S.J. Eglash, and T.C. McGill for providing the InAs/AlSb materials, to L.J. Mahoney and C.L. Chen for fabrication support, to D.L. Landers for valuable assistance in dicing and packaging, to R.A. Murphy and M.A. Hollis for useful comments on the manuscript, and to A.L. McWhorter for theoretical advice and useful comments on the manuscript. This work was sponsored by NASA through the Jet Propulsion Laboratory, by the Air Force Office of Scientific Research, and by the U.S. Army Research Office.

References

1. E.R. Brown, T.C.L.G. Sollner, C.D. Parker, W.D. Goodhue, and C.L. Chen, *Appl. Phys. Lett.* **55**, (1989), p. 1777.
2. E.R. Brown, C.D. Parker, A.R Calawa, M.J. Manfra, T.C.L.G. Sollner, C.L. Chen, S.W. Pang, and K.M. Molvar, *Proc. SPIE* **1288**, (1990), p. 122.
3. J.R. Söderström, E.R. Brown, C.D. Parker, L.J. Mahoney, and T.C. McGill, *Appl. Phys. Lett.* **58**, (1991), p. 275.
4. P. Boher, M. Renaud, J.M. Lopez-Villegas, J. Schneider, and J.P. Chane, *Appl. Surf. Sci.* **30**, (1987), p. 100.
5. D.B. Rutledge, Z.B. Popovic, R.M. Weikle, M. Kim, K.A. Potter, R.C. Compton, and R.A. York, *1990 IEEE MTT-S Int. Microwave Symp. Digest*, p. 1201.

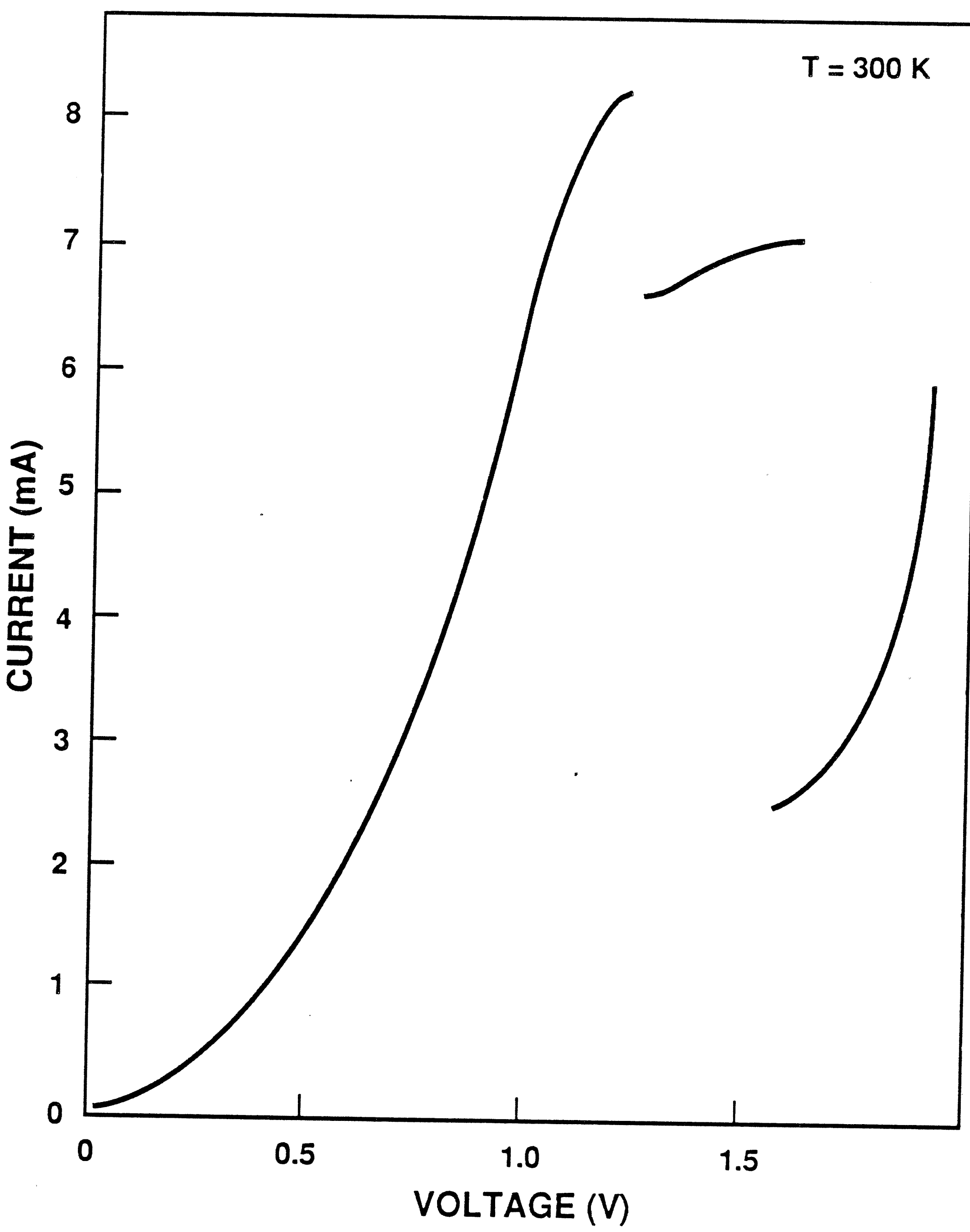

Fig. 1. I-V characteristics of a 1.8-μm-diameter InAs/AlSb RTD at room temperature. The step structure spanning the NDC region is caused by self-rectification of the oscillations.

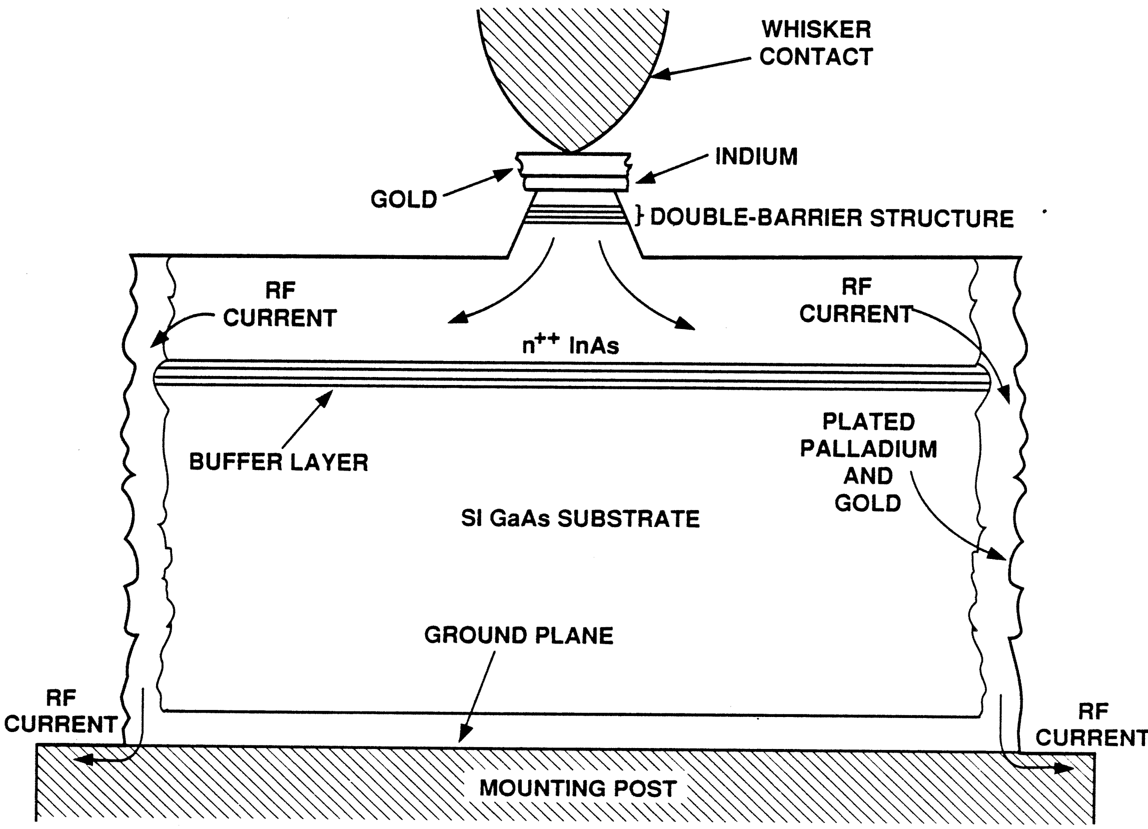

Fig. 2. Cross-sectional view of a fabricated InAs/AlSb RTD chip showing the current path followed between the diode mesa and the ground plane.

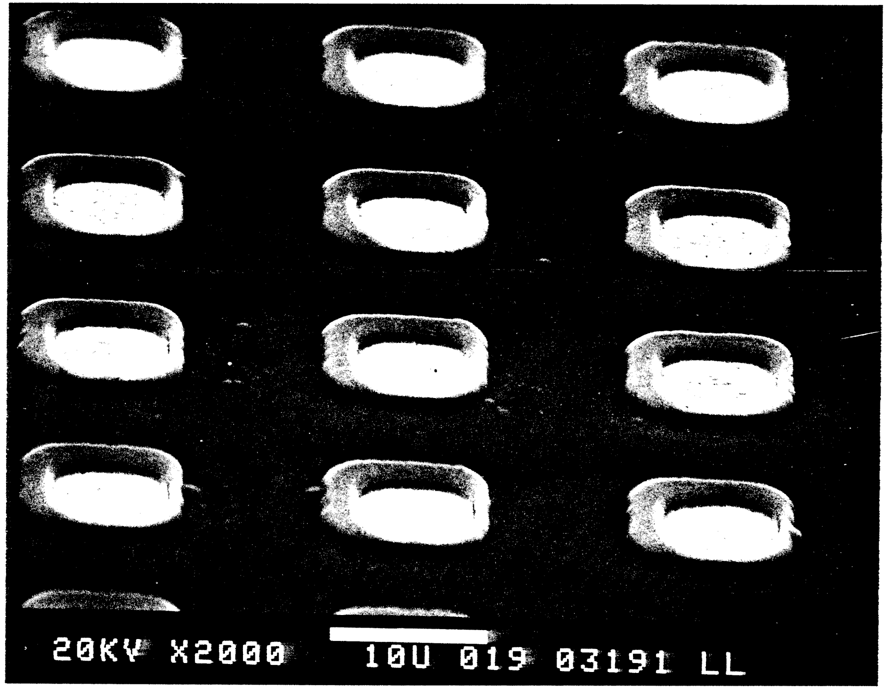

Fig. 3. Honeycomb pattern fabricated on top surface of RTD chip. The light regions are gold contacts on top of InAs mesas. The dark region is where a 1.0-µm-thick layer of Si_3N_4 covers etched InAs.

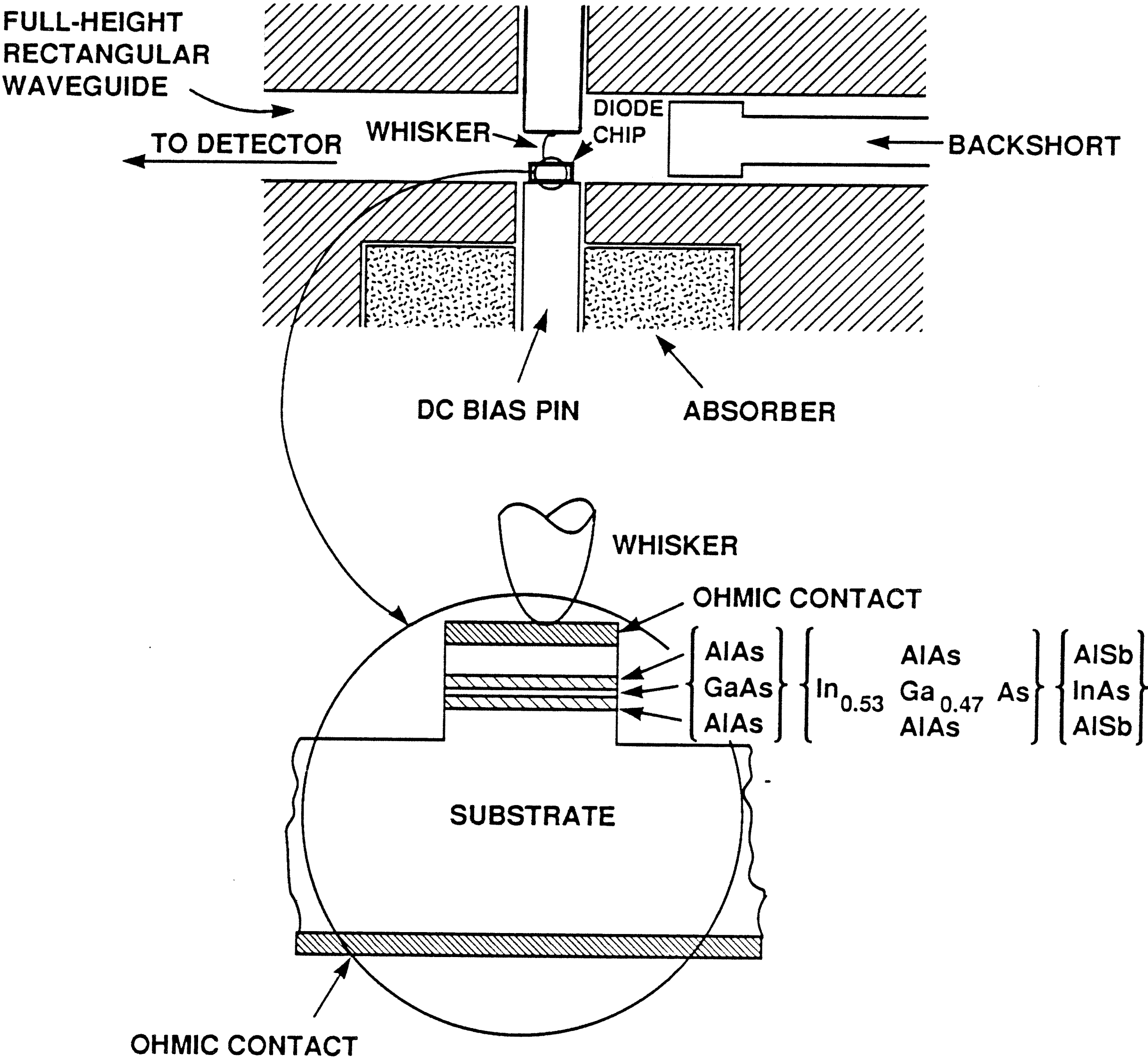

Fig. 4. Schematic diagram of waveguide resonator used to study RTD oscillators at frequencies above 100 GHz. The inset shows a cross-sectional view of a whisker-contacted RTD.

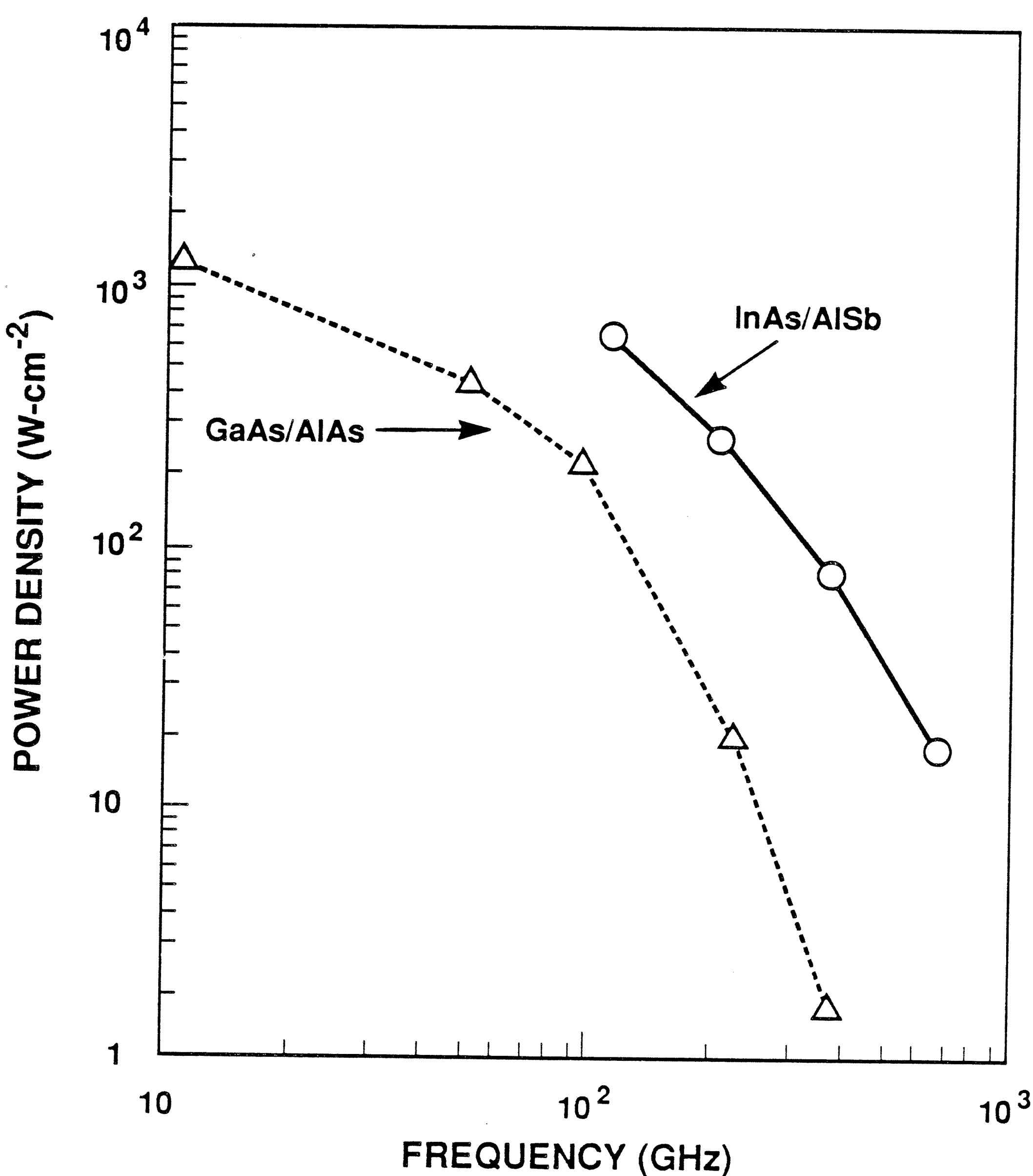

Fig. 5. Oscillator results for GaAs/AlAs and InAs/AlSb RTDs at room temperature.

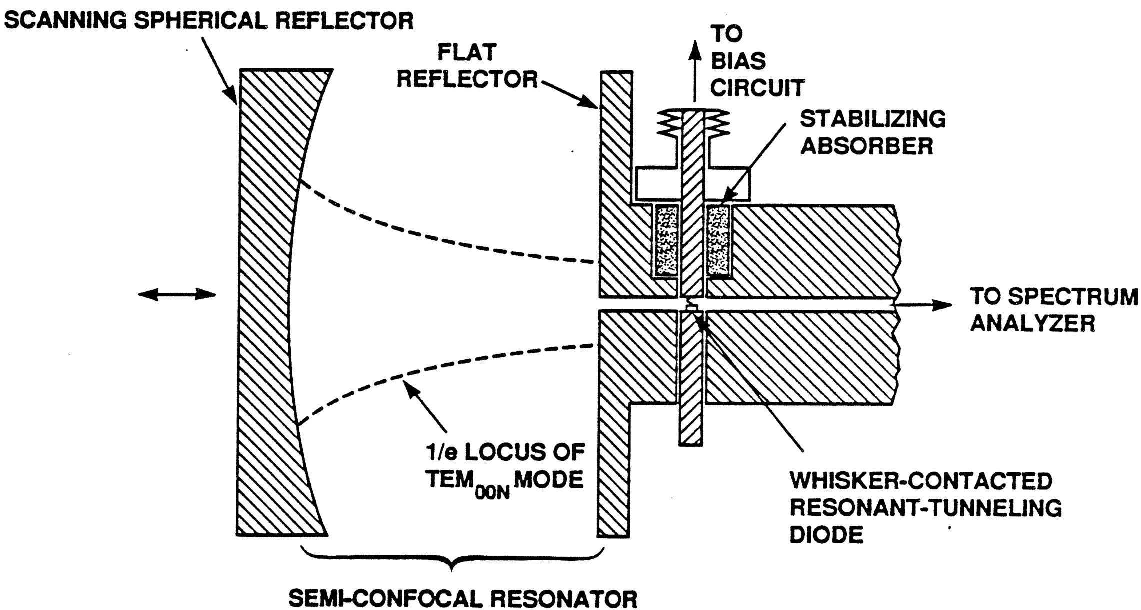

Fig. 6. Schematic diagram of quasioptical RTD oscillator designed to operate in the 100-GHz region.

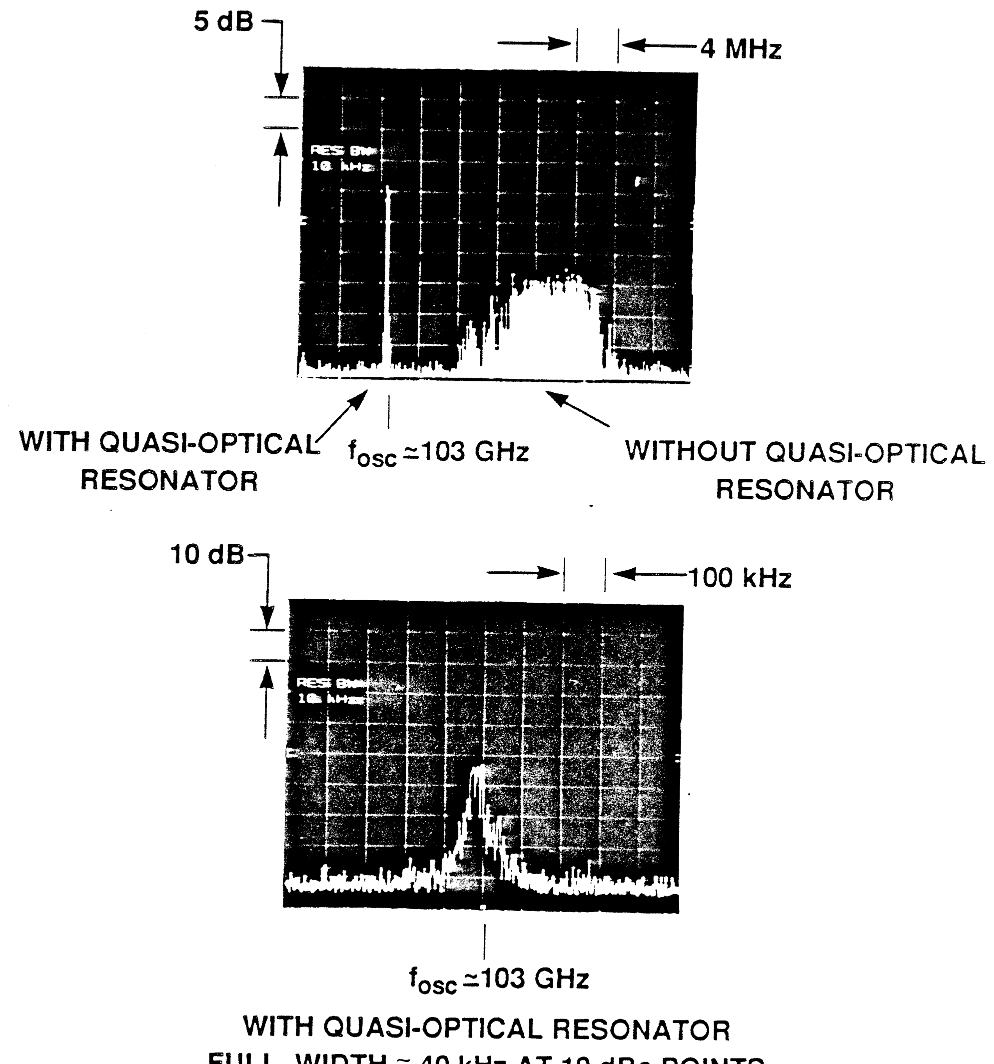

Fig. 7. (a) Power spectrum of the quasioptical oscillator with and without the benefit of the semiconfocal open resonator. (b) Expansion of the frequency axis of the power spectrum measured with the semiconfocal open resonator.

GaAs IMPATT DIODES FOR FREQUENCIES ABOVE 100 GHz: TECHNOLOGY AND PERFORMANCE

H. Eisele, R. K. Mains, G. I. Haddad, C. C. Chen

Center for Space Terahertz Technology
Department of Electrical Engineering & Computer Science
2231 EECS Building
The University of Michigan
Ann Arbor, Michigan 48109-2122

Abstract:

Recent experimental results have demonstrated good performance of GaAs IMPATT diodes around 94 GHz for both output power and noise measure. In this paper the first experimental results and some preliminary theoretical aspects for operation at higher frequencies are given together with an overview of the present status of the device technology. An improved small signal model and especially device simulations clearly depict that the device performance of GaAs IMPATT diodes is strongly limited by the contact resistance at frequencies above 100 GHz. These results agree well with experimental data obtained from W-band (75 - 110 GHz) IMPATT diodes operated at frequencies above their optimum frequency. A maximum output power of 30 mW with an efficiency of 0.73 % was obtained at 105.05 GHz in a W-band cavity. The highest oscillation frequency was 110.2 GHz with 8 mW and 0.2 % efficiency in a D-band cavity. Material parameters of electrons in GaAs for electric fields up to 900 $kVcm^{-1}$ allow a more accurate design of IMPATT diodes for D-band (110 - 170 GHz) operation. Preliminary tests on these IMPATT diodes show pure avalanche breakdown and prove that tunneling is significant only for electric fields above 1.0 $MVcm^{-1}$.

1. Introduction

It has recently been shown that GaAs IMPATT diodes are well suited for W-band operation [1] and exhibit excellent noise performance around 94 GHz [2]. GaAs single-drift flat-profile diodes show a clearly lower noise measure than Si single-drift flat-profile diodes operated in the same type of cavity and tested in the same measurement set up. Compared to Gunn devices these diodes offer better power capabilities, i. e. up to 320 mW, with nearly the same noise measure of 20 dB measured at 10 mW. To date only little is known about the CW performance at frequencies above 100 GHz [3,4].

Therefore, GaAs IMPATT diodes made from a material that was originally designed for 85 to 95 GHz were tested for CW operation at higher frequencies.

2. Design of single-drift flat-profile IMPATT diodes

As pointed out in References 5 and 6 the first derivative of the ionization rates of electrons and holes with respect to the electric field saturates around 500 $KVcm^{-1}$. Together with dead space effects in the avalanche zone [7] this saturation phenomenon favors a flat-profile structure for frequencies above V-band (50 - 75 GHz). The design of the single-drift structure is based on the assumption that the center of the avalanche region occurs where the electron concentration equals the hole concentration [8] for the applied bias voltage and that such a defined avalanche region is electrically equivalent to an avalanche region of the same width l_a but constant electric field and ionization rates [6]. Fig. 1 shows the electric field profile and the carrier concentration calculated for a doping concentration $N_D - N_A = 2.4 \times 10^{17}$ cm^{-3} in the active region at a current density $J_{tot} = 50$ $kAcm^{-2}$ and a junction temperature $T_j = 500$ K. The drift region - where ionization is to be neglected - is defined in its length l_d by the maximum in the well known transit-time function [9]

$$l_d = \frac{3\,v_s}{8 f_o} \quad , \qquad (1)$$

where v_s is the average saturated drift velocity (4.5×10^6 cms^{-1} for $T_j = 500$ K) and f_o the operating frequency.

3. Device technology

A selective etching technology for substrateless diodes on diamond heat sinks has successfully been established giving up to 600 diodes per cm^2 wafer area with high uniformity [9]. It implements an AlGaAs etch-stop layer between the substrate and the epitaxial layers for the device. In order to get the steep transitions for doping profiles in the submicron range, all wafers are grown by MBE [1]. Fig. 2 shows the flow chart of this technology process. The epitaxial side of the wafer is metallized with Ti/Pt/Au for a standard p^+-ohmic contact, then selectively plated with gold to form a grating for mechanical support and glued on a ceramic carrier. In the next step the substrate is removed by selective wet chemical etch and subsequently the etch-stop layer in a second selective wet chemical etch. A standard Ni/Ge/Au contact is evaporated on top of the n^+-contact layer and plated with gold. Contact patterns and diode mesas are defined by standard positive photoresist technology and wet chemical etching.

The diodes outside the supporting grating are tested and selected for good d.c. characteristics and exclusively thermocompression bonded on diamond heat sinks for optimum thermal resistance. The diamond heat sinks can be either in the form of copper blocks or similar to the standard ODS 138 packages. Electrical contact to the diode is basically provided by metallized quartz stand-offs thermocompression bonded onto the heat sink and tapered gold ribbons bonded on the diode and the stand-offs. For some diodes metallized quartz rings were very successfully used.

4. Experimental results

RF testing is performed in full height waveguide cavities with a resonant cap on top of the diode both in W-band (WR-10 waveguide) and D-band (WR-6 waveguide).

An output power of 17 mW at 103.8 GHz with an efficiency of 0.54 % and 30 mW at 105.05 GHz with an efficiency of 0.73 % were obtained in a WR-10 waveguide cavity. The highest oscillation frequency of 110.2 GHz could be observed in a WR-6 waveguide cavity. At this frequency the output power was 8 mW and the efficiency 0.2 %.

Table 1 summarizes the experimental results obtained from these diodes. The operating junction temperature was limited up to $T_j = 550$ K in order to ensure reliable long-term operation. As can be seen in Fig. 3 only the efficiency saturates at 6.0 % for 95.4 GHz while the output power monotonically increases up to the maximum bias current. This is also the case for the other results in Table 1 at higher frequencies and it means that the devices are thermally rather than electronically limited.

Table 1: Experimental results in W-band and D-band

Frequency [GHz]	93.4	94.7	95.4	103.8	105.0	110.2
Output power [mW]	140	217	320	17	30	8
Efficiency [%]	4.2	4.5	6.0	0.54	0.73	0.2
Cavity (W/D)	W	W	W	W	W	D

Fig. 4. shows the threshold current density J_{th} as a function of the operating frequency together with the values calculated by means of an IMPATT simulation program based on the drift-diffusion model [11]. Experiment and calculations are in good agreement and will be discussed in the next section.

Using the above discussed design rules, single-drift flat-profile structures for D-band operation were designed and the epitaxial layers grown in an MBE system. Processed devices were tested for d.c. characteristic and doping profile. As depicted in Fig. 5 the breakdown voltages of these IMPATT diodes are in good agreement with the breakdown voltages calculated from ionization rates evaluated in Reference 10. The I-V curve shown in Fig. 6. shows pure avalanche breakdown with a positive temperature coefficient. At present it cannot be determined whether the small leakage current just below breakdown is due to tunneling or surface effects.

5. Device simulation

In order to check the validity of the design at D-band frequencies device structures were simulated in a few preliminary runs using two IMPATT diode simulation programs, a drift-diffusion (DD) model [11] and an energy-momentum (EM) model [12]. Full details of the programs and the material parameters used in these programs will be given elsewhere. In contrast to the experimental results given in [10], slightly higher drift velocities for T_j = 500 K are used and the ionization rates are set equal for electrons and holes. However, the applied ionization rates give nearly the same breakdown voltages as shown in Fig. 5 and additionally, they take the temperature dependence of the breakdown voltages into account that were measured on IMPATT diodes for frequencies from Q-band up to W-band.

As previously mentioned, Fig. 4 shows the calculated J_{th} as a function of the oscillation frequency. As pointed out in [6,13], the oscillation starts at J_{th} when the real part $-R_D$ of the diode impedance $\underline{Z}_D$ just overcomes the series resistance. ($R_L << R_s$, $R_v << R_s$ in the inset of Fig. 4). In this case the series

resistance times unit area $R_s \times A_D$ is assumed to 2×10^{-6} Ωcm^2 as an upper limit and mainly due to the contact resistances in the diode [6]. The improved small signal model in Reference 6 gives similar results. At 140 GHz J_{th} is clearly above the thermal limit of 50 $kAcm^{-2}$ for the W-band diode (N_D - N_A = 2.4×10^{17} cm^{-3} in the active region) and below the expected thermal limit of 60 $kAcm^{-2}$ for one of the D-band diodes (N_D - N_A = 3.2×10^{17} cm^{-3}).

Table 2 shows calculated output power and efficiency at f = 95 GHz as preliminary results for both programs. The data for the device area A_D and current density J_{dc} are taken from Reference 1. The energy-momentum program shows slightly higher breakdown voltages and overestimates efficiency and output power. If a series resistance $R_s = 0.18\ \Omega$ is taken into account for this diode, the calculated output power and efficiency agrees very well with the measured values. This series resistance is comparable to the value obtained from small signal impedance measurements in forward direction at 32 MHz [6]. In Table 2 the prediction for one of the D-band structures is included. A smaller $R_s \times A_D$ (1×10^{-6} Ωcm^2) is assumed and demands significantly better technology for contacts on both p^+- and n^+-type GaAs.

Table 2: Calculated results

Area A_D: 8×10^{-6} cm^2 Current density: 50 $kAcm^{-2}$

Model	Voltage [V]	Frequency [GHz]	Power ($R_s = 0\ \Omega$) [mW]	Efficiency [%]	Power ($R_s = 0.18\ \Omega$) [mW]	Efficiency [%]
DD	12.2	95.0	550	11.3	320	6.5
EM	12.5	95.0	700	14.0	510	10.2

Area A_D: 5×10^{-6} cm^2 Current density: 60 $kAcm^{-2}$

Model	Voltage [V]	Frequency [GHz]	Power ($R_s = 0\ \Omega$) [mW]	Efficiency [%]	Power ($R_s = 0.20\ \Omega$) [mW]	Efficiency [%]
DD	10.4	140.0	120	3.8	35	1.1
EM	10.9	140.0	215	6.5	80	2.4

6. Conclusion

The above discussed experimental results prove that GaAs IMPATT diodes are powerful devices not only for frequencies below 60 GHz, but also above 100 GHz. Together with device simulation high output power can be expected for D-band operation. The simulation also reveals that the contact technology is very crucial for high output power and efficiency and must considerably be improved for GaAs D-band IMPATT diodes.

7. Acknowledgments

This work was supported by the Center of Space Terahertz Technology. A part of the experiments, measurements and calculations were performed by one of the authors (H. E.) at the Lehrstuhl für Allgemeine Elektrotechnik und Angewandte Elektronik, Munich, FRG. The authors are very grateful to Prof. W. Harth for his help.

8. References

[1] Eisele, H., and Grothe, H.: "GaAs W-band IMPATT diodes made by MBE", *Proc. MIOP '89*, Sindelfingen, FRG, Feb. 28th - March 3rd 1989, Session 3A.6.

[2] Eisele, H.: "GaAs W-band IMPATT diodes for very low-noise oscillators", *Electronics Letters*, **26**, 1990, pp. 109-110.

[3] Elta, M. E., Fettermann, H. R., Macropoulos, W. V., and Lambert, J.: "150 GHz GaAs MITATT source", *IEEE Trans. Electron. Device Lett.*, **EDL-1**, 1980, pp. 115-116.

[4] Chang, K., Kung, J. K., Asher, P. G., Hayashibara, G. M., and Ying, R. S.: "GaAs Read-type IMPATT diode for 130 GHz CW operation", *Electronics Letters*, **17**, 1981, pp. 471-473.

[5] Rolland P. A., Friscourt M. R., Lippens D., Dalle C., and Nieruchalski, J. L.: "Millimeter Wave Solid-State Power Sources", *Proc. of the International Workshop on Millimeter Waves*, Rome, April 2-4, 1986, pp. 125-177

[6] Eisele, H.: "GaAs W-Band IMPATT diodes: The first step to higher frequencies", *Microwave Journal*, to be published.

[7] Okuto, Y., and Crowell, C. R., "Threshold energy effects on avalanche breakdown voltage in semiconductor junctions", *Solid-State Electron.*, **18**, 1975, pp. 161-168

[8] Hulin, R.: "Großsignalmodell von Lawinenlaufzeitdioden", Ph.D. Thesis Techn. University Braunschweig, Braunschweig 1973

[9] Eisele, H.: "Selective etching technology for 94 GHz GaAs IMPATT diodes on diamond heat sinks", *Solid-State Electronics*, **32**, 1989, pp. 253-257.

[10] Eisele, H.: "Electron properties in GaAs for the design of mm-wave IMPATTs", *Int. Journal of Infrared and Millimeter Waves*, **4**, 1991, to be published.

[11] Bauhahn, P. E., and Haddad, G. I.: "IMPATT device simulation and properties", *IEEE Trans. Electron Devices*, **ED-24**, 1977, pp. 634-642.

[12] Mains, R. K., Haddad, G. I., and Blakey, P. A.: "Simulation of GaAs IMPATT Diodes Including Energy and Velocity Transport Equations", *IEEE Trans. Electron. Devices*, **ED-30**, 1983, pp. 1327-1338

[13] Adlerstein, M. G., Holway L. H., and Chu, S. L. G.: "Measurement of Series Resistance in IMPATT Diodes", *IEEE Trans. Electron Devices*, **ED-30**, 1983, pp. 179-182

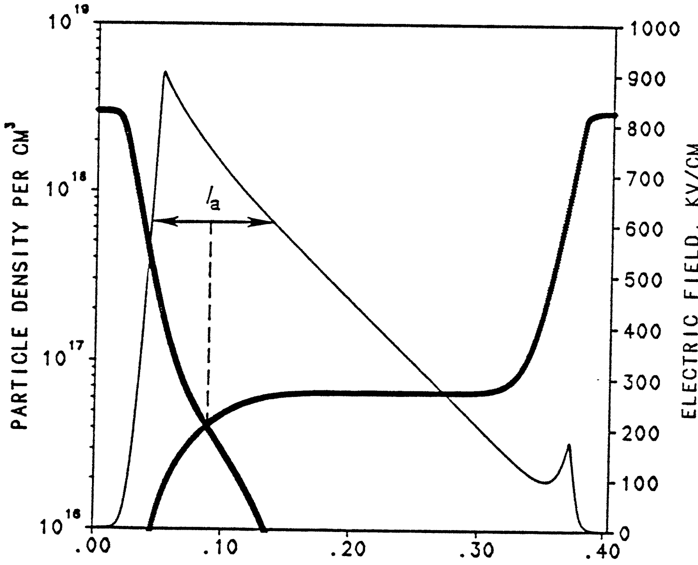

Fig. 1: Electric field E, electron and hole concentration n, p as a function of space x for $N_D - N_A = 2.4 \times 10^{17}$ cm^{-3} in the active region.

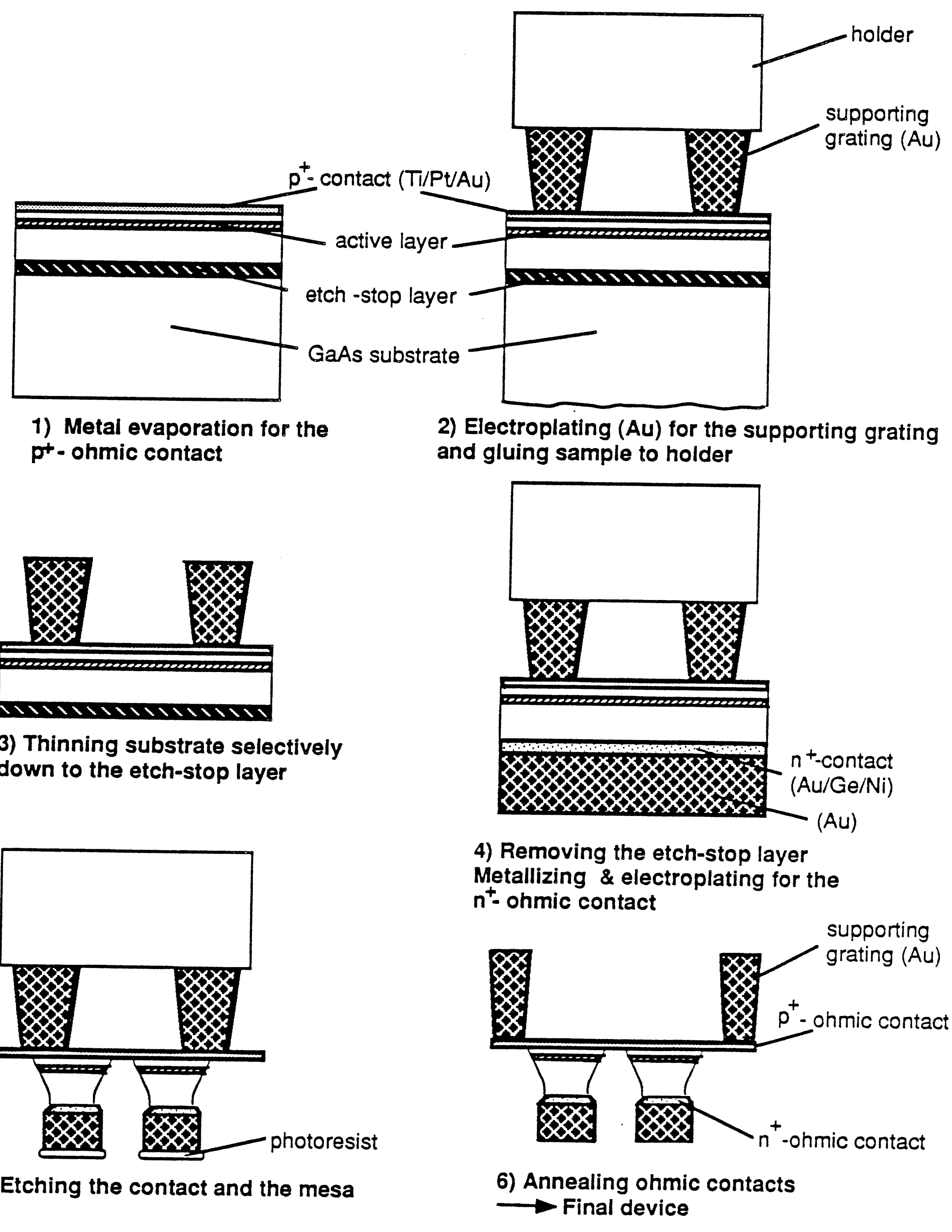

Fig. 2: Flow chart for IMPATT diodes device fabrication.

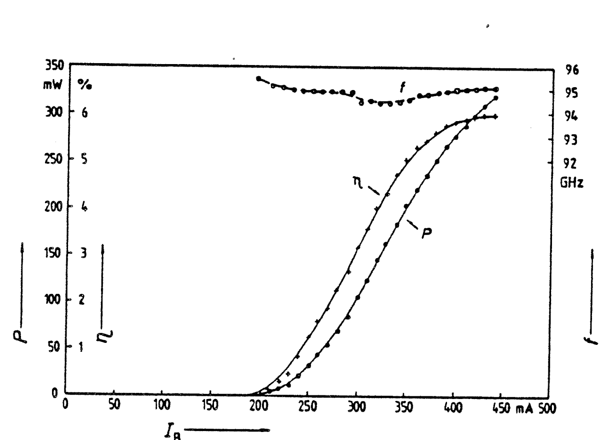

Fig. 3: Performance of a GaAs W-band single-drift flat-profile IMPATT diode.

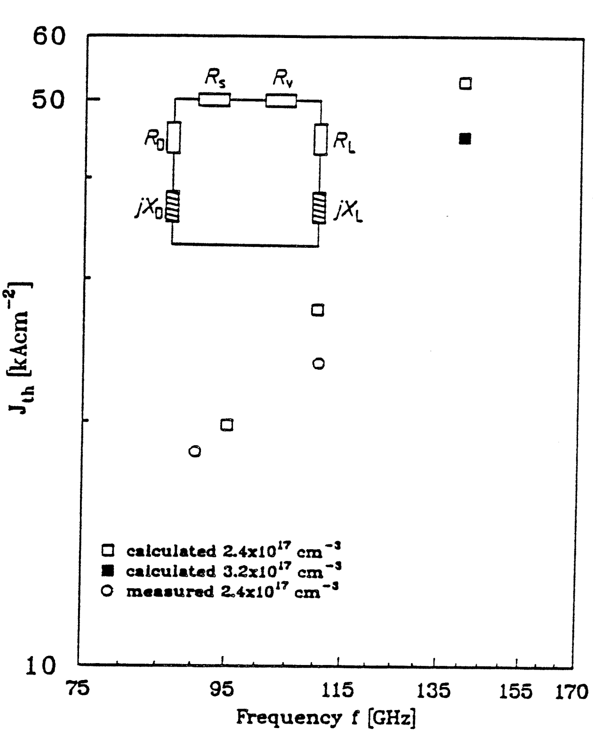

Fig. 4: Measured and calculated threshold current density J_{th} as a function of frequency for W-band and D-band single-drift flat-profile IMPATT diodes.

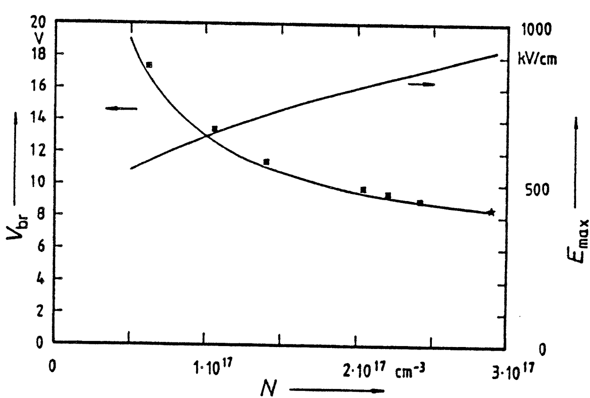

Fig. 5: Breakdown voltage V_{br} and peak electric field E_{max} of an abrupt p^+n-junction.

■ ★ : measured

—— : calculated.

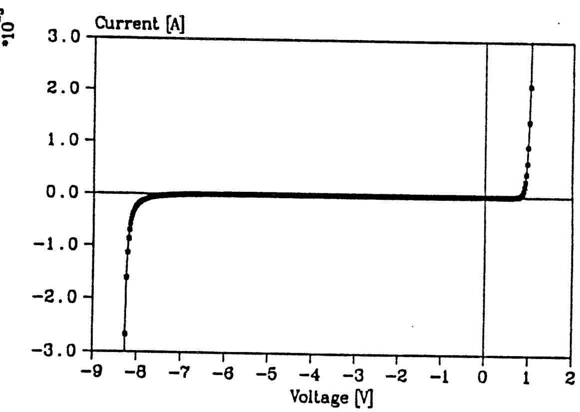

Fig. 6: I-V-curve of a D-band IMPATT diode with N_D - N_A = 2.9 × 10^{17} cm^{-3} in the active region.

LOSSY-LINE STABILIZATION OF NEGATIVE-RESISTANCE DIODES FOR INTEGRATED-CIRCUIT OSCILLATORS

Karl D. Stephan and Sai-Chu Wong
Department of Electrical & Computer Engineering
University of Massachusetts
Amherst, MA 01003

Elliot R. Brown
Lincoln Laboratory
Massachusetts Institute of Technology
Lexington, MA 02173-9108

ABSTRACT: Diodes that show negative differential resistance from DC up to 700 GHz are now available. To exploit these devices, a submillimeter-wave oscillator circuit must encourage oscillation near the upper frequency limit while discouraging oscillation at all lower frequencies. This is not easy. In this paper we describe a tool in the circuit designer's kit which may prove useful in the development of integrated-circuit submillimeter-wave oscillators using resonant-tunneling diodes or other negative-resistance devices. A lossy transmission line of sufficient length presents a nearly constant impedance to its load while furnishing a convenient pathway for DC bias. Following a Smith-chart presentation of the stabilization problem, we describe two microwave oscillator circuits that use lossy transmission lines for diode stabilization. One used a conventional tunnel diode in a quasioptical 2-GHz oscillator, and the other employed a resonant tunneling diode in a quasioptical-cavity-stabilized circuit at 9 GHz.

The Stabilization Problem

The designer of a submillimeter-wave oscillator using a negative-resistance device such as a resonant tunneling diode (RTD) faces a formidable engineering challenge. The need to increase the device's peak current for higher output power leads to difficulties in biasing and bypassing the device so that it will not oscillate at frequencies below the desired output frequency. This problem has been discussed extensively in a paper by Kidner et al. [1], who use a lumped-element circuit analysis to conclude that these stability problems pose a

grave difficulty in obtaining useful levels of output power from RTDs. While these cautions should be taken seriously, in this paper we will describe an idea that may alleviate some of the stability problems that circuit designers face in constructing RTD oscillators.

In Fig. 1 we show the equivalent circuit of a submillimeter-wave RTD whose maximum frequency of oscillation, given by

$$f_r = \frac{1}{2\pi R_d C_d}\sqrt{\frac{R_d}{R_S} - 1} \tag{1}$$

is 689 GHz. The differential negative resistance $-R_d = -20$ ohms is obtained by biasing the device in its negative-resistance region, typically 0.2–0.3 V at a few mA. The device capacitance $C_d = 20$ fF and series resistance $R_S = 5$ ohms are similar to devices reported by Brown et al. [2].

The oscillation design problem can be described by means of an oscillation criterion due to Esdale and Howes [3]. If Γ_d is the reflection coefficient of the one-port active device and Γ_ℓ is that of its load, then Esdale and Howes showed that steady-state oscillation is possible only if

$$\Gamma_\ell = \frac{1}{\Gamma_d}. \tag{2}$$

This implies the two conditions

$$|\Gamma_\ell| = \left|\frac{1}{\Gamma_d}\right|$$

and

$$\angle(\Gamma_\ell) = \angle\left(\frac{1}{\Gamma_d}\right).$$

The normalizing impedance used to define the reflection coefficients is completely arbitrary, and we have found it convenient to plot Γ_ℓ and $1/\Gamma_d$ on a Smith chart whose normalizing impedance Z_o is equal to the absolute value of the device's net negative resistance at DC:

$$Z_o = R_d - R_S = 20 - 5 = 15 \text{ ohms} \tag{3}$$

The advantage of this normalization is that the locus of the device's $1/\Gamma_d$ line as a function of frequency always starts at the center of the Smith chart and crosses the unit circle at the cutoff frequency f_r, as Fig. 2 shows.

Although Esdale and Howes do not address the issue of non-steady-state oscillation, it seems reasonable to assume that exponentially growing oscillations will occur at a given frequency if the following two conditions are satisfied:

$$|\Gamma_\ell| > |\frac{1}{\Gamma_d}| \tag{4}$$

$$\angle(\Gamma_\ell) = \angle\left(\frac{1}{\Gamma_d}\right) \tag{5}$$

The region of the Smith chart which satisfies these conditions is shaded in Fig. 2. If the load's reflection-coefficient locus $\Gamma_\ell(f)$ strays into this area, growing sinusoidal oscillations are possible. This portrayal shows why even extremely small values of inductance in series with the load can cause stability difficulties. For example, an inductance of only 25 picohenries has a reactance of 15 ohms at 100 GHz, which would place Γ_ℓ near the top of the Smith chart in Fig. 2, leading to possible problems with spurious "low-frequency" millimeter-wave oscillation in a submillimeter-wave circuit. Such parasitic inductance is difficult to avoid in lumped-element or waveguide circuits. However, integrated-circuit techniques may furnish a way around this problem.

Lossy Integrated-Circuit Transmission Lines

The ideal bias circuit for a submillimeter-wave RTD oscillator would be a voltage source with essentially zero internal impedance from DC up to the diode cutoff frequency f_r. No passive or active circuit achieves this ideal, but it is clear that a very broadband bias circuit design is called for, one whose impedance on the Smith chart of Fig. 2 would stay in the low-impedance left-hand side over the entire frequency range. Standard radio-frequency bypassing techniques can deal with this problem from DC up to the low GHz range, but above that it becomes very difficult to devise a low-loss filter structure whose input impedance never strays into the danger zone of Fig. 2 from, say, 10 GHz up to 700 GHz.

Fortunately, there are microelectronic components whose impedance can be made low and fairly constant over a wide frequency range. If a microstrip line is laid out on a highly-doped semiconductor substrate as shown in Fig. 3, it forms a slow-wave transmission

line under certain conditions. Such transmission lines have been investigated for possible signal-processing applications, but their very high attenuation values (up to 24 dB at 18 GHz in a 1.6 mm-long line reported by Krowne and Neidert [4]) have discouraged this application. However, one man's poison is another man's meat, and the very high loss factors which are such a disadvantage in signal processing turn out to be ideal for RTD biasing.

If these lines are made sufficiently wide, their characteristic impedance can fall below ten ohms. Moreover, the very high loss factors mean that a line a few millimeters long will present an essentially constant impedance to the oscillator circuit, regardless of how the bias-supply end of the line is terminated. This will not be the case at lower frequencies where the loss is not as great, but fortunately the conventional lumped-element circuit techniques can take over at that point.

Oscillators Using Lossy Lines

In some very preliminary experiments, we have used this biasing approach to stabilize negative-resistance devices in quasioptical oscillator circuits. One circuit is shown in Fig. 4. A thin slot antenna measuring 4.5 cm by 1 mm was fabricated on a single-clad microwave circuit substrate 0.508 mm thick, with a relative dielectric constant of 2.2. The low-impedance lossy transmission line, 2.8 mm wide and approximately 2.5 cm long, was fabricated on a 0.38 mm thick silicon wafer with a 7000 Å layer of silicon dioxide (SiO_2) grown on its top surface. The silicon was highly doped with a resistivity of less than 0.01 ohm-cm.

The microstrip line was mounted perpendicular to the slot. A packaged microstrip type tunnel diode was then mounted across the slot with its anode connected to one end of the microstrip line and its cathode to the ground across the slot. Tuning to the desired oscillation frequency was achieved by moving the location of the diode (and the microstrip line) along the slot. An oscillation frequency of 2.4 GHz was achieved by placing the diode 2-3 mm away from one end.

Another circuit in Fig. 5, described in more detail elsewhere [6], used a packaged RTD in a similar slot-antenna oscillator. In this case, the bias was fed through a 6.3-mm-wide parallel-plate transmission line made from 0.25-mm thick fiberglass circuit board material. Its 27-cm length and the lossy nature of its dielectric meant that, at least at high frequencies, its impedance at the diode end was independent of how the far end was terminated. The oscillator ran at 8.9 GHz, and demonstrated that an RTD oscillator's spectrum can be significantly improved if it is coupled to a high-Q cavity.

Conclusions

Despite the difficulties of designing oscillator circuits with submillimeter-wave negative-resistance devices, their promise as a useful source of power at those wavelengths has created a need for innovative oscillator circuit techniques. We hope that the notion of using integrated lossy transmission lines will encourage more efforts to exploit the great potential of resonant tunneling diodes to serve as a useful source of submillimeter-wave energy.

Acknowledgements

This work was sponsored by the U.S. Army Research Office, the National Aeronautics and Space Administration, and the Air Force Office of Scientific Research.

References

[1] C. Kidner, I. Mehdi, J.R. East, and G.I. Haddad, "Power and stability limitations of resonant tunneling diodes," *IEEE Trans. Microwave Theory Tech.*, vol. 38, pp. 864-872, July 1990.

[2] E.R. Brown, C.D. Parker, L.J. Mahoney, J.R. Söderström, and T. McGill, "Room-temperature oscillations up to 675 GHz in *InAs/AlSb* resonant-tunneling diodes," 1990 Device Research Conference, Santa Barbara, CA.

[3] D.J. Esdale and M.J. Howes, "A reflection-coefficient approach to the design of one-port negative impedance oscillators," *IEEE Trans. Microwave Theory Tech.*, vol. MTT-29, pp. 770-776, Aug. 1981.

[4] C.M. Krowne and R.E. Neidert, "Slow wave monolithic variable phase shifter," *Proceedings of Tenth Int'l. Conf. on IR and MM Waves*, pp. 275-276, Orlando, FL, Dec. 9-13, 1985.

[5] H. Hasegawa, M. Furukawa, and H. Yanai, "Properties of microstrip line on Si-SiO_2 system," *IEEE Trans. Microwave Theory Tech.*, vol. MTT-19, pp. 869–881, Nov. 1971.

[6] K.D. Stephan, E.R. Brown, C.D. Parker, W.D. Goodhue, C.L. Chen, and T.C.L.G. Sollner, "Resonant-tunneling diode oscillator using a slot-coupled quasioptical open resonator," submitted to *Electronics Letters.*

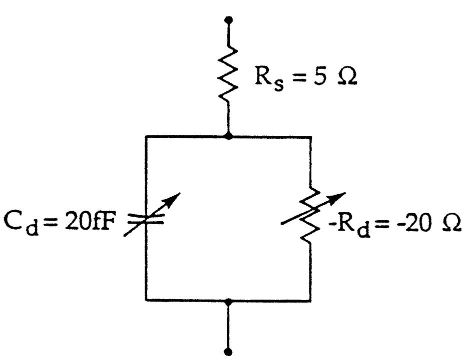

Fig. 1. Equivalent circuit of negative-resistance diode with cutoff frequency $f_r = 689$ GHz.

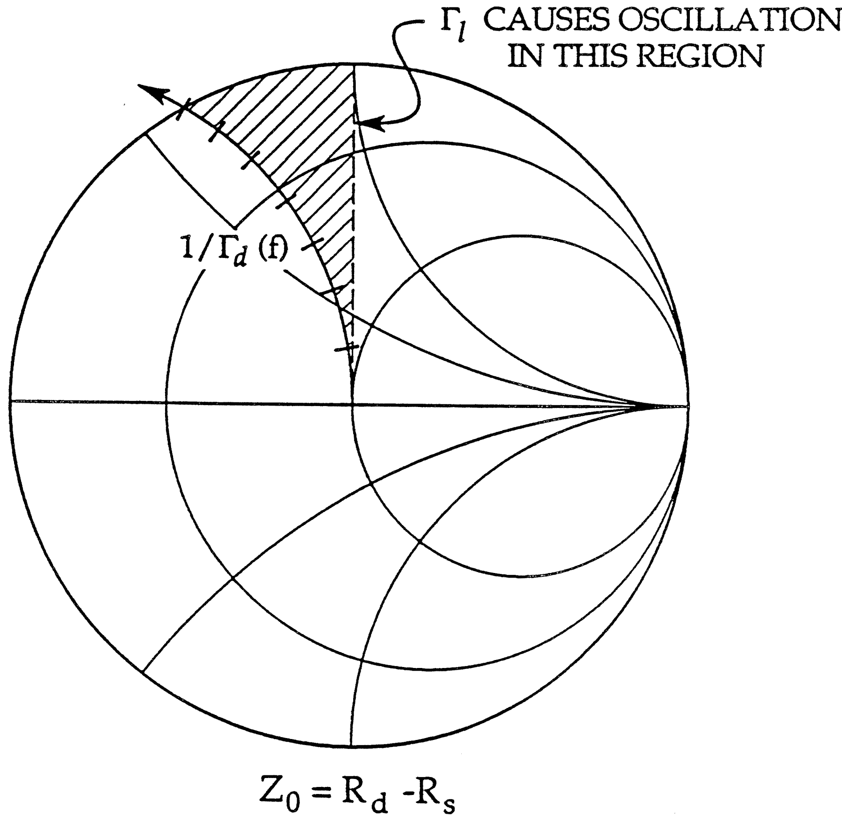

Fig. 2. Smith-chart plot of diode reflection coefficient inverse $1/\Gamma_d(f)$ and shaded area in which load impedance can cause oscillation.

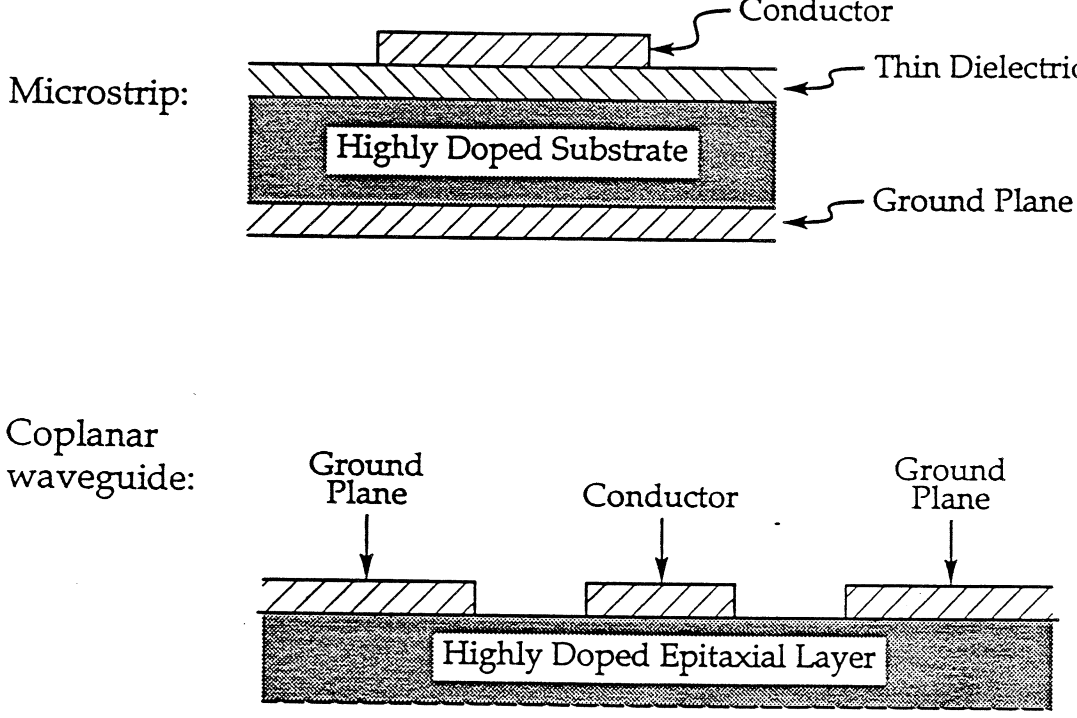

Fig. 3. Microelectronic low-impedance lossy transmission lines suitable for DC biasing negative-resistance devices.

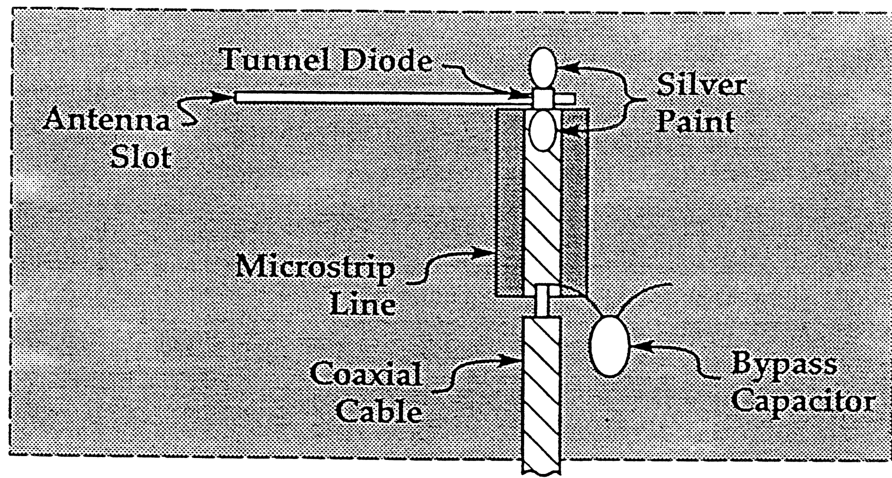

Fig. 4. Quasioptical oscillator using silicon lossy line for bias stabilization: $f_{osc} = 2.3$ GHz.

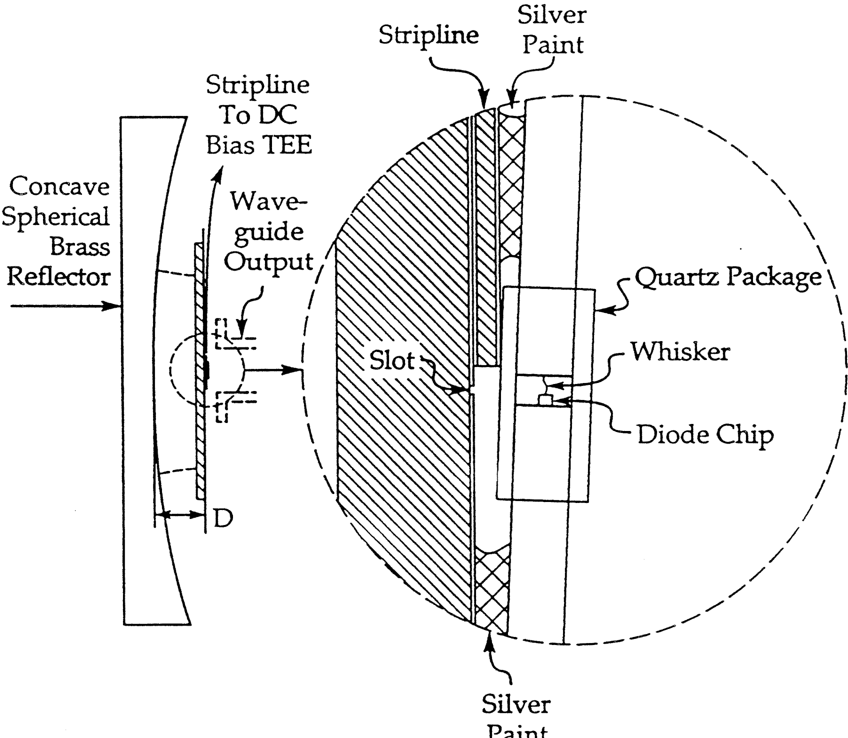

Fig. 5. Quasioptical cavity – stabilized oscillator using lossy-line bias: $f_{osc} = 8.9$ GHz.

Josephson Junction Oscillator Arrays

Matthew J. Lewis, Dale Durand, and Andrew D. Smith
TRW Space & Technology Group.

Peter Hadley*
Stanford University

Abstract

We have studied the stability and coherence of distributed Josephson junction array oscillators both theoretically, and experimentally. Distributed Josephson oscillator arrays successfully operate above 300 GHz with microwatt power levels.[1] The use of wavelength-long transmission lines between Josephson elements has overcome lithographic and stability difficulties plaguing earlier compact designs. In this paper, we study the dynamic stability and phase coherence of Josephson arrays.

We have extended lumped array stability analysis[2] both for more realistic embedding environments and to distributed arrays including element to element time delays. Stable oscillator operation in lumped arrays depends on both junction and drive parameters. Wide ranges of embedding impedances provide coherent output oscillations. For distributed arrays, the available oscillator output power increases with the total array size. These results are in good agreement with experimental observations.[1]

Experimentally, we have fabricated and operated a distributed array oscillator and observed at least 50 nW of power at 125 GHz using an on-chip detection circuitry.

Introduction

There is an increasing need for sub-millimeter wave sources for a wide range of applications ranging from astronomy to communications. Single Josephson junction oscillators have been successfully operated at frequencies up to hundreds of GHz, but these single junctions do not produce adequate power and have very low output impedance. Both of these limitations can be overcome by placing many junctions in a series array.

Early work in Josephson oscillator arrays concentrated on tightly spaced series arrays of junctions[3]. Workers quickly discovered successful high power operation of these arrays centered around obtaining

coherent, in-phase operation of the individual oscillator elements. Although the series array geometry imposes a uniform current requirement on the junctions, the oscillation voltages of the Josephson elements tend to destructively interfere unless specific feedback conditions are maintained.

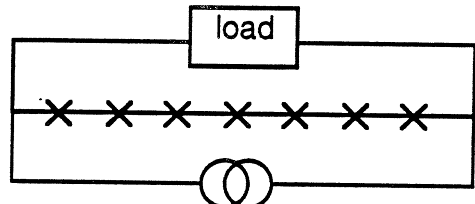

Figure 1. Lumped element Josephson array. Each cross represents an ideal Josephson element, shunt resistor, and shunt capacitance.

Hadley[2] and Jain et al[3] have studied electrically short, Josephson series arrays. (See Fig. 1). Coherent operation depends on the external load element(s), which provide feedback to the individual array elements. Hadley found separate parameter ranges leading to chaotic or very stable, coherent array operation, depending upon junction capacitance, critical current, bias current, and load.

These models, however, have their limitations. They neglect the parasitic inductance between junctions, as well as capacitance to ground of interconnecting lines. At low frequencies and for array lengths much shorter than a wavelength, these effects should be minimal. For sub-millimeter, microwatt oscillators these additional elements dominate the circuit dynamics.

In experimental work at Stony Brook, Wan, et al.[1] cleverly side-stepped the issue of long-array parasitics. Since interconnection wiring is unavoidable between Josephson elements, the Stony Brook design chooses the transmission line interconnection length to be precisely one oscillation wavelength long. (See Fig. 1.) Electrically, the transmission line appears identical to a zero-length interconnect for all frequencies which are multiples of the fundamental. Thus for any multiple of the fundamental frequency, solutions of the tightly-spaced array oscillator should also apply to the Stony Brook design array.

In this theoretical study we have extended the analyses for the lumped element array to include the reactance of the load. This analysis only applies to long arrays when the interconnects between the junctions are one wavelength long. We also consider more general distributed arrays. Here we find a

picture significantly more complex than simple wavelength arguments would predict. Some coherent solutions appear for operating frequencies which are a fraction of the junction spacing. In addition, some parameter choices which give stable short array solutions lead to out-of-phase solutions in Stony Brook array geometries.

Stability Theory for Oscillators

In-phase solution, where all of the junctions oscillate with the same frequency and phase, is an exact solution to the lumped element model for the arrays. Unless certain device parameter requirements are met, the in-phase solution is unstable and the oscillator will quickly decay into out-of-phase or aperiodic solutions. Previously simulations have been performed for junction arrays have been performed with a variety of β_c, current biases, and loads.[2] They show that the phase locking was strongest when $\beta_c \approx 1$ independent of the load. We were able to reproduce the earlier work and have extended it by calculating stability exponents for β_c as a function of load impedance. The equations of motion for the oscillator array are given by the conservation of current,

$$\beta_c \ddot{\varphi}_k(t) + \dot{\varphi}_k + \sin(\varphi_k(t)) + I_L(t) = I_B$$

and the voltage across the array,

$$V(t) = \sum_{k=1}^{N} \dot{\varphi}_k(t) = F(I_L(t))$$

using the usual reduced units: measuring current in units of I_c (critical current), voltage in units of I_cR_N (normal state resistance), resistance in units of R_N, capacitance in units of $\hbar/(2eI_cR_N^2)$, inductance in units of $\hbar/(2eI_c)$, and time in units of $\hbar/2eI_cR_N$.

The stability of the in-phase solution, φ_o, may be determined by considering small perturbations about that solution. Linearizing the previous equation around the in-phase solution we have

$$\beta_c \ddot{\eta}_k(t) + \dot{\eta}_k(t) + \sin(\varphi_o(t))\eta_k + i(t) = I_B$$
$$\sum_{k=1}^{N} \dot{\eta}_k(t) = F'(I_L(t))i(t)$$

After transforming to natural coordinates, we can simplify

$$\beta_c \ddot{\zeta}_k(t) + \dot{\zeta}_k(t) + \sin(\varphi_o(t))\zeta_k = 0 \qquad k = 1, 2, \cdots, N$$
$$\beta_c \ddot{\vartheta}_k(t) + \dot{\vartheta}_k(t) + \sin(\varphi_o(t))\vartheta_k + i(t) = 0$$
$$N\dot{\vartheta}(t) = F'(I_{o(t)})i(t)$$

The first equation arises frequently in physical problems and can be analyzed using Floquet theory. There are two independent solutions to the equation for ζ which have the form $\exp(\rho t)\chi(t)$ where $\chi(t)$ is a periodic function with the same period as φ_o and ρ is called the stability exponent The two solutions to the equation for ζ form a basis from which we can form any other solution. We can choose two independent solutions ζ_a and ζ_b which have the corresponding initial conditions $\zeta_a(0)=1$, $\dot{\zeta}_a(0)=0$, $\zeta_b(0)=0$, and $\dot{\zeta}_b(0)=1$. Since $\cos(\varphi_o)$ is a periodic function, $\zeta_a(t+T)$ and $\zeta_b(t+T)$ are also solutions of the equation. We can express this as

$$\begin{pmatrix} \zeta_a(t+T) \\ \zeta_b(t+T) \end{pmatrix} = \begin{pmatrix} \zeta_a(T) & \dot{\zeta}_a(T) \\ \zeta_b(T) & \dot{\zeta}_b(T) \end{pmatrix} \begin{pmatrix} \zeta_a(t) \\ \zeta_b(t) \end{pmatrix}$$

The eigenvectors of this equation are called Floquet solutions. The corresponding stability exponents determine the stability of the perturbations. They are related to the eigenvalues, λ_j, of the matrix, by $\rho_j = \ln(\lambda_j)/T$. If both $\mathrm{Re}(\rho_1)$ and $\mathrm{Re}(\rho_2)$ are less than 0 then the perturbation decays and the solution is stable. When $\mathrm{Re}(\rho_1) = \mathrm{Re}(\rho_2) = 0$ then the solution is neutrally stable and the perturbation neither grows nor decays. In this case second order terms control the stability. If either real part is greater than zero then the solution is unstable.

Lumped-Element Simulation

Our numerical studies began with a version of SPICE[4] developed at UC Berkeley we simulated a single junction voltage controlled oscillator. We were able to relate the results of this simulation to previous experimental work done by Smith, et al[5]. Once this was successful the design was extended to multi-junction arrays. The results indicated that both the array impedance and the array voltage increased as N.

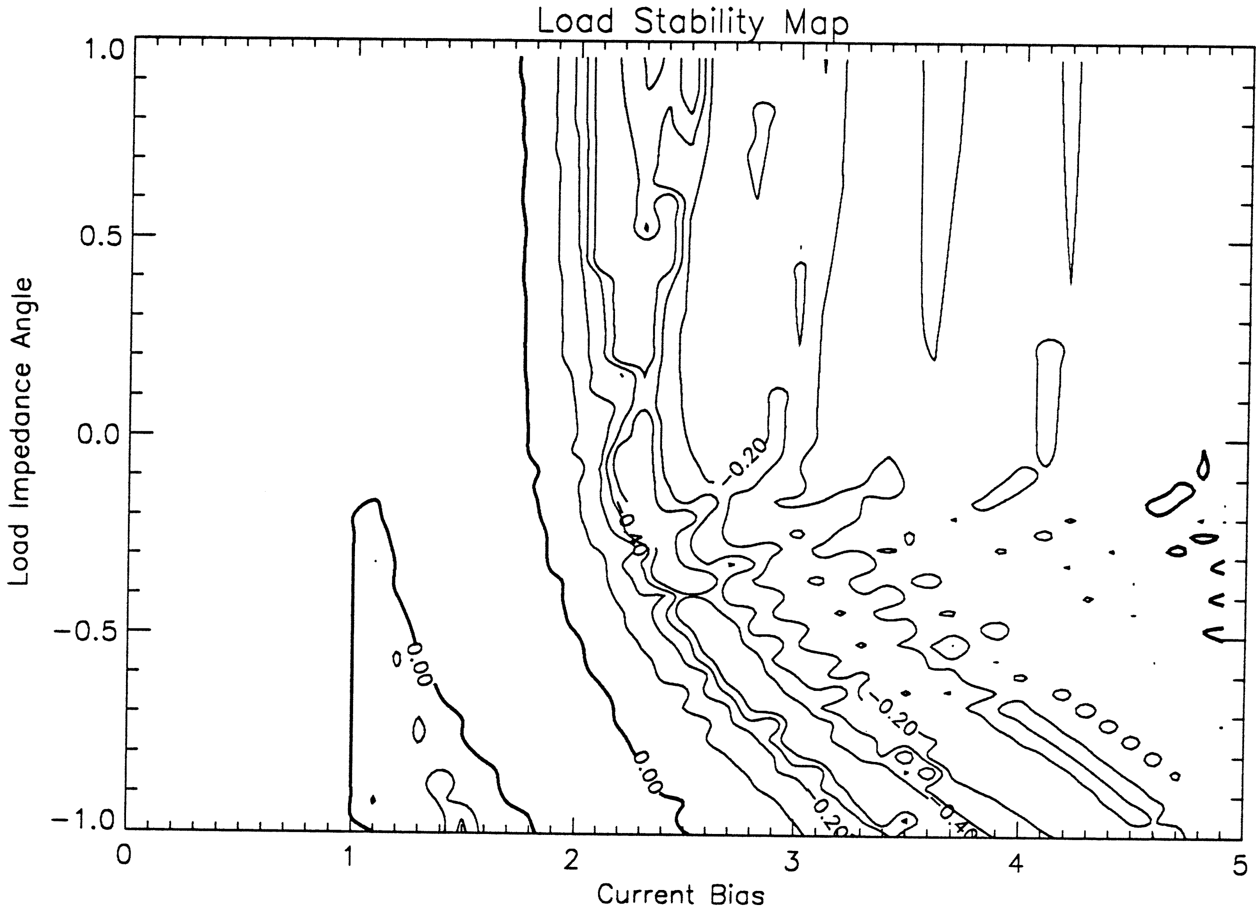

Figure 2. Floquet exponent stability plot at $\beta_c = 1.0$.

In a practical experiment, the circuit designer has good knowledge and control over internal circuit parameters of the oscillator: the critical current, shunting resistor, and junction capacitance. As a result,

tradeoffs are made to choose an appropriate β_c for stable, high power oscillation. Often it is the external load which is less well known. The oscillator design should either be unconditionally stable, or at least stable for a wide range of load impedances.

In our simulations we have chosen $\beta_c = 1.0$ in order to produce highly stable oscillations for a resistive load according to the Hadley calculations. We have then explored the dependence upon load impedance by running the simulation varying load impedance according to the following formula, parameterized by θ.

$\theta > 0$ series combination of a resistor and inductor

$\theta = 0$ a 1 ohm resistor

$\theta < 0$ parallel combination of a resistor and capacitor

In each case, the magnitude of the impedance at the signal frequency was held fixed.

The contour plot in figure 2 shows a typical Floquet exponent map with $\beta_c = 1.0$. The more negative the exponent the greater the stability when the array is phase-locked. The results show that both resistive and partially inductive loads have wide current ranges of stable in-phase oscillation. Capacitive loads also produce stable in-phase oscillation, although over a more limited range of bias current.

The lumped element, series array has several limitations. The simple model ignores series inductance and shunting capacitance which are unavoidably present between junctions. To more realistically model circuits, a transmission line was placed between Josephson elements in our SPICE simulations. Computer runs using this model showed that the physical spacing between the elements would play a major role in the array's ability to phase-lock. Unfortunately these simulations tended to exceed certain internal time-step memory requirements of this version of SPICE.

The dynamics of widely spaced junction arrays

The distributed array oscillator of Wan, et al.[1] consists of a large number of Josephson junction oscillators, separated by transmission line, as shown in Fig. 3. Each of the Josephson junctions is separated from its neighbors by a length of transmission line. DC bias current is supplied either along the array, as shown, or in parallel to each junction.

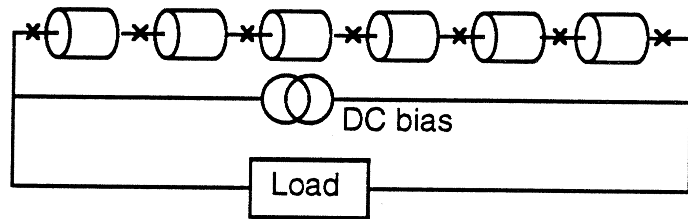

Figure 3. Distributed Josephson junction oscillator array. Identical transmission lines separate each Josephson junction.

The dynamics of the Stony Brook distributed array differs significantly from those of more tightly spaced oscillators. In the latter case, identical current passes through each oscillator element at every instant in time. Interaction between elements is rapid and quite strong. In contrast, coupling between elements of the array is moderated by the transmission lines. Each tunnel junction oscillator interacts with its nearest neighbors only after a time-of-propagation delay, τ.

In the absence of propagation losses, action of the transmission lines is straight forward to calculate. Each transmission line supports two travelling modes: right-going waves and left-going waves. (See Fig. 4.) Since action of the Josephson junction is most readily expressed in terms of a phase parameter, $\varphi(t)$, we define analogous phase quantities $\alpha(t)$ and $\beta(t)$ to describe the waveforms of the left-going and right-going waves. The time derivatives of $\alpha(t)$ and $\beta(t)$ gives the voltage waveforms at the ends of the transmission lines.

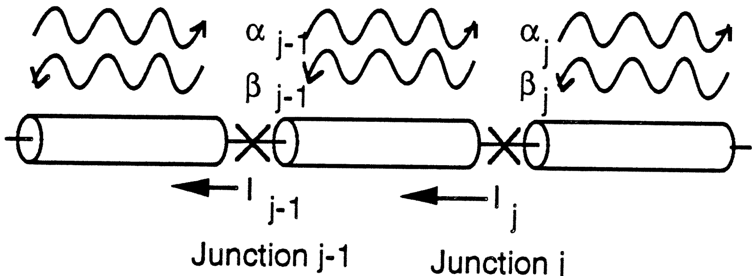

Figure 4. Detailed view of the distributed Josephson junction oscillator array. Each transmission line supports two travelling modes: a left-going wave with amplitude β(t), and a right-going wave with amplitude α(t).

The equations of motion of the large array are set by current continuity conditions, voltage consistency, Josephson dynamics, and external element boundary conditions. The condition that current through each junction must simultaneously equal the current through the ends of attached transmission lines gives rise to the first set of propagation equations:

Due to the propagation delay, a waveform which begins at time t -τ at junction j-1 appears at junction j at time t.

$$I_j(t) = \Phi_0/2\pi Z_0\ [\beta_j(t-\tau)' - \alpha_j(t)'] \quad (1)$$

$$I_j(t) = \Phi_0/2\pi Z_0\ [\beta_{j-1}(t)' - \alpha_{j-1}(t-t)'] \quad (2)$$

where Z_0 is the transmission line characteristic impedance. Similarly the voltage at the transmission line ends depend in part on earlier generated waveforms. The voltage across each junction can be expressed as the difference in voltage between adjacent transmission lines:

$$\varphi_j' = [\alpha_j(t)' + \beta_j(t-\tau)'] - [\alpha_{j-1}(t-\tau)' + \beta_{j-1}(t)'] \quad (3)$$

In addition, the current through each junction must satisfy the Josephson equations:

$$I_j(t) = I_c \sin\varphi_j + \Phi_0/2\pi R_j\ \varphi_j' + \Phi_0 C/2\pi\ \varphi_j'' \quad (4)$$

for the RSJ model. Finally, the total current and voltage across the array must satisfy the boundary condition imposed by the external load.

$$V_{total} = \Phi_0/2\pi \ [\varphi_N' + \alpha_{N-1}(t-\tau)' + \beta_{N-1}(t)'] \qquad (5)$$

$$I_{total} = I_N$$

for an N junction array. For the special case of a resistive load, R_{ext}, this requirement becomes:

$$I_N = \Phi_0/2\pi R_{ext} \ [\varphi_N' + \alpha_{N-1}(t-\tau)' + \beta_{N-1}(t)'] \qquad (6)$$

Numerical results

We have numerically solved the dynamical equations describing oscillator junctions separated by lossless transmission lines. For a system of N identical junctions with N-1 transmission lines, the equations readily reduce to a system of N second order differential equations. We computed solutions to these equations using standard Runge-Kutta integration. In all cases we chose junction parameters and the load to produce a stable, coherent oscillation according to lumped element calculations. Results of the calculations are in qualitative agreement with Stony Brook experimental results[1], and provide interesting insight into oscillator operation.

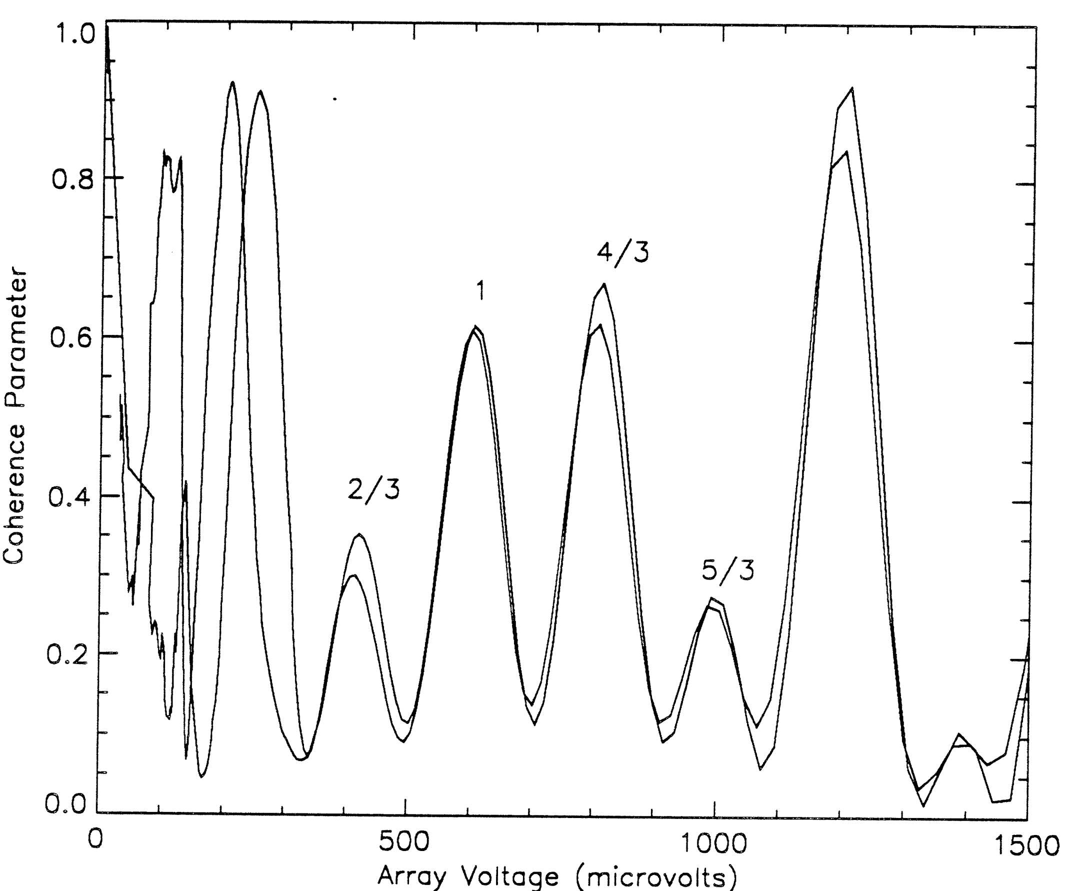

Figure 5. Numerical solution to 3 junction widely spaced junction. Fractions indicate the number of wavelengths between each junction.

Fig. 5 shows the results of a 3-junction simulation, the simplest non-trivial array. Taking account of time-of-propagation delay between junctions, we have tabulated a phase coherence parameter defined by:

$$\xi = < [\Sigma \sin (\varphi_j + j\tau)]^2 + [\Sigma \cos (\varphi_j + j\tau)]^2 > /N^2 \qquad (7)$$

where the average is taken over several oscillation cycles. This measure of phase should be one if the junctions waveforms add constructively, or less if cancellation reduces the total voltage output to a lower value.

Portions of the simulation data follow the predictions of theory. For frequencies which put precisely one oscillation wavelength between elements, the junction voltages add coherently and ξ approaches one. In

addition, the coherence parameter also is large at third sub-harmonics, where integer wavelengths fit in the *entire* array. This numerical prediction agrees with experimental observations of Wan, et al, who noted a large number of discrete frequencies of high output power.

Some aspects of the numerical simulations remain unexplained. Full phase coherence is not observed, despite the correspondence to in-phase stability in the equivalent lumped model. The reason for sub-harmonic response is yet unexplained.

Experimental Results

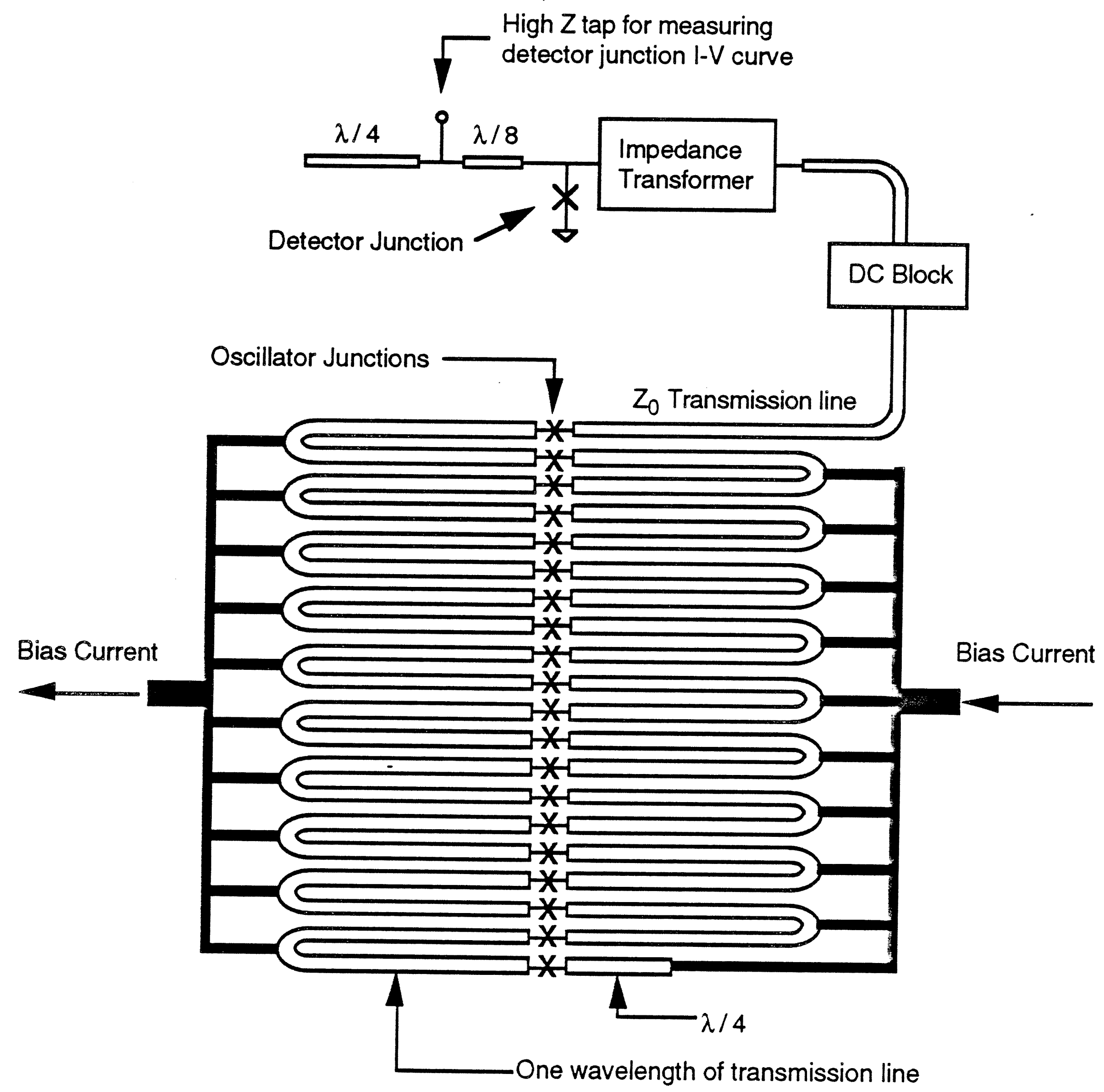

Fig. 7: A schematic diagram of the oscillator array and detection circuitry. The characteristic impedance of the line connected to the top of the array is matched to the output impedance of the array. Not shown are the damping resistors across each oscillator junction. The array is shunted by these resistors so that it can be voltage biased to produce a fixed frequency of RF.

We have fabricated and tested oscillator arrays of the general design suggested by Lukens[6]. In our tests, on-chip detection circuitry measures the RF power produced by the array. The detection circuitry consists of a Josephson junction and passive microstrip components designed to match the overall impedance of the

detector to the output impedance of the array (see Fig. 7). This method of power measurement is a realistic test of the power an array can deliver to an integrated superconducting microwave circuit.

The output of the array is fed through a DC block and an impedance matching network into a microwave detector consisting of a Josephson junction and a tuning stub. The effective conductance to the ground plane of the tuning stub cancels the shunting conductance of the junction capacitance at the operating frequency. Tuning the detector junction in this way increases its sensitivity. This kind of detector has been used successfully in the frequency range of 100 GHz.[7]

The circuit, shown in Fig. 7, is fabricated within TRW's standard Nb process based on $Nb/Al_2O_x/Nb$ junctions defined by selective anodization.[8] All the transmission lines are superconducting microstrip. The junction sizes and critical currents are within the standard range for the process used. The unshunted detector junction I-V characteristic is sharp. (See Figure 8) The oscillator junctions are 4 x 4 μm and the critical current is 1500 A/cm^2. We used these values, which are typical for our standard process, to facilitate incorporating this array design into integrated superconducting microwave circuits.

We fabricated and tested approximately 60 arrays, each with an on-chip power detection circuit as shown in Fig. 7. With the correct bias current flowing through the array, the array junctions oscillate coherently and RF induced steps in the quasi-particle portion of the detector junction I-V characteristic appear. Figure 8 shows the I-V characteristic of a detector junction with and without the array bias current on.

The steps in the quasi-particle portion of the I-V characteristic indicate power detection of approximately 100 GHz RF. We can easily estimate the minimum RF power required at the junction to produce the observed steps in the I-V curve such as those in Fig. 8 using Tucker's analysis[9]. The height of a small current step is given by $\Delta I = R \eta P$, where R is the responsivity of the junction which is at best equal to e/hf (R = 2400 A/W at 100 GHz), η is the impedance matching efficiency which is at best equal to unity, and P is the RF power incident on the junction. The RF power resulting in the step of 0.12 mA shown in Fig. 8 must be at least 0.05 μW.

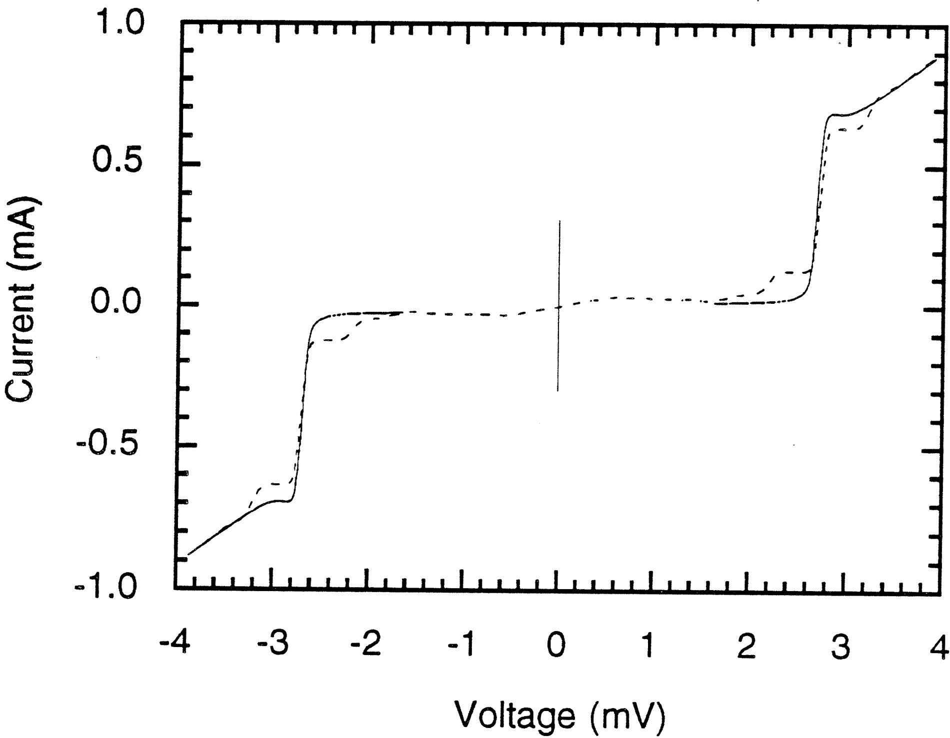

Fig. 8: The detector junction current-voltage curve with no array bias current (solid line), and with the array bias current set for maximum observed power (dashed line).

The distributed arrays produced detectable power when tested. The DC voltage across an array biased to produce power accurately determines the frequency of the oscillations. The voltage measurements were made using the four probe technique across the array while it is oscillating. All of the arrays oscillated at frequencies somewhat higher than the designed frequency of 100 GHz. Figure 9 shows a histogram of the arrays tested sorted by the frequency range of their oscillations. The size of the frequency error seems to be larger than one would expect to be due to miscalculation of the electrical length of the transmission line connecting the oscillator junctions in series. We believe this observation of power at a higher frequency than the nominal design value is consistent with that observed by Lukens and coworkers.[6]

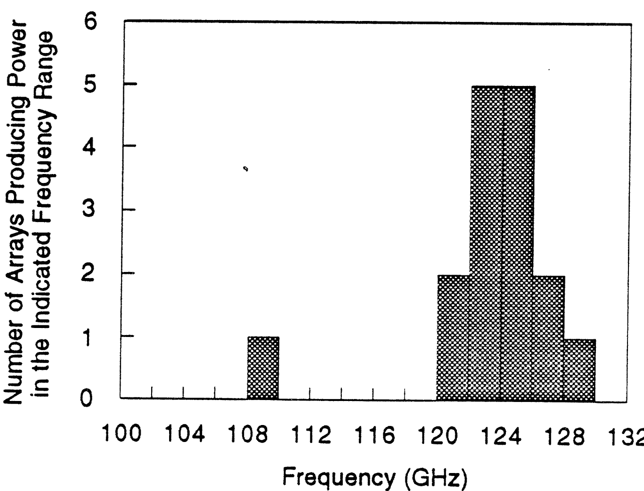

Fig. 9: The number of arrays tested which produced RF power in a given frequency range. All arrays were designed to oscillate at 100 GHz.

Conclusions

We have extended the lumped element analysis of Hadley, et al., to cover a particular case of practical importance: an oscillator array with optimum β_C feeding a complex load impedance. We find wide parameter ranges of stable, in-phase operation of oscillator elements.

We have also derived the equations of motion for the distributed array, and numerically solved the equations for several particular instances of interest. We find a significant deviation from simple extrapolations of lumped element analysis. Coherence in lumped element oscillator arrays does not guarantee stable coherent operation of distributed oscillators.

We have reported the fabrication and testing of several oscillator arrays. The on-chip detection circuitry provided a realistic test of the arrays operation in an integrated superconducting circuit. We observed at least 50 nW of 125 GHz power.

Acknowledgements

It is our pleasure to acknowledge important useful discussions with Jim Lukens and his group at SUNY Stony Brook and Arnold Silver. This work was sponsored by AF Contract F 19628-86-C-0154 with the

Electromagnetics Directorate of Rome Air Development Center, funded by the Innovative Science and Technology Office of the Strategic Defense Initiative Organization.

References

---

1 K. Wan, A. K. Jain, and J. E. Lukens, "Submillimeter wave generation using Josephson junction arrays", Appl. Phys. Lett., 54, (18), 1805-7, (1 May 1989).

2 P. Hadley, "Dynamics of Josephson Junction Arrays", Ph.D. Dissertation, Stanford University, March 1989.

3 A. K. Jain, K. K. Likharev, J. E. Lukens, and J. E. Sauvageau, "Mutual Phase-Locking in Josephson Junction Arrays", Physics Reports, 109, 6, 309-426, (1984).

4 R. E. Jewett, "Josephson Junctions in SPICE 2G5", University of California at Berkeley, 1982.

5 A. D. Smith, R. D. Sandell, A. H. Silver, and J. F. Burch, "Chaos and Bifurcation in Josephson Voltage-Controlled Oscillators", IEEE Trans. Mag, MAG-23, 2, March 1987.

6 James Lukens, "Josephson Arrays as High Frequency Sources", in *Superconducting Devices*, Edited by Steven T. Ruggiero and David. A. Rudman, Academic Press, Inc., (1990).

7 A. D. Smith, et al. to be published in the Proceedings of the ASC '90.

8 J. M. Murduck, J. Porter, W. Dozer, R. Sandell, J. Burch, J. Bulman, C. Dang, L. Lee, H. Chan, R. W. Simon, and A. H. Silver, "Niobium Trilayer Process for Superconducting Circuits", IEEE Trans. Magn. **25**, 1139 (1989).

9 John R. Tucker, "Quantum Limited Detection in Tunnel Junction Mixers", IEEE Journal of Quantum Electronics, **11**, 1234, (1979).

Terahertz Power-Combining with Coupled Oscillator Arrays

R. A. York and R. C. Compton

School of Electrical Engineering
Cornell University
Ithaca, New York 14853

Abstract — A quasi-optical method for solid-state power-combining is discussed, with application to high-power millimeter-wave generation. The approach uses two-dimensional planar arrays of coupled oscillators. These arrays are distinguished by the strength of the coupling, which is limited to weak interactions. This simplifies both the analysis and design of the arrays. A theoretical description of the coupled-oscillator arrays is briefly discussed, along with experimental results for two prototype arrays using Gunn and MESFET devices at X-band. Experiments indicate that mutual synchronization of the elements is facilitated by using a quasi-optical reflector to control the inter-element coupling.

Introduction

Devices such as resonant tunneling diodes and Josephson junctions have demonstrated modest power levels in oscillator circuits in the millimeter/sub-millimeter range. However, applications such as space communications or remote sensing and imaging will require much higher power levels than could be obtained from a single millimeter-wave device. A solid-state source for these applications must combine the output powers of thousands of devices. Clearly the traditional power-combining methods used for lower frequencies [1] are not feasible. For high efficiency and high power levels, a quasi-optical approach has been proposed in which the power-combining takes place in free-space [2].

This paper discusses one type of quasi-optical array, which incorporates many single-device oscillator elements in a classical antenna array. Weak mutual coupling synchronizes the array elements, enabling coherent summation of individual power outputs. This approach is not to be confused with another reported technique [10], using a distributed oscillator approach where the devices are mounted in a periodic grid structure and placed in an open quasi-optical cavity. The primary difference between the two methods is the amount of coupling between the elements. It is too early yet to articulate the relative merits of the two systems.

In the present approach, the strength of the coupling between elements is limited to ensure that each element operates close to its free-running state. In this configuration, the operating frequency is set by the design of the individual oscillator elements and biasing considerations. This technique is modular, as more elements can be added to increase the power without altering the operating frequency. Thus the important components in our power-combining arrays are the individual oscillator elements themselves.

The active radiating elements consist of a suitable device integrated into a printed radiating structure. The choice of device and radiating structure depends on many factors, such as operating frequency, power dissipation requirements, and substrate considerations. Several novel architectures have appeared in the literature [3-5] which creatively incorporate an active device in a planar microstrip antenna. The experimental arrays described later were constructed using two different active microstrip patch antenna designs, one with a Gunn diode [3] and the other with a MESFET [5]. The device is located at the point where it's impedance is matched to that of the antenna. Small signal device models, and simple analytical models for the antenna structures are usually sufficient for design purposes.

Coupled Oscillator Theory

The description of coupled oscillators is greatly simplified by the assumption of weak coupling between the elements. In this case, the individual oscillators are only slightly perturbed from their free-running state by the presence of the neighboring oscillators. It can then be argued that the steady-state behaviour is governed by the phase dynamics alone [7]. Similar arguments were put forth by Adler in connection with his famous injection-locking equation [6], which describes the phase dynamics of an oscillator under the influence of a weak injection signal. By suitably modifying Adler's equation, we can arrive at a dynamical equation for the coupled oscillator system.

Adler's equation for injection locking is

$$\frac{d\phi_0}{dt} = -\frac{A_{\text{inj}}}{A_0}\frac{\omega_0}{2Q}\sin(\phi_0 - \psi_{\text{inj}}) + (\omega_0 - \omega_{\text{inj}}) \tag{1}$$

where ϕ_0 = phase of oscillator, ψ_{inj} = phase of injected signal, ω_0 = free-running frequency of oscillator, ω_{inj} = frequency of injected signal from an external or neighboring oscillator, A_0 = free-running amplitude of oscillator (voltage), A_{inj} = amplitude of injected signal (voltage),

and Q = the external Q of the oscillator circuit. The oscillator phase is defined relative to the injected signal, so that $\omega = \omega_{\text{inj}} + d\phi_0/dt$ is the instantaneous frequency of the oscillator. Generalizing (1) to the case of several simultaneously injected signals, and describing the mutual coupling by a complex coupling coefficient, $\lambda_{ij}\ \exp(\jmath\Phi_{ij})$, gives the set of equations

$$\omega = \omega_i \left[1 - \sum_{j \neq i}^{N} \frac{\lambda_{ij}}{2Q_i} \frac{A_j}{A_i} \sin(\phi_i - \phi_j + \Phi_{ij}) \right] \qquad i = 1, 2, \ldots, N \tag{2}$$

where N is the number of oscillators in the system. Note that the instantaneous frequency ω is the same for all oscillators in the system *at synchronization.* Equation (2) describes a set of equations which can be used to determine the steady-state of the system.

Some simple analytical results can be derived from (2) by considering a linear chain of oscillators with only nearest neighbor interactions. Assuming that the coupling is the same between adjacent elements in the array, $\lambda_{ij} \equiv \lambda$ and $\Phi_{ij} \equiv \Phi$. Furthermore, let $Q \equiv Q_i$, $\lambda' \equiv \lambda/2Q$, $\rho_i \equiv A_{i-1}/A_i$, and $\Delta\phi_i \equiv \phi_i - \phi_{i-1}$. The set of governing equations becomes

$$\omega = \omega_i \left[1 - \lambda' \rho_i \sin(\Phi + \Delta\phi_i) - \lambda' \sin(\Phi - \Delta\phi_{i+1})/\rho_{i+1} \right] \qquad n = 1, 2, \ldots, N \tag{3}$$

Note that $\rho_1 = 1/\rho_{N+1} = 0$. Despite the simplification, this is still a set of coupled nonlinear equations. In general there are many possible phase distributions which satisfy (3), but not all are stable solutions. Stability of these modes can be investigated using a perturbation analysis. Recalling that $\omega = \omega_{\text{inj}} + d\phi_i/dt$, gives

$$\begin{aligned} \frac{d}{dt}\Delta\phi_i &= \omega_i \left[1 - \lambda' \rho_i \sin(\Phi + \Delta\phi_i) - \lambda' \sin(\Phi - \Delta\phi_{i+1})/\rho_{i+1} \right] \\ &\quad - \omega_{i-1} \left[1 - \lambda' \rho_{i-1} \sin(\Phi + \Delta\phi_{i-1}) - \lambda' \sin(\Phi - \Delta\phi_i)/\rho_i \right] \end{aligned} \tag{4}$$

The phase is then perturbed by a small amount by letting $\Delta\phi_i \rightarrow \Delta\phi_i + \delta_i$. After some algebra this leads to

$$\begin{aligned} \frac{d}{dt}\delta_i &= a_i\delta_{i-1} + b_i\delta_i + c_i\delta_{i+1} \qquad i = 2, 3, \ldots, N \\ \text{where} \quad a_i &= \lambda' \rho_{i-1} \omega_{i-1} \cos(\Phi + \Delta\phi_{i-1}) \\ b_i &= -\lambda' \omega_i \rho_i \cos(\Phi + \Delta\phi_i) - \lambda' \omega_{i-1} \cos(\Phi - \Delta\phi_i)/\rho_i \\ c_i &= \lambda' \omega_i \cos(\Phi - \Delta\phi_{i+1})/\rho_{i+1} \end{aligned} \tag{5}$$

This is of the form of a matrix equation, $d\underline{\delta}/dt = \mathbf{A}\underline{\delta}$, where $\mathbf{A}$ is a tridiagonal matrix, and $\underline{\delta}$ is a column vector with elements δ_i. A stable solution for the phase distribution requires $\underline{\delta}$ to decay with time. This is satisfied when all the eigenvalues of $\mathbf{A}$ have negative real parts.

For power combining applications, we desire a mode of operation where all elements are in phase ($\Delta\phi = 0$). Substituting this into (3) for a chain of identical oscillators, we find that the allowed values of coupling phase are determined by the boundary elements, and are given by $\Phi = n\pi$, where $n = 0, 1, 2 \ldots$. Note that for an infinite chain, any value of coupling phase would satisfy (3). From the stability analysis (5), we find that the eigenvalues of the matrix can have negative real parts only if $\cos\Phi > 0$, so a stable, in-phase mode is only possible if $\Phi = 0, 2\pi, \ldots$.

There are several ways of accomplishing the desired inter-element coupling. Simple proximty-coupling, through free-space and surface waves, could be used, but this means that the elements must be spaced at multiples of one wavelength. Such spacing is generally unacceptable because of grating lobes in the antenna patterns. Another possibility is to use a quasi-optical reflector element (such as a dielectric slab) over the array. This is an attractive alternative since the coupling can be varied by moving this reflector element above the array, thus introducing additional flexibility into the design. Consistent with the weak-coupling assumption, the reflectivity of this element must be small. Another alternative is to use a microstrip coupling circuit to provide a weak coupling signal at the required phase angle.

Since we have chosen to characterize our arrays by this complex coupling parameter, some mention should be made regarding its measurement. Recently a technique has been described [8] for the measurement of mutual coupling between two oscillators. Using this technique, it is possible to determine the complex coupling coefficient directly.

Experimental Array Results

The first experimental array of weakly coupled oscillators was a 16-element array using packaged Gunn diodes, shown in figure 1 [9]. This array design uses individual bias to each device, which was required due to device non-uniformities. Elements of the array are spaced a half free space wavelength apart, a distance which was initially selected based on curves

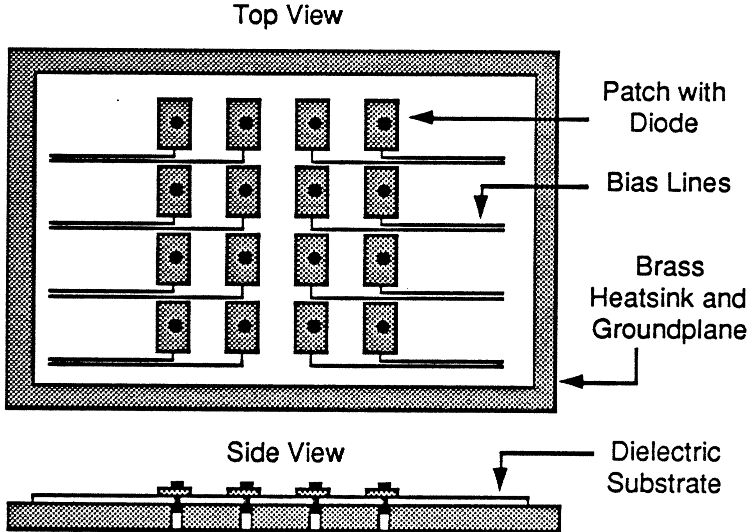

Figure 1 — Diagram of Gunn diodes mounted into a 4×4 array of microstrip patches. The brass block serves as a groundplane, heatsink, and DC bias return. Individual bias to each element is applied at an RF null.

in [2]. Thus a reflector proved necessary for proper operation. The array was designed on a 60 mil substrate with $\varepsilon_r = 4.1$.

Each diode was first biased, one at a time, to establish a common operating frequency. These individual biases were then applied simultaneously. Single frequency operation was verified with a spectrum analyzer, as shown in figure 2b. Spectra resembling figure 2a result when the elements are not all in synchronization. Radiation pattern measurements were made at the final oscillation frequency of 9.6 GHz. The total radiated power was estimated from these patterns to be 415 mW, giving an effective radiated power (ERP) of 22 Watts. The overall DC to RF conversion efficiency was low, typical of Gunn diodes, around 1%.

A second array was constructed with MESFET devices. Much higher efficiency, larger tuning range, and better noise properties can be obtained using FET devices. The experimental MESFET array is depicted in figure 3. The individual element design [5] uses a general purpose Fujitsu device (FSX02). Half as many bias lines were used in this array design, with bias isolation between the elements provided using a 6-turn coil. The gate resistor was used to supress bias circuit oscillations. Again, the spacing was chosen to be less than one wavelength to avoid grating lobes, which meant that a reflector element was required for in-phase operation. The array was fabricated on a 93 mil Duroid 5870 substrate ($\varepsilon_r = 2.33$).

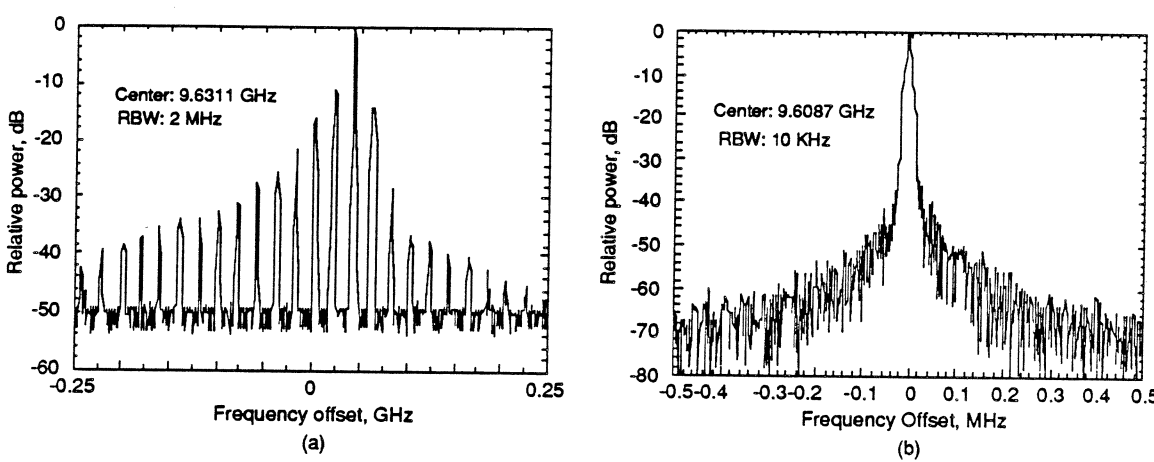

Figure 2 — (a) Spectrum of the Gunn array on the threshold of synchronization, and (b) at full synchronization. These measurements were made with the dielectric reflector in place.

As with the Gunn array, the power-on sequence was to tune each group of elements individually to set a common operating frequency, and then apply DC power to all elements at once. Varying the reflector element spacing is then usually sufficient to enforce mutual synchronization. With single frequency operation verified at 8.27 GHz , the patterns of figure 4 were measured. These patterns closely correspond to the expected pattern when the elements are all in phase. A total radiated power of 184 mW was estimated from the pattern measurements, giving a 10 Watt ERP and 11.5 mW per device at 26% efficiency. The results of the MESFET array are seen to be similar to that of the Gunn array, but with a much higher DC-to-RF efficiency, which makes it a more attractive design.

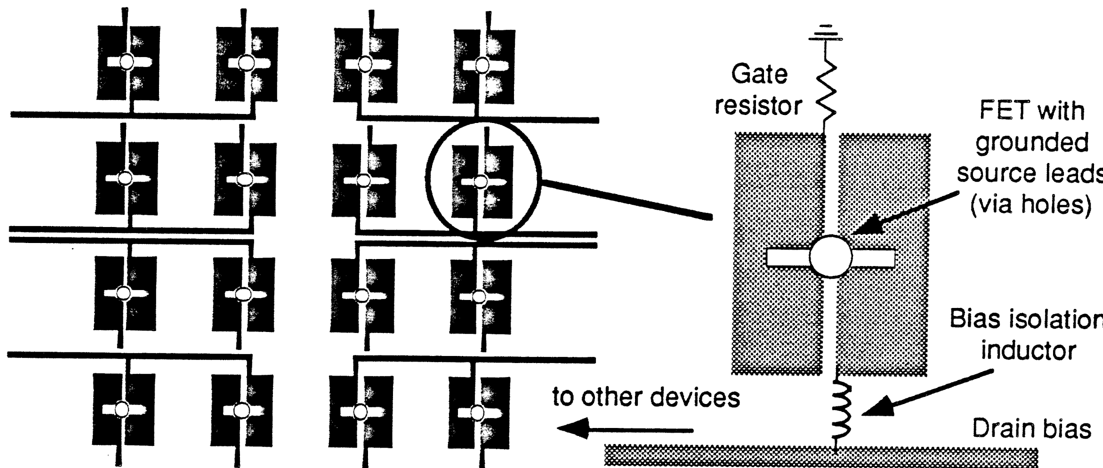

Figure 3 — Sketch of the array which uses Fujitsu fsx02 MESFETs, showing bias arrangement and individual element design. Elements measure 11 mm by 15 mm and the spacing of the elements is 0.67 λ_0 between centers. The bias inductor reduces element interactions along the bias line.

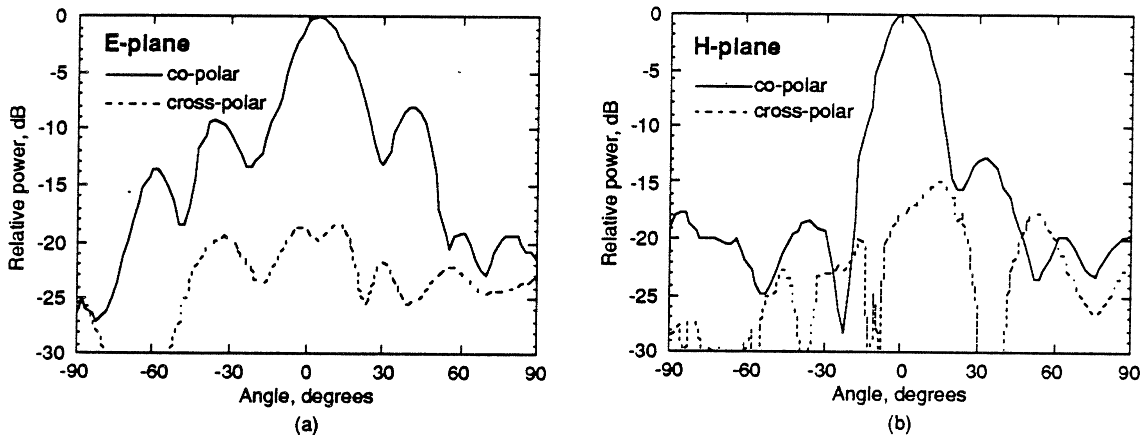

Figure 4 — (a) E-plane and (b) H-plane patterns for the 4×4 MESFET array. The measurements were made at 8.27 GHz, using a flat, 2.5 cm thick dielectric reflector with a dielectric constant of 4. The good patterns indicate in-phase operation.

Conclusion

An architecture for quasi-optical power combining has been discussed, which involves mutually synchronized arrays of single-device oscillators. The oscillators are allowed to interact weakly in order to synchronize the frequency and phase relationships. A quasi-optical reflector element was found to aid in establishing a desired phase relationship. A simple theory based on Adler's equation has also been presented, which establishs certain design guidelines for these types of arrays.

The proposed concepts have been verified using two 16-element X-band arrays. Both of the arrays were constructed using hybrid assembly techniques. For large arrays, biasing will be an important issue. Individual bias to each element also allows the system to degrade gracefully—for multiple devices on a single bias, failure of one device often leads to failure of all of the devices. However, individual bias to all the elements of a large array containing several hundred devices is impractical. Proper operation of the array requires that the elements have nearly identical characteristics, which would allow them to be biased from a common source. Monolithically fabricated arrays could yield the required uniformity between elements to make this technique possible, and are expected to be the best test of theory and design concepts presented here.

Acknowledgements

The authors are indebted to Professor B. Z. Kaplan for helpful discussions regarding coupled oscillator theory, and to Professors D. B. Rutledge at Caltech and K. D. Stephan at U. Mass. for their advice and encouragement. This work is supported by the U.S. Army Research Office and General Electric.

References

[1] K. Chang and C. Sun, "Millimeter-Wave Power-Combining Techniques," *IEEE Trans. on Microwave Theory Tech.*, vol. MTT-31, pp. 91–107, Feb. 1983. Contains an extensive reference list on classical combining techniques.

[2] J. W. Mink, "Quasi-Optical Power Combining of Solid-State Millimeter-Wave Sources," *IEEE Trans. on Microwave Theory Tech.*, vol. MTT-34, pp. 273–279, Feb. 1986.

[3] H. J. Thomas, D. L. Fudge, and G. Morris, "Gunn source integrated with microstrip patch", *Microwaves & RF*, pp. 87-89, Feb. 1985.

[4] N. Camilleri and B. Bayraktaroglu, "Monolithic mm-wave IMPATT Oscillator and Active Antenna", *IEEE Trans. Microwave Theory Tech.*, vol. MTT-36, pp. 1670–1676, Dec. 1988.

[5] R. A. York, R. M. Martinez and R. C. Compton, "Hybrid Transistor and Patch Antenna Element for Array Applications", *Electron. Lett.*, vol. 26, pp. 494–495, March 1990.

[6] R. Adler, "A Study of Locking Phenomena in Oscillators", *Proc. IRE*, vol. 34, pp. 351–357, June 1946; also reprinted in *Proc IEEE*, vol. 61, no. 10, pp. 1380–1385, Oct 1973.

[7] B. Z. Kaplan and K. Radparvar, "Canonic Coupling of Oscillators in a Chain", *J. Franklin Inst.*, vol. 325, no. 1, pp. 49–60, 1988.

[8] W. P. Shillue and K. D. Stephan,"A Technique for the Measurement of Mutual Impedance of Monolithic Solid-State Quasi-Optical Oscillators", *Microwave and Opt. Tech. Lett.*, Dec 1990

[9] R. A. York and R. C. Compton, "A 4×4 array using Gunn diodes", *IEEE Antennas and Propagation International Symposium* (Dallas), May 1990.

[10] Z. B. Popovic, R. M. Weikle, M. Kim, K. A. Potter, and D. B. Rutledge, "Bar-Grid Oscillators", *IEEE Trans. on Microwave Theory Tech.*, vol. MTT-38, pp. 225–230, March 1990.

Millimeter and Submillimeter Wave Quasi-optical Oscillator with Multi-elements

M.Nakayama, M.Hieda, T.Tanaka, H.Kondo, K.Osakabe and K.Mizuno

Research Institute of Electrical Communication, Tohoku University, Sendai, 980 Japan

ABSTRACT

Multi-elements oscillators with a quasi-optical resonator are reported. The resonator consists of a Fabry-Perot cavity with a grooved mirror and concave mirror. The oscillator has capability for power-combing of solid-state sources in the millimeter and submillimeter wave region. X-band models consisting of Gunn diodes or GaAs MESFET's have been demonstrated. Coherent power combining and frequency-locking of 18 diodes (6x3 grid) and 6 FET's (3x2 grid) have been successfully observed at X-band. We have also succeeded frequency-locking of 3 Gunn diodes at U-band. A W-band InP Gunn diode oscillator using a same configration is also reported.

INTRODUCTION

Recently, many kinds of oscillators have been developed for use of millimeter and submillimeter wave frequencies. Solid-state devices have many advantages: small size, light weight, and low-voltage power supplies. As frequency increases, however, output power becomes small. In addition, the dimensions of conventional waveguide cavities become very small and ohmic losses in the metal wall increase. Therefore, coherent power combining of a large number of devices using quasi-optical resonators is attractive. A wide variety of quasi-optical power-combining method using Gunn diodes and MESFET's have been demonstrated [1],[2]. We have proposed a Fabry-Perot resonator with a grooved mirror for solid-state oscillators [3],[4]. In this paper, we report the results of experiments with an X-band model consisting of Gunn diodes and GaAs MESFET's and the results of a U-band Gunn diodes oscillator.

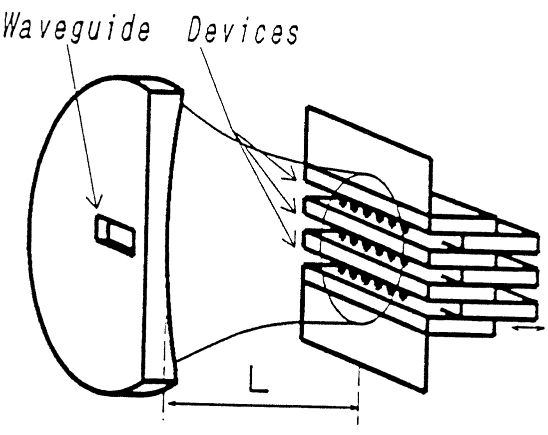

Fig. 1 Resonator configuration.

CONFIGURATION

The configuration of the resonator is shown in Figure 1. It consists of a grooved mirror and a concave spherical mirror facing each other. Figure 2 shows the structure of the grooved mirror. The groove pitch D must be less than oscillator wavelength to avoid diffraction losses. The Gunn diodes are mounted in grooves and biased by the top and the bottom plates of each groove (Fig.2a). These plates are insulated by thin (80μm)teflon tape. Similarly, FET's(Fujitsu FSX52-LF) are mounted on the surface of the groove. Gate and drain ribbons are connected to adjacent insulated plates. The spherical mirror's radius of curvature is 200mm or 400mm. The groove depth t could be continuously changed to adjust the impedance of the groove. Output power is taken out by a waveguide at the center of the spherical mirror.

The U-band and W-band resonators consist of spherical mirror which radius of curveture are 100mm and 60mm respectively.

The resonator proposed here has the following advantages: it has a large heat dissipation capacity, can mount large number of devices, is lager enough than wave length, and has simple bias circuit.

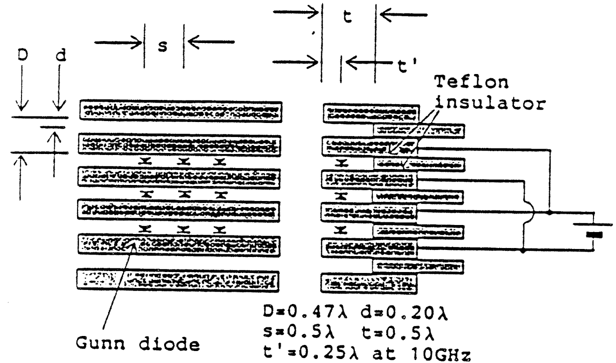

Fig. 2a Grooved mirror for diodes.

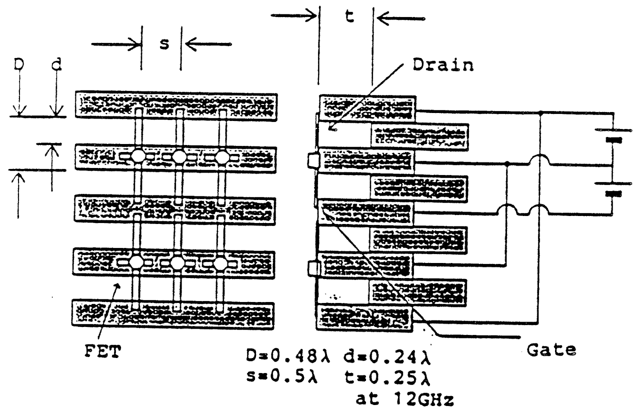

Fig. 2b Grooved mirror for FET's.

X-band Gunn diode oscillator

Figure 3 shows the spectra for the Gunn diode(JRC NJX4410) oscillators. We have succeeded in frequency locking and power combining. Furthermore, it is seen that the spectrum for nine diodes is much narrower than that for a single diode. The optimum depth of each groove was about $\lambda/2$. The optimum spacing between elements in a groove has been chosen experimentally. Good results were obtained with spacing of $\lambda/2$. At present, we have succeeded in frequency locking and power combining for up to 18 diodes (6×3 grid), obtaining an output power of

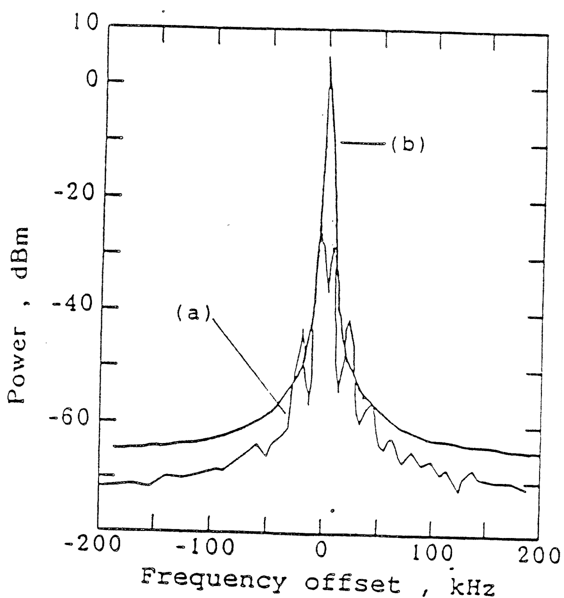

Fig. 3 Spectra of Gunn diode oscillators.
(a) Single diode. (L=107.2mm,fc=10.0336GHz)
(b) Nine (3×3 grid) diodes.
(L=104.2mm,fc=10.2293GHz)

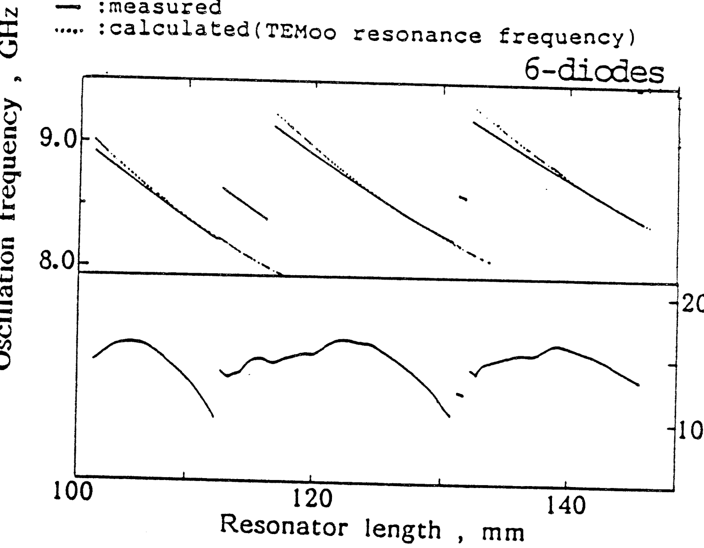

Fig. 4 Oscillation frequency and output power of 6(6×1grid) diodes oscillator versus resonator length. Calculated line shows resonance frequency of TEM_{00} mode.

123mW at 8.3GHz. This is roughly 18 times the power from a single diode oscillator with a waveguide cavity. The C-N ratio is 83dB/Hz at a 12.5kHz offset.

Figure 4 shows how the oscillation frequency varies with the length of the resonator with 6 Gunn diodes. The mechanical tuning range is about 11%. Oscillation frequency agrees with theoretical resonant frequency of the fundamental (TEM_{00}) mode of the Fabry-Perot resonator. Resonant modes were identified by measuring the field distribution in the cavity. This was measured by moving a small ($< \lambda/10$) piece of absorber through the cavity.

12GHz FET oscillator

We have succeeded in frequency locking and power combining 6 FET's in a 3 × 2 grid at 12GHz. Noise reduction was observed just as in the case of the Gunn diode oscillator. We had 6dB more power with locked 6FET's than single FET. As the resonator length varies, the oscillator frequency shifts over 600MHz. The oscillation frequency agree with the calculated resonant frequency of fundamental mode(TEM_{00}).

U-band Gunn diode oscillator

We have succeeded frequency locking and power combining with U-band Gunn diodes. Figure 5 shows the spectra for U-band Gunn diode oscillator. The spectrum for three diodes is narrower than that for single diode. The 3dB more output power have been obtained with three diodes. The Gunn diodes(Alpha DGB8266) are mounted in the same groove. The spacing of the diodes s and groove depth t are same as X-band model experiments.

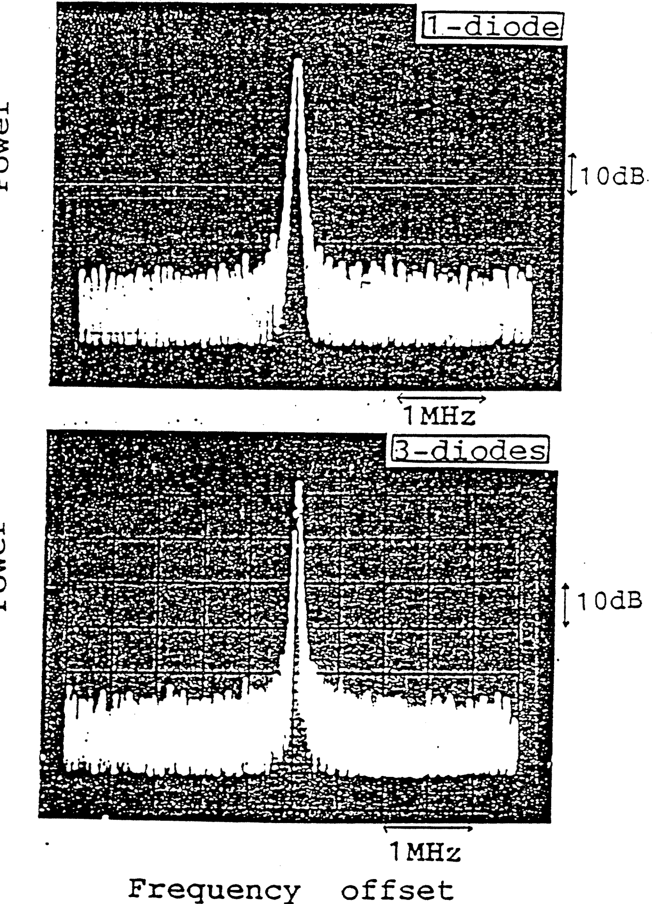

Fig. 5 Spectra of U-band diodes oscillators.
(a) Single diode.
(b) Locked 3 diodes.

W-band Gunn diode oscillator

We have constracted W-band InP Gunn diode oscillator with same resonator configration. Figure 6 shows how oscillation frequency varies with the resonator length. The mecanical tuning range is 2.6%. The maximum output power is 4dBm. The InP Gunn diode (Acrotec NT-W50) is mounted at the center of grooved mirror.

CONCLUSION

We have demonstrated the utility of a quasi-optical oscillator with multi-elements. The resonator consists of Fabry-Perot cavity with a grooved mirror. It has the capability of power combining many solid-state sources at millimeter and submillimeter wave regions. Frequency-locking and coherent power combining of 18 Gunn diodes and 6 GaAs FET's have been successfully observed at X-band. The oscillation mode is the fundamental mode (TEM_{00}) of the Fabry-Perot resonator. We have also reported U-band 3 Gunn diodes oscillator and a W-band Gunn diode oscillator with the same configuration.

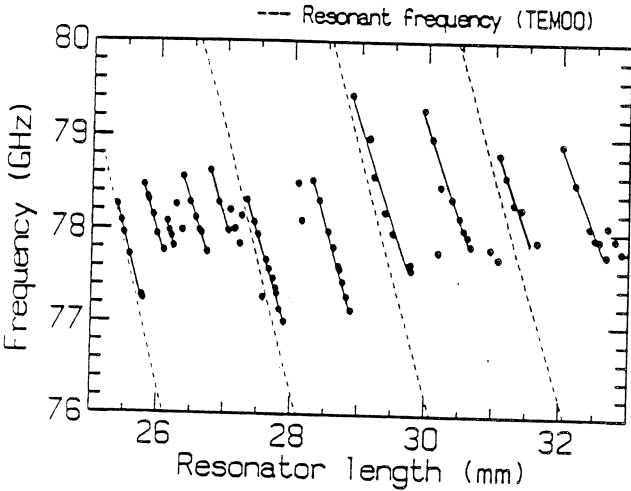

Fig. 6 Oscillation frequency W-band diode oscillator versus resonator length. Broken line shows resonance frequency of TEM_{00} mode.

REFERENCES

[1] D.B.Rutledge, Z.B.Popović, R.M.Weikle II, M.Kim, K.A.Potter, R.C.Compton, R.A.York, 'Quasi-Optical Power-Combining Arrays', IEEE Microwave Symposium 1990, MTT-S Digest, pp1201-1204, 1990

[2] K.D.Stephan and T.Itoh, 'Recent Efforts on Planar Components for Active Quasi-optical Applications' IEEE Microwave Symposium 1990, MTT-S Digest, pp1205-1208, 1990

[3] K.Mizuno, T.Ajikata, M.Hieda, and M.Nakayama, 'Quasi-Optical Resonator for Millimeter and Submillimeter Wave Solid-state Sources', Electronics Letters, Vol.24, pp.792-793, June 1988

[4] M.Nakayama, M.Hieda, T.Tanaka, and K.Mizuno, 'Quasi-Optical Resonator for Millimeter and Submillimeter Wave Solid-State Sources', IEEE Microwave Symposium 1990, MTT-S Digest, pp.1209-1212, 1990.

Network Analysis of Planar Spatial Power Combining

Tatsuo Itoh
Dept. of Electrical Engineering
University of California, Los Angeles
Los Angeles, CA 90024-1594

ABSTRACT

Planar multiple-device power combining fundamental and harmonic oscillators based on the periodic structure are presented. A small signal analysis based on a network theory leading to the design of such oscillator is described. A large signal analysis based on a new voltage-frequency updating method is used for characterizations of typical configurations.

1. INTRODUCTION

As the frequency of operation is increased, output power from any solid state device tends to decrease. In order to achieve a meaningful amount of power, a power combining is a remedy [1]. At millimeter-wave frequencies and beyond, the loss in the waveguide structures increases. Thus the spatial power combining becomes attractive [2]. More recently, the integrated circuit technology has been advanced in such a degree that many millimeter-wave circuits can be built in an integrated circuit form. In addition to typical advantages of the integrated circuits, its open nature can be used for an additional benefit. The radiating function can be incorporated directly so that a component that can be used in a quasi-optical system can be developed. Several examples of such circuits have been reported [3,4]. In addition, it is often more advantageous to generate a harmonic directly from a planar oscillator, because most solid state devices exhibit nonlinearity in addition to negative resistance [5].

This paper deals with the modeling aspect of a planar periodic power combining oscillator. In its original form this is a planar integrated circuit version of the single cavity multiple-device Kurokawa oscillator [6]. However, due to its open nature, it can be used for a quasi-optical power combining. In what follows, the structure and operating principle are briefly described. This is followed by a simple application of the eigenvalue equation for operation according to Kurokawa. Finally, a new voltage-frequency update method [7] will be applied to a typical power combining oscillation.

2. STRUCTURE AND OPERATING PRINCIPLE

Fig.1 shows a typical configuration of the periodic power combining oscillator. In this particular example, Gunn diodes are used for circuit demonstration at X band, although different types of devices such as QWITT are likely to be used at higher frequencies. In Fig.1, the inductive stub essentially resonates out the shunt capacitance of the device which is assumed to be expressed as a parallel combination of such capacitance and a negative resistance. The equivalent circuit for this structure is shown in Fig.2. If one chooses the distance d equal to one half of guide frequency, this periodic structure falls into the surface wave stopband region so that the devices are mutually locked in the oscillation. On the other hand if the spacing between the devices is one guide wavelength, the periodic structure falls into the leaky wave stopband so that the oscillation signal radiates into the

broadside direction. Hence, if the multiple-device oscillator oscillates at the frequency corresponding to the surface wave stop band, and subsequently generates the second harmonic due to nonlinearity in the device, then the second harmonic coincides with the leaky wave stop band, provided that the dispersion of the connecting transmission line is negligible. Since the phases of the second harmonic at each device are identical, the radiating beam is in the broadside direction. Fig.3 shows an example of such a harmonic space combiner.

3. EIGENVALUE EQUATIONS FOR PERIODIC STRUCTURES

The theory developed by Kurokawa [6] and Peterson [8] can be applied to the structure under discussion here. For an N element construction, the impedance matrix seen from the device ports can be described by the elements z_{ij} (i, j = 1,..., N). The modes of operation can be identified by finding the eigenvalues and the eigenvectors of this impedance matrix. In the case where the spacing between the devices loading the transmission line periodically and the periodic structure is terminated by a load R as shown in Fig.2, z_{ij} can be derived readily from the network analysis. The problem of interest is the case where the periodic structure falls into the stopband region. In the case of the surface wave stopband, only resistive load appearing in this network is R in the figure. Since the electrical length of each period is one half of the wavelength, the impedance matrix becomes

$$Z = R\begin{bmatrix} 1 & -1 & 1 & -1 & . & . & . \\ -1 & 1 & -1 & 1 & . & . & . \\ 1 & -1 & 1 & -1 & . & . & . \\ -1 & 1 & -1 & 1 & . & . & . \\ . & . & . & . & . & . & . \end{bmatrix} \qquad (1)$$

There are N eigenvalues and N eigenvectors. However, all but one eigenvalues are zero. The nonzero eigenvalue is NR. This means that at the fundamental frequency only one mode oscillates because all device ports are short circuited for all other N-1 modes. For the nonzero mode, the oscillation condition is satisfied if one chooses R such that

$$R = -Z_{device}/N \qquad (2)$$

This is the usual oscillation condition. On the other hand, the structures with distributed loads such as those shown in Fig.3, the impedance matrix for the fundamental oscillation is obtained by replacing R in (1) with Z_{in}/N where Z_{in} is the input impedance of the patch structure at the connecting point to the device. Therefore, once again only one mode has nonzero eigenvalue and the oscillation condition for this mode is

$$Z_{in} = -Z_{device} \qquad (3)$$

For the second harmonic oscillation, the period between the devices becomes one full wavelength so that the electrical length is 2π. Therefore all the elements in the impedance matrix become unity. Once again, only one mode has a nonzero eigenvalue for which the oscillation condition is given by (3) except that both sides of the equation need to be evaluated at the second harmonic frequency. The discussions presented in this chapter do not provide information at frequencies other than the design frequency.

4. LARGE SIGNAL MODELING

In the periodic power combining oscillator such as those presented above, the coupling of the devices is very strong. Hence, the ability to self-lock to each other cannot be correctly predicted by the weakly coupled formulation by Adler. Although the eigenvalue analysis developed by Kurokawa [6] is useful for finding the modal behavior of the configuration, it does not include the effect of higher harmonics and assumes that the large signal device impedances are a function of amplitude only.

In the present paper, the voltage-frequency update method developed in [7] is applied to the periodic power combining oscillators. Since the three types presented above operate essentially on the same mechanism, the one shown in Figs.1 and 2 are used for modeling here. However, before presenting a specific application, the basic procedure in [7] is given, although the details are left in [7].

In this method, the harmonic balance equation is solved consistently by means of the modified relaxation technique. The voltage across each port joining the passive and active subcircuit is expressed either in terms of the time series or the Fourier spectrum. This voltage applied to the device side provides the current at the joining port. The current is then applied to the passive subcircuit to find the updated voltage. In updating the voltage, we use a relaxation method with appropriate relaxation constant. This technique is quite standard in many amplifier analysis techniques [9]. In the case of free-running or self-locking oscillators, the oscillation frequency is another unknown. Therefore, the frequency must also be updated in a relaxation process. This is introduced in [7].

The structure to be analyzed has two resonant mechanisms. At the each device terminal, an inductive stub is attached to nullify the shunt capacitance of the device. This arrangement makes the device impedance purely resistive to satisfy the oscillation condition in (2). In addition, the half wave spacing between the devices provides another mechanism for resonance. In the example of calculation, it is assumed that the X band Gunn diode rated for 10 mW output follows a simple cubic law of $i = -0.01v + 0.0015\, v^2 + 0.001v^3$. The device capacitance is assumed to be 0.4 pF. The transmission line used is a 50 Ω microstrip line. In the calculations, a total of twelve harmonics is used. The device resonance determined by the device capacitance and the inductive stub is varied in the test calculations. It is found that as the number of diodes is increased, the importance of the periodicity decreases in comparison with the individual device resonances. When the deviation of the device resonance from the half wave frequency of the periodic structure, no convergent solution can be found and hence the diodes do not lock to each other any more.

The output power from the power combining oscillator is studied as a function of the device resonance. It is found that the output power increases as the device resonance is tuned away from the half wave frequency of the periodic structure. The degree of power increase is more pronounced as the number of diodes is increased from 2 to 4. Since the environment to each device changes as the frequency is detuned, the power generated from individual devices can be different.

5. CONCLUSIONS

A simple design rule for a number of power combining oscillators based on the periodic structure is presented. A new voltage-frequency updating method is used for characterizing the large signal operation of these oscillators.

ACKNOWLEDGMENT

The work reported here was supported by Army Research Office Contract DAAL03-88-K-0005. The author acknowledge the numerical and experimental effort expended by former graduate students, A. Mortazawi and H. D. Foltz at The University of Texas at Austin.

REFERENCES

[1] K. Chang and C. Sun, "Millimeter-wave power combining techniques," IEEE Trans. Microwave Theory and Techniques, Vol. MTT-31, No.2, pp.91-107, February 1983.

[2] J. W. Mink, "Quasi-optical power combining of solid-state millimeter-wave sources," IEEE Trans. Microwave Theory and Techniques, Vol. MTT-34, No.2, pp.273-279, February 1986.

[3] J. Birkeland and T. Itoh, "FET-based planar circuits for quasi-optical sources and transceivers," IEEE Trans. Microwave Theory and Techniques, Vol. 37, No.8, pp.1452-1459, August 1989.

[4] A. Mortazawi and T. Itoh, "A periodic planar power combining oscillator," IEEE Trans. Microwave Theory and Techniques, Vol. 38, No.1, pp.86-87, January 1990.

[5] A. Mortazawi and T. Itoh, "A periodic second harmonic spatial power combining oscillator," 1990 IEEE MTT-S International Microwave Symposium Digest, pp.1213-1216, May 1990, Dallas, TX.

[6] K. Kurokawa, "The single-cavity multiple-device oscillators," IEEE Trans. Microwave Theory and Techniques, Vol. MTT-19, No. 10, pp.793-801, October 1971.

[7] H. D. Foltz, J. H. Davis and T. Itoh, "Voltage-frequency update for nonlinear analysis of free-running and injection-locked multiple-device oscillators," to appear in 1991 IEEE MTT-S International Microwave Symposium Digest, June 1991, Boston, MA.

[8] D. F. Peterson, "Harmonic power combining of microwave solid-state active devices," IEEE Trans. Microwave Theory and Techniques, Vol.MTT-30, No.3, pp.260-268, March 1982.

[9] V. D. Hwang and T. Itoh, "An efficient approach for large-signal modeling and analysis of the GaAs MESFET," IEEE Trans. Microwave Theory and Techniques, Vol.MTT-35, No.4, pp.396-402, April 1987.

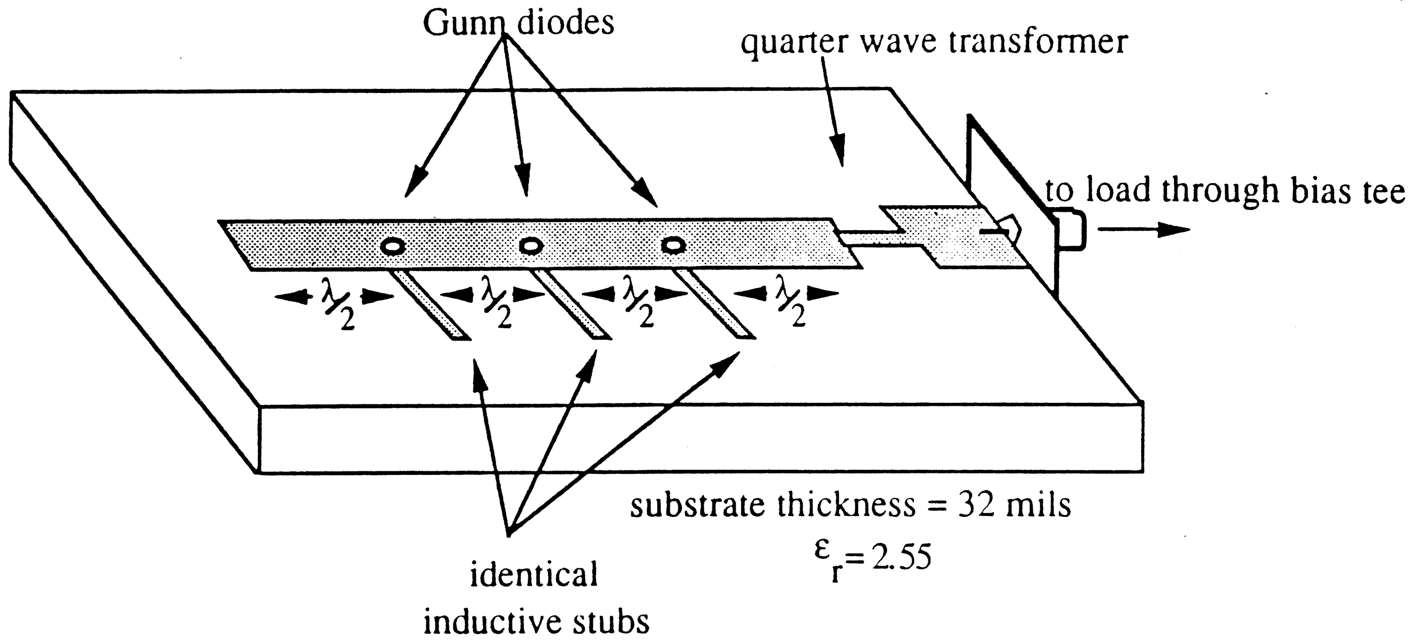

Fig.1 Three diode periodic power combining oscillator

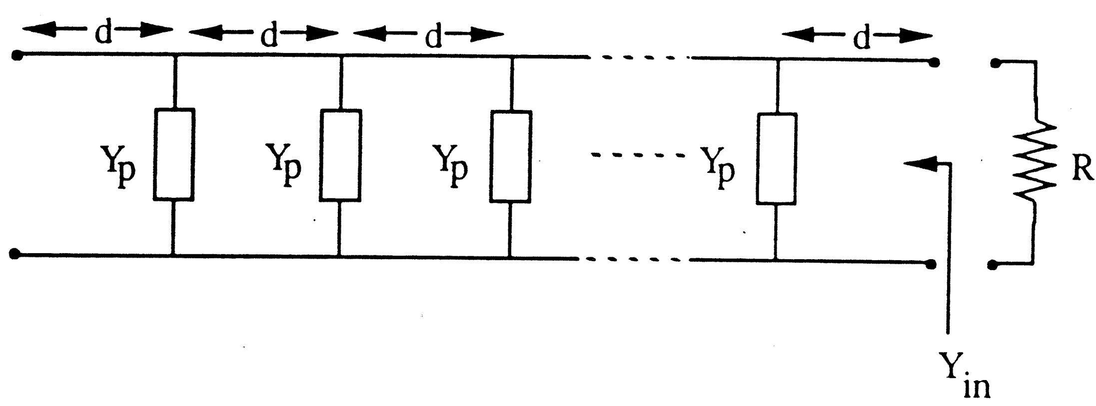

Fig.2 Transmission line loaded periodically with admittance Y_p

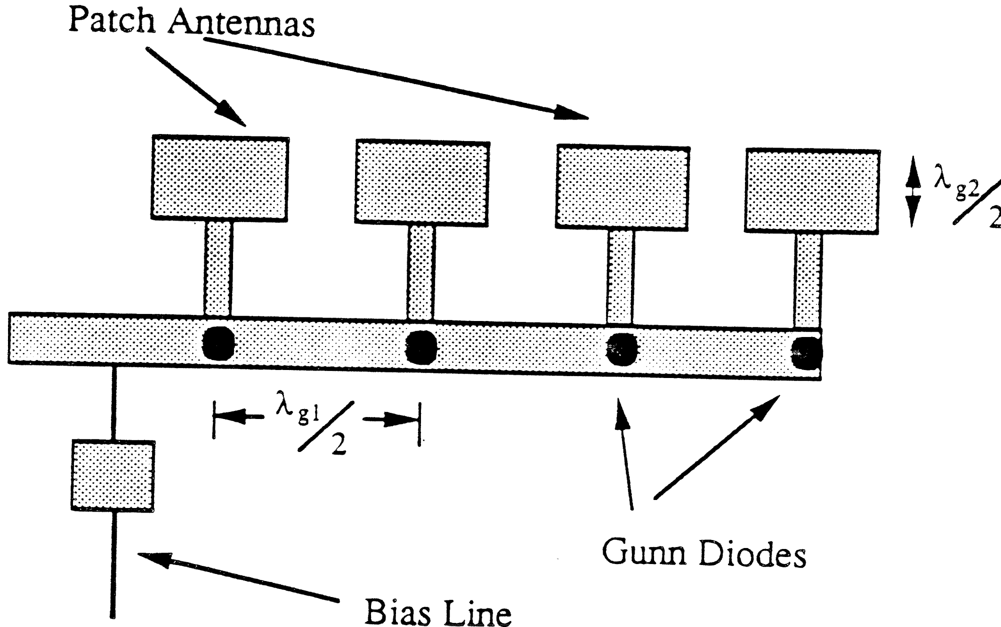

Fig.3 Four diode spatial second harmonic power combiner

THEORETICAL EFFICIENCY OF MULTIPLIER DEVICES

Timo J. Tolmunen and Margaret A. Frerking
Jet Propulsion Laboratory
California Institute of Technology
Pasadena, California 91109, U.S.A.

Abstract

During the past few years, several new devices have been proposed for use in frequency multipliers at millimeter and submillimeter wavelengths. Candidate diodes include a quantum well diode, a single barrier varactor, a barrier-intrinsic-N diode, a delta-doped varactor and a high electron mobility varactor. In comparison to the conventional Schottky varactor, these new diodes have some potential advantages in their characteristics, such as a stronger nonlinearity or a special-symmetry, which make them very attractive for millimeter and submillimeter wave frequency multiplication. This paper gives an overview of these novel devices and their potential benefits in comparison to the conventional Schottky-barrier varactor. Their performance has been analyzed theoretically in various low and high order multipliers for 200 GHz and 1 THz.

Introduction

Basic scientific research including radio astronomy, remote sensing of the atmosphere, plasma diagnostics and laboratory spectroscopy has long been the primary application for shorter millimeter and submillimeter wave technology. More recently this spectral range is also being considered for space-borne radar and communication systems. Fundamental local oscillator sources available today for low-noise heterodyne receiver systems include tube oscillators, gas lasers and solid-state sources. The tube oscillators and lasers can cover frequencies well above 1 THz, but especially for space-borne applications, these sources

require considerable improvement to reduce size or to increase lifetime and reliability. Solid-state sources such as Gunn oscillators do not have these disadvantages, but operate only up to about 200 GHz. Therefore, frequency multipliers are needed to achieve higher frequencies.

The standard "workhorse", the GaAs Schottky-barrier varactor multiplier, is extensively used for signal generation at millimeter and submillimeter wavelengths. Although there are still some incomplete areas in the study and optimization of this diode, such as the behaviour of the C-V characteristics close to the built-in potential or the effect of multiplier cooling, the Schottky varactor has shown to be an efficient device, both theoretically and experimentally [1,2] at millimeter and lower submillimeter wavelengths. However, considerable improvement is still required at frequencies over 500 GHz in order to fulfill input power requirements of mixer devices.

While standard Schottky varactor technology is still maturing, several novel diodes have been proposed for use as multipliers at millimeter and submillimeter wavelengths. These diodes include a quantum well diode [3], a single barrier varactor [4], a BIN diode (barrier-intrinsic-n^+) [5], a delta-doped varactor [6] and a high electron mobility varactor [7].

In comparison to the Schottky varactor, these new diodes have some potential advantages in their characteristics, such as a stronger nonlinearity or a special-symmetry, which make them very attractive for millimeter and submillimeter wave frequency multiplication. Stronger nonlinearities allow more efficient harmonic generation with smaller input signal levels, and more efficient higher-order harmonic generation with unoptimized idler terminations.

By using a device having a symmetric C-V curve or an antisymmetric I-V curve, only odd-harmonics are generated. Therefore, there is no need for an idler termination in the case of a frequency tripler. Similarly a frequency quintupler requires only one idler termination at the 3rd harmonic for optimum operation. Schottky varactors, or other devices, having asymmetric curves generally require an idler termination at each intermediate harmonic frequency.

This paper gives a brief overview of these novel diodes and their theoretical performance as multipliers at millimeter and submillimeter wavelengths. All of these diodes are considerably less mature than the conventional Schottky varactor. Therefore, there should be opportunity for device optimization for each application.

Devices

The quantum well diode (QWD) has been the subject of theoretical and experimental studies since 1970 [8]. Its high speed [9] and the negative differential resistance make it attractive for millimeter-wave oscillators and its highly nonlinear antisymmetric I-V curve is suitable for frequency multiplication. The quantum well diode has a thin (20–60 Å) undoped layer (well) sandwiched between two thin barriers (10–50 Å) of material having a larger band-gap than the well (Fig. 1a). This structure acts as a resonator which exhibits peaks in electron transmission (current) at certain values of incident electron energy (voltage). Therefore, the QWD has regions of negative differential resistance when the voltage is just greater than the resonance.

In addition to a voltage-dependent resistance (Fig. 1b), the quantum well diode has a highly nonlinear capacitance related to the epitaxial layers exterior to the barriers. Under the assumption that no current flows through the device, the capacitance can be approximated as

$$C = \frac{C_0}{1 + \sqrt{(2\epsilon/qN_d w^2)|V_j|}}, \qquad C_0 = \frac{\epsilon A}{w}, \tag{1}$$

where C_0 is the zero-bias capacitance, which depends on the diode area A and the total thickness of the double barrier structure w ($w = 2w_{barrier} + w_{well}$); ϵ is the dielectric constant, q is the electron charge, N_d is the doping concentration outside the barriers and V_j is the junction voltage. If the epitaxial layer width and doping concentration is equal in both sides of the double barrier structure, the C-V curve is symmetric and can generate only odd harmonics without external biasing. Quantum well diodes have been demonstrated as a tripler to 200 GHz [10]. The tripling mechanism has since been determined to be the nonlinear C-V characteristic rather than the I-V characteristic. Recent capacitance measurements of the quantum-well diodes have revealed that the C-V curve is less nonlinear at small voltages and exhibits an extra peak in the capacitance at voltages close to the negative differential resistance (Fig. 1c) [11].

Theoretically the resistive multiplication is far less efficient than the reactive and it often merely decreases the device performance as a multiplier. Therefore, it is reasonable to suppress the effects of the nonlinear resistance, if this is possible. The structure of the quantum well diode can be modified by replacing the well and dual barriers with a single barrier which is thick enough (150–200 Å) for suppressing the current flow through the device. The resulting diode, a single barrier varactor (SBV) [4], has a theoretical capacitance which is symmetric and follows Eq. (1) (Fig. 1c). This makes the SBV (also called quantum

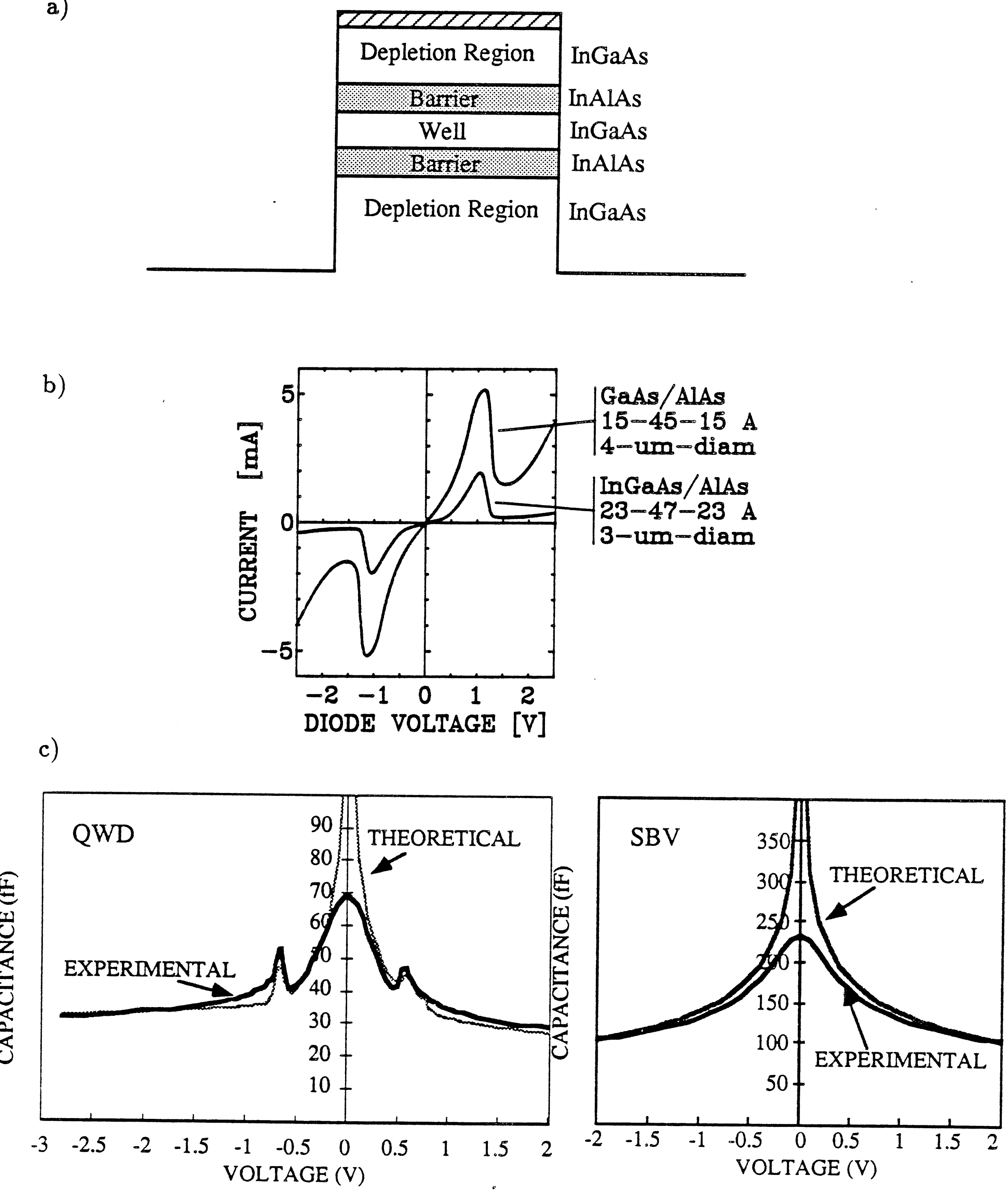

Figure 1. a) Structure of the quantum well diode. In a single barrier varactor only one barrier is used between epitaxial layers. This barrier is made thick enough in order to suppress the current flow through the device. **b)** Examples of measured I-V curves of quantum well diodes. **c)** Theoretical and experimental C-V curve of a quantum well (left) and a single barrier varactor diode (right). The theoretical curve of the quantum well diode is based on a more detailed model which takes into account current flow through the device.

barrier varactor, QBV) very attractive in millimeter wave multiplier applications.

The Barrier-Intrinsic-N (BIN) diode has been proposed as an improved varactor diode for harmonic multiplication [5]. Unlike quantum well diodes or single barrier varactors which consist of a heterostructure and two ohmic contacts as terminals, the BIN diode is essentially a Schottky varactor with an unique doping profile that yields a sharper C-V characteristic. The diode consists of a Schottky-contact, a barrier layer (thickness d_1), a sheet doping layer and an intrinsic layer (thickness d_2) on a highly doped substrate (Fig. 2a). Generally, the diode may be designed so that at zero or low reverse bias, the sheet doping layer is just barely depleted and the capacitance is

$$C_{max} \approx \frac{\epsilon A}{d_1}. \tag{2}$$

As the reverse voltage increases the depletion region switches to $d_1 + d_2$. Because further increase of the bias has no effect on the capacitance due to the high doping of the substrate, the minimum capacitance can be expressed as

$$C_{min} \approx \frac{\epsilon A}{d_1 + d_2}. \tag{3}$$

Therefore, a single BIN diode has an asymmetric C-V curve (Fig. 2b) which is sharper than that of the Schottky varactor. By contacting two diodes back-to-back, a symmetric "pulse"-like curve results (Fig. 2c). More importantly, the back-to-back BIN is an inherently planar device having both terminal contacts on the same surface. This is an advantageous feature, especially for space-borne applications.

Due to the intrinsic layer, the series resistance of the BIN diode is relatively high, which results in a low cut-off frequency. In a modification of the BIN diode, the BNN (barrier-n-n^+) or delta-doped varactor structure [6,12], a moderately-doped layer is used instead of the intrinsic layer to decrease the resistance in the undepleted epitaxial layer.

A high electron mobility varactor is another inherently planar diode which incorporates the proven performance of a standard Schottky varactor technology with the electron properties of the two-dimensional electron gas formed, e.g in a GaAs/AlGaAs heterostructure. In these structures the electrons have higher mobility than in conventional varactors, especially if the device is cooled [7]. The high electron mobility varactor consists of a Schottky-contact followed by a two-dimensional electron gas (2-DEG) modulation region (Fig. 3). By applying a reverse bias to the anode contact, the 2-DEG in the modulation region will become depleted near the Schottky-contact, reducing contact capacitance. As the bias is further increased, more of the layer will be depleted. The geometry of the structure results in a sheet-like variable capacitor which has an inversely logarithmic dependence on voltage.

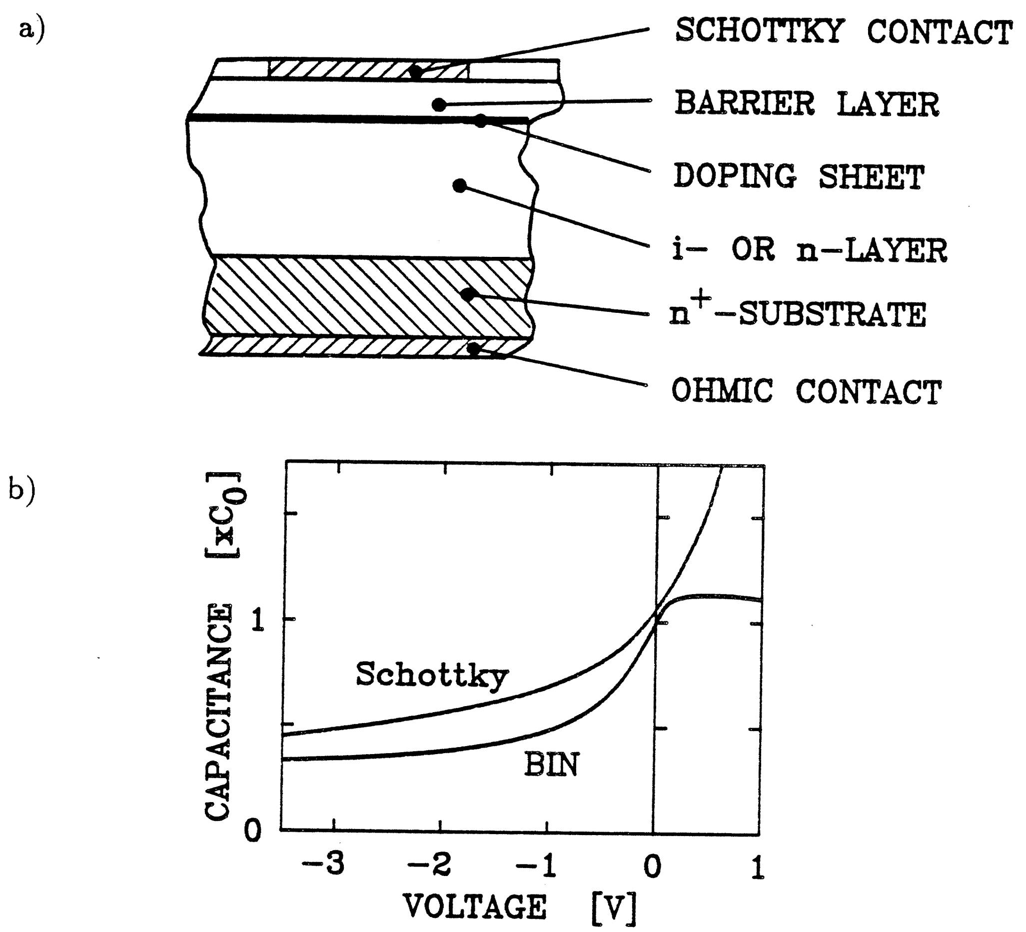

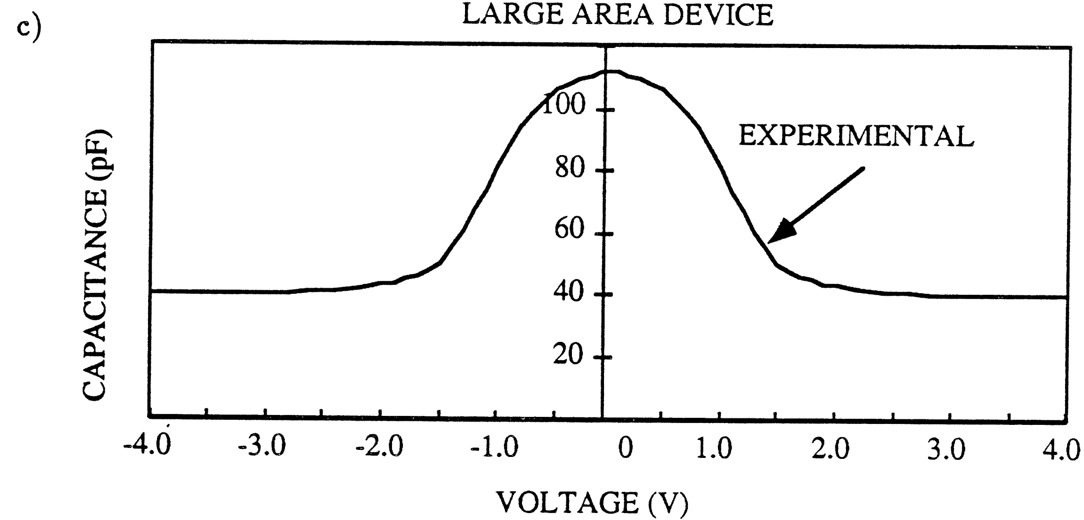

Figure 2. Structure of a single BIN or BNN diode a) its C-V characteristic compared to the C-V curve of a conventional Schottky b), and an experimental C-V characteristic of a large area back-to-back BNN diode c).

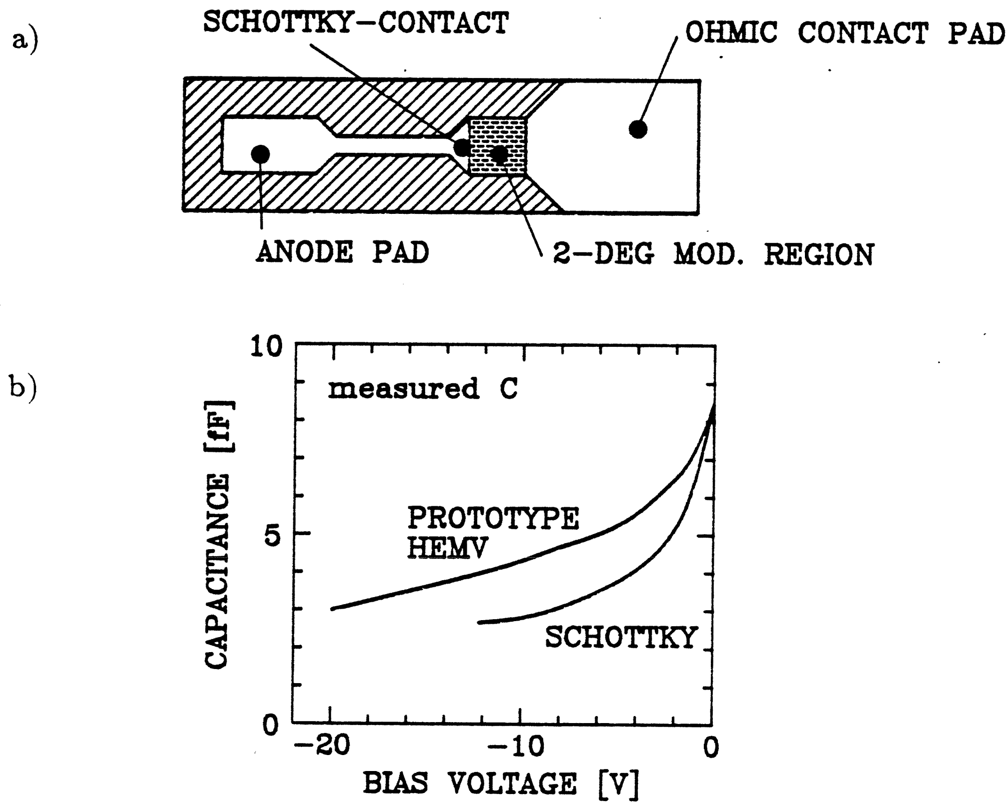

Figure 3. Structure of the high electron mobility varactor a) and its C-V characteristic b).

The equivalent circuit of each diode described above is similar to that of the Schottky varactor. It consists of a parallel combination of a voltage-dependent capacitance and conductance, in series with a frequency (and voltage) dependent resistance. For the present work the simulations were carried out using this diode model and a modified version of the large signal analysis program by Siegel and Kerr [13].

Multipliers for 200 GHz

For diodes having an asymmetric C-V curve, the basic multiplier configuration is a doubler. Fig. 4 illustrates the theoretical efficiency of a delta-doped varactor or BNN and three Schottky varactor (6P2 and 5M2 by University of Virginia and VD011 by Farran Technology) doublers for 200 GHz. Although the nominal diode parameters (Table I) are rather different, the dynamic cut-off frequency is almost equal, which results in the same peak-efficiency. This peak is reached with a voltage swing from near forward conduction

Table I. Parameters used in the analyses of multipliers for 200 GHz. Parameter K is $2\epsilon/qN_dw^2$, see Eq. (1).

200 GHz multipliers				
VD011	$C_0 = 12$ fF, $\gamma_0 = 0.45$,	$R_s = 12\ \Omega$,	$V_{BR} = -15$ V,	$f_{cd} = 3.0$ THz
6P2	$C_0 = 21$ fF, $\gamma_0 = 0.45$,	$R_s = 9\ \Omega$,	$V_{BR} = -20$ V,	$f_{cd} = 2.7$ THz
5M2	$C_0 = 21$ fF, $\gamma_0 = 0.50$,	$R_s = 10\ \Omega$,	$V_{BR} = -15$ V,	$f_{cd} = 2.8$ THz
SBV	$C_0 = 50$ fF, $K = 18$ V^{-1},	$R_s = 15\ \Omega$,	$V_{BR} \approx \pm 10$ V,	$f_{cd} = 2.3$ THz
BNN	$C_{max}/C_{min} = 17/5$ fF,	$R_s = 9\ \Omega$,	$V_{BR} = -8$ V,	$f_{cd} = 2.5$ THz
bbBIN	$C_{max}/C_{min} = 18/5$ fF,	$R_s = 24\ \Omega$,	$V_{BR} \approx \pm 7$ V,	$f_{cd} = 1.0$ THz
bbBNN	$C_{max}/C_{min} = 15/5$ fF,	$R_s = 15\ \Omega$,	$V_{BR} \approx \pm 7$ V,	$f_{cd} = 1.4$ THz

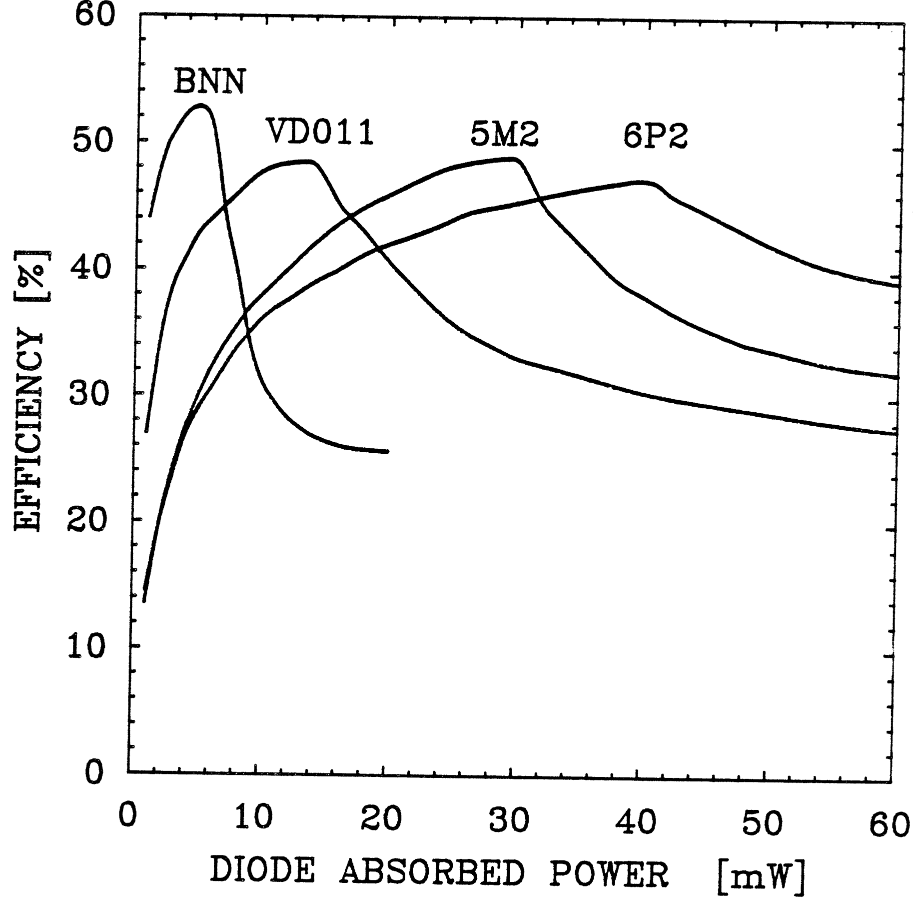

Figure 4. Theoretical efficiency of frequency doublers for 200 GHz. Simulations are based on measured (DC) nonlinearities of the devices.

to the break-down. These diodes can handle more input power, but due to the forward conduction, multiplication then becomes partly resistive which results in a decrease in efficiency. For diode absorbed power, below the peak, the efficiency is determined by the strength of the non-linearity. Hence, the BNN or delta-doped varactor results in excellent performance if the input power level is relatively low.

In general the input power level for peak efficiency is a function of the zero-bias capacitance of a diode. For example, a Schottky varactor having a small area and hence a small C_0 is favorable for applications where input power is limited. Small capacitance results in high input impedance and hence larger voltage swing across the diode for a given input power. Therefore, the break-down voltage limit is reached with rather small input power levels. When higher input power levels are available, a larger capacitance is a better choice, especially if the nonlinearity is sharper (5M2) or break-down limit is higher (6P2).

The prototype high electron mobility varactors had a C-V characteristic which was

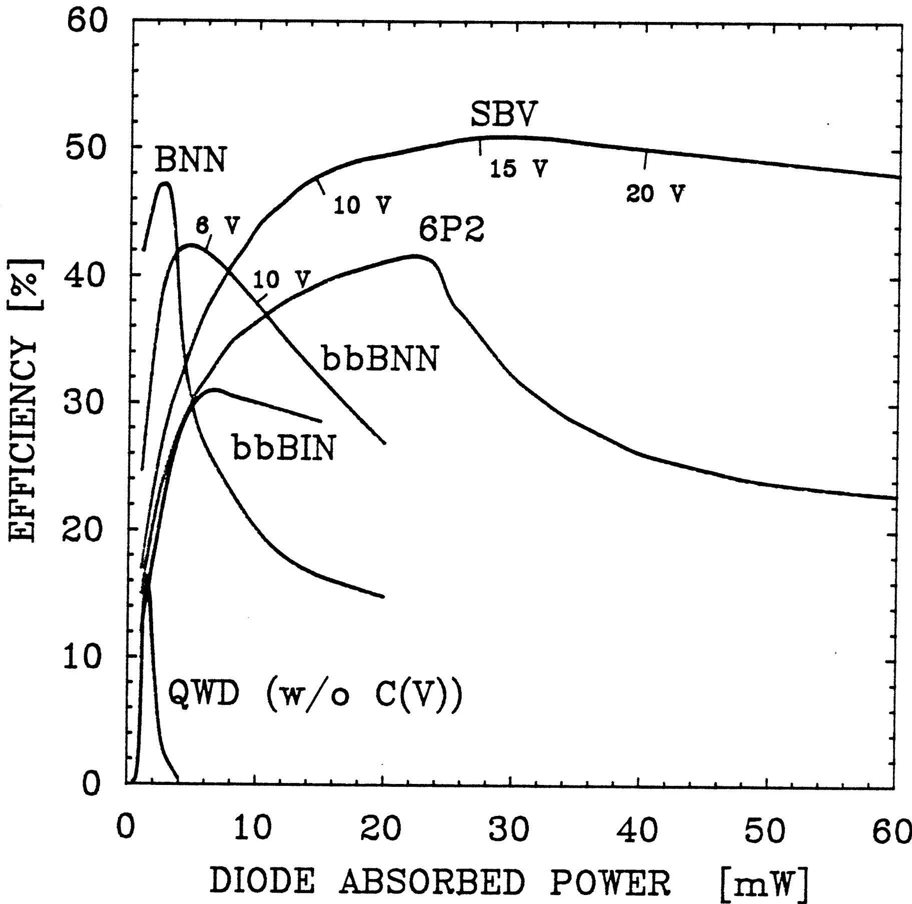

Figure 5. Theoretical efficiency of frequency triplers for 200 GHz.

slightly less nonlinear than that of the conventional Schottky varactor [7]. This was partly due to rather large parasitic capacitance related to the structure. However, it is expected that a reduction of this parasitic capacitance will result in a curve which is as steep as that of the conventional Schottky [14]. This together with a measured high break-down voltage [7] make this device very attractive especially for applications, where the input power level is high.

Comparison of triplers to 200 GHz is shown in Fig. 5. Below the peak, where the multiplication is purely reactive, the theoretical tripling efficiency of the 6P2 and the BNN or delta-doped varactor is close to their doubling efficiency. This is because the input impedance of a tripler for 200 GHz is higher than the impedance of a doubler for the same output frequency, causing more efficient capacitance modulation. This partly "compensates" additional losses in the diode series resistance at the idler frequency. However, because a good idler termination is crucial for the operation of both devices, degradation of efficiency will be more severe in practice, due to the difficulty of arranging separate tuning for each harmonic.

The need for an idler can be avoided using a device having a symmetric C-V curve, such as a single barrier varactor (SBV) or back-to-back BNN (bbBNN). If there is no current leakage through the single barrier varactor, its highly nonlinear C-V curve together with a high dynamic cut-off frequency, results in an excellent 3rd harmonic generation without the need of an idler. As a hypothetical extreme, a similar size ($\approx$4-μm-diam.) quantum well diode (QWD) was analyzed assuming that multiplication is purely resistive (Experimentally, the voltage variable capacitance dominates the multiplication). The dramatic difference between resistive and reactive multiplication can be seen in Fig. 5. Despite the highly nonlinear I-V curve of the quantum well diode, its theoretical performance for varistor operation is much less than the varactor's performance.

The back-to-back BIN (bbBIN), also has a sharp symmetric C-V curve, but its rather low dynamic cut-off frequency decreases the conversion efficiency. A doped version, a back-to-back BNN, has a lower series resistance and therefore higher cut-off frequency. This results in better performance at moderate pump power. Doping in the epitaxial layer degrades the sharpness of the C-V curve so that the efficiency at low pump power is reduced.

Experimentally, the efficiencies available from multipliers will be lower due to resistive losses, which in the 200-GHz range in a well-made waveguide mount are typically around 1.5–2 dB, with an additional 0.5–1 dB for each idler frequency. The efficiency will further decrease due to the difficulty to provide the device with optimum terminations at each harmonic frequency. For the best performance, the diode should be matched at the input

Table II. Parameters used in the analysis of the multipliers for 1000 GHz.

1 THz multipliers				
2T2	$C_0 = 5.5$ fF, $\gamma_0 = 0.45$,	$R_s = 12\ \Omega$,	$V_{BR} = -10$ V,	$f_{cd} = 5.8$ THz
SBV	$C_0 = 15$ fF, $K = 18\ \mathrm{V}^{-1}$,	$R_s = 20\ \Omega$,	$V_{BR} \approx \pm 10$ V,	$f_{cd} = 5.0$ THz
QWD(C)	$C_0 = 50$ fF, $K = 112\ \mathrm{V}^{-1}$,	$R_s = 20\ \Omega$,	$V_{BR} \approx \pm 3$ V	
BNN	$C_{max}/C_{min} = 4.5/1.2$ fF,	$R_s = 17\ \Omega$,	$V_{BR} = -8$ V,	$f_{cd} = 5.7$ THz
bbBIN	$C_{max}/C_{min} = 7.5/2.1$ fF,	$R_s = 40\ \Omega$,	$V_{BR} \approx \pm 5$ V,	$f_{cd} = 1.4$ THz
bbBNN	$C_{max}/C_{min} = 5.6/2.0$ fF,	$R_s = 20\ \Omega$,	$V_{BR} \approx \pm 5$ V,	$f_{cd} = 2.6$ THz

and output frequency, and terminated at the idler(s) with an inductance which resonates with the average capacitance at that particular frequency. At harmonic frequencies higher than the output an optimum termination is an open circuit, because other terminations

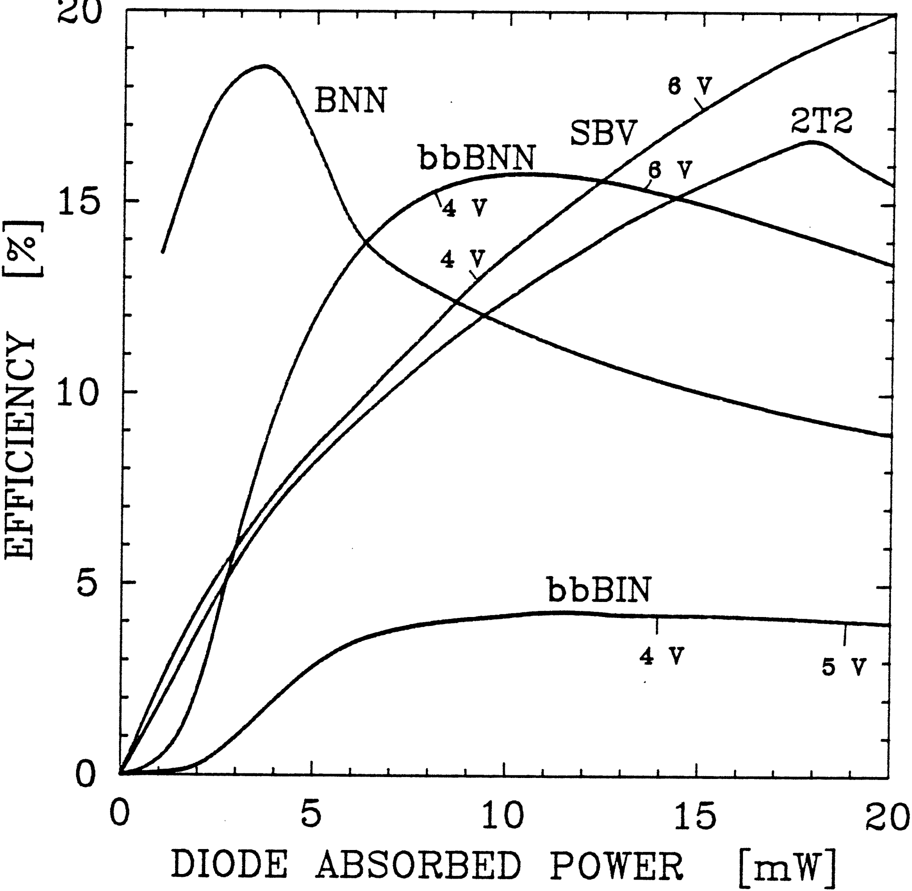

Figure 6. Theoretical efficiency of frequency triplers for 1000 GHz.

(worst case is an inductance which resonates the capacitance) allow current flow which generally introduces extra losses in the diode series resistance.

Multipliers for 1000 GHz

Accurate analyses of multipliers for 1 THz are more complicated due to various effects which become more important at high frequencies, or when the order of multiplication increases. These effects include current saturation and the limited speed of the edge of the depletion region. In the following analyses, the basic equivalent circuit is used and the emphasis is based on the nonlinearities of the devices. This will give an optimistic upper limit for the performance of the devices. A more detailed discussion on the current saturation can be found elsewhere in this proceedings [15].

Fig. 6 illustrates the theoretical efficiency of various devices working as a tripler for 1 THz. The maximum input power available from present solid-state sources at 333 GHz

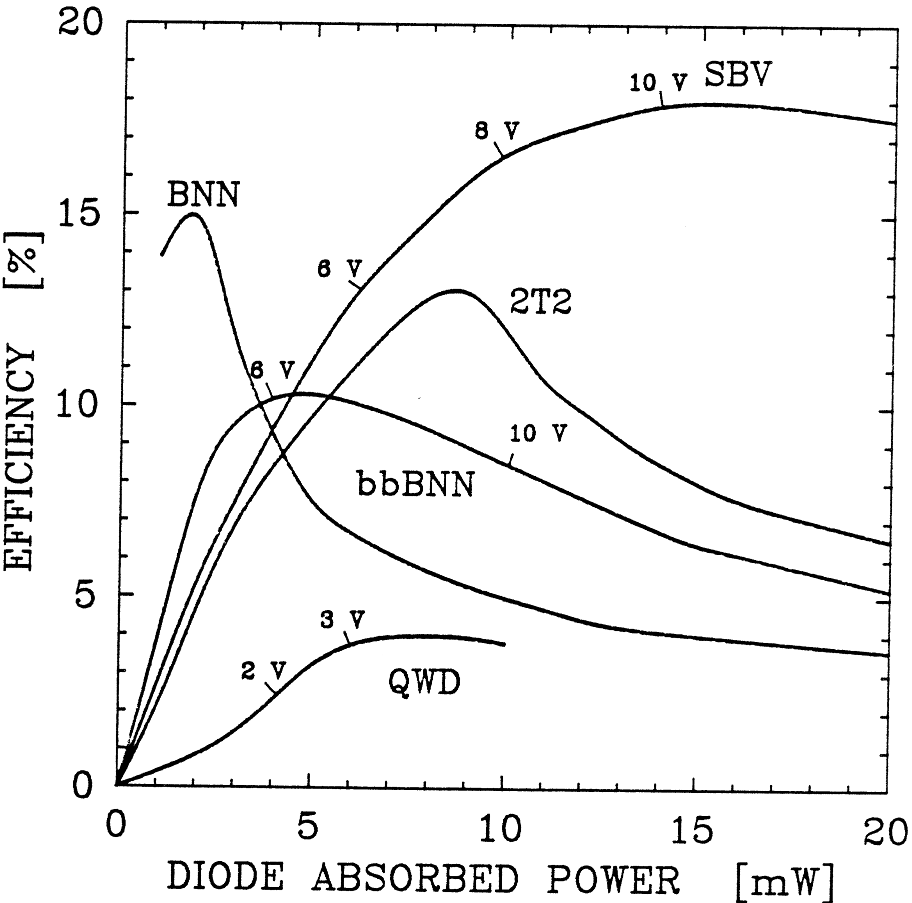

Figure 7. Theoretical efficiency of frequency quintuplers for 1000 GHz.

is below 5 mW. At this pump power, the BNN or delta-doped varactor will be superior, exceeding the efficiency of the 2T2 (U.Va) and the single barrier varactor by a factor of three. Also, the back-to-back BNN configuration works very well, and has an additonal advantage that no idlers are needed. Similarly, Fig. 7 illustrates the theoretical efficiency of various quintuplers for 1 THz. In this case, the maximum input power level available from solid-state sources at 200-GHz input range is around 10–20 mW, which makes the single barrier varactor the most attractive device. In the quintupler case, it should also be remembered that devices having asymmetric curves (BNN and standard Schottky) require three idler terminations for the performance shown in Fig. 7. The 2nd harmonic idler termination is essential, but idlers at the 3rd and 4th harmonics are "alternative". However, the theoretical efficiency of a Schottky varactor, for instance, decreases at least by a factor of two if either of these is missing. Devices having symmetric curves require only one idler termination (which is essential) at the 3rd harmonic frequency. Therefore, the symmetric devices will suffer less from unoptimized idler terminations.

Conclusions

The GaAs Schottky varactor has long been the only efficient component for millimeter and submillimeter wave frequency conversion. However, during the past few years growing interest in novel structures and semiconductor materials have brought to light several new devices which utilize a stronger nonlinearity or a special-symmetry in their characteristics.

The sharp C-V dependence of the barrier-n-n^+ diode (delta-doped varactor) improves performance at low input power levels, making it very attractive in the submillimeter wave regime. The highly nonlinear, symmetric C-V curve of the single barrier varactor yields excellent performance theoretically, whereas the antisymmetric I-V curve of the quantum well diode, since it suffers resistive losses, is less efficient. The structure of back-to-back BIN/BNN diodes and the high electron mobility varactor is inherently planar which yields higher reliability, especially for space-borne applications.

In conclusion, these novel devices have some benefits which make them attractive in specific applications, especially at submillimeter wavelengths. In the near term, the conventional Schottky varactor will continue to be the device of choice for most applications. However, all of the novel diodes are considerably less mature than the Schottky varactor. Therefore, there should be a great opportunity for future device optimization.

Acknowledgements

The research described in this paper was performed by the Center for Space Microelectronics, Jet Propulsion Laboratory, California Institute of Technology and was sponsored by the National Aeronautics and Space Administration, Office of Aeronautics, Exploration, and Technology. The authors wish to thank P. Batelaan, T. Crowe, E. Kollberg, U. Lieneweg, J. Maserjian, B. Peatman, D. Rutledge and P. Siegel for valuable discussions.

References

[1] N. Erickson, "High effieciency submillimeter frequency multipliers." 1990 IEEE MTT-S International Microwave Symposium Digest, 1301–1304, 1990.

[2] T. Tolmunen, "High-efficiency Schottky-varactor frequency multipliers at millimeter waves." Helsinki University of Technology, Radio Laboratory, Report S180, 1989. (Partly published in *Int. J. of Infrared and Millimeter Waves*, Vol. 8, 1987, pp. 1313–1353 and Vol. 10, 1989, pp. 475–518.)

[3] T.C.L.G. Sollner, W.D. Goodhue, P.E. Tannenwald, C.D. Parker and D.D. Peck, "Resonant tunneling through quantum wells at frequencies up to 2.5 THz." *Appl. Phys. Lett.*, Vol. 43, 588–590, (1983).

[4] E. Kollberg, A. Rydberg, "Quantum-barrier-varactor diodes for high-efficiency millimeter wave multipliers,"*Electron. Lett.*, Vol. 25, No. 25, 1696–1697, (1989).

[5] U. Lieneweg, B.R. Hancock, J. Maserjian, "Barrier-Intrinsic-N^+ (BIN) diodes for near-millimeter wave generation", Conference Digest for the Twelft International Conference on Infrared and Millimeter Waves, 6–7, 1987.

[6] B.J. Rizzi, T.W. Crowe, and W.C.B. Peatman, "A δ-doped varactor diode for submillimeter wavelengths", Conference digest for the 15th International Conference on Infrared and Millimeter Waves, SPIE Cat. No. 90-50878, pp 478–480, 1990.

[7] W.C.B. Peatman and T.W. Crowe, "A high electron mobility varactor." Conference digest for the 15th International Conference on Infrared and Millimeter Waves, SPIE Cat. No. 90-50878, pp 473–474, 1990.

[8] L. Esaki and R. Tsu, "Superlattice and negative differential conductivity in semiconductors,"*IBM J. Res. Develop.*, Vol. 24, 61–65, (1970).

[9] E.R. Brown, T.C.L.G. Sollner, C.D. Parker, W.D. Goodhue and C.L. Chen,

"Oscillations up to 420 GHz in GaAs/AlAs resonant tunneling diodes," *Appl. Phys. Lett.*, Vol. 55, 1777–1779, (1989).

[10] P.D. Batelaan and M.A. Frerking, "Quantum well multipliers," Conference Digest for the Twelfth International Conference on Infrared and Millimeter Waves, 14–15, 1987.

[11] O. Borić, T.J. Tolmunen, M.A. Frerking, J.B. Hacker and D.B. Rutledge, "S parameter measurements of quantum well diodes." Conference digest for the 15th International Conference on Infrared and Millimeter Waves, SPIE Cat. No. 90-50878, pp. 251–253, 1990.

[12] U. Lieneweg, T. Tolmunen, M. Frerking and J. Maserjian," Design of planar varactor frequency multiplier devices with blocking barriers," Second International Symposium on Space Terahertz Technology, this proceedings.

[13] P.H. Siegel, A.R. Kerr and W. Hwang, "Topics in the optimization of millimeter-wave mixers," NASA Technical Paper 2287, 512 p., 1984.

[14] Private discussions with B. Peatman, U.Va.

[15] E. Kollberg, T. Tolmunen, M. Frerking, J. East, "Current Saturation in Submillimeter Wave Varactors," Second International Symposium on Space Terahertz Technology, this proceedings.

MULTIPLIERS FOR THz HETERODYNE SYSTEMS

B.L.A. Rydberg, B.N. Lyons and U.S. Lidholm
Farran Technology Ltd.
Ballincollig, Cork, Ireland

Abstract:

The development of a 750 GHz tripler having a measured output power and efficiency of more than 120 μW and 0.8 % respectively at a frequency of 803 GHz is described. The output powers and efficiencies are the highest reported for this frequency. The development of a 250 GHz tripler to be used as a pump source for the 750 GHz tripler is also described.

Introduction:

Due to the development of mixers, for example SIS-mixers, at frequencies around 1 THz, the demand for solid state local oscillators has been steadily increasing. In 1988 Farran Technology was commissioned by the European Space Agency to investigate and develop solid state sources based on Schottky diode multipliers to be used as local oscillators in such receivers. One of the targets has been to develop a 750 GHz solid state source with a predicted output power of 50 μW based on two triplers pumped by an 83 GHz InP-TED oscillator. We here report on the progress and results in developing such a source.

Theoretical study and mount design:

Using a large signal multiplier analysis program based on the principle of harmonic balance developed by Siegel et al. [1], different Schottky varactor diodes were investigated for the two multipliers. The output power for four different devices ranging from $C_j(0)=1.6$ to 3.4 fF was calculated for the 750 GHz tripler, see Fig.1. The input power in the investigation was varied between 1-6 mW since this was assumed to be a reasonable estimate of what it is possible to achieve from a 250 GHz tripler. The description of the devices used in the simulation was simplified in that a

fixed layer thickness and doping of 0.49 μm and $9{\cdot}10^{16}$ cm^{-3} respectively was used for the low doped epitaxial region. The breakdown voltage V_b varied between 4 - 7 V for the devices, see Fig.1. The series resistance was set to 20 ohm, which is assumed to be a reasonable value for diodes having a capacitance $C_j(0)$ of 1.6 - 3.4 fF.

The marked region in Fig.1 shows the operating condition when the maximum voltage V_{max} that is the bias voltage plus the peak rf-voltage is approximately equal to the breakdown voltage. Thus diodes with a capacitance between 2.2 - 2.8 fF should be the most suitable ones. The device capacitance was chosen to be 2.8 fF. The calculated output power for such a device is about 500 μW, allowing 10 dB matching and circuit losses, yields the required output power of ⩾50 μW. Experimental results have shown that twice the pump power needed for V_{max} to reach V_b can be used [2]. Therefore it should be possible to use a pump power of approximately 5 mW thereby increasing the output power by a factor of two.

A cross sectional view of the 750 GHz tripler is shown in Fig.2. The function of the idler resonator, see Fig.2, used in the multiplier is based on the principle developed by Erickson [3]. The step in the outer diameter of the coaxial resonator is incorporated in order to achieve a better short circuit at the end of the idler [4]. The input waveguide is a reduced height WR-3 waveguide. The wide dimension of the output waveguide is 0.258 mm, thus being cutoff at 581 GHz. A conical horn was used for the output port due to the ease with which it could be machined. By proper selection of the length and horn opening it is possible to have a nearly identical beam pattern in the E and H planes [5]. The waveguide is matched to the horn using a 5λ long taper with a square cross section at the horn throat, having the same cutoff frequency as the circular horn throat. Thus the impedance discontinuity between the horn and the waveguide becomes very small.

A scaled model of the mount (scaling factor = 83.31) was designed in order to investigate and optimize the embedding

impedances seen at the input, idler and output frequencies by the diode. Using the scaled model it was found that most resonances in the embedding impedance were due to higher order mode excitation in the rf-filter, see Fig.3. These resonances were particularly strong close to the cutoff frequency for the particular mode. Due to mechanical limitations it was not possible to shift the coaxial TE_{11}-mode cutoff frequencies for the rf-filter above the highest operating frequency except for the last rf-filter section. The TE_{11}-mode cutoff frequencies for the other filter sections were instead shifted to the frequency region between the input and the idler frequency, thereby minimizing the influence of the resonances related to the cutoff frequency. The rf-filter is extended by a $\lambda/2$ coaxial section in order to make the middle block easier to machine, see Fig.2.

A theoretical model was developed for the mount, where the coupling between the rf-filter and the input waveguide was calculated using the theory by Williamson [7]. For the output port a simplified theoretical model was used based on the assumption that the embedding impedance seen by the diode is the sum of the impedances from (i) the output waveguide in parallel with the backshort, (ii) the rf-filter and (iii) the idler. Though this simplified model is not sufficient to fully describe the output port it was used in the absence of a more accurate one. The bias filter was assumed to present a short circuit at the input frequency.

Using the theoretical and the scaled models of the mount the embedding impedances seen by the device at the input, idler and output frequencies were calculated and measured respectively, see Fig.4. The bias filter was short circuited in the measurements.

It can be seen in Fig.4 that there is a difference in reactance between the measurements and the calculated values. The discrepancy in reactances is believed to be related to the simplifications in the theoretical model used in the calculations. The increased capacitance due to the measurement cable - waveguide junction compared to the

actual device was found to add a capacitance of only about 43 fF to the actual values. Thus this capacitance does not account for the noted discrepancy.

In Figure 4 is also plotted the complex conjugate of the diode impedance, Z_d^x, or the reactance, X_d^x, at the input, idler and output frequencies. Comparison between Z_d^x or X_d^x and the measured embedding impedance shows that a match to the device could be achieved particularly at the high frequency end of the output frequency range 675 - 825 GHz wanted for the tripler.

Simulations using the theoretical model of the mount gave a maximum efficiency for the tripler of 11 % at 750 GHz, compared to the theoretical value of 12.2 % found in the diode simulations for 2.5 mW in input power.

The 250 GHz tripler which very recently has been assembled has a similar design to the 750 GHz tripler. However the low pass filter structure for the bias filter is replaced with a radial-line resonator filter [8]. The step in the outer diameter of the idler resonator, see Fig.2, was not used in this design due to better mechanical control. The 250 GHz tripler is designed for a 17 fF, varactor diode from Farran Technology, nr. VD10A. Simulations using this device have shown that output powers of about 22 mW can be generated for input powers of 64 mW. However due to mount losses, impedance mismatch etc., this power is reduced by a factor of 2 - 4 [2]. Thus it is reasonable to expect about 5 mW of output power for a well optimized mount, since output powers of 1 - 3 mW are commonly achieved for this type of mount [9].

Measurements:

In the initial test phase a carcinotron was used as the pump source for the 750 GHz tripler.

The mount was developed for a 2.8 fF varactor diode. However due to lack of a suitable diode with this capacitance a 5.4 fF varactor diode having a series resistance of 11 ohm was tested in the mount, see Fig.5. The use of a higher capacitance device means in principle that

more pump power is needed in order to achieve the same output power as for a 2.8 fF device, assuming the same series resistance for the diodes. However this is compensated for by the much smaller series resistance for the 5.4 fF, 11 ohm as compared to 20 ohm assumed for the 2.8 fF device.

Computer simulations of the tripler using the theoretical model showed that it is possible to match the 5.4 fF diode, by reducing the whisker length to 50 µm compared to 60 µm for the 2.8 fF device, though with a loss in maximum efficiency. Thus it was found using computer simulations that a maximum efficiency of 12.8 % for the mount compared to a maximum of 16.3 % using optimum embedding impedances could be achieved at 750 GHz, at 6 mW input power. This can be compared to an efficiency of 18.4 % for the 2.8 fF diode at optimum embedding impedances using the same input power. The small difference, that is 16.3 - 18.4 % is mainly due to the difference in cutoff frequency for the devices.

The measured results for the 750 GHz tripler using the 5.4 fF diode are shown in Fig.5. The output power and efficiency are as can be seen in Fig.5, very sensitive to the input power. The higher input power means that a larger backbias voltage or in this case a smaller forward bias voltage can be used thereby making the diodes work more in varactor mode, see Fig.6. Thus the output power and efficiency using this operating point are greater, compare Fig.5 and 6. It can be seen, comparing Fig.6 with Fig.5, that the operating points vary according to the pump power available from the carcinotron and seem to be less dependent on the pump frequency Thus the passband for the rf-filter seems to have little variation in attenuation over the investigated frequency range, which was also anticipated.

The work on optimizing the 250 GHz tripler is about to commence. Initial output powers of 1 mW at 250 GHz has been achieved.

Future work:

The 250 GHz tripler will be optimized as a pump source for the 750 GHz tripler.

The 5.4 fF varactor will be replaced by a 2.8 fF device which we have now fabricated, having a series resistance of 16 ohm.

Single barrier varactors (SBV) will be tested in the mount. Due to the symmetrical I-V and C-V characteristic of the SBV-diodes only odd harmonic are generated in these devices [10]. Thus they are particularly suitable for use in example triplers since no idler resonator is needed, thereby reducing the losses at the idler frequency to zero [11].

Conclusions:

The design and development of a solid state source for 750 GHz consisting of two triplers has been described. State of the art output powers of more than 120 μW has been achieved at 803 GHz using a carcinotron as the initial test source for the 750 GHz tripler.

Acknowledgements:

We would like to thank Dr. D. Vizard for helpfull discussions and Mr. J. Pike for assistance in selecting the diodes and diode manufacture. Messrs. K. Barrett and M. Fehilly are thanked for skilful manufacturing and assembly of the multipliers as well as technical ideas. Miss M. Tubridy is also thanked for help with optimization of the mount using Touchstone.

The European Space Agency (ESA) is acknowledged for financial support (ESA contract no. 7898/88/NL/PB).

References:

1. P.H. Siegel, A.R. Kerr and W. Hwang, Topics in the optimization of millimeter-wave mixers," NASA tech. paper 2287, 1984.

2. N.R. Erickson, "Very high efficiency frequency tripler for 100-300 GHz," Proc. of the 10th Int. Conf. on Infrared and Millimeter Waves, pp. 54-55, 1985.

3. N.R. Erickson, "A high efficiency frequency tripler for 230 GHz," Proc. of the 12'th European Microwave Conf., pp. 241-246, 1982.

4. N.R. Erickson, "High efficiency submillimeter frequency multipliers," Proc. of IEEE-MTT Conf. 1990, pp. 1301-1304, 1990.

5. R.C. Johnson and H. Janik, Antenna engineering handbook, second edition, McGraw-Hill, pp. 15-13 - 15-17, 1984.

6. T.J. Tolmunen and A.V. Raisanen, "An efficient Schottky-varactor frequency multiplier at millimeter waves, Part II: Tripler," Int. Journal of Infrared and Millimeter Waves, vol. 8, pp. 1337-1353, 1987.

7. A.G. Williamson, "Analysis and modelling of "two-gap" coaxial-line rectangular waveguide junctions," IEEE Trans. on Microwave Theory and Tech., vol. MTT-31, pp. 295-302, 1983.

8. A. Rydberg, "Calculation of microwave radial-line filters," Microwave and Optical Technology Lett., vol.1, pp. 4-7, 1988.

9. A. Rydberg, "Oscillator and multiplier development for millimeterwave radioastronomy," Proceedings of the workshop on solid state sources at millimeter and submillimeter wavelengths, Ulm, BRD, October 1987.

10. E. Kollberg and A. Rydberg, "Quantum-barrier-varactor diodes for high-efficiency millimeter-wave multipliers," Electron. Lett., vol. 25, pp. 1696-1698, 1989.

11. A. Rydberg, H. Gronqvist and E. Kollberg, "Millimeter- and submillimeter-wave multipliers using Quantum-Barrier-Varactor (QBV) diodes," IEEE Electron Device Lett., vol. 11, pp. 373-375, 1990.

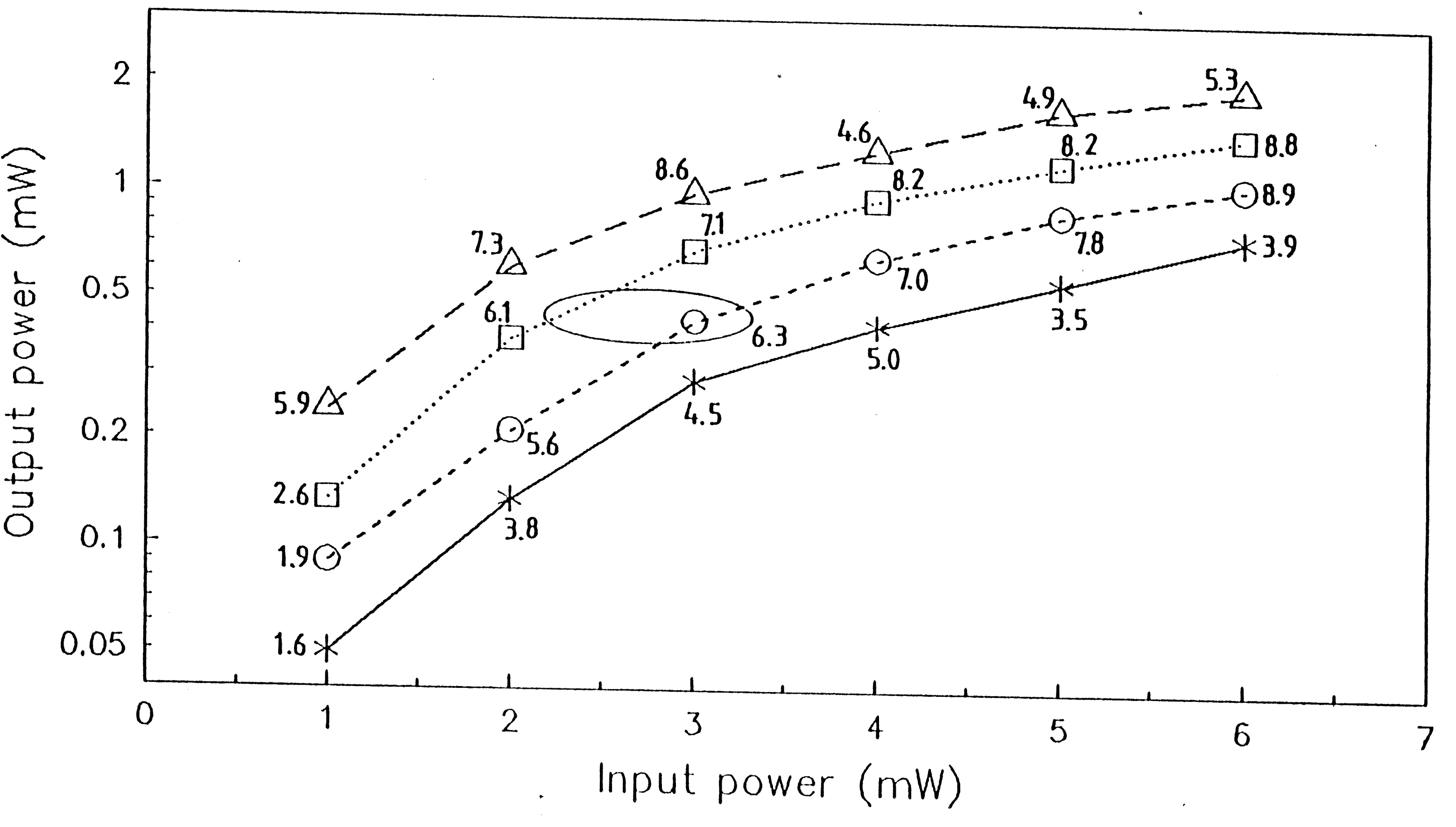

Fig.1 Calculated output power as a function of input power for Schottky varactor diodes having a capacitance $C_j(0)$ of between 1.6 - 3.4 fF. The bias voltage is optimized for best efficiency. The numbers along the curves are the maximum voltages V_{max} across the device at the particular operating point.

(Δ): $C_j(0)$ is 1.6fF, V_b = 4 V.

(□): $C_j(0)$ is 2.2fF, V_b = 6 V.

(O): $C_j(0)$ is 2.8fF, V_b = 6.5 V.

(x): $C_j(0)$ is 3.4fF, V_b = 7 V.

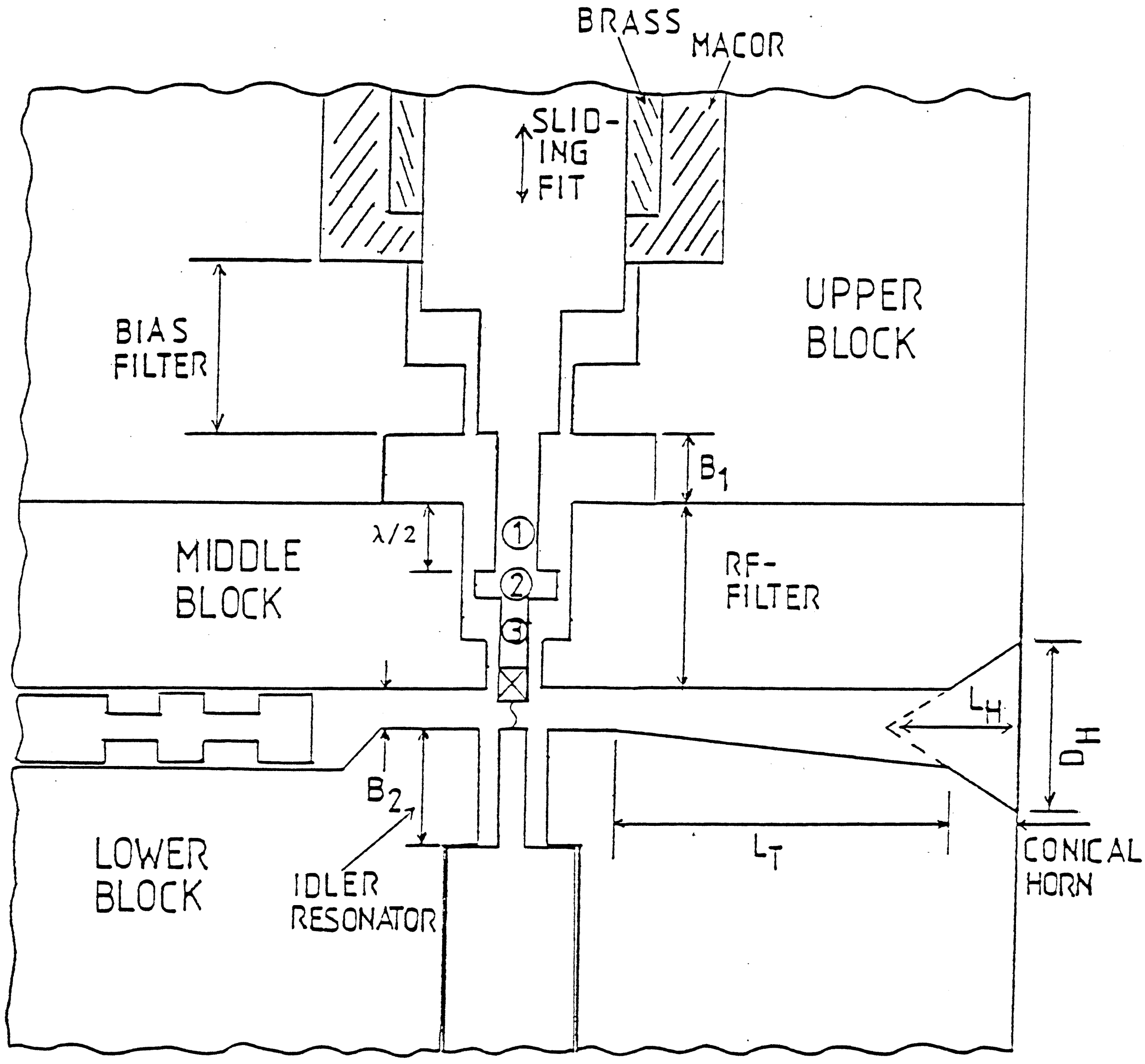

Fig.2 Cross-sectional view of the 750 GHz tripler. (Not to scale). B1=0.091 mm, B2=0.041 mm, $L_H=2\lambda$, $D_H=2.54\lambda$, $L_T=5\lambda$.

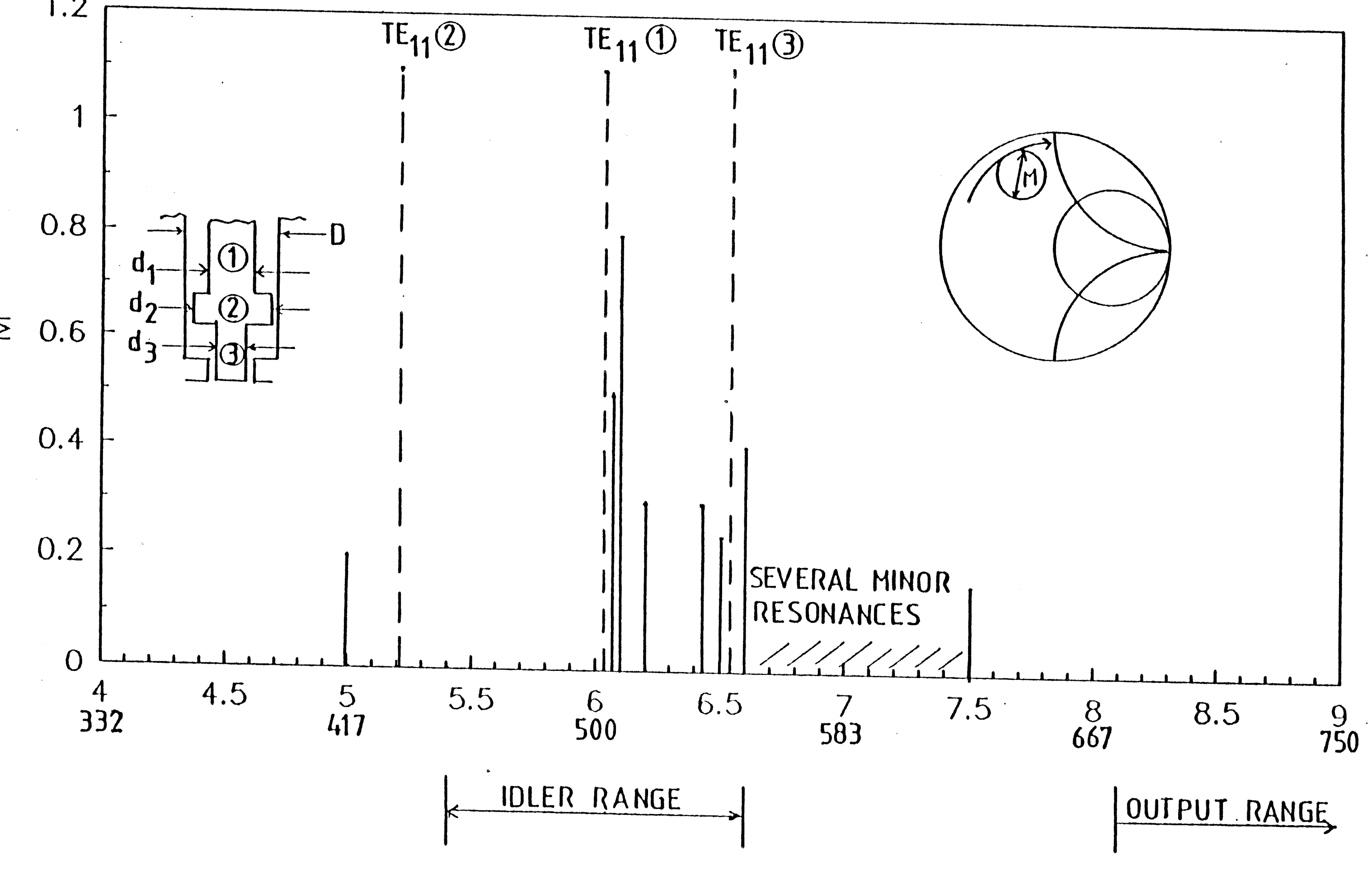

Fig.3 Measured resonances and calculated coaxial TE_{11}-mode cutoff frequencies for the rf-filter as a function of frequency. The measured resonances are plotted as the diameter of the resonance loop "M", see sketch in Fig.3. The maximum value of "M" is 1. The frequency is plotted both as the real and the scaled model frequencies for the multiplier. D=0.25 mm, d_1=0.13 mm, d_2=0.19 mm, d_3=0.1 mm.

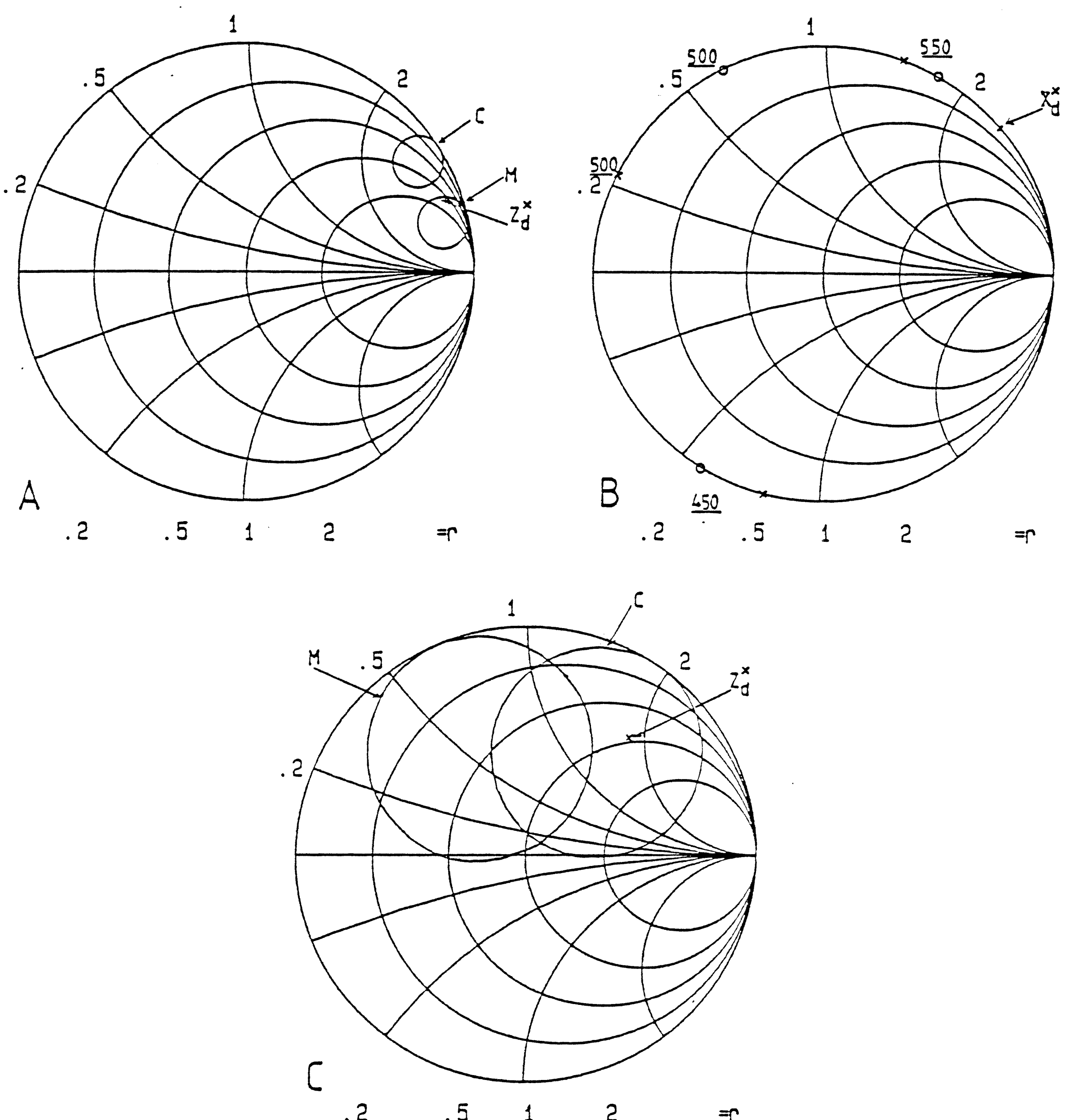

Fig.4 Measured and calculated embedding impedances seen by the diode at the input, idler and output frequencies. Z_d^x and X_d^x are the complex conjugate of the diode impedance and reactance respectively at 250, 500 or 750 GHz. M is measured and C is calculated in the figures, except for the idler where "o" = calculated and "x" is measured.

A: input frequency, 250 GHz.

B: idler frequencies, 450, 500 and 550 GHz.

C: output frequency, 750 GHz.

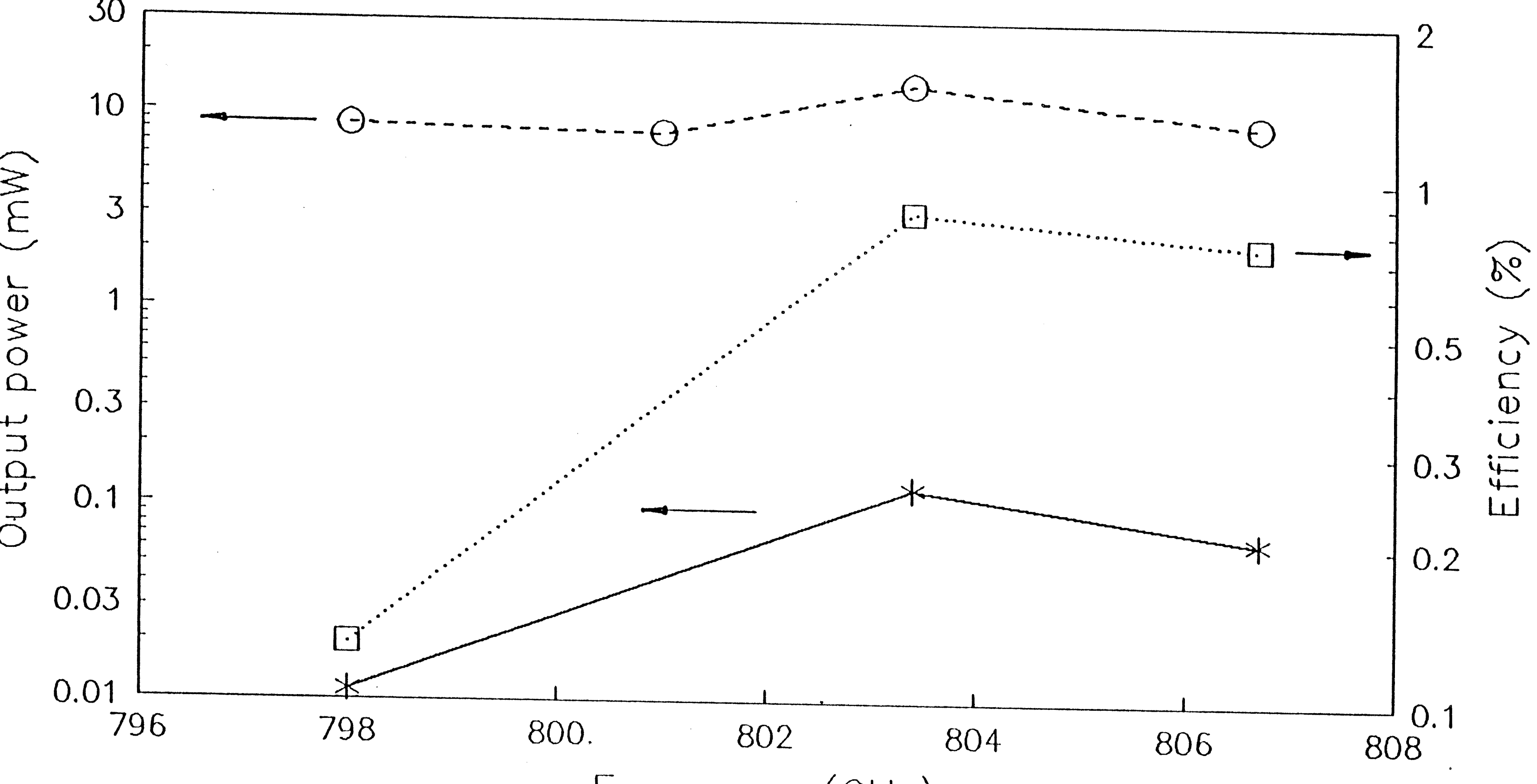

Fig.5 Output power and efficiency for the 750 GHz tripler as a function of the output frequency. The output power for the pump source (carcinotron) is also shown.
(x): output power from the tripler.
(□): efficiency for the tripler.
(o): output power from the carcinotron.

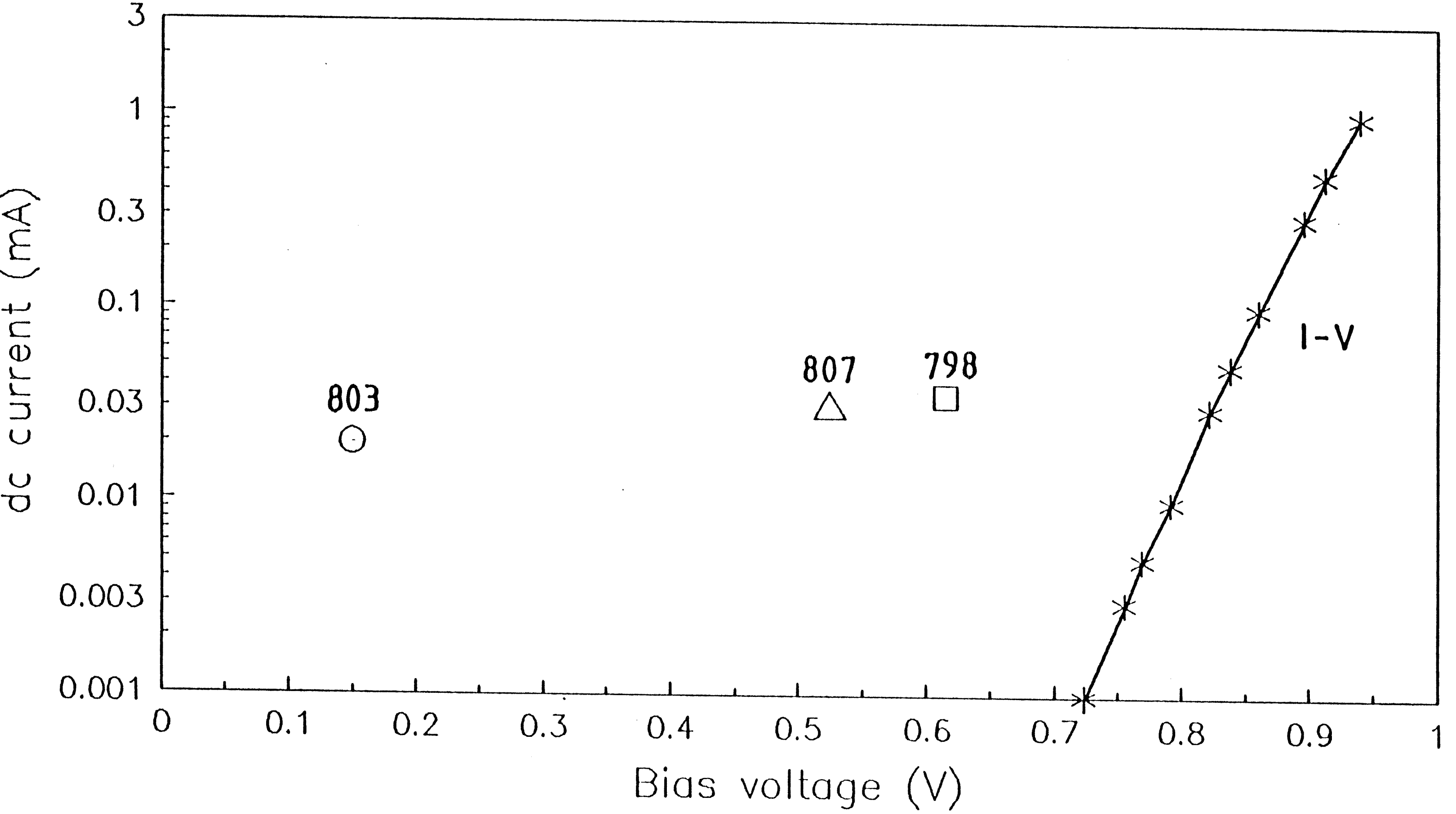

Fig.6 I-V curve and operating points for the 5.4 fF diode. The numbers at the operating points refer to the operating frequency in GHz for the particular operating point.

QUANTUM WELL DIODE FREQUENCY MULTIPLIER STUDY

R. J. Hwu

Department of Electrical Engineering

University of Utah

N. C. Luhmann, Jr.

Department of Electrical Engineering

University of California, Los Angeles

Abstract

Quantum well devices which show negative resistance in the I-V characteristic offer very strong nonlinearity for efficient frequency harmonics generation. Furthermore, the structure can be tailored to eliminate unwanted harmonics and optimize higher harmonics in the same device. The Wafer uniformity is a key issue when making an array and requires more study.

Quantum Well Diode Odd Harmonic Frequency Multipliers

The varactor diode multiplier is extensively used for generating power at millimeter-wave frequencies, and it has been shown theoretically to be quite efficient in doubler to quintupler configurations [1]. However, the theoretical calculations assume that the input and output impedances are matched and that optimum reactive loads at all idler frequencies are realized, a requirement which in practical cases is not possible to implement fully due to a number of limitations. Thus, measured efficiencies are often considerably smaller than those theoretically estimated [1]. By using a device with a symmetrical current-voltage and/or capacitance-voltage characteristic, only odd harmonics are generated. Thus, for example, using such a device in a quintupler configuration, there is only one idler at the third harmonic to consider. This can be compared to the three idlers needed in a Schottky varactor quintupler.

The presence of a peak and valley in the I-V curve combined with the overall antisymmetry of the I-V curve about the origin [i.e., I(V) = -I(-V)], offers the potential for efficient odd-harmonic generation with an unbiased quantum well diode [2]. The key lies in pumping the diode so that the peak amplitude of the voltage across the diode occurs above the resonant current peak. This will produce, at least, three local maxima to occur in the diode current waveform over one cycle, corresponding to third or higher odd harmonic generation. The quantum well resonant tunneling multiplier has two distinct advantages over existing resistive multipliers, which are usually based on Schottky barrier diodes. First, the symmetrical response provides the potential for efficient odd harmonic frequency multiplication with an unbiased resonant-tunneling diode due to cancellation of the even harmonics, therefore greatly simplifying the circuit design. Second, the maximum harmonic generation efficiency of a quantum well device is significantly higher than the $1/n^2$ (n is the harmonic number) value that applies to standard resistive multipliers because of its negative resistance [3] (i.e., nonmonotonically increasing function I-V characteristic).

To demonstrate the feasibility of this analysis, Fig. 1 shows the polynomial I-V curve ($I = aV + bV^3 + cV^5$) which is used in the large-signal multiplier study [4,5]. It should be mentioned that the large-signal multiplier analysis has been performed under the zero-bias condition to preserve the symmetrical polarity characteristic of the I-V curve. A constant capacitance was assumed in the computation to ensure that the diode is operating in the purely varistor mode. The delivered power values at the third and fifth harmonic frequencies have been plotted versus frequency as can be seen in Figs. 2 and 3, respectively. The embedding impedances at the fundamental and third harmonic frequencies are optimized for each frequency case. The tripling and quintupling efficiencies corresponding to these power relations are shown in Figs. 4 and 5 to facilitate the comparison. Based upon these results, it is seen that the output power decreases dramatically with increasing frequency for both cases. Harmonic conversion efficiency, therefore, decreases significantly as frequency increases. As also can be seen from these

plots, the maximum tripling efficiency is actually very close to the maximum quintupling efficiency. This illustrates that the cut-off frequency of negative resistance diode frequency multipliers is not determined by the $1/n^2$ (n is the output harmonic number) limitation as for the standard positive resistance varistor diode. It can also be seen that the highest efficiency has been obtained in the negative conductance region of the device.

Power and Stability Considerations

Biasing in the Negative Differential Resistance Region

As discussed in previous publications [6,7], the diode-grid array approach is attractive because a grid is monolithically integrated with thousands of solid state diodes thereby overcoming the power limitations of a single diode multiplier since the power is distributed among the many diodes making possible watt-level CW output power throughout the millimeter-wave region. However, the pumping power for a diode grid is significantly higher than that for a single diode (proportional to the number of the diodes). Therefore, it is important to minimize the amount of input power required to pump each individual diode. In order to efficiently utilize the symmetrical I-V characteristic of a quantum well multiplier, one needs to pump the diode sufficiently hard so that the peak amplitude of the voltage across the diode occurs above the resonant current peak. This means an input power higher than 10 mW for each diode which, most likely, is too high for the diode grid concept as thousands of diodes are integrated and need to be pumped at the same time. The major thrust of this section is to investigate the possibility of minimizing the amount of power required to efficiently pump each individual diode without losing multiplication capability. For example, the almost symmetrical characteristic of the quantum well diode at the center of the negative resistance region can also be used in odd harmonic mode multiplication. This arrangement requires a dc bias. However, highly

efficient frequency multiplication can be achieved with relatively small pumping power for each diode.

To study the possibility of biasing the diode to minimize the pumping power level, the I-V curve of a quantum well diode is modelled with a fifth order polynomial (Fig. 6). The efficiency for a quantum well tripler to 100 GHz, using the I-V curve shown in Fig. 6, was calculated. The calculations are made using a large-signal nonlinear circuit analysis program for multipliers. The curves are calculated assuming a 1.5 ohm series resistance and a constant capacitance of 10 fF. By pumping the unbiased quantum well diode using a sinusoidal signal (peak voltage of 3.0 V), the tripling efficiency of the diode was analyzed as a function of pumping voltage as shown in Fig. 7. Maximum tripling efficiency can be obtained when the diode is pumped with a high power level of close to 10 mW (V_p = 2.0 V). The same calculation has been performed for the doubling efficiency which is always very close to zero. It can be seen from this result that the even harmonics are cancelled and reduced at the symmetrical I-V point along the I-V curve.

As can be seen from Fig. 8, the almost symmetrical characteristic of the quantum well diode near the center of the negative resistance region provides highly efficient odd harmonic mode multiplication. The tripling efficiency drops quickly as the dc bias point moves away from the center of the negative resistance region. In addition, the power required to achieve the maximum tripling efficiency reduces to 5 mW (V_p = 1.414 V) for each diode.

Biasing in the Positive Differential Resistance Region

The difficulty of operating in the negative differential resistance region can be seen from the stability consideration. However, if one biases the device in the positive differential resistance region, the conditions are considerably relaxed. The positive differential resistance can be utilized to relax the stringent requirements.

As can be seen from the results shown in Fig. 9, if the diode is biased in the positive differential resistance region close to the resonant current peak, the diode can be easily driven into the negative differential resistance region to achieve a high multiplication efficiency of 20%. This arrangement minimizes the required pumping power and relaxes the stringent requirements on the stability consideration. However, the tripling efficiency is lower than can be expected from biasing the device near the center of the negative differential resistance region. The doubling efficiency which can be obtained from this operation is also calculated and shown in Fig. 10. A maximum doubling efficiency of 30% can be achieved which is slightly higher than the maximum tripling efficiency from the same operation. This efficient doubling operation can be explained by the symmetrical behavior of the I-V characteristic at the peak resonant current region.

Another biasing possibility for utilizing the positive differential resistance region to relax the stability condition is to operate around the voltage region right above the occurrence of the valley current. The tripling efficiency of the quantum well diode multiplier has been calculated assuming a DC bias value of 2.2 V and is shown in Fig. 11. The maximum tripling efficiency of this operation is much lower than the above mentioned biasing cases due to the high dc current conduction and power dissipation (see Fig. 6). The positive varistor mode dominates in this bias region which can also be seen from the point that the maximum tripling efficiency is actually limited to 11% (i.e., $1/n^2$, n = output harmonic number).

Summary

The shape of the I-V curve suggests that there should be large harmonic content to the current waveform, and the antisymmetry implies that only odd harmonics should be present. From the large-signal nonlinear circuit results, the differential negative resistance allows efficiencies greater than the limit $1/n^2$ for monotonically increasing I-V curves. In conclusion, the Q factor (f_c/f_o) is the major parameter on determining the multiplication

efficiency of a quantum well diode. It is clear that the multiplication performance of a negative resistance quantum well diode is determined by the capacitance, series resistance and negative differential resistance at the operating point. However, detailed studies need to be conducted to obtain a better understanding of this phenomenon.

Power and stability considerations have been carried out for the quantum well diode multiplier application. Highly efficient odd harmonic generation can be obtained when operating a quantum well diode at the origin and the center of the negative resistance region. The power requirement for operating at the origin and the stability consideration for operating in the negative resistance region suggest the alternative choice of biasing the diode at the positive resistance region. This arrangement requires less pumping power and relaxes the stability condition; however, the odd harmonic generation efficiency is reduced due to the loss of the symmetry characteristic.

References

[1] T. J. Tolmunen, "High Efficiency Schottky-Varactor Frequency Multipliers at Millimeter Waves," J. Infrared and Millimeter Waves, **Vol. 9**, pp. 475-518, 1989.

[2] T. C. L. G. Sollner, P. E. Tannenwald, D. D. Peck, and W. D. Goodhue, Appl. Phys. Lett. **Vol. 45**, P. 1319, 1984.

[3] C. H. Page, "Harmonic Generation with Ideal Rectifiers," Proc. IRE, **Vol. 46**, pp. 1738-1740, 1958.

[4] A. R. Kerr, IEEE Trans. Microwave Theory Tech., **MTT-23**, No. 10, P. 828, 1975.

[5] H. Siegel, A. R. Kerr, and W. Hwang, NASA Tech. Paper #2287, 1987.

[6] C. F. Jou, UCLA Ph.D. Thesis, 1987.

[7] R. J. Hwu, C. F. Jou, W. W. Lam, U. Lieneweg, D. C. Streit, N. C. Luhmann, Jr., J. Maserjian, and D. B. Rultedge, IEEE Microwave Theory Tech. Symposium, Digest of Technical Papers, P. 533, 1988.

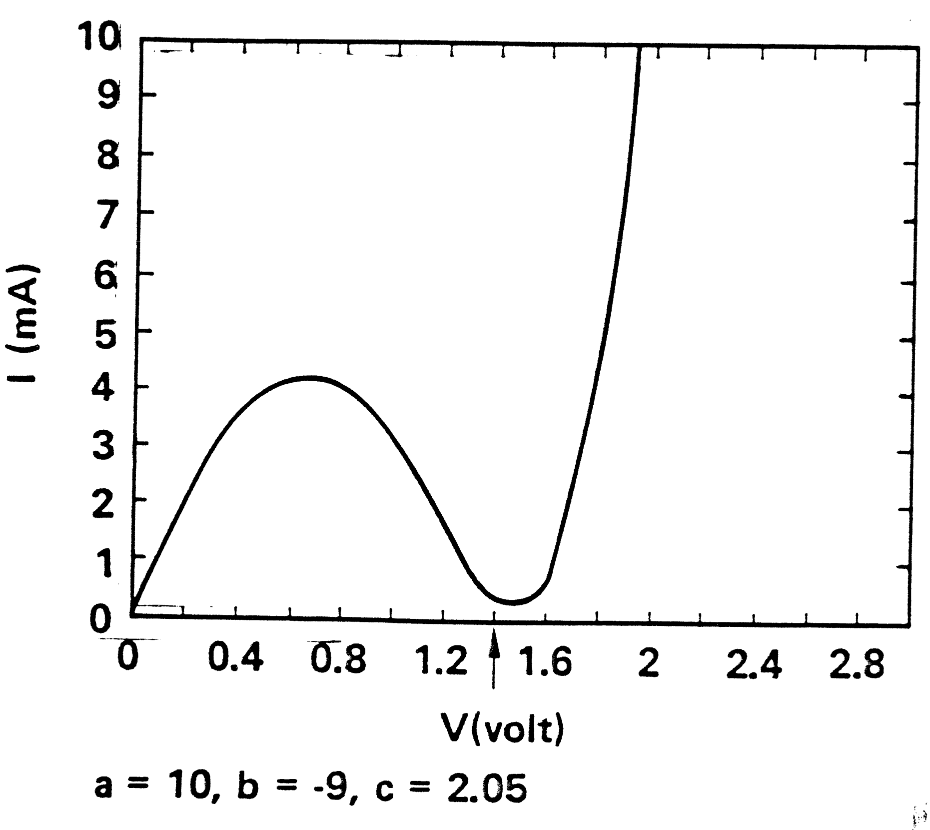

Fig. 1 The polynomial I-V curve used in the initial large-signal negative resistance quantum well diode multiplier study.

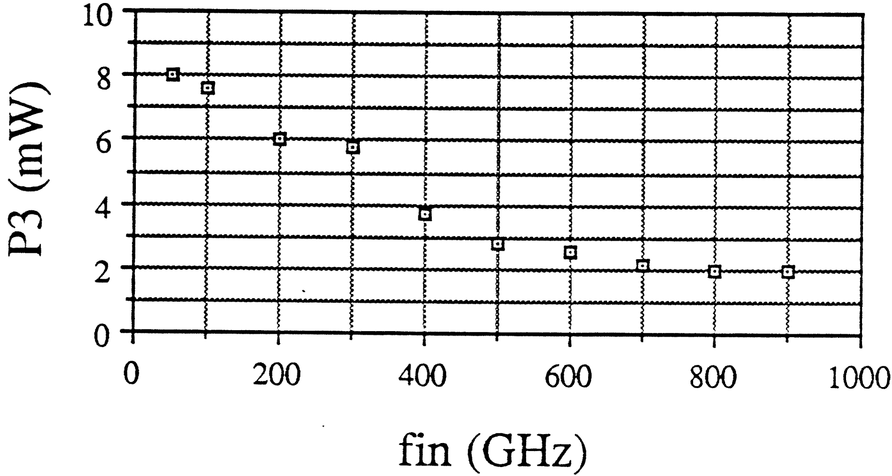

Fig. 2 Delivered power versus frequency for quantum well tripler.

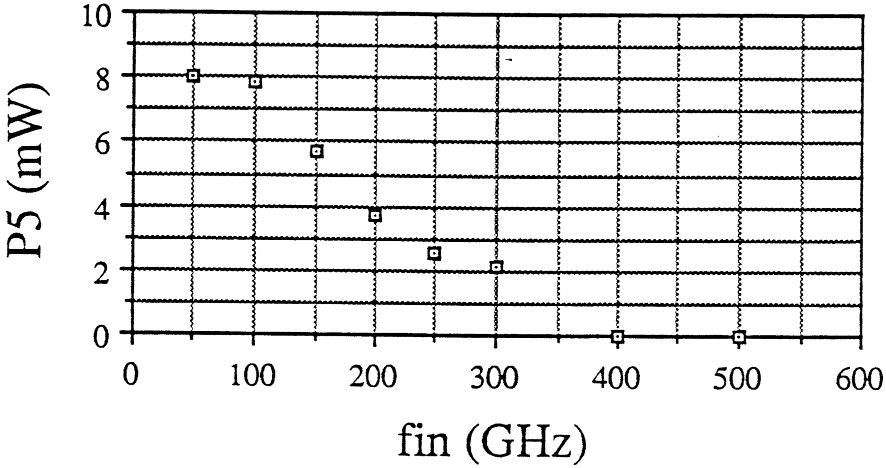

Fig. 3 Delivered power versus frequency for quantum well quintupler.

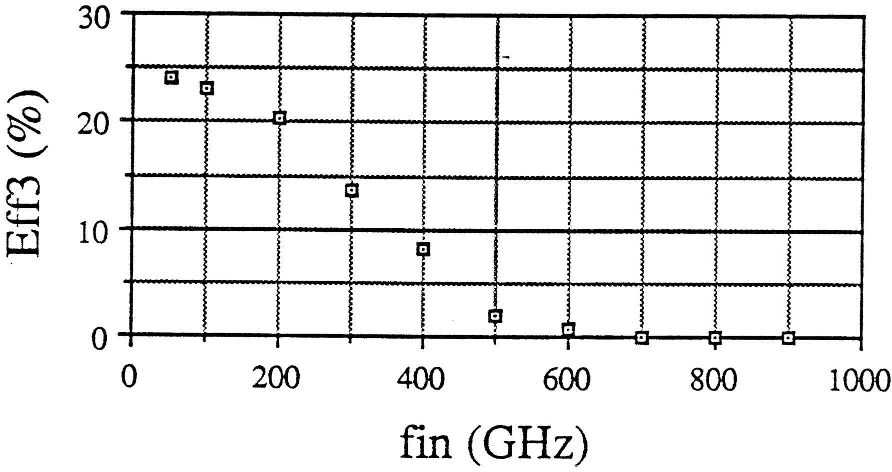

Fig. 4 Tripling efficiency versus frequency corresponding to the power shown in Fig. 7.2.

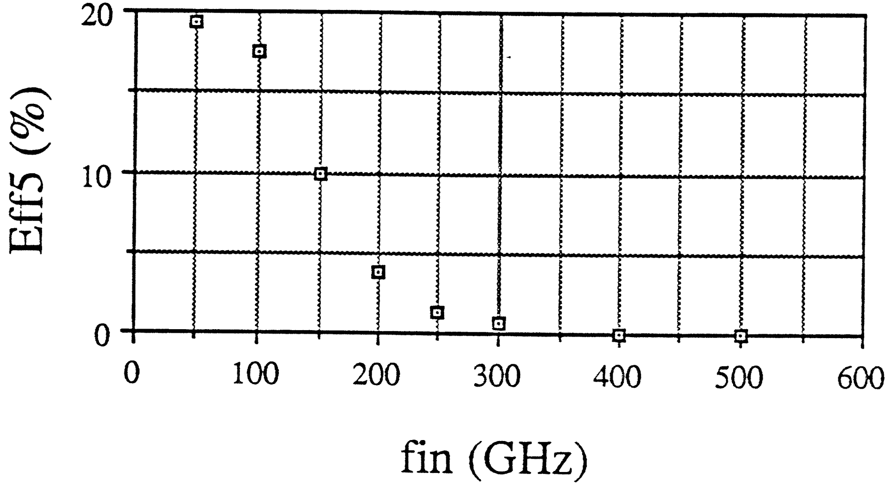

Fig. 5 Quintupling efficiency versus frequency corresponding to the power shown in Fig. 7.3.

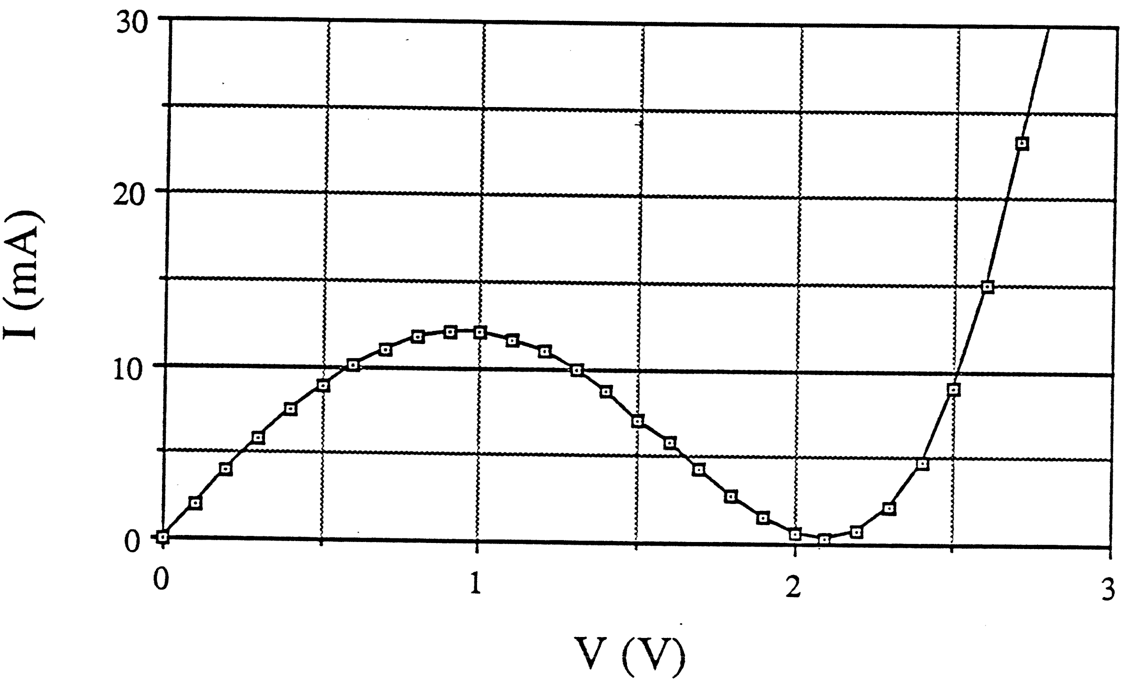

Fig. 6 The polynomial I-V curve used for the following large-signal nonlinear circuit analysis.

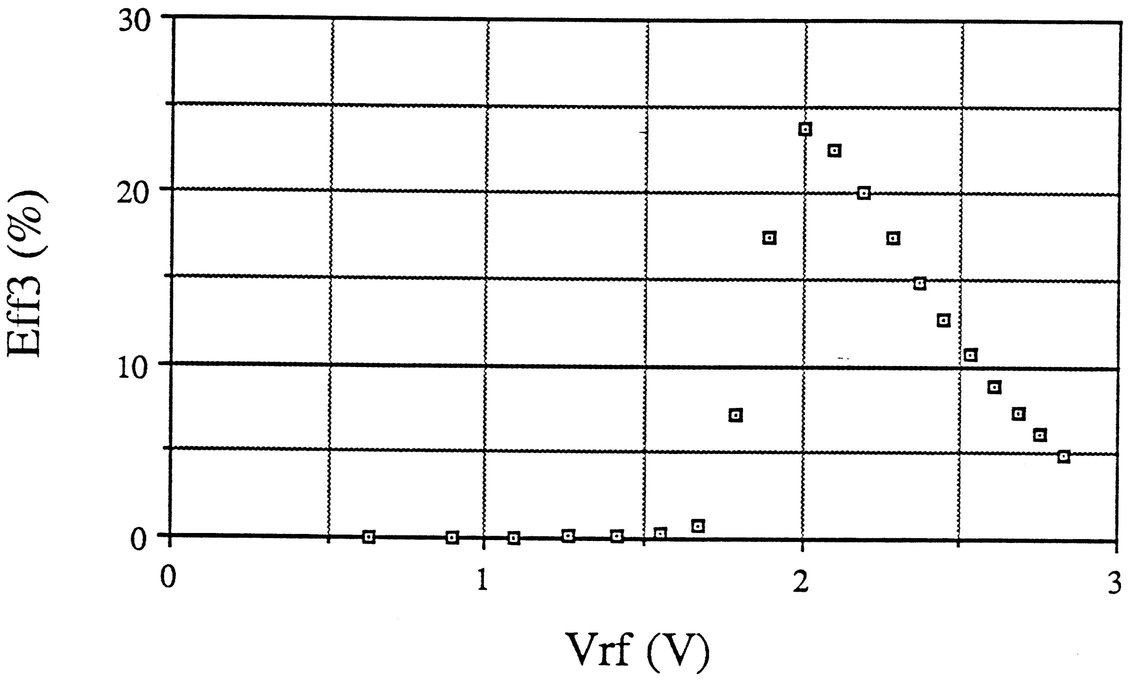

Fig. 7 Tripling efficiency versus RF voltage for the quantum well diode with zero DC bias.

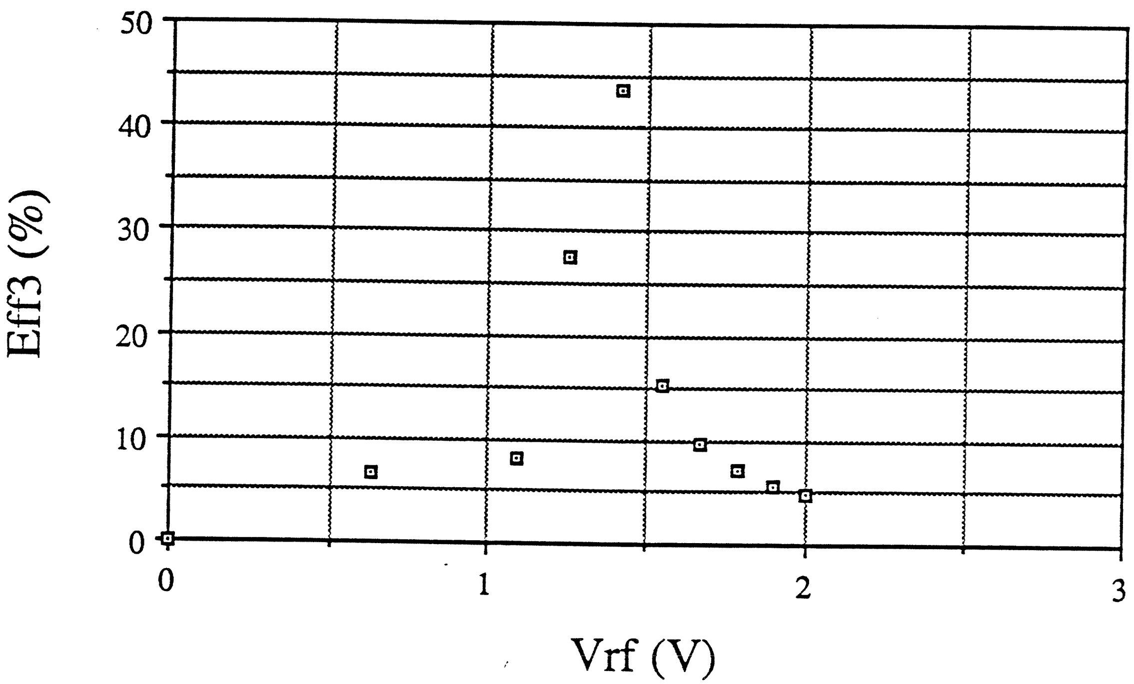

Fig. 8 Tripling efficiency versus input power for the quantum well diode biased at 1.5 V.

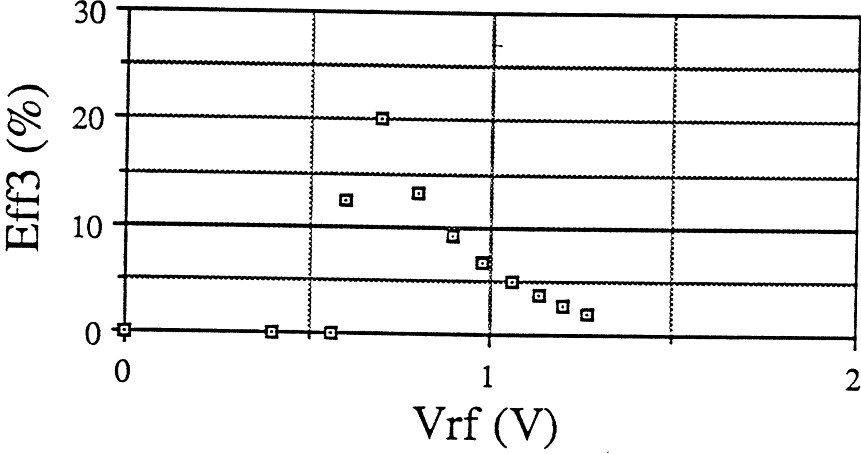

Fig. 9 Tripling efficiency versus input power for the quantum well diode biased at 0.8 V.

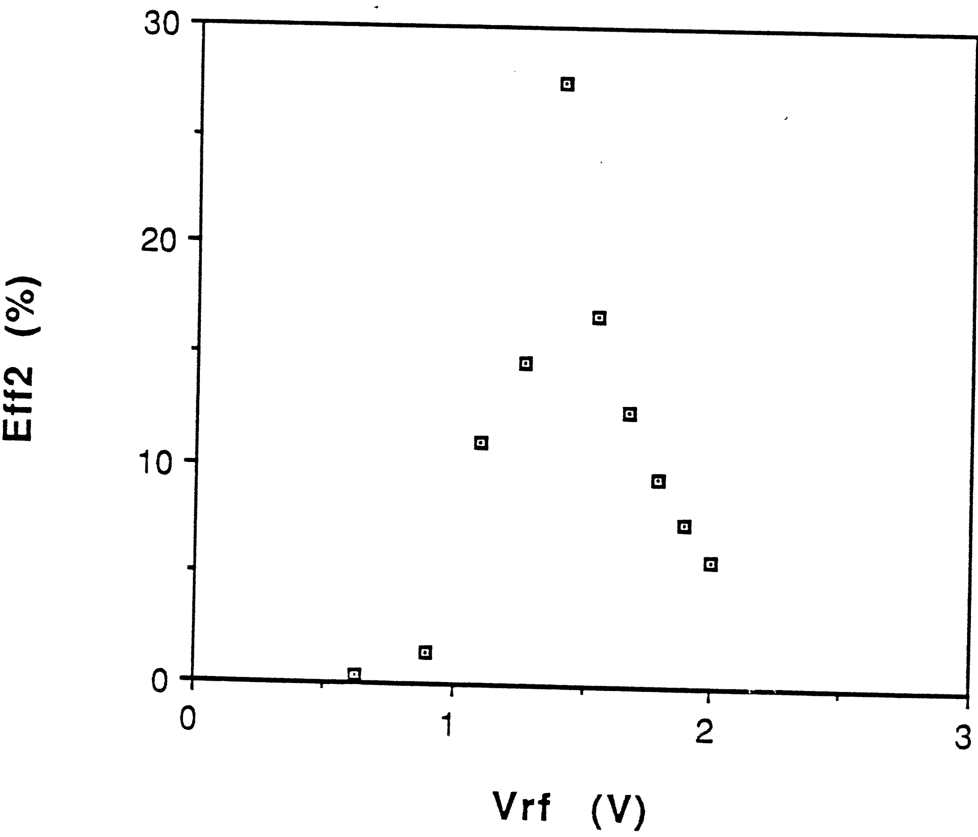

Fig. 10 Doubling efficiency versus input power for the quantum well diode biased at 0.8 V.

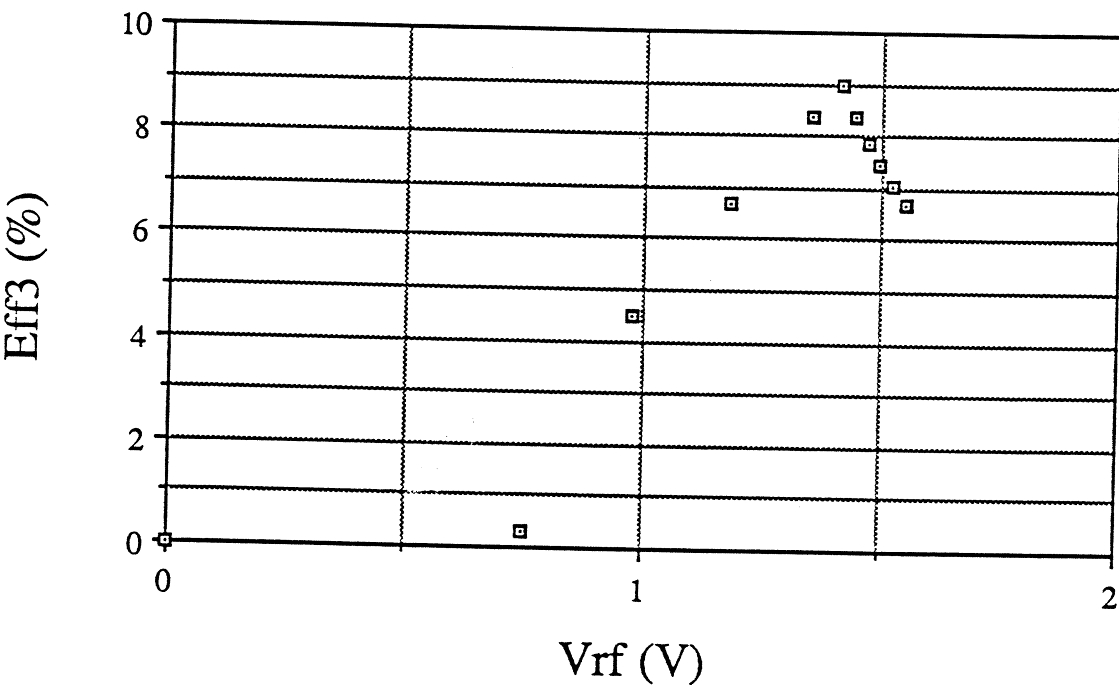

Fig. 11 Tripling efficiency versus input power for the quantum well diode biased at 2.2 V.

90-180 GHz Heterostructure Monolithic Integrated Doubler*

Y. Kwon, D. Pavlidis, P. Marsh, M. Tutt, G.I. Ng and T. Brock
Center for Space Terahertz Technology
Solid State Electronics Laboratory
Department of Electrical Engineering and Computer Science
The University of Michigan, Ann Arbor, MI 48109-2122, USA

Abstract

This paper demonstrates the design, theory, monolithic integrated circuit (MMIC) implementation, and 180 GHz operation of a doubler based on HEMT technology. Doublers were fabricated on an InP substrate using submicron ($0.1\mu m$) InAlAs/InGaAs HEMT's. Microstrip lines were utilized for the various matching components. The doubler 90 GHz input drive was varied from approximately -10 dBm to +8 dBm as measured at the test fixture input. Conversion loss varied from approximately 6dB to 10dB and was minimum at an input drive level of approximately 0 dBm.

Introduction

Space based sensor applications where gas molecule resonances are studied at several hundred GHz require high frequency receiver functions such as frequency mixing and oscillation. Two terminal device sources such as IMPATT's and TUNNET's are reported to operate at frequencies which are normally below 200 GHz. The traditional approach for extending the frequency limits of oscillator sources above 100 GHz is frequency multiplication. This is usually performed using two-terminal multiplier diodes. The high frequency characteristics of FET's, however, suggest the possibility of three-terminal devices for such applications. In fact, the transistor approach can allow conversion gain and better efficiency than diodes which normally require relatively higher power drive levels. Also, input and output isolation is superior in FET structures. Monolithic implementations of GaAs FET doublers are also possible and have, for example, been demonstrated up to 40 GHz [1][2]. Three terminal devices such as MESFET's and

*Work supported by NASA under the contract NAGW-1334

HEMT's also offer the possibility of integrating the various receiver functions on the same chip. Amplifiers, mixers, oscillators and multiplier could consequently be realized through the use of monolithic integrated circuit technology.

HEMT's based on InAlAs/InGaAs material system have shown state-of-the-art discrete device performance with maximum oscillation frequency (f_{max}) of 450 GHz [3]. Furthermore, strained designs with excess indium in the channel show improved carrier confinement and improved characteristics [4]. Monolithic integrated circuits using this system have started emerging recently, including X-band amplifiers [5] and W-band mixers [6]. A W-band monolithic oscillator using InAlAs/$In_{0.6}Ga_{0.4}As$ HEMT's has been demonstrated by the authors and showed 81 GHz oscillation with output power of -7 dBm at the chip level [7].

This work demonstates the first experimental characteristics of a monolithic HEMT doubler from 90 GHz to 180 GHz using InAlAs/InGaAs heterostructure circuits above 100 GHz.

1. Submicron ($0.1\mu m$) Gate HEMT Fabrication

A cross-section of the InAlAs/$In_{0.65}Ga_{0.35}As$ HEMT is shown in Fig. 1. The details of the design optimization were reported by the authors in the past [4]. The layers were grown by MBE as described by Hong et. al. [8]. The active device used for the monolithic doubler is a $0.1\mu m \times 90\mu m$ mushroom-gate HEMT. A mix-and-match method is employed for this purpose whereby optical lithography is used for all levels except the submicron gates which require e-beam writing. The first level is the mesa isolation which is achieved using wet chemical etching (H_3PO_4:H_2O_2:H_2O). Next an image-reversal process (Shipley 5214-e photoresist) is used to define the ohmic patterns (2 μm source-drain spacing) and Ge/Au/Ni/Ti/Au is evaporated and lifted off using PRS100 solution. The ohmic metal is then rapid thermal annealed at $375°C$ for 7s. Good electrical characteristics and surface morphology can be obtained at the same time. This allows small acess resistance to the device and facilitates e-beam writing.

To obtain the $0.1\mu m$ gate, a bi-layer electron-beam resist technology was developed. The gates were written using the JEOL JBX 5DIIF e-beam system which is equipped with 50keV e-beam energy capability. The higher electron energy allows better beam

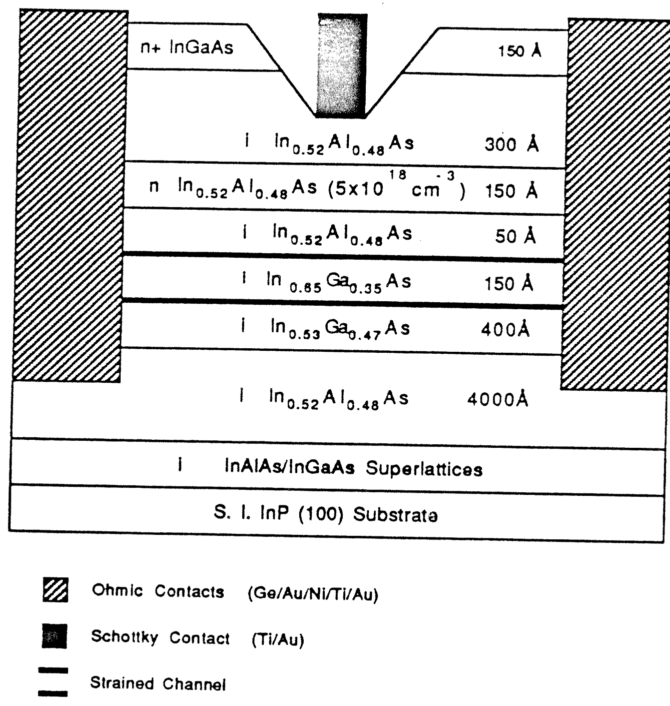

Figure 1: Device cross-section of a single-heterojunction InAlAs/$In_{0.65}Ga_{0.35}As$ HEMT

directionality which causes less back scattering in the resist during exposure and hence less broadening of the exposed area. This feature permits one to obtain a small (0.1μm) gate foot print by implementing a bi-layer resist technique rather than using a tri-layer resist technology. The advantages of the bi-layer resist technique include shorter time and fewer steps for resist preparation, excellent gate aspect ratio and higher lift-off yield for both pads and gates. 0.1μm gates are obtained with this approach in a very reproducible way and the technology lends probably itself to even shorter gate lengths.

The bi-layer resist consists of a bottom PMMA (1500Å) layer and a top P(MMA-MAA) (5500Å) layer as shown in Fig. 2. A side-lobe exposure technique is employed to obtain submicron mushroom-gate with excellent aspect ratio (4:1). This technique consists of three beam exposures. The first exposure is used to define the 0.1μm foot print. As mentioned earlier, the higher directionality of the electron-beam allows the definition of very small foot print of 0.1μm or smaller. The other two beam exposures with weaker dosage are used to obtain the top mushroom-gate profile. After exposures, the e-beam resist is developed using a MIBK:IPA solution. A SEM picture of the bi-layer resist profile is shown in Fig. 2.

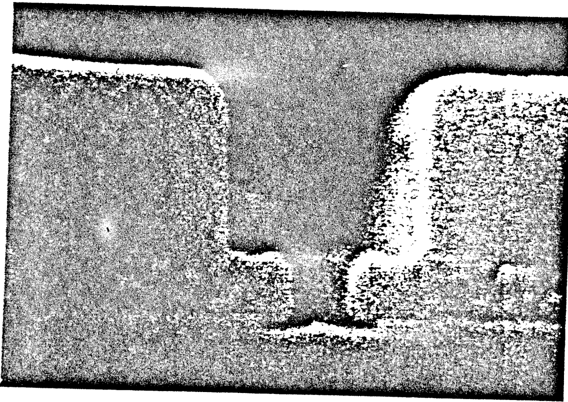

Figure 2: SEM picture of a bi-layer E-beam resist profile of the 0.1 μm mushroom gate

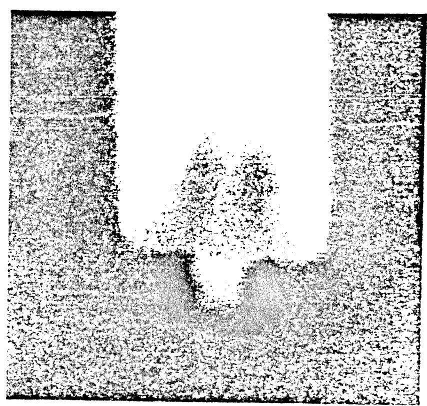

Figure 3: SEM picture of a 0.1 μm mushroom gate using bi-layer resist and side-lobe exposure technique

The next critical step after the e-beam writing is the gate recess. Before that, the wafer is descumed in an oxygen plasma to remove any resist residues in the opened areas. Next, the native oxide layer is removed using buffered HF and immediately followed by gate recess using an citric acid:H_2O_2:H_2O etchant. The gate recess is stopped when a predetermined drain-source current is reached. The wafer is then subjected to a short buffered HF etch and loaded immediately into the e-beam evaporator. Ti/Pt/Au is evporated and lifted off using acetone. After lift-off, wafers are inspected and a yield estimate is made. This is normally exceeding 90%. A complete SEM picture of a 0.1μm mushroom- gate is shown in Fig. 3.

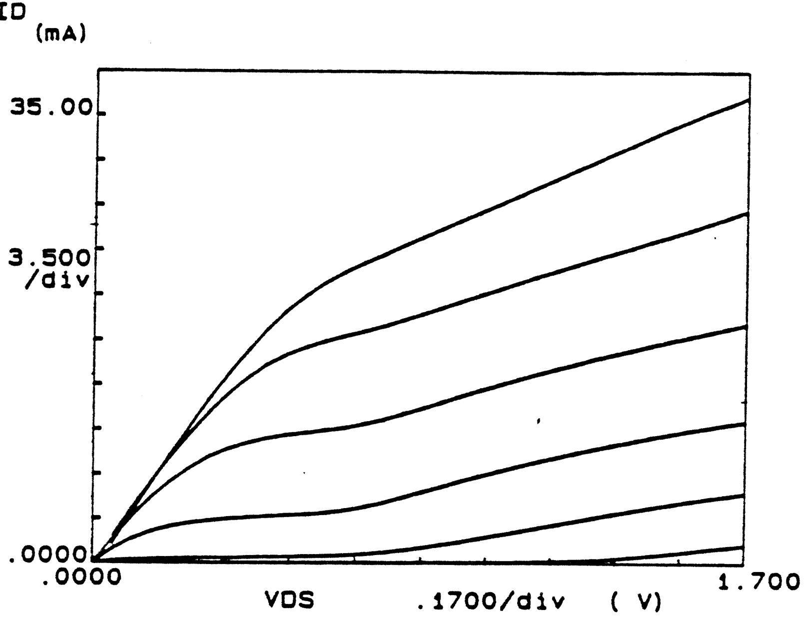

Figure 4: DC I-V characteristics of a 0.1 μm × 45 μm InAlAs/$In_{0.65}Ga_{0.35}As$ HEMT

2. DC and Microwave Characterization

Before proceeding to the next fabrication steps, the devices are tested both at DC and RF. This allows one to evaluate the suitability of the wafer for MMIC processing and monitor the degree of possible degradation when the active devices are subjected to the subsequent MMIC processing steps.

Fig. 4 shows a typical I-V characteristics of a fabricated 0.1μm×45μm HEMT's. These devices exhibit good pinch-off characteristics which is important for good doubler operation. A drain-source current as high as ~820mA/mm at V_{ds}=1.7V and V_{gs}=0.4V was obtained. Fig. 5 shows the corresponding transfer characteristics of the same device. The extrinsic g_m is ~920mS/mm with an associated I_{ds} of 550mA/mm at V_{ds}=1.5V and V_{gs}=0.18V. However, these devices also give high output conductance (G_{ds}~180mS/mm) which is typical of the single-heterojunction design using this material system [9]. As a result, th gain factor g_m/G_{ds}~5 is rather low and limits the microwave power gain performance.

The devices were also characterized using on-wafer probing from 0.5GHz to 26.5GHz. Fig. 6 shows the microwave performance of a 0.1μm×90μm HEMT. A high extrinsic f_T of 180GHz was extracted for this device following a -6dB/oct slope. The maximum power gain at 26.5GHz was ~15.5dB. The estimated f_{max} for this device is also of the same

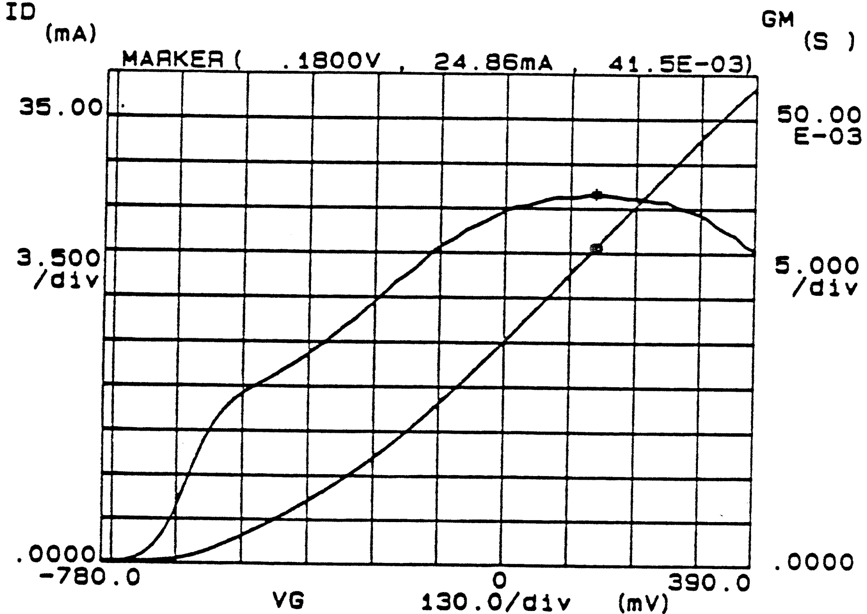

Figure 5: DC transfer characteristics (g_m-V_{gs},I_{ds}-V_{gs}) of the device corresponding to Fig. 4. Peak extrinsic g_m=920mS/mm with an associated I_{ds}=550mA/mm.

magnitude (~180GHz). Higher f_{max} values can be expected by optimizing the device structure and growth technique to suppress the high G_{ds} [9] and by improving the device technology using techniques such as double-recess gate [10].

Following the device characterization, the wafer was carried through the remaining MMIC processing steps to realize the complete doubler circuit. After the wafer has been thinned down to ~100μm and diced, the discrete HEMT's were once again being characterized. These results reflect more closely the true device performance capability since they are obtained at the end of the complete MMIC fabrication cycle. The results obtained for the doubler run reported in this paper revealed degradation in device performance. DC g_m's values on the average have dropped from 900mS/mm to 600mS/mm which corresponds to a substantial g_m decrease by 30%. Likewise, both f_T and f_{max} have decreased to ~ 130GHz. Similar degradation have also been observed in other wafers after processing steps involving heat treatment. Preliminary studies indicate that this may be related to the material and the growth conditions. A more detailed study of this phenomenal will be reported elsewhere [11].

The bias-dependent extrinsic f_T characteristics of the 0.1μm×90μm HEMT are shown in Fig. 7. The f_T's increase with V_{ds} under all gate bias conditions. The best f_T for this

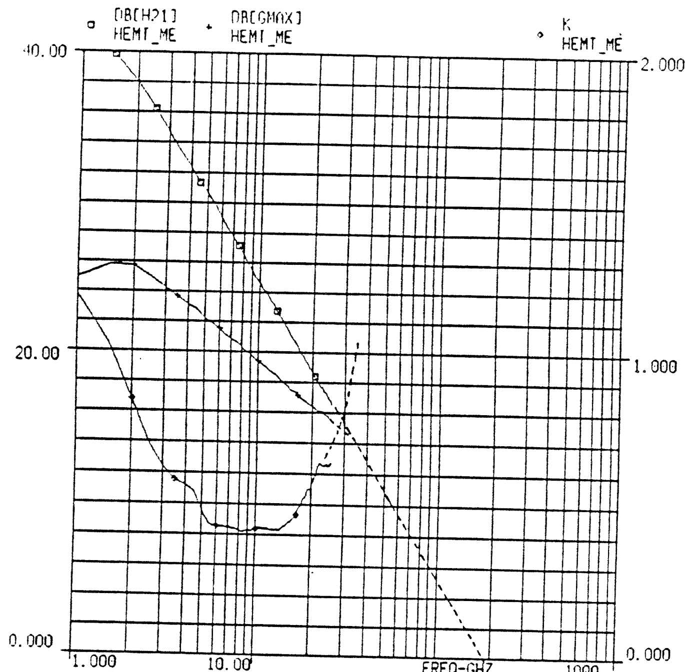

Figure 6: Microwave characteristics of a 0.1 μm × 45 μm InAlAs/$In_{0.65}Ga_{0.35}As$ HEMT right after active device fabrication. The maximum extrinsic f_T and f_{max} are approximately 180 GHz.

device is ~130GHz at V_{ds}=1.5V and V_{gs}=0V. This corresponds to a decrease of ~30% which was primarily due to the same order of magnitude degradation in the g_m of the device.

Although the device performance at the end of the MMIC processing does not demonstrate the maximum possible capability of the HEMT's, it is sufficiently good to permit the demonstration of a functional 90GHz to 180GHz doubler. This is due to the fact that the frequency of the doubler input signal is below f_T and thus the device nonlinearity can still be effective. Much better doubler performance such as lower conversion loss can be expected if the interity of the devices can be preserved throughout the processing steps.

3. Passive MMIC Component Fabrication

Following the active devices, the passive MMIC components are fabricated. These include biasing and matching capacitors, interconnect metals for microstrip stubs and bonding pads, and air-bridges.

To realize the capacitors, a sputtered lift-off technique is used which allows selective deposition of the SiO_2 without any influence on the active device characteristics. The

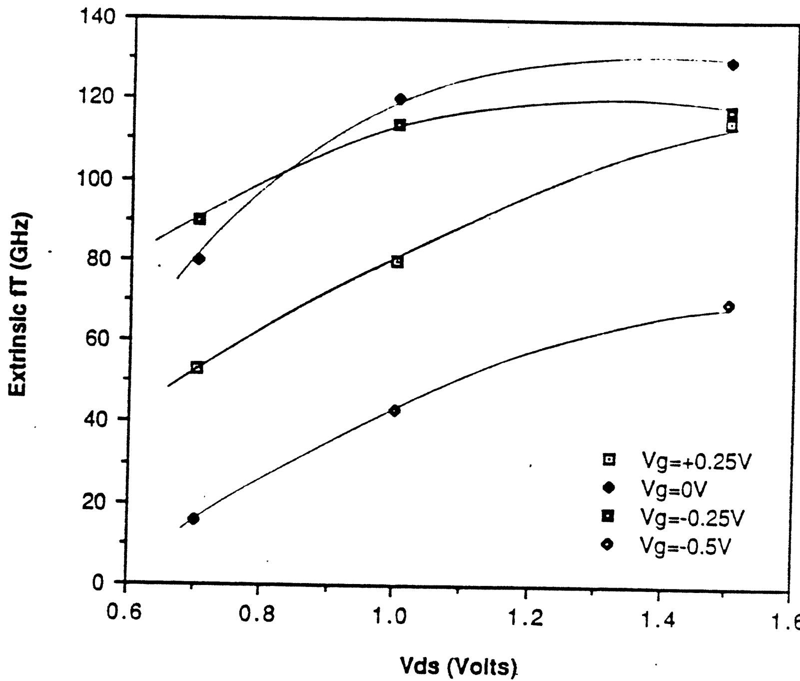

Figure 7: Bias-dependent microwave characteristics of a 0.1 μm × 90 μm HEMT after the complete MMIC fabrication cycle.

capacitor consists of the bottom plate (Ti/Au), sputtered SiO_2 as the dielectric material, and finally the top plates (Ti/Au) which also serve as the interconnect metal. All these levels are defined using optical lithography and a chlorobenzene lift-off technique.

Next, air-bridges are fabricated in a two-step process. First, the pillars of the air-bridges are defined and the entire wafer is sputtered with Ti and Au to form the pillars and also to serve as the conductive path for the subsequent electroplating. Next, the air-bridges are opened up and followed by electroplating of thick Au layer. The photoresists are then removed and the thin sputtered Ti and Au layers are etched away using buffered HF and TFA gold etchant respectivley. The integrity of the air-bridges is excellent as confimed by their stability after wafer thinning (~100μm) and dicing. The latter are the final two steps of the complete MMIC fabrication cycle used for the reported doubler. Finally, the individual chips are mounted and bonded in a specially designed text fixture for 180GHz testing.

4. 90 to 180 GHz Doubler Circuit Design

FET frequency doublers can operate in two typical bias conditions - one corresponds to a gate-source voltage (V_{gs}) near pinch-off (V_p) (class B) and the other requires an almost near V_{gs} = 0 V condition. The transconductance is used as a major source of

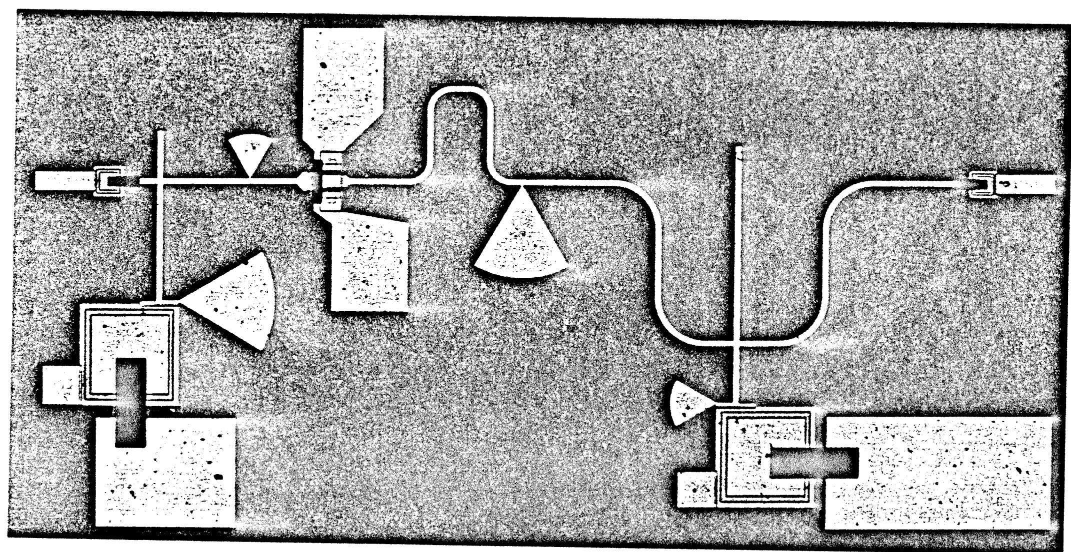

Figure 8: Photograph of a monolithic integrated doubler using InAlAs/InGaAs HEMT

nonlinearity in class B operation. For an operation with $V_{gs} = 0$, the output conductance is the predominant device nonlinearity necessary for harmonic generation. There is no major difference in conversion efficiency between these two cases for low frequency operation because both can provide efficient drain current clipping which is the main source of second-harmonic generation. However, the RF leakage current which is represented by the displacement current in the gate-source capacitance (C_{gs}) for high frequency operation prohibits the ideally expected square-wave-like waveform generation and thus degrades the efficiency significantly. Even if the device provides greater transconductance at $V_{gs} = 0$, it is advisable to use the $V_{gs} = V_p$ bias condition for high frequency multiplication to minimize the RF leakage current. This design philosophy was applied to the 90 to 180 GHz doubler reported in this paper.

A photograph of the fabricated chip is shown in Fig. 8. Right next to the HEMT one distinguishes two radial stubs used to realize bandreject filter characteristics. The left stub acts as a 180 GHz resonator prohibiting the doubled signal from leaking towards the input, while the right one functions as a 90 GHz resonator cutting off the fundamental 90 GHz from the output terminal. The radial stubs have 10 % bandwidth and a maximum rejection of more than 25 dB. These filters also serve as means to isolate the input and output ports. The bandreject filters are placed so as to provide proper reactive termination at the FET for the fundamental and doubled frequencies. Gate bias is

achieved through an overlay capacitor connected to the 90 GHz radial stub. This is quarter-wavelength transformed to yield perfect open conditions at the input line. The drain bias decoupling circuit is realized in a similar fashion. The matching networks at the input and output of the circuit are realized using narrow 90 Ω open-ended stubs and tuning capacitors.

In order to determine the large signal matching impedances and simulate the nonlinear operation of the HEMT doubler, a special nonlinear transistor modeling procedure has been developed and combined with harmonic balance analysis routine. The method allows the exact reproduction of experimental microwave data over the bias range of interest even with limited number of measurements. For the actual circuit simulation, the whole circuit was driven with a variable power source and the output power was evaluated at a 50 Ω load connected to the output port of the doubler circuit.

The conversion loss dependence on the gate bias was also studied. The time-domain characteristics of the output drain voltage after clipping resemble a truncated sinusoidal function. The DC gate bias determines the time duration over which the transistor is conductive (duty ratio). When $V_{gs} = V_p$, the duty ratio is 50 % and optimum conversion efficiency is expected theoretically. This is not, however, true in practice, due to the high frequency displacement current which leaks through C_{gs} and contributes to a parasitic signal. For this reason, the optimum gate bias condition is found to be slightly more positive than the pinch-off voltage.

The theoretical conversion loss vs. input power level obtained from the nonlinear analysis is shown in Fig. 9. For increased power levels, the conversion loss is seen to reduce and subsequently increase. The first reduction of conversion loss can be explained by a more efficient pumping with increased input power which results in a larger effective nonlinear transconductance swing. The deterioration of conversion loss with excess input power is attributed to the reduction of transconductance with increased power level in HEMT's due to parasitic "MESFET"-type operation. The theoretically estimated minimum conversion loss is of the order of 7.2 dB with 2 dBm LO power level using an InAlAs/InGaAs HEMT with f_T of 135 GHZ.

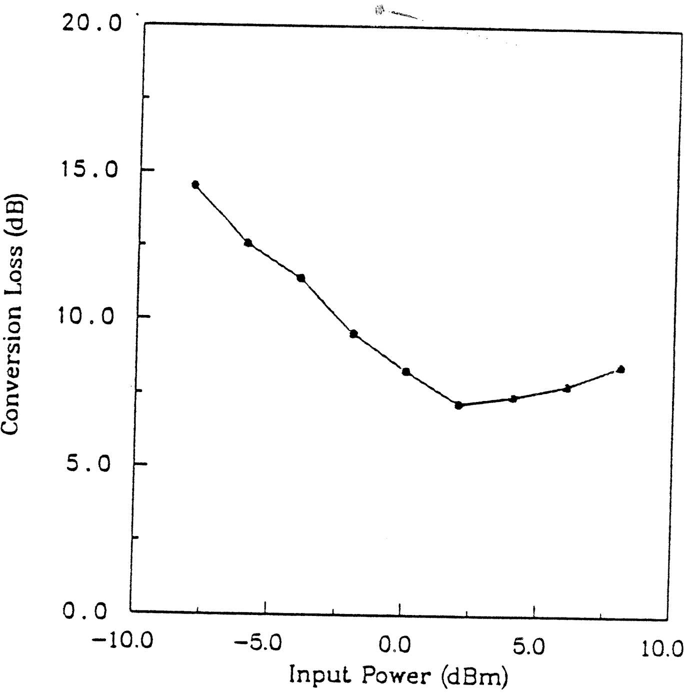

Figure 9: Theoretical conversion loss versus input power for HEMT doubler

5. High Frequency Doubler Tests and Results

Since the goal of this project is to produce working doublers, characterization is needed to verify the doubler design. Initially, the goal of characterization was to see conversion of 90 GHz to 180 GHz, i.e. a go - no go test. Thus, the test fixture design philosophy was to produce a fixture that could be designed and constructed with minimal effort, while promoting easy device mounting and reasonable testing repeatability. Doubler performance was evaluated in terms of conversion loss vs. RF drive level at 180 GHz output.

5.1 Test Fixture Design

The test fixture used to house the doubler needed to provide: a 90 GHz WR-10 waveguide input; a 180 GHz WR-3 waveguide output; two dc supply lines for drain and gate bias; and a smooth supportive surface to mount the doubler chip. The overall dimensions of the doubler test fixture were chosen to minimize waveguide lengths, yet provide adequate room for waveguide flanges, screws and other hardware (See Figure 10.). A finline to microstrip transition was selected for the WR-10 port. Theoretically, finline transitions are more lossy than probe transitions. However, finline transitions have the advantage of lower sensitivity to dimensional variations than probes [12].

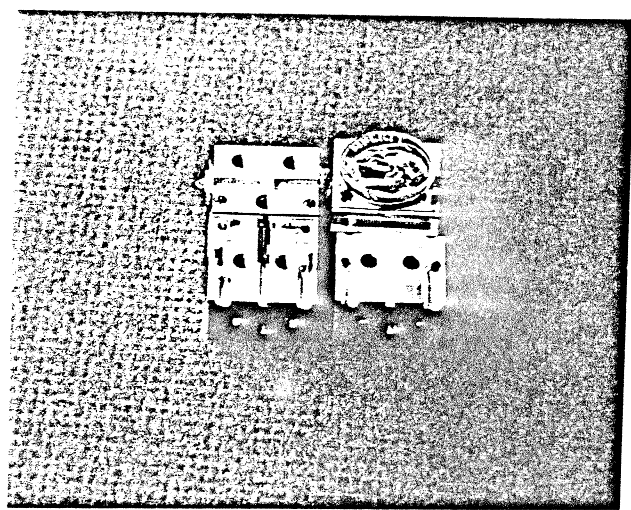
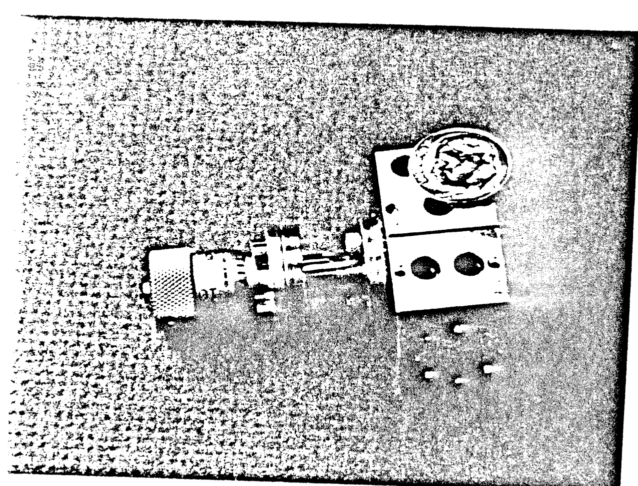

Figure 10: Photograph of the doubler test fixture

At the 180 GHz (WR-3) port, it was necessary to regress to the use of a microstrip probe transition because the minimum feasible finline transition substrate thickness of 5 mils was an appreciable fraction of the waveguide dimensions. It was expected that the addition of a WR-3 variable backshort would provide 180 GHz tuneability to offset design uncertainties in the probe. Since the microstrip probe lies in the center of the WR-3 guide, the variable backshort may be mounted on either of the two WR-3 ports. The actual WR-3 microstrip probe was realized using a microstrip realized on a 100 micron thick GaAs substrate free of backside metalization.

The 90 GHz WR-10 transition was realized using a waveguide to finline to microstrip transition (hereafter called a finline transition) on 5 mil thick fused quartz. Low dielectric constant, low losses, and a firm substrate that allows wirebonding make quartz the material of choice for this application. The transition itself is about one guide wavelength long near 94 GHz. In order to prevent evanescent waveguide modes from coupling past the transition, the quartz microstrip was made about one guide wavelength long at 94 GHz.

The finline transition is designed to present a smooth, gradual change from the waveguide TE01 mode configuration to a microstrip mode. First, the traveling waveguide E-field encounters the finline substrate. Provided that the product of the finline thickness and one minus the dielectric constant is small, the waveguide E-field sees little reflection here and proceeds to become concentrated within the substrate, between the finline edges.

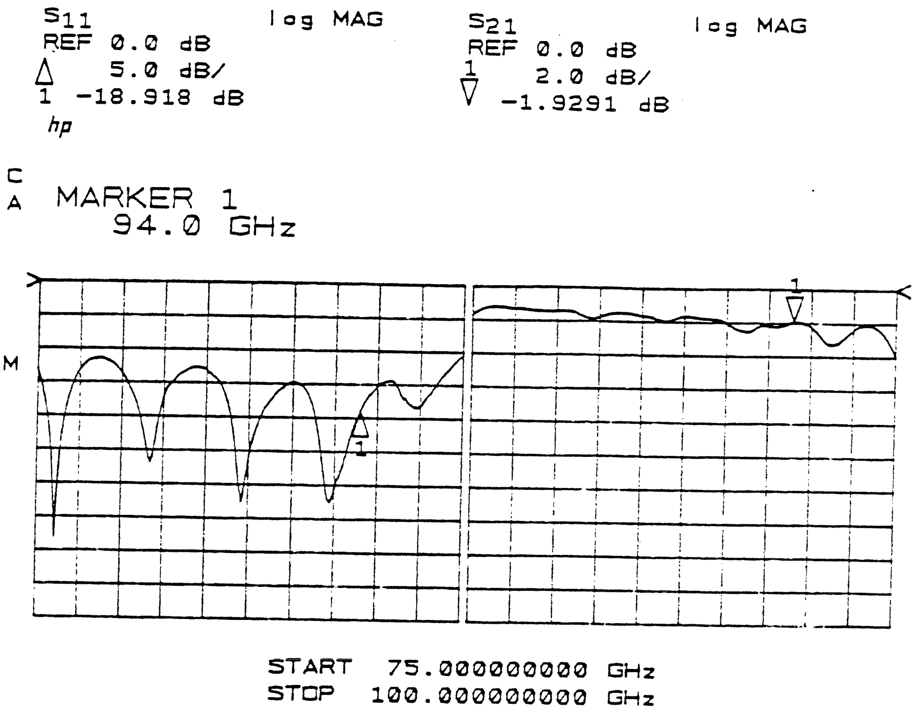

Figure 11: Double-ended finline W-band performance

From here, the antipodal finlines gradually overlap, causing the E-field to rotate towards 90 degrees as it propagates toward the microstrip. Eventually, the finline becomes a microstrip, thus carrying the E-field in a microstrip mode. In the section of the transition containing the microstrip, the backside metalization of the microstrip forms a waveguide below cutoff, thus insuring the that only the microstrip mode survives the transition.

The WR-3 microstrip probe was designed to couple to the TE01 mode of the WR-3 waveguide. In a lossless circuit, the backshort is capable of adjusting the reactance of the probe.

5.2 Test Fixture Characterization

In order to obtain reasonable measurement accuracy, it was necessary to characterize the performance of both the 90 GHz finline and 180 GHz probe transitions. Test results show that the finline - GaAs microstrip - finline has a loss of about 4.8 dB total with reflection below -30dBm at 90 GHz. This meant that the 90 GHz finline transition and bondwire in the doubler test fixture was estimated to have a 90 GHz loss of $4.8/2 = 2.4$ dB.

Next, it was necessary to characterize the doubler test fixture's 180 GHz probe transition. First, 180 GHz characteristics of the doubler test fixture's finline transition

were estimated from 180 GHz loss measurements taken on the finline - GaAs microstrip - finline configuration discussed above. This resulted in a 10 dB loss at 180 GHz. Thus, the doubler test fixture's finline loss was estimated to be 5dB at 180 GHz. To complete the characterization of the doubler test fixture's 180 GHz probe transition, a 1mm long GaAs microstrip section was installed to bridge the finline to the 180 GHz probe. Total insertion loss was about 15.5 dB at 180 GHz . Subtracting the finline loss from the measured total loss placed the doubler test fixture's 180 GHz probe transition loss at about 10.5 dB. The test results reflect the performance of test fixture of our first iteration design.

5.3 Doubler Test Procedure

Figure 12 illustrates the test setup used for the doubler characterization. One KHz square wave modulation was provided to the 90 GHz Gunn source and lock-in amplifier. The 90 GHz RF drive level was monitored using the 10 dB coupler and power meter and regulated by the continuously variable attenuator. A diode detector in conjunction with a lock in amplifier provided sensitive, detection of 180 GHz. Synchonous detection of the weak square wave output of the diode detector enables the lock-in amplifier to reduce the noise floor of these measurements. Because the diode detector exhibits broadband performance, it was necessary to eliminate the pickup of the 90 GHz fundamental. A one inch section of WR-3 waveguide provided a very effective high pass filter. To demonstrate that the detected signals were arising exclusively from the multiplying action of the doubler, the output from the 90 GHz isolator was connected through a one inch section of WR-3 waveguide to the diode detector. Under these conditions, the diode detector registered only a weak signal, about 40dB below that typical of the doubler output. Of course, with these results, one could not rule out the possibility that the doubler produced significant power at higher harmonics. However, theoretical calculations lead one to believe that the second harmonic is dominant.

5.4 90 to 180 GHz High Frequency Results

The behavior of the HEMT doubler showed some interesting features. Conversion loss was minimized at V_{ds} = 1V, I_{ds} = 5.1 mA (no input signal) and V_{gs} = -0.2 V. (The pinch-off voltage for the device tested was -0.25 V.) As expected from the simulation, the best conversion loss occurred just above pinch-off. Test results given here reflect doubler performance for the optimum bias conditions, namely those given above. Conversion loss

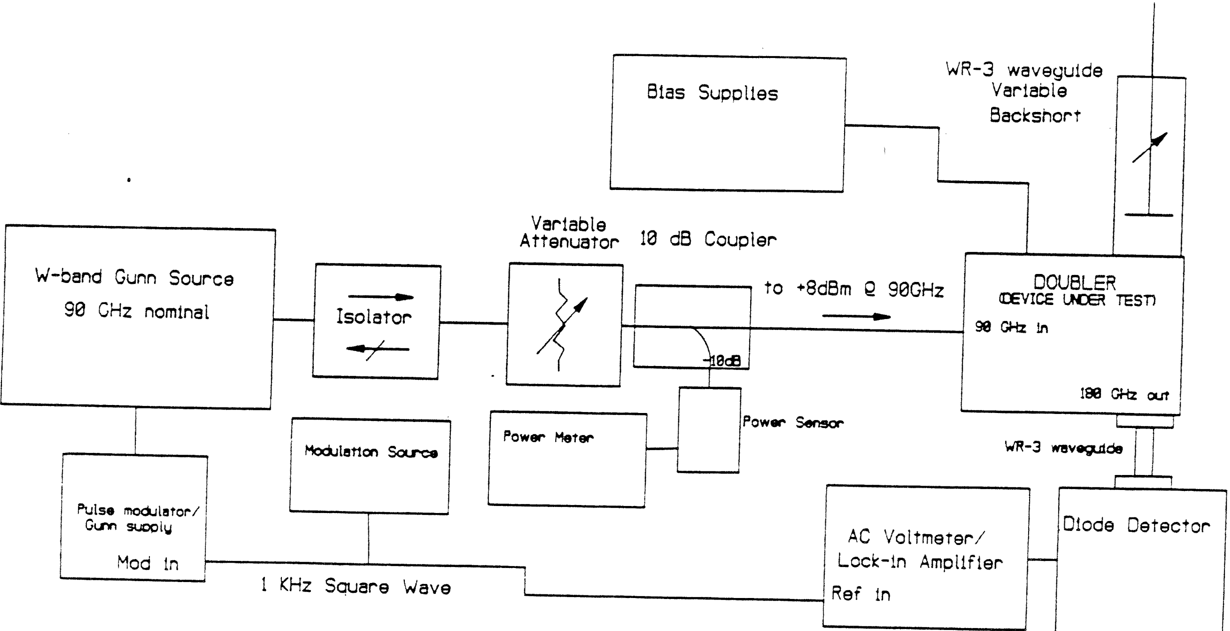

Figure 12: Doubler test setup

was found to be minimum at 0 dBm input power drive, which was close to the theoretical predictions. Over the input power range of our test (-10 dBm to 8 dBm), the conversion loss varied from 6 dB to 10 dB. This is not far off the result obtained by using hybrid diode doublers at 200 GHz. It should finally be noted that the small amount of input drive level necessary for minimum conversion loss is compatible with the limited amount of LO power available at millimeter-wave frequencies and makes the doubler compatible with other HEMT MMIC components such as, for example, oscillators [7].

Conclusion

At frequencies well above 100 GHz, and using MMIC technology, any measurable value of conversion would have been an encouraging step. The performance levels achieved (6 dB to 10 dB conversion loss for doubling from 90 to 180 GHz) was very satisfactory and even exceeded expectations. One should notice that this performance was obtained without the benefit of via hole technology. Future plans call for the implementation of via holes and further optimization of the HEMT output conductance, f_T, and f_{max} using advanced gate technologies such as offset T-gate and double recess. Eventually, these doublers will be coupled with the author's demonstrated W-Band MMIC oscillators [7] to generate milliwatt levels at 180 GHz and beyond from MMIC technology.

Acknowledgments

The authors would like to thank Professor P. K. Bhattacharya, his graduate students, Y. J. Chan and W. Q. Lee for material growth and J. Morgan for his skill in fabrication of the test fixtures. Gratitude also goes to Professor G. Rebeiz and his students, B. Kormanyos and C. Ling whose help with the lock in amplifier and diode detector made the doubler characterization possible.

References

[1] A. M. Pavio, S. D. Bingham, R. H. Halladay and C. A. Sapashe, "A Distributed Broadband Monolithic Multiplier," *IEEE, MTT-S Digest,* 1988, pp. 503-505

[2] S. Meszaros, C. J. Verver, R.J.P. Douville and W.J. R. Hoefer, "An Integrated 18.75/37.5 GHz FET Frequency Doubler," *IEEE, MTT-S Digest,* 1988, pp. 815-818

[3] P. K. Smith, P. C. Chao, P. Ho, K. H. G. Duh, M. Y. Kao, J. M. Ballingall, S. T. Allen and A. Tessmer, "Microwave InAlAs/InGaAs/InP HEMTs: Status and Application," *Proceedings of 2nd International Conf. on InP and Related Materials,* 1990, pp. 39-43.

[4] G. I. Ng, D. Pavlidis, M. Jaffe, J. Singh and H. F. Chau, "Design and Experimental Characteristics of Strained $In_{0.52}Al_{0.48}As/In_xGa_{1-x}As$ (x > 0.53) HEMT's", *IEEE, Trans. on Electron Devices,* Vol. 36, No. 9, October 1990, pp 2249-2259

[5] M. Weiss, G. I. Ng and D. Pavlidis, "New generation MMIC amplifiers using InGaAs/InAlAs HEMTs". *IEE, Electronics Lett., 1990,* Vol. 26, No. 4, pp. 264-266

[6] Y. Kwon, D. Pavlidis, M. Tutt, G. I. Ng and T. Brock,"W-band Monolithic Mixer using InAlAs/InGaAs HEMT's", *IEEE, GaAs IC Symposium,* New Orleans, LA, October, 1990, pp. 181-184.

[7] Y. Kwon, D. Pavlidis, M. Tutt, G. I. Ng, R. Lai and T. Brock,, "W-Band Monolithic Oscillator Using InAlAs/InGaAs HEMT's," *Electronics. Letters,* Vol. 26, No. 18, August 1990, pp. 1425-1426.

[8] W. P. Hong, G. I. Ng, P. K. Bhattacharya, D. Pavlidis and S. Willing, "Low and High Field Transport Properties of Psudomorphic $In_xGa_{1-x}As$/ $In_{0.52}Al_{0.48}As$ ($0.53 \leq x \leq 0.65$) Modulation Doped Heterostructures," *J. Applied Physics,* Vol. 64, No. 4, pp. 1945–1949, August 1988.

[9] G. I. Ng, R. Lai, D. Pavlidis, J. Pamulapati, P. K. Bhattacharya and K. Studer-Rabeler, "Submicron Double Heterojunction Strained InAlAs/InGaAs HEMT's: An Experimental Study of DC and Microwave Properties," *Proceedings of 2nd International Conf. on InP and Related materials,* Denver, Colorado, pp. 424, 1990.

[10] L. F. Lester, P. M. Smith, P. Ho, P. C. Chao, R. C. Tiberio, K. H. G. Duh and E. D. Wolf, "0.15μm gate-length double recess pseudomorphic HEMT with f_{max} of 350 GHz", *Proceeding of IEDM conference,* pp. 172, 1988.

[11] M. Tutt, G. I. Ng, D. Pavlidis and J. Mansfield,"Reliability Issues of InAlAs/InGaAs High-Electron-Mobility Transistors," *To be presented in the 3rd International Conf. on InP and Related Materials,* Cardiff, Wales, U. K., April, 1991.

[12] J. H. C. Van Heuven,"A new integrated waveguide-microstrip transistion," *IEEE, Trans. on Microwave Theory and Techniques,* Vol. 24 No. 3, pp.144–147, March 1976.

RECENT DEVELOPMENT OF BARRIER-INTRINSIC-N+ (BIN) DIODE FREQUENCY TRIPLER

R. J. Hwu

Department of Electrical Engineering

University of Utah

N. C. Luhmann, Jr.

Department of Electrical Engineering

University of California, Los Angeles

Abstract

Potential problems of the back-to-back GaAs Barrier-Intrinsic-N+ (BIN) diode tripler concept along with the associated device physics will be presented in this paper. The back-to-back GaAs BIN diode structure was originally proposed to have an intrinsic cut-off frequency close to 1 THz and be a highly efficient millimeter-wave frequency tripler device [1-3]. The device frequency limitations will be discussed to explain the failure of the GaAs BIN diode as a millimeter wavelength device.

Introduction

Recently, a novel metal-semiconductor homostructure, the Barrier-Intrinsic-N+ (BIN) diode structure, in which the capacitance switches rapidly between two values and behaves in a similar fashion to the punch through diode, has been proposed as a highly efficient millimeter-wave frequency tripler [1-3]. The nonlinear element of a punch through diode is a capacitor with a step-like transition in the C-V characteristics. An analytical study of the multiplication efficiency of the punch through diode was carried out and compared to that of the varactor diode [4-6]. The results show that the punch-through diode is always more efficient than the junction varactor for the same cut-off frequency. To overcome the power limitations of a single-diode multiplier, spatial power combining [7] of

the outputs of large planar arrays of nonlinear frequency multiplication devices has been implemented by the design of a diode grid [8,9]. The BIN diode concept has been adapted for the construction of diode-grid frequency tripler arrays [10,11]. Thousands of GaAs BIN diodes were integrated with a periodic grid in this approach to investigate the possibility of producing watt-level CW output power in the millimeter-wave region. This is an attractive approach to combine the power of each distributed device using monolithic integrated circuit techniques, thereby, resulting in potentially low cost fabrication and small size realization. Ideally, this approach should provide inexpensive, watt-level CW solid-state sources in the millimeter-wave region.

In the last two years, fifteen GaAs BIN diode-grid frequency tripler arrays have been fabricated with high-frequency measurements performed on each wafer. The highest tripling efficiency obtained was 8.5% at an output frequency of 100 GHz [11]. This wafer was destroyed shortly after by pumping it with too much power. Efforts have been devoted to repeat this result with additional samples. It has not been possible to reproduce the results of this measurement; in fact, no output power has been detected at the frequency of 100 GHz from any of the other wafers. Through this study, however, it was noticed that power could be obtained at the output port (W-band detector) before the detector was shielded from the input source radiation. It was further observed that once the detector was sealed all around by absorbers the detected power disappeared. At least part of the results obtained from this particular sample are believed to be due to scattered power sensed by the diode detector since no effort had been taken to shield the detector from random radiation at that time. The cut-off frequency of these GaAs BIN devices was determined to be 600 GHz assuming an average drift velocity of 3×10^7 cm/sec. A maximum tripling efficiency of 24% at an output frequency of 100 GHz was, therefore, predicted for these GaAs BIN diode-grid tripler arrays [10]. It should be pointed out that the assumed measured tripling efficiency (8.5%) was even smaller than that from an equivalent diode structure using Si

material. The major thrust of this paper is to explore the potential problems and limitations of the back-to-back BIN diode frequency tripler.

Device Concept

The Barrier-Intrinsic-N^+ (BIN) diode incorporates a thin undoped semiconductor layer (I) on a heavily doped layer (N) serving as a back contact. On top of the undoped layer, there is an ultrathin electron-blocking barrier layer (B) in contact with a metal top layer [1-3]. This blocking layer can be formed by an insulator, a semiconductor with a very wide band gap, or a Mott barrier [1-3]. With the low doping region, the action of the device depends upon the charge which is injected from the substrate into the epitaxial layer under forward bias. The device can be switched rapidly between two capacitance states which correspond to accumulation of electrons at the barrier and depletion of the intrinsic layer, respectively, by the applied bias. This results in a highly nonlinear capacitance-voltage characteristic which is needed for efficient harmonic generation. The maximum cut-off frequency of the BIN diode is determined by the time it takes electrons to transit the epitaxial layer. With a thin epilayer, intrinsic cut-off frequencies close to 1 THz have been projected in GaAs material [2,3].

The construction of a BIN diode on a III-V compound semiconductor entirely by the Molecular Beam Epitaxy (MBE) growth process (shown in Fig. 1) has been described [2,3]. A Mott-barrier is formed by a thin intrinsic layer sandwiched between the top metal contact and a charge sheet created by selective doping. This structure eliminates the problem of low fabrication yield associated with the thin MOS structure [12]. In the proposed GaAs Mott-BIN diode frequency tripler concept [2,3], it was assumed that GaAs is always superior to silicon due to the higher mobility and maximum velocity which will reduce the transit time and render negligible the parasitic resistance of the back contact. Therefore, based on the arguments above, higher intrinsic cut-off frequencies should be achieved using this structure. For example, an ideal diode with a 1000 Å epilayer thick is

predicted to have a transit time of 0.3 ps and an intrinsic cut-off frequency of 960 GHz assuming a drift velocity of $3x10^7$ cm/sec [2,3]. The validity of the possibility of achieving terahertz cut-off frequencies is investigated in the next section.

RC Time Constant

To study the properties of a BIN diode, one needs to study the large-signal series resistance of the space charge varactor in detail. The basic action of the BIN diode varactor is the movement of mobile space charge into the epilayer under forward bias conditions and out of it under reverse bias conditions. As discussed in references 1 and 4, under high field conditions, i.e., when the electron travels most of the cycle with their saturation velocity, v_d, the series resistance from the epilayer can be calculated as follows:

$$R_{epi} = V_s/(2i) = d^2_{epi}/(2\varepsilon_s v_d A)$$

The losses in the bulk are described by the spreading resistance given by

$$R_{bulk} = \rho_B(t/A + s/(lt))$$

where ρ_B is the resistivity of the bulk, t is the thickness of the back contact layer, s is the spacing between two diodes, and l is the length of the active device.

Combining these two losses, the series resistance becomes

$$R_s = R_{epi} + R_{bulk}$$
$$= d^2_{epi}/(2\varepsilon_s v_d A) + \rho_B(s/(lt))$$

The capacitance of the epilayer, on the other hand, is given by

$$C_{epi} = \varepsilon_s A/d_{epi}$$

This results in an RC time constant expressed as

$$R_{max}C_{min} = R_s C_{epi} = \varepsilon_s A(d^2_{epi}/(2\varepsilon_s v_d A) + \rho_B(s/(lt)))/d_{epi}$$
$$= (d_{epi}/(2v_d) + \rho_B \varepsilon_s As/(d_{epi}lt))$$

The dependence of the RC time constant on the device area can be neglected when the back contact layer thickness is large and/or doping is high enough. In this case, one has

$$R_{max}C_{min} = R_{epi}C_{epi} = d_{epi}/(2v_d)$$

The $R_{max}C_{min}$ time constant is then mainly dependent upon the epilayer thickness and saturation drift velocity. If we assume that quasi-static approximation is valid here, then the upper limit on the maximum operation frequency for the BIN diode is roughly the inverse of the RC time constant or $2v_d/d_{epi}$ (a more exact value would be $v_d/(\pi d_{epi})$). It is then clear that the maximum operating frequency of a BIN diode is strongly dependent on the epilayer thickness and saturation drift velocity. It should be pointed out that the device geometry can improve the upper limit of the maximum operating frequency only when the resistivity of the back contact layer is large and/or the thickness of this layer is small.

Due to overshoot or ballistic motion, drift velocity values much higher than those corresponding to the final steady-state conditions can possibly be achieved in semiconductors. These phenomena, occurring under non-steady state conditions, might be achieved in submicron devices [13,14]. Thus, they can be used to strongly increase the velocity of the carriers with the objective to further reduce their transit time along the active region. Based on this type of study, one can argue that the average drift velocity in the thin epilayer of the BIN diode can be much higher than the steady-state saturation velocity. This possibility is carefully investigated below.

The average transient velocity versus distance for different values of electron energy was calculated by Iafrate et. al. using Monte Carlo techniques [13,14]. The calculation makes use of the assumption that the applied electric field is constant in time, and is assumed to be turned on instantaneously [13,14]. These results were used in a feasibility study on the BIN diode frequency tripler carried out by Lieneweg et. al. [2,3]. However, this situation is not expected to occur in a real device structure. Additional numerical results obtained by using a configuration where the electric field increases proportionally to time have also been reported [14]. For this case, which may roughly simulate the electric field applied to the carriers when travelling through the active region of a common

submicron device, the average velocity remains lower than that obtained by using a simple time step for the whole region considered.

The transit velocities achievable in gallium arsenide can be quite large, however, achievement of such high velocities does not only depend upon the injection energy and the transit distance, but also is highly sensitive to the electric field [13,14]. The average drift velocity distributions for different external electric field strengths have also been calculated by Iafrate et. al. using Monte Carlo techniques. This study shows the dramatic decrease of the average drift velocity as the external electric field strength increases. The physical explanation for this velocity versus distance behavior is simple. Initially, the electrons assume the small effective mass of the central Γ valley, whereupon they are accelerated by the electric field in the forward direction. For modest injection energies and electric fields, electrons suffer little intervalley scattering. However, for injection energies approaching the L and X minima and strong electric fields, the electrons are promoted to the high effective-mass satellite X and L valleys, and the strong intervalley scattering reduces the drift velocity of carriers after a relatively short transient distance.

With suitable electric field temporal dependences, it seems possible, by using the overshoot phenomenon, to strongly increase the carrier velocity during very short times, which in the spatial scale corresponds to submicron distances. Ruch first demonstrated the velocity overshoot effect by calculating the transient response of carriers in a temporal electric field step function by the the Monte Carlo method [15-17]. In order to relate his results more pertinently to device performance, he plotted the result versus distance. The distance was obtained by integrating the ensemble velocity over time. This practice was used in many subsequent works [13,14]. However, it is somewhat misleading because most of these works were simulations of temporal velocity overshoot only but were often used as spatial overshoot.

Pan et. al. [18] clarified the significant difference between the spatial velocity overshoot and the temporal overshoot and presented the simulated spatial velocity

overshoot results for Si semiconductors. The physical condition for the temporal velocity overshoot should be a large homogeneous sample with a uniform electric field suddenly turned on. Any transient diffusional effect will be cancelled in the current because of the homogeneity of the situation. On the other hand, if a spatial step function of electric field is applied to a sample, the carrier's average velocity may show an overshoot over a short distance near the step of the electric field. In general, this spatial velocity overshoot should not be obtained from the temporal velocity overshoot by the simplified transformation. This is because transient diffusional effect should play an important role in this case. Differences between the temporal and spatial overshoot are found by Pan et. al. to be of a factor as large as three to five for Si [18].

No direct determination of the drift velocity can be achieved since the current depends not only on the carrier velocity, but also on the number of carriers injected into the active region. In addition, the presence of parasitic elements, such as series resistances, can introduce spurious effects which are difficult to fully and properly account for. In conclusion, the average drift velocity for GaAs semiconductor (3×10^7 cm/sec) used in the proposed work on the BIN diode tripler [2,3] is overly optimistic. No simulation work has been published for the spatial velocity overshoot in GaAs semiconductors. Based upon the above studies and the high electric field distribution of the GaAs BIN diode structure as will be discussed later in this paper, the average drift velocity in the GaAs BIN diode should be very close to the saturation drift velocity of the gallium arsenide material system, i.e., 6×10^6 cm/sec. This value will be used below to calculate the intrinsic cut-off frequency and series resistance of BIN diode frequency triplers. The calculated series resistance of $\approx 200\ \Omega$ has been shown to be more in agreement with the high-frequency impedance measurement results of this study.

Back-to-Back Diode Configuration

1. Capacitance-Voltage Characteristic

Due to the blocking barrier of the BIN structure, two diodes should be able to operate back-to-back generating a symmetrical capacitance-voltage curve. The sharp spike in the capacitance-voltage curve eliminates even harmonics and thus favors tripling operation [2,3]. In addition, the height and width of this capacitance-voltage curve can, in principle, be adjusted by doping control alone [2,3]. This arrangement needs no external ohmic contact, thereby making a highly efficient frequency tripler in which the efficiency does not degrade with high fundamental power. Only one metal layer is required which greatly simplifies the fabrication task [10,11]. In addition, no idler is needed in the circuit design, again, making the circuit construction much simpler [10,11]. This back-to-back configuration is considered to be a very important feature of the BIN structure. In this section, the back-to-back diode configuration will be studied and carefully discussed to illustrate the possibility of employing this concept in odd-harmonic frequency multiplication.

The C-V characteristics measured from both a single diode and from two-back-to-back connected GaAs BIN diodes are shown in Fig. 2. It can be seen from these results that the capacitance from two back-to-back connected (in series) BIN diodes can not be scaled directly from that of a single diode. Specifically, C_{max} of two back-to-back connected diodes is approximately half of that of a single diode as what one might expect. However, C_{min} of a single diode is only slightly higher than that of two back-to-back connected diodes. This is due to the symmetrical nature of the back-to-back BIN structure; when one diode is strongly reversed biased, the other diode will be strongly forward biased. Therefore, when one BIN diode is in the depletion mode, the other BIN diode is in the accumulation mode. In other words, when one diode has a capacitance value of C_{min}, the other diode has a capacitance of C_{max}. The total minimum capacitance of two back-to-back connected BIN diodes is, therefore, much higher than half of the minimum

capacitance of one single diode. The back-to-back diode configuration results in a much smaller ratio of C_{max}/C_{min} and smoother (i.e., lower gradient slope) C-V characteristic which, therefore, reduces the nonlinearity which is utilized to generate harmonics (see Fig. 2).

This can also be illustrated assuming a capacitance ratio, k ($k = C_{max}/C_{min}$), the total capacitance of a back-to-back BIN diode system when one BIN diode is under a large forward bias and the other BIN diode under a large reverse bias (i.e., when one diode is strongly forward biased, the other diode will be strongly reverse biased) is $kC_{min}/(k+1)$ as shown below:

$$C_{bb} = 1/(1/C_{max}+1/C_{min}) = 1/(1/(kC_{min})+1/C_{min}) = kC_{min}/(k+1) \approx C_{min}$$

where C_{bb} is the equivalent capacitance of two back-to-back (series) connected BIN diodes. This value is very close to C_{min} of one single diode, especially when the capacitance ratio, k, is large. Therefore, the GaAs BIN structure which has a capacitance ratio close to 4.5 in a single diode configuration, however, has a capacitance ratio of ≈ 2.3 for the back-to-back diode arrangement (as can be seen in Fig. 2).

2. Cut-Off Frequency

In the back-to-back diode configuration, when one diode is under forward bias, the other diode is always reverse biased, one may, therefore, question which series resistance should be used - the series resistance of one single diode or of two back-to-back diodes. It can be seen from Table. I that the operation of one single diode is very different from that of two back-to-back connected diodes. For example, when a single diode is strongly reverse biased, the epilayer is completely depleted, the capacitance is close to C_{min}, and the series resistance is close to zero. However, applying the same large reverse bias to the BIN diode in the back-to-back configuration will result in a much different situation. While the epilayer of one diode is completely depleted and provides the minimum capacitance, C_{min}, the other diode shows a series resistance of R_s due to the undepleted epilayer. The

back-to-back diode operation increases the effective series resistance one should use for calculating the cut-off frequency of two back-to-back connected diodes. To determine this effective series resistance, a series of high frequency impedance measurements were performed on one single diode, as well as on two back-to-back diodes. It should be mentioned that the high frequency impedance measurements were performed on approximately 25 devices per wafer. The capacitance of the diode can be deduced from the reactance values obtained from the high-frequency impedance measurements. The ratio of the RC time constant of a single diode to that of two back-to-back connected diodes can then be used to determine the effective series resistance for the back-to-back BIN diode configuration. The value of the effective series resistance is determined to be between $1.5R_S$ and $2R_S$.

Device Simulation Results

In this work, a computer program was developed to solve exactly the Poisson Equation in multilayer semiconductor devices having a step-wise doping profile [11]. The program developed in this paper allows for detailed simulation of the device and provides crucial physical insight into the key performance parameters. In this model, Poisson's equation is solved exactly by a set of coupled analytical expressions which accurately describe each region of the BIN diode. Band and carrier continuity between layers is included and properly accounted for. The final expressions derived are transcendental and require carefully structured algorithms to avoid inaccurate and unrealistic convergent difficulties. This method does not require large computer memory arrays and lengthy computer time as numerically intensive programs such as PISCES [11].

Using the device simulation model developed, the electric field of the BIN diode structure is studied in detail. The original structure proposed for the BIN diode tripler [2,3] has an aluminum metal gate in intimate contact with a layered GaAs structure consisting of a 300 Å thick undoped GaAs, a 100 Å thick $2x10^{18}$ cm^{-3} heavily doped n^+ layer, another

1500 Å thick undoped layer, and a thick heavily doped n^+ region grown on top of a semi-insulating GaAs substrate. The electric field distributions of this structure under different bias conditions are shown in Fig. 3. As can be seen from this result, the electric fields in both the barrier and epitaxial layers are fairly high. It should be pointed out that the high electric field strength in the epilayer results in low average drift velocity as discussed in the above section [13,14]. In addition, the electric field in the barrier region are very close to the breakdown field of GaAs and may actually cause the breakdown of the BIN diode structure. The results of the theoretical simulation model show good agreement with the experimental measurement of the BIN diode as shown in Fig. 2.

Summary

The intrinsic cut-off frequency of the original GaAs BIN diode is close to 50 GHz using the average drift velocity of 6×10^6 cm/sec. This result explains the low device-performance measurement from the GaAs BIN diode-grid frequency tripler arrays. The calculated series resistance also agrees well with the high-frequency impedance measurement results. Due to the large RC time constant and the reduced capacitance-voltage variation of the back-to-back BIN structure, the BIN diode frequency tripler employing a back-to-back configuration is not very efficient for high frequency generation.

References

[1] U. Lieneweg and J. Maserjian, "Harmonic Generation in the Near-Millimeter-Wave Range by Thin MOS Structures," 6th Intl. Conf. and Millimeter Waves, Tech. Dig., P. F-5-6, 1981.

[2] J. Maserjian and U. Lieneweg, "BIN Diode Harmonic Multiplier," A Concept Proposal at JPL/Cal. Tech., 1987.

[3] U. Lieneweg, B. R. Hancock, and J. Maserjian, "Barrier-Intrinsic-N^+ (BIN) Diodes for Near-Millimeter Wave Generation," 12th Intl. Conf. Infrared and Millimeter Waves, Tech. Dig., pp. 6-7, 1987.

[4] D. P. Howson, B. Owen, and G. T. Wright, "The Space-Charge Varactor," Sol. St. Electron. **Vol. 8**, pp. 913-921, 1965.

[5] R. P. Rafuse and D. H. Steinbrecher, " Harmonic Multiplication with Punch-Through Varactors," Intl. Solid-State Circuit Conf., Tech. Dig., pp. 68-69, 1966.

[6] K. Schunemann and B. Schiek, "Optimal Efficiency of Charge-Storage Multipliers II," **A.E.U. 22**, pp. 293-302, 1968.

[7] J. W. Mink, "Quasi-Optical Power Combining of Solid-State Millimeter-Wave Sources," IEEE Trans. Microwave Theory and Tech., **MTT-34**, No. 2, pp. 273-279, 1986.

[8] D. B. Rutledge and S. E. Schwarz, "Planar Multimode Detector Arrays for Infrared and Millimeter-Wave Applications," IEEE J. Quantum Electronics, **QE-17**, P. 407, 1981.

[9] C. F. Jou, W. W. Lam, H. Chen, K. Stolt, N. C. Luhmann, Jr., and D. B. Rutledge, "Millimeter-Wave Monolithic Schottky Diode-Grid Frequency Doubler," IEEE Trans. Microwave Theory and Tech., **MTT-36**, No. 11, pp. 1507-1514, 1988.

[10] R. J. Hwu, C. F. Jou, W. W. Lam, U. Lieneweg, N. C. Luhmann, Jr., and D. B. Rutledge, "Millimeter-Wave Monolithic Diode-Grid Frequency Multipliers," 1988 IEEE MTT-S Digest, pp. 533-536, 1988.

[11] R. J. Hwu, L. P. Sadwick, N. C. Luhmann, Jr., and D. B. Rutledge, "DC and Millimeter- Wave Performance of Watt-Level Barrier-Intrinsic-N^+ Diode-Grid Frequency Multipliers Fabricated on III-V Compound Semiconductors," 1988 IEDM, Tech. Dig., pp. 191-194, 1988.

[12] C. F. Jou, U. Lieneweg, D. Zheng, J. Bean, D. B. Lawson, J. Maserjian, P. Tong, P. Frerking, D. S. Pan, P. Zimmermann, D. B. Rutledge, and N. C. Luhmann, Jr., "Thin MOS Millimeter Wave Frequency Multipliers and Phase Shifters," 9th Intl. Conf. Infrared and Millimeter Waves, Tech. Dig., pp. 256-257, 1984.

[13] L. Reggiani, "Hot Electron Transport in Semiconductors," Springer-Verlag, 1985.

[14] D. K. Ferry, "Gallium Arsenide Technology," 1985.

[15] J. G. Ruch and G. S. Kino, J. Appl. Phys., **Vol. 174**, P. 921, 1968.

[16] J. G. Ruch and W. Fawcett, J. Appl. Phys., **Vol. 41**, No. 9, pp. 3843-3847, 1970.

[17] J. G. Ruch, IEEE Trans. Electron Devices, **ED-19**, No. 5, pp. 652-654, 1972.

[18] R. Y. Chen and D. S. Pan, "Accurate Simulations of Spatial and Temporal Velocity Overshoot in Silicon," to be published, 1990.

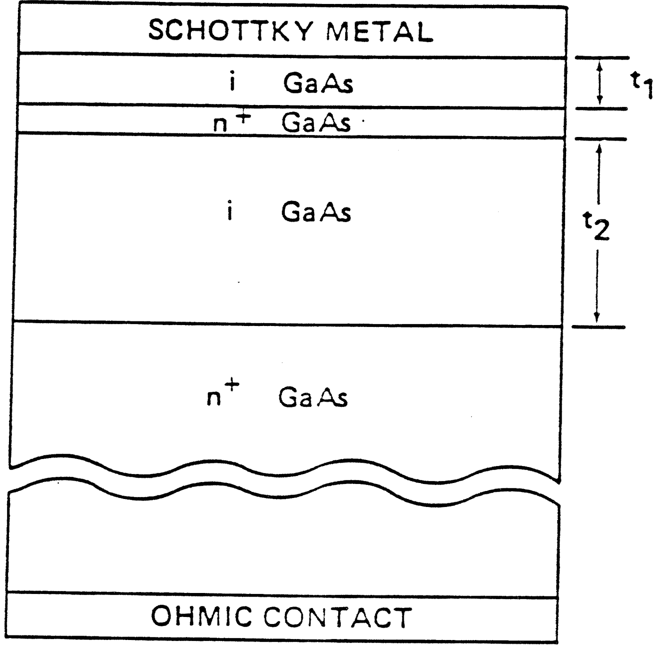

Fig. 1 The GaAs BIN diode structure.

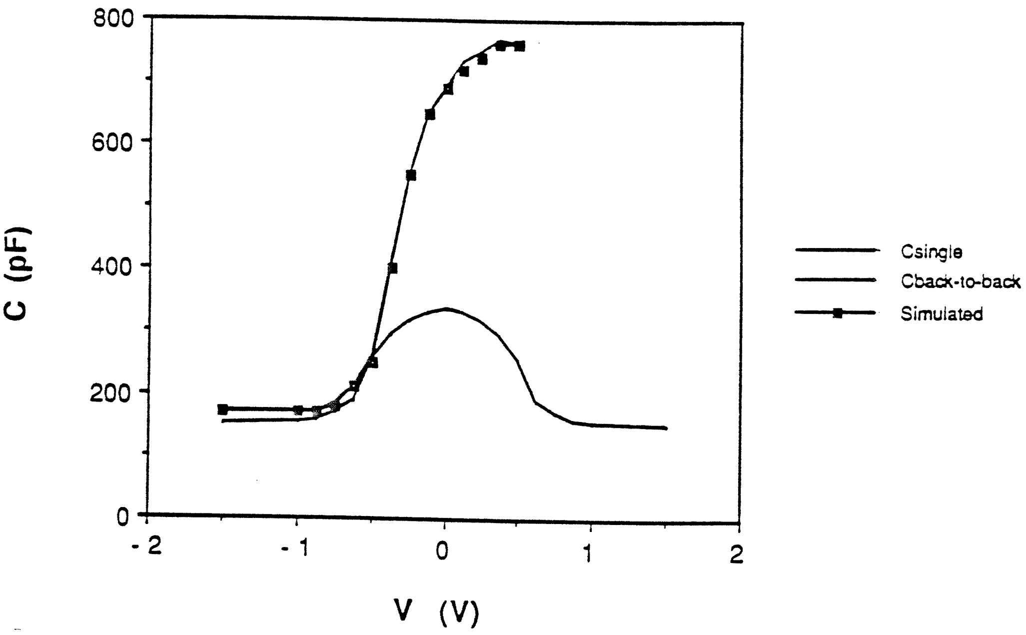

Fig. 2 The C-V characteristics measured from a single and two back-to-back connected GaAs BIN diodes.

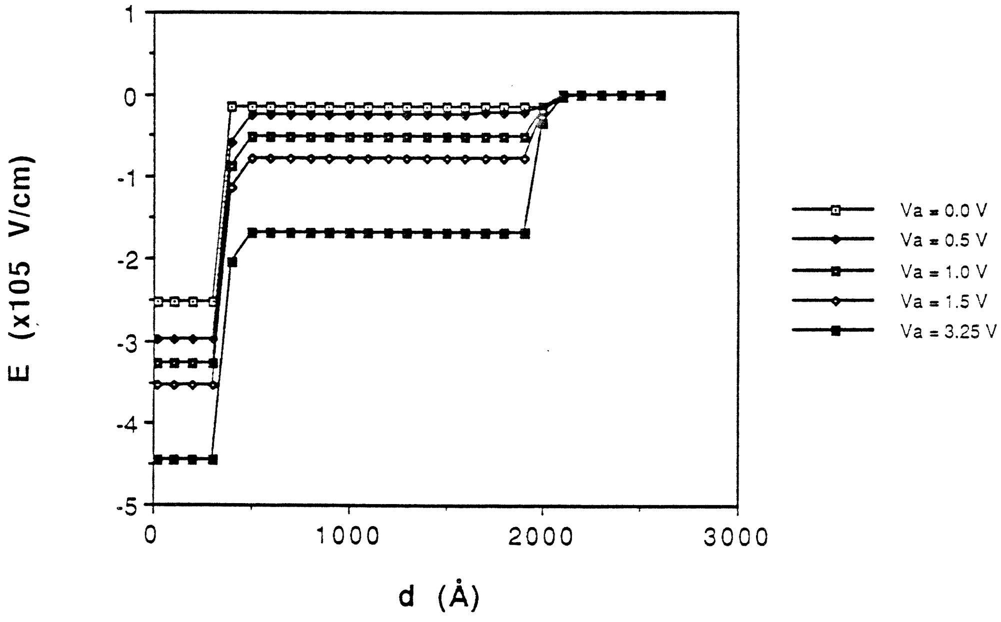

Fig. 3 The electric field distributions of the "original" GaAs BIN diode structure under different bias conditions.

Table 1.

	Large Forward Bias	Large Reverse Bias
Single BIN		
R	R_s	0
C	$C_{max,s}$	$C_{min,s}$
Back-to-Back BIN		
R	R_s	R_s
C	$C_{min,b} \approx C_{min,s}$	$C_{min,b} \approx C_{min,s}$

Design of Planar Varactor Frequency Multiplier Devices with Blocking Barriers *

U. Lieneweg, T. Tolmunen, M. Frerking, and J. Maserjian
Jet Propulsion Laboratory, California Institute of Technology
Pasadena, CA 91109

Abstract

Design principles for optimization of planar frequency triplers with symmetrical $C-V$ curves are presented. Role and limitation of various blocking barriers (oxide, Mott, heterojunction) are discussed. Devices with undoped drift regions (BIN+) have moderate efficiency but a broad range of power operation, whereas devices with doped drift regions (BNN+) have high efficiency in a narrow power window. In particular, an upper power limit of the BNN+ is caused by electron velocity saturation. Implementations in SiO_2/Si and AlAs/GaAs and means for increasing the power of BNN+ structures are considered.

In contrast to conventional varactor diodes with a Schottky barrier, diodes with a Mott or heterojunction barrier (B) allow one to construct devices with a symmetric capacitance-voltage ($C-V$) characteristic of high Cmax/Cmin ratio by connecting two diodes back-to-back. Each diode is constructed, top to bottom, of a Schottky metal contact, the

*This work was performed at the Jet Propulsion Laboratory, California Institute of Technology, with support from the Director's Discretionary Fund and under contract with the Army Research Office.

barrier with a thickness $d_{bar} \approx 10 \ldots 30$ nm, an N-type doping sheet, a drift region $d_{drift} \approx 50 \ldots 150$ nm, and an N^+ back contact. This construction leads naturally to a planar back-to-back configuration with no ohmic contacts. No bias is required as the sheet doping controls the operating point of the diodes. A simple planar process is desirable for construction of highly reliable integrated multiplier structures with high yield for multidiode arrays. Fig. 1 shows the device structure and its equivalent circuit. Thanks to the favorable geometry the parasitic series resistance is minimal and does not degrade due to skin effect. Isolation can be achieved by mesa etching and deposition of SiO_2. An optional etch stop layer allows the removal of the substrate for minimizing the parasitic capacitance and transmission line losses of the leads.

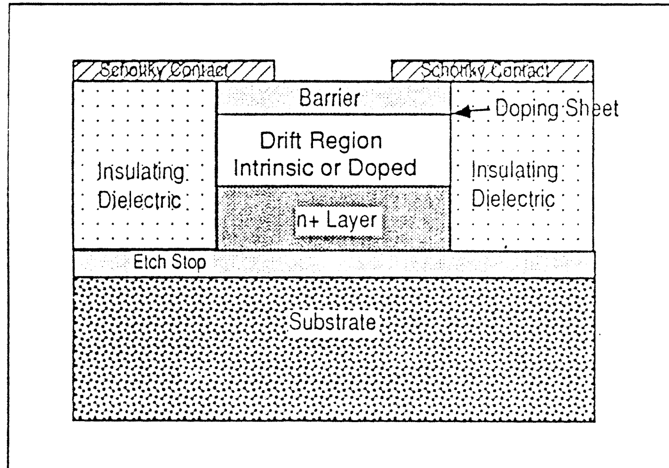

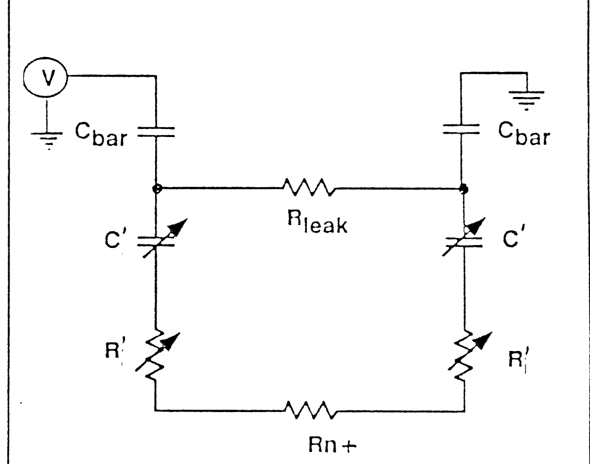

Figure 1: Planar blocking barrier varactor: cross section and equivalent circuit

If the drift region is intrinsic (I), electrons injected from the N^+ back contact carry a space charge limited current with a transit time limited frequency response (BIN+ diode) [1]. The $C - V$ characteristic in this case has a steep transition, $(\mathrm{d}C/\mathrm{d}V)/C = q/kT$, between C_{min} and C_{max} enabling to generate a frequency spectrum of high harmonic content suitable for triplers, quintuplers, etc. at low power levels. The validity of the BIN+ concept was proven earlier with a single SiO_2/Si diode operating as a frequency

doubler in a waveguide mount [2] and performing closely to the predictions of a large signal analysis for a stepfunction $C - V$ [3]. A similar theory for pulse-like $C - V$, as exhibited by back-to-back BIN+ diodes, was developed by the same group [4] but proved to be unrealistic. Therefore we resorted to a simulator [5], shown in Fig. 2, which optimizes the embedding impedances at input and output frequencies for an arbitrary $C(V_C)$ curve, a fixed series resistance R, and a given input power P_{in} in order to find the maximum output power P_{out}.

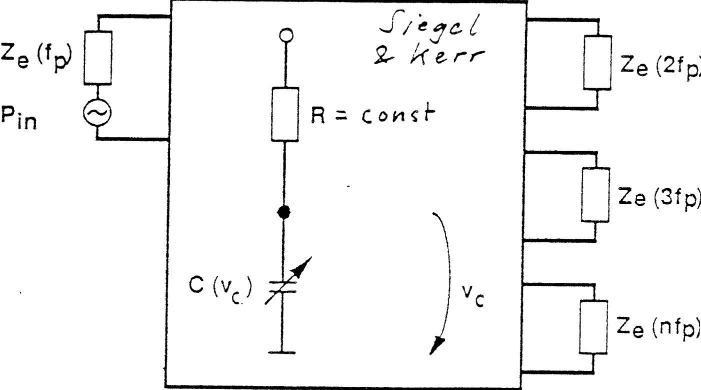

Figure 2: Varactor multiplier signal simulator with embedding impedances Z_e at fundamental f_p and harmonics. For tripler $\Re\{Z_e(nf_p)\} \gg R$ for $n = 2, 4, 5, 6, 7$ was chosen. Simulator maximizes output power by optimizing $Z_e(f_p) = R_1 + jX_1$ and $Z_e(3f_p) = R_3 + jX_3$.

Fig. 3 shows a schematic $C - V$ curve from a back-to-back BIN+ with its characteristic values related to physical diode properties as follows. The maximum capacitance is reached when both diodes are in accumulation, whereas at the minimum capacitance one diode is in accumulation and the other fully depleted, leading to

$$C_{max} = C_{bar}/2 \tag{1}$$

and

$$C_{min} = \frac{C'_{min} C_{bar}/2}{C'_{min} + C_{bar}/2} \tag{2}$$

with $C_{bar} = \epsilon_{bar} A/d_{bar}$ and $C'_{min} = \epsilon_{drift} A/d_{drift}$, where A is the area of each single diode. The halfwidth of the $C-V$ curve is close to $2V_f$, where V_f is called flatband voltage because at that voltage the field at the barrier is zero, marking the transition between accumulation and depletion of the drift region. The flatband voltage is determined from the sheet doping N_{sheet} together with the barrier height at the metal interface, Φ_M, the barrier height at the interface with the drift material, Φ_D, and a small potential step at the border between drift and N^+ region Φ_{N+}(≈ 0.1 V at room temperature) as

$$V_f = qN_{sheet} d_{bar}/\epsilon_{bar} + \Phi_D - \Phi_M + \Phi_{N+}. \tag{3}$$

As the capacitance changes, the series resistance changes,too, as shown in the figure. The maximum,

$$R_{max} = 2R'_{max} + R_{N+}, \tag{4}$$

is the resistance of both drift regions in accumulation plus the parasitic series resistance, whereas the minimum,

$$R_{min} = R'_{max} + R_{N+}, \tag{5}$$

is the resistance of only one accumulated diode plus parasitic because the other diode is fully depleted. As a reasonable average value we have used $R = 1.5R'_{max} + R_{N+}$ in the simulations. For the BIN+ one obtains [6]

$$R'_{max} = d^2_{drift}/2\epsilon_{drift} v_s A, \tag{6}$$

where v_s is the electron saturation velocity.

Fig. 4 shows a simulated result for a tripler to 200 GHz. For a given halfwidth $2V_f$ the efficiency η peaks at a certain input power with the peak shifting to higher powers,

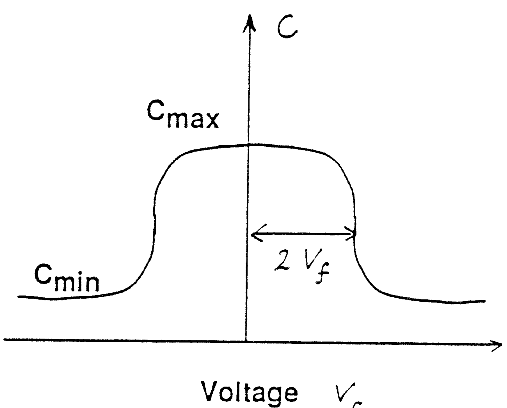

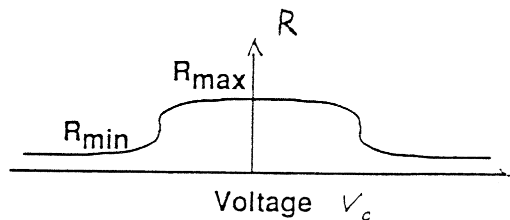

Figure 3: Capacitance and series resistance of back to back BIN+ diodes as function of voltage drop over capacitance. Halfwidth equals twice the flatband voltage of single diode.

broadening, and reaching a saturation value for larger halfwidths. Furthermore, the input power is related to the peak voltage drop over the capacitance, $\hat{V}_C$, by $P_{in} \propto \hat{V}_C^2$. The condition for maximum efficiency, obtained from many simulations, can be described by

$$2V_f = 0.6\frac{C_{min}}{C_{max}}\hat{V}_C, \qquad (7)$$

where $2V_f$ should be much larger than kT/q for a BIN+ structure.

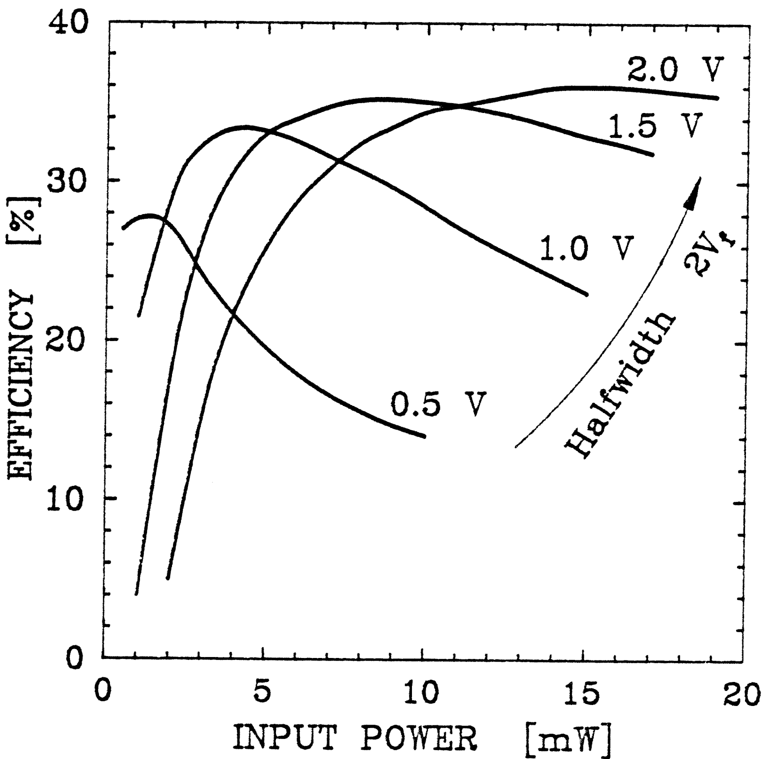

Figure 4: Simulated efficiency for BIN+ tripler to 200 GHz as function of input power with halfwidth of $C - V$ as parameter. $C_{max} = 15$ fF, $C_{min} = 5$ fF, $R = 20\ \Omega$.

The question of what limits $\hat{V}_C$ is investigated in Fig. 5. Here the conduction band edge of a back-to-back BIN+ structure with Mott barriers has been plotted from a d.c. PISCES [7] calculation. The fields are high in the reverse biased and low in the forward biased diode as long as the input frequency is much smaller than the cut-off frequency.

We define now "breakdown" by the following conditions: The forward biased barrier exhibits a leakage current of density, see, e.g., [8],

$$j_{TE} = \frac{4\pi q m_{bar} k^2 T^2}{h^3} \exp[-\frac{q\Phi_B}{kT}], \tag{8}$$

which is caused by thermionic emission (TE) over the barrier with m_{bar} being its effective mass and Φ_B its effective height. The leakage current in the reverse biased barrier is dominated by Fowler-Nordheim (FN) tunneling with a density [8]

$$j_{FN} = \frac{m_0}{m_{bar}} \frac{q^3 E_{bar}^2}{8\pi h \Phi_M} \exp\{-\frac{8\pi\sqrt{2m_{bar}q}\Phi_M^{3/2}}{3hE_{bar}}\}, \tag{9}$$

which, in contrast to the thermionic current, is a strong function of the the field in the reverse biased barrier, $E_{bar} > 0$.

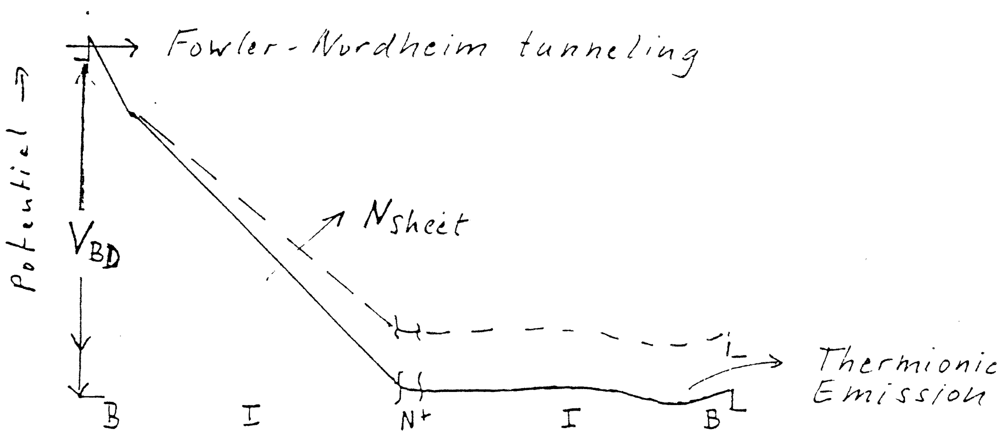

Figure 5: Potential distribution in back-to-back BIN+ at breakdown, voltage V_{BD}, caused by tunneling through reverse biased barrier. Increased sheet doping decreases V_{BD}.

Postulating that the FN current becomes nearly equal to the TE current by equating the exponents of Eqs. (8) and (9) leads to the barrier breakdown field

$$E_{bar,BD} = \frac{8\pi\sqrt{2m_{bar}q\Phi_M}}{3h} \frac{\Phi_M}{\Phi_B} \frac{kT}{q} \tag{10}$$

$$= \frac{1.7\times 10^6}{\mathrm{V}^{1/2}\mathrm{cm}} \sqrt{\frac{m_{bar}}{m_0}\Phi_M} \frac{\Phi_M}{\Phi_B} \text{ at } T = 300 \text{ K} . \tag{11}$$

The above derivation of the breakdown holds not only for (triangular) Mott barriers but also for the trapezoidal heterojunction and oxide barriers as long as these barriers are not so thin that the current tunnels through the full barrier at breakdown,i.e., $\Phi_M - E_{bar,BD}d_{bar} \leq 0$ must be fulfilled.

The breakdown voltage of a single diode is related to the barrier breakdown field by

$$V_{BD,s} \approx E_{bar,BD}(\frac{\epsilon_{bar}}{\epsilon_{drift}} d_{drift}) - \frac{qN_{sheet}}{\epsilon_{drift}} d_{drift} + \Phi_D - \Phi_M. \tag{12}$$

Applying $Q = \int C\mathrm{d}V$ to the single and the back-to-back diodes, the breakdown voltage of the latter becomes

$$V_{BD} \approx \frac{C_{min,s}}{C_{min}}(V_{BD,s} - V_f) + 2V_f \tag{13}$$

with

$$\frac{C_{min,s}}{C_{min}} = \frac{d_{bar}}{d_{bar} + d_{drift}} + 1. \tag{14}$$

Note the decrease of V_{BD} with increased sheet doping as illustrated in the figure.

Table 1 lists the properties of various barriers starting with the simple GaAs Mott barrier, suitable only for low power applications, and progressing to AlGaAs/GaAs with about 50% Al, AlAs/GaAs, and SiO_2/Si.

With these parameters and the maximum allowed voltage drop over the capacitance, max($\hat{V}_C$), set equal to V_{BD}, the results for the AlGaAs/GaAs heterojunction barrier tripler in Table 2 have been obtained. Since already $V_f \approx 1$ V, the effective height of the forward biased heterojunction barrier, Φ_B, was set to Φ_D. The area has been chosen to achieve matchable impedance levels.

If bulk doping N is added to the drift region (BNN+ diode), the current is no longer space charge limited, and the cut-off frequency becomes intrinsically determined

Table 1: Properties of various barriers

Barrier Type	Material	Drift Region		Φ_M[V]	Φ_D[V]	m_{bar}/m_0
Mott	GaAs	GaAs		0.8	0	0.07
Heterojunction	AlGaAs	GaAs		1.2	0.4	0.10
Heterojunction	AlAs	GaAs	Γ:	2.0	1.0	0.15
			X:	1.4	0.6	0.19
Oxide	SiO_2	Si		3.2...4.1	3.2	1.0

Table 2: Simulated Performance of a AlGaAs/GaAs BIN+ Tripler to 200 GHz

Parameter	Value
d_{bar} [nm]	20
d_{drift} [nm]	80
N_{sheet} [cm^{-2}]	5.5×10^{12}
A [μm^2]	6
C_{max} [fF]	15
C_{min} [fF]	5
R [Ω]	20
$2V_f$ [V]	2.0
$\hat{V}_C$ [V]	11.5
P_{in} [mW]	19
η [%]	35.5
P_{out} [mW]	6.7
R_1 [Ω]	48
X_1 [Ω]	300
R_3 [Ω]	35
X_3 [Ω]	50

by dielectric relaxation. The transition from the first mechanism to the second occurs when the Debye length $L_{Debye} = \sqrt{2\epsilon_{drift}kT/q^2N}$ becomes less than d_{drift} [9]. As a side effect, the transition from high to low capacitance becomes more gradual. This should have little effect on tripling for high enough powers as long as the diodes "punch through", i.e., the maximum depletion width reaches d_{drift}. If punch through is reached exactly when the barrier breaks down, then

$$V_{BD,s} \approx E_{bar}(\frac{\epsilon_{bar}}{\epsilon_{drift}}\frac{d_{drift}}{2} + d_{bar}) - \frac{qN_{sheet}}{\epsilon_{drift}}\frac{d_{drift}}{2} + \Phi_D - \Phi_M, \quad (15)$$

i.e., a reduction of almost a factor 2 in comparison to the BIN+, if N_{sheet} is not reduced.

Table 3 summarizes differences between BIN+ and BNN+ structures with the intrinsic cut-off frequency defined as

$$\omega_{ci} = 1/R'_{max}C'_{min}. \quad (16)$$

Table 4 gives numerical values for the intrinsic cut-off showing the superiority of GaAs BNN+ at low fields. Unfortunately the relaxation time degrades when the field in the drift region exceeds the critical field. The formulas given in Table 3 are based on a simple monotonous model for the field dependent mobility

$$\mu(E) = \frac{\mu}{1 + E_{drift}/E_{crit}} \quad (17)$$

with $E_{crit} = v_s/\mu$. Estimates of the value of the average electron velocity in 100 nm GaAs layers range from 0.6×10^7 cm/s for space averaging [10] to 3×10^7 cm/s for time averaging[11]. A simulation for transit time devices [12] gave values $1 \ldots 2 \times 10^7$ cm/s.

In our large signal simulations it was easier to monitor the total current rather than the field in the drift region. Since the current reaches 1/2 of its saturation value at the critical field , cf. $\mu(E)$, this should be the maximum current allowed to flow in the diode

Table 3: Comparison of BIN+ and BNN+ diodes

BIN+ ($L_{Debye} \gg d_{drift}$)	BNN+ ($L_{Debye} \ll d_{drift}$)
Steep transition $(dC/dV)/C = q/kT$	Gradual transition $C \propto 1/\sqrt{V}$
High harmonic content at low power	3rd harmonic little affected at high power
Space charge $n(x, V)$ injected into drift region from N+	$n = N$ in undepleted drift region $n = 0$ in depleted part
$R'_{max} = d^2_{drift}/2\epsilon_{drift}v_s A$	$R'_{max} = d_{drift}(1 + E_{drift}/E_{crit})/qN\mu A$
Transit time limited response $\omega_{ci} = 2v_s/d_{drift}$ for $E_{drift} > E_{crit} = v_s/\mu$	Relaxation time limited response $\omega_{ci} = 1/\epsilon\rho(1 + E_{drift}/E_{crit})$ with $1/\rho = qN\mu$

Table 4: Calculated intrinsic cut-off frequency for $d_{drift} = 100$ nm and $N = 10^{17}/\text{cm}^3$

	ϵ/ϵ_0	$\mu(N)$ [cm²/Vs]	v_s [cm/s]	$E_{crit}(N)$ [kV/cm]	f_{ci}(BIN+) [GHz]	f_{ci}(BNN+) [THz]
Si	12	700	1×10^7	15	300	1.5
GaAs	13	4500	$1 \ldots 2 \times 10^7$	$2 \ldots 4$	$300 \ldots 600$	8.6

without serious degradation in the frequency response. Fig. 6 shows results of a back-to-back AlGaAs/GaAs BNN+ tripler with $N = 1 \times 10^{17}$ cm^{-3}, $d_{bar} = 20$ nm, $d_{drift} = 100$ nm, $N_{sheet} = 4 \times 10^{12}$ cm^{-2}, and $A = 13$ μm^2. The maximum current is calculated as

$$I_{sat}/2 = qNv_sA/2 = 20 \text{ mA}. \tag{18}$$

This restricts the input and output powers to $P_{in} < 2$ mW and $P_{out} < 0.8$ mW, which is clearly below the optimum. Increasing the doping to 2.5×10^{17} cm^{-3} would increase the maximum current to 50 mA and input and output power to about 10 mW and 5.5 mW, respectively, if we use the curves in Fig. 6 for scaling. Qualitatively, the degradation of the efficiency due to the smear-out of the $C - V$ should be offset by the higher cut-off frequency due to the reduction in the intrinsic part of the series resistance. A still higher doping would cause the peak voltage exceed the breakdown limit, cf. Table 2.

As a consequence, the output power of the BNN+ is not higher than that of the BIN+ although the efficiency is. The power levels ($\propto A$) could be increased by increasing the area A if lower impedance levels ($\propto 1/A$) could be matched. Another approach would be to replace each BNN+ diode by a stack of several back-to-back BNN+'s in series in order to bring the impedance up again. Actually, no metal or N+ layers would be necessary between barriers in each stack. The device approaches then the configuration of a stack of single barrier varactors [13] while preserving the planarity with Schottky contacts at the surface barriers.

We are presently implementing an AlAs/GaAs BNN+ tripler to 200 GHz with a target of 5 mW output power in a waveguide configuration with flip-mounting of a thinned chip to a quartz substrate, which carries the filter and coupling structures. We are also collaborating with Prof. N. C. Luhman and his students at UCLA on a quasioptically coupled tripler array with an integrated antenna structure using the AlAs/GaAs system. Our analysis shows, however, that the SiO_2/Si BIN+ system should be revisited because

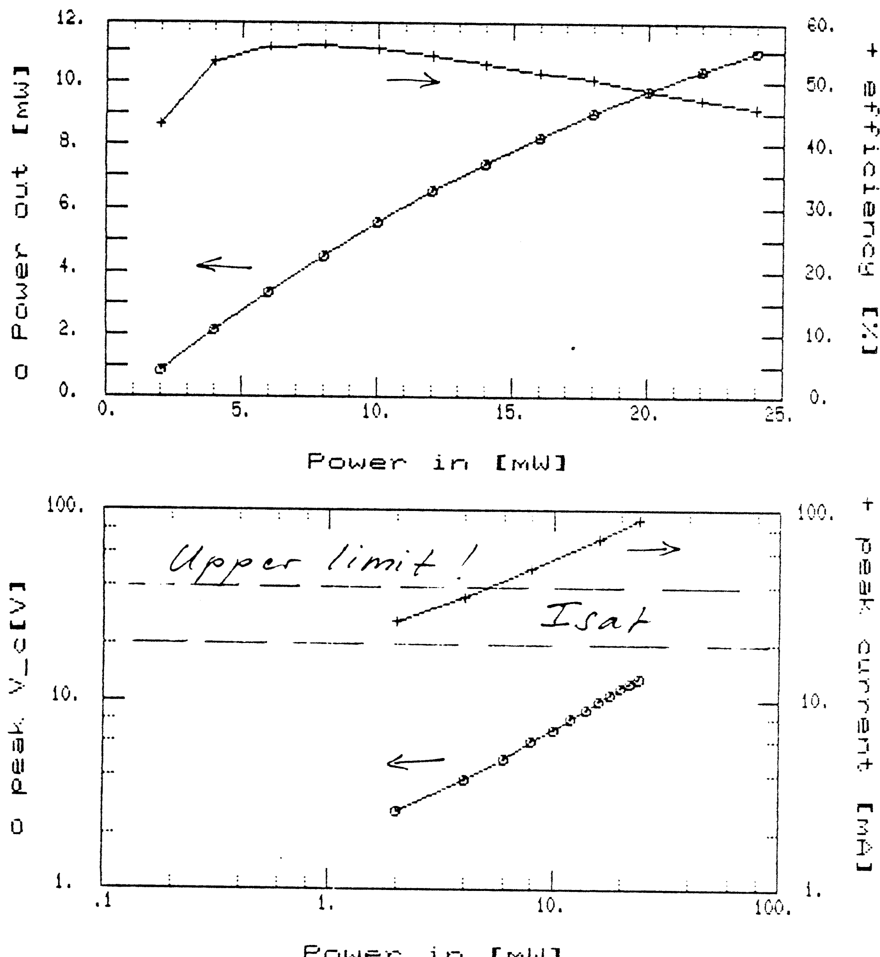

Figure 6: Simulated performance of BNN+ tripler. $C_{max} = 30$ fF, $C_{min} = 11$ fF, $R = 5\ \Omega$

of the theoretically superior breakdown resistance of the thin, grown oxide with no loss in saturation current at high fields in comparison to GaAs. Earlier experienced low yields due to oxide pinholes should be overcome due to improved cleanroom control.

ACKNOWLEDGEMENT

The heterojunction devices are being fabricated in the Microdevices Laboratory of the Center for Space Microelectronics Technology at JPL. We thank B. Hancock, K. Delgadillo, and J. Rosenberg for their efforts.

REFERENCES

1. U. Lieneweg and J. Maserjian, 6th Intern. Conf. IR & MM Waves, Miami, 1981
2. C. Jou, Ph.D. Thesis, Electr.Sc., UCLA (1987)
3. K. Schunemann and B. Schiek, A. E. U. (German) 22, 293 (1968)
4. B. Schiek and J. Marquard, A. E. U. (German) 24, 237 (1970)
5. P. H. Siegel, A. R. Kerr, and W. Hwang, NASA Technical Paper 2287 (1984)
6. D. P. Howson, B. Owen, and G. T. Wright, Solid St. Electron. 8, 913 (1965)
7. M. R. Pinto, C. S. Rafferty, H. R. Yeager, and R. W. Dutton, PISCES IIB, Stanford Electronics Laboratory (1985)
8. A. van der Ziel, Solid State Physical Electronics, 3rd ed., Englewood Cliffs (1976)
9. U. Lieneweg and J. C. Bean, Solid St. Electron. 27, 867 (1984)
10. D. S. Pan, UCLA, private communication
11. G. J. Iafrate, in Gallium Arsenide Technology (D. K. Ferry, Ed.), Indianapolis (1985)
12. R. O. Grondin, P. A. Blakey, and J. R. East, IEEE Trans. ED-31, 21 (1984)
13. cf. papers presented by H. X. L. King and E. Kollberg at this symposium

MONOLITHIC METAL-INSULATOR-SEMICONDUCTOR (MIS) VARACTOR FREQUENCY MULTIPLIERS IN THE MILLIMETER AND SUBMILLIMETER WAVE REGION

R. J. Hwu and L. P. Sadwick

Department of Electrical Engineering

G. B. Stringfellow

Department of Material Science and Engineering

The University of Utah, Salt Lake City, Utah 84112

Abstract

Unintentionally doped layers of AlGaInP with energy gaps of approximately 2.0 eV were grown lattice matched to GaAs. Metal-insulator-semiconductor (MIS) capacitors were made with the AlGaInP layer for the insulator on n-type GaAs. The accumulation mode was successfully demonstrated. This MIS varactor structure can be grown using MOCVD technique and planar diode array can be easily achieved.

Introduction

We have investigated the electrical properties of various $(Al_xGa_{1-x})_yIn_{1-y}P$/ GaAs epitaxial structures. In particular, capacitance versus voltage (C-V) and current versus voltage (I-V) were used to ascertain the electrical behavior of the structures and the metal contacts to these structures. This work continues in the direction established by Casey et. al. [1] on the properties of AlGaInP/GaAs MIS structures. As can be seen from the raw and analyzed C-V data shown in Figs. 1 through 3, epilayers of $(Al_xGa_{1-x})_yIn_yP$ with x=0 (i.e. GaInP, which will be referred to as sample #1) grown on N^+ GaAs form virtually perfect Schottky diodes with highly uniform parametric characteristics. The addition of Al to form AlGaInP produces a highly resistive (approximately 10^{12} to 10^{13} Ohm-cm) epitaxial layer. AlGaInP epilayers of identical thickness (1 μm) to that of sample #1 grown

on N^+ GaAs displayed a constant capacitance over the bias range of +/- 30 volts, and a resistivity of approximately 10^{13} Ohm-cm, indicative of a dielectric insulator.

C-V and I-V Characteristics

In this work, a multitude of samples were investigated. Schottky contacts to AlGaInP-containing samples W375 and W407 represent the general trend found for conventional metal Schottky contacts to GaAs-based (i.e GaAs and AlGaAs) semiconductors. Sample W375 consisted of a 0.6 μm AlGaInP layer with a multiple GaInP/AlGaInP quantum well on top of a 1 μm GaAs low-doped layer grown on a highly conductive N^+ GaAs substrate. Sample W407 consisted of a 0.1 μm AlGaInP layer, a 84 Å GaInP layer, and a 0.6 μm AlGaInP layer on top of a 1 μm GaAs low-doped layer grown on a highly conductive N^+ substrate. Large area Ohmic contacts were made to the back of the N^+ GaAs substrate by sintering AuGe for 1 minute at approximately 430 ^oC. Schottky contacts to the AlGaInP epilayers were made using the conventional tri-level TiPtAu metalization scheme. Fig. 4 shows the C-V curve of a W375 Schottky contact dot (area 1.05×10^{-3} cm^2). There is considerable hysteresis between the forward and reverse direction C-V curves. This hysteresis was seen in all Schottky contact samples as further evidenced by the C-V curve (Fig. 5) of a W407 Schottky contact dot (area 1.05×10^{-3} cm^2). This is a general feature observed for all the Schottky contacts to AlGaInP which were studied. The large shift in flatband voltage of the C-V curve of sample W407 compared to that of W375 is due, in part, to the thin GaInP layer inserted in the AlGaInP epilayer.

The I-V characteristics of these samples have also been studied. Depending on the exact structure of the AlGaInP/GaInP epitaxial layers, current behavior ranging from Frenkel-Poole emission to a modified Schottky emission/conduction process were experimentally observed for the AlGaInP-containing Schottky contact samples. A 1 μm,

unintentionally doped n-type GaAs layer was grown on the substrate and then the undoped AlGaInP layer was grown. The breakdown voltage of this structure is close to 35 V.

High-Frequency Performance

Since a very thin AlGaInP layer can be grown by MOCVD technique. The epilayer of the AlGaInP/GaAs MIS varactor can be made thin enough to reduce the transit time for electrons to travel through this layer, therefore, the cut-off frequency in the submillimeter wavelength can be easily achieved. The high breakdown voltage of the AlGaInP/GaAs MIS varactor structure also provides the capability of high power operation. Using the high resistivity AlGaInP layer for the insulator, different MIS varactor structures are designed as efficient millimeter-wave frequency multipliers. These MIS varactor structures contain either a 100 Å or 200 Å thickness of AlGaInP insulator layer. The predicted cut-off frequencies of these different MIS varactor structures as functions of the epilayer thickness are shown in Fig. 6. The predicted high-frequency performances of two different MIS varactor frequency doublers are shown in Fig. 7. The structures of these two different MIS varactor frequency doublers can also be seen in Fig. 7. More studies are needed to fully develop and utilize the novel AlGaInP/GaAs MIS diode. However, planar diode-grid array of the MIS varactor on the III-V compound semiconductors can be easily achieved. Using the monolithic integrated circuit technique, thousands of MIS varactors will be fabricated on a wafer to make frequency multiplying surface [2].

References

[1] H.C. Casey, Jr., J.S. McCalmont, H. Pandharpurkar, T.Y. Wang, and G.B. Stringfellow, "Current-voltage and Capacitance-voltage Behavior of High Resistivity AlGaInP on GaAs", Applied Physics Letters, Vol. 54, No. 7, p. 650, 1989.

[2] R. J. Hwu, L. P. Sadwick, N. C. Luhmann, Jr., and D. B. Rutledge, "DC and Millimeter Wave Performance of Watt-Level Barrier-Intrinsic-N^+ Diode Grid Frequency

Multipliers Fabricated on III-V Compound Semiconductors," 1988 IEDM, Tech. Dig., pp. 191-194, 1988.

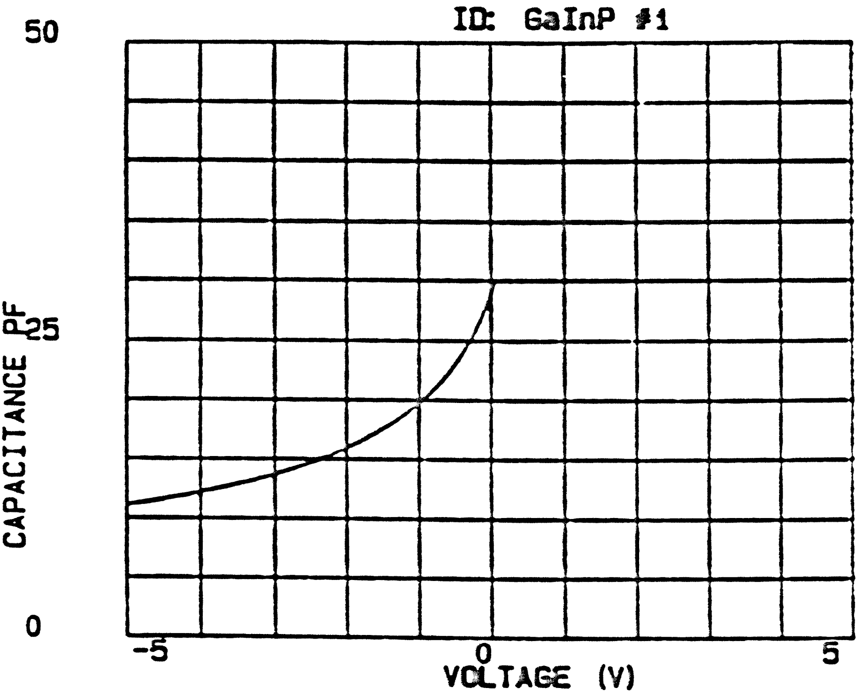

Fig. 1 C-V curve of GaInP sample.

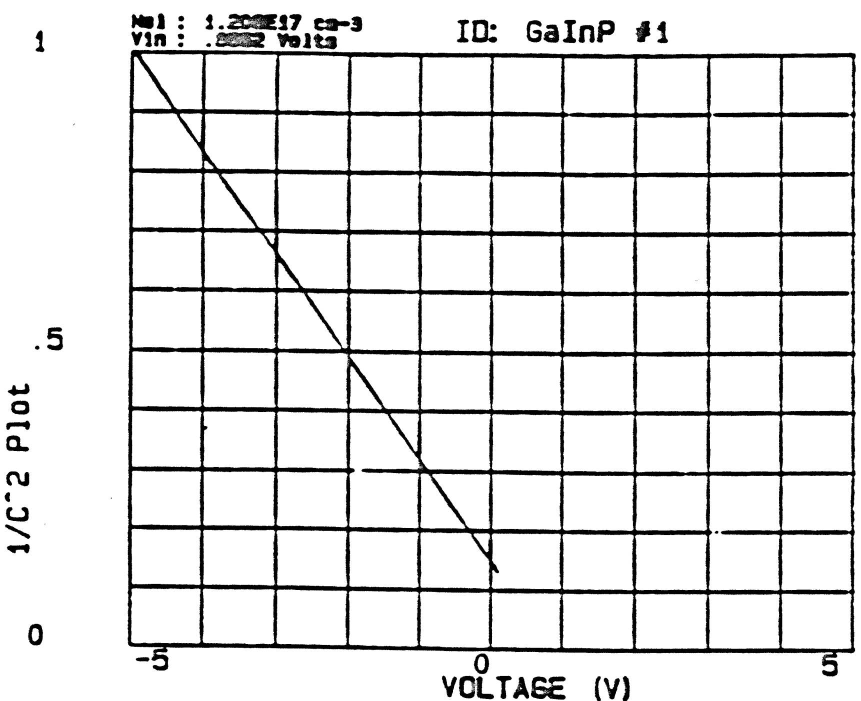

Fig.2 $1/C^2$ versus V curve of GaInP sample.

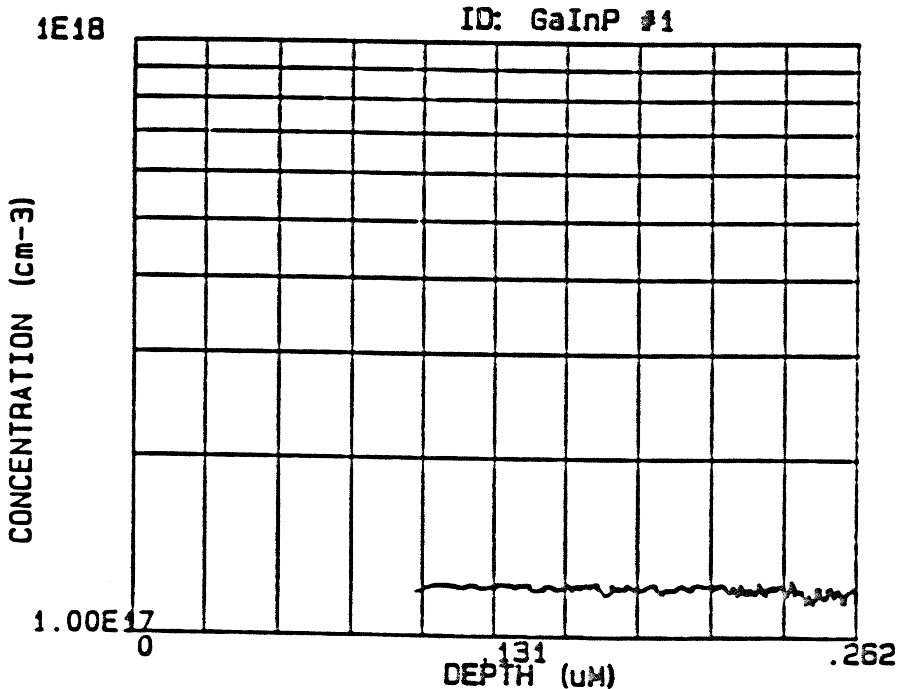

Fig. 3 Doping profile of GaInP sample.

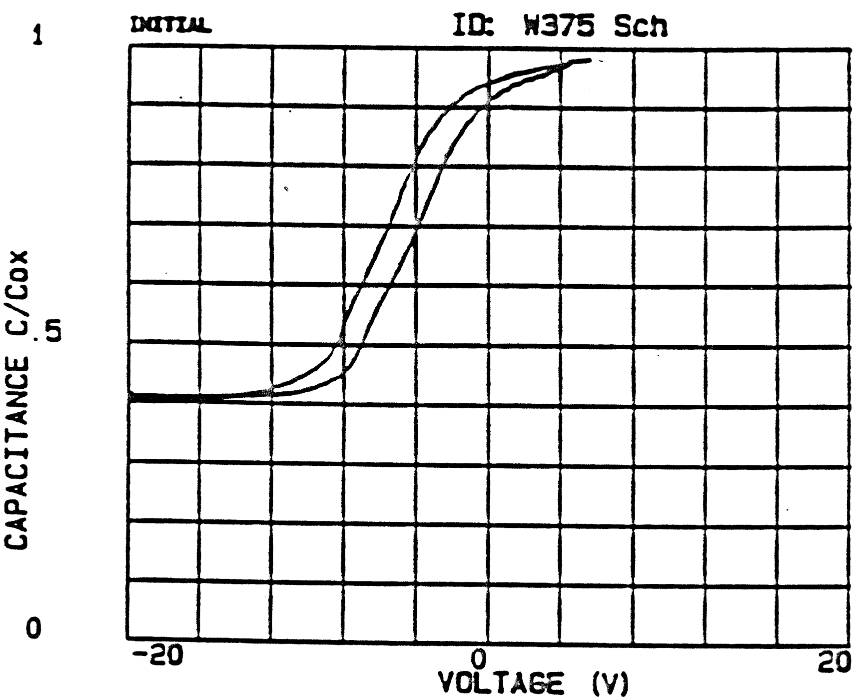

Fig.4 C-V curve of AlGaInP-containing sample W375.

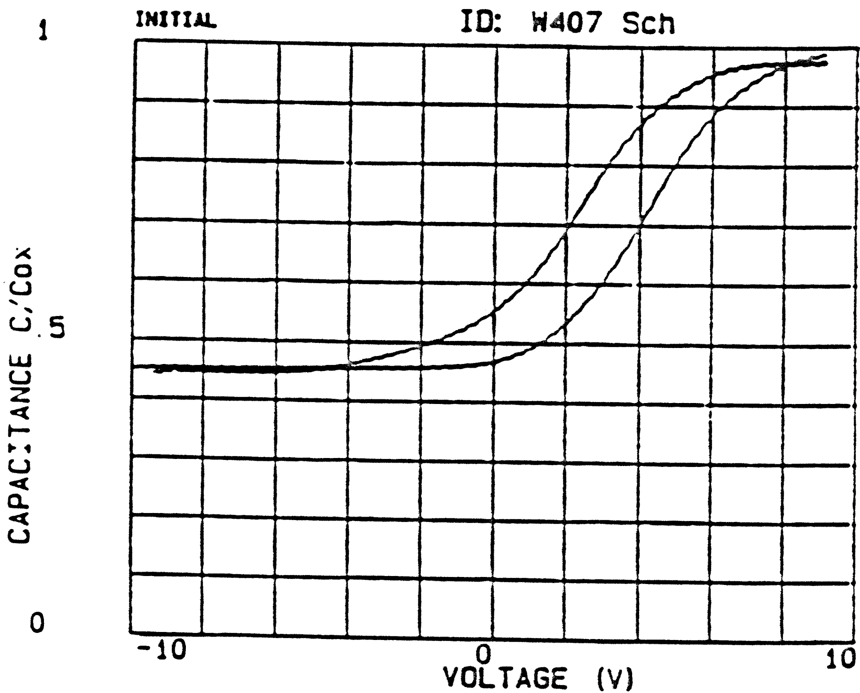

Fig. 5 Representative C-V curve of AlGaInP-containing sample W407.

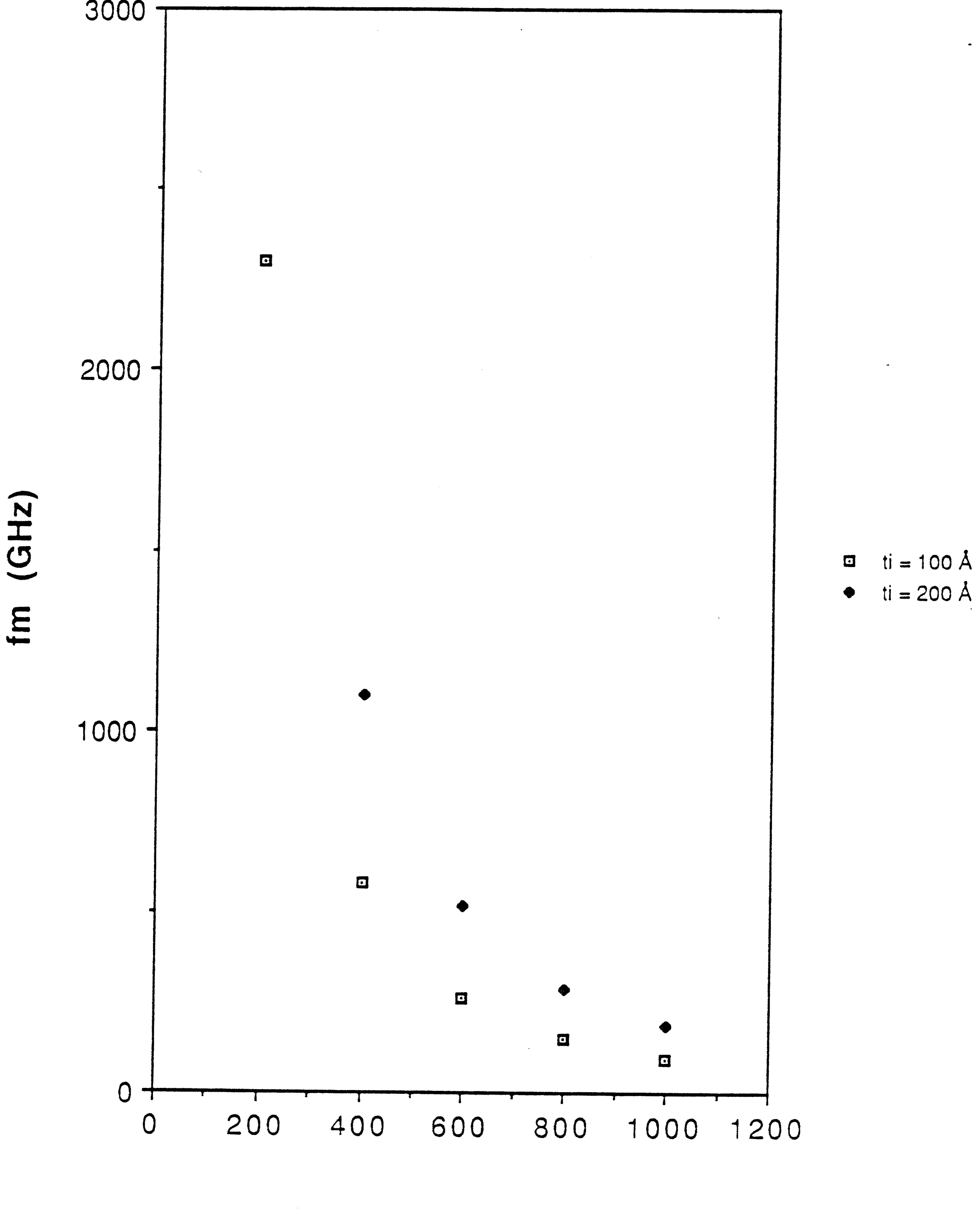

Fig. 6 Calculated cut-off frequency versus epilayer thickness for the MIS varactor structures contain either a 100 Å or a 200 Å thick of AlGaInP insulator layer.

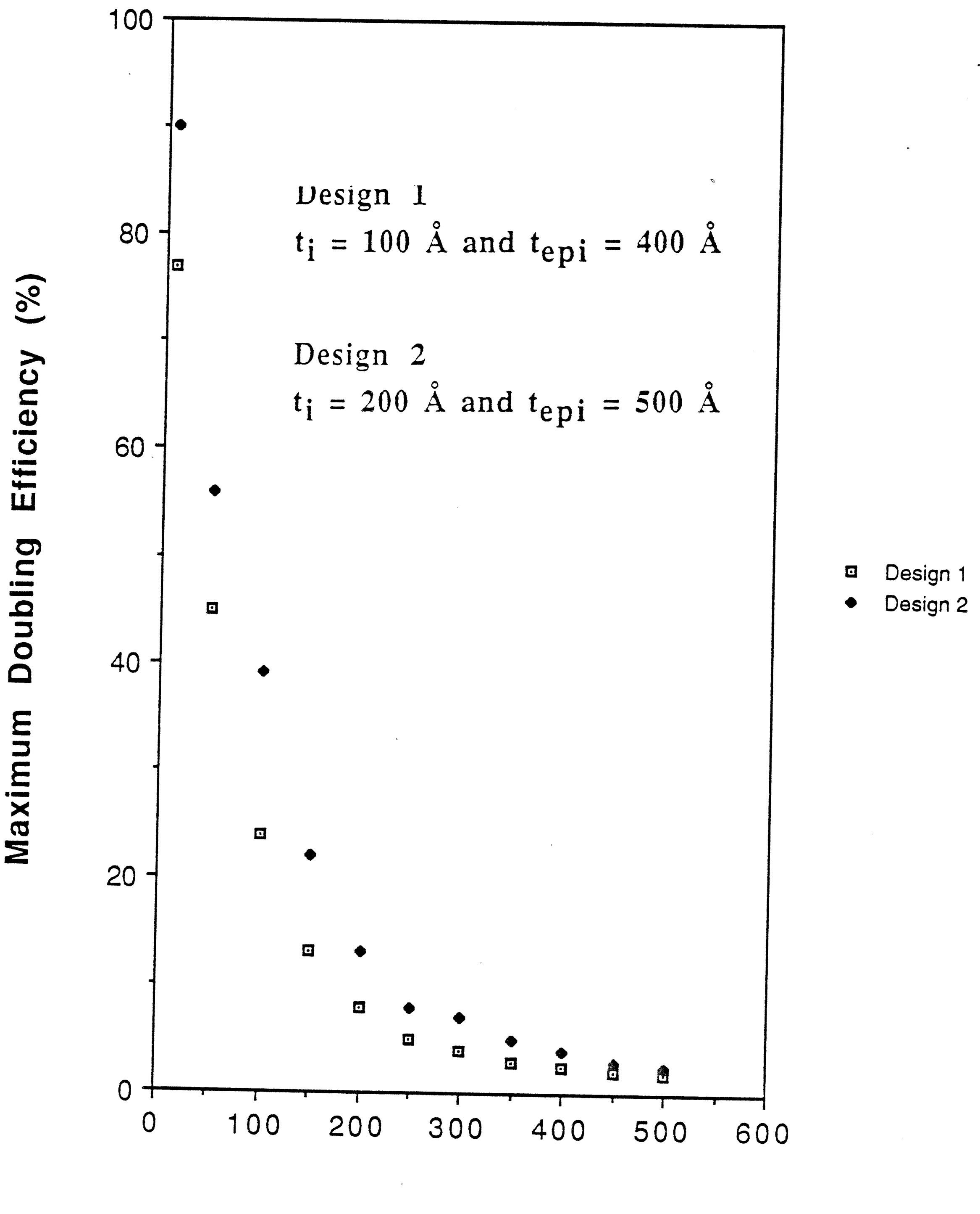

Fig. 7 Predicted maximum doubling efficiency versus input frequency for two different MIS varactor frequency doublers.

Millimeter Wave Monolithic Solid State Device Arrays

H-X.L. King, N.C. Luhmann,Jr., X. Qin, L.B. Sjogren, W. Wu, D.B. Rutledge[(1)], J. Maserjian[(2)], U. Lieneweg[(2)], C. Zah[(3)], and R. Bhat[(3)]
Department of Electrical Engineering, University of California
Los Angeles, CA. 90024

ABSTRACT

Current research efforts involve the design and fabrication of two-dimensional grids loaded with oscillators, frequency multipliers and electronic beam steerers which employ quasi-optical coherent spatial combining of the outputs of a large number of solid state devices. This paper is specifically connected with our work on diode frequency multipliers, resonant tunneling oscillators, and Schottky diode beam steerers and focussers.

(1) Department of Electrical Engineering, California Institute of Technology, Pasadena, CA. 91109.
(2) Jet Propulsion Laboratory, Pasadena, CA. 91109.
(3) Bellcore, Red Bank, NJ. 07701.

INTRODUCTION

Major advances in materials technology, solid state electronics, integrated circuit technology, quasi-optics and quantum theory promise a new generation of high frequency devices and systems to solve critical problems in radar, electronic warfare and countermeasures, remote sensing, communications, and imaging. Such systems require power sources up to the THz region for transmitters ($\simeq$1 W to 100 W) and low noise local oscillators for receivers. Those needs have been traditionally satisfied by electron tube oscillators and amplifiers. However, the size, cost, and lifetime of the tube sources have severely limited their usage. This dictates the use of solid state sources. However, it is well known that the power handling capability of solid state devices is relatively low, especially at higher frequencies. Therefore, we have employed quasi-optical spatial power combining of the outputs of large planar arrays of devices to provide the required power levels, as well as to avoid the Ohmic losses and limitations associated with conventional power combining techniques. Monolithic integration is essential so that the required output power can be obtained without excessive cost and the performance can be more easily optimized. Current development efforts involve frequency multiplier arrays, Schottky diode beam steering arrays, and resonant tunneling oscillator arrays. This work is discussed in the following sections.

QUANTUM WELL ARRAYS

a) Quantum Barrier Varactor (QBV)

The concept of a single quantum barrier varactor (QBV) for frequency multiplication has been impressively demonstrated by Rydberg et al [1] with output at frequencies up to 280 GHz with 5% efficiency. However, it has also been observed that the large thermionic current as well as large Ohmic contact resistance of the GaAs/AlGaAs QBV limited its performance. Our approach is to utilize the InGaAs/InAlAs system with the InGaAs lattice matched to the InP substrate. with $In_{0.32}Al_{0.68}As$ serving as the barrier. A composition of 68% of AlAs has been chosen in order to obtain a high barrier ($\simeq$800 mV) with an acceptable lattice mismatch (1%). Also, InGaAs is a narrow band gap material, so that the Ohmic contact resistance is significantly smaller than GaAs. In addition, InGaAs has superior electronic transport properties. However, this system has its high power limitations. The main limitation to our device is due to avalanche breakdown because of the narrow band gap of InGaAs. Space charge effects and thermal heating will also degrade the device performance at high power. However, these effects can be greatly ameliorated by employing the new concept of stacking many barriers in the epitaxial structure. Since each QBV only shares part of the pumping power, very high power generation is feasible. Besides improving high power generation, the use of many QBVs in series also increases the cutoff frequency, since C_{min} can be dramatically reduced. Alternatively, the series resistance can be reduced by increasing the active area while the C_{min} is still sufficiently low. The other important advantage of many QBVs in series is in

improving the yield of the array. The so called "back-to-back" fabrication method can be employed [2]. Using this method, only one metalization is required. On the other hand, since a larger area can be employed, higher lift-off yield can be obtained. Figure 1 shows the profile of four QBVs in series. The epitaxial structure provides two QBVs while the "back-to-back" process doubles the numbers of QBVs in series.

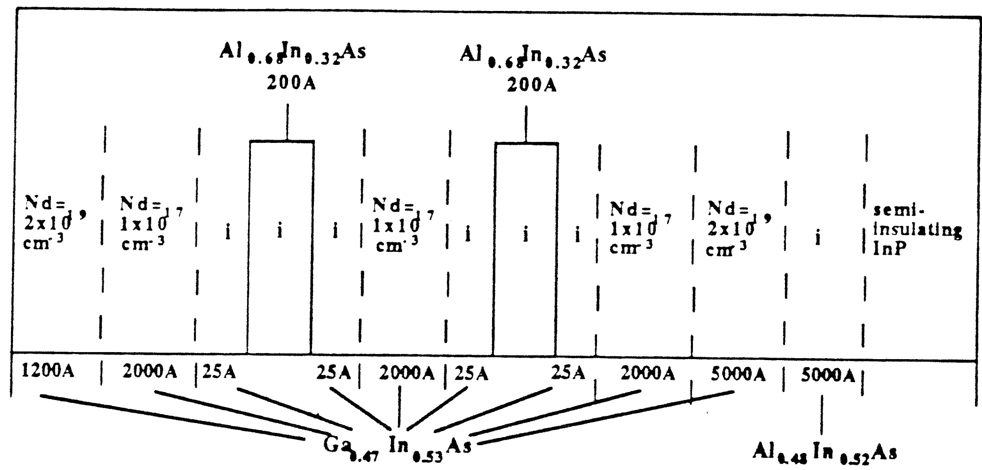

Figure 1. The profile of four QBVs in series.

The output power versus pumping power at 1.5 THz has been simulated as shown in Fig.2.

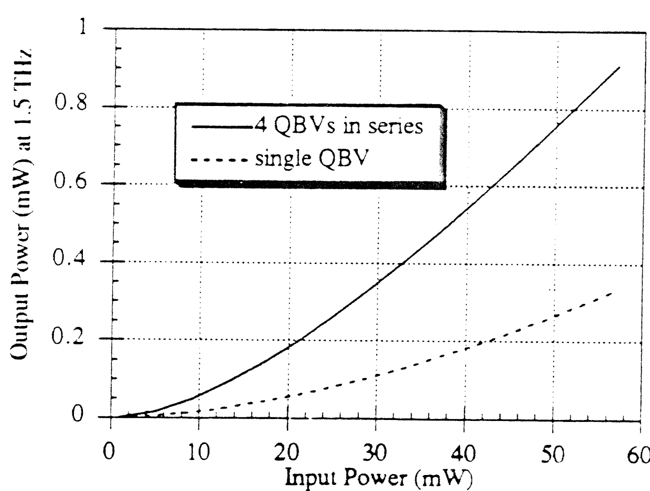

Figure 2. Comparison of the output power of four QBVs with single QBV.

The efficiency of four QBVs in series is almost four times larger than the single QBV at a pumping power level of 30 mW. This indicates that many QBVs in series provide a promising approach for THz multiplification. The setup for testing a proof-of-principle tripler array is demonstrated in Fig.3.

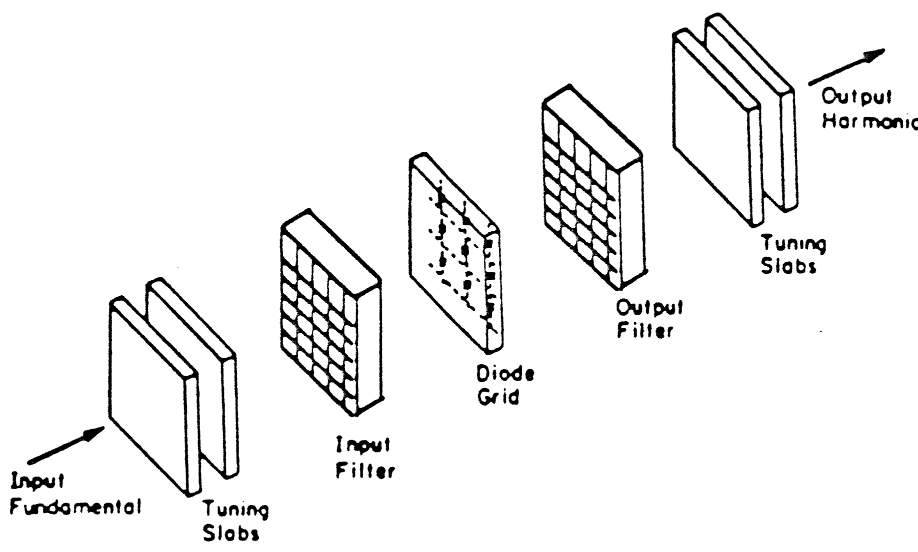

Figure 3. Quasi-optical tripler configuration.

The quasi-optical input filter consists of inductive strip arrays on both sides of a quarter wavelength quartz slab, while the output filter consists of two capacitive slot arrays on a like slab. The dual quartz tuning slabs are used for impedance matching.

b) Resonant Tunneling Diode (RTD) Arrays

In addition to the development efforts on QBV arrays, a study of resonant tunneling device (RTD) [3] [4] for multiplier as well as oscillator applications is being conducted. Test devices have been fabricated using an MOCVD wafer provided by Bellcore. Figure 4 shows that a current peak-to-valley ratio of 19:1 with peak current density of $1.6\text{x}10^5$ A/cm^2 has been achieved at room temperature, which is the highest current peak-to-valley ratio achieved for MOCVD wafers at such a high current density.

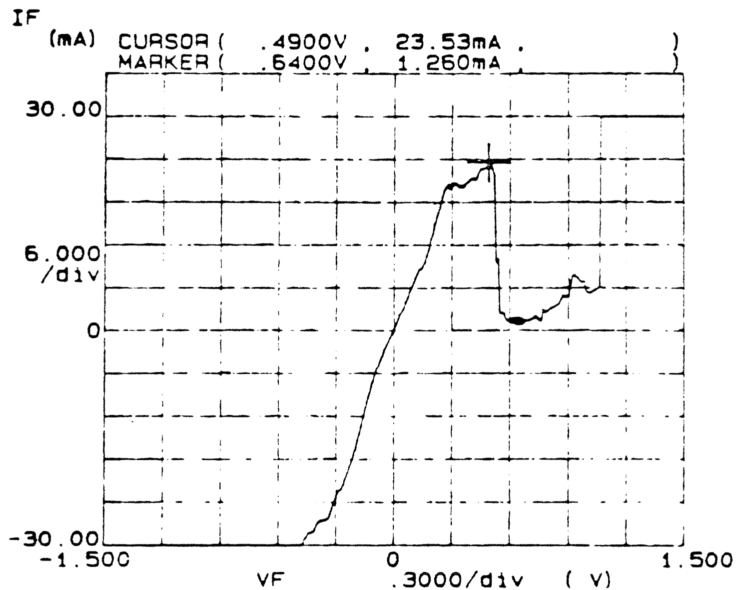

Figure 4. Measured I-V characteristics of RTD.

The RTD oscillator array presents a significant challenge due to the difficulty in stabilizing the low frequency oscillations resulting from the large negative differential resistance. Based on the equivalent circuit analysis of the grid array, work has been initiated on simulating the frequency dependent characteristics of the RTD array.

LINEAR SCHOTTKY VARACTOR ARRAY

The linear Schottky varactor array is being developed because it has the potential for a number of quasi-optical circuit functions. When the array is operated with a uniform DC bias to all the diode rows, the array can function as a reflection phase shifter, transmission amplitude modulator, or reflection polarizer as shown in Fig.5.

Phase shifter

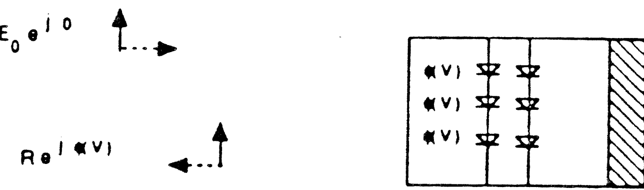

Electronic shutter

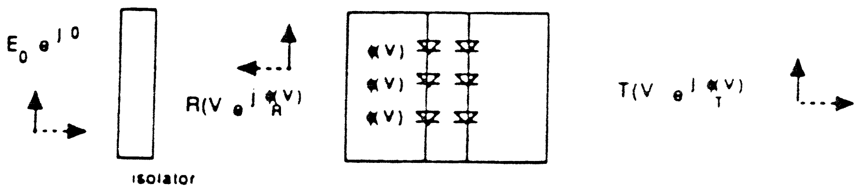

Polarizer

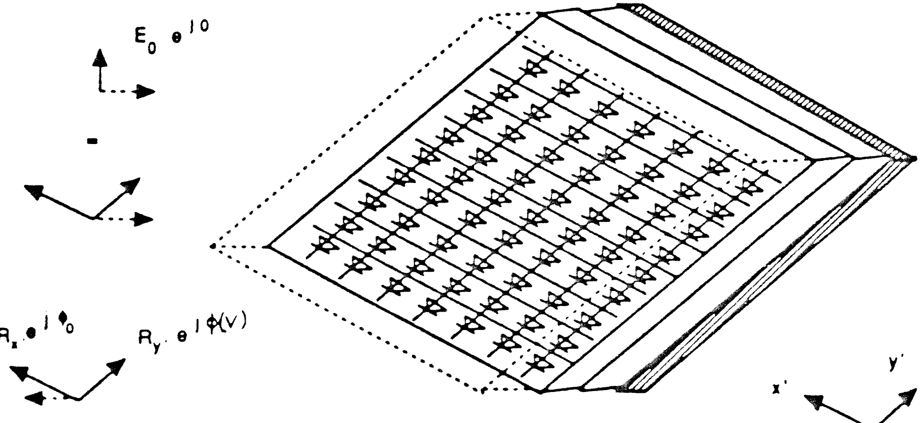

Figure 5. Capabilities of stacked varactor array under uniform bias.

When different bias is applied to the rows of the array, the grid can be operated as a phased array beam steerer, electronically focusable mirror, or phase conjugation surface (Fig.6).

Beam steerer

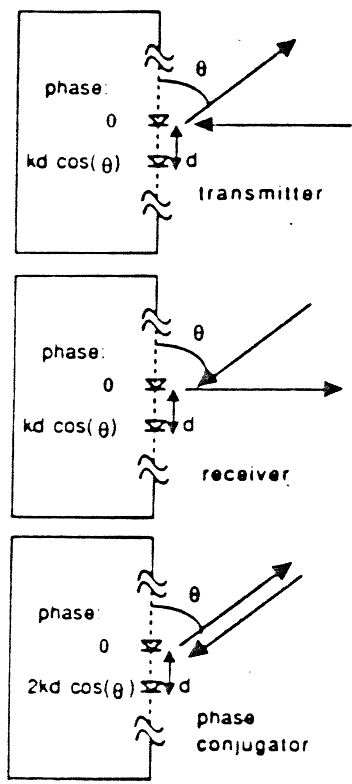

Focusable mirror

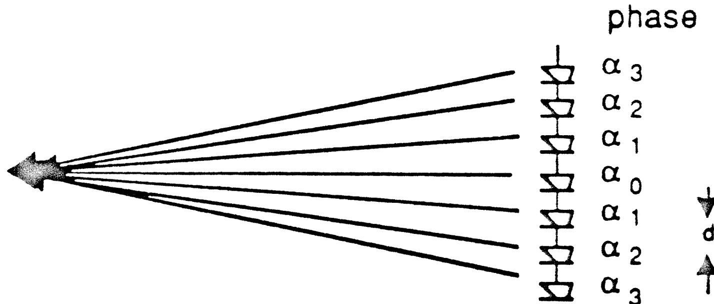

Figure 6. Capabilities of stacked varactor array under nonuniform bias.

The concept was pioneered by W. Lam, who successfully demonstrated the use of such an array as a phase shifter, with 70 degrees of phase and 6.5dB loss [5]. Lam also proposed an extension of the phase shifter array concept to achieve a full 360 degrees of phase. The design involves stacking two phase shifter arrays with a quarter wavelength separation (Fig.7).

Schematic view

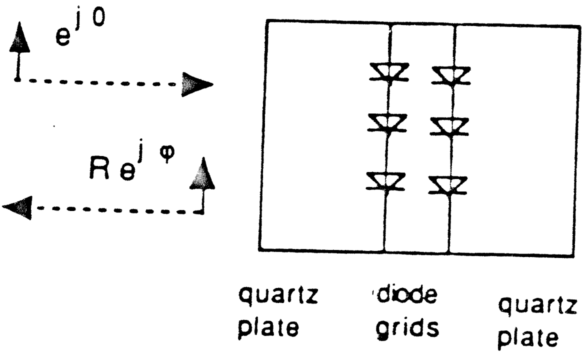

Quasi-optical circuit

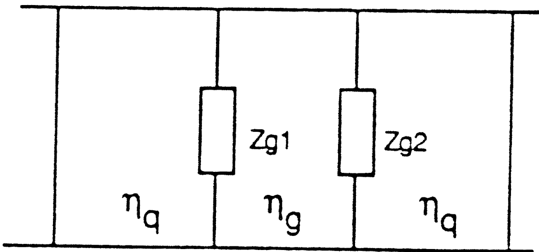

Layers are odd multiple quarter wavelength thick

Figure 7. Two layer stacked linear varactor array

This is the concept we are pursuing. Using the full phase range with different phasing of the rows allows beam steering operation as well. The model used for a diode array is that of a lumped impedance in a transmission line system. Lam obtained good agreement between theory and experiment using an impedance consisting of an inductance in series with the diode impedance. His array had a rather large diode C_{min}, however, which hid the effect of the "gap capacitance" associated with the non-uniformity of the strip current at the gap as shown in Fig.8.

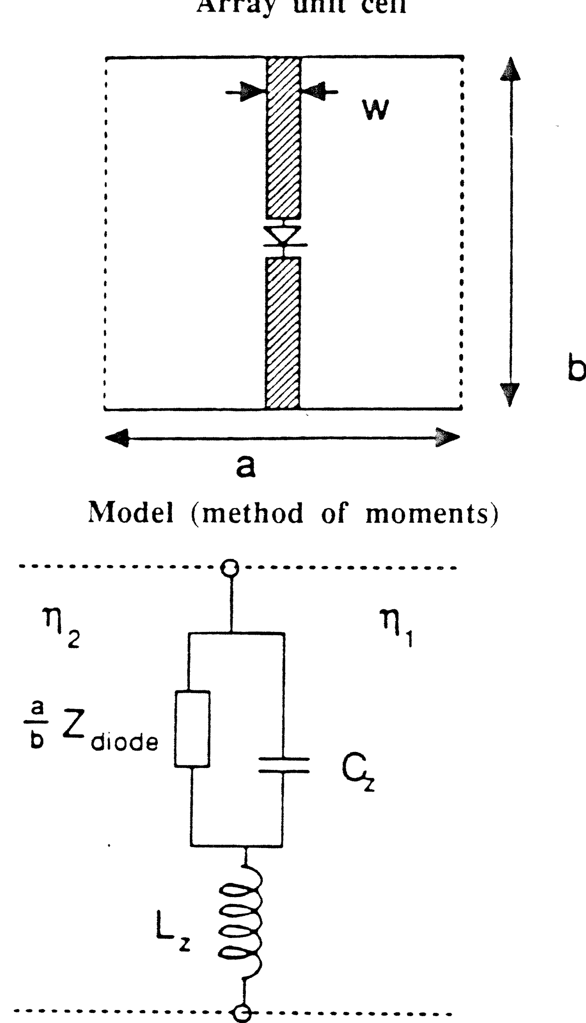

Figure 8. Quasi-optical impedance model of the diode array.

A method of moments simulation developed for the current work has shown that at small diode capacitance the gap capacitance will severely degrade the grid performance. However, a small C_{min} is essential to achieve the 360 degree phase shifting. Fortunitely, the gap capacitance effect can be reduced to an acceptable level by use of a rectangular array unit cell (Fig.9).

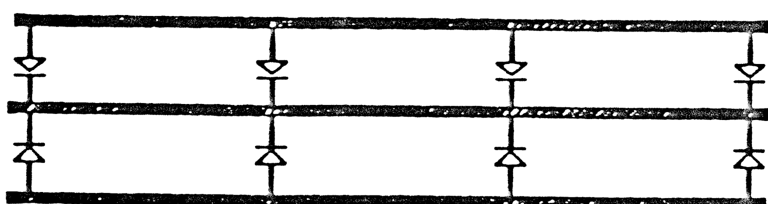

Figure 9. Rectangular unit cell array design.

A rectangular array requires a larger diode, which, fortunitely, is easier to fabricate with high yield and improves power handling capability. Based on the electromagnetic model of the diode array, C-V characteristics of the diode, and transmission line circuit model, simulations of the reflection phase shifting and transmission amplitude modulation as functions of DC bias have been carried out as displayed in Fig.10.

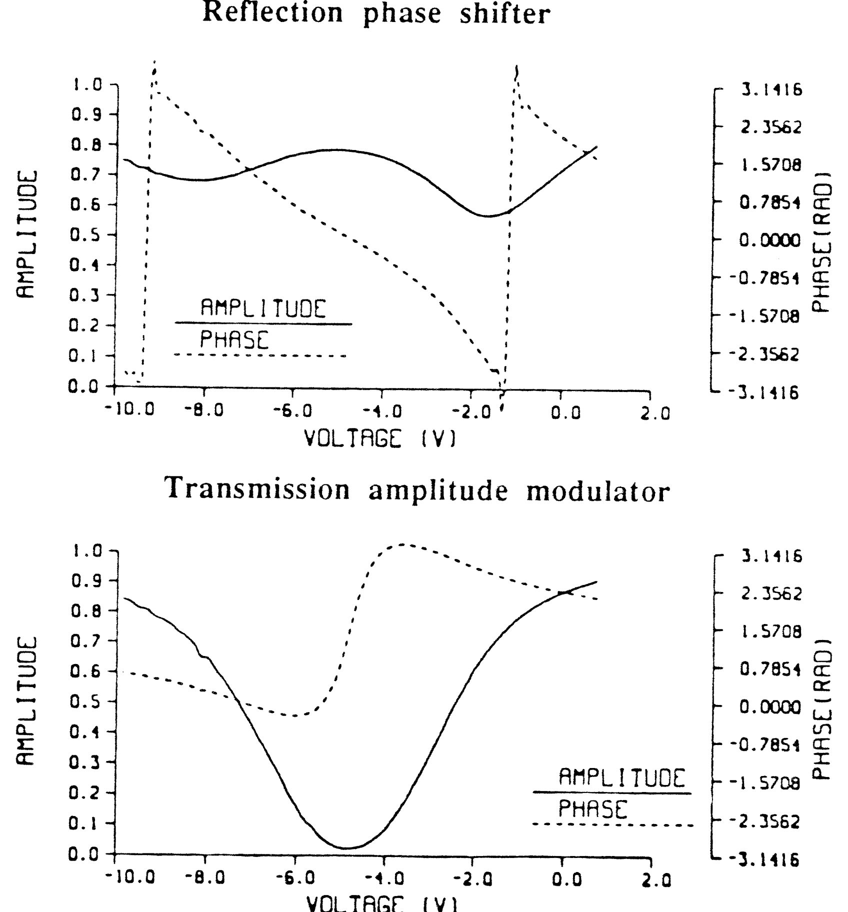

Figure 10. Simulated performance of the stacked linear varactor arrays

It is observed that 360 degrees of phase shifting and an amplitude modulation of 3% to more than 90% are both achievable. A high breakdown voltage is essential to achieve a small diode capacitance. An AlGaAs barrier layer with 50% of AlAs has therefore been used to improve the breakdown voltage. The testing of the array will be performed using a reflectometer based on Lam's design [6].

BNN VARACTOR ARRAY

This work, is an extension of the work of Jou [7] and of Hwu [8]. By using a hyperabrupt Schottky diode array, Jou successfully demonstrated a frequency multiplification from 33 GHz to 66 GHz. The small breakdown voltage of the Schottky diode motivated the follow-in work on the BIN diode array by Hwu. However, the intrinsic region of the BIN causes a large space charge resistance. As a result, the efficiency and the cutoff frequency are severely degraded. The space charge effect can be suppressed by adding doping in the previous intrinsic region while still preserving a reasonably high C-V nonlinearity. A comparison of the C-V characteristics of the hyperabrupt Schottky, BIN and BNN diodes is shown in Fig.11.

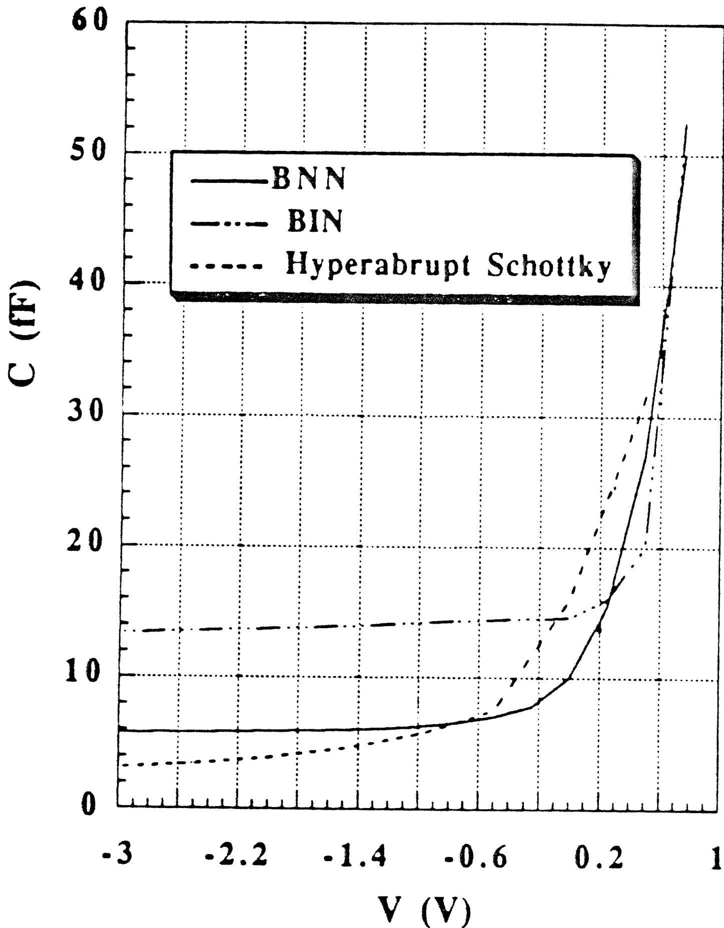

Figure 11. Comparison of the C-V characteristics of hyperabrupt Schottky, BIN, BNN diodes.

Both BNN doubler and tripler array work is underway. Figure 12 shows the measured C-V characteristics of the BNN back-to-back tripler and its profile.

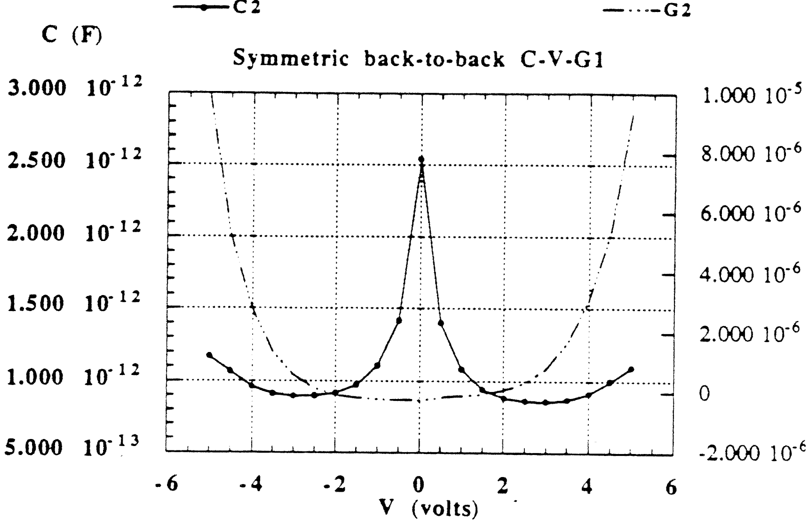

Figure 12. Measured C-V characteristics of back-to-back BNN.

The testing of the BNN doubler array will be demonstrated using the configuration of Jou [7], while the BNN tripler array will be tested using the setup arranged for the QBV tripler array.

CONCLUSION

We are actively working on the development of millimeter wave monolithic solid state device arrays. The new concept of many QBVs in series and BNN monolithic quasi-optical arrays offer great promise for THz frequency multiplification. The linear Schottky varactor array has numerous useful quasi-optical functions. In the design of this array, a more accurate electromagnetic model has been developed.

ACKNOWLEDGEMENTS

The work described here is supported by the US Army Research Office and by Northrop Corporation and the California MICRO Program.

REFRENCES

1 A. Rydberg, H. Gronqvist, and E. Kollberg, "Millimeter-and-Submillimeter-wave Multipliers Using Quantum-barrier-varactor (QBV) Diodes", *IEEE Elec. Dev. Lett.*, 11, No. 9, p.373, 1990.

2 R.J. Hwu, C.F. Jou, N.C. Luhmann,Jr., M. Kim, W.W. Lam,Z.B. Popovic, and D.B. Rutledge, "Array Concept for Solid State and Vacuum Microelectronics Millimeter Wave Generation", *IEEE Tran. Elec. Dev.*, 36, No. 11, 1988.

3 T.C.L.G. Sollner, H.Q. Le, and W.D. Goodhue, "Resonant Tunneling Through Quantum Wells at Frequencies up to 2.5 THz", *Appl. Phys. Lett.*, 45, p. 1319, 1984.

4 E.R. Brown, T.C.L.G. Sollner, W.D. Goodhue, and C.D. Parker, "High Speed Resonant Tunneling Diodes", *Proc. SPIE Conf. Quantum Well Superlattice Phys. II*, 943, p. 2, 1988.

5 W.W. Lam, C.F. Jou, N.C. Luhmann,Jr., and D.B.Rutledge, "Millimeter-wave Diode-Grid Phase Shifters", *IEEE Tran. Microwave Theory Tech.*, 36, No. 5, p. 902, 1988.

6 W.W. Lam, "Millimeter-wave Monolithic Schottky Diode-grid Phase Shifter", Ph.D Thesis, California Institute of Technology, 1987.

7 C.F. Jou, W.W. Lam, H.Z. Chen, K.S. Stolt, N.C. Luhmann,Jr., and D.B. Rutledge, "Millimeter Wave Diode-grid Frequency Doubler", *IEEE Tran. Microwave Theory Tech.*, 36, No. 11, p. 1507, 1988.

8 R.J. Hwu, N.C. Luhmann,Jr., D.B. Rutledge, D. Streit, T.O'Neill, and U. Lieneweg, "Monolithic Watt-level Millimeter Wave Barrier Intrinsic N+ (BIN) Diode-grid Frequency Tripler Array", *Proc. 13th International Conf. Infrared Millimeter Waves*, p. 328, 1988.

Current Saturation in Submillimeter Wave Varactors

E. Kollberg[1], California Institute of Technology,
T. Tolmunen and M. Frerking, JPL,
J. East, University of Michigan

Abstract

In semiconductor devices the speed of electrons cannot exceed certain limits. This phenomenon will affect varactor multipliers as well as other high frequency devices where the RF current through the active part of the device is primarily displacement current. Hence, we expect at some point "saturation" of the varactor output power. We will in this paper discuss this phenomenon in some detail and show that it severely deteriorates the multiplier performance at higher frequencies. Single barrier varactors (SBV) should have an advantage to ordinary GaAs Schottky diode varactors because they can be fabricated on InAs and stacked in a series array, allowing for lower current densities and higher power handling.

1. Introduction.

Computer analysis can be used to accurately predict the performance of millimeter and submillimeter wave Schottky barrier diode mixers and frequency multipliers over a wide range of operating conditions [1,2]. However, these analyses depend on an accurate equivalent circuit for the nonlinear element over the range of RF drive levels and frequencies expected in actual operation. The commonly used varactor diode equivalent circuit consists of a parallel combination of voltage dependent capacitance and conductance in series with a diode resistance (Fig. 1a). The nonlinear capacitance is due to the voltage variable width of the depletion layer and the nonlinear conductance is due to the I-V curve of the diode. Both can be found from an analytic approximation or from measured data. The resistance term is more difficult to obtain from experimental measurements. It can be approximated from information on the device undepleted layer width, the spreading resistance, and the contact resistance (see e. g. ref. [3,4]). The resistance can be constant or voltage variable, depending on the nature of the solution. The best multiplier efficiency theoretically occurs when the multiplication is purely reactive. If the diode is

[1] on leave from Chalmers University of Technology

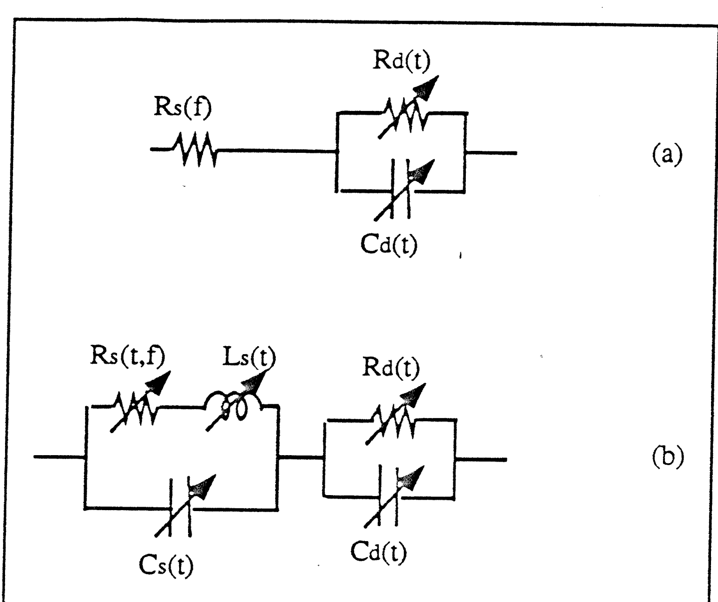

Figure 1: Schottky diode varactor models with: (a) constant series resistance; (b) series resistance, a parallel displacement current capacitance both changing with the width of the undepleted epitaxial layer, and added inductance L_s related to the inertia of the electrons.

driven into forward conduction, multiplication becomes a hybrid of resistive and reactive multiplication which degrades the efficiency. This equivalent circuit approach has worked well in the design of harmonic multipliers at lower frequencies or power levels. However, as the frequency and power level increase disagreement between theory and experiment increase. Erickson [5] has reported efficiencies in harmonic multipliers that match the computer simulation results at low pump power levels, but not at higher power levels. The experimental degradation of efficiency occurs well before the diode is driven into forward conduction. He suggested that the problem might be caused by device heating at the higher power levels. The purpose of this paper is to analyze limitation on varactor performance and then to compare the modified models with the experimental results.

2. Basic Limitations.

In the most common model for the Schottky diode varactor (see Fig. 1a), the *displacement current* (i_d) through the depleted region is

$$i_d(t) = C_d(t) \cdot \frac{dV_d(t)}{dt} \tag{1}$$

where $C_d(t)$ is the depletion capacitance and $V_d(t)$ is the voltage over the depletion region. Hence we expect i_d to increase with the pump power and the pump frequency. In the varactor diode model of Fig. 1a the displacement current must be matched by the *electron conduction current* (i_e) *through*

the undepleted semiconductor, where i_e is

$$i_e = A_d \cdot n_e \cdot v_e(t) \cdot e \tag{2}$$

A_d is the diode area, n_e the electron density (in our case $n_e = N_d$, the doping density), v_e the electron velocity and e the charge of the electron. Basically all millimeter wave and submillimeter wave varactor multipliers use GaAs Schottky diodes. Since it is well known that in a DC electric field, the electron velocity in GaAs reaches a maximum of about $2.2 \cdot 10^5$ m/s at about 3.2 kV/cm [6], a saturation phenomenon is expected when $i_d > i_{sat}$ where

$$i_{sat} = i_{e,max} = N_d \cdot v_{e,max} \cdot e \cdot A_d \tag{3}$$

This current limiting phenomenon can be modelled as an *effective series resistance* which increases rapidly with higher power levels, causing a considerable deterioration in the multiplier performance.

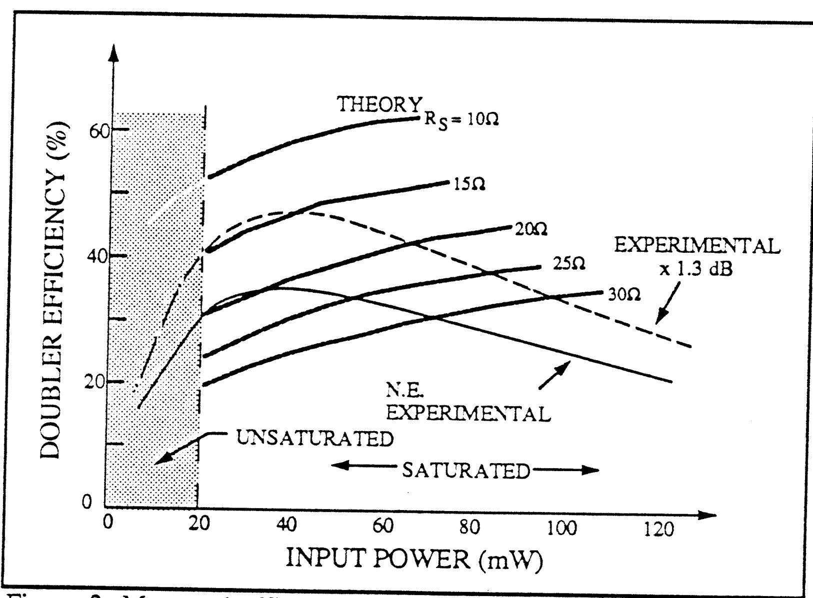

Figure 2: Measured efficiency (full line: measured; dashed line: ohmic losses of 1.3 dB subtracted) for the 2x80 GHz multiplier [5] compared to theoretical efficiencies obtained for different series resistances. The shadowed area indicates where theory suggests the multiplier is unaffected from current saturation.

Experimental evidence can be found by studying the 2x80 GHz multiplier reported by Erickson [5]. This high efficiency doubler uses two diodes (6P4 from the University of Virginia) in a balanced configuration. Erickson found that the fall off of the measured efficiency versus power did not follow the theoretical predictions. We confirmed this in an independent calculation using the Siegel and Kerr program [1] as shown in Fig. 2. The maximum electron current i_{sat} as calculated from Eq. (3) for this particular diode (6P4; see Table 1) is 44 mA. The displacement current i_d equals this electron current i_e for a pump power of 11 mW

(per diode). Furthermore, with this current through the 11 Ω series resistance the field over the 1 μm epitaxial layer will be greater than 3.2 kV/cm.

The maximum pump power used experimentally by Erickson was 120 mW or 60 mW per diode; hence the maximum displacement current i_d exceeds i_{sat} a large margin (compare Table 2). We consequently decided to investigate how the efficiency of the 2x80 GHz multiplier varies with increasing series resistance. The graph shown in Fig. 2 shows calculation of the efficiency versus input power with an increasing series resistance as a parameter. In addition it shows the experimentally obtained results as obtained by Erickson. We have also scaled these results by 1.3 dB, the estimated loss in the waveguide multiplier mount. We conclude that a series resistance that increases from 11 Ω a low pump powers to about 30 Ω at high pump powers can explain the measured efficiency degradation for input powers above about 20 mW (10 mW per diode).

In addition, several other phenomena may play a role in explaining the fall off in efficiency at higher pump powers. One is that *the edge of the depletion region cannot move faster than allowed by the maximum electron velocity*, i. e. $dW(t)/dt < v_{s,max}$ where W is the width of the depletion region. Hence the capacitance variation $C(t) \sim 1/W(t)$ may not vary as rapidly as calculated by the multiplier simulation computer program. Investigating dW(t)/dt for the Erickson doubler, shows that $dW(t)/dt > 3 \cdot 10^5$ m/s for input powers >40 mW (20 mW per diode). Hence, for this multiplier we will assume that this phenomenon is less important than the saturation of the current. However, for higher frequency multipliers the limited speed of the capacitance variation may be a more serious concern.

The acceleration of the electrons is finite and introduces an inductance L_s as shown in Fig. 1b (see e.g. ref. [7,8]). An approximate calculation shows that $\omega L_s \ll R_s$ for pump frequencies below about 100 GHz (f_{es} is about 800 GHz).

$$\omega L_{epi}(t) = R_{epi}(t) \cdot \frac{\omega}{\omega_{es}} \approx R_{epi}(t) \cdot \frac{f_{GHz}}{f_{es}} \qquad (4)$$

Further *the displacement current through the undepleted epitaxial layer* (represented in Fig. 1b by $C_{Rs}(t)$) is not of any major concern at pump frequencies of about 100 GHz and below. However, for higher frequencies it must be taken into account.

Heating of the diode seems not to be of any particular importance for the diodes investigated. Estimates of the heating suggests that when each 6P4 diode absorbs 48 mW, the heating will not exceed 30 °C, increasing the series resistance (decreasing the mobility [6]) by less than 5%. For another diode discussed below, 2T2 (see Table 1), the maximum power absorbed by the diode is of the order 20 mW yielding a temperature increase less than that for the 6P4 diode. The saturation velocity in the 2T2 diode will drop with about 10 % [6] for a 30 °C temperature increase.

Basically, the *spreading resistance* in the heavily doped substrate can be ignored. For a typical varactor, the epitaxial layer region is 5000 to 10000 Å. Since the epitaxial layer resistivity is much larger than the bulk resistivity, and since a large fraction of the epitaxial layer is undepleted during most of the pump cycle, R_{epi} will most of the series resistance. In fact, when the varactor is driven at about the maximum allowable power, R_{epi} is time-varying between a maximum value (R_{epimax}) valid when the W_{depl}≈0, and a minimum value approximately equal to zero.

The time variation of the width of the undepleted epitaxial layer causing $R_s(t)$, $L_s(t)$ and $C_{Rs}(t)$ to be time varying, also does not change the general picture. Raisanen et. al. [9] have investigated the influence of the time variation of $R_s(t)$, $L_s(t)$ and $C_{Rs}(t)$. They found a considerably increased theoretical efficiency at low drive levels, while for a large pump power the theoretical efficiency is only slightly higher than assuming a constant series resistance ($R_s \approx R_{epimax}$) and neglecting the influence from C_{Rs} and L_s. This can be understood, since the mean of the time varying series resistance is lower than the experimentally determined series resistance, which is measured during heavily forward bias conditions. For high pump powers our computer simulations shows that the maximum current through the diode is obtained for near zero and moderately small negative

voltages when most of the epitaxial layer is still undepleted, indicating that the effective series resistance then becomes nearly equal to the experimentally determined one.

3. Analysis Using a Drift Diffusion Model Approach.

To gain more insight into the current saturation problem, a large signal time dependent version of a device simulation has been modified to assess the large signal equivalent circuit of varactors. The simulation solves Poison's equation and the current continuity equation self consistently in the time domain to find the total current (the sum of the electron current and the displacement current) as a function of time through the structure. The simulation is driven with an RF voltage and the resulting current waveform is found. The in-phase Fourier component of the current at the drive frequency is associated with the resistance, and the 90 degree phase component is associated with the reactance. The device large signal capacitance can be found from the reactance and the frequency. A simple approximation for the velocity that includes a constant low field mobility region and a saturated high field velocity is used. The inductance L_s related to the inertia of the electrons is neglected. This simulation has been used to study a variety of varactor operating conditions.

A wide variety of dynamic or velocity overshoot effects are possible in GaAs. These effects can modify the simple current transport model discussed above. A large signal Monte Carlo simulation of the epitaxial region using a technique described in [10] was modified to include impurity scattering. This simulation was then used to find the RF mobility of electrons in GaAs as a function of frequency and drive level. The results of this simulation were used to set the mobility and saturated velocity in the diffusion model. The varactor structure used in the Monte Carlo simulation is that of the submillimeter wave varactor 2T2 from the University of Virginia. It has a 0.5 micron long epitaxial layer with a doping of $1 \cdot 10^{17}$ cm^{-3}.

Fig. 3 shows the large signal resistance of the complete device pumped with a pure sinusoidal voltage at 200 GHz. Similar effects has been studied in IMPATT diodes [7, 8 and references at end

of 10]. For such combinations of RF drive level and frequencies that produce a small current where the fields and voltages in the epitaxial region are small, the mobility is approximately equal to the low field mobility and the device resistance is small. As the RF drive level increases, the current through the device increases, the voltages and fields in the undepleted region increase, the mobility goes down and the resistance increases. In fact, since the device is being driven by a sinusoidal wave, the current through the device is a non-sinusoidal function of time. The resistance shown in Fig. 3 is an average resistance over the 200 GHz RF pump cycle. Although part of this device resistance is related to power loss at harmonic frequencies in the series resistance, the major contribution is due to the decreased mobility. The result in Fig. 3 shows a major limitation on the combination of RF pump power and frequency in varactor multipliers. This resistance information is used to study efficiency reduction in multipliers. Based on this simulation, a current dependence for the diode series resistance is derived.

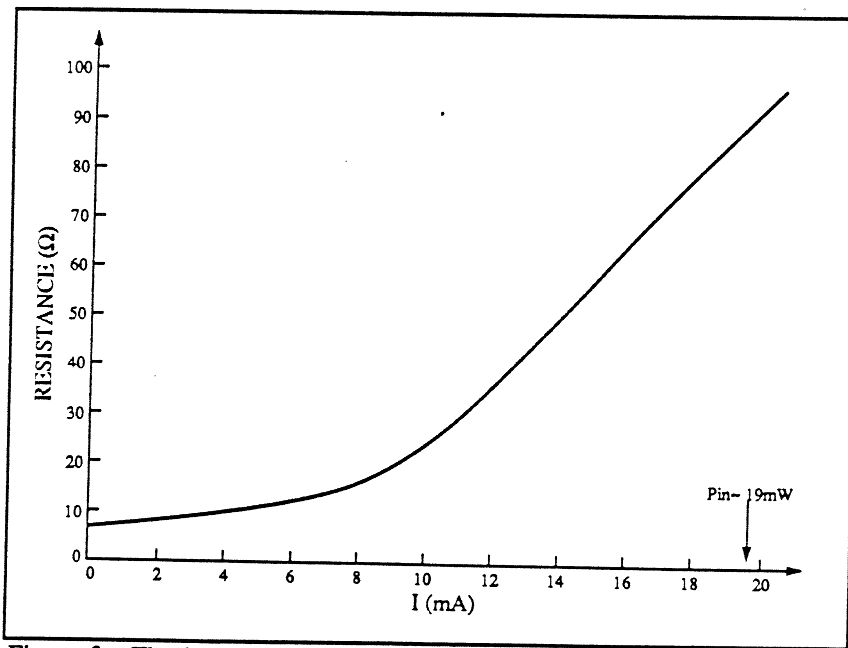

Figure 3: The large signal series resistance at 200 GHz for the 2T2 diode as obtained from the drift-diffusion model.

The varactor equivalent circuit must be further modified at higher frequencies. Consider the varactor equivalent circuit shown in Fig. 1b where the capacitance C_{Rs} shunting the epitaxial resistance accounts for the displacement current through the undepleted part of the epitaxial layer. At "low" frequencies and small drive powers, the impedance of this extra capacitance is usually much larger than the resistor impedance. Most of the RF current will flow through the resistance and the effect of this capacitance will be small. However, conditions will change as the drive level or frequency increase. The parallel combination of the resistor and capacitor will act like a current divider.

Increasing the RF drive at a constant frequency will increase the impedance of the resistor as shown in Fig. 3. This will shunt a larger fraction of the current through the capacitance. If the undepleted epitaxial layer capacitance were to completely shunt the resistance, the device would appear to be a series combination of two capacitors, the net capacitance would go down and become constant. This phenomenon is illustrated in Fig. 4. Notice that this saturation effect would also degrade the harmonic multiplier performance since the multiplier performance depends on the nonlinear nature of the device capacitance.

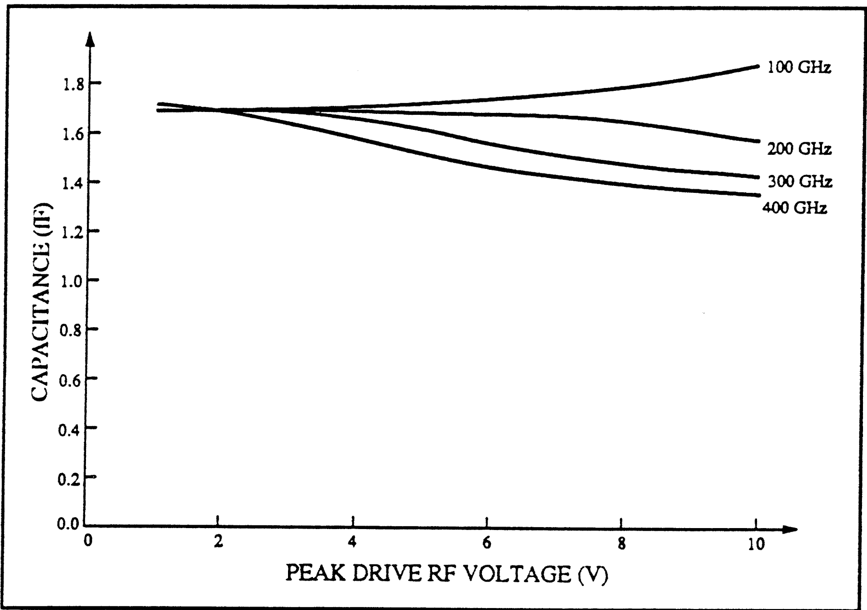

Figure 4: Device capacitance versus drive voltage as obtained from the drift diffusion model for different frequencies.

This brief description of varactor models shows several limitations with the simple equivalent approach typically used with large signal device circuit programs. The problems include (1) large signal current limits in the undepleted epitaxial region which can occur at all frequencies, (2) large signal shunting of the undepleted region which can reduce the device nonlinearity and occurs at frequencies of several hundred GHz, and (3) inductive electron effects which can be ignored for most varactor applications but will have a major impact on very high frequency mixers. The results will be used in the next section to see the effect on varactor frequency multipliers.

4. Approximate Approach Using a Current and Time Dependent Series Resistance.

As mentioned above, in GaAs, the electron velocity in a DC electric field reaches a maximum of about $2.2 \cdot 10^5$ m/s [6]. Electron velocities in bulk GaAs have been calculated for different RF electric fields at 50, 250 and 1000 GHz using Monte Carlo simulations [10]. At 250 and 1000

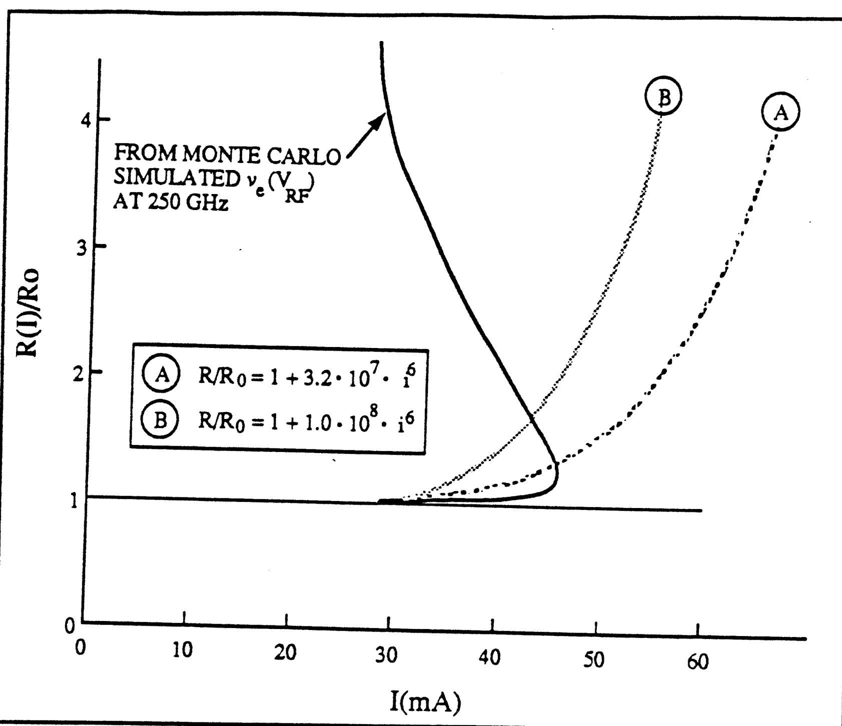

Figure 5: Resistance versus drive current obtained from Monte Carlo simulations and Eq. (4), and resistance versus drive current according to Eq. (5) ((A) and (B)) and used for calculation of efficiencies as described in Fig. 6.

GHz in addition to the in phase component v_o, an inductive, i. e. delayed velocity component v_1, is present . Hence in a high frequency electric field, the net electron velocity $(v_o^2 + v_1^2)^{1/2}$ is slightly larger due to overshoot phenomena. The maximum velocity at 50, 250 and 1000 GHz is about $2.85 \cdot 10^5$, $2.9 \cdot 10^5$ and $3.4 \cdot 10^5$ m/s at approximately 4.5, 4.5 and 10 kV/cm, respectively. Extrapolating this data to DC, the velocity is $2.8 \cdot 10^5$ m/s at about 4 kV/cm, which can be compared with $2.2 \cdot 10^5$ at 3.2 kV/cm [6]. It is evident from the discussion above that the velocity versus field dependence at high frequencies is considerably modified as compared to the DC curve [6].

Although the current (velocity) can be divided up into one in phase ($i_0 \propto v_o$) and one 90 degrees out of phase ($i_1 \propto v_1$) component, we can also model this as a series configuration with a total current $(i_o^2 + i_1^2)^{1/2} = (v_o^2 + v_1^2)^{1/2} \cdot N_d \cdot e \cdot A_d$ with one voltage component in phase and one inductive voltage component out of phase with the current. The "inductive voltage" can be tuned out by a proper choice of embedding circuit. The effective series resistance can then be identified as

$$R_s(E) = \frac{i_o(E)}{i_o^2(E) + i_1^2(E)} E \cdot L \qquad (5)$$

In Fig. 5, $R(E)/R(E \approx 0)$ is shown as a function of the total current $(i_o^2 + i_1^2)^{1/2}$ for the field E for the 6P4 diode. (E is the electric field and L is an arbitrary length and will disappear upon normalization.)

Since the current is limited at high frequencies, an approach with a current dependent series resistance was chosen. In order to have a single valued R(i) curve, we define the current dependent series resistance accordingly:

$$R_s(i) = R_{so}\left(1 + a \cdot i_{mA}^6\right) \qquad (6)$$

By a proper choice of the parameter "a" and the power for the current (here chosen equal to 6 although this is not critical), $R_s(i(t))$ will increase dramatically for currents near and above the maximum current defined by Eq. (3) or the curve in Fig. 5 for $R(E)/R(E \approx 0)$. This choice of the current dependent series resistance will

i. cause the apparent series resistance at the pump frequency and the harmonics to increase with the pump power (compare Fig. 2), and

ii. modify (clip) the current waveform approximately as required.

In Fig. 5 $R_s(i)$ is depicted for two values of the parameter "a" to be used for multiplier performance simulation in the next paragraph.

5. Results.

In Table 1 information is presented for two diodes, the 6P4 millimeter wave varactor diode, and the 2T2 submillimeter wave varactor diode. Both are built at University of Virginia. Erickson used the 6P4 diode in the 2x80 GHz multiplier, and the 2T2 diode in a 3x160 GHz multiplier. The maximum measured efficiency of the 2x80 GHz multiplier was 34%. Since the losses in the mount were about 1.3 dB, the intrinsic conversion efficiency is about 46%. The 3x160 GHz multiplier had a maximum output power of 0.7 mW for an input power of about 25 mW. We assume losses of about 5 dB for the 3x160 GHz multiplier by scaling the 1.3 dB waveguide loss for the 2x80

GHz multiplier. This results in an intrinsic efficiency is about 9%. The efficiency of these multipliers were investigated theoretically using ta large signal analysis computer program. The relevant data for the diodes are summarized in Table 1.

Table 1: ***Diode Data for the U. Va varactor diodes 6P4 and 2T2.***

	2x80 GHz f_p*=80 GHz* *6P4*	3x160 GHz f_p*=160 GHz* *2T2*	*3x330 GHz* f_p*=330 GHz* *2T2*
N_d nominal (cm^{-3})	$3.0 \cdot 10^{16}$	$1.0 \cdot 10^{17}$	$1.0 \cdot 10^{17}$
N_d used by us (cm^{-3})	$3.5 \cdot 10^{16}$	$1.0 \cdot 10^{17}$	$1.0 \cdot 10^{17}$
t_{epi} (µm)	1.0	0.5	0.5
R_{so} (Ω) measured	10	14[1], 12[2]	14[1], 12[2]
C_0 (fF) measured	21	5.5[1], 6.5[2]	5.5[1], 6.5[2]
$V_{break\text{-}down}$ measured (Volts)	20	11[1], 8.5[2]	11[1], 8.5[2]
Area (μm^2) Nominal/Adjusted[3]	33/33	5/6[3]	5/6[3]
assumed v_{max} (m/s)	$2.4 \cdot 10^5$	$2.4 \cdot 10^5$	$2.4 \cdot 10^5$
$i_{sat} = AN_d e v_{max}$ (mA)	44	23	23

1) Univ. Va.; 2) From Ref. [2]. 3) Adjusted according to measured C_0. See the text.

2x80 GHz Multiplier.

For the 2x80 GHz multiplier, R_{so} was chosen equal to the measured series resistance of 10 Ω. We selected two values for "a" in Eq. (6), as indicated in Fig. 5 and 6. In estimating i_{sat} we have assumed the doping concentration to be $3.5 \cdot 10^{16}$ cm^{-3} rather than the nominal doping concentration of $3.0 \cdot 10^{16}$ cm^{-3}. A best fit to the experimental curve is obtained by using a value between the two values for "a" used for the $R_s(i)$ curves shown in Fig. 5. The results are summarized in Table 2.

Table 2: ***Calculated performance of the Erickson 2x80 GHz and 3x160 GHz multipliers.***

	P_{in} (mW)	i_{RF} (mA)	dW/dt 10^5(m/s)	η	R_s (Ω)	a
2x80 GHz	11	42.0	2.0	52	10	–
$i_{sat} \approx$	40	69.0	2.8	54	10	–
44 mA	11	41.5	1.7	46	$R(i)$	$3.2 \cdot 10^7$
	40	62.7	2.6	41	$R(i)$	$3.2 \cdot 10^7$
3x160 GHz	2	23.7	≈1.7	22	12	–
$i_{sat} \approx$	12	47.0	3.5	>40	12	–
23 mA	2	23.0	1.6	20	$R(i)$	$1.53 \cdot 10^9$
	20	33.0	2.8	9	$R(i)$	$1.53 \cdot 10^9$

It is quite obvious from Table 2 that the relation $i_{RF}<i_{sat}$ is violated for input powers as low as of 11 mW. The depletion edge velocity exceeds the maximum electron velocity at larger powers. For 40 mW input power per diode (60 mW/diode was used as a maximum in Erickson's experiment) the $i_{RF}>>i_{sat}$, and $dW/dt>v_{max}$. Due to these effects, the calculated efficiency is decreased with about 25% from its unsaturated value.

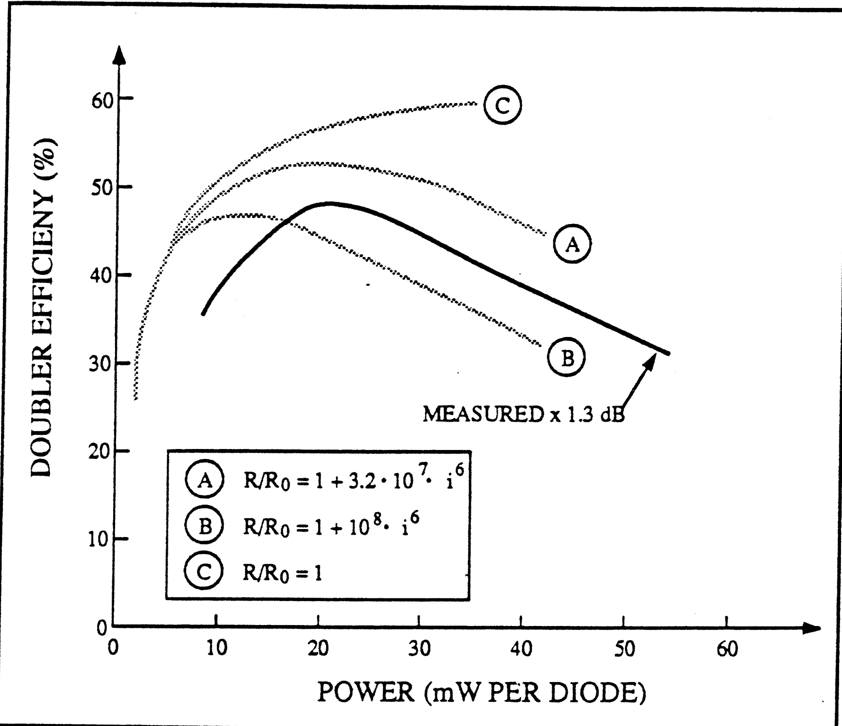

Figure 6: Intrinsic efficiency versus pump power (see Fig. 2) for the Erickson 2x80 GHz multiplier compared to calculated efficiency using the current dependent series resistance (A) and (B) as suggested in Fig. 5.

The agreement between theoretical calculations and the experiments are shown in Fig. 6. These results give some confidence in evaluating the 3x160 GHz multiplier using the same technique.

<u>*3x160 GHz Multiplier.*</u>

From Table 2 it is seen that i_{RF} is greater than i_{sat} for input powers as low as 2 mW. The situation seems now much worse than for the 2x80 GHz multiplier. For the analyses, the lower value of the parameter "a" was used, scaled taking into account the area and the doping concentration of the 2T2 diode. The area is actually more uncertain for this small area diode than for the 6P4 diode. We determined an "effective area" by comparing the capacitances as measured by Erickson [5] of the 6P4 and 2T2 diodes, and scaling from the area of the 6P4 diode; $A(2T2)=A(6P4)\cdot\{C(2T2)/C(6P4)\}\cdot\{N_d(6P4)/N_d(2T2)\}^{1/2}$. Computed results are shown in Table 2. The efficiency calculated including the saturation effect is now deteriorated by a factor of almost five as compared to the efficiency expected for the constant series

resistance case (R_s=12 Ω). The predicted efficiency of 9% for large pump power coincides with the measured one assuming the ohmic losses of the mount is 5 dB. Interestingly Erickson pointed out that the reverse bias voltage for optimum performance of this tripler was near the break-down voltage (V_{bias} = 5-6 volts, $V_{break\text{-}down}$= 8.5 volts), and the negative voltage swing was considerably larger than 8.5 volts.

3x330 GHz Multiplier.

A theoretical case of a 3x330 GHz multiplier was also analyzed. Results are shown in Table 3. Again, the saturation severely deteriorates the efficiency: at large input powers, the efficiency drops from almost 12% to 0.6%, a factor of 20! In fact, assuming these calculation are valid, it may not be possible to obtain more output power than 60 μW at 1 THz using the 2T2 diode. If no deterioration due to current saturation were present, the maximum predicted output power would be 1.2 mW.

Table 3: ***Calculated performance of 990 GHz Schottky Barrier Diode Varactor (2T2) Multiplier.***

	P_{in} (mW)	i_{RF} (mA)	dW/dt 10^5 (m/s)	η	R_s (Ω)	a
3x330	2	24	2.3	4.1	12	–
GHz	10	53	4.6	11.6	12	–
i_{sat}=	2	23	2.0	2.3	R(i)	$1.53\cdot10^9$
23 mA	10	31	2.9	0.6	R(i)	$1.53\cdot10^9$

Discussion

Whether a more exact theory using a more precise device model will predict lower or higher efficiency is not known. There are several approximations involved in our calculations, as mentioned above. There are also inconsistences such as that the velocity of the depletion edge calculated in two different ways as demonstrated in Eq. (6) do not agree, viz.

$$v = \frac{A\varepsilon}{\Delta t}\cdot\left(\frac{1}{C(t)} - \frac{1}{C(t+\Delta t)}\right) \neq \frac{i_d(t)}{N_d e A} \tag{7}$$

where $i_d(t)$ is the current through the varying capacitance. Typically the maximum velocity determined from the depletion current $i_d(t)$ is the larger one and the maxima do not occur

simultaneously. It is, however, quite clear that the current dependence of the series resistance is very important and will deteriorate the performance of the multiplier. For 1 THz, diodes with higher doping than 2T2 and correspondingly thinner epitaxial layer (the break-down voltage will be lower, and the corresponding epitaxial layer thickness smaller) will suffer less from saturation, and are expected to be more efficient.

The Single Barrier Varactor (SBV).

The single barrier varactor is an MBE-grown mesa diode, with ohmic contacts. It has been shown experimentally that this diode has a considerable potential as a varactor diode for multiplier applications [11]. In GaAs, an AlGaAs barrier in the middle of the mesa blocks all conduction current. The diode exhibits a symmetrical C-V characteristic, which causes only odd harmonics to be created when the varactor is pumped (zero bias assumed). The SBV exhibits a symmetric C-V characteristic similar to a back-to-back configuration of two Schottky varactors. Since this diode relies on a voltage variable depletion region to generate the nonlinear capacitance, it will have exactly the same problem with current saturation in a multiplier application as the common Schottky varactor diode.

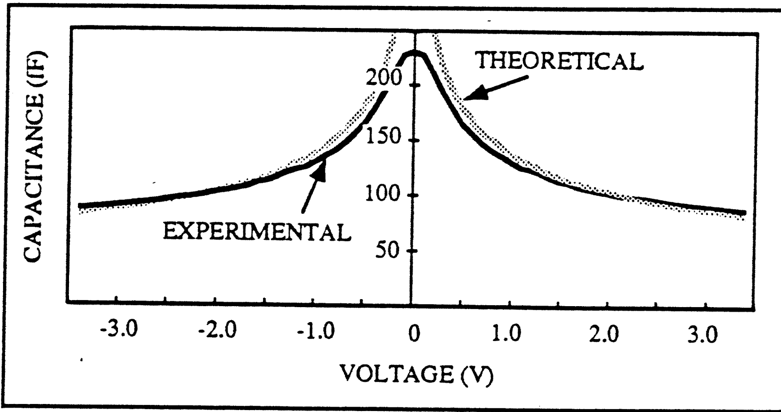

Figure 7: Capacitance versus bias voltage for a single barrier varactor.

We have measured the C-V characteristic of such a diode (see Fig. 7). We found that the zero bias capacitance deviated from the capacitance expected from the simple calculation, $C_{max} = (A_d \varepsilon)/W_{barrier}$, by about a factor of three. An interpretation of this phenomenon is that the effective barrier thickness is larger than $W_{barrier}$. The lower zero bias capacitance indicates an effective barrier thickness of 600 Å rather than 200Å. An obvious possible contribution to this excess barrier

thickness stems from the fact that there are 50Å undoped regions on both sides of the barrier. In addition, the deviation may arise from the discontinuity of the Fermi level at the doped/undoped barrier interface.

A few simulations of a SBV diode multiplier have been carried out, showing similar results as for the Schottky varactor multiplier as summarized in Table 4. For the particular case shown in Table 4, it is assumed that $N_d = 2\cdot10^{17}$ cm^{-3}, $W_{barrier}$=200 Å (this is now an *effective* width), C_0=20 fF, R_s=12 Ω. It is seen that this device suffers less from saturation while the velocity of the edge of the depletion region seems to be a more serious problem. InAs based devices have fewer problems in this respect since the electron velocity is two to three times higher than for GaAs.

Table 4. *Predicted performance of a Single Barrier Varactor 3x330 GHz Multiplier.*
($N_d = 2\cdot10^{17}$ cm^{-3}, $W_{barrier}$=200 Å, C_0=20 fF, R_s=12 Ω;
GaAs: $v_{max} \approx 2.4\cdot10^5$ m/s, $i_{sat} \approx 88$ mA; InAs: $v_{max} \approx 5\cdot10^5$ m/s, i_{sat} >100 mA)

P_{in} (mW)	i_{RF} (mA)	dW/dt 10^5 (m/s)	η	R_s (Ω)	a
2	18	3.6	7.2	12	–
10	39	6.6	17.9	12	–
2	17	3.6	6.9	R(i)	$1.53\cdot10^9$
10	31	5.1	6.8	R(i)	$1.53\cdot10^9$

A limitation of these devices as the are currently made is that they start conducting at a finite voltage. Multiplier simulation shows that when the diode is pumped to the extent that the magnitude of the resistive current (as determined from the I-V curve) becomes approximately equal to the magnitude of the capacitive current, the efficiency of the multiplier is deteriorated. This limitation can be overcome by using a number of diode in series. It should be possible to make an epitaxial layer with a stack of e. g. four diodes in series. If each is 7500 Å thick, a stack of four results in an epitaxial layer of 3 μm. Such a diode offers several advantages:

i. The area can be made n times larger for a given impedance, where n is the number of stacked barriers.

ii. The influence of the ohmic contact will become n times less important due to the larger area.

iii. The worries about current saturation and the depletion edge speed will be considerably relaxed since for constant power the current density goes down with the number of series diodes (area), leading to higher efficiency.

iv. The lower current density or drive voltage per series diode will allow using low bandgap materials such as InAs, yielding still lower series resistance and higher cut-off frequencies.

Mixers.

Most likely GaAs Schottky barrier diode mixers will also experience current saturation. An analysis of a 600 GHz mixer using a 1 μm diameter diode with a driving power of 1 mW shows diode currents that exceed $i_{e,max}$ with a factor of 6 (private communication with Dr. I. Mehdi).

6. Suggestions for Future Research.

We have identified a serious limitation of semiconductor multipliers using a voltage variable depletion region to generate reactive multiplication when operating at high frequencies and/or high input power levels. This arises from the saturation of electron velocity in the semiconductor. To date most varactors have been fabricated from GaAs which exhibits a saturation velocity of about 2-$3 \cdot 10^5$ m/s. Other semiconductors, such as InAs have higher saturation velocities and may provide a more optimum material for the varactors. However, other parameters affect varactor performance as well. In particular, the break-down voltage of the device is critical. More studies are needed to determine the relative tradeoff of these effects in the GaAs and the InAs materials systems. In addition, different varactor architectures, which reduce the impact of the current saturation may be available, such as forming a series stack of single barrier varactors.

Acknowledgements.

We would like to acknowledge valuable discussions with Neal Erickson during the course of this study. E. Kollberg would like to thank Caltech and Prof D. Rutledge, who made it possible for him to spend six months in Pasadena. The research described in this paper was performed, in part, by the Center for Space Microelectronics Technology, Jet Propulsion Laboratory, California Institute of Technology and was sponsored by the National Aeronautics and Space Administration, Office of Aeronautics, Exploration, and Technology.

7. References.

1. P. H. Siegel, A. R. Kerr and W. Hwang, "Topics in the optimization of Millimeter Wave Mixers," NASA Technical Paper 2287, March 1984

2. J. W. Archer, "Multipliers and Parametric Devices," *Handbook of Microwave and Optical Components, Vol. 2*, editor Kai Chang, Wiley, New York, 1990.

3. E. Bava, G. P. Bava, A. Godone, and G. Rietto, "Analysis of Schottky-Barrier Millimetric Varactor Diodes," IEEE Trans. of Microwave Theory and Techniques, Vol. MTT-29, pp. 1145-1149, 1981.

4. T. Crowe, "GaAs Schottky Barrier Mixer Diodes for the Frequency Range 1-10 THz," Int. J. Infrared and Millimeter Waves, Vol. 10, No. 7, pp. 765-777, 1989.

5. N. Erickson, "High Efficiency Submillimeter Frequency Multipliers", 1990 IEEE MTT-S International Microwave Symposium Digest, Vol III, pp. 1301-1304, 1990.

6. S. M. Sze, "Physics of Semiconductor Devices", Wiley, New York, 1981

7. P.A. Blakey, B. Culshaw and R.A. Giblin, "The flat field approximation - A model for the drift region in high-efficiency GaAs IMPATT's", IEEE Journal of Solid State and Electron Devices, vol. 1, pp. 57-61, Jan. 1977.

8. H. Statz, H.A. Haus and R.A. Pucel, "Large-signal dynamic loss in gallium arsenide Read avalanche diodes", IEEE Trans. on Electron Devices, vol. ED-25, pp. 22-23, Jan. 1978.

9. A. Raisanen and M. Sironen, "Capability od Schottky Diode Multipliers as Local Oscillators at 1 THz," Conference Proceedings for First International Symposium on Space Terahertz Technology, pp.293-303, Mar 1990.

10. R. O. Grondin, P. A. Blakey and J. R. East, "Effects of Transient Carrier Transport in Millimeter-Wave GaAs Diodes," IEEE Trans. on Electron Devices, vol. ED-31, pp. 21-28, 1984.

11. H. Gronqvist, E. Kollberg, A. Rydberg, "Quantum Well and Quantum Barrier Diodes for Generating Sub-Millimeter Wave Power," Optical and Microwave Techn. Lett., Jan. 1991.

GaAs Schottky Diodes for Mixing Applications Beyond 1 THz †

Thomas W. Crowe and W.C.B. Peatman

Semiconductor Device Laboratory
Department of Electrical Engineering
University of Virginia
Charlottesville, VA 22903

ABSTRACT

In the frequency range from about 600 GHz to over 3 THz, GaAs Schottky barrier diodes are the most sensitive mixer element for use in heterodyne receivers. Although there is hope that superconductor-insulator-superconductor (SIS) junctions will soon replace semiconductor diodes over all, or part, of this frequency range, there are many technological challenges, and perhaps fundamental problems, that must be overcome before this can be achieved. Since there are many scientific research programs that require receivers in this frequency range, and a variety of NASA missions are planned for the near future, it is imperative that the performance and reliability of GaAs diodes be increased to the highest level possible. This paper reviews the performance of heterodyne receivers in this frequency range, discusses qualitatively how the mixer diode limits the receiver performance, considers potential improvements to receiver performance, and overviews research at the University of Virginia. The paper begins with a very brief overview of the previous research that has lead to the present Schottky technology.

I. BACKGROUND

A great deal of research has been necessary to bring GaAs Schottky technology to the point where it is suitable for use in THz receiver applications. Although it is beyond the scope of this paper to outline this research in detail, it is helpful to acknowledge several of the major milestones. The first such milestone was the initial development of the "honeycomb" Schottky diode by Young and Irvin in 1965 [1]. This work used modern photolithographic technology to

† *This work has been supported by the National Science Foundation under contract ECS-8720850, the Jet Propulsion Laboratory, and the U.S. Army.*

define the metal-semiconductor junction in a reproducible and controlled manner. Their basic chip design, shown in Fig. 1, is still in use today, mainly because the whisker contact adds minimal series resistance and shunt capacitance to the diode circuit. In addition, microwave engineers have used the whisker to couple the high-frequency radiation into the diode, and have even used the whisker inductance to tune out part of the shunt capacitance.

Once the basic chip design of Young and Irvin was recognized as a suitable structure for high-frequency receivers, many groups began investigations to determine the optimum design for the GaAs epitaxial layers and to improve the fabrication technologies. Major contributions to this work were made by over a dozen research teams including those at Bell Labs, MIT, University College in Ireland, Chalmers University in Sweden, and the University of Virginia. Theoretical research has resulted in a great advance in the understanding of electronic conduction in the diode, including the effect of electron tunneling on the IV curve [2] and the increase in series resistance due to the skin effect [3] and plasma resonance [4]. The generation of noise in the diode was intensively studied by many groups, culminating in the *Unified Noise Theory* of Viola and Mattauch [5], which was later extended to include the so called hot-electron noise [6]. Modern fabrication technology allowed the reduction of the anode size and vastly improved control of the thickness and doping concentration of the epitaxial layer, reducing junction capacitance and series resistance. The fabrication of highly reliable metal-semiconductor

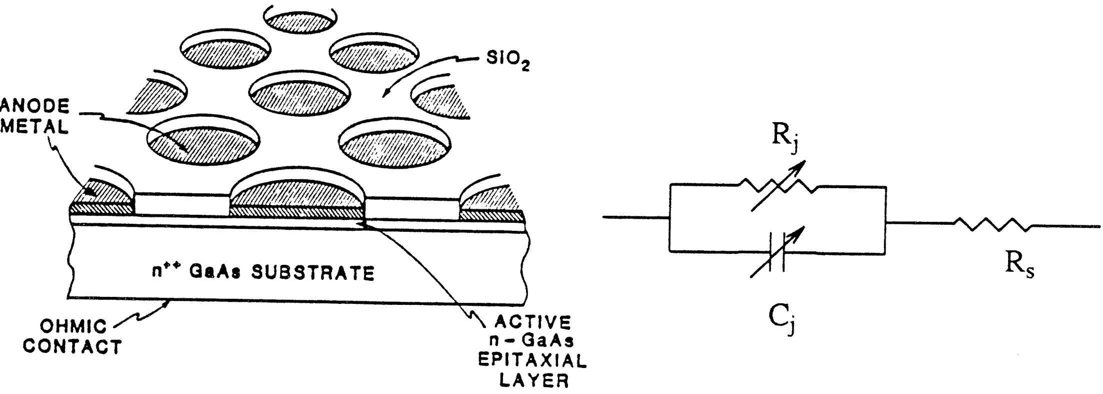

Fig. 1. A cross-section view of a typical Schottky diode chip and an equivalent circuit.

interfaces was seen as a major prerequisite to the fabrication of devices without excess noise, and many papers were written on this subject [7,8,9,10].

Research by Kerr and his colleagues lead to the development of a powerful computer program that predicts the performance of a heterodyne receiver once the fundamental properties of the mixer element and the RF circuit are known [11,12]. This analysis is used not only by receiver designers, but also by device designers, in an effort to understand how to optimize the mixer element for higher frequencies. The program has since been extended to incorporate greater understanding of the operation of the diodes at THz frequencies [13,14].

The coupling of RF radiation into the diode has always been a problem. The major advance that lead to the first THz receivers was the development of the corner-cube mixer, initially proposed by Kräutle [15]. Although the corner-cube is often maligned for its poor efficiency and difficult use, it remains the best structure for THz Schottky receivers, and minor changes have been made to improve reliability and coupling to the IF amplifier [16,17]. There have been several attempts to develop planar Schottky diodes that eliminate the whisker contact and use integrated antenna structures [18,19,20,21]. However, this work is only now becoming successful at millimeter and long-submillimeter wavelengths.

Molecular gas lasers have been developed as suitable local oscillators for heterodyne receivers throughout the submillimeter wavelength range [22,23]. Although these systems are large, power inefficient, and require excessive maintenance and tuning, lasers are the only sources available that generate sufficient power with low noise and high spectral purity throughout this wavelength range.

The current status of heterodyne receivers employing Schottky diodes is summarized in Table I. The frequency coverage is from 300 GHz through nearly 3 THz. It is clear that the noise temperatures are well above the quantum limit. It is important to ask why this is so and to determine what limits the sensitivity of these receivers.

II. LIMITATIONS TO THE PERFORMANCE OF SCHOTTKY RECEIVERS

A simplified block diagram of a heterodyne receiver is shown in Fig. 2. The receiver noise temperature is essentially determined by the signal losses and the noise generated within the system. The major losses occur between the antenna and the mixer, within the mixer itself, and between the IF amplifier and the mixer. The major sources of noise are the mixer diode, the IF amplifier and thermal noise from passive components. For the purposes of this paper, we will neglect noise and losses from passive components and the receiving antenna.

Table I: Submillimeter Wavelength Performance of Some Whisker Contacted Schottky Barrier Mixer Diodes

ν_{RF} (GHz)	T_{rec}^{SSB} (K)†	ν_{IF} (GHz)	BW_{IF} (GHz)	Temp.(K)	Reference
326	1900	1.4	1	300	Röser, 1986 [17]
460-490	1740	1.45	0.3	20	Keen, 1986 [42]
693	4850	1.4	1	300	Röser, 1986 [17]
800	6300	6.4	1	77	Harris, 1989 [24]
1,963	21,000*	6.7	0.2	77	Boreiko, 1989 [43]
2,520	17,000	1.4	1	300	Röser, 1986 [17]
2,528	31,000*	-	-	77	Betz, 1990 [32]

† *In order to express all of the data in a uniform manner it is assumed that* $T^{SSB} = 2T^{DSB}$ *when the values are quoted as DSB in the references.*

* *Measured on the Kuiper Airborne Observatory.*

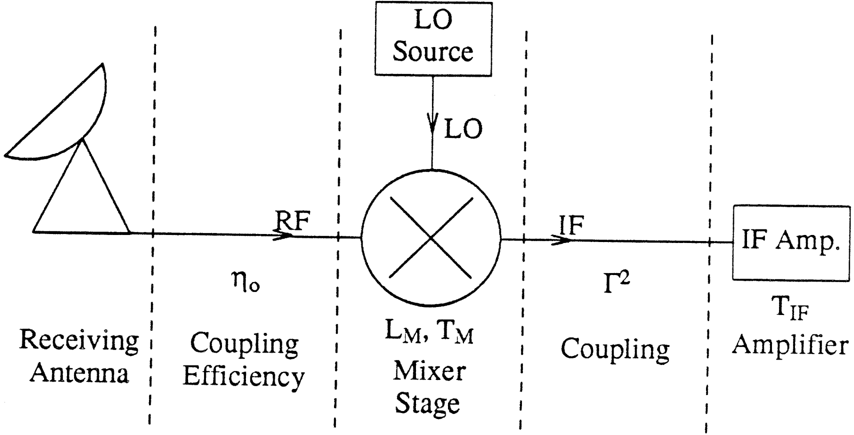

Fig. 2. A simplified block diagram of a typical heterodyne receiver.

To determine the best method to optimize the receiver it is useful to consider the breakdown of receiver noise. A recent paper by Harris [24] has closely analyzed the noise of a Schottky heterodyne receiver at 800 GHz. They have achieved a receiver noise temperature of 6300 K single-sideband †. They express the receiver noise temperature in terms of an effective mixer temperature, T_m', and an effective mixer conversion loss, L_m',

$$T_{rec} = T_M' + L_M' T_{IF} \tag{1}$$

where T_{IF} is the noise temperature of the IF amplifier. The effective mixer noise temperature and conversion loss are defined as

$$T_M' = L_M' \Gamma^2 T_{t,RJ} + \frac{L_o T_M}{\eta_o} \tag{2}$$

$$L_M' = \frac{L_o L_M}{\eta_o (1-\Gamma^2)} \tag{3}$$

where

η_o is the RF coupling loss due to the corner-cube antenna efficiency, 0.5
L_o is the matched optical resistive loss factor, 0.86
Γ^2 is the mismatch reflection coefficient between the mixer and the IF amplifier, 0.25
$T_{t,RJ}$ is the effective Rayleigh-Jeans temperature of the isolator used between the mixer and the IF amplifier, 58K

and L_M and T_M are the true mixer conversion loss and noise temperature. The mixer noise temperature is caused by the noise generated in the diode, but is also a function of the losses in the mixer [25],

$$T_M = (L_M - 2) T_{D,eff} \tag{4}$$

where $T_{D,eff}$ is the effective diode noise temperature at the IF while the diode is dc biased and pumped by the LO. This is a function of both the shot and hot-electron noise in the diode. The calculated value of $T_{D,eff}$ for this case is 630K. At millimeter wavelengths, values as low as 50K have been reported [26]. However, it will be shown below that such a low value cannot be achieved at THz frequencies.

† In this paper we will use single-sideband noise temperatures and conversion losses. All double-sideband values taken from the literature are converted to single-sideband by multiplying by two.

Table II shows how the receiver noise can be reduced by improving the various system parameters. We have tried to assume optimum values that do not violate any fundamental principles, but it is by no means clear that such values can actually be achieved. This table indicates that T_{IF} and Γ^2 have only a small effect, while the other terms are considerably more important. The mixer conversion loss is the product of two distinct terms which are not separable by this type of empirical analysis. These are the actual loss incurred in the mixing process, $L_{M,d}$, and the losses incurred due to the impedance mismatch between the diode and its antenna at the signal frequency, $L_{M,c}$. The assumed ideal value ($L_M=2$) is the best that can be achieved with a real, resistive mixer with zero coupling loss [25].

III. OPTIMIZATION OF SCHOTTKY DIODES FOR THz FREQUENCIES

The three terms that contribute most to the receiver noise temperature are the efficiency of the corner-cube antenna, the mixer conversion loss, and the diode noise. In this section we will consider the possible reduction of each of these terms.

A. Diode Noise

To discuss the reduction of $T_{D,eff}$, we will consider two very successful diodes, whose parameters are shown in Table III. The 2P9 has achieved shot-noise-limited performance at millimeter wavelengths [26] and the 1E7 has been very successful at frequencies near 1 THz. The 1E7 is also the same diode used by Harris [24]. Fig. 3 shows the noise temperature of these diodes as a function of dc current at 1.4 GHz. At low currents, the junction impedance is much

Table II: Contribution to the Noise of a Schottky Receiver at 800 GHz

Parameter	L_M^{SSB}	η_o	Γ^2	$T_{D,eff}$(K)	T_{IF}(K)
Estimated Value	7.1	0.5	0.25	630	36
Assumed ideal value	2	1	0	100	1
ΔT_{rec} (K)	-6090	-3150	-382	-4690	-584

Table III: Comparison of Two Schottky Diodes

Batch	Diameter (μm)	doping (cm^{-3})	R_s (Ω)	C_{jo} (fF)	ΔV (mV)	ν_{co} (THz)
2P9	2.5	$3x10^{16}$	12	6.5	66	2
1E7	0.8	$2x10^{17}$	12	1.4	73	9

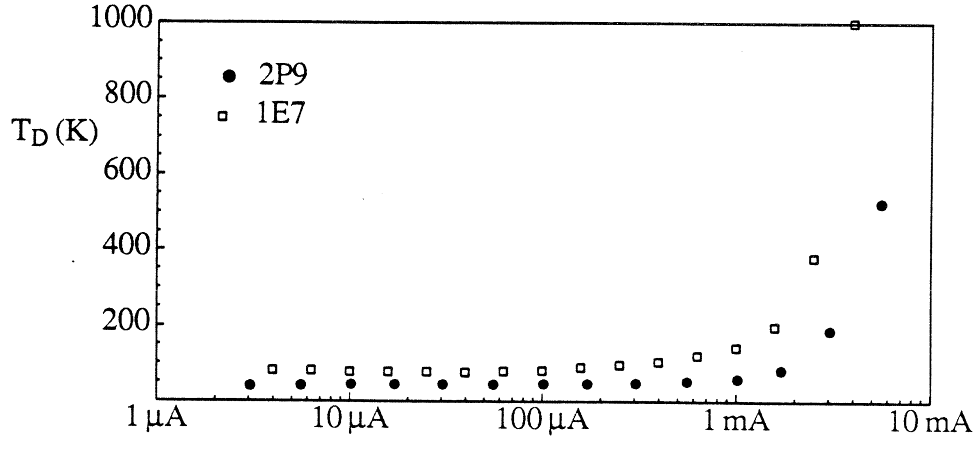

Fig. 3. The equivalent noise temperature of two Schottky diodes as a function of dc current. The noise was measured at 1.4 GHz with a noise reflectometer

larger than the series impedance of the diode and the junction shot-noise dominates, yielding a nearly constant noise temperature [5]. As the current is increased the junction resistance is decreased exponentially and the series resistance becomes significant. Also, the electron distribution in the series resistance becomes heated, causing a rapid increase in the diode noise temperature, the so called hot-electron noise [6]. Clearly, it would be beneficial for receiver performance if the diode could be used in such a manner that the current never approached the range where the hot-electron noise becomes significant. The 2P9 diode has achieved this goal at 100 GHz, and the result is shot-noise-limited performance with $T_{D,eff}=50$ K [25].

If the 2P9 diode is used at significantly higher frequencies, the junction capacitance will short the junction resistance over a larger current range, forcing the higher current portion of the diode IV curve to be used for mixing. This will cause the hot-electron noise to have a greater

effect and $T_{D,eff}$ will increase. Although, we can make the diode area smaller, thereby reducing the junction capacitance, this will also increase the series resistance, making the hot-electron noise turn-on at a lower current level. The only way to achieve shot-noise-limited performance at higher frequencies is to increase the doping density in the epitaxial layer, thereby reducing the $R_s C_{jo}$ product [27]. Comparing the 1E7 diode to the 2P9, the epilayer doping density is increased by roughly an order of magnitude. This has reduced the $R_s C_{jo}$ product by a factor of about five, but has also increased the shot-noise, as seen in Fig. 3. This is directly attributed to increased tunneling current caused by the higher doping density [2]. However, since Harris reports $T_{D,eff} = 630\,K$, the doping density of the 1E7 must be increased to an even higher level, if shot-noise-limited performance is to be achieved at 800 GHz. To summarize, as the frequency increases, the doping density must be increased to reduce the $R_s C_{jo}$ product. This causes the shot-noise to increase, so that even though shot-noise-limited performance is achieved, the receiver noise temperature increases with frequency.

Mixer Conversion Loss

From the above argument, it is clear that to increase the cut-off frequency the epilayer doping density must be increased. The choice of the anode diameter has only a secondary effect on the cut-off frequency, but a major impact on the coupling between the diode and its antenna. The impedance of the corner-cube antenna as seen by the diode is roughly 145 Ω [28]. As the frequency is increased, the effect of the junction capacitance becomes more pronounced and the total diode impedance is reduced, making coupling to the corner-cube more difficult. For example, we would like to bias the diode and adjust the LO power so that the small-signal junction resistance is nearly 145 Ω. However, at 1 THz a 2 fF junction capacitance would have an impedance of only j80, effectively shunting the junction resistance. Thus, the junction capacitance must be reduced.

The 1E7 diode has a much smaller anode than the 2P9, and therefore its capacitance is smaller. As can be seen from Fig. 3, this also causes the hot-electron noise to turn-on at a lower current. However, since the lower capacitance allows the diode to be used at lower voltages, this is not a problem and the increased small-signal junction impedance will improve coupling to the antenna. However, the capacitance of the 1E7 is still large enough to cause a substantial amount of signal power to be shorted around the junction, particularly when we acknowledge that the junction capacitance at forward bias is substantially larger than the zero-bias value. Therefore, it is expected that the diode conversion loss will be reduced by a further reduction in anode diameter.

For each frequency there is an optimum anode diameter - epitaxial layer doping pair. Typically, the determination of these values has been achieved empirically, although it is clear that the trends at higher frequency must be smaller anodes and higher doping. This optimization is particularly challenging at THz frequencies, where effects such as charge carrier inertia, dielectric relaxation, and the skin effect become significant, and diode design is limited by the fabrication technology. Although modern electron-beam lithography has been used by industry to fabricate tenth micron lines, high-quality Schottky diodes have only been fabricated with anode diameters as small as 0.4 microns [29].

Antenna Efficiency

The corner-cube mixer has only about 50% antenna efficiency, causing the receiver noise temperature to be about a factor of two higher than would be possible with ideal coupling. Although this is quite poor in comparison to waveguide mixers, it is still the best that is commonly achieved at THz frequencies. Since planar Schottky diodes are now available, it would seem that the integration of an optimized planar diode with a high efficiency planar antenna should lead to significant improvement. Also, such an integrated structure could easily evolve into an array technology that would significantly reduce observing time. Part of the reason that

this has not yet been achieved is a lack of close interaction between the device and RF researchers. Hopefully, this situation will be overcome in the near future.

Potential Receiver Performance at 800 GHz

If we assume the breakdown of noise contributions in the 800 GHz receiver described by Harris [24], it should be possible to design a diode that will significantly improve performance. The goal of this sub-section is to make reasonable assumptions about how the diode can be improved and predict a possible receiver noise temperature. The 1E7 diode has a shot-noise temperature of less than 100 K, but an effective noise temperature of 630 K, implying that the hot-electron noise is having a great impact. This can be alleviated by significantly increasing the epitaxial layer doping density. Although this will increase the shot-noise temperature, the elimination of the hot-electron noise will be more significant. If we assume the new diode has an ideality factor of 1.5 at room temperature (a reasonable guess for high doping density), the shot-noise temperature will be roughly 225K [5]. Assuming shot-noise-limited performance yields $T_{D,eff}=225$ K, which will reduce the receiver temperature to 2800 K (SSB).

The next improvement should come in the mixer conversion loss, which is estimated to be 7.1 (8.5 dB). The increase in doping, mentioned above, should increase the cutoff frequency, thereby improving $L_{M,d}$. Also, if the anode diameter is reduced sufficiently the coupling between the diode and the corner-cube antenna should also be improved, reducing $L_{M,c}$. Although it seems reasonable that L_M can be reduced, it is difficult to estimate how much. For the sake of this discussion, a value of $L_M=6$ is assumed. In combination with the reduction of $T_{D,eff}$, this yields a receiver temperature of 2,244 K (SSB).

The final significant improvement is in the antenna efficiency. It is doubtful that the corner-cube efficiency can be significantly improved. However, if we assume that a planar diode can be developed with an integrated planar antenna, it is possible that a large improvement may be possible [30]. If we assume an efficiency of 75%, the receiver temperature is reduced to 1500

K (SSB). This is a factor of four better than the present value and is roughly 40 hv / k. Although, a significant amount of work is necessary before this is achieved, none of the assumptions are unreasonable and we consider these proposed improvements to represent our design goals.

IV. RESEARCH AT THE UNIVERSITY OF VIRGINIA

The University of Virginia Semiconductor Device Laboratory is involved in the research of GaAs Schottky diodes for THz applications. This includes theoretical evaluation of device operation, design of optimized diodes for high-frequency applications, research of fabrication technologies for improved devices, and the fabrication and evaluation of prototype diodes. Presently, these prototype devices are in use around the world for a variety of applications, with radio astronomy being the most common. In this section several of the individual research projects are outlined.

Theoretical Analysis of THZ conduction in the GaAs Substrate

A computer program that determines the electromagnetic fields in the diode chip and performs a very accurate calculation of the diode series impedance has been developed [31]. This is the first such analysis that accurately incorporates all of the known phenomena at THz frequencies, including skin effect, charge carrier inertia, dielectric relaxation and the distributed nature of the series impedance. It is also the first analysis to accurately consider real diode structures that have nonideal ohmic contacts and epitaxial layers of lower doping than the substrate. This has led to proposed diode designs that are optimized for frequencies as high as 5 THz, shown in Table IV.

We have used a mixer analysis program [11,12] to evaluate mixer performance to frequencies as high as 1 THz. This was made possible by the extension of the diode noise model to include the correlated components of the diode's hot-electron noise [14]. We are presently working to improve the diode model to include the accurate analysis of the high-frequency series

Table IV. Optimized Schottky Diodes for THz Operation

frequency	1 THz	3 THz	5 THz
anode diameter	0.50 µm	0.20 µm	0.15 µm
epilayer thickness	0.046 µm	0.033 µm	zero
epilayer doping	1.0×10^{18} cm^{-3}	2.0×10^{18} cm^{-3}	-
R_s	15.3 Ω	35.7 Ω	40.8 Ω
X_s	9.9 Ω	53.1 Ω	82.0 Ω
C_{jo}	0.74 fF	0.19 fF	0.16 fF
f_{co}	14 THz	23 THz	25 THz

resistance. This should extend the useful range of the mixer analysis program to at least 5 THz and should greatly facilitate diode optimization.

Fabrication of Whisker Contacted Diodes

We have performed extensive research on the fabrication of prototype diodes for experimental evaluation and use in scientific applications. We have fabricated diodes with anode diameters as small as 0.4 microns and figure-of-merit cut-off frequencies as high as 15 THz. A summary of the characteristics of several recent diode batches is given in Table V. These diodes have lead to consistently decreasing noise temperatures throughout the 1-3 THz range [32]. Also, these new diodes have had the added benefit of requiring less LO power than previous diodes[33]. The reduced LO power requirement is achieved because the smaller anode diameter improves the coupling of both the signal and the LO from the corner-cube antenna to the diode. This work is continuing with the goal of fabricating the diodes described in Table IV. We are also developing a fabrication technology for membrane diodes that will eliminate the skin effect component of the substrate resistance, significantly increasing the cut-off frequency.

Fabrication of Planar Diodes

The Semiconductor Device Laboratory is vigorously pursuing research of planar diode structures that are leading to the replacement of whisker contacted diodes [34,35,36,37].

Scanning electron micrographs of two recent diode chips are shown in Fig. 4 and characteristics of several recent batches are given in Table V. We have fabricated single anode diode chips that are competitive with whisker contacted diodes at millimeter wavelengths [35]. We have also recently developed a dual-diode chip structure which integrates an anti-parallel pair of anodes. This yields an anti-symmetric IV characteristic, which is ideal for subharmonically pumped mixing. This device has yielded excellent results at 183 GHz [37] and is being scaled to 640 GHz for use in a radiometer for the Eos Microwave Limb Sounder.

Investigation of Varactor Diodes

We have also begun to focus attention on varactor diodes. These diodes are used to multiply the output from a solid-state source, typically a Gunn diode, to a higher frequency. The goal is to achieve sufficient power for use as local oscillator sources through the submillimeter wavelength range, replacing the molecular gas laser with a reliable, light weight, and cost effective solid-state source. Standard varactors have been developed that have generated suitable amounts of power up to 600 GHz [38,39]. A novel δ-doped diode has been developed to increase the sharpness of the diode capacitance-voltage characteristic [40]. This will increase the efficiency of high-frequency multipliers when the available input power is small. Our first planar varactor diodes have also been fabricated. These have generated milliwatt power in a tripler to 275 GHz with encouraging efficiency [41]. This work will be expanded in the near future to consider series arrays of varactors to increase power handling ability and novel varactor structures.

V. SUMMARY AND FUTURE WORK

A great deal of work by many researchers has led to the development of heterodyne receivers based on GaAs Schottky diodes that are suitable for use throughout the submillimeter wavelength range. Although Schottky receivers will not approach the quantum noise limit, this is the most sensitive technology throughout most of this frequency range. Thus, it is important to consider methods to improve the performance of these receivers.

Table V: Recent Diode Batches

Whisker Contacted Diodes for THz Frequencies

Batch	Diameter (µm)	doping (cm^{-3})	R_s (Ω)	C_{jo} (fF)	ΔV (mV)	V_{br} (V)	ν_{co} (THz)
1T9	0.9	$2x10^{17}$	11-12	1.4	71-72	>5.5	10
1T11	0.4	$4x10^{17}$	25±5	0.4-0.5	80±1	>4	14
1T12	0.5	$4x10^{17}$	25±5	0.45-0.55	79±1	>4.5	13

Recent Planar Diode Batches

Batch	Diameter (µm)	doping (cm^{-3})	R_s (Ω)	C_{jo} (fF)	ΔV (mV)	V_{br} (V)	C_T (fF)
SC2R4	2.5	$2x10^{17}$	5.5	6	70	5-6	10
SQ2S1	2.5	$3x10^{17}$	3	8	72	5-6	5
SC2T1	1.5	$2x10^{17}$	10	3	72	6	10
SD2T3	1.5	$2x10^{17}$	7.4	4.5	72	6	19
SR2T1	1.2	$2x10^{17}$	6.3	3.0	72	4	9.5
SD1T1 *	<1.2	$2x10^{17}$	11	-	73	6.5	-
SD1T2 *	<1.2	$2x10^{17}$	12.5	-	73	-	-

** Denotes preliminary data.*

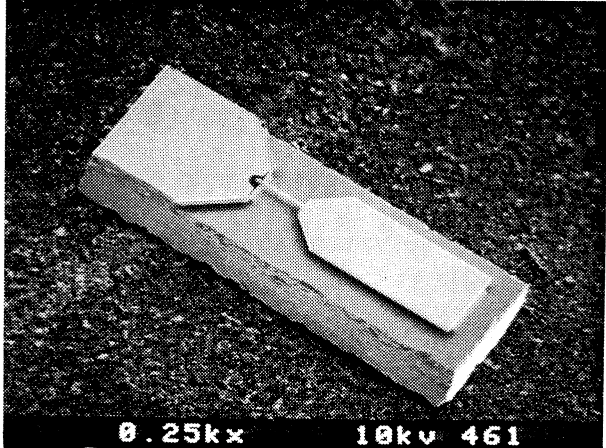

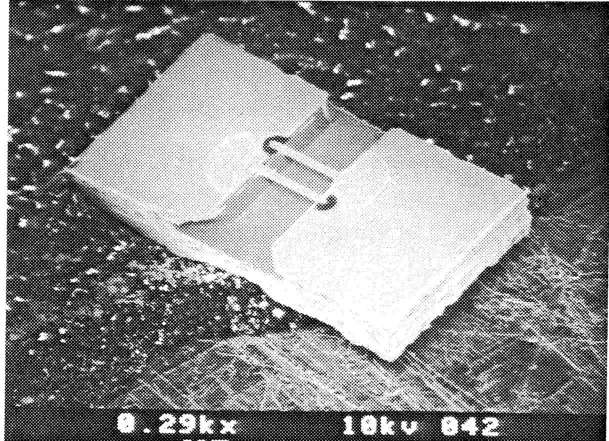

Fig. 4. *Scanning electron micrographs of a planar diode (SC2T1) with junction capacitance of only 3 fF and total capacitance of 13 fF (left) and a dual-anode diode chip (SD2T3) for subharmonic mixing (right).*

Our research goals for the continued improvement of Schottky diodes at THz frequencies are as follows:

1) Fabricate diodes following the design rules given in Table IV for 1-5 THz. This requires anode diameters as small as 0.15 micron.
2) Fabricate diodes that are shot-noise-limited to as high a frequency as possible. This will be achieved first in the 600 - 800 GHz range, and then at higher frequencies.
3) Continue to investigate the RF coupling between the diode and the corner-cube antenna and develop methods to improve the coupling where possible. This can be achieved either by increasing the impedance of the diode or reducing the impedance of the antenna.
4) Develop planar diodes for THz applications. This will involve research of novel fabrication technologies and integrated antennas.

Through work in these four areas we will continue to increase the sensitivity of heterodyne receivers. A proposed set of goals should result in a single-sideband receiver temperature of 1500 K at 800 GHz (approximately 40 $h\nu/k$). Similar improvements should be expected at higher frequencies, provided suitable fabrication technology can be developed.

VI. REFERENCES

[1] D.T. Young and J.C. Irvin, "Millimeter Frequency Conversion Using Au-n-Type GaAs Schottky Barrier Epitaxial Diodes with a Novel Contacting Technique," Proceedings of the IEEE, pp. 2130-2131, Dec. 1965.

[2] F.A. Padovani and R. Stratton, Field and Thermionic-Field Emission in Schottky Barrier Diodes," Solid-State Electron., Vol. 9, pp. 695-707, 1966.

[3] L.E. Dickens, "Spreading Resistance as a Function of Frequency," IEEE Trans. Microwave Theory Tech., Vol. MTT-15, No. 2, pp. 101-109, 1967.

[4] K.S. Champlin and G. Eisenstein, "Cutoff Frequency of Submillimeter Schottky-Barrier Diodes," IEEE Trans. Microwave Theory Tech., Vol. MTT-26, No. 1, pp. 31-34, 1978.

[5] T.J. Viola and R.J. Mattauch, "Unified Theory of High-Frequency Noise in Schottky Barrier Diodes,"J. Appl. Phys., Vol. 44, pp. 2805-2808, June 1973.

[6] H. Zirath, "High-Frequency Noise and Current-Voltage of Millimeter Wave Platinum n-n^+ GaAs Schottky Barrier Diodes," J. Appl. Phys., Vol. 60, No. 4, pp. 1399-1407, 1986.

[7] M.V. Schneider, "Metal-Semiconductor Junctions as Frequency Convertors," in *Infrared and Millimeter Waves,* Vol. 6, K. Button, Ed., New York: Academic Press, pp. 226-229, 1982.

[8] M.V. Schneider, A.Y. Cho, E. Kollberg and H. Zirath, "Characteristics of Schottky Diodes with Microcluster Interface," Appl. Phys. Lett., Vol. 43, pp. 558-560, 1983.

[9] G.K. Sherrill, R.J. Mattauch, and T.W. Crowe, "Interfacial Stress and Excess Noise in Schottky Barrier Mixer Diodes," IEEE Trans. Microwave Theory Tech., Vol. MTT-34, No. 3, pp. 342-345, March 1986.

[10] K.M. Kattmann, T.W. Crowe, and R.J. Mattauch, "Noise Reduction in GaAs Schottky Barrier Mixer Diodes," IEEE Trans. Microwave Theory Tech., Vol. MTT-35, No. 2, pp.

212-214, Feb. 1987.

[11] D.N. Held and A.R. Kerr, "Conversion Loss and Noise of Microwave and Millimeter-Wave Mixers: Part 1 - Theory, and Part 2 - Experiment," IEEE Trans. Microwave Theory Tech., Vol. MTT-26, Feb. 1978.

[12] P.H. Siegel and A.R. Kerr, "The Measured and Computed Performance of a 140-220 GHz Schottky Diode Mixer," IEEE Trans. Microwave Theory Tech., Vol. MTT-32, pp. 1579-1590, Dec. 1984.

[13] G. Hegazi, A. Jelenski, and S. Yngvesson, "Limitations of Microwave and Millimeter-Wave Mixers Due to Excess Noise," IEEE Trans. Microwave Theory Tech., Vol. MTT-33, pp. 1404-1409, Dec. 1985.

[14] T.W. Crowe and R.J. Mattauch, "Analysis and Optimization of Millimeter- and Submillimeter-Wavelength Mixer Diodes," IEEE Trans. Microwave Theory Tech., Vol. MTT-35, Vol. 2, pp. 159-168, Feb. 1987.

[15] H. Kräutle, E. Sauter and G.V. Schultz, "Antenna Characteristics of Whisker Diodes Used as Submillimeter Receivers," Infrared Physics, Vol. 17, p. 477, (1977).

[16] J. Zmuidzinas, A.L. Betz, and R.T. Boreiko, "A Corner-Reflector Mixer Mount for Far Infrared Wavelengths," Infrared Phys., Vol. 29, No. 1, pp. 119-131, (1989)

[17] H.P. Röser, R. Wattenbach, E.J. Durwen, and G.V. Schultz, "A High Resolution Spectrometer for 100 μm to 1000 μm and Detection of CO (J=7-6), CO (J=6-5) and ^{13}CO (J=3-2)," Astron. Astrophys., 165, 287-299, (1986).

[18] J.A. Calviello, J.L. Wallace, P.R. Bie, "High-Performance GaAs Beam-Lead Mixer Diodes for Millimetre and Submillimetre Applications," Electronics Letts., Vol. 15, No. 17, pp. 509-510, Aug. 1979.

[19] B.J. Clifton, G.D. Alley, R.A. Murphy, and I.H. Mroczkowski, "High-Performance Quasi-Optical GaAs Monolithic Mixer at 110 GHz," IEEE Trans. Elec. Dev., Vol. ED-28, No. 2, pp. 155-157, Feb. 1981.

[20] J.L. Heaton, W. Fabian, and F. Spooner, "High-Performance Millimetre-Wave Mixer Diodes Fabricated Using A Deep Mesa Etch Approach," Electronics Letts., Vol. 19, No. 19, pp. 749-750, Sept. 1983.

[21] B.J. Clifton and R.A. Murphy, "Surface-Oriented Schottky-Barrier Diodes for Millimeter and Submillimeter Wave Applications," Tech. Dig. IEDM, pp. 124-129, 1978.

[22] D.T. Hodges and T.S. Hartwick, "Waveguide Laser for the Far-Infrared Pumped by a CO_2 Laser," Appl. Phys. Lett., Vol. 23, No. 5, 1973.

[23] R. Densing, P.B. van der Wal, D. Galleguillos, H.P. Röser, and R. Wattenbach, "Investigation of a Compact Laser System for the Frequency Range 300 - 3000 GHz," SPIE Vol. 598 *Instrumentation for Submillimeter Spectroscopy, 1985.*

[24] A.I. Harris, J. Stutzki, U.U. Graf, and R. Genzel, "Measured Mixer Noise Temperature and Conversion Loss of a Cryogenic Schottky Diode Mixer Near 800 GHz," Intl. J. Infrared and Millimeter Waves, Vol. 10, No. 11, Nov. 1989.

[25] S. Weinreb and A.R. Kerr, "Cryogenic Cooling of Mixers for Millimeter and Submillimeter Wavelengths," IEEE J. Solid State Circuits, Vol. SC-8, pp. 58-63, Feb. 1973.

[26] C.R. Predmore, A.R. Räisänen, N.R. Erickson, P.F. Goldsmith, and J.L.R. Marrero, "A Broad-Band, Ultra-Low-Noise Schottky Diode Mixer Receiver for 80 to 115 GHz," IEEE Trans. Microwave Theory Tech., Vol. MTT-32, pp. 498-506, May 1984.

[27] T.W. Crowe, "GaAs Schottky Barrier Mixer Diodes for the Frequency Range from 1 - 10 THz," International Jour. Infrared and Millimeter Waves, Vol. 10, No. 7, July 1989.

[28] E.N. Grossman, "The Performance of Schottky Diodes as Far-Infrared Modulators," Int. J. Infrared and Millimeter Waves, Vol. 8, No. 10, pp. 1293-1312, (1987).

[29] W.C.B. Peatman and T.W. Crowe, "Design and Fabrication of 0.5 micron GaAs Schottky Barrier Diodes for Low-Noise Terahertz Receiver Applications," *Int. Journal on Infrared*

and Millimeter Waves, Vol. 11, No. 3, 1990, pp. 355-365.

[30] S.S. Gearhardt, C.C. Ling, G.M. Rebeiz, "Intergrated Millimeter-Wave Corner-Cube Antennas," accepted for publication, IEEE Trans. Antennas and Prop., 1991.

[31] U.V. Bhapkar, "An Investigation of the Series Impedance of GaAs Schottky Barrier Diodes," M.S. Thesis, University of Virginia, May 1990, pp. 99-101.

[32] A.L. Betz and R.T. Boreiko, "Far-Infrared Heterodyne Technology," Proceedings of the 29th Liege International Astrophysical Colloquium "From Ground-Based to Space-Borne Submillimeter Astronomy," Liege, Belgium, July, 1990.

[33] R.U. Titz, H.P. Röser, G.W. Schwaab, T.W. Crowe, W.C.B. Peatman, M. Crawford, J. Neilson, J. Prince, P. Wood, H. Alius, G. Dodel, "Investigation of GaAs Schottky Barrier Diodes in the Frequency Range from 1-3 THz," Int. J. IR & MM Waves, Vol. 11, No. 7, July 1990.

[34] W.L. Bishop, K. McKinney, R.J. Mattauch, T.W. Crowe and G. Green, "A Novel Whiskerless Schottky Diode for Millimeter and Submillimeter Wave Applications," Proc. 1987 IEEE MTT-S Intl. Symp., Las Vegas, NV, 607-610, June 1987.

[35] D.G. Garfield, R.J. Mattauch, and S. Weinreb, "RF Performance of a Novel Millimeter-Wave Diode Incorporating an Etched Surface Channel," IEEE Trans. Microwave Theory Tech., Vol. MTT-39, No. 1, pp. 1-5, Jan. 1991.

[36] W.L. Bishop, T.W. Crowe, R.J. Mattauch and P.H. Ostdiek, "Planar Schottky Barrier Mixer Diodes for Space Applications at Submillimeter Wavelengths," Microwave and Optical Technology Lett., Special Issue on Space THz Tech., Vol. 3, No. 1, pp. 44-49, Jan. 1991.

[37] P.H. Ostdiek, T.W. Crowe, and I. Galin "Integration of an Anti-parallel Pair of Schottky Barrier Diodes in Millimeter Wave Mixers" The Digest of the 15th International Conference on Infrared and Millimeter Waves, pp. 401-402, Orlando, Dec. 1990.

[38] N. Erickson, "High Efficiency Submillimeter Frequency Multipliers," The Digest of the 1990 IEEE MTT-S Intl. Microwave Symp., Dallas, TX, pp. 1301-1304, May 1990.

[39] A. Räisänen, "Capability of Schottky Diode Multipliers as Local Oscillators at 1 THz," First International Symposium on Space Terahertz Tech., Ann Arbor, MI., March 1990.

[40] B.J. Rizzi, T.W. Crowe, and W.C.B. Peatman, "A δ-Doped Varactor Diode for Submillimeter Wavelengths," The Digest of the 15th International Conference on Infrared and Millimeter Waves, pp. 478-480, Orlando, Dec. 1990.

[41] H. Dossal, "Planar GaAs Varactor Diodes for Millimeter and Submillimeter Wavelengths," Master of Science Thesis, University of Virginia, in preparation, May 1991.

[42] N.J. Keen, K.-D. Mischerikow and G.A. Ediss, "Three Facility Low-Noise Receivers for Millimeter and Submillimeter Radio-Astronomy," 16th European Microwave Conf., Dublin, Sept. 1986.

[43] R.T. Boreiko and A.L. Betz, "Heterodyne Spectroscopy of the J=17-16 CO Line in Orion," Astrophys. J., Vol. 337, No. 1, pp. 332-341, Feb 1989.

Millimeter Wave Planar Doped Barrier Detector Diodes

Yogi Anand and Jack Hillson
M/A-COM Inc.,
Burlington, Mass. 01803

Abbas Torabi
Georgia Tech Research Institute
Atlanta, Georgia 30332

Jack East
Dept. of Electrical Engineering and Computer Science
The University of Michigan
Ann Arbor, Michigan 48109

Abstract

Planar Doped Barrier (PDB) diodes are semiconductor devices for high frequency detector and mixer applications. In these devices a thin layer of highly p doped GaAs is sandwiched between two layers of lightly n doped material to produce a potential barrier. The height of this potential barrier as well as the device capacitance can be adjusted by varying the doping density and thickness of the various layers. We are developing millimeter wave "zero bias planar doped barriers" for low level detector (zero bias) and low barrier mixer applications in the frequency range of 30 to 140 GHz. These devices exhibit low level signal sensitivity, (TSS) of −58 dBm (bandwidth = 2 MHz) at Ka band frequencies. The PDB detectors are found to be relatively insensitive to electrostatic discharge. The MBE material growth, device fabrication, RF performance and electrostatic burn out characteristics of the PDB detectors will be discussed in this paper.

1. Introduction

The planar doped barrier is a structure that uses intrinsic layers, ohmic contacts and heavily doped spikes or barriers to produce desired terminal current vs. voltage characteristics. The structure first proposed by Malik et. al. [1] used two intrinsic layers with a p^+ doping spike in the middle to produce an anti-symmetric current vs. voltage characteristics. This type of structure can be used as a single diode subharmonically pumped mixer. Experimental results have been obtained at low frequencies [2] and in W [3] and D bands [4]. A summary of the theory and performance of these subharmonic results is given by Lee et. al. [5]. The doping spike can be offset from the center of the intrinsic region to produce a diode like current vs. voltage characteristic. Since the barrier height is controlled by the structure dimensions and sheet doping levels, and not by a metal-semiconductor barrier height, a range of low barrier height mixer and detector characteristics are possible. Initial work on planar doped barrier detectors was described by Dale et. al. [6]. In this paper we will discuss the design and performance of conventional planar doped barrier detector diodes and then point out the potential advantages of using doped spacer layers in place of the conventional intrinsic ones. The next section of this paper will discuss a model for arbitrary doping layer structures. Section 3 will describe the experimental video detector and burnout performance. The results are summarized in section 4.

2. Planar Doped Barrier Detector Characteristics

A range of models for barrier limited current flow are available. The two extremes for analytic models are thermionic emission models and the diffusion theory. A complete review of the possible models and approximations is given in chapter 5 of Sze [7]. The two models both predict an exponential current current vs. applied voltage characteristic, although the internal assumptions and saturation currents are different.

The thermionic emission model is useful when describing current flow over a barrier, and for a variety of other analytic approximations. The diffusion theory theory is easier to implement in a device simulation where charge redistribution effects and space charge effects are possible. A large signal time dependent version of a device simulation has been modified to study the current vs. voltage characteristics of planar doped barrier structures. The simulation solves Poissons' equation and the electron continuity equation self consistently in time to find the total current through the device as a function of time. A simple approximation for the velocity that includes a constant low field mobility region and a saturated high field velocity is used. The Einstein relation is used for the diffusion coefficient. The solution is stepped through a range of bias voltages to obtain the device characteristic.

The purpose of this study is to characterize planar doped barrier devices for low barrier zero bias detector application. The detector properties depend on the curvature of the device current vs. voltage characteristic at the bias point. Since we want a zero bias detector, we need a low barrier height structure, with a low forward resistance and a blocking reverse characteristic. The current vs. voltage characteristic of a planar doped barrier with a p^+ doping spike of $10^{12}/cm^2$ and intrinsic layer widths of 100 and 500 angstroms is shown in figure 1. The doping in the p^+ spike determines the barrier height and the ratio of the lengths of the two intrinsic layers determines the relative resistance in the forward and reverse directions. This figure also shows a potential problem with low doped structures. The low doped regions have a relatively large space charge resistance. The current knee in the forward direction is low, only about 0.1 volts, but the forward characteristic rapidly becomes resistive. This limiting effect caused by the i layers can limit the device performance. One way to reduce this effect is to reduce the thickness of the i layers. This can cause several additional problems. Material growth problems can occur in very thin layers. The thin top i layer combined with a thin top n^+ ohmic cap layer is difficult to process and wire bond.

3.Video Detector Results

The devices discussed in this paper are fabricated from MBE grown GaAs. The devices are fabricated by lapping the semiconductor wafer to 100 microns thickness, depositing ohmic contact metal on both sides, etching a mesa to the final required size and dicing into individual chips. The X and Ka band devices are tested in standard microwave pill packages. The W band results use a whisker contact in a full height waveguide. Typical current vs. voltage characteristics for a zero bias PDB detector are shown in figure 2 and in Table 1. These devices exhibit voltages of 0.11 volt at 10 microamps and 0.20 volts at 100 microamps. The output voltage vs. input power for these detectors at 10 and 35 GHz is shown in figure 3. The power compression point is several milliwatts. Additional detector performance information is shown in Table 2. These devices exhibit a zero bias TSS of −50 to −58 dbm at frequencies between 10 and 35 GHz. The video bandwidth was 2 KHz to 2 MHz and the amplifier noise figure was 2 db. The video impedance varies between 2 and 50 Kohms. A coaxial mounted package with a bias Tee was used between 10 and 20 GHz and a waveguide mount was used at 35 GHz. No matching circuit or tuner was used to optimize the measurement. Broad band low level detector performance was observed in the 75–110 GHz frequency range. These results are shown in Table 3. These initial results were obtained in a broadband waveguide mixer mount. Improvements of 3 to 6 db should be possible.

Electrostatic and RF burnout performance is important in several applications at millimeter wave frequencies. Because of their small active egion planar doped barrier and Schottky barrier diodes are limited in power handling ability. Single junction PDB diodes were subjected to electrostatic pulses. The pulses simulate electrostatic discharge through the human body. The circuit consists of a 100 pf capacitor in parallel with a 1000 ohm resistor and discharges in less than 100 nanoseconds. Table 4 shows the burnout results for PDB detectors along with Schottky barrier results for

comparison purposes [8-9]. The Schottky devices withstand 500 to 1500 volts in the forward direction and 300 volts in the reverse direction. The PDB devices survived up to 2500 volts in both directions. The PDB detectors were also tested for CW power handling capability at 10 GHz. A sweeper and TWT amplifier were used along with a precision attenuator to expose the PDB's to gradually increasing amounts of power. High barrier Schottky diodes and PDB's have similar CW power capabilities.

4. Conclusions

This paper gives an overview of zero bias planar doped barrier diodes for video detector applications. The PDB's have excellent video detector performance up to 35 GHz and promising results to W band. They exhibit high resistance to electrostatic burnout and have CW burnout limits similar to high barrier Schottky barrier diodes. These devices should be useful video detectors at microwave and millimeter wave frequencies.

Acknowledgments The authors wish to thank Yulan Tan of GTRI for MBE growth assistance, Joyce Park, Brian Brown , W. Martin and Robert Nelson of M/A-COM for help in diode fabrication and characterization, and N. Deo of Millitech and G. Haddad of the University of Michigan for many helpful discussions.

References

1. R. Malik, T. AuCoin, R. Ross, K. Board, C. Wood, and L. Eastman, "Planar Doped Barriers in GaAs by Molecular Beam Epitaxy," *Electronics Letters*, vol. 23, pp. 836–837, 23 October 1980.

2. S. Dixon and R. Malik, "Subharmonic Planar Doped Barrier Mixer Conversion Loss Characteristics," *IEEE Trans. on Microwave Theory and Techniques*, vol. MTT-31, No. 2, pp. 155–158 (1983).

3. J. Chen and D. Wong, "W-Band Beam Lead Planar Doped barrier Subharmonic Mixer," IEEE Microwave Symposium Technical Digest, pp. 178–180 (1985).

4. U. Guttich, K. Strohm and F. Schaffler, "D-Band Subharmonic Mixer with Silicon Planar Doped Barrier Diodes," *IEEE Trans. on Microwave Theory and Techniques*, vol. MTT-39, No. 2, pp. 366–368, February 1991.

5. T. Lee, J. East and G. Haddad, "Planar Doped Barrier Subharmonic Barrier Mixers," *Microwave and Optical Technology Letters*, vol. 4, No. 1, pp. 53–66, January 1991.

6. I. Dale, A. Condle, S. Neylon and J. Kerney, "Planar Doped barrier Mixer and Detector Diodes As Alternatives to Schottky Diodes For Both Microwave and Millimeter Wave Applications," IEEE MTT Symposium Technical Digest, pp. 467–470, 1989.

7. S. M. Sze, *Physics of Semiconductor Devices*, second edition, Wiley, chapter 5, 1981.

8. Y. Anand and W. J. Moroney, "Microwave Mixer and Detector Diodes," Proc. of the IEEE, vol. 59, pp. 1182–1190, August 1970.

9. Y. Anand, "X-band High Burnout Resistance Schottky Barrier Diodes," *IEEE Trans. on Electron Devices*, vol. ED-24, pp. 1330–1336 (1977).

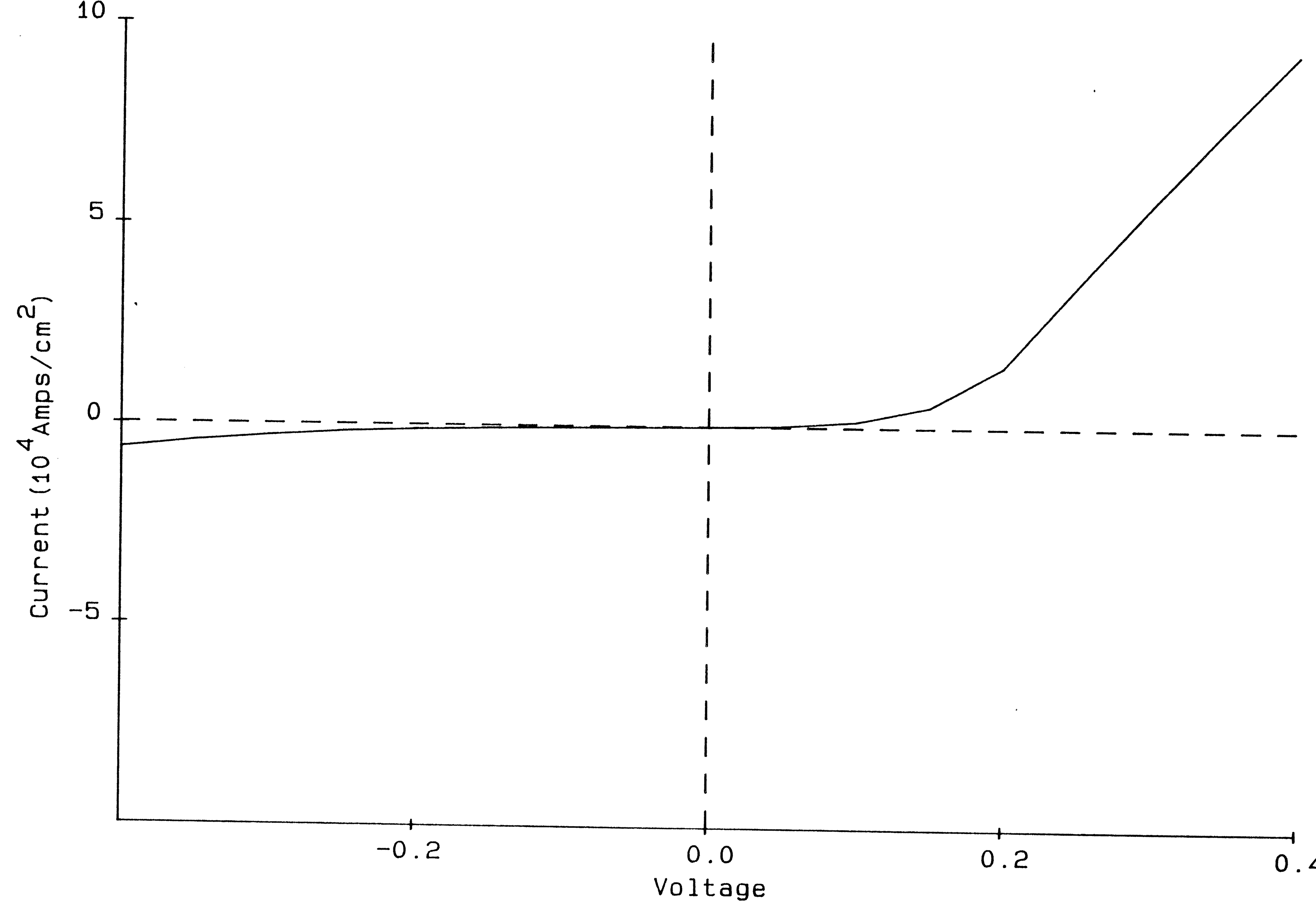

Figure 1. 100 angstrom/500 angstrom intrinsic structure.

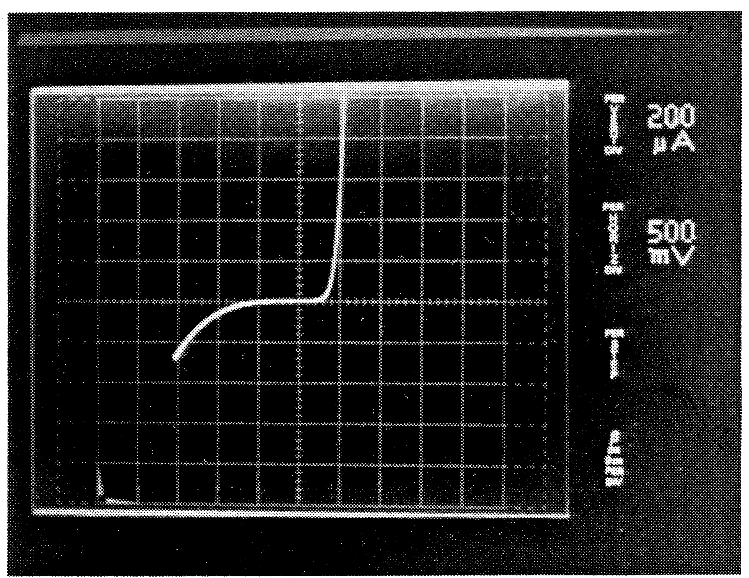

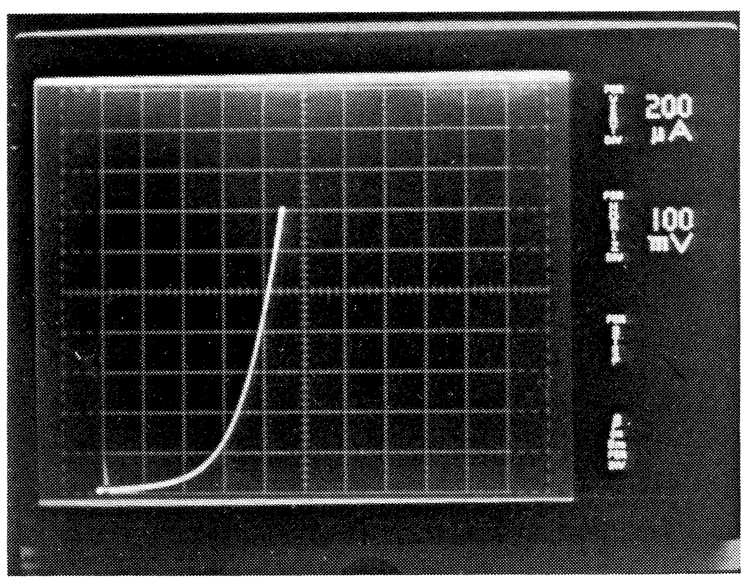

Figure 2. Typical experimental zero bias current vs. voltage results.

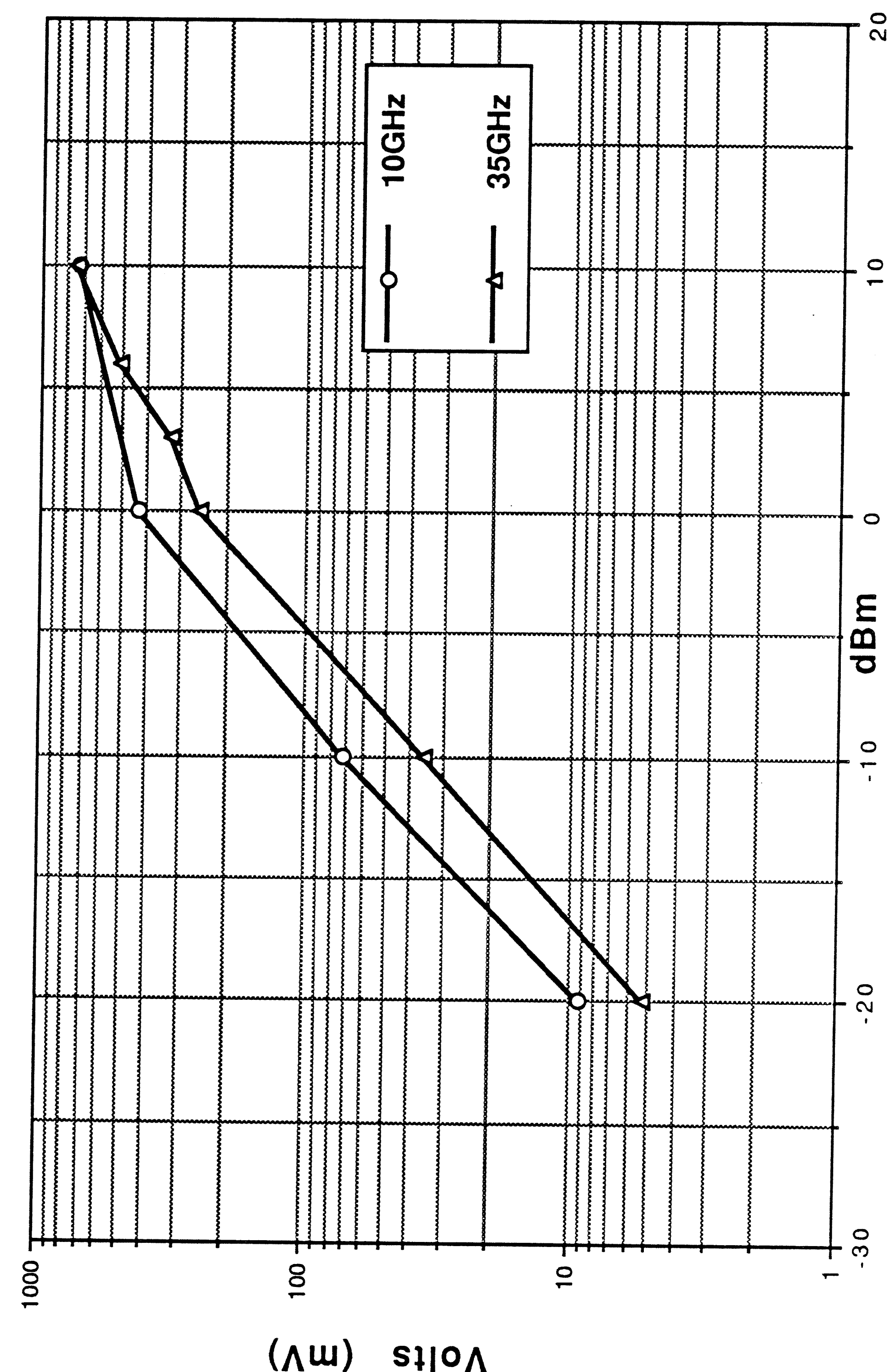

Figure 3. Video detector performance at 10 and 35 GHz.

DC CHARACTERISTICS OF PDB (ZERO BIAS) DIODES

(10 GHz - 40 GHz PILL PACKAGE)

Vf @ 10μA	0.11 Volts
Vf @ 100μA	0.20 Volts
Vb @ 10μA	0.8 Volts
Vb @ 100μA	1.5 Volts
Cj (calculated)	60fF
Rs	20 ohms

TABLE 1

Table 1. Details of low barrier characteristics.

RF PERFORMANCE OF ZERO BIAS PDB DIODES

(10 GHz - 40 GHz PILL PACKAGE)

Detector Performance	10 GHz	35 GHz
Video Impedance; Rv	2-50Kohms	2-50Kohms
Tangential Sensitivity; TSS	-50 to -58dBm	-50 to -58dBm
Voltage Out Put @ -10dBm (RL > 1m ohms)	70mV	40mV

Table 2. Details of video performance at 10 and 35 GHz.

OUTPUT VOLTAGE VS. RF POWER AT W-BAND FREQUENCIES

RF POWER	Vout 92.6 GHz	Vout 94.6 GHz
- 6 dBm	6mV	5mV
- 9 dBm	2mV	1.5mV
-12 dBm	0.7mV	0.6mV
-15 dBm	0.32mV	0.28mV

Table 3. W band detector performance.

ELECTROSTATIC & CW BURNOUT AT 10.0 GHz

	Low Barrier Si-Schottkys	Med. Barrier Si-Schottkys	High Barrier Si-Schottkys	PDB Si-Schottkys
Electrostatic (three pulses)				
Forward	800V	1100V	1500V	2500V
Reverse	300V	300V	300V	2500V
CW Operation	0.2 - 0.4W	0.3 - 0.5W	0.4 - 0.6W	0.4 - 0.6W

Table 4. Video detector burnout performance.

Two-Dimensional Electron Gas ("2DEG") Hot-Electron Mixers For Millimeter Waves and Submillimeter Waves

J.-X. Yang, W. Grammer, F. Agahi, K.-M. Lau, and K.S. Yngvesson

Abstract

The lowest noise temperature for any receiver in the 0.5 to 1 THz range has been achieved with the *InSb* hot electron mixers, which unfortunately suffer from the problem of having a very narrow (1–2 MHz) bandwidth. We are investigating two–dimensional electron gas (2DEG) devices as hot electron detectors and mixers in order to circumvent this problem. High–quality heterojunction material has been grown in–house with OM-CVD, and devices fabricated with dimensions in the range 10–100 micrometers. We have designed and tested a 35 GHz mixer, operating at 77K, which has demonstrated a band-width of at least 2 GHz. We are also working on a 94 GHz mixer for 4.2K operation. The theory of 2DEG hot electron mixers, and their potential for low–noise receivers in the THz range are discussed.

This work was supported by the National Aeronautics and Space Administration, under grant NAGW–1659

The authors are with the Department of Electrical and Computer Engineering, University of Massachusetts, Amherst, MA 01003.

I. INTRODUCTION

Receivers at frequencies close to 1 THz have equivalent noise temperatures which are from one to two orders of magnitude higher than the ultimate limit for the noise temperature of a coherent receiver - the quantum noise limit, see Figure 1. The frequency-dependence of the noise temperature of cooled Schottky-barrier and SIS mixers is also quite steep, as seen in this figure. The lowest noise temperature in this frequency range has been demonstrated with the *InSb* hot-electron mixer [1], which is a bulk device, and therefore has very small parasitic reactances. It is noteworthy that the frequency-dependence of the noise temperature of the *InSb* mixer is less steep – presumably this can be explained in general terms by the low reactance of the device. In contrast, Schottky-barrier and SIS devices for this frequency range have to be fabricated with extremely small dimensions in order to minimize their reactance (primarily capacitive). The main disadvantage of the *InSb* mixer is its very narrow bandwidth (at most a few MHz), which has limited its application in practical systems. A natural question to ask is then: Are there bulk-type devices which will result in a wider bandwidth? A paper by Smith et al. [2] proposed a two-dimensional electron gas device, operating at liquid helium temperature, and demonstrated photoconductive detection at 100 and 200 GHz, as well as at 119 micrometer wavelength. This device is essentially constructed as a fairly large HFET (heterojunction FET, also known as HEMT), without the gate. The structure of the device is shown in Figure 2. It makes use of a two–dimensional "sheet" of electrons (the two-dimensional electron gas, or "2DEG"), streaming from what would be the source of the HFET, to the drain, i.e. it is the two-dimensional analogue of the bulk *InSb* device.

The two-dimensional geometry results in many of the same advantages, which derive from the three-dimensional geometry of the *InSb* mixer, with a few differences which we will explore below. Most importantly, however, the bandwidth is predicted to be in the GHz range, which is sufficient for most THz applications.

We have proposed new versions of the 2DEG hot electron mixer [3], in particular we will present measured data for a 2DEG mixer, which operates at 77K. This mixer demonstrates the wide bandwidth of the 2DEG type of mixer for the first time. The paper first discusses the basic features and theory of 2DEG hot-electron detectors and mixers,

with emphasis on the latter. We then describe designs for mixers at 35 and 94 GHz, respectively, and the data obtained so far.

II. THEORY OF HOT-ELECTRON DETECTORS AND MIXERS

A. *Basic Nonlinear Mechanism*

The nonlinear mechanism behind hot electron detectors and mixers is substantially different from that of Schottky barrier and SIS mixers. In the latter, the currents at the RF and LO frequencies basically follow the I–V–curve, which can be measured at DC. The hot electron device, on the other hand, responds to the power at the RF or LO frequency, not the instantaneous voltage. This power heats the electron gas above the lattice temperature, and as a result the resistance of the device changes. The change in resistance with electron temperature can come about because of a change in electron mobility, or electron density, or a combination of these. A typical curve of resistance versus dissipated power, derived from measured data on one of our devices at 77K, is shown in Figure 3. Note that in this particular case, the slope of the curve is approximately constant, i.e.

$$R_B = C \times P \tag{1}$$

If both RF and LO power are coupled to the device, then the resistance will vary in response to the total instantaneous power as shown in Figure 4, provided that the IF frequency (f_{IF}) is such that

$$f_{IF} < \frac{1}{2\pi\tau_e} \tag{2}$$

The energy relaxation time, τ_e, determines the rate at which the average energy of the electron gas (at least approximately given by the "electron temperature") can change in response to the dissipated power imposed. If (2) is fulfilled, we will thus find that the resistance varies at the IF frequency. Given a constant current bias source, a voltage will then be developed across the load at the IF frequency, R_L, in the equivalent circuit of Figure 5. This circuit will enable us to calculate the responsivity of the device as a detector, and the conversion loss as a mixer. The useable bandwidth extends from DC to the frequency given by (2). It may be of interest to point out that the theory of hot electron mixers safely can ignore any higher order LO harmonics or sidebands.

The value of τ_e for $InSb$ in the liquid helium temperature range is about 2×10^{-7} sec, resulting in a bandwidth of about 1–2 MHz. The energy relaxation time of the 2DEG in heterostructures has been the subject of fairly intensive study, over the temperature range from 4K through 300K. In the lower temperature range, Sakai et al. [4] measured values between 10^{-10} and 10^{-9} seconds, indicating that bandwidths of about 1 GHz are attainable. Shah [5] has summarized work related to the energy loss rate of the 2DEG at higher temperatures, from 50K to 150K. Values for τ_e of 10^{-11} to 10^{-10} seconds have been obtained, which indicate bandwidths of a 2DEG mixer in this temperature range up to 10 GHz.

B. *Calculation of the Conversion Loss*

Expressions for the conversion loss of hot electron mixers were given by Arams et al. [6]. These are based on the equivalent circuit in Figure 5. The conversion loss must be optimized with respect to the value of several parameters in this circuit. It is assumed that the DC power (P_{DC}) and the LO power (P_{LO}) have the same effect on the device resistance. Reference [6] derives the optimum ratio of P_{DC}/P_{LO}, for which the conversion loss is minimized, under the constraint that the total dissipated power, P_O, is constant. We also introduce $R_{BO} = V/I$, which is the equivalent device RF resistance at an operating point for which the total power dissipated is P_O. The following expression can then be obtained for the conversion loss:

$$L_c = 8\left(\frac{R_{BO}}{CP_O}\right)^2 \left[\frac{(R_L + R_{BO})^2}{4R_L R_{BO}}\right] \left[1 - \frac{CP_O}{R_{BO}}\left(\frac{R_L - R_{BO}}{R_L + R_{BO}}\right)\right] \left[1 - \left(\frac{R_{BO} - Z_O}{R_{BO} + Z_O}\right)^2\right] \left[1 + (\omega_{IF}\tau_e)^2\right] \quad (3)$$

The optimum DC power and the optimum load resistance are found from:

$$(P_{DC})_{opt} = \frac{P_O}{2 - \frac{CP_O}{R_{BO}}\left(\frac{R_L - R_{BO}}{R_L + R_{BO}}\right)} \quad (4)$$

$$(R_L)_{opt} = R_{BO}\sqrt{\frac{1 + \frac{CP_O}{R_{BO}}}{1 - \frac{CP_O}{R_{BO}}}} \quad (5)$$

We can thus calculate L_c from (3), and plot it as a function of P_{LO} by using $P_O = P_{DC} + P_{LO}$, as well as (4), given representative values for the RF circuit impedance Z_O (100 ohms), and $R_L = 50$ ohms. Figure 6 shows the measured I-V-curve for the 77K device which will be described later*). The conversion loss calculated from this curve is given in Figure 7. For convenience, an analytical fit to the I-V-curve was used, given by:

$$I = \left(\frac{2I_O}{\pi}\right) \tan^{-1}(\alpha V) \qquad (6)$$

Experimental LO power was in the range of 1-4 mW, and the predicted conversion loss thus is of the order of 15–20 dB. Other devices fabricated from wafers which have been grown in-house have shown greater nonlinearity. By using these data, and assuming reasonable changes in the device dimensions, we have estimated that we can expect to improve the I-V-curve considerably. On the basis of the improved I-V-curve, we predict a considerably lower conversion loss of close to 8 dB, see Figure 8. The ultimate theoretical limit for the conversion loss is 6 dB [6]. We also calculated L_C for $InSb$, based on an I–V–curve from [1], and obtained an optimum value of about 12 dB, which is consistent with published data for this material.

C. *Variation of Device Resistance with Device Dimensions*

One of the advantages of using the two-dimensional device geometry is that it allows a great deal of flexibility for choosing the device dimensions, in order to match the requirements for an optimum detector or mixer. Its surface resistance is found from:

$$\rho_s = \frac{1}{eN_s\mu} \text{ ohms}/\square \qquad (7)$$

where e is the electron charge, N_s is the electron density (cm^{-2}), and μ is the mobility. The device resistance is found by multiplying (7) by L/W, where L is the length, and W the width of the device. According to (7), devices with the same L/W can be fabricated with different areas, while maintaining the same resistance, which may be matched to a particular microwave circuit. For typical materials, ρ_s is conveniently close to the

* This device was fabricated on MBE material, courtesy of Dr. D. Masse' of Raytheon Company

impedance of microwave integrated transmission lines. For example, if $N_s = 10^{12}$ cm^{-2}, and $\mu = 63,000$ cm^2/Vs, $\rho_s = 100$ ohms.

Briefly, by using (3), we find that mixer devices are optimized if the initial (linear) resistance is small, while the RF and LO impedances are matched to R_{BO} at the operating point. The optimum IF impedance is 2–4 times higher than the RF impedance. The LO power required should scale with the area of the device, since the energy loss rate per electron is constant for a given electron temperature [4]. Optimum detectors should also be RF matched to R_{BO}, and the responsivity is predicted to increase with decreased area.

D. *Equivalent Circuit, Including Parasitics*

So far we assumed that the device equivalent circuit was purely resistive. In order to assess the potential of the device for THz applications, we must calculate the parasitic elements in the circuit, however. An important effect to take into account is the electron inertia which is related to the finite momentum relaxation time, τ_m [7,8].

The value of τ_m is found from the mobility as follows:

$$\tau_m = \frac{\mu m^*}{e} \tag{8}$$

As demonstrated in [7], the equivalent circuit at very high frequencies is as shown in Figure 9a. The impedance (Z_s) of the series portion of the circuit is

$$Z_s = \rho_s \times \frac{L}{W}(1 + j\omega\tau_m) = R_B + j\omega L_B = R_O(1 + j\omega\tau_m) \tag{9}$$

in terms of the low-frequency resistance, R_0. C_0 is the (frequency–independent) capacitance. The configuration of the device makes it easy to minimize C_0, in which case it is sufficiently accurate to use only Z_s for the equivalent circuit. The inductive part of Z_s becomes appreciable at a frequency for which $2\pi \times f \times \tau_m = 1$. Let's define this frequency as f_m. For typical room temperature mobilities, (8) and (9) predict that f_m is from 0.5 to 1 THz, and these phenomena are consequently not important in devices below the THz range**).

** Carrier inertia phenomena have very noticeable effects in THz harmonic multipliers, see the paper at this conference by E.L. Kollberg, T. Tolmunen, M. Frerking, and J. East, "Current Saturation in Submillimeter Wave Varactors".

At lower temperatures, however, τ_m is longer, and significant effects can be seen at frequencies of tens of GHz. At 77K, for example, a typical μ for our materials is 100,000 cm^2/Vs, and $f_m = 42$ GHz. As LO and DC power is applied, the electron temperature rises, and f_m increases as well, since τ_m becomes shorter at the higher T_e's. This effect will have to be taken into account in the mixer design. It is also not clear how good the model is, which assumes a specific value for τ_m, although it has been shown to work well in some cases for which Monte Carlo simulation was used for comparison [8]. Since f_m is as low as 30–40 GHz, it is possible to measure the equivalent circuit, however, as described below.

The reactive nature of the response of the electrons has been shown to give rise to a decrease of the responsivity of $InSb$ detectors with increasing frequency, starting at about 200–300 GHz [1]. One can circumvent this limitation by applying a small magnetic field, tuning the electrons to the cyclotron resonance. As a result, the responsivity (and the conversion loss of a mixer) becomes essentially independent of frequency up to about 2 THz. The experiment of Smith et al. [2], showed that the 2DEG device also acts as a detector at the cyclotron resonance. There are thus two conceivable methods for obtaining good response for 2DEG devices up to THz frequencies:

(1) Make use of the cyclotron resonance for enhancement. This should be feasible for devices at 4K, as well as at 77K.

(2) Add a capacitance in series, in order to tune out the 2DEG inductive reactance, as shown in the circuit model of Figure 9b.

We are planning to try both of these approaches.

E. *Noise Properties*

As shown in [6], the DSB noise temperature of a hot electron mixer receiver is approximately:

$$T_{RX} = L_c \times (T_e + T_{IF}) \tag{10}$$

Here, T_e is the electron temperature, and it is assumed that the electrons radiate thermal noise at this temperature. Shot noise has been neglected, and T_{IF} is the noise temperature of the IF amplifier, which is assumed to be matched to the mixer. For a mixer operating

at a physical temperature of 77K, T_e may be about 150K. If T_{IF} is 10K, and $L_c = 10$ dB, we find $T_{RX} = 1600$K. From the noise temperature point of view, it is clearly desirable to operate the mixer at as low a temperature as possible. For example, a 4.2K device might have $T_e = 10$ K, and $T_{RX} = 200$K for the same L_c and T_{IF}.

III. MATERIALS GROWTH AND FABRICATION OF DEVICES

The 2-DEG structures were grown by low pressure organometallic chemical vapor deposition (OMCVD) on undoped semi-insulating *GaAs* (100) substrates oriented 2° off towards the (110) planes. The sources used were trimethylaluminum, trimethylgallium, 100% arsine, and silane as n-type dopant. A typical device structure includes a 1μm *GaAs* buffer, a 100Å undoped *AlGaAs* spacer, a 500Å uniformly doped *AlGaAs*, and a 200Å doped GaAs contact layer. The *Al* content in the *AlGaAs* layers was between 29 and 33%. The dopant concentration in the doped *AlGaAs* was in the high 10^{17} to 1×10^{18} range. The reaction chamber pressure was kept at 50 torr and the growth temperature was at 700°C. A V/III ratio of > 200 was used for the growth of the *AlGaAs* layers. The thicknesses of the thin layers were nominal thicknesses determined by the growth of thick calibration layers. Hall measurements were made on the as-grown layers using the van der Pauw technique at room, liquid nitrogen, and liquid helium temperatures. The best sample obtained thus far has a sheet charge density (N_s) of 1×10^{12}/cm^2 and a 77K mobility (μ_{77}) of 95,000 cm^2/V-s. At 4.2K these values were 1×10^{12}/cm^2 and 166,000 cm^2/V-s. A carefully calibrated slow etchant was used to remove materials from the surface between 77K measurements. There were no noticeable changes in the measurements as the surface doped layers were being step-etched, indicating that there was minimal conduction in these layers competing with the 2-DEG. A standard Hall bar was fabricated on a sample piece for drift mobility and Shubnikov-de Haas measurements. Shown in Fig. 10 is the low field (mV/cm) drift mobility measured at 4.2K, which agrees well with the Hall mobility. Very strong Shubnikov-de Haas oscillations of the magnetoresistance and quantum Hall effects were observed (Fig. 11).

A double channel structure consisting of a 1μm *GaAs* buffer, a 500Å undoped *AlGaAs* buffer, a 500Å doped *AlGaAs*, a 100Å undoped *AlGaAs* spacer, a 1000Å undoped *GaAs*, a 100Å undoped *AlGaAs* spacer, and doped cap layers of *AlGaAs* and *GaAs* was also

grown. Two 2-DEG channels are formed at the top and bottom of the 1000Å *GaAs* layer. This structure has resulted in an $N_s = 2 \times 10^{12}/\text{cm}^2$ with $\mu_{77} = 64,400\text{cm}^2/\text{V-s}$. The $N_s\mu$ product is very high compared with any MODFET structures made with any material systems.

We believe the high sheet charge densities from the relatively low doped *AlGaAs* ($10^{17}/\text{cm}^3$ range) are a result of the high quality of the *AlGaAs* layers and interfaces, leading to very efficient transfer of electrons to the 2-DEG channels.

IV. MIXER CIRCUIT DESIGN AND EXPERIMENTAL RESULTS

A. *A 35 GHz Mixer for 77K Operation*

We plan to use the 2DEG devices with Tapered Slot Antennas (TSAs) or arrays, which makes it convenient to couple experimental mixer designs from a waveguide/finline transition inside a split block. The device is inserted across a slot-line, just outside the split block, by using a flip-chip technique, see Figure 12. The circuit is fabricated on a high-resistivity silicon substrate, 0.33 mm thick, see Figure 13. A slot-line/coplanar waveguide (CPW) transition is placed $3/4\lambda$ from the device, with a quarter-wave open CPW stub $\lambda/4$ from the transition, serving as an RF matching element and low-pass filter for the IF (1 GHz). We have chosen to use the combination of slot-line/CPW transmission lines, for the convenience of being able to produce circuits on a single side of the substrate. Wire bonds are used at all CPW discontinuities to keep ground currents in phase. A monolithic version of the mixer will use air bridges and an integrated IF amplifier, and be fabricated on a semi-insulating *GaAs* substrate.

The uniplanar silicon circuits are being developed and tested by probing them with a Cascade Microprobe. Many different configurations can be tested on a single chip, see Figure 14. We also plan to measure devices at liquid nitrogen temperature in order to derive the equivalent circuit of the device (compare the discussion in section III.D.).

The mixers are being tested in a simple cryogenic setup, which cools them to liquid nitrogen temperature. Figure 15 gives the measured onversion loss, versus frequency, for two different bias voltages. The conversion loss becomes very large for zero DC bias, as it should (see (3)). The measured conversion loss also was essentially unchanged as the IF frequency was changed between 1 and 2 GHz, a behavior which is expected since $\frac{1}{(2\pi \times \tau_e)}$

is estimated to be about 10 GHz. The conversion loss is about 10 dB higher than the theoretical prediction from Figure 7. The discrepancy in this initial experiment appears to be a circuit effect, based on the evidence that the return loss for both RF and IF is better than 10 dB, while variation of the bias has only a very small effect on the return loss. On the other hand, the conversion loss behaves as predicted when the bias and LO power are varied. Further circuit studies are expected to solve this problem.

B. *A 94 GHz Mixer for 4.2K Operation*

A similar circuit to that described above is being used to implement a 94 GHz mixer. The initial experiments are being performed to detect the cyclotron resonance in the 2DEG, and confirm the results of [2]. So far, these have been unsuccessful, but the initial device (from the same batch as the one used in the 35 GHz mixer) had a much too small impedance (about 10 ohms) when used as a detector device and was not well matched to the slotline. New devices are under fabrication, which will have closer to optimum parameters.

V. CONCLUSION

The challenge of this work is to duplicate the excellent noise temperatures achieved by *InSb* hot electron mixers in the frequency range 0.5–1 THz, while providing a much wide bandwidth, in a 2DEG device. So far, our first device has demonstrated a wide bandwidth (at least 2 GHz), while operating at 77K. Further circuit work is expected to bring the conversion loss of this mixer down to values close to those predicted by theory (about 10 dB or less). Noise temperature measurements on this mixer will enable us to establish a theoretical framework for the noise performance. The experiments by Smith et al. [2] indicate that a 4.2K device is also feasible. For a device cooled to this temperature, we can expect the noise temperature to be as low as that of the *InSb* mixer.

REFERENCES

[1] Brown, E.R., Keene, J., and Phillips, T.G., "A Heterodyne Receiver for the Submillimeter Wavelength Region Based on Cyclotron Resonance in *InSb* at Low Temperature," *Intern. J. Infrared and Millimeter Waves*, 6, 1121 (1985).

[2] Smith, S.M., Cronin, N.J., Nicholas, R.J., Brummel, M.A., Harris, J.J., and Foxon, C.T., "Millimeter and Submillimeter Detection Using $Ga_{1-x}Al_xAs/GaAs$ Heterostructures," *Intern. J. Infrared and Millimeter Waves*, 8, 793 (1987).

[3] Yang, J.-X., Grammer, W., Agahi, F., K.-M. Lau and K.S. Yngvesson, "High Mobility Hot Electron Mixers for Millimeter Waves and Submillimeter Waves," *Fifteenth Intern. Conf. Infrared and Millimeter Waves*, Orlando, FLA, Dec. 1990 (Digest), p. 248.

[4] Sakaki, H. Hirakawa, K., Yoshino, J., Svensson, S.P., Sekiguchi, Y., Hotta, T., and Nishii, S., "Effects of Electron Heating on the Two–Dimensional Magnetotransport in $AlGaAs/GaAs$ Heterostructures," *Surface Science*, 142, 306 (1984).

[5] Shah, J., "Hot Carriers in Quasi-2-D Polar Semiconductors," *IEEE J. Qu. Electronics*, QE–22, 1728 (1986).

[6] Arams, F., Allen, C., Peyton, B., and Sard, E., "Millimeter Mixing and Detection in Bulk $InSb$," *Proc. IEEE*, 54, 612 (1966).

[7] Champlin, K.S., Armstrong, D.B., and Gunderson, P.D., "Charge Carrier Inertia in Semiconductors," *Proc. IEEE*, 52, 677 (1964).

[8] Grondin, R.O., Blakey, P.A., and East, J.R., "Effects of Transient Carrier Transport in Millimeter Wave GaAs Diodes," *IEEE Trans. Electron Devices*, ED-31, 21 (1984).

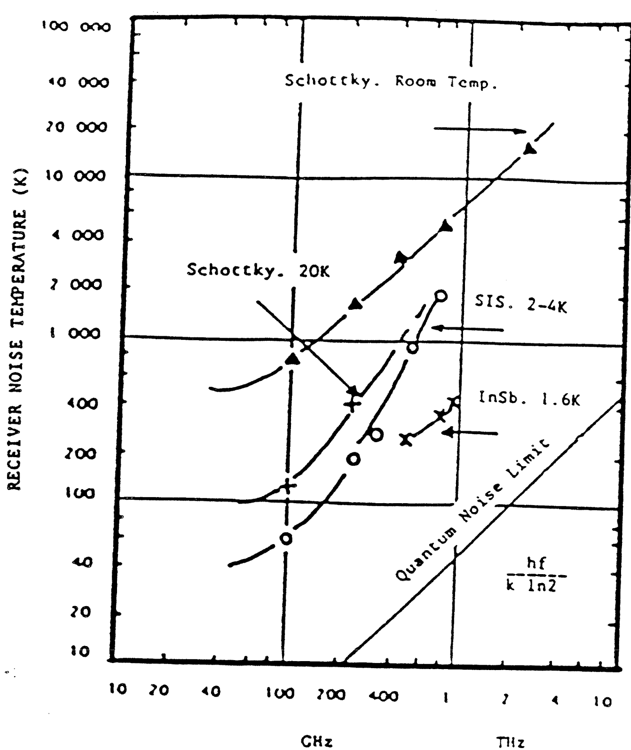

Figure 1. Best noise temperatures achieved for receivers from 100 GHz through 2 THz.

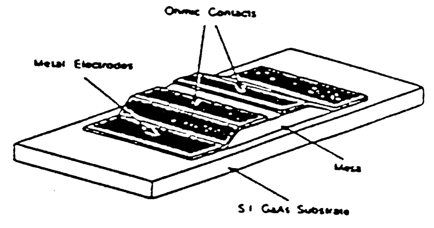

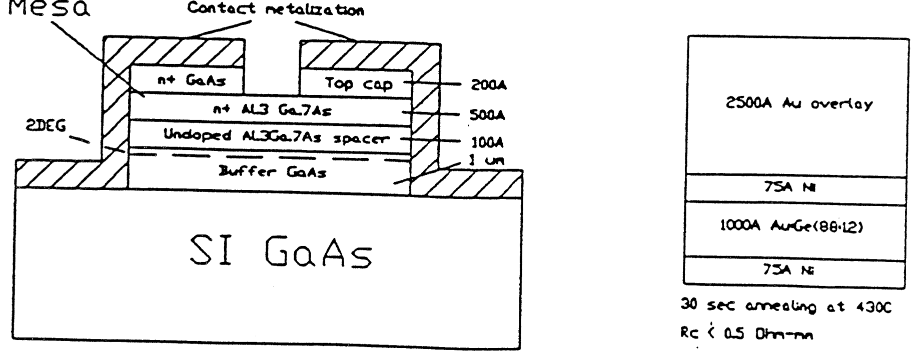

Figure 2. Outline and cross-section of the 2DEG device.

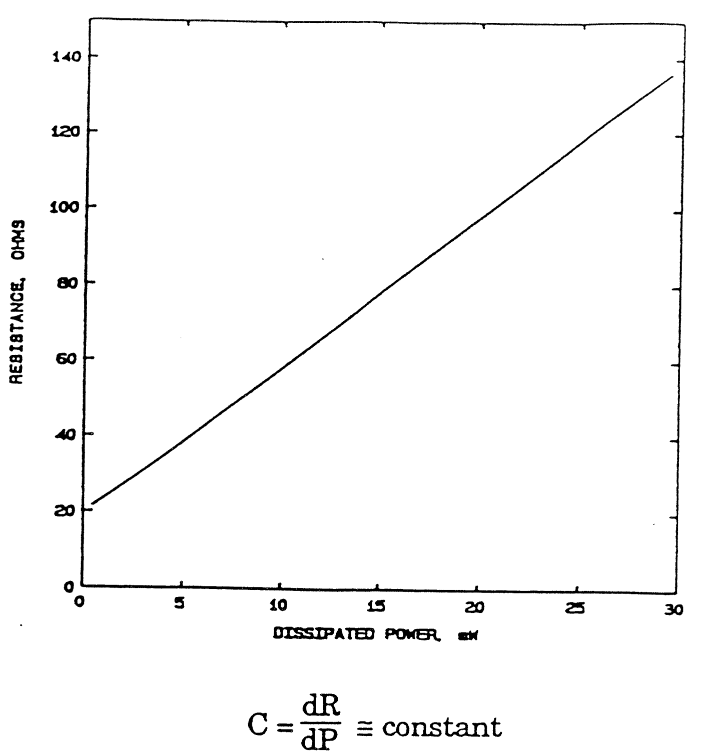

$$C = \frac{dR}{dP} \cong \text{constant}$$

Figure 3. Resistance versus dissipated power for 2DEG device at 77K.

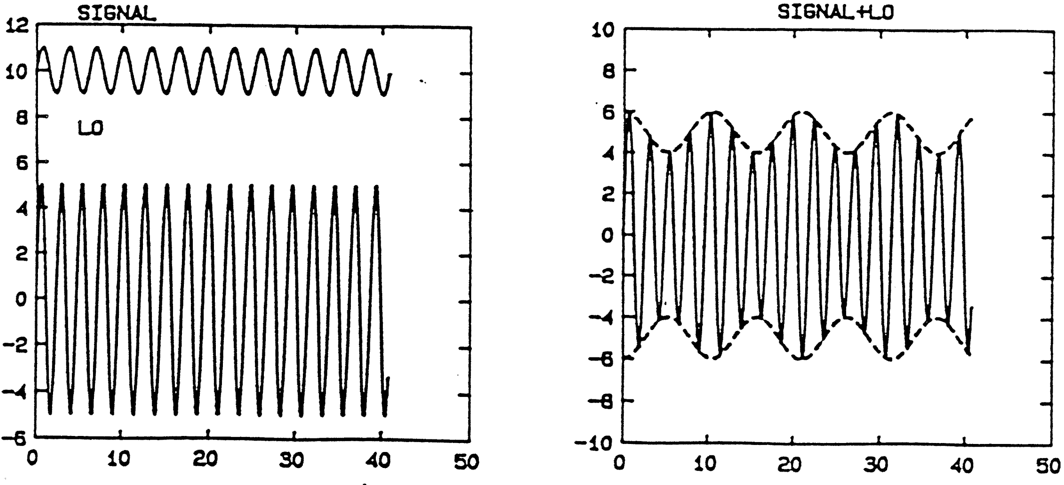

Figure 4. Illustration of the operation of a hot electron mixer.

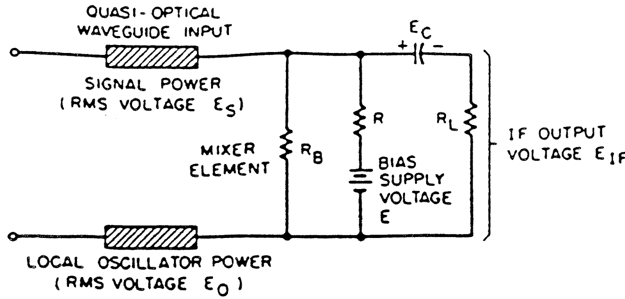

Figure 5. Equivalent circuit of hot electron mixer device.

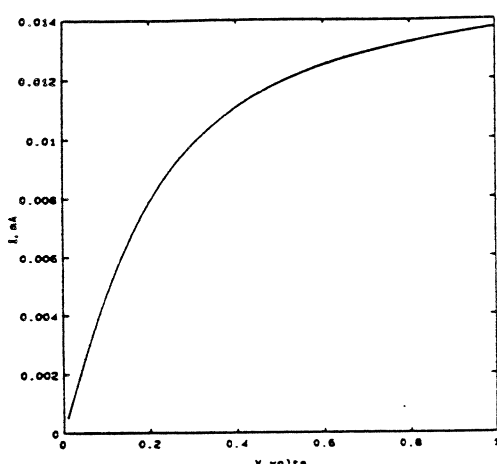

Figure 6. I–V–curve for 2DEG device at 77K.

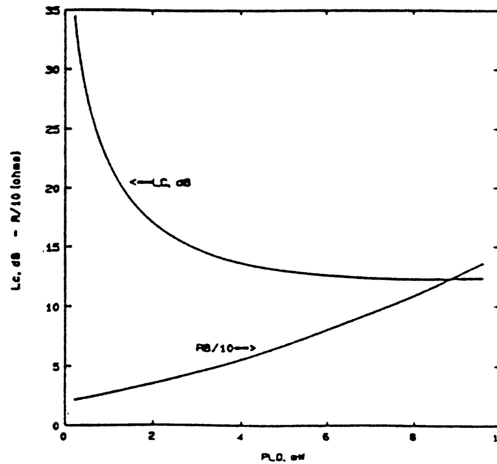

Figure 7. Calculated conversion loss of 2DEG mixer, based on I–V–curve of Figure 6.

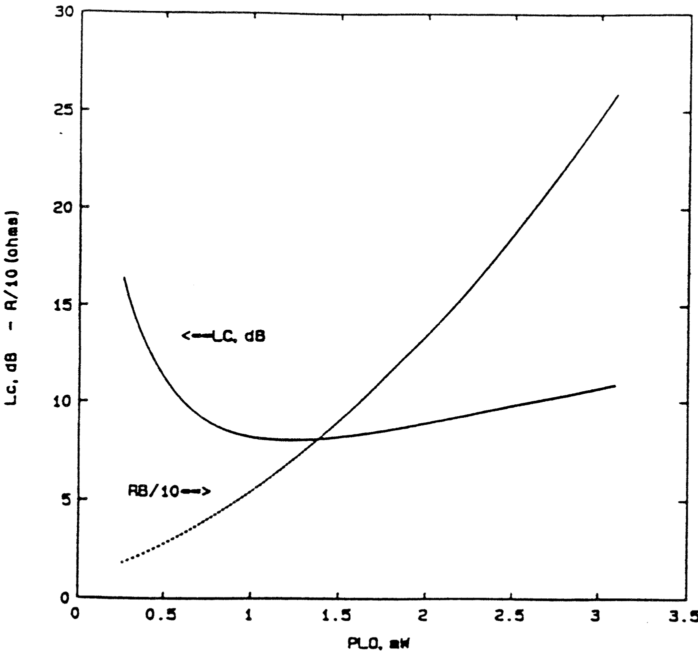

Figure 8. Calculated conversion loss for 2DEG device at 77K, based on improved I–V–curve.

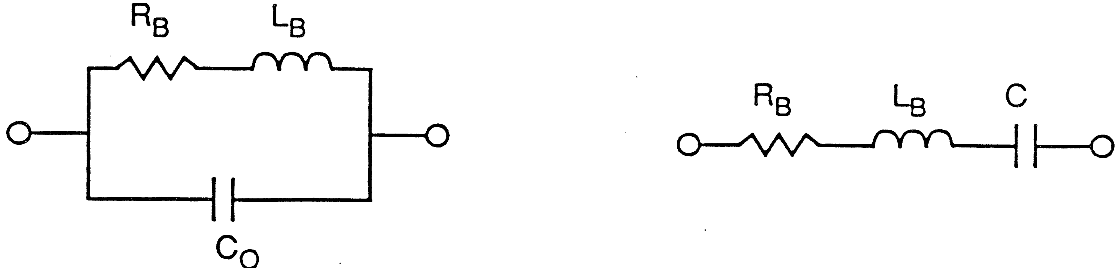

Figure 9. a) Equivalent circuit of 2DEG devices, with parasitics. b) Inductance of device is tuned out with series capacitance.

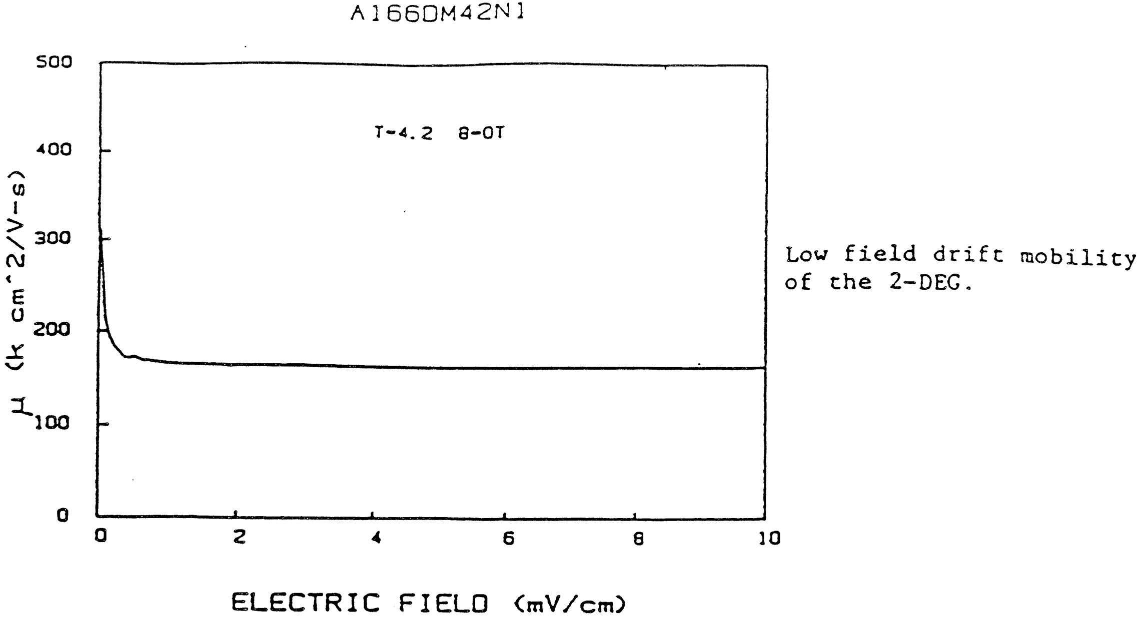

Low field drift mobility of the 2-DEG.

Figure 10.

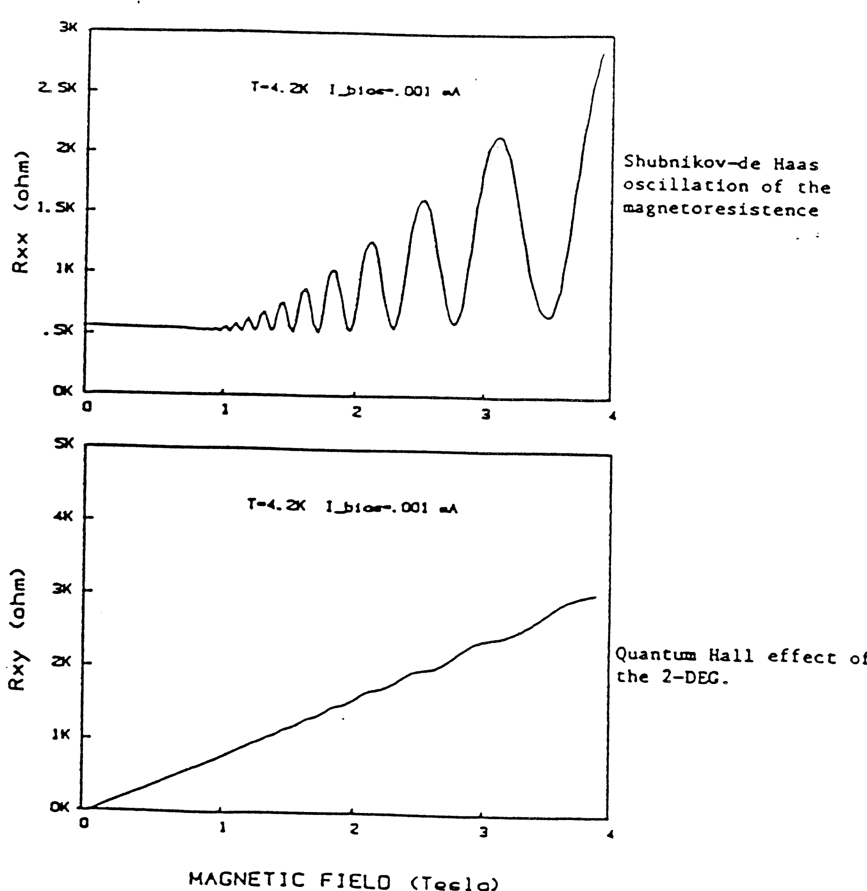

Shubnikov-de Haas oscillation of the magnetoresistence

Quantum Hall effect of the 2-DEG.

Figure 11.

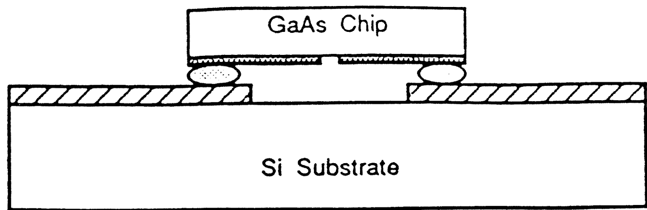

Figure 12. Flip-chip mounting of the device across slot-line circuit.

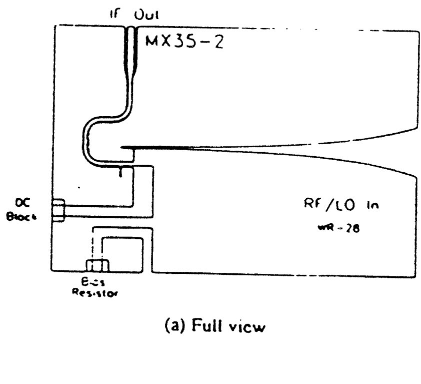

(a) Full view

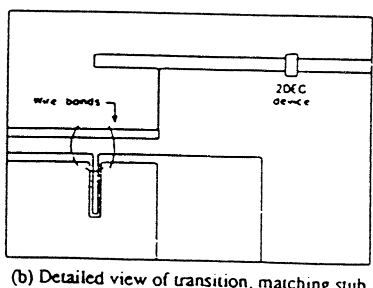

(b) Detailed view of transition, matching stub

Figure 13. Circuit for 35 GHz mixer.

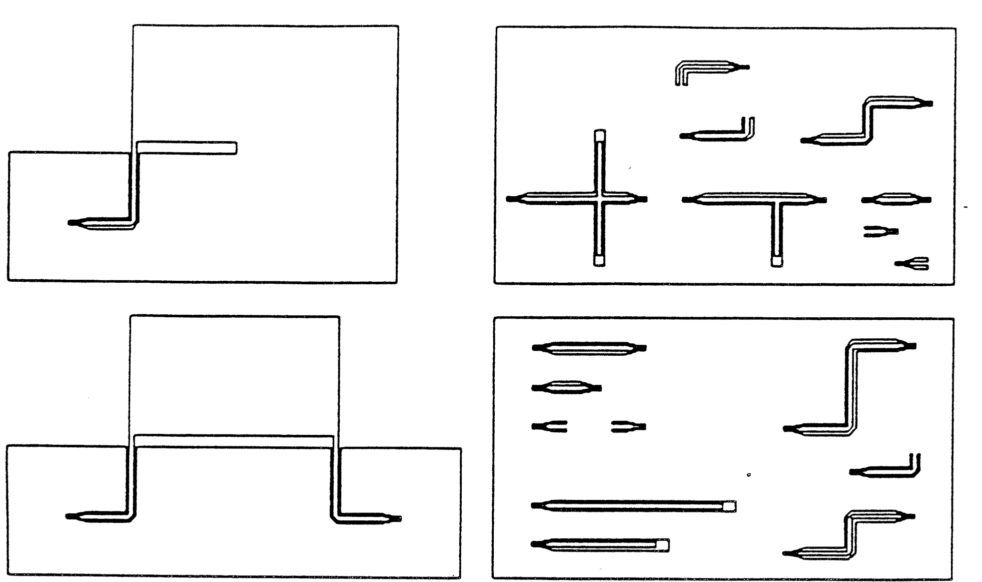

Figure 14. Test chip for microprobing of uniplanar circuit elements.

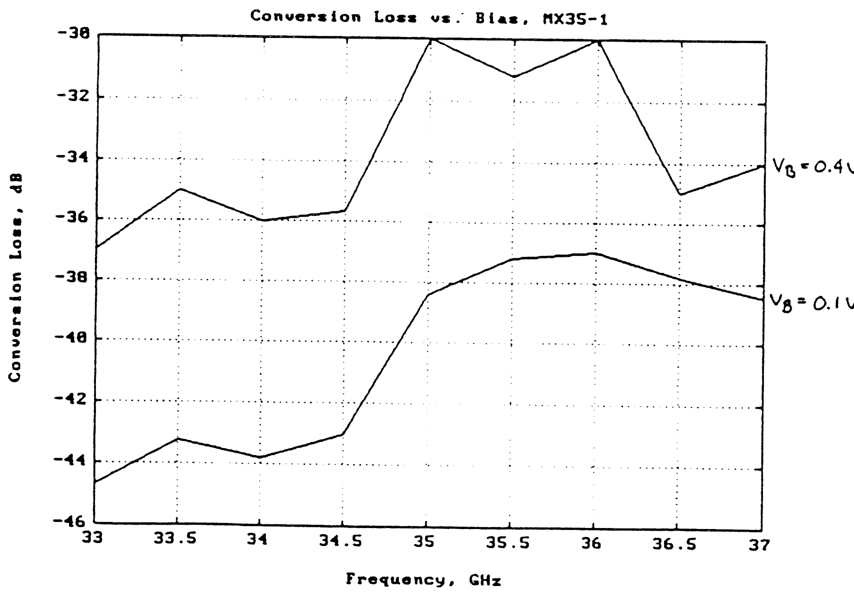

Figure 15. Measured conversion loss of 35 GHz 2DEG mixer at 77K.

InGaAs SCHOTTKY BARRIER MIXER DIODES FOR MINIMUM CONVERSION LOSS AND LOW LO POWER REQUIREMENTS AT TERAHERTZ FREQUENCIES *

U.V. Bhapkar, T.A. Brennan and R.J. Mattauch

Semiconductor Device Laboratory
Department of Electrical Engineering
The University of Virginia
Charlottesville, VA 22903-2442

ABSTRACT

This paper presents a theoretical investigation of the conversion loss of mixers using InGaAs Schottky barrier diodes as well as experimental findings on these diodes.

The conversion loss study is based on a multi-port mixer analysis developed by Held and Kerr. This analysis requires a knowledge of the embedding impedance presented to the diode, as well as the diode parameters, such as the series resistance, the junction capacitance, and the current-voltage characteristic. We have performed an analysis of the current-voltage characteristics of Schottky diodes based on the work of Crowell, Chang and Sze. This model considers the effects of electron tunneling and image force lowering of the barrier. The conversion loss studies indicate that InGaAs diodes will offer comparable conversion performance to that of GaAs diodes with DC bias. The calculations also show that non-biased InGaAs diodes are expected to require about one-sixteenth of the LO power required by non-biased GaAs diodes. We also present conversion loss predictions of sub-harmonically pumped, anti-parallel diodes, and show that to achieve minimum conversion loss, $In_{0.53}Ga_{0.47}As$ diodes will require one-eighth of the power required by GaAs diodes.

Several batches of back-contacted InGaAs diodes with indium mole fractions of 0.2 and 0.3 have been fabricated on GaAs substrates. The fabrication procedure used to make the InGaAs diodes is similar to that used for high frequency GaAs devices. The DC testing indicates that the InGaAs diode performance compares favorably with that of the best GaAs devices in terms of the ideality factor, parasitics, and the breakdown voltage. These devices had a lower turn-on voltage than conventional GaAs devices, as expected.

* This work was supported in part by NASA through the University of Michigan Space Terahertz Technology Center under grant Z-25251, and by the National Science Foundation under grant ECS-8720850-02.

I. Introduction

GaAs Schottky diodes are frequently used as mixer elements in heterodyne receivers for the few hundred gigahertz to 1 terahertz frequency range. At present a major limitation of these devices is the difficulty in obtaining sufficient local oscillator (LO) power from solid state sources at these frequencies. One solution to this problem is to use sub-harmonically pumped, anti-parallel diode pairs. This will halve the frequency at which the LO power is needed to a range where obtaining sufficient LO power is less of an obstacle. GaAs diodes can be used in such a configuration, but unfortunately, they require a significant DC bias or high LO power for optimum conversion performance, and it is very difficult to bias diodes used in this manner. To solve this problem, InGaAs has been proposed as a material for use in sub-harmonically pumped, anti-parallel diode structures. Schottky barriers formed from $In_xGa_{1-x}As$ have a height that decreases with increasing indium mole fraction. The Schottky barrier height is critical in mixer operation because it determines the turn-on voltage of the diode. A diode with a lower turn-on voltage requires less DC bias to reach its optimal operating range. An added benefit of using InGaAs is its mobility, which is superior to that of GaAs. This is important because the high mobility will lead to a lower series resistance, which is a parasitic that lowers the overall conversion efficiency of the diode.

This paper presents a report on progress towards the goal of developing an InGaAs Schottky diode mixer having superior performance and LO power requirement for use at frequencies up to 1 THz. The effort thus far has consisted of both theoretical and experimental work. The theoretical work has focused on predicting InGaAs diode parameters as well as the conversion efficiency of mixers using these diodes. The experimental work has focused on perfecting the fabrication sequence of InGaAs diodes formed on GaAs substrates.

Section II of this paper presents the diode models that have been used in the conversion loss analysis. A major effort of our research has been the development of a computer program that calculates the current-voltage characteristics of Schottky diodes while taking into consideration the quantum mechanical reflection of electrons at the Schottky barrier. This analysis, based on the work of Crowell, Chang, and Sze, also takes into consideration the image force lowering of the Schottky barrier [1,2]. A new model of the RF series impedance is also outlined [3]. This model considers the structure of diodes with epitaxial layers, and automatically incorporates into the calculation high frequency phenomena such as the skin effect and charge-carrier inertia. Section III presents the results of conversion loss calculations of both single diode and anti-parallel GaAs and InGaAs diodes. These calculations are based on a multi-port mixer analysis developed by Held and Kerr [4,5]. We have used a modified version of a computer program by S. Maas to perform the analysis [6]. The modifications to the program include the use of our own current-voltage analyses, rather than the standard thermionic-emission model. This analysis requires a knowledge of the embedding impedance presented to the diode, as well as the diode parameters discussed in Section II. Section IV presents experimental work. The fabrication technology which produces InGaAs diodes with predictable, desirable mixer characteristics is discussed. The DC characteristics of four batches of InGaAs diodes are reported, along with those of typical GaAs diodes for comparison. The InGaAs devices compare well with the GaAs diodes even though their fabrication procedure has not yet been optimized. Section V concludes this paper and indicates areas of present and future work.

II. Diode Models

The diode parameters needed for the implementation of the conversion loss analysis are:

A. the Schottky barrier height,
B. the junction capacitance,
C. the RF series resistance, and
D. the current-voltage characteristic.

Because the study of InGaAs Schottky diodes is in its infancy, the experimental base to provide some of these parameters, particularly the last two, is inadequate. Therefore, to obtain valid predictions of the conversion loss, we first performed new, more accurate calculations of the RF series impedance and the current-voltage characteristic.

A. Schottky Barrier Height

The Schottky barrier height of $In_xGa_{1-x}As$ as a function of the mole fraction, x, is given by the following empirical formula [7]:

$$\phi_B = 0.95 - 1.90x + 0.90x^2. \tag{1}$$

The Schottky barrier height, given by (1), is plotted in Fig. 1, and decreases very rapidly with increasing indium mole fraction. This is of critical importance to mixer operation because the Schottky barrier height determines the diode turn-on voltage, and diodes with a low turn-on voltage may require the application of less bias and/or LO voltage. Thus, InGaAs diodes are expected to require less LO power in comparison to that required by GaAs diodes. Also, InGaAs diodes will improve the performance of mixer configurations in which it is not possible to bias the diodes, such as in sub-harmonically pumped, anti-parallel pairs.

B. Junction Capacitance

The junction capacitance, C_j, is a parasitic element that affects the conversion loss of the diode, and is given by

$$C_j = \frac{C_{jo}}{(1-V/\phi_B)^{1/2}}, \tag{2}$$

where C_{jo} is the zero-biased junction capacitance. In whisker-contacted diodes, C_{jo} is given by [8]

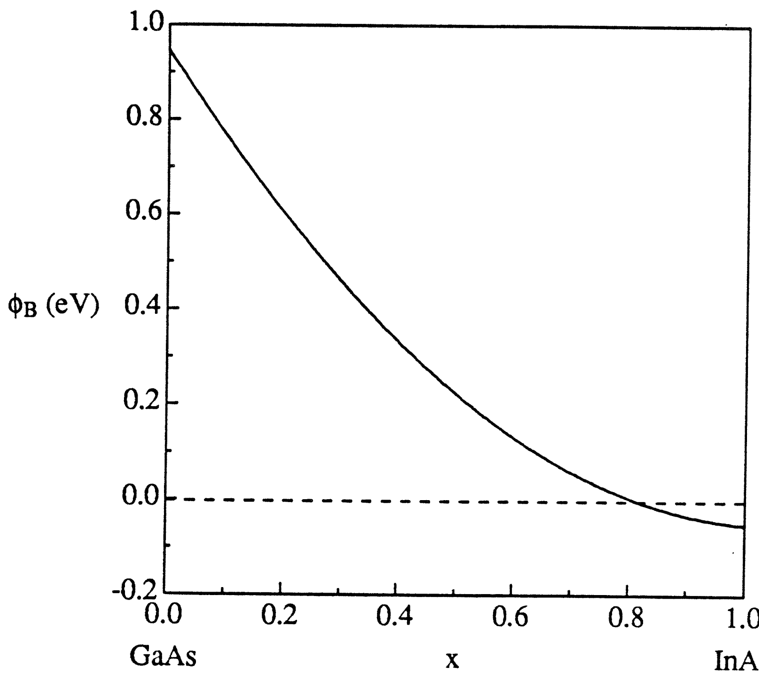

Figure 1. Schottky barrier height of $In_xGa_{1-x}As$ as a function of indium mole fraction.

$$C_{jo} = \frac{\varepsilon A}{W} + \frac{3\varepsilon A}{2a}, \tag{3}$$

where ε is the permittivity of the semiconductor, a is the anode radius, A is the anode area, and W is the zero-biased depletion depth, given by

$$W = \left[\frac{2\varepsilon\phi_B}{qN}\right]^{1/2}, \tag{4}$$

where N is the doping concentration in the region below the anode. The second term in (3) is due to the fringing of the electric field near the anode edges.

C. RF Series Impedance

The RF series impedance of Schottky barrier diodes is a complicated function of the frequency, and no analytic formulae of sufficient accuracy are available. Dickens' formula of the series impedance has commonly been used [9], but it is accurate only for simple diodes without epitaxial layers and with the ohmic contact encircling the diode chip. Real Schottky diodes usually have epitaxial layers and have the ohmic contact on the back or on top of the chip. In addition, the formula loses accuracy at frequencies greater than several hundred gigahertz. Therefore, we have developed a finite difference calculation of the RF series impedance that considers these factors [3]. These computer programs obtain the solution to the electromagnetic field over the entire diode chip, which, for ease of calculation, is assumed to be cylindrical. The actual diode chip of the planar structure, as shown in Fig. 2, is rectangular, and the whisker-contacted structure, as shown in Fig. 3, is square-shaped. Use of the cylindrical approximation causes only a small error in the series impedance calculation of the whisker-contacted chip. For the planar diode structures our finite difference calculations offer a less accurate prediction of the series impedance because it models the ohmic contact as entirely encircling the anode. In an actual chip, the ohmic contact occupies only about half of the wafer's top surface. In spite of these simplifications, our model is useful for comparing the series impedance of different diodes. Figures 4 and 5 depict two-dimensional cross sections of the current contours within whisker-contacted and planar diodes, respectively.

The series impedance of course depends on the electron mobility μ of each layer in the diode. We have proposed the following empirical formula for the electron mobility at 300 K, expressed in $cm^2V^{-1}s^{-1}$:

$$\mu = \frac{7250(1+2.9x)}{1+1.6\times10^{-9}N^{1/2}}, \tag{5}$$

where N is the doping concentration of the semiconductor in cm^{-3}. This formula was obtained from experimental data on the mobility of doped GaAs [10] and InAs [11], and assumes a linear dependence of the mobility on the indium mole fraction. The predicted mobility agrees with a simulation of the mobility of $In_{0.53}Ga_{0.47}As$ doped at 10^{18} cm^{-3} [12]. Experimental findings indicate that the mobility of $In_{0.53}Ga_{0.47}As$ on lattice matched InP is somewhat lower than predicted by (5), but is significantly greater than that of GaAs [13]. This will lead to lower series impedance in devices using $In_{0.53}Ga_{0.47}As$ on lattice matched InP than in standard GaAs devices. However, devices with InGaAs epilayers on GaAs substrates will have strained lattices, which may affect the mobility of the InGaAs layer.

The thickness of the epilayer also affects the series impedance. The epilayer of Schottky diodes is usually made to approximate the zero-biased depletion width, given by (4). Due to its dependence on the Schottky barrier height, the depletion width decreases with increasing indum mole fraction. Therefore, it is possible to fabricate InGaAs diodes with thinner epilayers than those in GaAs diodes, leading to lower series impedance in these devices.

D. Current Voltage Characteristic

A highly accurate model of the current voltage characteristic of the Schottky diode is essential to obtain a reasonable estimate of the conversion loss. The most frequently used models, such as Bethe's thermionic emission model [14] and Padovani and Stratton's field-thermionic emission model [15], are

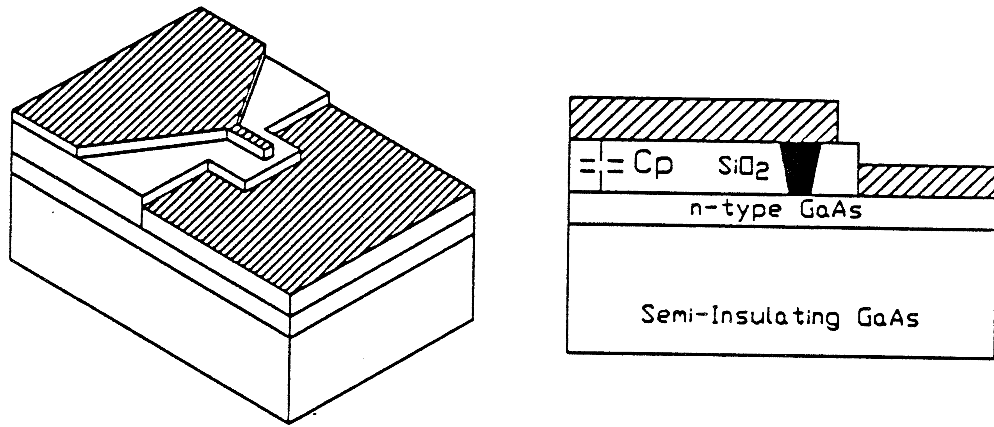

Figure 2. Planar diode chip.

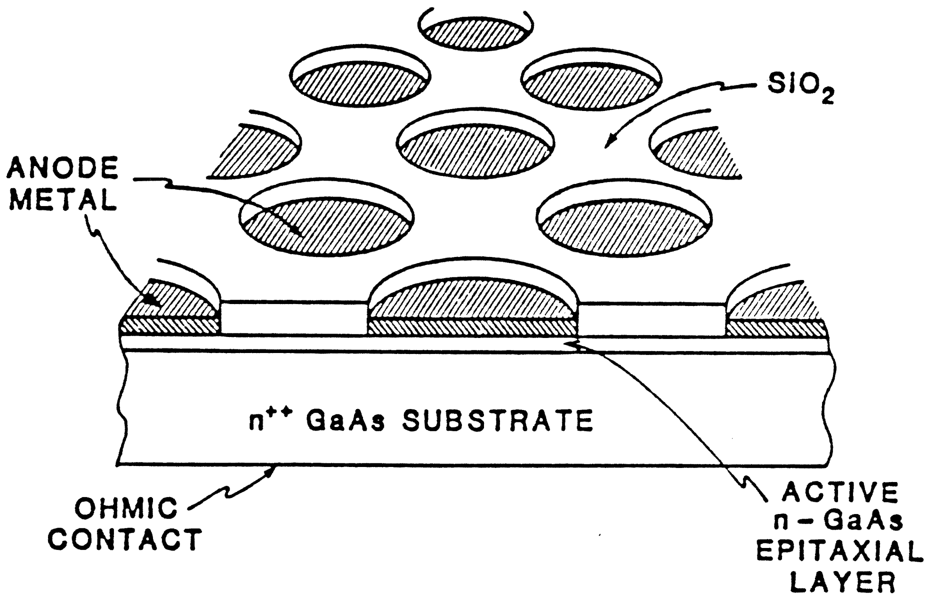

Figure 3. Whisker-contacted diode chip.

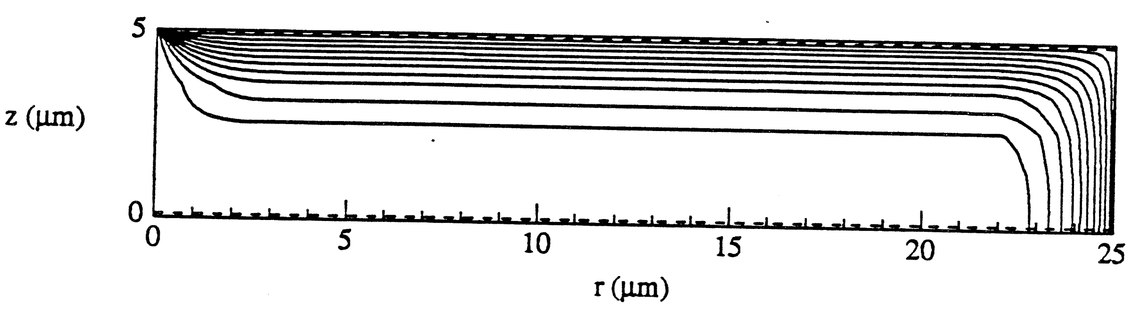

Figure 4. Current contours within whisker-contacted diode chip.
Each line represents 10 percent of the total current.

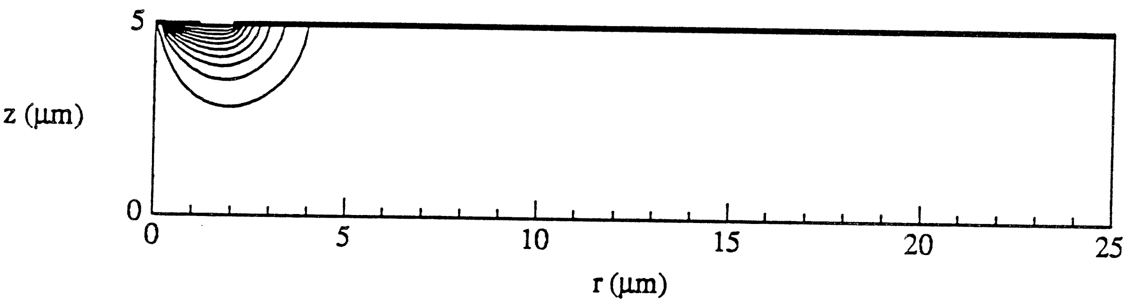

Figure 5. Current contours within planar diode chip.

either insufficiently accurate, or are applicable only in a limited voltage range. We therefore use a more sophisticated model similar to that of Crowell, Chang and Sze [1,2].

According to the thermionic emission model, the diode I-V characteristic is given by

$$I = I_{sat}\exp(V/V_o) \tag{6}$$

where I_{sat} is the saturation current and V_o is the inverse slope parameter, given by

$$V_o = \eta\frac{kT}{q}, \tag{7}$$

where η is the ideality factor. The ideality factor is an attempt to match the observed I-V characteristics of Schottky diodes with the thermionic emission model. The saturation current is expressed as

$$I_{sat} = ART^2\exp(-\phi_B/V_o), \tag{8}$$

where A is the anode area, R is the Richardson constant, and T is the temperature. The Richardson constant is given by

$$R = \frac{4\pi qm^*k^2}{h^3}, \tag{9}$$

where k is Boltzman's constant, h is Plank's constant, and m^* is the electron effective mass in the semiconductor. The electron effective mass in $In_xGa_{1-x}As$ varies with the indium mole fraction. We used a linear fit between the InAs and GaAs electron effective masses, given by

$$m^* = (0.067 - 0.044x)\, m_e, \tag{10}$$

where m_e is the free electron mass. Because the dominant factor in the saturation current is the barrier height, the saturation current increases very rapidly with the mole fraction. An important question therefore is whether the greater saturation currents of InGaAs diodes will decrease their conversion performance relative to that of GaAs diodes.

Due to various other phenomena, the actual I-V characteristic of a Schottky diode is more complicated than predicted by (6). Electron tunneling, for example, is an important effect, and has been investigated by Padovani and Stratton [15] and Crowell, Chang and Sze [1,2]. Chang and Sze's model also includes image force lowering of the Schottky barrier, and is the most sophisticated model available.

Padovani and Stratton have obtained analytic formulae for the case of thermionic-field emission, in which most of the emitted electrons have an energy greater than the Fermi energy, but tunnel through the barrier. These equations have been found to accurately predict the I-V characteristics at low and intermediate applied bias, but fail at bias voltages close to or exceeding the barrier voltage; in the latter regime, the dominant transport mechanism is not tunneling, but thermionic emission. Their method therefore cannot be used to obtain a continuous I-V relationship over the entire operating range of a Schottky diode mixer, from negative applied voltage to forward voltage exceeding the barrier voltage. The method of Crowell, Chang, and Sze resolves this deficiency, and also allows accurate consideration of image force effects.

Crowell and Sze [1] have developed a method that comprehensively calculates the transmission probability of an electron through the Schottky barrier. The model calculates the quantum mechanical transmission coefficient T(E,V) as a function of the electron energy E for a particular applied bias V. The method is applicable for both tunneling (in which the electron energy is less than the barrier height) and thermionic emission (in which the electron energy is greater than the barrier height). The model is based on a solution of Schrodinger's equation in one dimension,

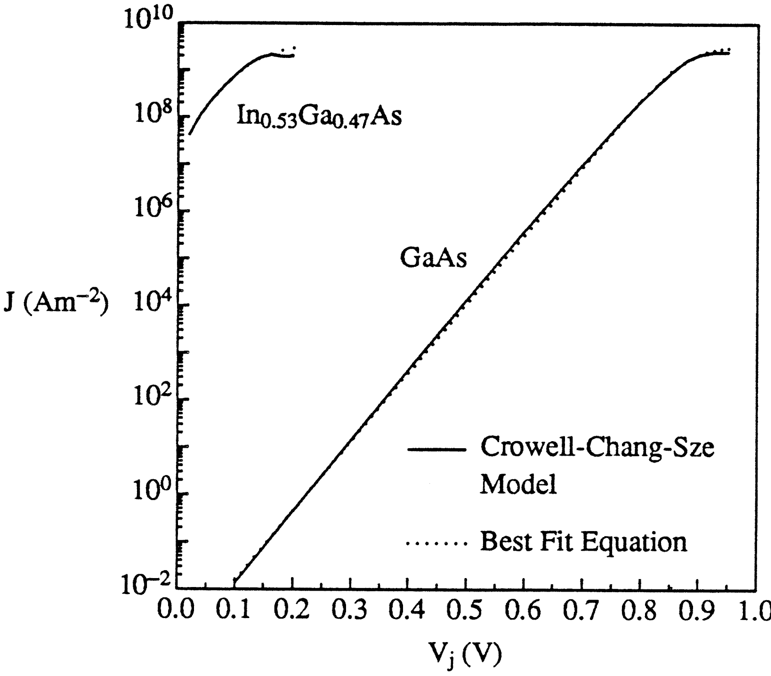

Figure 6. Predicted current-voltage characteristics of GaAs and $In_{0.53}Ga_{0.47}As$ Schottky diodes.

$$-\frac{\hbar^2}{2m}\frac{d^2\Psi}{dx^2} + V(x)\Psi(x) = E\Psi(x), \tag{11}$$

which is solved by imposing continuity relationships on the wavefunction $\Psi(x)$ and $\frac{1}{m}\frac{d\Psi}{dx}$ at the edge of the depletion region and at the metal-semiconductor boundary. V(x) is the potential in the depletion region, given by

$$V(x) = q\phi_B - \frac{q^2N}{\varepsilon}\left[Wx - \frac{x^2}{2}\right] - \frac{q^2}{16\pi\varepsilon x}. \tag{12}$$

The first term represents the potential due to the Schottky barrier, the second term is the potential in the depletion region, and the last term is due to the image force. After obtaining the wavefunction, we calculate the quantum transmission coefficient by comparing the probability density of the transmitted to the incident current. The probability current density is given by

$$j = \frac{q\hbar}{2im}\left[\Psi^*\frac{d\Psi}{dx} - \Psi\frac{d\Psi^*}{dx}\right]. \tag{13}$$

Chang and Sze have developed a method that incorporates Crowell's calculation of the transmission coefficient to obtain the diode I-V characteristic [2]. The total current density in this analysis is given by

$$J(V) = \frac{RT}{k}\int_0^\infty T(E,V)\,[F_s(E,V) - F_m(E)]\,dE, \tag{14}$$

where F_s and F_m are the Fermi-Dirac distributions in the semiconductor and the metal, respectively. The above expression considers the current in both directions, and as noted earlier, considers the tunneling current as well as the current due to electrons traveling over the barrier. The calculation requires T(E,V) to be calculated at several hundred discrete energies for each applied voltage, in order to obtain reasonable accuracy. The only drawback to this algorithm is that several million floating point operations are required to generate each (I,V) pair. This model, as well as the other models mentioned, assume thermal equilibrium electron distribution functions. At very high applied bias, this assumption may not be reasonable.

Figure 6 shows the I-V characteristics of various Schottky diodes as predicted by the preceding algorithm. The logarithm of the current, plotted versus the applied bias, has a fairly constant slope at low bias, but the slope decreases as the applied bias approaches the barrier voltage. Therefore, it is not sufficient to characterize the Schottky I-V relationship by a single parameter V_o; the reduction of the slope at high applied voltage must be taken into consideration. This is particularly important in mixer diodes that are operated at high bias and/or LO voltage, which is usually done in order to obtain the lowest possible conversion loss.

Rather than input the discrete (I,V) pairs into the conversion loss program, we used the following best-fit equation:

$$I(V) = \frac{1}{\frac{1}{I_{max}} + \frac{1}{I_{sat}[\exp(qV/\eta kT) - 1]}}, \tag{15}$$

where the parameters I_{max}, I_{sat}, and η were obtained from a fit to the I-V output of the Crowell-Chang-Sze analysis. As seen in Fig. 6, a fairly good fit can be obtained.

Figure 7 shows a comparison of the I-V characteristics obtained from this model with experimental data collected on an InGaAs diode, SDL33/1/5. The area of the diode was deduced from the measured capacitance along with other diode parameters, using (3). The indium mole fraction was deduced by matching the magnitude of the current at low applied voltage to that predicted by the theoretical model. The value of the deduce indium mole fraction was lower than that specified by the material supplier. We speculate that this discrepancy may be due to strain on the non-latice matched InGaAs of this sample. The strain may increase the energy gap and the Schottky barrier height of the semiconductor, and

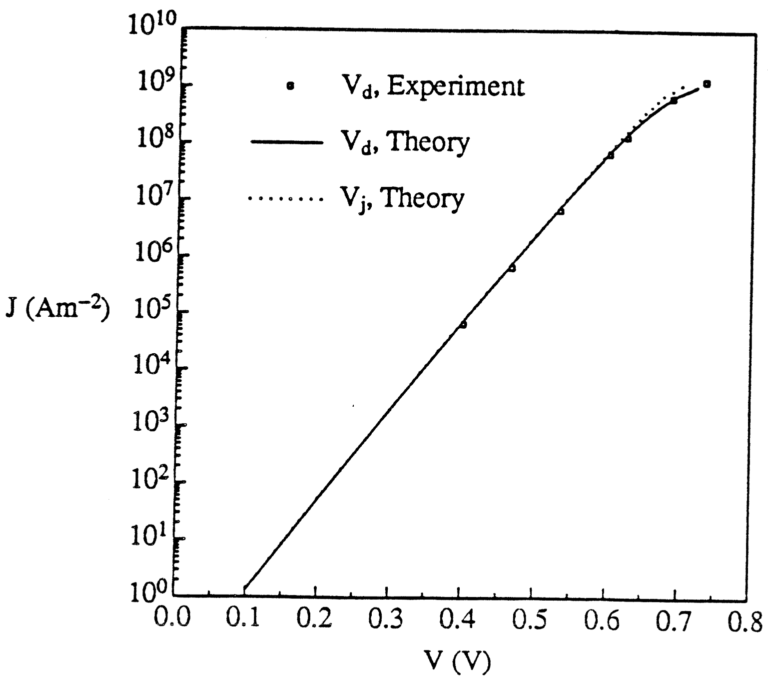

Figure 7. Theoretical and experimental current-voltage characteristics of InGaAs diode SDL 33/1/5. The theoretical calculations assume $x = 0.11$, $R_s = 13.2\ \Omega$, and anode diameter = 1.3 μm.

therefore make it behave as InGaAs with a smaller amount of indium. An excellent fit between theory and experiment was obtained throughout the voltage range. Apparently, deviations from thermal equilibrium statistics are not significant for this diode in the voltage range considered.

III. Conversion Loss Analysis

The conversion loss calculations that we have performed are based on the so-called multiple reflection algorithm developed by Held and Kerr [4,5]. A Pascal language computer program by S. Maas, known as DIODEMX, was used to perform the calculations [6]. Our only modification to the program was to use the I-V model described above, rather than the thermionic emission model.

A. Theory

The analysis discussed here is based on the assumption of a large signal LO source, upon which is superimposed a small signal RF. The time-dependent conductance of the diode is determined through a non-linear analysis known as the large signal algorithm, through use of the multiple reflection algorithm. The diode waveform is then resolved into the small signal admittance, represented in the frequency domain through its Fourier coefficients, which in turn is used to calculate the conversion performance of the diode. This analysis assumes a knowledge of the diode parameters as well as the embedding impedances.[1]

[1] The discussion in this section follows Maas, *Microwave Mixers*, to which the reader is referred for more details [6].

1. Large Signal Analysis

The mixer equivalent circuit is described by a series of loop equations at the mixing frequencies ω_n:

$$\omega_n = \omega_o + n\omega_{LO}, \tag{16}$$

where

$$n = -N, \cdots -2, -1, 0, 1, 2, \cdots N.$$

The value of N is necessarily finite for computation purposes, although in theory the current and voltage exist at an infinite number of harmonics. The loop equations are

$$V_{sn} - Z_{sn}I_{dn} - V_{dn} = 0, \tag{17}$$

where

$$V_{s0} = V_{DC} \tag{18}$$

and

$$V_{s1} = V_{LO}, \tag{19}$$

and all other V_{sn} are equal to zero. I_{dn} and V_{dn} are the diode current and voltage at the nth harmonic, which are obtained through use of the multiple reflection algorithm, which we shall not describe here [4,5]. Z_{sn} is the large-signal embedding impedance presented to the diode at the nth harmonic. The available LO power, P_{LO}, is given by

$$P_{LO} = \frac{V_{LO}^2}{8\,\mathrm{Re}(Z_{s1})}, \tag{20}$$

where Z_{s1} is the LO source embedding impedance.

2. Small Signal Analysis

The small signal voltage and current of the diode may be represented by

$$v(t) = \exp(j\omega_o t) \sum_{-N}^{N} V_n \exp(jn\omega_{LO}t) \tag{21}$$

and

$$i(t) = \exp(j\omega_o t) \sum_{-N}^{N} I_n \exp(jn\omega_{LO}t). \tag{22}$$

The time varying impedance may be represented by its Fourier series

$$z(t) = \sum_{-N}^{N} Z_n \exp(jn\omega_{LO}t), \tag{23}$$

where Z_n includes the series resistance R_s as well as the Fourier coefficients of the junction conductance and capacitance of the diode. Using Ohm's Law, these equations may be written in matrix form as

$$\mathbf{V} = \mathbf{Z}\,\mathbf{I}, \tag{24}$$

where **I**, **V**, and **Z** are matrices consisting of the coefficients discussed above.

Calculation of the conversion performance requires that the 2N + 1 port network discussed above be converted into a two port network consisting of the RF and the IF ports, at frequencies ω_1 and ω_0, respectively. This is achieved by modifying **Z** by adding the embedding impedances Z_{en} to its diagonals. The resulting augmented matrix, $\mathbf{Z}^a$, is inverted to form an admittance matrix, **Y**. Finally, all voltages, except at the RF and IF frequencies, are set to zero.

The conversion loss L of the mixer is defined as

$$L = \frac{P_{IF}}{P_{RF}} = 4|Y_{01}|^2 \mathrm{Re}(Z_{e1})\mathrm{Re}(Z_{e0}), \tag{25}$$

where P_{IF} is the power dissipated in the IF load and P_{RF} is the available power from the source.

B. Calculations

Tables I and II show the assumed and calculated diode parameters, respectively, and Table III indicates the non-zero embedding impedances assumed for the conversion loss calculations. The broadband assumption was used, that is, the impedances of the RF and the image terminations were assumed equal. According to an analysis by Grossman [16], the input impedance of a corner cube antenna is equal to approximately 145 Ω near the RF frequency. The other embedding impedances were chosen through impedance matching considerations with the diode. We chose an IF load impedance of 250 Ω, which in most cases was close to the small signal output impedance of the diode. The LO source impedance was assumed to be 100 + j 100 Ω, to match the input impedance of a typical diode.

Table I. Diode dimensions and doping concentrations.

epilayer material	GaAs	$In_{0.2}Ga_{0.8}As$	$In_{0.53}Ga_{0.47}As$
anode diameter	0.5 μm	0.5 μm	0.5 μm
chip diameter	100 μm	100 μm	100 μm
chip thickness	125 μm	125 μm	125 μm
epilayer thickness	807 Å	655 Å	389 Å
epilayer doping	5.0×10^{17} cm^{-3}	5.0×10^{17} cm^{-3}	5.0×10^{17} cm^{-3}
substrate doping	5.0×10^{18} cm^{-3}	5.0×10^{18} cm^{-3}	5.0×10^{18} cm^{-3}

Table II. Predicted diode parameters.

epilayer material	GaAs	$In_{0.2}Ga_{0.8}As$	$In_{0.53}Ga_{0.47}As$
C_{jo}	0.56 fF	0.67 fF	1.13 fF
R_s at 1THz	23.3 Ω	17.3 Ω	13.0 Ω
X_s at 1THz	18.8 Ω	16.0 Ω	12.2 Ω
I_{sat}	1.16×10^{-16} A	2.06×10^{-11} A	1.07×10^{-5} A
I_{max}	0.70×10^{-3} A	0.70×10^{-3} A	0.70×10^{-3} A
η	1.152	1.184	1.271

Table III. Mixer embedding impedances.

ω_{RF}	145 Ω
ω_{image}	145 Ω
ω_{LO}	100 + j 100 Ω
ω_{IF}	250 Ω

Figure 8 indicates the predicted conversion loss, as a function of V_{LO}, for a whisker-contacted GaAs diode. In general, the conversion loss decreases as the LO voltage is increased. Also, the LO voltage (and therefore power) requirement can be reduced by biasing the diode. Figure 9 shows the predicted conversion loss of various un-biased InGaAs and GaAs diodes. It is highly significant that the minimum conversion loss of $In_{0.53}Ga_{0.47}As$ diodes is only 1 to 2 dB greater than that of GaAs diodes. The much greater saturation current of $In_{0.53}Ga_{0.47}As$ diodes is not expected to significantly degrade their performance vis-a-vis GaAs diodes. Of even greater importance is that they will achieve this performance with only one-fourth of the LO voltage as required by GaAs diodes. The corresponding LO power requirement for $In_{0.53}Ga_{0.47}As$ diodes is about 0.1 mW, one-sixteenth that of GaAs diodes.

We also calculated the conversion loss of a sub-harmonically pumped, anti-parallel, whisker-contacted diode pair, operated without bias voltages. We caution that this is a preliminary analysis that was done before we performed the more accurate I-V analysis using the Crowell-Sze-Chang model, and therefore the predictions cannot be precisely compared with those of single diodes. To perform the conversion loss analysis, we used the single-diode equivalent circuit, in which the anti-parallel pair is modeled as a single diode in a mixer with twice the embedding impedance at even harmonics, and zero embedding impedance at odd harmonics [6]. Figure 10 shows that is possible to achieve a minimum conversion loss of 10 dB or better for all of the diodes by using sufficient LO power. However, to achieve this performance, a GaAs diode requires about 0.8 mW of LO power, compared to 0.5 mW for an $In_{0.2}Ga_{0.8}As$ diode and 0.1 mW for an $In_{0.53}Ga_{0.47}As$ diode.

These predictions are especially noteworthy because the proposed anti-parallel, sub-harmonically pumped diode structure is very difficult to bias, and because obtaining sufficient LO power at frequencies in the 600 GHz to 1 THz range has been a major limitation of Schottky diode mixer performance. Therefore, with their ability to provide good conversion efficiency using LO sources of modest power, at roughly half the RF frequency, sub-harmonically pumped, anti-parallel $In_{0.53}Ga_{0.47}As$ diode mixers will offer significant performance advantages to those using GaAs diodes.

IV. Experimental Results

The objective of this facet of our work is to develop a device fabrication technology which will enable us to produce $In_xGa_{1-x}As$ mixer diodes with predictable electrical characteristics. This was implemented by fabricating several batches of $In_xGa_{1-x}As$ diodes and comparing their DC characteristics with those of nearly equivalent GaAs diodes.

A. Fabrication Technology

In order to proceed with the fabrication of initial devices while the aforementioned theoretical analysis was being carried out, a simple model was used to estimate the diode performance for various values of indium mole fraction, x. Based on the lumped element diode model, the device impedance in the low conductivity state, Z_{off}, and the impedance in the high conductivity state, Z_{on}, were calculated in order to estimate the ratio Z_{off}/Z_{on}, which is infinite in the ideal case. We imposed a minimum allowable value of $Z_{off}/Z_{on} = 100$; this lead to preliminary values of $x = 0.2$ and $N_D = 2x10^{17}$ cm^{-3}. It was felt at the time that the significant leakage current predicted for $In_{0.53}Ga_{0.47}As$ devices would degrade mixer performance seriously; thus a lower mole fraction was chosen for our initial fabrication work. Unfortunately, $In_{0.2}Ga_{0.8}As$ is not lattice matched to any known usable substrate; therefore it was grown on GaAs, which presents the closest lattice match.

Whisker-contacted Schottky diodes were fabricated on $In_xGa_{1-x}As$ using virtually the same processing steps as are employed in the fabrication of GaAs diodes. They are as follows:

1. Active Layer Thinning. The active layer of the InGaAs is intentionally grown thicker than required for device fabrication. This allows impurity concentration profiling by a standard C(V) technique. The active layer is subsequently thinned electrochemically to a

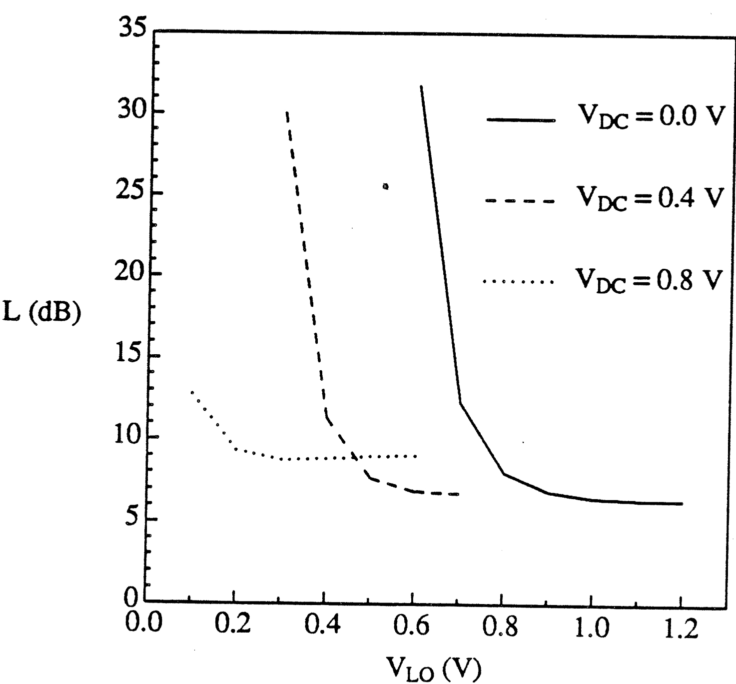

Figure 8. Predicted conversion loss of GaAs Schottky diode mixers at various bias at f_{LO} = 1 THz. Diode and mixer parameters are given in Tables I - III.

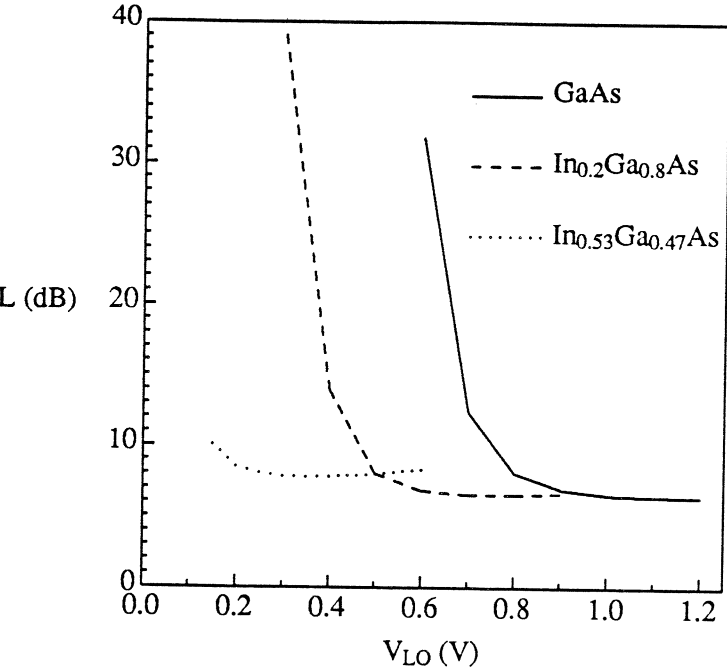

Figure 9. Predicted conversion loss of various single diode mixers at zero bias at f_{LO} = 1 THz.

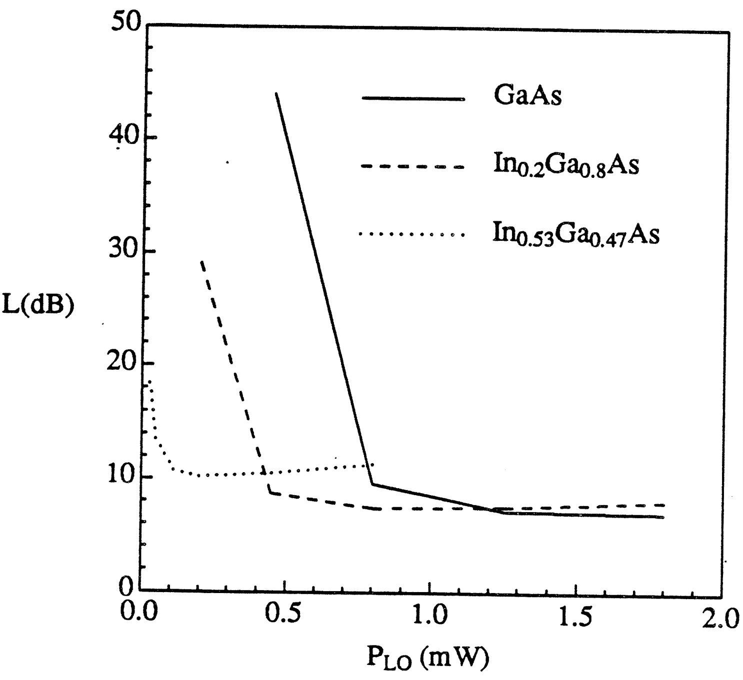

Figure 10. Predicted conversion loss of various anti-parallel, sub-harmonically pumped mixers at f_{LO} = 500 GHz and f_{RF} = 1005 GHz.

thickness slightly greater than the zero-bias depletion depth.

2. Oxide Deposition. A thin (4200 A) layer of SiO_2 is pyrolitically deposited on the active layer. This serves to not only passivate the resulting devices but also as an anode definition mask.

3. Anode Definition. Standard photolithography and reactive ion etching are employed to define anode windows in the SiO_2 layer. Anode metals (Pt and Au) are electroplated through these windows onto the underlying active semiconductor material to form the device anodes.

4. Ohmic Contact Formation. For back-contact devices, the n^{++} substrate is thinned mechanically and an ohmic contact is formed by electroplating Sn-Ni/Ni/Au and subsequent alloying at 425 °C.

Due to the lattice mismatch between the $In_{0.2}Ga_{0.8}As$ active layer and the GaAs substrate, cross-hatching was evident (as expected) on the surface, however it was observed to be minimal in samples which included a graded region from x = 0 to x = 0.2. The non-uniformity of the surface was manifested in the SiO_2 layer as well, but did not significantly hamper the fabrication procedure.

The most crucial step in device fabrication is anode formation. The detail of this step is specific to the semiconductor material and metal used. Early attempts at anode formation on $In_xGa_{1-x}As$ resulted in a device current-voltage characteristic which was changed, often irreversibly, by the application of high forward current. (This phenomenon is termed diode creep.) In addition, I-V characteristics varied greatly from device-to-device on the same 10 mil x 10 mil chip. These problems were ultimately overcome by slight adjustments of the processing parameters.

B. Measured Diode Characteristics

$In_xGa_{1-x}As$ diodes, as expected, have a lower forward turn-on voltage than do corresponding GaAs devices. This is illustrated in Fig. 11 which shows the actual I-V characteristics of both an $In_{0.2}Ga_{0.8}As$

diode and a GaAs diode. The difference in diode turn-on sharpness is due to differences in the active layer dopings, which is related to the ideality factor.

Figure 12 shows an I-V plot of data measured for four diodes with varying indium mole fractions. Diode 1T2/30 was fabricated on GaAs, while the others were fabricated on $In_xGa_{1-x}As$. Diode SDL33/1/5 has x = 0.3, and SDL25/3/5 and QED1/11/3 have x = 0.2. The straight lines represent the best fit through the three "low current" points, i.e., 100 nA, 1 µA, and 10 µA, where the characteristic is very nearly linear. The series resistance for each diode was inferred from the distance between that line and the measured voltage at a current of 1 mA. It can be noted that all of the devices have nearly the same ideality factor in that "low current" region.

C. Analysis

The device physical and electrical parameters are listed in Table IV. The first column lists the diode identification number; the next three columns indicate values of the indium mole fraction, active layer doping, and thickness, as specified to the material supplier. The diameters of the anodes were inferred from the measured zero-bias capacitance, and are listed in the fifth column.[2] The remaining columns contain values obtained from the measurement of the DC or low frequency characteristics of each diode. The voltage measured due to a bias of 10 µA, which is designated in the table as $V_{10\mu A}$, is listed for each device for comparison purposes.

Table IV shows that in devices with approximately the same epilayer thicknesses (within 200 A), R_s for the $In_xGa_{1-x}As$ devices is significantly less than that for the GaAs diode. This is due primarily to two factors: the larger diameter anodes of the InGaAs devices and the higher electron mobility of InGaAs. The other InGaAs devices, which have a thicker epilayer and lower doping than the GaAs diode, have relatively large R_s values. The capacitance values of the InGaAs diodes are greater than that of the GaAs diodes due to their greater device area. Their larger anode diameters were not intentional, but occurred due to the non-optimization of our initial processing parameters.

As was previously noted, all of the diodes have similar measured values of the ideality factor. The breakdown voltages, as expected [17], decrease with decreasing values of the energy gap, that is, with increasing values of x. Note that V_{BR} also depends on the epilayer thickness and doping, which accounts for V_{BR} of SDL25/3/5 being greater than that of the GaAs diode, in spite of its smaller energy gap.

The voltages measured at a current of 10 µA clearly indicate that the InGaAs devices require a substantially smaller voltage to achieve the same current density as the GaAs diode. It is this property of InGaAs that will be exploited in the anti-parallel configuration.

V. Conclusion

The difficulty of obtaining sufficient LO power from solid-state sources at frequencies above 600 GHz has become a limiting factor in the design and operation of heterodyne receivers in that frequency range. One method of circumventing the problem is to employ sub-harmonic mixing, which requires power at about half the frequency of the RF signal. The simplest configuration that relies on sub-harmonic pumping uses two anti-parallel diodes. However, GaAs diodes used in such an arrangement require a substantial bias for optimum conversion performance, and it is quite difficult to bias diodes in this configuration. We have therefore proposed the use of InGaAs mixer diodes, which have a low turn-on voltage, and can therefore efficiently operate without DC bias. The $In_xGa_{1-x}As$ material system allows for a controllable lowering of the Schottky barrier height and a corresponding reduction in turn-on voltage. Our work here has focused on both theoretical studies of the conversion performance and experimental development of InGaAs Schottky diodes. The theoretical studies have included the

[2] We note that the diameters listed here are greater than the diameters of the diodes in the 1 THz simulations discussed in the preceding two sections.

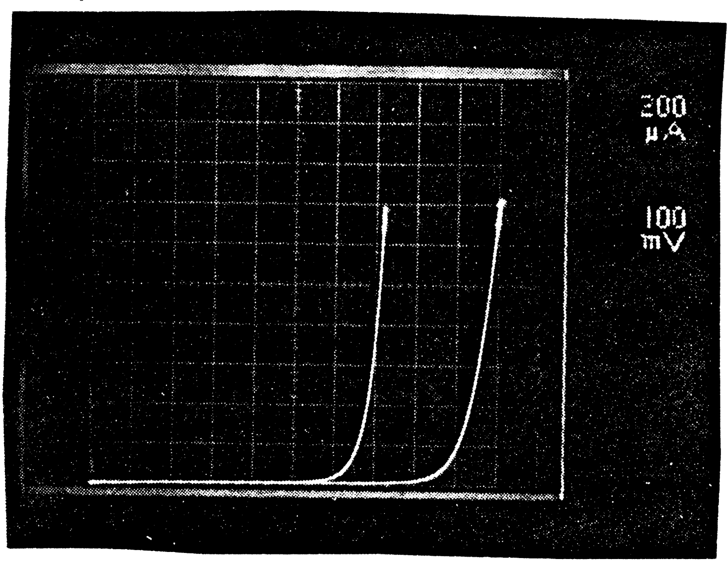

Figure 11. A comparison of the I-V characteristics of an $In_{0.2}Ga_{0.8}As$ diode (left-most trace) and a GaAs diode.

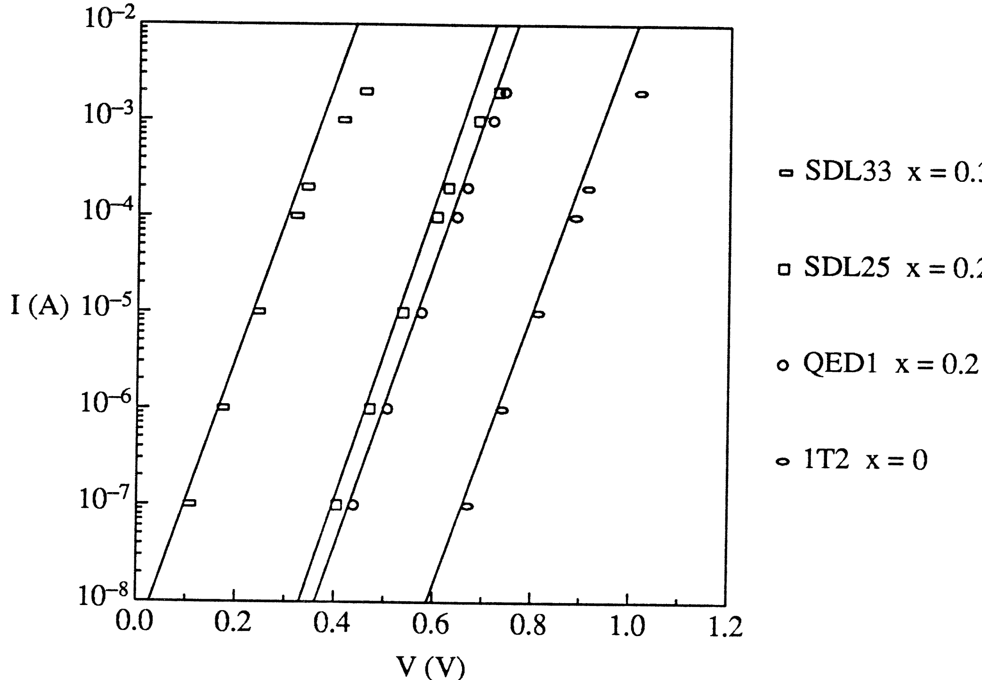

Figure 12. Current-voltage plot of four diodes with the indicated indium mole fractions.

Table IV. Measured and specified diode parameters.

Diode	x	N_D (cm^{-3})	t_{epi} (A)	d (μm)	R_s (Ω)	C_{jo} (fF)	η	V_{BR} (V)	$V_{10\mu A}$ (mV)
1T2/30	0.0	4×10^{17}	1000	0.97	20.5	0.95	1.21	5.8	799.8
SDL25/3/5	0.2	1.3×10^{17}	1500	1.3	22.0	2.16	1.11	7.3	525.6
QED1/11/3	0.2	2×10^{17}	800	1.5	10.5	3.10	1.15	4.1	564.2
QED2/11/2	0.2	2×10^{17}	800	1.5	11.0	3.42	1.15	4.2	569.1
SDL33/1/5	0.3	2×10^{17}	1500	1.3	27.0	2.34	1.19	< 1	232.3

prediction of diode parameters as well as the study of conversion loss and LO power requirements of InGaAs diodes.

Our studies of the diode characteristics have centered on the RF series resistance, an important parasitic, and the current-voltage relationship. We have performed calculations of the RF series resistance using a finite difference technique that considers high frequency phenomena such as the skin effect and charge carrier inertia. The calculations indicate that the series resistance of these devices will be lower than that of conventional GaAs devices, and thereby reduce the conversion loss. We have also written a program to predict the current-voltage relationship of Schottky diodes. Our program uses the model of Crowell, Chang and Sze, and takes into consideration quantum-mechanical reflection and image force lowering of the Schottky barrier. The results indicate that $In_{0.53}Ga_{0.47}As$ will have a much lower turn-on voltage than GaAs diodes, as expected. More importantly, the ideality factor of these diodes will be only slightly greater than that of GaAs diodes.

We have performed conversion loss studies of single and anti-parallel diode mixers using a computer program by Maas, modified for the more sophisticated I-V relationship discussed above. The results indicate that unbiased $In_{0.53}Ga_{0.47}As$ diodes will require about one-sixteenth of the LO power required by GaAs diodes, and will have an optimum conversion loss within 1 to 2 dB of comparably sized GaAs diodes. Simulations of sub-harmonically pumped, anti-parallel diodes have produced similar results.

In addition to the theoretical investigations, we have refined fabrication technology so that InGaAs diodes with stable, predictable electrical characteristics can be reproduced reliably. Initial problems with the electrical stability of devices were resolved by small modifications to the processing parameters; however, some optimization remains to be completed. Our results obtained thus far agree well with our I-V model and indicate that InGaAs devices can match or exceed the performance of GaAs diodes in terms of series resistance and the slope of the current-voltage characteristic.

This work is continuing with the investigation of $In_{0.53}Ga_{0.47}As$ diodes on InP substrates, in both the whisker-contacted and planar anti-parallel configurations. Additional variations to the fabrication procedure are anticipated for material with indium mole fraction greater than about 0.3, and although the changes are expected to be relatively minor, the optimization process will have to be repeated to ensure reliable reproducibility. DC and RF testing will be performed on the new devices to determine how well our model predicts device behavior.

Acknowledgments

We would like to thank Drs. J. East and G. Haddad of the University of Michigan Center for Space Terahertz Technology for their guidance and many helpful suggestions.

REFERENCES

[1] C.R. Crowell and S.M. Sze, "Quantum-Mechanical Reflection of Electrons at Metal-Semiconductors Barriers: Electron Transport in Semiconductor-Metal-Semiconductor Structures," *Journal of Applied Physics*, Vol. 37, No. 7, June 1966, pp. 2683-2689.

[2] C.Y. Chang and S.M. Sze, "Carrier Transport Across Metal-Semiconductor Barriers," *Solid-State Electronics*, Vol. 13, pp. 727-740.

[3] U.V. Bhapkar, "An Investigation of the Series Impedance of GaAs Schottky Barrier Diodes," M.S. Thesis, University of Virginia, May 1990.

[4] A.R. Kerr, "A Technique for Determining the Local Oscillator Waveforms in a Microwave Mixer," *IEEE Transactions*, Vol. MTT-23, Oct. 1975, pp. 828-831.

[5] D.N. Held and A.R. Kerr, "Conversion Loss and Noise of Microwave and Millimeter-Wave Mixers: Part I -- Theory," *IEEE Transactions*, Vol. MTT-26, Feb. 1978, pp. 49-55.

[6] S.A. Maas, *Microwave Mixers*, Artech House, 1986, pp. 89-128, pp. 315-339.

[7] K. Kajiyama, Y. Mizushima, and S. Sakata, "Schottky Barrier Height of n–$In_xGa_{1-x}As$ Diodes," *Applied Physics Letters*, Vol. 23, No. 8, 15 Oct. 1973, pp. 458-459.

[8] J.A. Copeland, "Diode Edge Effects of Doping-Profile Measurements," *IEEE Transactions*, Vol. ED-17, No. 4, May 1979, pp. 404-407.

[9] L.E. Dickens, "Spreading Resistance as a Function of Frequency," *IEEE Transactions*, Vol. MTT-15, No. 2, Feb. 1967, pp. 101-109.

[10] S.M. Sze, *Physics of Semiconductor Devices*, 2nd Ed., Wiley-Interscience, 1981, p. 29.

[11] Sze, p. 849.

[12] J. Costa, A.Peczalski, and M. Shur, "Monte Carlo Studies of Steady-State Electronic Transport in Compensated $In_{0.53}$GaSub0.47As," *Journal of Applied Physics*, Vol. 65, No. 12, 15 June 1989, pp. 5205-5206.

[13] E.H.C. Parker, *The Technology and Physics of Molecular Beam Epitaxy*, Plenum Press, p. 129.

[14] Sze, pp. 255-257.

[15] F.A. Padovani and R. Stratton, "Field and Thermionic-Field Emission in Schottky Barriers," *Solid State Electronics*, Vol. 9, 1966, pp. 695-707.

[16] E.N. Grossman, "The Performance of Schottky Diodes as Far-Infrared Modulators," *Int. Journal on Infrared and Millimeter Waves*, Vol. 8, No. 10, 1987, pp. 1293-13.

[17] Sze, p. 104.

HIGH GAIN AND NOISE IN SIS MIXERS AT SUBMILLIMETER WAVELENGTHS

Michael J. Wengler, Noshir Dubash, Gordana Pance
Electrical Engineering, University of Rochester, Rochester, NY 14627

and

Ronald E. Miller
AT&T Bell Labs, Murray Hill, NJ 07974

Abstract

Superconducting tunnel diode (SIS) mixers are used for radio astronomy from 100 to 500 GHz. They are being considered for NASA spaceborne astronomy at frequencies near 1,000 GHz. We report measurements of gain and noise in SIS mixers at 230 and 492 GHz. We measure high gain and noise associated with Josephson currents which have not been previously reported. These measurements show that Josephson currents are increasingly important as operating frequencies are raised.

We discuss the techniques we use to make these measurements. Measurements made with hot and cold blackbodies are shown to be inaccurate at high frequencies. The problem is that SIS's do not always respond linearly to the signal power incident on them. This is particularly important when 1) very broad band mixers are used and 2) Josephson effect currents are important. Both of these circumstances are present in the quasioptical SIS mixers favored for 500 GHz and higher. We use monochromatic signals to measure gain and noise to get around these problems.

Introduction

Mixers using superconducting tunnel diodes called SIS's (Superconductor-Insulator-Superconductor) as their detector are the most sensitive available for millimeter spectroscopy. They are the front end of choice for millimeter radio astronomy [1-5]. SIS's are predicted to work well at submillimeter wavelengths [6], and are now in astronomical use at 492 GHz [7]. Excellent reviews of the field are available [8, 9].

There are two charge carriers in the SIS: 1) superconducting or Cooper pairs of electrons and 2) quasiparticles or single electrons. The SIS can be thought of as a pair-device and a

quasiparticle-device connected in parallel. The pair-device is a Josephson junction which has a non-linearity in its IV at 0 V. The quasiparticle-device has an IV similar to the forward conduction IV of a regular diode. It has a non-linearity in its IV at its gap voltage, V_{GAP}. We are working with lead alloy SIS junctions. The dc current-voltage curve (IV) for our junction can be seen in both fig. 1 and fig. 2. The pair and quasiparticle non-linearities are both present. 1) The portion of the IV labeled S_0 is a non-zero current at 0 mV due to the pair-device. It can be seen to disappear when a magnetic field is applied to the SIS. 2) There is a sudden rise in current at V_{GAP} = 2 mV due to the quasiparticle device. This is only slightly affected by the presence of the magnetic field.

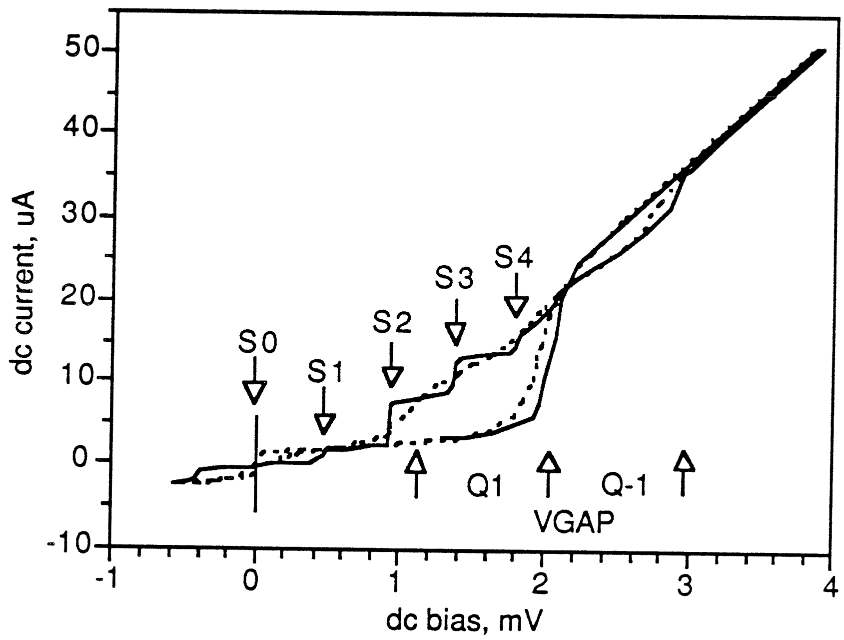

Fig. 1) SIS IV curves with and without 230 GHz radiation applied. The dashed lines are with magnetic field applied to suppress the Josephson effect, the solid are without. Shapiro step voltages and quasiparticle photon steps are shown.

Both the pair and the quasiparticle devices respond to incident radiation. In fact, both devices are so sensitive that they respond in a quantum fashion to radiation at frequencies as low as 100 GHz (even lower for SIS's fabricated from other materials). The SIS IV with 230 GHz radiation is shown in fig. 1. The structures in the IV labeled S_n are the Shapiro steps due to mixing of the incident radiation with Josephson currents in the pair-device. They are labeled

sequentially as they appear above the Josephson nonlinearity at 0 V. They are spaced in voltage by hf/2e, the energy of a photon divided by the charge of a carrier in the Josephson junction. The quasiparticle device has steps in its response as well. They are labeled Q_n and are labeled sequentially away from the quasiparticle non-linearity at V_{GAP}. Q_1 is only clearly seen when the magnetic field is applied to suppress S_2, S_3, and S_4. Their spacing in voltage is hf/e, twice as large as Shapiro step spacing because the quasiparticle carrier charge is only half as much as a pair.

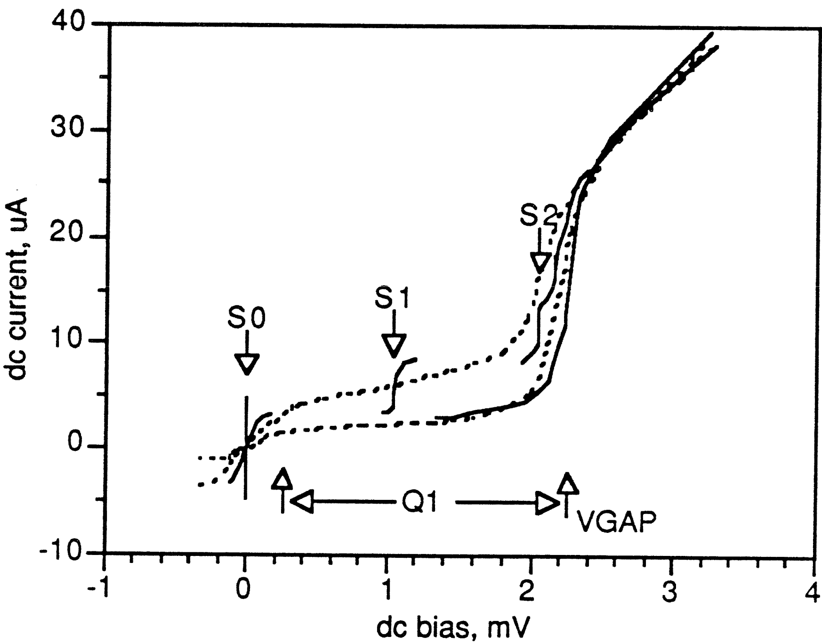

Fig. 2) SIS IV curves with and without 492 GHz radiation. The dashed lines are with a magnetic field applied, solid lines are without. Broad ranges of dc bias are not possible unless a magnetic field applied.

At 492 GHz, the quasiparticle steps are spaced 2 mV apart, and the Josephson step separation is 1 mV. An IV for an SIS at 4.2 K is shown in fig. 2. At this high frequency, there is only one quasiparticle step below the gap, and only two Shapiro steps. Without magnetic field applied, the SIS cannot be stably biased over most of the range from 0 to 2 mV. The SIS switches hysteretically between S_0, S_1, and S_2 in this range. This has very important implications for an SIS mixer at 492 GHz. At many frequencies, best SIS mixing performance occurs for a dc bias on Q_1 at about 1.9 mV. In fig. 1 it can be seen that stable bias is possible at this and all other dc bias voltages whether or not the pair currents are suppressed by magnetic field. But at 492 GHz and

(we presume) higher frequencies, it is only possible to have stable dc bias points on Q_1 if magnetic field suppresses pair currents. Just from the IV curves, we can see the increased importance of pair currents as frequency of SIS mixer operation is increased!

Quasioptical SIS Mixer

For work comparing SIS mixer performance over a broad range of millimeter and submillimeter wavelengths we require a radiation coupling structure which works over a very broad range. The mixer we use is identical to the quasioptical SIS mixer used at the Caltech Submillimeter Observatory [7]. The SIS is coupled to a planar spiral antenna, which is placed on the back of a quartz hyperhemispherical lens. This structure is similar to the original bowtie SIS mixer [10]. Both of these are coupled to radiation over a large spectral range including 100 to 500 GHz. Thus, we can measure a single junction's response to a broad range of frequencies.

The receiver at Caltech has been operated at 492 GHz with receiver noise temperatures below 1,500 K. Our receiver is about ten times as noisy. Much of this inferiority may be due to our use of lower current density SIS's. In this case, we are losing proportionally more of our signal due to SIS capacitance than the Caltech workers. Even though our receiver is noisier, we believe the effects we report here are relevant to the performance of lower noise receivers.

Gain and Noise Measurements

Hot and cold loads (blackbodies at 295 and 77 K) are usually used to calibrate astronomical receivers. The load provides a signal power of $S_{RF} = k_B T_L B$ where k_B is Boltzmann's constant, T_L is the temperature of the blackbody, and B is the bandwidth in which the power is measured. B is defined by a bandpass filter in the IF circuit. The total IF power measured includes both signal and noise,

$$P_{IF}(T_L) = S_{IF}(T_L) + N_{IF}.$$

The signal and noise portions of this are

$$S_{IF}(T_L) = GS_{RF} \quad \text{and} \quad N_{IF} = Gk_B T_N B.$$

G is the conversion gain of the mixer, T_N is its noise temperature. The mixer has a signal to noise

ratio SNR = 1 if $T_L = T_N$.

Two major difficulties arise in the measurement of some receivers using hot and cold loads. First, the accuracy in the determination of T_N is bad when T_N is larger than a few thousand degrees. Second, a change in P_{IF} as T_L is changed is not necessarily due to linear mixing. SIS diodes with Josephson currents in them are sensitive to very small power levels. This non-linear response to incident signal power is particularly severe when an SIS is dc biased near a Shapiro step. Submillimeter SIS mixers seem always to be biased between very strong Shapiro steps, so this non-linear response is a particular problem for high frequency SIS mixers.

The non-linear response of SIS mixers to hot and cold load radiation seems generally to increase P_{IF} as T_L is raised. In the normal way of finding G and T_N from measurements with two values of T_L, this produces an overestimate of G and an underestimate of T_N. In extreme cases, values of T_N below zero have been calculated.

The problem of using blackbodies as calibration signals is that they are incoherent. There is no way to distinguish at the mixer output what portion of P_{IF} is due to down-conversion of S_{RF}, and what portion is due to mixer noise. We can get around this problem by using monochromatic or coherent signals. In this case, a spectrum analyzer at the IF frequency is used to find S_{IF} and N_{IF}. The down-converted coherent signal, S_{IF}, appears as a spike well above the noise background. N_{IF} is just the height of the noise background. P_{IF} is now made up of two clearly distinguishable components, a spike which is signal and a smooth, broadband background which is noise.

Unfortunately, it is difficult to know accurately the power coupled from a coherent source into a mixer. First, it is not easy to make accurate power measurements of monochromatic millimeter and submillimeter signals, especially signals of low enough power to be useful in heterodyne measurements. More importantly, it is difficult to focus and align optics between the coherent source and the mixer so that nearly 100% of the signal power is coupled into the mixer. Blackbody loads do not have this problem as they can be made much bigger than necessary. But the coherent source radiates into only a single mode of the radiation field which must be made to

overlap with the radiation mode to which the mixer responds.

As a result, we make measurements assuming that our signal oscillator power is unknown, but constant in time. In this case, we cannot make an absolute measurement of gain or noise temperature, but we can make relative measurements. In particular, we can say how gain or noise changes as things are varied: LO power level, dc bias voltage, magnetic field strength, & c.

All of the relative measurements of gain and noise can be made absolute if even one good hot and cold load measurement of noise temperature can be made. Perhaps we have reason to believe we do not see non-linear response to hot and cold load in mixers operated with high LO power and biased near the gap voltage. Then measurement of gain and noise with hot and cold loads under this condition give an absolute calibration to all relative measurements made, even to relative measurements made under bias conditions in which it is known that the mixer responds in a non-linear way to hot and cold loads.

Two Oscillators

The simplest and most versatile set up to measure gain and noise of a mixer with a coherent signal is to use two rf oscillators, one to act as LO and one to serve as the signal. The signal oscillator must supply orders of magnitude less power to the mixer than the LO does. A major problem of the two oscillator system of gain measurement is the expense of submillimeter oscillators. On the other hand, astronomical groups will often keep two oscillator systems around for reliability. Also, sources which have insufficient power output to serve as LO's can still be used as signals.

Sidebands

A cheaper way to produce coherent signals is to weakly modulate the LO source at the IF frequency. The radiation leaving the oscillator will now have low power sidebands spaced an IF frequency away from the LO. It will now carry small signals at the signal and image frequencies. This modulation is straightforward with almost any millimeter or submillimeter source. A standard submillimeter oscillator is a 100 GHz Gunn diode oscillator driving a Schottky diode multiplier. The Schottky diode will usually have a coaxial connection for its dc bias. We use a coaxial-T and a

dc block to couple a 1.5 GHz signal into the Schottky diode along with its dc bias. In the simplest picture, we are modulating the bias on the multiplier, and therefore modulating its efficiency. The resulting LO leaving the oscillator is amplitude-modulated, and thus has sidebands at the signal and image frequencies of the mixer. Their intensity with respect to the LO can be controlled by varying the amplitude of the 1.5 GHz diode modulation.

We assume that virtually any LO source can be made to produce sidebands. In particular, a Gunn or YiG oscillator could have a 1.5 GHz signal superimposed on its dc bias. A Klystron could have its reflector voltage modulated by 1.5 GHz.

Receiver Gain with Coherent Signals

Measurements at 492 GHz have been made using both the two oscillator method and the sideband method. Measurements at 230 GHz have been made using the sideband method and hot and cold loads (we did not have access to two independent oscillators at this frequency).

One measurement that can be made with two oscillators that cannot be made with the sideband method is mixer gain as a function of LO power. With the sideband method, changing the LO power also changes the signal power, so different IF power out of the mixer is no longer simple to interpret as a mixer gain change. However, if the LO and its carriers were passed through a calibrated attenuator, the change in signal powers would be known as the LO power was varied, and it would be possible to learn how gain varies with LO power.

Gain at 492 GHz

We show gain measurements of our 492 GHz mixer as LO power is varied in fig. 3. The measurements on S_0 and S_2 are made with no magnetic field applied to the SIS. The gain measured on Q_1 corresponds to the usual way an SIS is used as a mixer at millimeter wavelengths. A magnetic field is applied to suppress Josephson currents for the measurement of gain on Q_1. Interestingly, if the magnetic field is turned off we see that a dc bias on two of the Shapiro steps has a gain which is over twice as high as mixing on the quasiparticle step. We see that gain on S_0 is a sharply peaked function of LO power, while mixing on S_2 and Q_1 have very similar

dependences on LO power. We suspect that this similarity is because mixing on S_2 comes from a complicated interaction between quasiparticle and pair current mechanisms.

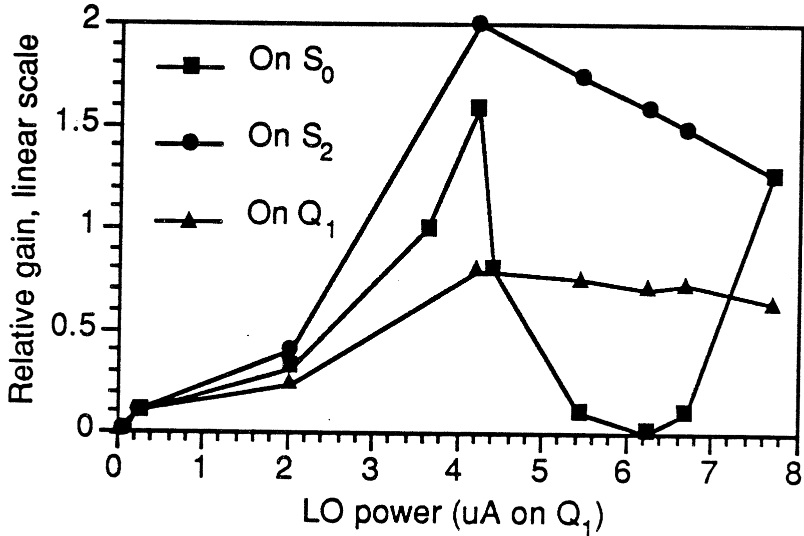

Figure 3) Relative gain at 492 GHz is measured as LO power is increased. Two of these curves are for bias points at the gain maxima near S_0 and S_2, with no magnetic field. The third is at the gain maximum of Q_1 with magnetic field.

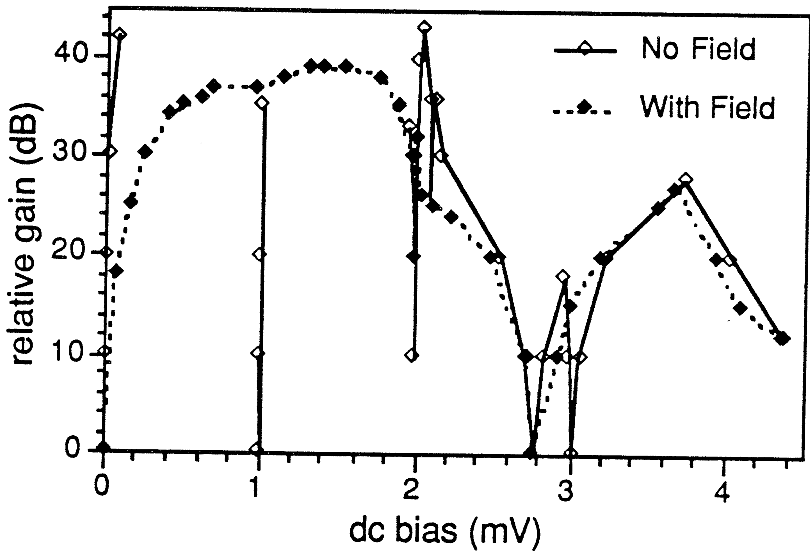

Figure 4) Relative gain at 492 GHz with and without magnetic field applied to suppress Josephson effects.

Fig. 4 shows relative gain at 492 GHz as a function of dc bias voltage. LO power for the No Field case is set to maximize the gain peak at 2 mV (on S_2). The LO power for the With Field case is set to maximize gain at 1.6 mV. Relative gain is now shown on a logarithmic scale; great

dynamic range is possible in gain measurements with coherent signals. The broad gain peak between 0 and 2 mV measured with magnetic field present shows that relatively high gain can be found nearly everywhere on Q_1, the broad quasiparticle photon step. With no field, we again see that higher gain is available on S_0 and S_2 then on Q_1. We also see that gain on the Shapiro steps is zero at their low dc voltage end, and the gain maximum occurs at their high dc voltage end. It is not easy to see in fig. 2, but the Shapiro steps actually have a finite slope. This may be an artifact of our bias circuit. It may be more correct to say that the Shapiro step gain is zero at its low current end and high at its high current end.

Sideband Coherence: No Effect on Gain

The sideband method generates both an upper and a lower sideband. However, these are not independent signals, they are phase referenced to the carrier and each other by virtue of arising from an amplitude modulation of that carrier. There are mixing processes such as parametric amplification which may actually rely on a phase modulation of the LO by the signal. Our sideband system might drastically underestimate the gain in such systems.

We checked the validity of the sideband technique against the two oscillator technique at 492 GHz. We did this by simultaneously modulating the LO at 1.5 GHz, and running the second signal oscillator at slightly more than 1.5 GHz above the LO frequency. We looked at the IF on a spectrum analyzer and could see both signals side by side. We then varied dc bias voltage and watched the IF power of both techniques. Relative gain measured both ways was identical. This was particularly important on the high gain Shapiro steps which we thought might be doing some parametric mixing, and would therefore show a lower relative gain when measured by sidebands. They didn't, so we see no evidence that gain due to the Josephson effect is parametric.

Gain at 230 GHz

Fig. 5 shows the gain of our SIS mixer at 230 GHz as a function of dc bias voltage. This was measured using the sideband method. Without field applied, dc biases between S_0, S_1, S_2, and S_3 showed gain which was visibly fluctuating on the spectrum analyzer. We assume that the SIS IV is actually slightly hysteretic between these steps. This hysteresis is masked in fig. 1

because our dc bias circuit uses feedback to achieve a constant voltage bias. We show gain with no field only where we found it to be stable. With magnetic field applied, all dc bias points show stable gain.

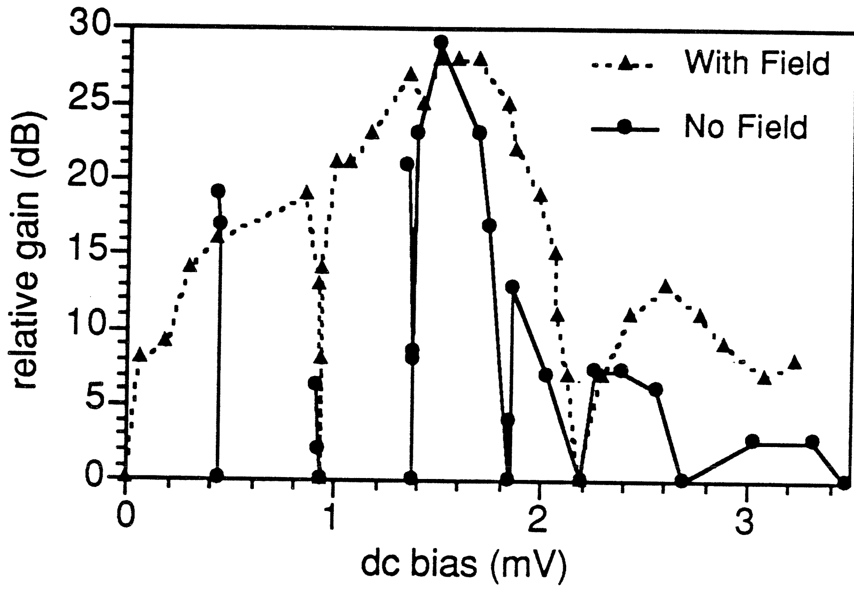

Figure 5) Relative gain at 230 GHz, with and without magnetic field to suppress Josephson effect.

The higher mixer gain is found with no field applied, as it was at 492 GHz. However, the gain is only about 1 dB higher than with field, and it is not occurring on a Shapiro step, but rather between them. We believe that mixing at this point is not influenced by pair currents. We believe the gain is a little higher without field applied because the underlying quasiparticle IV is a little bit better quality when no magnetic field is applied, as can be seen in fig. 1.

When magnetic field is applied, we might hope to see clear differences between the gain on Q_1 and Q_2. We do see higher gain in the region of Q_1 then in the region of Q_2. However, our magnetic field does not completely suppress Josephson currents. As a result, the shape of the gain curve shows deep minima at S_2 and S_5 which make it harder to distinguish clearly the quasiparticle step.

Gain Calculated From Current Responsivity

Information about SIS mixer gain can be gotten from measurements of the dc IV at two

slightly different LO power levels. This is explained by the Amplitude Modulation model of SIS mixer gain [11]. The current responsivity of a detector is

$$R_I(V,P_{LO}) \approx \frac{I(V,\, P_{LO}+dP_{LO}) - I(V,\, P_{LO})}{dP_{LO}}\,.$$

where I is the dc current through the detector, V is the dc bias voltage, and dP_{LO} is a small change in the applied LO power. A relative responsivity can be calculated numerically from two IV curves taken at slightly different LO powers without knowledge of absolute power levels.

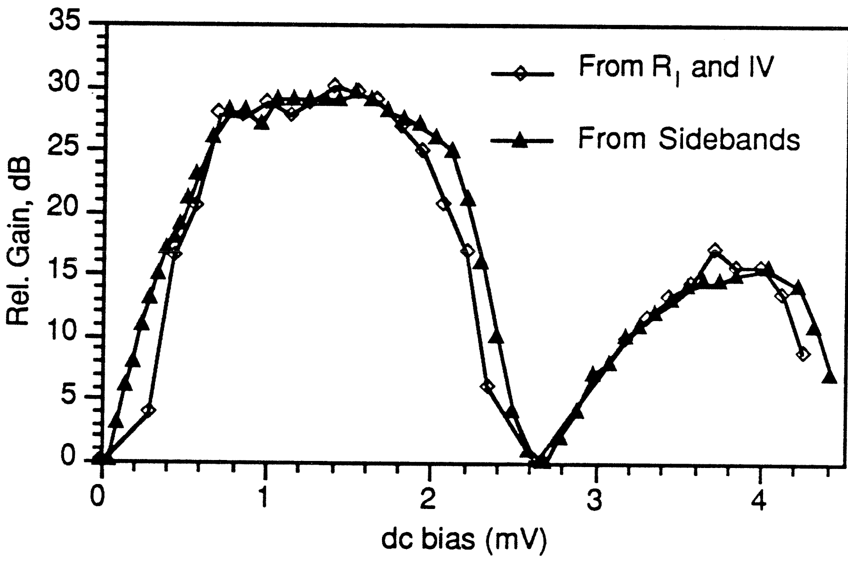

Figure 6) Relative gain at 492 GHz, measured with sidebands and calculated from IV curve measurements.

The total rf power P_{RF} incident on the SIS when illuminated by a signal P_S and P_{LO} is

$$P_{RF}(t) = P_{LO} + P_S + \sqrt{2P_{LO}P_S}\cos\omega_{IF}t.$$

The time varying part of this power causes a time varying current which is coupled into the following IF amplifier as IF power. Taking into account the output admittance G_D of the SIS mixer, the mixer's available gain is

$$G_A = R_I^2 P_{LO}/G_D.$$

In fig. 6, available gain from this expression is plotted along with gain measured using the sideband method. An arbitrary scaling factor is used to make the two relative gain curves overlap. The agreement is quite good over the whole range of bias voltage and gain magnitude. We have

made these measurements with Josephson currents suppressed, but we see some preliminary evidence that the high gain on Shapiro steps can also be explained in terms of an Amplitude Modulation model.

Noise Measurements with Coherent Signals

Relative gain measurements are really just a measure of mixer IF output power for a constant but unknown input signal. Of primary importance with SIS receivers for astronomy is signal to noise ratio (SNR). As with gain, we wish to know how this varies with changing LO, dc bias voltage, etc. Again, as with gain, a relative measure of SNR will yield valuable information.

If we use a very broad filter in the IF, we can measure mixer noise power N_{IF} with the input signal turned off. This is a more accurate way of measuring the noise floor surrounding the signal on a spectrum analyzer, as discussed above. S_{IF} is the IF power measured in a narrow band filter with the coherent signal turned on. Then the signal to noise ratio of the mixer is SNR = S_{IF}/N_{IF}. This SNR will be proportional to the inverse of the mixer noise temperature, SNR $\propto T_N^{-1}$.

SNR at 230 GHz

In fig. 7, we show the SNR calculated from coherent signal measurements at 230 GHz. Even though the maximum gain with and without the magnetic field applied are nearly the same (fig. 5), the SNR of the mixer is about 40% better when no field is applied. However, this SNR is sharply peaked as plotted against dc bias voltage. In fig. 1, it can be seen that the IV with no LO applied is somewhat degraded by the presence of magnetic field. It may be that this accounts for the better noise performance of the SIS here without field applied.

SNR at 492 GHz

Figure 8 shows the SNR measured at 492 GHz with and without magnetic field. Here we see the surprising fact that the high gain of the mixer on the Shapiro steps is not associated with a high SNR. In fact, the SNR on the broad quasiparticle step Q_1 is about twice as high as the SNR at the top of S_2, even though its gain is only half as high!

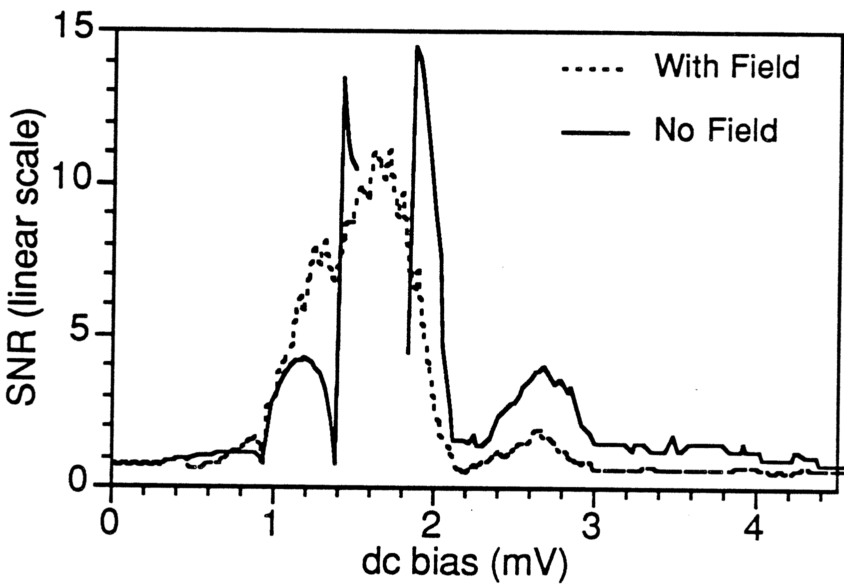

Figure 7) SNR found using sidebands at 230 GHz. Where No Field curve disappears, no stable bias was possible.

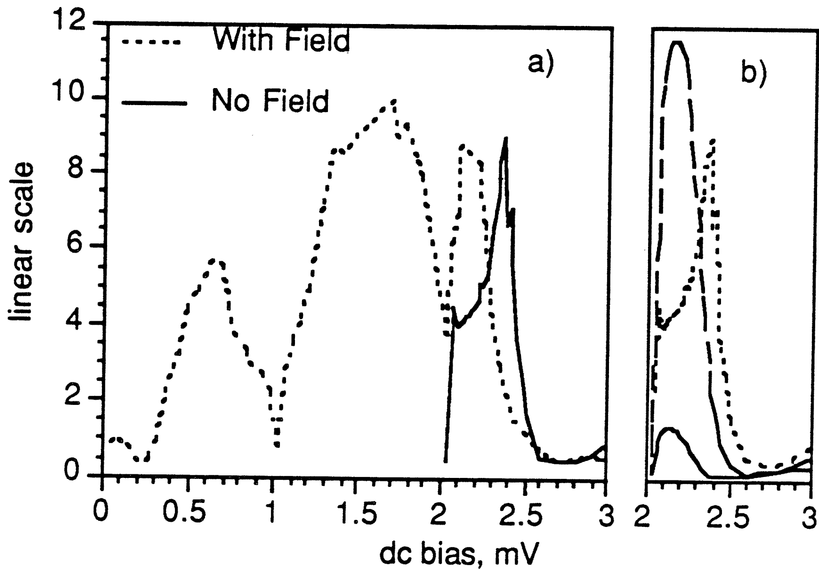

Figure 8) SNR at 492 GHz. a) SNR compared with field on and off. With no field, dc biases between 0 and 2 mV are not stable. b) the dashed line is gain, the solid line is noise, and the dotted line is SNR, done with no field.

Some clues about the nature of the high noise and high gain on S_2 are seen in fig. 8b. The raw data for IF signal (S_{IF}) and noise (N_{IF}) are plotted along with their ratio (SNR) at S_2 and higher dc biases. We see the gain rising quickly as S_2 (at 2 mV) is approached from above. But the noise rises even more quickly as S_2 is approached from above. So the SNR is falling even as

gain is rising. The data shown here reinforce the original claim that magnetic field is necessary for submillimeter operation of SIS mixers [10].

Hot and Cold Load Measurement Problems

We described above how an SIS mixer is usually measured using hot and cold blackbodies as calibrated signal sources. In fig. 9, we superimpose gain calculated from hot an cold load measurements with gain measured using a coherent sideband signal. The curves are arbitrarily scaled to be equal at 1.65 mV.

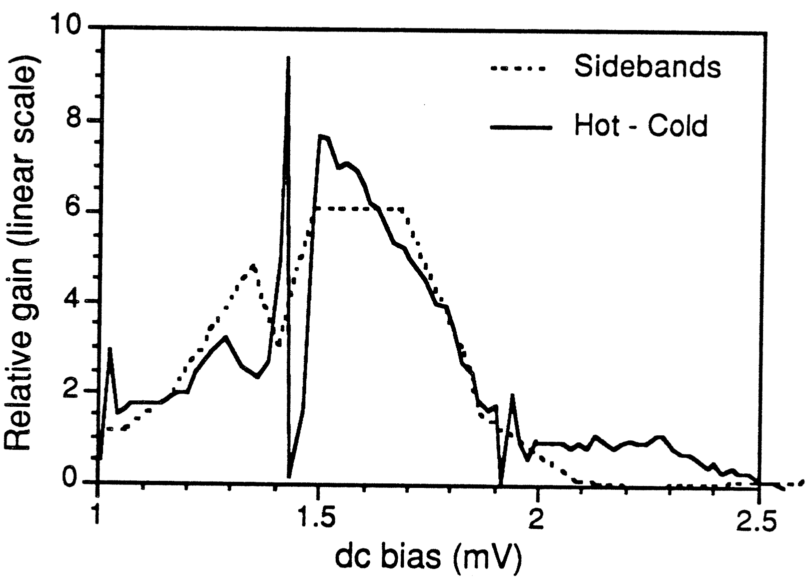

Figure 9 230 GHz relative gain inferred from hot and cold load measurements, and sidebands. The sideband gain here is the same as in fig. 5, but on a linear scale. Curves are scaled to be equal at 1.65 mV. Done with magnetic field on.

The hot and cold load method produces some wild structure near S_3 and S_4. It also overestimates gain at dc biases above 2 mV. Measurements of gain with sidebands showed that the mixer gain was actually quite smooth through the Shapiro steps, and was quite low at voltages above 2 mV. We believe that the reason for this deviation is non-linear response of the SIS mixer to the blackbody radiation, as discussed above. Essentially, the SIS is acting as a noise generator where the magnitude of its generated noise varies as the magnitude of broadband noise from the blackbody is changed. Above 2 mV, we may actually be seeing the effects of direct detection by the SIS of the hot and cold load radiation. A detector current has fluctuations in it which reflect the

statistics of the incident radiation. Even a small detected current from a hot thermal source may have a fairly large amount of fluctuation, since thermal sources have large fluctuations.

The conditions under which the SIS is most apt to act as a noise generator are 1) high frequency operation (it seems to be more of a problem in the submillimeter than in the millimeter), 2) broadband coupling structures: low capacitance SIS's coupled to planar antennas will be coupled to hundreds of GHz of blackbody noise, and 3) strong Josephson effects, especially if the SIS is biased very near to one of the Shapiro steps S_n.

The sideband and two-oscillator techniques are not susceptible to the same kind of misinterpretation between excess noise vs. actual down-conversion. A narrow band IF signal cannot be produced by any other mechanism than linear down-conversion of a narrow band signal. Our effort with sidebands may result in more reliable and simpler ways of calibrating SIS mixers. At minimum, we will develop protocols for verifying that mixer noise is not being mistaken for signal.

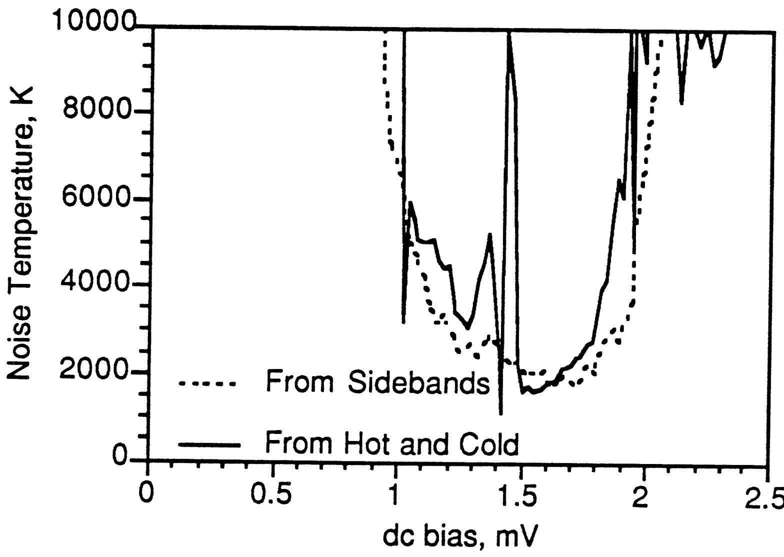

Figure 10) Noise temperature at 230 GHz calculated from hot and cold load measurements is shown as a solid line. The dashed line shows a/SNR where a is a scaling constant and SNR is from sidebands as shown in fig. 7.

Hot and cold load measurements establish mixer noise temperature. The solid line in fig. 10 shows the noise temperature of a 230 GHz receiver as dc bias is varied. The dashed line is

a graph of 1/SNR measured with sidebands, multiplicatively scaled so that it fits the solid line. The region of low noise shows good overlap with Q_1, the first quasiparticle photon step below the SIS gap voltage.

Even with magnetic field applied to suppress Josephson currents, we see glitches in the hot-cold measurement at all Shapiro steps near Q_1. Magnetic field is not able to fully suppress Josephson currents. More importantly, it does not suppress them enough to remove non-linear response to hot and cold loads. But again, the sideband measurement shows a smooth variation of mixer noise temperature through the Shapiro steps.

Because of the high receiver noise temperature at 492 GHz, gain and noise calculated from hot and cold load measurements were too noisy to use. We anticipate that the problems we report for hot and cold measurements at 230 would be much worse for 492 GHz. We expect to make better measurements at 492 GHz when we have a lower noise receiver.

Summary

SIS mixers at submillimeter frequencies are much more influenced by the presence of Josephson currents and Shapiro steps than are lower frequency mixers. At 492 GHz, twice as much gain is available when Josephson currents are not suppressed by magnetic field. Unfortunately, this high gain is associated with an even higher noise in these mixers, so that maximum signal to noise at 492 GHz is achieved with a magnetic field present to suppress Josephson currents.

The SIS mixer at 230 GHz has about the same gain available whether or not its Josephson effect currents are suppressed by magnetic field. It has lower noise at some biases when no field is applied, but those low noise regions are very narrow and might be difficult to use in a radio-astronomical receiver. But the trend in which it is more important to apply magnetic field to higher frequency SIS mixers is clearly seen comparing 230 and 492 GHz SIS mixer results here.

We have described two useful methods for measuring relative gain and noise in SIS mixers. One of these methods uses two oscillators, one as LO and one as signal. The other

requires only a single submillimeter source, which is modulated at the IF so that it serves as both LO and signal. We have discussed how to make these measurements absolute by calibrating them with hot and cold load measurements. We have shown that the Amplitude Model of SIS mixing can be used to predict relative gain even without mixing measurements.

We have discussed the relation of sideband-measured relative gain and noise to hot and cold load measurements. We have described how hot and cold load measurements can err, particularly near Shapiro steps, and have shown direct measurements of the errors at 230 GHz. We have suggested these effects will be much stronger at 492 GHz. We have laid the groundwork for SIS receiver calibration schemes which could augment hot - cold load techniques.

Acknowledgements

We are pleased to be supported in this work by NASA grant NAG 2-539 and NSF grant ECS-8857868.

References

1. Woody, D.P., R.E. Miller, and M.J. Wengler, "85-115 GHz receivers for radio astronomy," *IEEE Trans. Microwave Theory and Techniques,* vol. MTT-33, pp. 90-95, 1985.

2. Ellison, B.N. and R.E. Miller, "A low noise 230 GHz receiver," *Int. J. of IR and MM Waves,* vol. 8, pp. 608-625, 1987.

3. Blundell, R., M. Carter, and K.H. Gundlach, "A low noise SIS receiver covering the frequency range 215-250 GHz," *Int. J. of IR and MM Waves,* vol. 9, pp. 361-370, April, 1988.

4. Kerr, A.R., S.-K. Pan, and M.J. Feldman, "Integrated tuning elements for SIS mixers," *Int. J. of IR and MM Waves,* vol. 9, pp. 203-212, 1988.

5. Ellison, B.N., *et al.*, "A 345 GHz receiver for radio astronomy," *Int. J. of IR and MM Waves,* vol. 10, pp. 937-947, 1989.

6. Wengler, M.J. and D.P. Woody, "Quantum noise in heterodyne detection," *IEEE Journal of Quantum Electronics,* vol. QE-23, pp. 613-622, May, 1987.

7. Büttgenbach, T.H., *et al.*, "A broad-band low-noise SIS receiver for submillimeter astronomy," *IEEE Trans. Microwave Theory and Technique,* vol. 36, pp. 1720-1726, December, 1988.

8. Richards, P.L. and Q. Hu, "Superconducting components for infrared and millimeter-wave receivers," *Proc. IEEE,* vol. 77, pp. 1233-1246, 1989.

9. Tucker, J.R., "Quantum limited detection in tunnel junction mixers," *IEEE J. Quantum Electron.,* vol. QE-15, pp. 1234-1258, November, 1979.

10. Wengler, M.J., *et al.*, "A low noise receiver for millimeter and submillimeter wavelengths," *Intl. J. of IR and MM Waves,* vol. 6, pp. 697-706, 1985.

11. Phillips, T.G. and D.P. Woody, "Millimeter- and submillimeter wave receivers," *Ann. Rev. Astron. Astrophys.,* vol. 20, pp. 285-321, 1982.

TERAHERTZ DETECTORS BASED ON SUPERCONDUCTING KINETIC INDUCTANCE

E.N. Grossman, D.G. McDonald, J.E. Sauvageau*

Abstract – **The inductance of a superconducting stripline varies with the concentration of Cooper pairs in the superconductor. This inductance variation may be used as the basis for highly sensitive radiometers, bolometers, and heterodyne mixers. We describe recent progress on three kinetic inductance devices: a large-area, absolute radiometer intended for use in the NIST Low-Background Infrared Calibration Facility, and small, antenna-coupled devices used either in a bolometric mode as direct detectors, or in a non-equilibrium, "photoinductive" mode as heterodyne mixers. The photoinductive mixers are of particular interest because their frequency coverage starts at approximately the energy gap, 2Δ, and extends upward. The impedance matching concerns which make extension of SIS mixers to high frequencies so difficult in practice are greatly relaxed for photoinductors because they lack the large parasitic capacitances inherent in a junction-like geometry.**

I. Introduction

Kinetic inductance is a property of superconducting thin films that has long been recognized as playing a major role in the propagation velocities and impedances of superconducting transmission lines. However, it was only fairly recently [1] that its potential usefulness in a host of other applications was recognized. As was emphasized in that original work, one of the main reasons kinetic inductance can serve as the basis for sensitive transducers of any kind is the fact that it is naturally compatible, both in terms of impedance matching and fabrication processes, with one of the most sensitive amplification devices known, namely the SQUID [2]. At NIST,we have lately begun a program to explore some of the applications of kinetic inductance devices in infrared and submillimeter wave detection. The goal of this presentation is to provide an overview of this work.

The (low-frequency) inductance per unit length of a superconducting stripline, when normalized to the ordinary, magnetic inductance, without field penetration, of a normal stripline with the

* The authors are with the Electromagnetic Technology Division of the National Institute of Standards and Technology, Boulder, CO 80303. This work is supported by the SDI Metrology Program, the Innovative Science and Technology Program of SDIO, and by NASA's Office of Space Science and Applications. U. S. government publication, not subject to copyright.

same dimensions is given by [3]

$$L \propto \left(1 + \frac{\lambda_1}{d}\coth\frac{t_1}{\lambda_1} + \frac{\lambda_2}{d}\coth\frac{t_2}{\lambda_2}\right) \tag{1}$$

where t_1 and t_2 are the thicknesses of the two superconductors, d their separation, and λ_1 and λ_2 the two superconducting penetration depths. (The penetration depth is a characteristic length scale of a superconducting material, equal to the e-folding length over which the magnetic field decays due to Meissner effect at the surface of a bulk sample.) The reason far-i.r. radiation enters the picture is that the penetration depth is related to the density of superconducting pairs, N_s,

$$\lambda^2 = \frac{m}{\mu_0 e^2 N_s}\left(\frac{\xi_0}{l_e}\right) \quad , \tag{2}$$

and N_s can be altered both by very small changes in temperature, or by direct application of pair-breaking radiation ($h\nu > 2\Delta(T)$, where Δ is the temperature-dependent superconducting energy gap). In (2), m and e are the mass and charge of the electron, and μ_0 the permeability of free space. The term in parentheses is a correction to what would otherwise be just the conventional London penetration depth. It accounts for the effect of impure or otherwise "dirty" materials. ξ_0 is the superconducting coherence length (roughly speaking, the "size" of a Cooper pair) and l_e the electronic mean free path. From (1) and (2) it is clear that, other things being equal, dirty materials, i.e. those with l_e small, will produce the greatest inductance changes for a given change in the pair density. As will be seen, this leads to our choice of metallic alloys such as NbTi and NbZr, in which l_e is comparable to the interatomic spacing, for the photoinductive elements in our devices.

The microscopic mechanism by which pair-breaking radiation is converted into changes in N_s is indicated schematically in Fig. 1. Both direct pairbreaking and electromagnetic absorption by quasiparticles lead to an effective temperature T^* of the quasiparticle population which can, in general, be different from the bulk temperature of the lattice. Energy is exchanged between the quasiparticle population and the lattice through inelastic electron-phonon scattering, the same interaction as is responsible for the electron pairing of (conventional, low-T_c) superconductivity in the first place. The thermalization of the quasiparticle population through electron-phonon scattering takes place on a sub-nanosecond timescale; therefore, this "non-equilibrium" response in N_s has sufficient speed to be useful for a heterodyne mixer. The detailed dynamics of this response, and the way in which the quasiparticle and pairbreaking phonon populations are coupled, is a subject of some complexity which has been studied for many years [4]. In addition to this non-equilibrium response, there is also a slower, bolometric response due to the bulk heating of

the photoinductive element relative to the substrate. In this case, N_s is determined simply by equilibrium thermal generation of quasiparticles, with approximately the canonical $1 - (T/T_c)^4$ dependence. Near T_c this leads to a very sensitive dependence of inductance on temperature. This is a conventional microbolometer response [5]. For the typical sizes of our devices, it can be expected to yield bandwidths of 100's of kHz, and phonon-limited noise-equivalent powers (NEP's) even at temperatures as high as 8 – 9 K.

The balance between the non-equilibrium and bolometric responses may be conveniently characterized by two thermal conductances in series, a microscopic G_m related to the electron-phonon scattering, and a macroscopic G_M determined by bulk and surface thermal conductivities. The details depend on the assumptions made for substrate material and superconducting film properties, but are typically as indicated by the dependence shown in Fig. 2, (which we have calculated using the formalism described in reference [4]). For a given detector geometry, the bolometric response dominates at temperatures near T_c, and the non-equilibrium response dominates at temperatures well below T_c. Early experiments on the response of superconducting films to fast laser pulses [6] showed this behavior very explicitly; near T_c the electrical pulses were heavily rounded due to the bulk heat capacity of the superconducting film, but as the temperature was lowered, the pulses grew progressively sharper until the rise times matched those of the laser pulses.

II. Radiometer

The first project undertaken at NIST which exploits kinetic inductance for infrared detection is an absolute radiometer intended for installation at the NIST Gaitherburg, Low-Background Infrared (LBIR) calibration facility [7]. The radiometer is intended for standards-grade intercomparisons of 300 K black-body emitters in the 10 – 150 THz frequency range, with spectral resolution $\Delta\nu/\nu \approx 0.01$. Its design is therefore optimized for high accuracy, i.e. large dynamic range, and not simply for high sensitivity. In other words, the important figure of merit for this application is not raw NEP, but rather the ratio of NEP to the largest signal power detectable without saturation, (which must be of the order of 10^{-7} W).

This leads to a somewhat different design strategy than that used in conventional i.r. bolometers. Since the NEP of a thermal detector may be expressed as the product of the bulk thermal conductance G [W/K] and a temperature noise spectral density S_T [K/Hz$^{1/2}$], lowering the thermal conductance of a conventional detector always improves the performance, even in the phonon-limited case, where $S_T \propto G^{-1/2}$. Typically, bolometer designers do very extensive thermal engineering to obtain the minimum G possible at any given operating temperature. (Lower oper-

ating temperature can be thought of as a "brute force" method of attaining lower G.) However, saturation power also scales linearly with G, so in our case, in which high accuracy is the important figure of merit, lowering G does not improve performance at all. Rather, G is chosen so as to accommodate the largest signal powers employed, and all the effort is concentrated on lowering S_T, i.e. on building a sensitive thermometer.

The method we employ is outlined schematically in Fig. 3 and has been described in further detail in Ref. 7. Four inductive superconducting striplines are arranged in a Wheatstone bridge configuration. The Nb striplines are approximately 3 μm wide and have a stretched-out length of 4 cm each, yielding inductances in the convenient range of 0.1 μH at our typical operating temperatures of 0.6 – 0.9 T_c. Two of the inductors are thermally isolated from the rest of the chip by etching a trench on the back side of the Si, surrounding a square island at the center of the chip, of 2 mm^2 area. The island is physically attached to the rest of the chip only by the 9 μm thick, boron-doped, etch stop layer. This etch stop layer, which forms a relatively flexible, thin membrane, determines the thermal conductance G between the temperature-sensitive inductors and the substrate. A resistive heater lies on the island along with the thermally isolated inductors. A small inductance mismatch is built into the bridge to allow it to be balanced even with the maximum anticpated powers absorbed in the island. The bridge is driven with a large audio-frequency current, typically 5 mA at 3 kHz. The imbalance current is sensed by a commercial DC SQUID amplifier, located off chip and operated in flux-locked mode.

Thermal responsivity and noise measurements were performed on the bridge over an operating temperature range (of the chip, not the island) of 4.0 – 7.0 K. The thermal conductance was determined independently by using the resistive superconducting transition of the island inductors as a thermometer. Responsivity was measured from the change in in-phase and quadrature components of the demodulated SQUID output as small (10 nW) pulses of electrical power were applied to the island heater. Noise was determined from the RMS voltage noise level at the SQUID output measured directly on an audio-frequency spectrum analyzer. The responsivity measurements are shown in Fig. 4 as the filled circles. The curve is a theoretical model, with no free parameters except the geometric aspect ratio of the inductors (which is known from optical microscopy to $\sim$ 10 %), and assuming the canonical $N_s \propto 1 - (T/T_c)^4$ dependence of the pair density. The measured NEP of the bridge is NEP $= 4.4 \times 10^{-11}$ W/Hz$^{1/2}$ at an operating temperature of 6.6 K. The measured thermal conductance is $G = 1.0 \times 10^{-4}$ W/K, which implies $S_T = 440$ nK/Hz$^{1/2}$. As discussed above, the high NEP, some 3 orders of magnitude higher (i.e. worse) than conventional liquid-He temperature bolometers optimized for sensitivity, is a direct result of the high value of G, which in

turn is the result of our design emphasis on absolute accuracy. In terms of temperature sensitivity, the result is in fact somewhat better than any other i.r. bolometer we know of (most of which are based on semiconductor thermistors). The most important conclusion from this experiment is perhaps the fact that no excess noise source is observable. That is, the measured voltage noise level agrees with that implied by the parameters of the SQUID to within the measurement accuracy.

III. Antenna-coupled Bolometers and Mixers

Given the impressive level of temperature sensitivity attainable with kinetic inductance elements coupled to SQUID amplifiers, it is natural to explore the possibilities of i.r. detectors when the relevant thermal conductances are made very small. The desirability of an entirely lithographic fabrication method and an interest in large arrays have led us to consider a strategy of obtaining low G by antenna-coupling the incident radiation into a very small ($\ll \lambda$) inductor as opposed to using a large area, surface-absorbing detector similar to the radiometer. Although the short wavelength limit of lithographic antenna performance has not been well explored beyond 119 μm [8], there seems to be no fundamental obstacle besides lithographic resolution to extending high efficiency antennas to the thermal infrared, where many of our array applications exist. At 119 μm and longward, where our heterodyne mixer work is concentrated, on the other hand, high efficiencies have already been achieved [9].

The basic physical structures of our microbolometers and our heterodyne mixers are identical. This structure is illustrated in Fig. 5. The thin film photoinductive element lies at the feed of a lithographic antenna. The size of the photoinductive element is taken to be 1 μm $\times$ 1 μm $\times$ 10 nm in our calculations. In general, it should be as small as possible, but submicron lithography is not required in order to achieve very interesting levels of sensitivity. The photoinductive element forms one section of the loop of a DC SQUID. The SQUID loop, as shown in the lower, cross-sectional view of the feed region, consists of the lower photoinductive element, which contacts the two antenna feed points, the two Josephson junctions, and an upper photoinductive film, identical to the lower one, which closes the loop. I.r. radiation concentrated by the antenna is dissipated in the photoinductive elements, where, either through non-equilibrium effects or through bolometric heating, the pair population is reduced, increasing the inductance of the two photoinductive films. The DC SQUID is operated in a somewhat unusual way, as a 3-terminal inductance transducer rather than as a magnetic flux transducer. As shown in the inset of Fig. 6, a large DC bias or "control" current, I_c, analogous to the magnetic bias of a conventional SQUID magnetometer, is passed through the photoinductive film. This is in addition to the conventional bias current,

I_b, passed through the two Josephson junctions in parallel. The control current serves to set the operating point on the steep section of a high-order lobe in the SQUID's voltage-flux (V - Φ) pattern (Fig. 6). As the loop inductance varies with incident i.r. radiation, the V - Φ pattern accordions in and out, modulating the SQUID output voltage. This turns out to be an extremely sensitive way to read out very small changes in inductance.

The fundamental reason this device is expected to be sensitive can be summarized in one word: impedance-matching. At frequencies above the energy gap, $\nu > 2\Delta(T)/h$, which is the range for which the detector is intended, the thin film superconductor has the surface impedance of a normal metal. Thus, for $\sim$ 10 nm thicknesses, sheet resistances will be 10 – 40 Ω/square for Nb or Nb alloys. This is ideal for matching to lithographic antennas. Note that, unlike SIS mixers, Schottky diodes, or other devices with a junction-like geometry, there will be no large parasitic capacitance associated with the photoinductive element. On the other hand, at i.f. frequencies and below, the thin film is a superconducting (i.e. inductive) short. This is ideal for matching to SQUID amplifiers. Thus, without any special matching structures or tuning elements, the device is naturally impedance-matched to the rest of the circuit at both the RF and the i.f. frequencies.

Given that we have not discussed anything regarding non-linearities in the I-V curve, there might be some who would ask how such a device can operate as a sensitive heterodyne mixer. This is a parochial viewpoint, however, arising out of the accidental fact that Schottky diodes and SIS mixers happen to dominate the mixer world at millimeter frequencies, and both of those devices mix through the non-linearity in their I-V curves. In fact, any sensitive direct detector can also act as a sensitive heterodyne mixer. This occurs because the electromagnetic field *amplitudes* (signal and local oscillator (LO)) add, while the detector senses total power, which is proportional to the square of the total field amplitude. In other words, $E = E_{LO}\cos\omega_{LO}t + E_s\cos\omega_s t$, (where $E_s \ll E_{LO}$), which implies that $P = P_{LO} + 2\sqrt{P_{LO}P_s}\cos\omega_{IF}t + P_s + P_{2\omega} + ...$ Heterodyne mixers of this type, which includes the InSb hot-electron mixer and the 2D electron gas mixer [10] are often called "total power" or "envelope" mixers. Although it is true that any direct detector will also function as a heterodyne mixer, the question of whether it can serve as *useful* heterodyne mixer is more complicated. In particular, the device's usefulness strongly depends on its speed. Unlike diode-like mixers, the available i.f. bandwidth of total power mixers is limited by the basic physics of the detection process. In the case of the photoinductive mixer, the bandwidth is limited by the microscopic processes of quasiparticle recombination, quasiparticle scattering with pairbreaking phonons, and pairbreaking phonon escape. The size of our SQUID is small enough that self-resonance effects should be a less restrictive limit on the bandwidth than the quasiparticle

recombination.

We have done a thorough design analysis of the photoinductive mixer which has been described in more detail elsewhere [11]. The heart of the analysis is calculation of the device's voltage responsivity. This has three main parts: calculation of the SQUID's sensitivity as an inductance transducer (in V/H), calculation of the photoinductive film's inductance sensitivity, $\partial L/\partial N_s$, (which follows from Eqns. 1 and 2), and calculation of the quasiparticle population's response to incident i.r. photons, which includes all the complicated dynamics of quasiparticle and phonon recombination and scattering. These dynamical processes are still the subject of active research; nonetheless, a basic theoretical framework does exist and has been, to some extent, confirmed by experiment. The Rothwarf-Taylor equations are a pair of coupled rate equations for the quasiparticle and pairbreaking phonon populations, and they represent the simplest level of approximation for treating these dynamical processes. By performing a small-signal stability analysis of these rate equations, we have made predictions (shown in Fig. 7) of the response of the quasiparticle density perturbation to a harmonically varying (at frequency ω_{IF}) quasiparticle injection rate. This is proportional to the device's responsivity as a function of i.f. frequency. The response is nearly Lorentzian, and the 3 dB bandwidths are strongly dependent on temperature, varying from 200 MHz to 1 GHz as T/T_c varies from 0.5 to 0.9. The absolute levels of the response shown in Fig. 7 assume the LO power level is held fixed, which is not realistic. In fact, at the higher temperatures, the optimum LO power also rises rapidly, so that there is a tradeoff between LO power requirement and available i.f. bandwidth. However, the levels of LO power required, even at the higher temperature, are still very low, only 10's of nW, many orders of magnitude less than Schottky diodes, and comparable to the levels required for mm-wave SIS mixers. In short, the bandwidths are large enough, 200 – 1000 MHz, and the required LO powers low enough, 10's of nW, to make the device extremely interesting as a practical THz mixer.

It is unknown whether the complicated scattering and recombination processes of the quasiparticle/phonon system will introduce excess noise into the device's response. So long as this recombination noise is no more than a factor of a few greater than the shot noise limit, however, the total noise should be dominated by the noise of the SQUID amplifier. The noise of well designed SQUIDs is tantamount to just the Johnson noise of the two junction shunt resistors in parallel. For our design, this amounts to a Johnson noise of roughly 1 Ω at T = 4 – 8 K, appearing at the SQUID output. Using this, and the estimate of voltage responsivity described above, the heterodyne noise performance of the device may be estimated, as shown in Fig. 8. Well above the gap frequency, noise temperatures should be approximately $10h\nu/k$, comparable to the best SIS

receiver results at frequencies well below the energy gap. As shown however, this performance is only achieved by using metallic alloy superconductors such as NbZr and NbTi, which have both high critical current densities (allowing large control currents to be used in the SQUID transducer), and large penetration depths, which yield larger inductance sensitivities (Eqns. 1 and 2). Pure niobium photoinductors are expected to yield performance comparable to current Schottky diodes. In both cases, however, the SQUID junctions can and will be made of conventional Nb/Al-AlO_x/Nb trilayers.

IV. Recent Experimental Results

These theoretical estimates are sufficiently promising to have encouraged us to begin an experimental program to investigate antenna-coupled kinetic inductance bolometers and mixers. Initially, we are confining ourselves to pure Nb devices for ease of fabrication. Fig. 9 shows an early device, fabricated as indicated by the schematic in Fig. 5, but which lacks the SQUID junctions. The rectangular areas on each side of the antenna feed are windows in the SiO insulation layer where the SQUID junctions would lie. In this device, the sloped edges of the 100 nm thick antenna layer, needed for obtaining contact with the the thin photoinductor, were fabricated by reactive-ion etching at high O_2 concentration. In later devices, we have switched to a different geometry, in which the photoinductive layer is deposited first, and a Au antenna deposited on top of it. A typical low temperature I-V curve of such a device is shown in Fig. 10. The measurement is performed in vacuum, and the I-V curve is therefore highly hysteretic due to self-heating. This fact can be used to estimate, in a very unambiguous way, the bulk thermal conductance from the device to the substrate. First the T_c of the film is measured by heating the entire substrate, and then, at any given operating temperature $T < T_c$, the I-V curve is measured. The power dissipated at the point just before the device switches back into the zero-voltage state yields G. The basic parameters of the device as derived from these measurements are listed in table I.

Table I. Cryogenic Properties

Thickness	20 nm
Length × Width	2.5 μm × 1.0 μm (nom.)
T_c	7.25 K
Z_{normal}(DC)	20 Ω
G_M (6 K)	2.4×10^{-7} W/K
$NEP_{phonon} = (4kT^2G)^{1/2}$	2.2×10^{-14} W/Hz$^{1/2}$

Finally, we have measured the optical responsivity of the large-area, radiometer chip using a

1.3 μm wavelength laser diode coupled into the cryostat with an optical fiber. The silicon chip is transparent at 1.3 μm and the fiber illuminates the chip from the back side. The purpose of this experiment was to try to find a definite non-equilibrium response of the photoinductive stripline when it is illuminated with pairbreaking radiation. (1.3 μm is about 300 times the gap energy.) Unfortunately, we have not yet been able to set up the appropriate driver electronics to allow us to modulate the laser diode. A component of the response that remained essentially flat at frequencies well above the thermal time constant of the island (which corresponds to about 600 Hz) would be an unambiguous sign of non-equilibrium response. The optical responsivities we have so far measured at d.c. are shown as a function of temperature in Fig. 4 alongside the thermal responsivity data. Over the temperature range covered, they track the thermal responsivities to within the experimental error. This is expected on the basis of the very large volume of the photoinductor (the microscopic G_m scales with detector volume) and the fact that the fiber illuminated the island approximately uniformly. We hope to separate out the thermal and non-equilibrium responses in in future experiments of this type on the radiometer chip.

V. References

[1] D.G. McDonald, "Novel Superconducting Thermometer for Bolometric Applications", *Appl. Phys. Lett.*, vol. 50, p. 775 (1987)

[2] M. B. Ketchen, "DC SQUIDs 1980: The State of The Art", *IEEE Trans. Magn.*, vol. MAG-17, no. 1, p. 387 (1981)

[3] T. Van Duzer and C. W. Turner, *Principles of Superconductive Devices and Circuits*, Elsevier, New York, 1981, p. 112 ff.

[4] See for example W. H. Parker, "Modified Heating Theory of Nonequilibrium Superconductors", *Phys. Rev. B,* vol. 12, p. 3667 (1975), and S. B. Kaplan, C. C. Chi, D. N. Langenberg, J. J. Chang, S. Jafarey, and D. J. Scalapino, "Quasiparticle and Phonon Lifetimes in Superconductors", *Phys. Rev. B*, vol. 14, p.4854 (1976)

[5] T. L. Hwang, S. E. Schwartz, and D. B. Rutledge, "Microbolometers for Infrared Detection", *Appl. Phys. Lett.*, vol. 34, p. 773, (1979)

[6] L. R. Testardi, "Destruction of Superconductivity by Laser Light", *Phys. Rev. B.*, vol.4, p. 2189 (1971)

[7] J. E. Sauvageau, D. G. McDonald, and E. N. Grossman, "Superconducting Kinetic Inductance Radiometer", accepted for publication in *IEEE Trans. Mag.*, MAG-27, (1991)

[8] The only quantitative work on antennas at 10 μm, A. Sanchez, C. F. Davis, K. C. Liu, and A.

Javan, "The MOM Tunneling Diode", *J. Appl. Phys.*, vol. 49, p. 5270 (1978) and J. G. Small, G. M. Elchinger, A. Javan, A. Sanchez, F. J. Bachner, and D. L. Smythe, "AC Tunneling at Infrared Frequencies", *Appl. Phys. Lett.*, vol. 24, p. 275, (1974), was done before many of the basic properties of lithographic antennas were known, and quoted coupling efficiencies never exceeded 2 – 3 %.

[9] D. P. Neikirk, P. P. Tong, and D. B. Rutledge, "Imaging Antenna Array at 119 μm", *Appl. Phys. Lett.*, vol. 41, p. 329, (1982), and recent work described by S. Gearhart and G. Rebeiz in these proceedings.

[10] For the InSb hot electron mixer, T. G. Phillips and K. B. Jefferts, "A Low Temperature Bolometer Heterodyne Receiver for Millimeter Wave Astronomy", *Rev. Sci. Inst.*, vol. 44, p. 1009 (1973), for the 2D Electron Gas Mixer, see J. X. Yang, W. Grammer, F. Agahi, K. M. Lau, and K. S. Yngvesson, "2-Dimensional Electron Gas Hot Electron Mixers for Millimeter and Submillimeter Waves" these proceedings.

[11] E. N. Grossman, D. G. McDonald, and J. E. Sauvageau, "Far-Infrared Kinetic Inductance Detectors", accepted for publication in *IEEE Trans. Mag.*, vol. MAG-27, (1991)

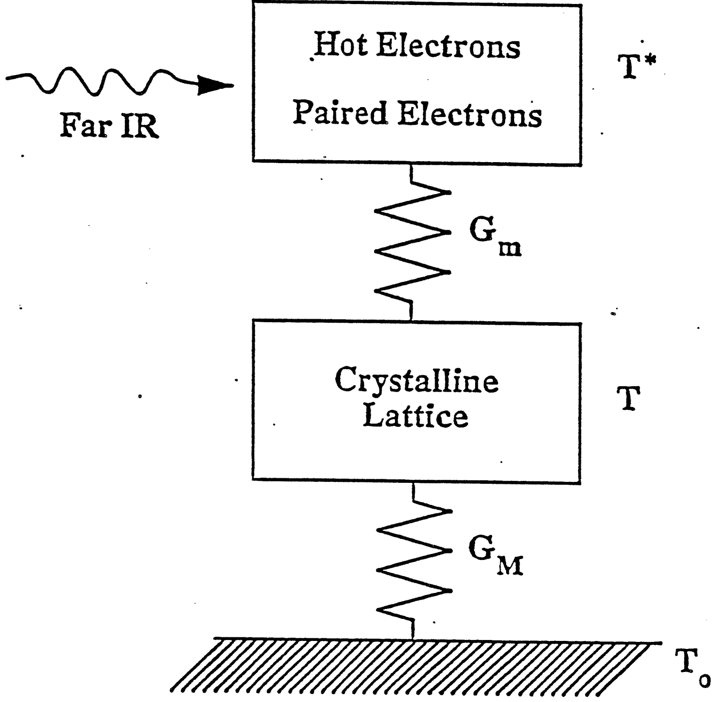

Figure 1 Thermal circuit showing how the far IR power flows through the system. The device is a conventional bolometer if $G_M \ll G_m$.

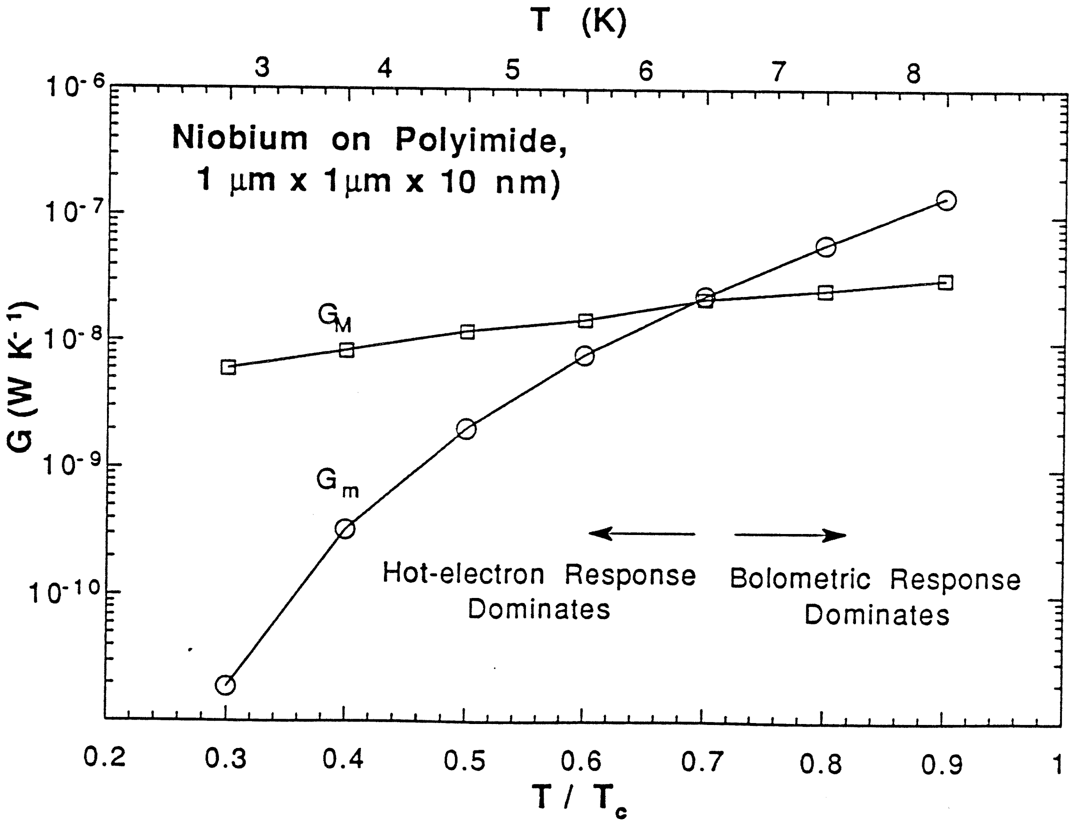

Figure 2. Distinction between bolometric and hot-electron regimes, in terms of microscopic and macroscopic thermal conductances.

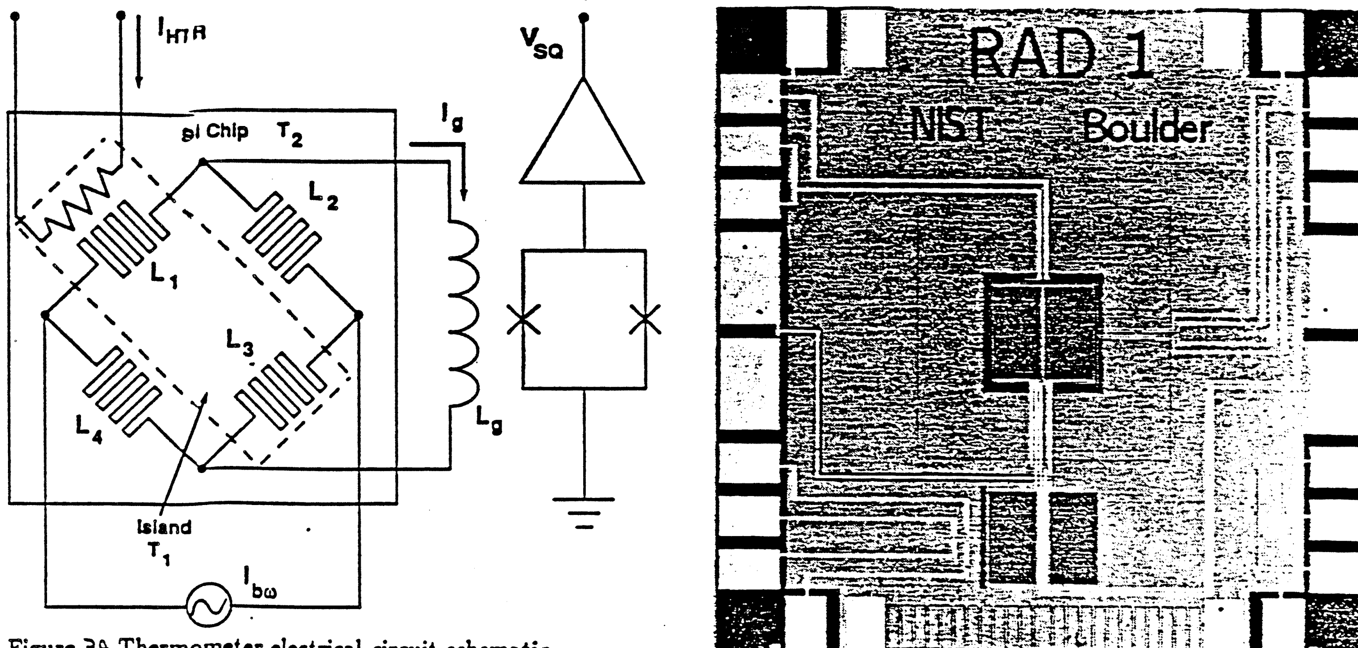

Figure 3A Thermometer electrical circuit schematic.

Figure 3B Typical radiometer thermometer chip fabricated and tested. The central region in the figure is the thermally isolated island. This region is surrounded by the boron-doped membrane and contains the two kinetic inductors L_1 (left) and L_3 (right). The chip is 1 cm on a side.

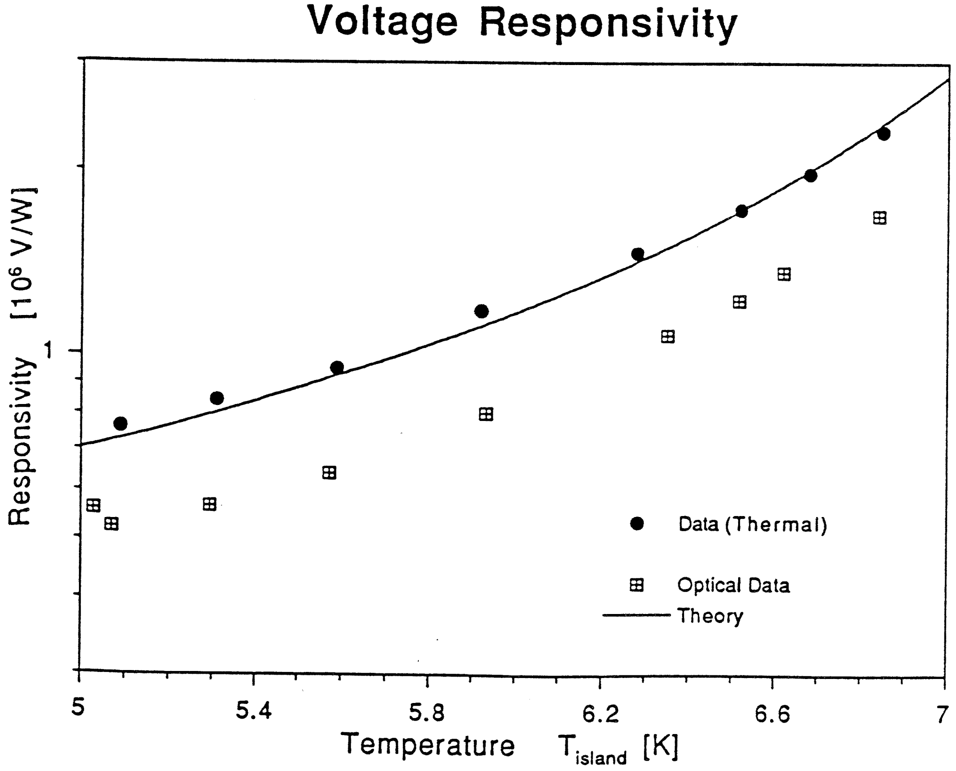

Figure 4. Measured thermal and optical responsivities of the radiometer. The theoretical model assumes a conventional $N_s \alpha 1 - (T/T_c)^4$ dependence.

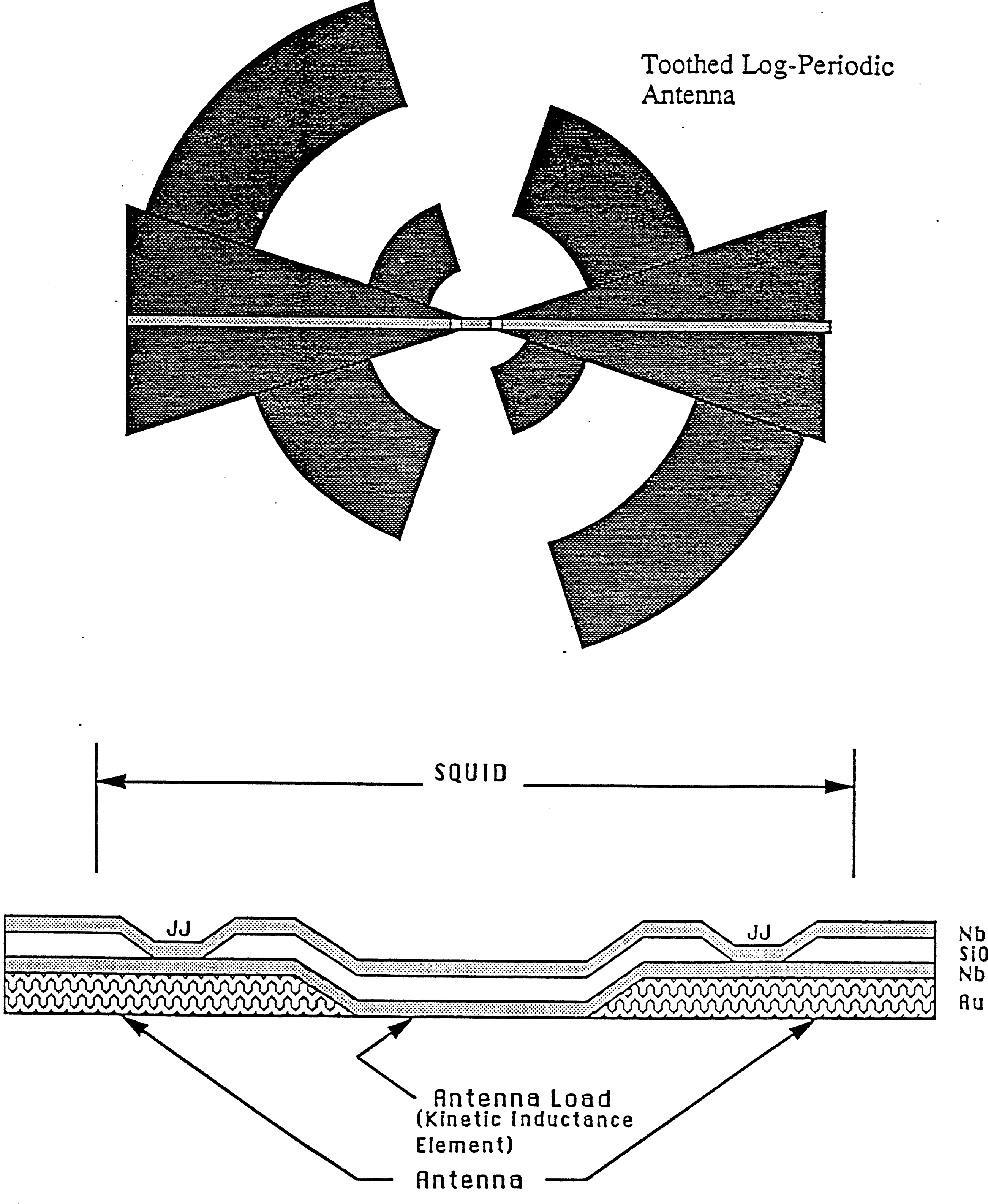

Figure 5 Top: Example antenna with detector.
Bottom: Schematic drawing of the detector, the kinetic inductance element, between the terminals of the antenna. The SQUID loop is shown connecting the Josephson junctions (JJ). The side view is a magnified cross sectional view at the center of the antenna. The length of the antenna load is about 1 μm. Other features are not to the same scale.

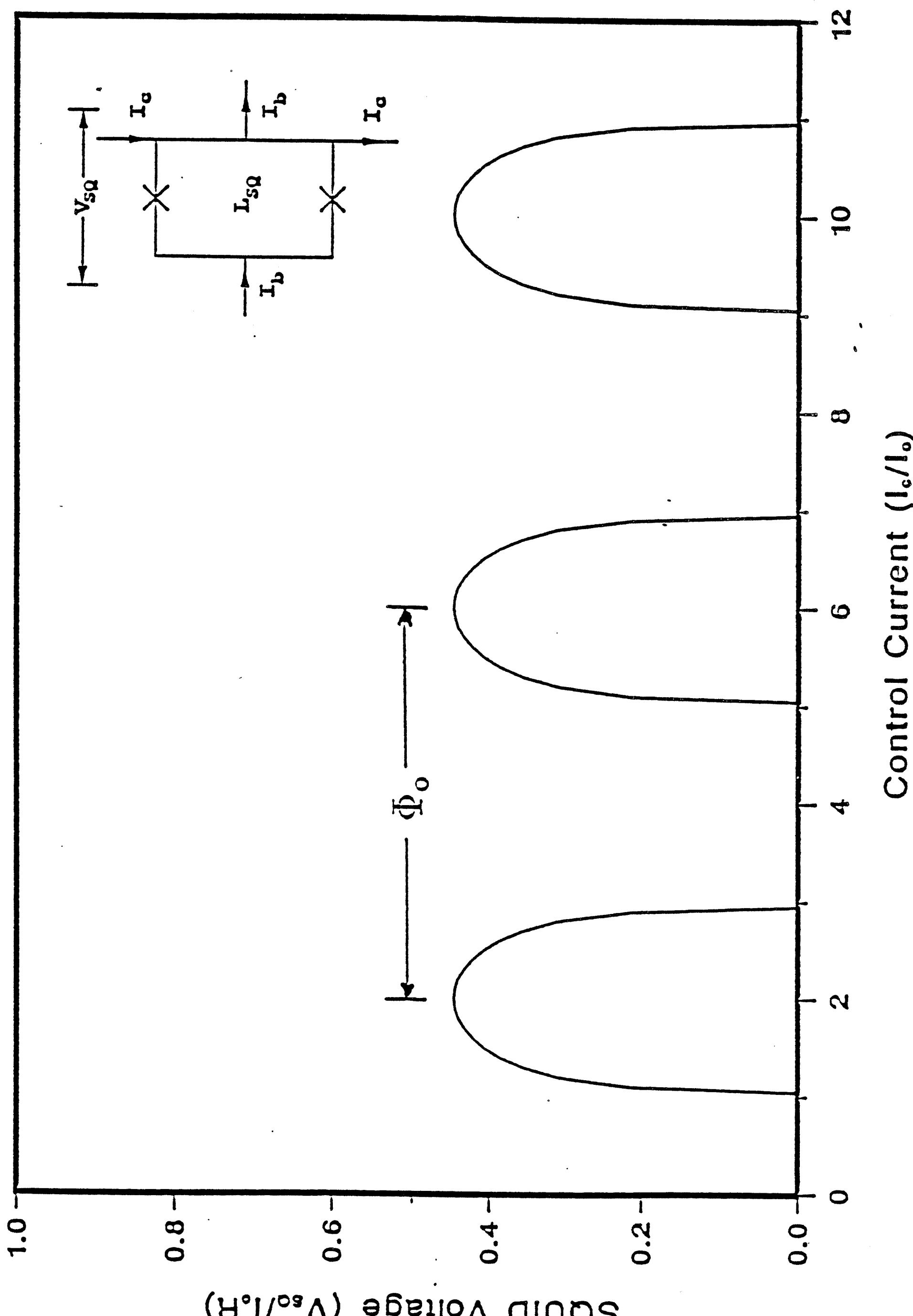

Figure 6 SQUID voltage response as a function of control current I_c. The inset shows the SQUID schematic, with Josephson junctions denoted by ×.

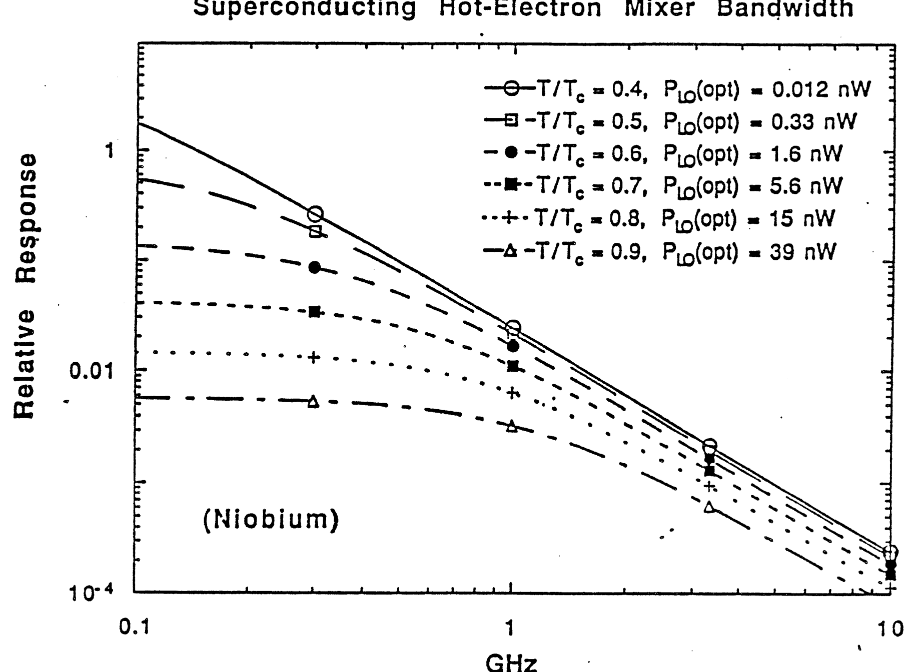

Figure 7 Frequency response of hot-electron photoinductive mixer.

Figure 8. Comparison of predicted photoinductive mixer performance with current SIS and Schottky mixers

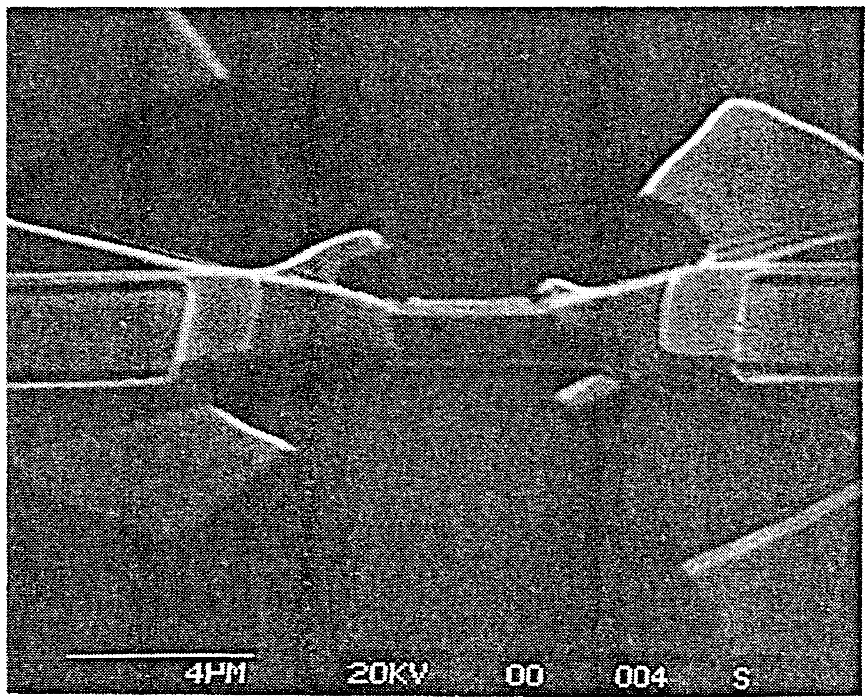

Figure 9. SEM photograph of an early device fabricated without SQUID junctions.

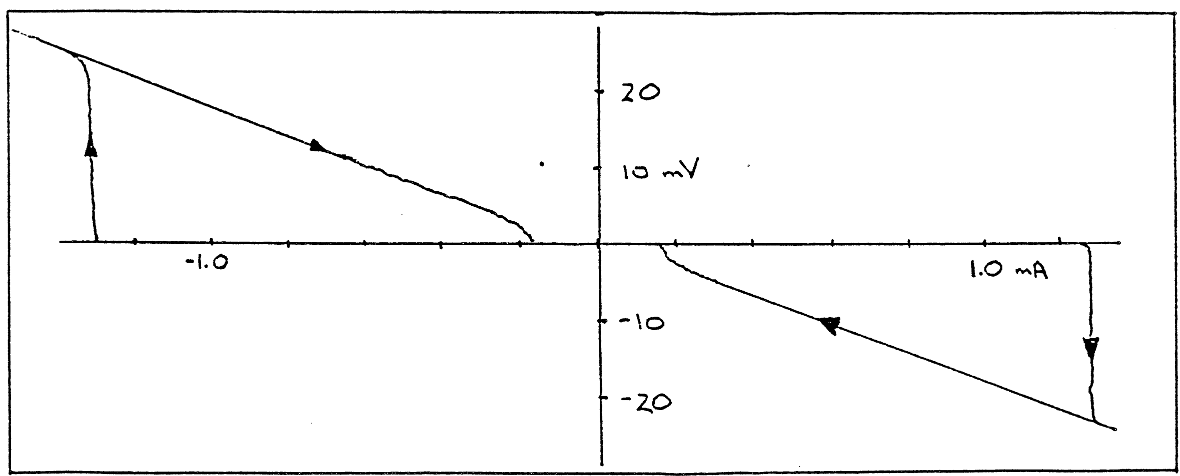

Figure 10. Hysteretic current-voltage curve of a photoinductive element at the feed of a lithographic antenna, at 5 K.

JPL

LOW-NOISE 205GHz SIS MIXERS USING HIGH CURRENT DENSITY Nb AND NbN TUNNEL JUNCTIONS

W.R. McGrath, H.H.S. Javadi, S.R. Cypher, B. Bumble, B.D. Hunt, H.G. LeDuc

Center for Space Microelectronics Technology
Jet Propulsion Laboratory
California Institute of Technology
Pasadena, CA 91109

JPL

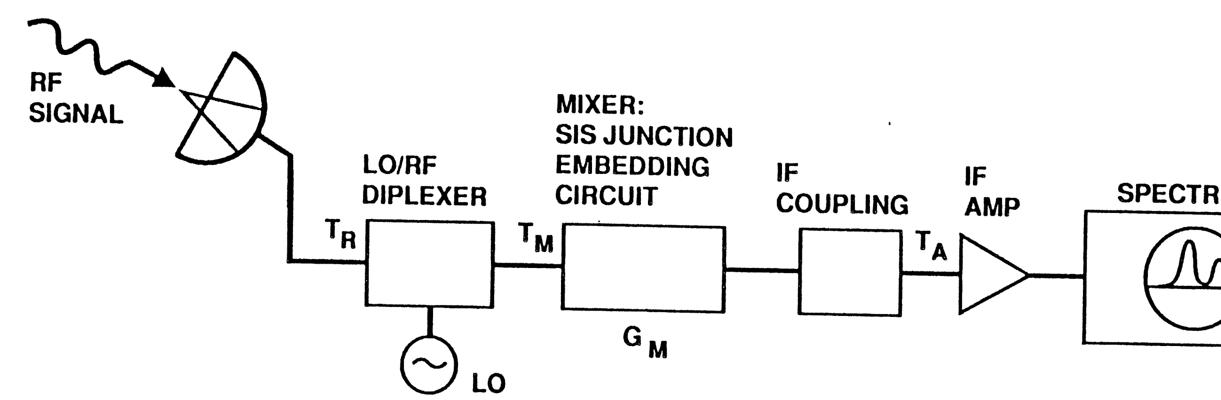

HETERODYNE RECEIVER $T_R = T_M + T_A / G_M$

SIS MIXER: $G_M > 1$, $T_M \rightarrow \frac{h\upsilon}{k}$, $P_{LO} \sim 50$ nW @ 200 GHz

IMPORTANT REQUIREMENTS: (Tucker Theory 1979)

- PROPER RF EMBEDDING CIRCUIT (TUNE OUT JUNCTION CAPACITANCE)
- IMPEDANCE MATCH AT THE IF
- SHARP NONLINEARITY $\frac{h\upsilon}{e} > \Delta V_g$
- LOW SUBGAP CURRENT $I_{sg} << \Delta I$

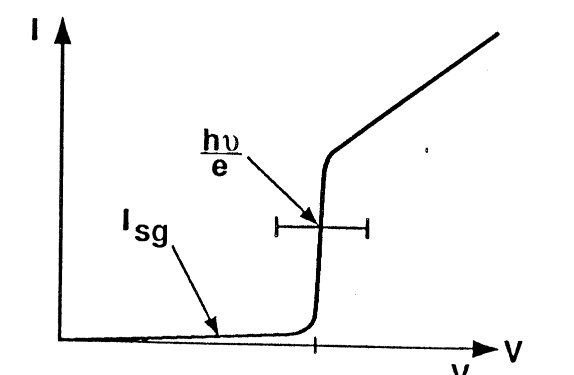

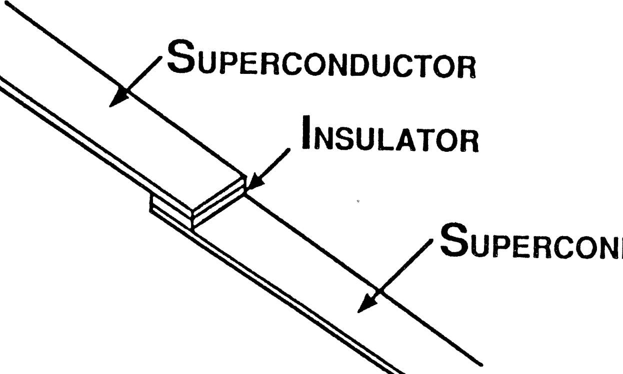

JPL

GOAL: Develop Low Noise SIS Mixers for Submillimeter Wave Applications using High Current Density, Submicron Area, Refractory Metal Tunnel Junctions: NbN, Nb

(Ground-based: Caltech, KAO, SMMM)

APPROACH:

I.
Area $\geq 1\ \mu^2$
Current Density Jc: moderate to high (10^3 - 10^4 A/cm^2)
ωRC: high (8 - 10)
Good Mixer Performance with Integrated Tuning Elements.
(Last year; First Space Terahertz Technology Conference)

II.
Area $<< 1\ \mu^2$ ($0.25\ \mu^2$)
Current Density: high (10^4 A/cm^2))
ωRC: low (2 - 4)
Excellent Mixer Performance without Integrated Tuning Elements.

Impedance Smith Chart

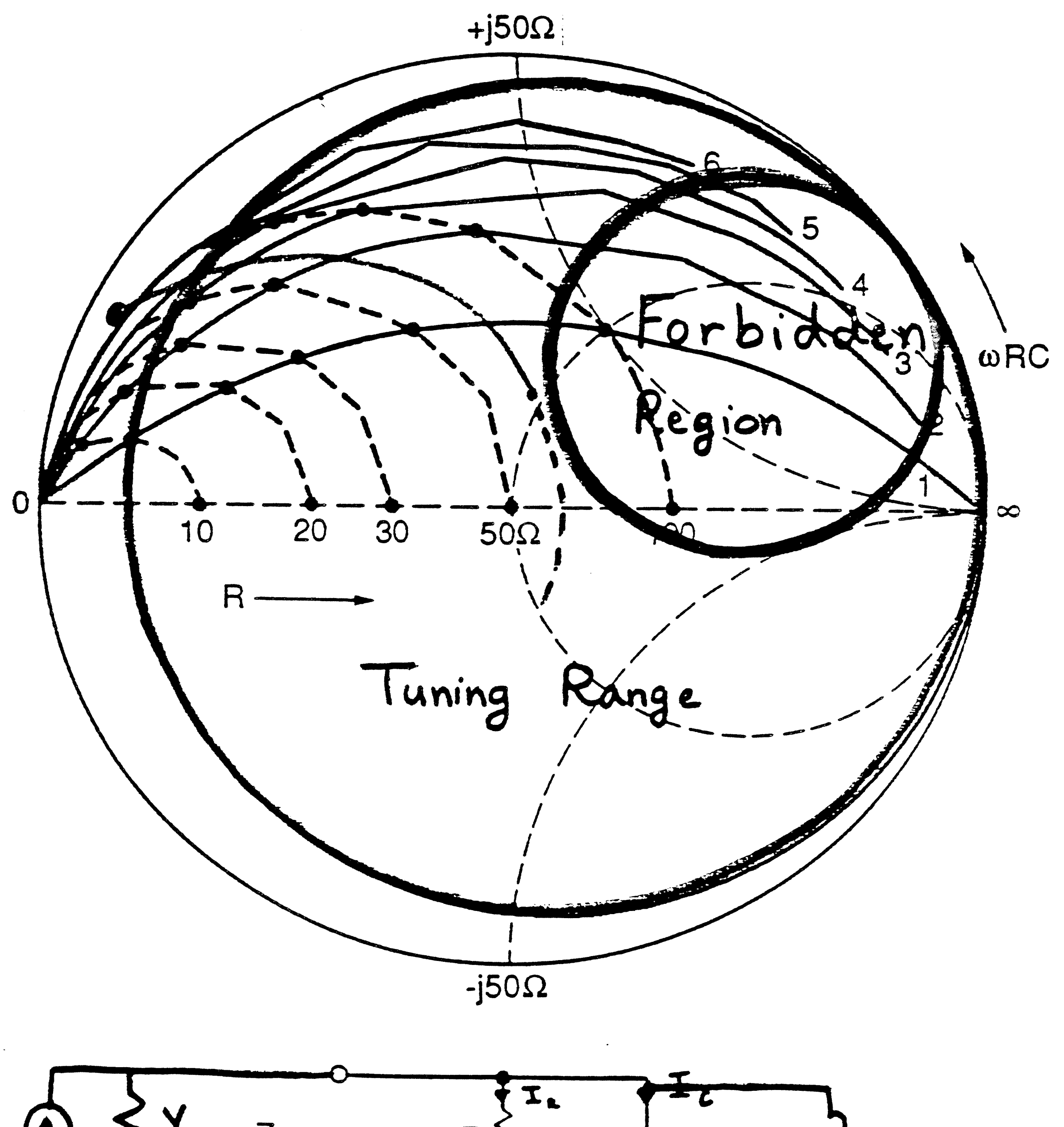

$$\omega R C = \frac{I_c}{I_R} = \frac{\omega}{\Delta\omega}$$

EDGE JUNCTION PROCESS

(1) SPUTTER NbN AND Aℓ LAYERS, PATTERN Aℓ ELECTRODE

(2) LIFTOFF $A\ell_2O_3$ MILLING MASK

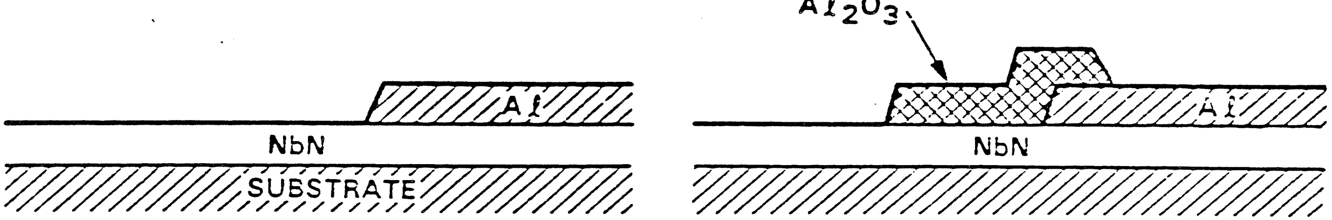

(3) ION MILL NbN EDGE

(4) SPUTTER MgO BARRIER AND NbN COUNTER-ELECTRODE/RIE NbN

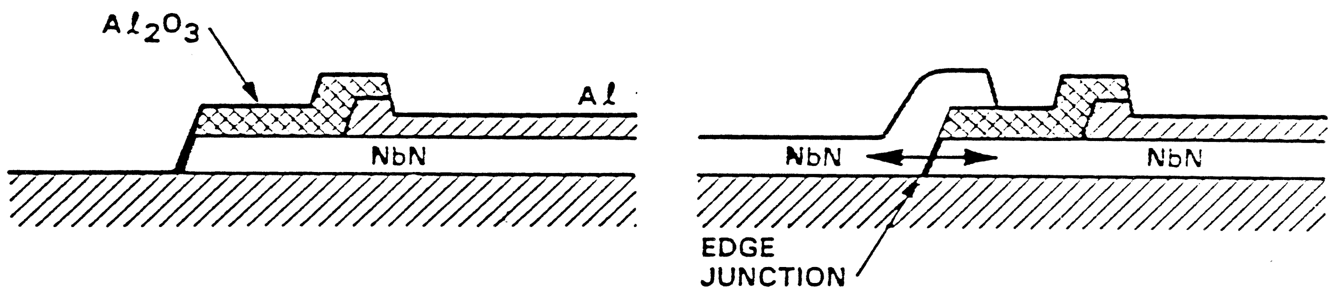

(5) TOP VIEW

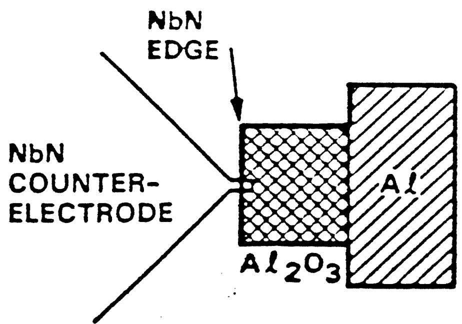

NbN/MgO/NbN EDGE JUNCTION

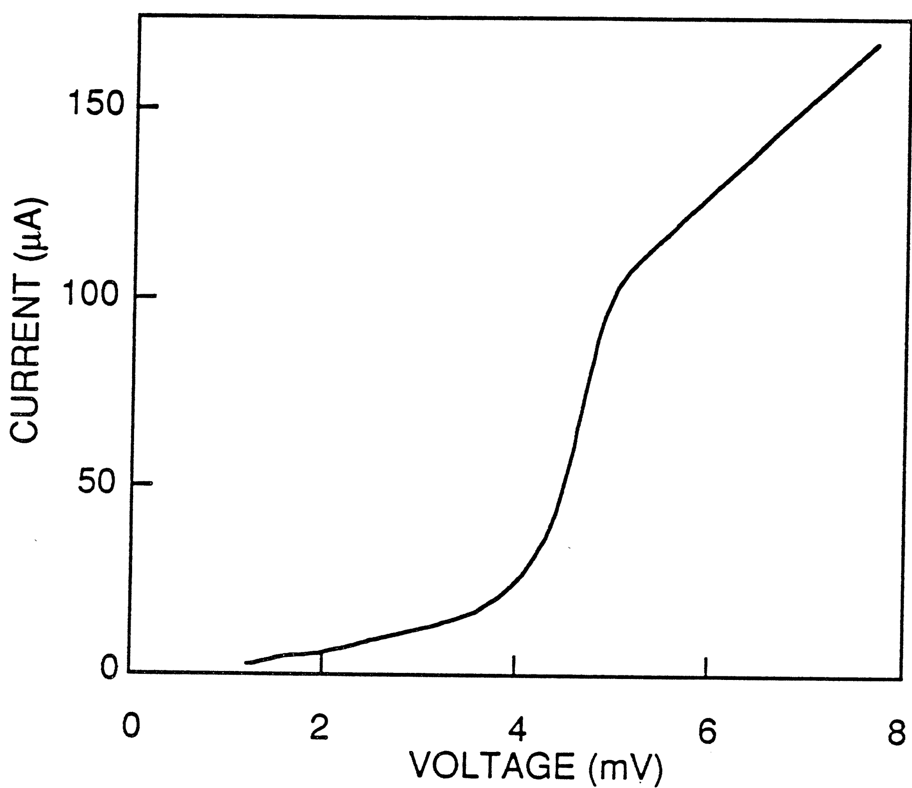

TYPICAL JUNCTION PARAMETERS

AREA ≈ 0.3μ^2 Jc = 18 - 25 kA/cm^2 R = 40 -70 Ω

Vg = 4.8 mV ΔVg ≈ 1 -2 mV $\frac{h\nu}{e} \simeq 0.85\,mV \rightarrow \Delta V_g > \frac{h\nu}{e}$

Capacitance ≈ 35 - 50 fF ωRC ≈ 2.5 - 3.5 @ 205 GHz

For recent improvements in edge junction I-V curves, see:
H.G. LeDuc, A. Judas, S.R. Cypher, B. Bumble, B.D. Hunt, and J.A. Stern
"Submicron Area NbN/MgO/NbN Tunnel Junctions for SIS Mixer Applications"
Applied Superconductivity Conference Proceedings, IEEE Trans. Magn. March 1991.

Nb-AlOx-Nb E-beam Mesa Junction

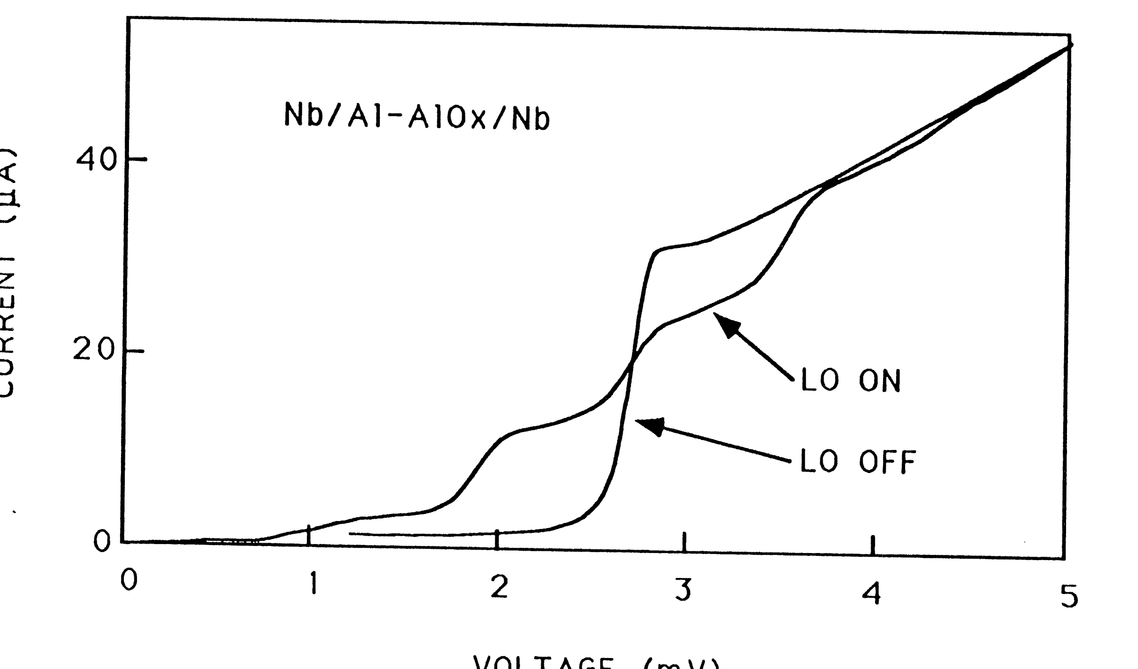

JUNCTION PARAMETERS

AREA ≈ 0.25 μ^2 Jc ≈ 10 kA/cm^2 R = 95 Ω

Vg = 2.7 mV ΔVg ≈ 0.3 mV hν/e ≈ 0.85 mV ΔVg < hν/e

ωRC ≈ 2 @ 205 GHz

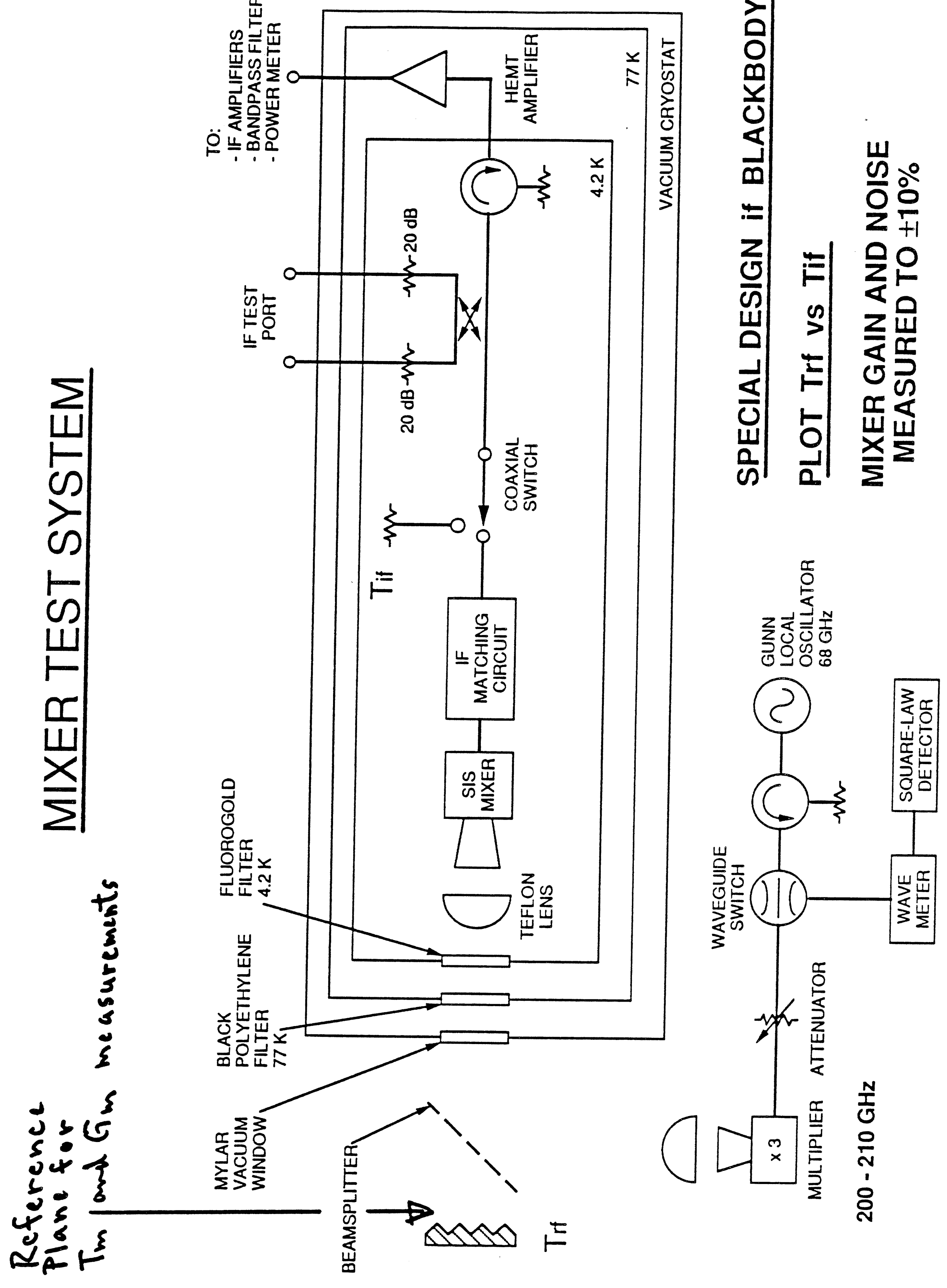
MIXER TEST SYSTEM
Reference Plane for Tm and Gm measurements
TO:
- IF AMPLIFIERS
- BANDPASS FILTERS
- POWER METER
HEMT AMPLIFIER
77 K
VACUUM CRYOSTAT
4.2 K
IF TEST PORT
20 dB
20 dB
COAXIAL SWITCH
Tif
IF MATCHING CIRCUIT
SIS MIXER
TEFLON LENS
FLUOROGOLD FILTER 4.2 K
BLACK POLYETHYLENE FILTER 77 K
MYLAR VACUUM WINDOW
BEAMSPLITTER
Trf
SPECIAL DESIGN if BLACKBODY
PLOT Trf vs Tif
MIXER GAIN AND NOISE MEASURED TO ±10%
GUNN LOCAL OSCILLATOR 68 GHz
SQUARE-LAW DETECTOR
WAVEGUIDE SWITCH
WAVE METER
ATTENUATOR
x 3
MULTIPLIER
200 - 210 GHz

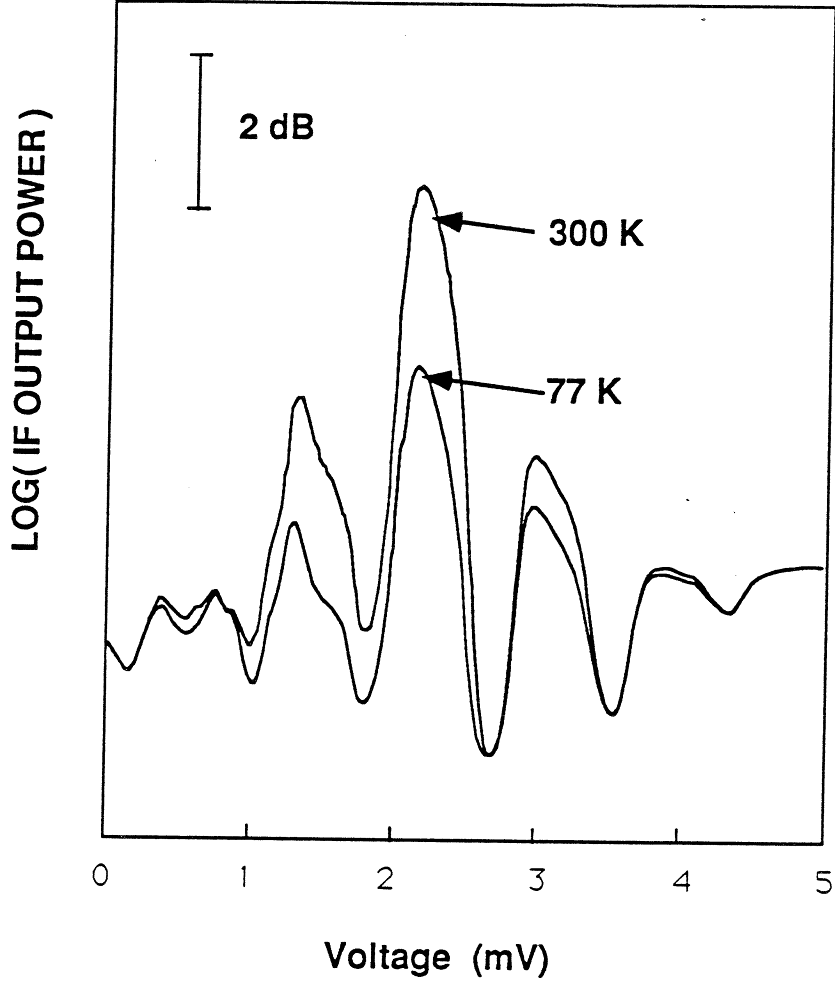
2 dB
300 K
77 K
LOG(IF OUTPUT POWER)
0
1
2
3
4
5
Voltage (mV)

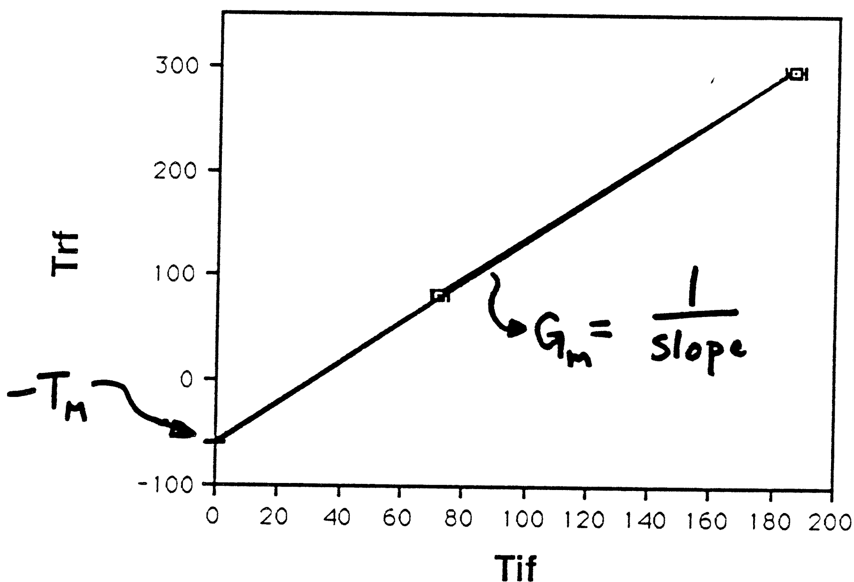
MIXER PERFORMANCE
300
200
100
0
-100
Trf
-T_M
G_m = 1/slope
0
20
40
60
80
100
120
140
160
180
200
Tif

JPL

SUMMARY OF BEST RESULTS

JUNCTION TYPE	BATH TEMP.[K]	SIDEBAND RATIO [dB]	T_m [K]	AVAILABLE G_m [dB]	T_R* [K] (T_{IF}=5K)	STUB LENGTH [μ]
Nb MESA (0.25μ²)	4.2	19 ± 3	60 ± 10	-2.1	70	NO STUB
Nb MESA (1μ²)	4.2	***	78 ± 7	-6.5	100	NO STUB
NbN EDGE (0.3μ²)	4.2	0 ± 3	145 ± 10	-10.7	215	NO STUB
NbN MESA**	4.2	0 ± 3	185 ± 10	-12.4	290	80
	1.5	0 ± 3	134 ± 10	-11.2	212	80

* CALCULATED

** W.R. McGrath, K. Jacobs, J. Stern, H.G. LeDuc, R.E. Miller, M.A. Frerking, First Int. Symp. on Space Terahertz Technology, University of Michigan, 1990.

JPL

COMPUTER SIMULATION OF MIXER PERFORMANCE

Tucker Theory

Three - Port Mixer Model

Inputs: DC I-V Curve, V_{dc}, V_{LO}, Z_{USB}, Z_{LSB}, Z_{IF}

Outputs: Mixer Noise Temperature, Mixer Conversion Efficiency

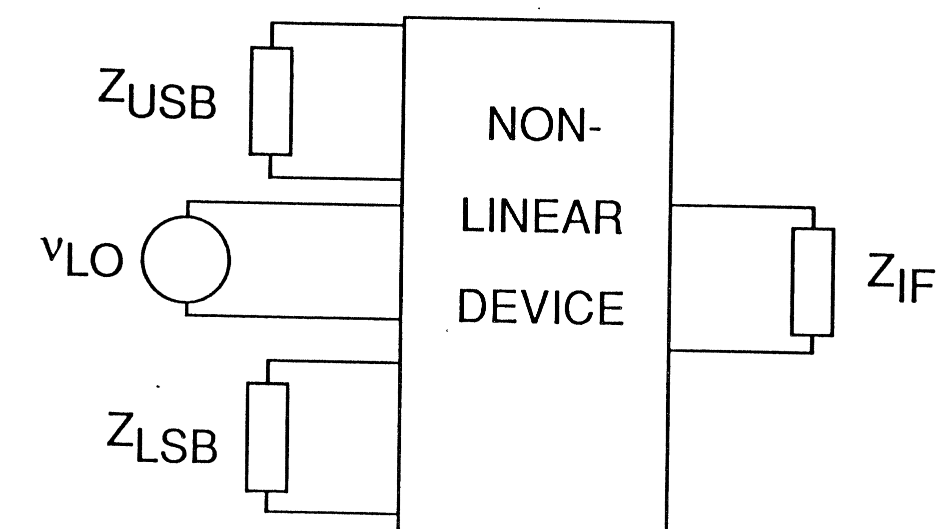

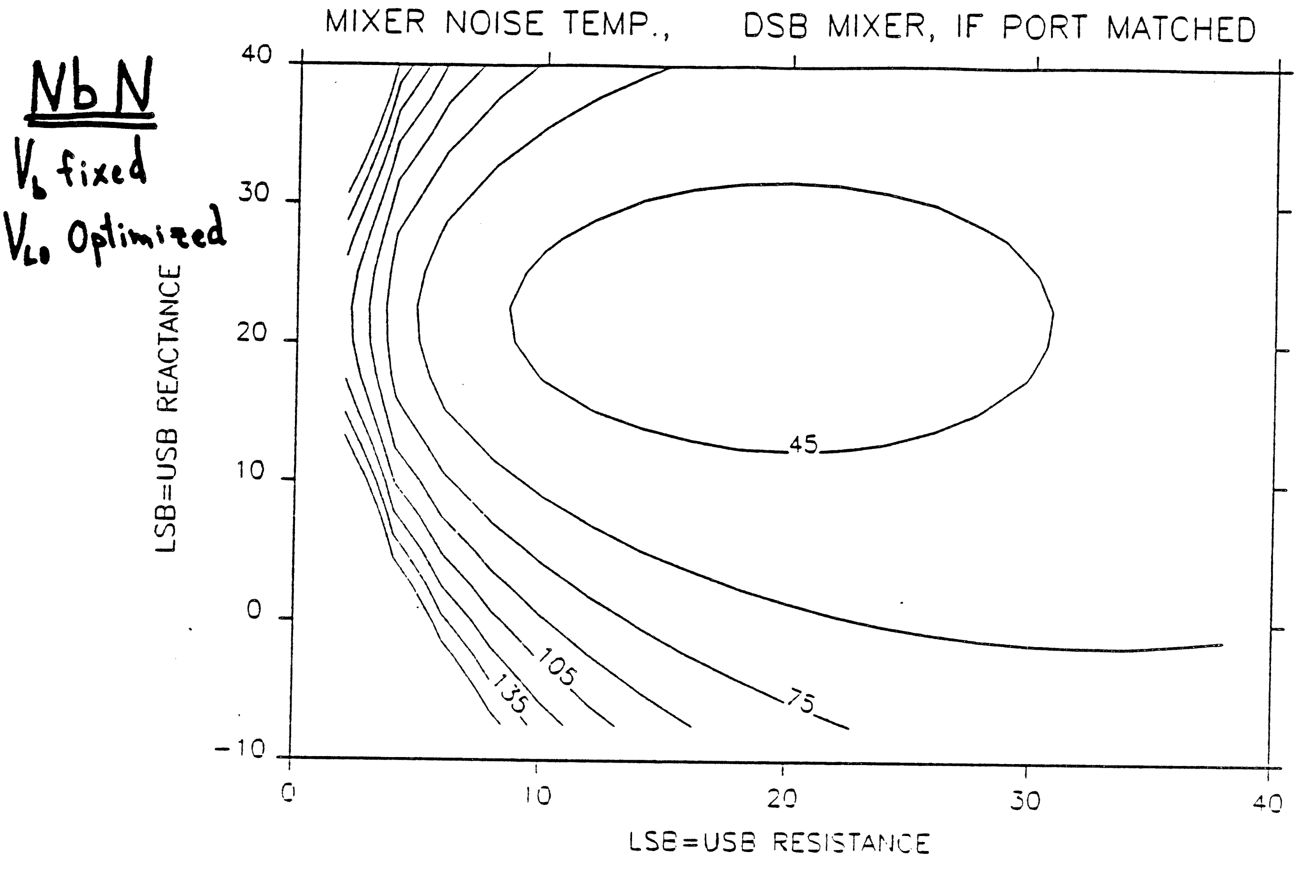
MIXER NOISE TEMP., DSB MIXER, IF PORT MATCHED
NbN
Vb fixed
VLO Optimized
LSB=USB REACTANCE
LSB=USB RESISTANCE
40
30
20
10
0
−10
0
10
20
30
40
45
75
105
135

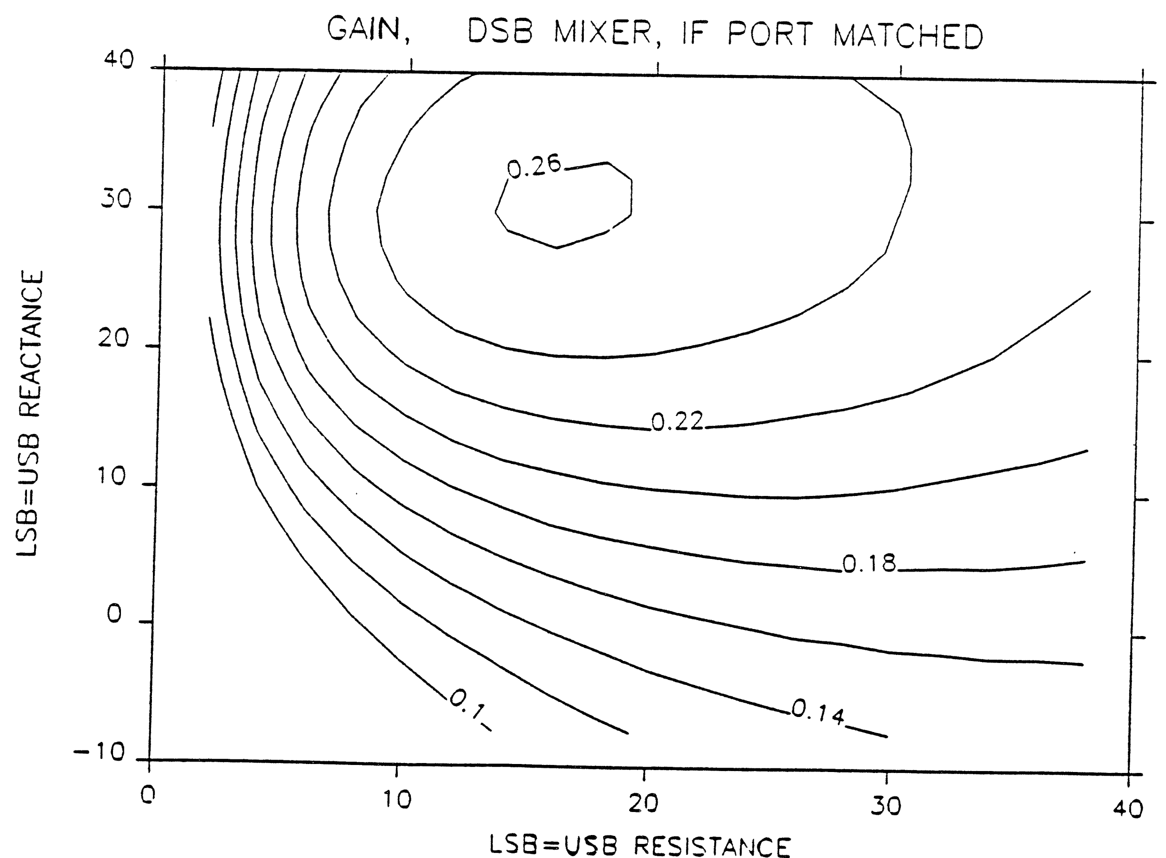
GAIN, DSB MIXER, IF PORT MATCHED
LSB=USB REACTANCE
LSB=USB RESISTANCE
40
30
20
10
0
−10
0
10
20
30
40
0.26
0.22
0.18
0.14
0.1

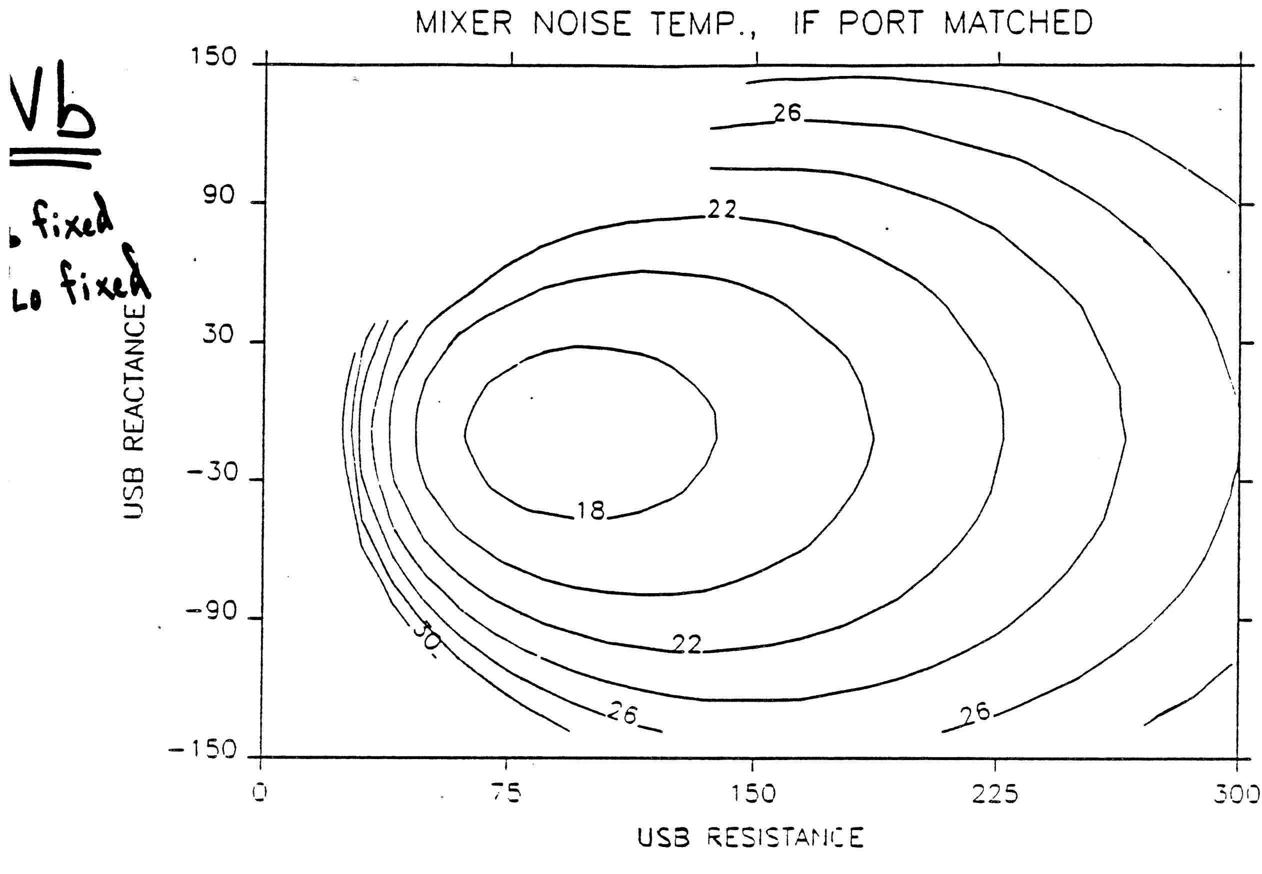
MIXER NOISE TEMP., IF PORT MATCHED
Vb
fixed
Lo fixed
150
90
30
−30
−90
−150
0
75
150
225
300
USB REACTANCE
USB RESISTANCE
26
22
18
22
30
26
26

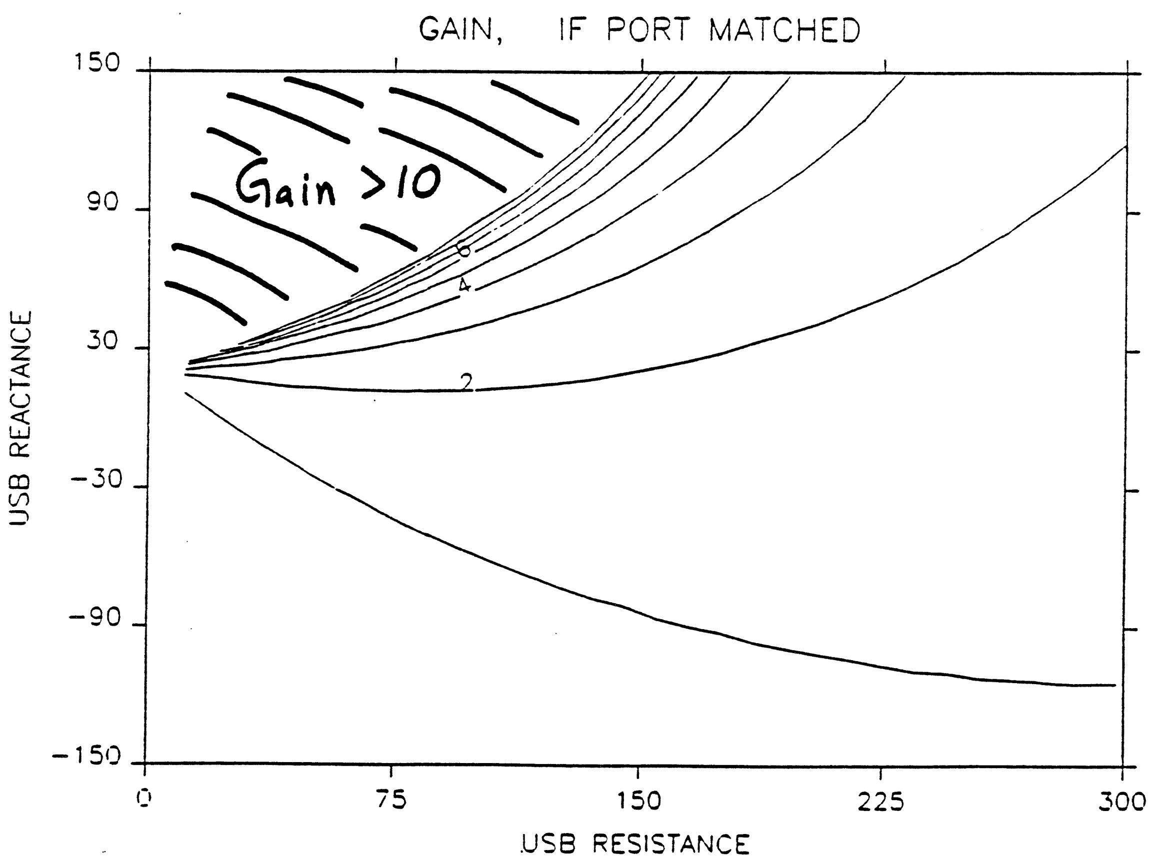
GAIN, IF PORT MATCHED
Gain >10
6
4
2
150
90
30
−30
−90
−150
0
75
150
225
300
USB REACTANCE
USB RESISTANCE

Comparison:

	NbN		Nb	
	Gain	T_M	Gain	T_M
Tucker's Theory	-6^{dB}	45	Large	18
Experiment	-11^{dB}	145	-2^{dB}	60

JPL

CURRENT PROGRAMS

* 630 GHz SIS MIXER ----- Presently being tested.

Waveguide Mount
NbN, Nb Tunnel Junction (JPL)
Pb-Alloy (R.E. Miller, Bell Labs)

* Si Micromachined Waveguide ----- 1000 GHz

Y.C. Tai, C. K. Walker, M. Yap: Campus
W.R. McGrath, H.S. Javadi, H.G. LeDuc: JPL

Fabricate waveguides with 1μ thick SiN membranes in E-field dir.
Fabricate SIS junctions or probes directly in the waveguide
Solves the mounting problem !

JPL

SUMMARY

Fabricated and tested submicron area, refractory tunnel junctions as SIS mixers at 205 GHz.

No integrated tuning elements: $\omega RC \approx 2\text{-}4$.

Accurate measurements of mixer noise and conversion efficiency.

Nb-AlOx-Nb: Tm(SSB) = 60K   Gm(SSB) = -2 dB Best to date!

NbN-MgO-NbN: Tm(DSB) = 145K   Gm(DSB) = -10.7 dB

Preliminary calculations of mixer performance with the Tucker Theory.

630 GHz SIS mixer currently being tested.

Extenion of waveguide circuits to 1000GHz using Si micromachining techniques.

Nb BASED MIXER ELEMENTS FOR MILLIMETER AND SUBMILLIMETER WAVELENGTHS

A.W. Lichtenberger, D.M. Lea, and A.C. Hicks

Superconductive Device Laboratory
Department of Electrical Engineering
University of Virginia
Charlottesville, Virginia 22903

J.D. Prince, R. Densing, D. Peterson, and B.S. Deaver

Far Infrared Receiver Laboratory
Department of Physics
University of Virginia
Charlottesville, Virginia 22903

ABSTRACT

The superconductor-insulator-superconductor (SIS) junction is the most sensitive nonlinear element for millimeter-wave heterodyne detection. We have developed a Nb/Al–Al_2O_3/Nb junction fabrication process which is compatible with the use of planar tuning circuits integrated with the junctions. Recent results have yielded a double sideband receiver noise temperature less than 50K from 205 to 240 GHz and 44K at 230 GHz.

We are also extending our Nb/Al–Al_2O_3/Nb trilayer technology to the fabrication of sub-square-micron area junctions for submillimeter wavelengths. Two fabrication techniques are at present under investigation. The first involves a modification of our *trilevel* resist junction insulation process to augment the currently used SiO_2 masking layer with a more CF_4 etch-resistant Cr layer which should extend the capabilities of this insulation process to sub-square-micron junction areas. A trilayer insulation planarization (TIP) process, which avoids the drawbacks of machine aligned and liftoff insulation techniques, is also under investigation. TIP uses an SiO_2 deposition process to planarize, and hence insulate, a previously defined sub-square-micron junction area. Progress on the modified trilevel resist and TIP techniques will be described, and the results of recent direct detection experiments at 585 GHz and 763 GHz will be presented.

This work was supported in part by the National Science Foundation under grant #AST8922155, the National Aeronautic Space Administration under grant #1056546, and the U.S. Army.

I. Introduction

$Nb/Al-Al_2O_3/Nb$ trilayer junctions have surpassed those made by all other SIS technologies in leakage current and uniformity. They are currently the element of choice for ultra low noise millimeter wave heterodyne detection. We are investigating both Nb and NbCN superconductors in the planar and edge junction geometries for submillimeter wavelengths. In this paper we discuss the future direction of our Nb trilayer technology.

There have generally been two approaches to SIS mixers at millimeter wavelengths: (1) the use of very small area high current density junctions to minimize $\omega R_N C$ [1,2,3,4,5] and (2) the use of integrated tuning elements to tune out the junction capacitance while keeping the benefits of a larger junction capacitance [6,7,8,9,10,11]. For millimeter wavelengths, both approaches have been rather successful. At higher frequencies the use of increasingly smaller junction areas and higher J_c values may be restricted by fabrication limitations and the properties of available superconductors. For example, with $C_s = 45fF/\mu m^2$, $I_C R_N = 1.8mV$ [12], and $R_N = 100\Omega$, a choice of $\omega R_N C = 1$ at 100 GHz with the $Nb/Al-Al_2O_3/Nb$ system requires a junction area of approximately 0.35 μm^2 and a $J_c = 5.1 \times 10^3$ A/cm^2. Even if we ignore the $J_c \alpha f^2$ relationship found by Kerr and Pan for $\omega R_N C = 4$[10], at 600 GHz and 1 THz the desired junction areas and J_c values would still be 0.06 μm^2 and 3×10^4 A/cm^2, and 0.035 μm^2 and 5×10^4 A/cm^2 respectively. These numbers, particularly the J_c values, are certainly optimistic estimates. The fabrication of such planar trilayer junctions having reasonable electrical characteristics may be difficult, making the use of integrated tuning elements, which permit the use of larger junction areas and smaller J_c values, more attractive. Additionally, the expected difficulty in suppressing Josephson currents (and the resulting Josephson noise) for very small junction areas argues for the choice of junctions with the largest area. However,

resistive loss in superconductor films at frequencies approaching $2\Delta/h$ ($\approx$ 700 GHz for Nb) will prevent the use of superconductive tuning elements above these frequencies, and normal metal tuning elements [9] or alternative mixer designs will need to be developed.

Superconductor-Insulator-Normal (SIN) junctions are also attractive at high frequencies. Although the nonlinearity of the SIN junction is weaker than that of an SIS junction, and the theoretical upper frequency limit ($2\Delta/h$) is half that of an SIS mixer[13], the SIN junction has no pair currents and is thus free of Josephson noise. This advantage could be extremely important, as Josephson noise may severely limit the high frequency performance of SIS mixers.

II. Millimeter Wavelength Device Research

A. SIS Elements with Integrated Tuning Elements

In our earlier work [9,14], we reported utilizing a trilevel resist to pattern junction areas in Nb/Al–Al_2O_3/Nb films. After reactive ion etching to define the junction area, the perimeter of the junction is revealed and a liftoff structure is defined with an oxygen plasma shrink of the exposed polyimide sidewalls. A subsequently deposited insulation layer seals the sides and the perimeter of the Nb counter electrode button (Fig. 1). The excellent liftoff profile that is obtained with this technique allows the use of thick insulation layers. An off-axis SiO insulation deposition with wafer rotation results in good step coverage and a nonabrupt surface for the subsequent Nb wiring layer (Fig. 2). We have repeatably utilized this technique to fabricate high-quality junctions of 1.5 μm diameter and current density as large as 1 x 10^4 A/cm^2.

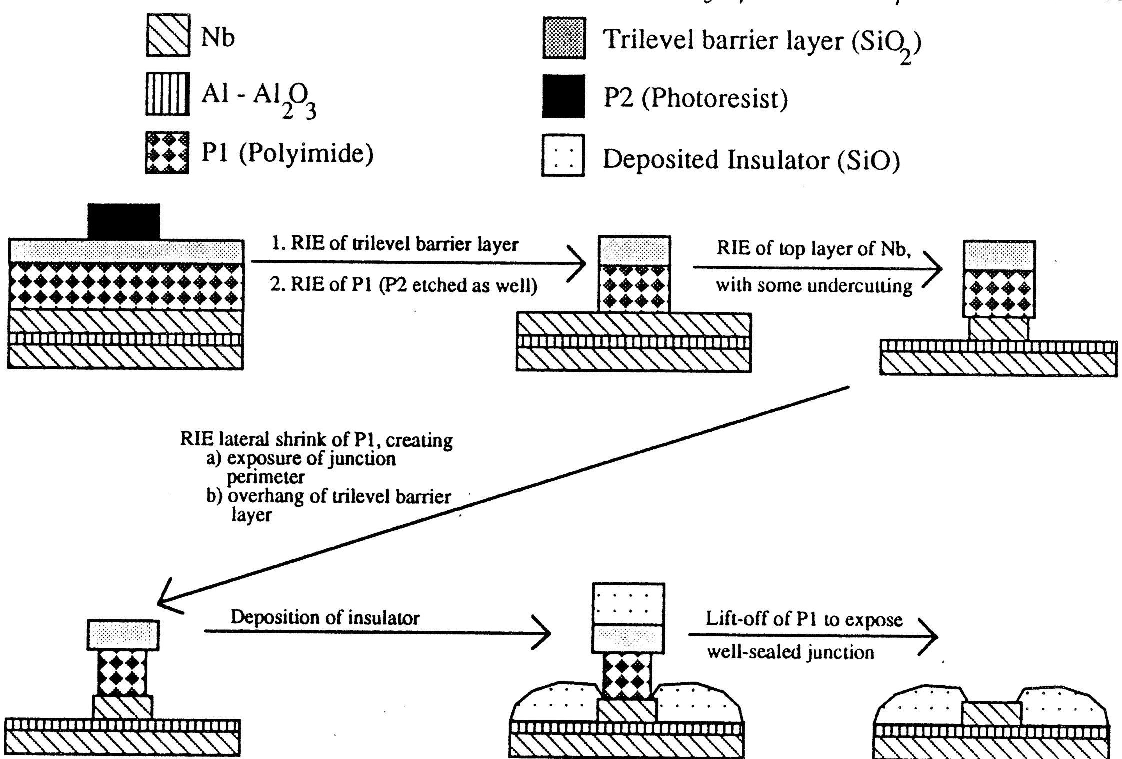

Figure 1. Outline of the trilevel resist insulation process.

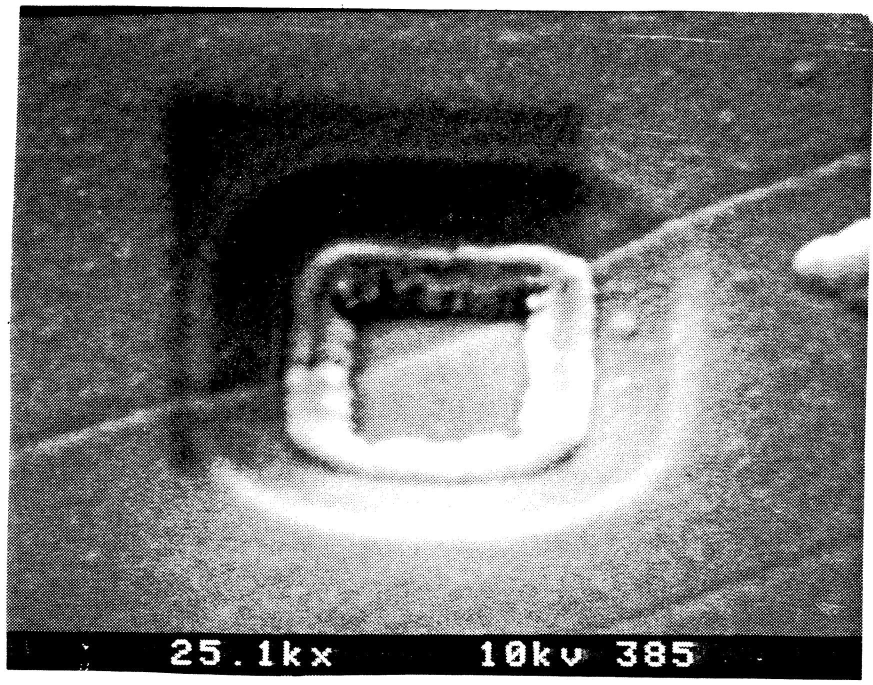

Figure 2. SEM view of an Nb junction area insulated with SiO. Due to the shadowing effect of the trilevel resist, the SiO deposition results in a gradual profile as the SiO reaches the Nb button.

For SIS mixers, the use of relatively large area junctions with relativity large $\omega R_N C$ has two advantages: (i) The large capacitance tends to short-circuit currents at the LO harmonics and harmonic sidebands, and (ii) Undesired effects of the AC Josephson currents in the junction are reduced. For good mixer performance it is necessary to tune out the junction capacitance at the signal frequency. To do this, we have used inductive tuning circuits integrated with the individual junctions [9,12,14]. The most recent results at 230 GHz are shown in Figure 3. An NRAO receiver [15] using these junctions has a DSB noise temperature (T_R) of 44K at 230 GHz, and a T_R below 50K from 205 GHz to 240 GHz. These figures are believed to be the lowest reported for a receiver operating over this frequency range.

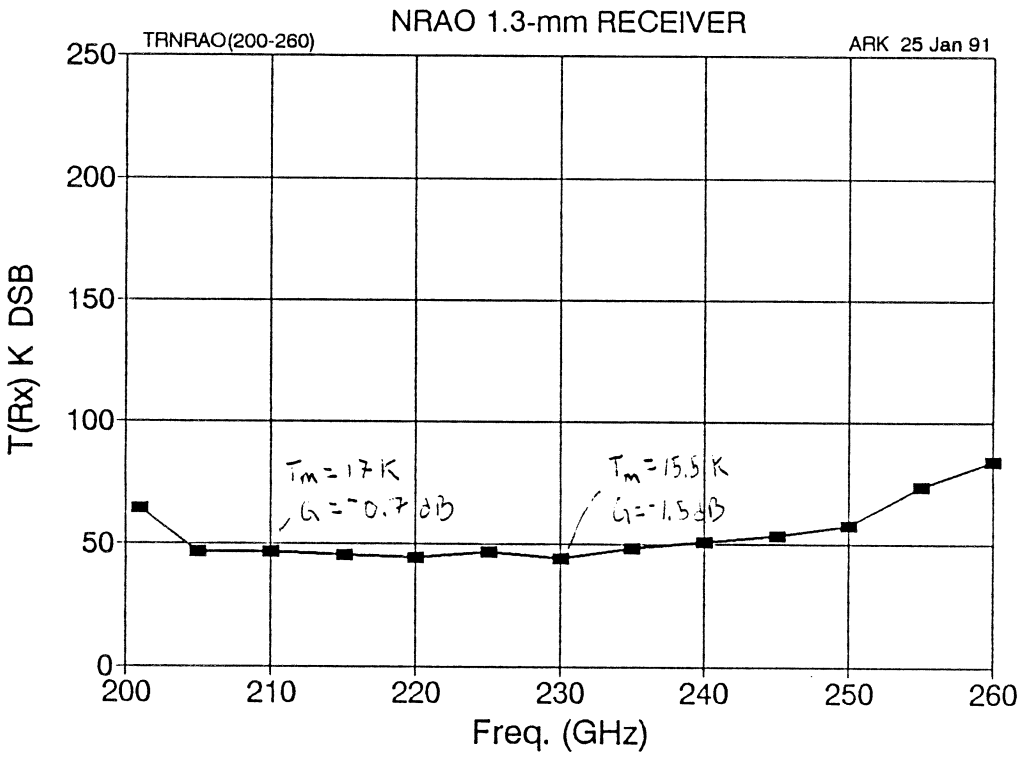

Figure 3. Noise temperature measurements from 205 GHz to 260 GHz for a NRAO receiver incorporating Nb/Al–Al_2O_3/Nb junctions fabricated at the University of Virginia [15]. The DSB mixer noise temperature at 230 was 44K.

III. Submillimeter Wavelength Device Research

A. Cr/SiO_2 *Quadlevel Resist Insulation*

The optimal performance of SIS mixers requires that the junction area be decreased as the frequency of operation increases. Consequently, we have attempted to apply our existing trilevel resist process to the fabrication of sub-square-micron area junctions. These efforts have now convinced us that repeatability in etching limits our present trilevel process to the fabrication of junctions with an area of $\approx 1\mu m^2$. The limitation arises from an unfortunate characteristic of the SiO_2 masking layer: the trilevel SiO_2 etches rapidly in low-pressure CF_4 based etches which are otherwise well-suited for defining the counter electrodes of our junctions. Because the SiO_2 masking layer must remain intact during the Nb counter electrode etch, it is necessary to perform this etch at a significantly higher pressure (300 mTorr) in order to minimize etching of the SiO_2. However, the higher pressure appreciably increases lateral etching, or "undercutting," of the Nb counter electrode; this is especially true for small features. In the case of submicron junctions, the undercutting either etches the feature away entirely or leaves an area so small that the subsequent shrink of the polyimide layer to expose the counter electrode perimeter can not be repeatably performed (Fig. 4).

Recently, we have developed what we believe to be a viable solution to this problem. The new approach involves the addition of a 1000 Å Cr layer sputtered on top of the 1500 Å SiO_2 layer to form a *quadlevel* structure (Fig. 5). The Cr layer's resistance to etching in a low-pressure CF_4+O_2 plasma allows it to protect the quadlevel structure; as a result, the Nb counter electrode layer may be etched with little or no undercutting. A vertical etch of the Nb is desirable because it reduces the required amount of shrinkage of the polyimide features in the next step of the process; it will only be necessary to perform the O_2 plasma shrink long enough

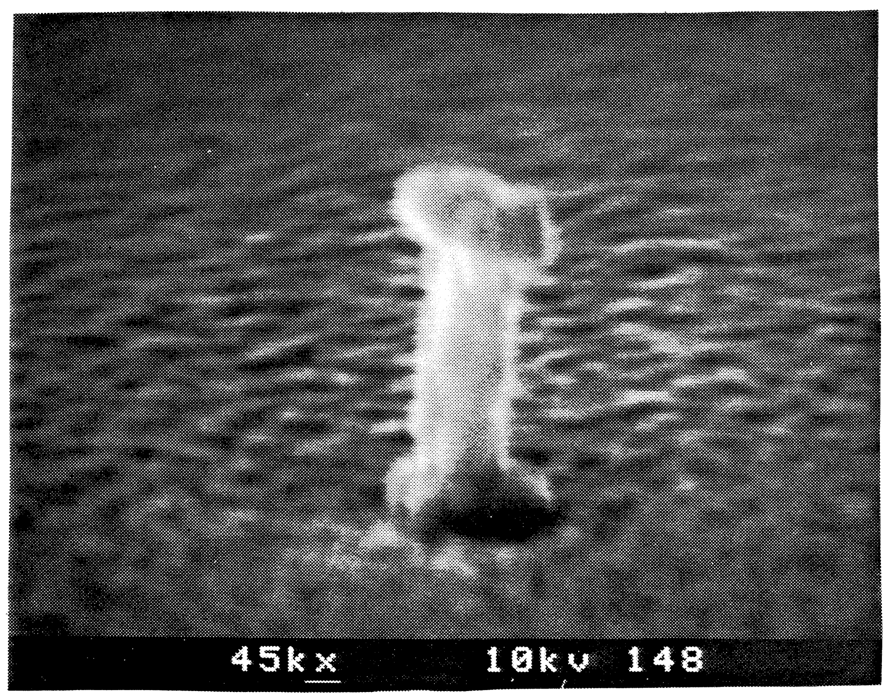

Figure 4. An SEM micrograph of a 0.3 μm x 0.3 μm Nb junction area for which a successful SiO_2 based trilevel resist feature was obtained. The shrinkage from the mask feature size of 0.8 μm x 0.8 μm is primarily due to the "undercutting" of the Nb film in the high pressure $CF_4 + O_2$ etch. A lateral shrinkage of $0.25\ \mu m < x_{shrink} < 0.35\ \mu m$ was therefore required for this successful polyimide shrink step. This step is performed, however, without quantitative information on the extent of the Nb undercutting, resulting in poor repeatability.

to create an adequate liftoff profile. A relatively thin Cr layer is desired to avoid undercutting from the wet etch used to define it. The SiO_2 layer is still required so that the SiO_2 and Cr together will form a masking layer thick enough to serve as the top layer of liftoff features. Initial tests of the quadlevel technique have resulted in Nb counter electrode buttons which are actually slightly *larger* than the defining quadlevel resist structure. We have also determined that the polyimide shrink step can be performed *prior* to the Nb counter electrode etch without any apparent effect on the subsequent Nb etch (Fig. 6). The anisotropic Nb etch results in a counter electrode circumference size which is controlled by the Cr/SiO_2 mask and not the pre-

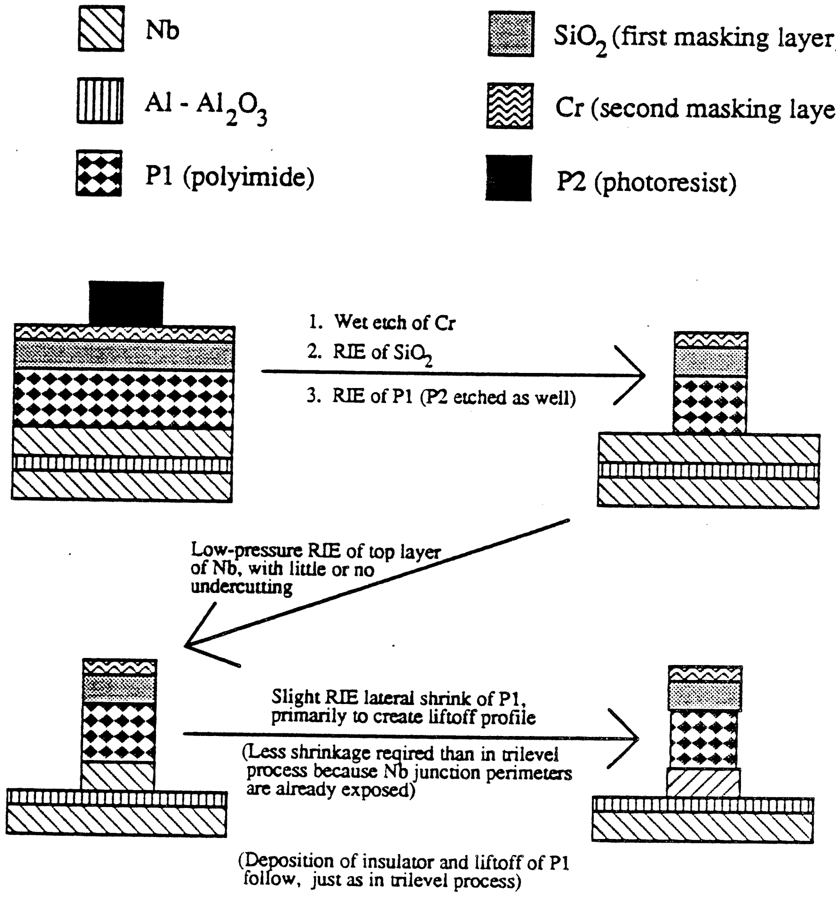

Figure 5. Outline of the quadlevel resist insulation process.

shrunk polyimide perimeter. Performing the polyimide shrink prior to the junction definition results in a more uniform and controlled shrink process since difficulties in polyimide shrinkage due to PRIST hardening [9] from the Nb etch are not encountered. It is expected that with the use of a new sub-micron feature mask, we will be able to accurately and repeatably fabricate sub-square-micron junction areas. We will also investigate the use of Cl based RIE chemistry for Al etch mask definition to replace the Cr/SiO_2 bilayer. The resulting Al based trilevel resist would have fewer steps and avoid the wet etch of the Cr based quadlevel technique.

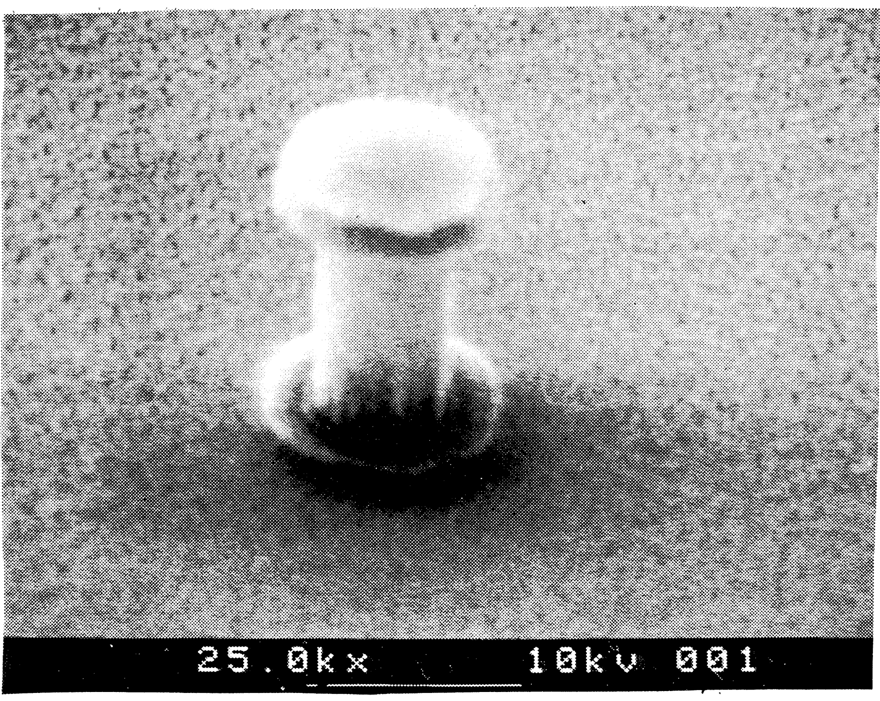

Figure 6. An SEM micrograph of a quadlevel resist defined Nb counter electrode. The excellent liftoff profile has been obtained with a pre-shrink of the polyimide prior to definition of the junction area. The subsequent SiO_2 deposition should easily insulate the junction area. Note that the perimeter of the counter electrode is slightly larger than the defining Cr/SiO_2 mask. By adjusting the RIE parameters, we should be able to control the size of the junction circumference, making it larger or smaller than the defining Cr/SiO_2 mask.

B. Trilayer Insulation Planarization

Although the use of self-aligned liftoff insulation techniques is common [12, 16-22], there is an intrinsic drawback in the use of the defining film as both an etch mask for junction definition and as a liftoff structure for junction insulation. If moderately thick base electrode and insulation layers are desired (e.g., for some tuning element designs), then a relatively thick liftoff structure with an overhang is required for a successful liftoff. Such structures may become unstable and difficult to define for sub-half-micron feature sizes.

We have been investigating an alternative trilayer insulation planarization (TIP) process [23] which avoids the difficulties of self-aligned liftoff techniques (Fig. 7). The basic idea of this process is to separate the junction definition from the junction insulation step while *not* requiring a machine-aligned or self-aligned liftoff process. Following RIE definition of the junction, the entire wafer is covered conformally with an insulator. The wafer is then planarized with an aggressive rf bias sputter deposition. The planarization is based on the dependency of sputter etching rate on angle. While a near zero deposition rate is occurring on the planar regions of the wafer, the edges of the surface features will be rapidly etched. A subsequent etchback of the planarized insulation layer, which reveals the Nb junction area, can be monitored with a surface profiler. The desired end result of the TIP process is an insulation layer which seals the edges of the junction and presents a planarized surface for the subsequent Nb wiring. This insulation technique should properly seal any size junction area, limited only by the ability to define submicron Nb features with lithography and RIE. The TIP process is also compatible with the incorporation of integrated tuning elements, permitting the use of a wide range of insulator thicknesses.

Our experiments with the TIP process have utilized a rf diode sputtering system for insulator planarization. It was initially determined that a light bias deposition was necessary in order to obtain good conformal coverage by the initial insulation layer. Excellent planarization was then obtained after 4 hours of more aggressive bias deposition at the following conditions: 5 μm Ar pressure, 3.9 W/cm^2 and 1900 Volts on the target electrode, and 0.38 W/cm^2 and 180 Volts on the substrate electrode. Uniform planarization was only obtained when the wafers were not heat-sunk to the H_2O cooled substrate platter.

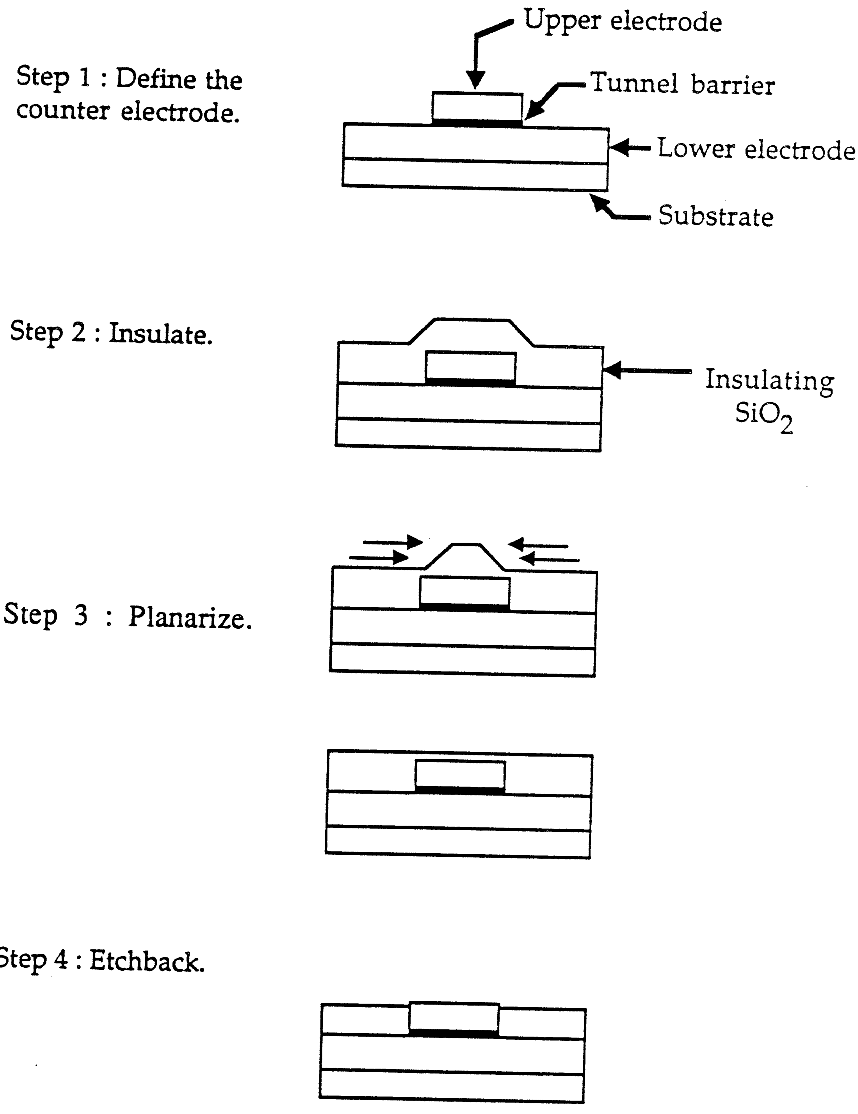

Figure 7. The trilayer insulation planarization TIP process

A CF_4 RIE etchback technique was initially investigated (under conditions similar to our trilevel SiO_2 etch), yet the planarized films had an extremely small etch rate (<10 Å/min). It was suspected that these low rates were due to film contamination from the chamber during the high power planarization process. Instead, a buffered hydrofluoric etch (BOE) was used successfully to thin the planarized SiO_2 film until the conformal SiO_2 layer was revealed. The CF_4 etchback technique was then utilized until the Nb counter electrode junction button was revealed (Fig. 8). The use of BOE for the entire etchback step resulted in a poor interface between the SiO_2 and the sidewalls of the Nb counter electrode (Fig. 9).

We are encouraged by these results; however, due to the lack of wafer cooling during the planarization process, the wafers are subjected to high temperatures, resulting in severe damage

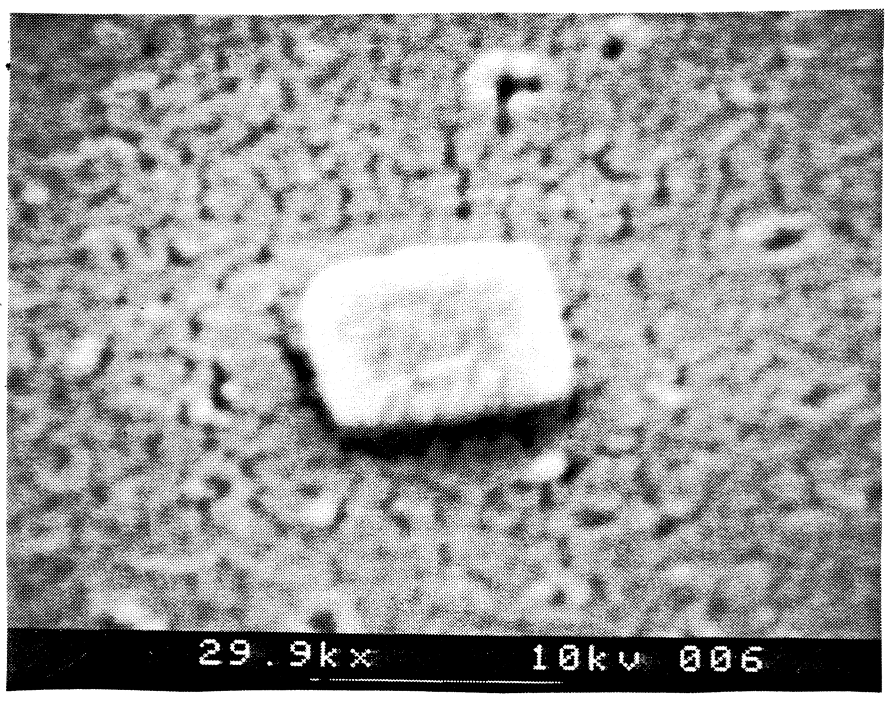

Figure 8. An SEM micrograph of a Nb counter electrode button insulated by the TIP process

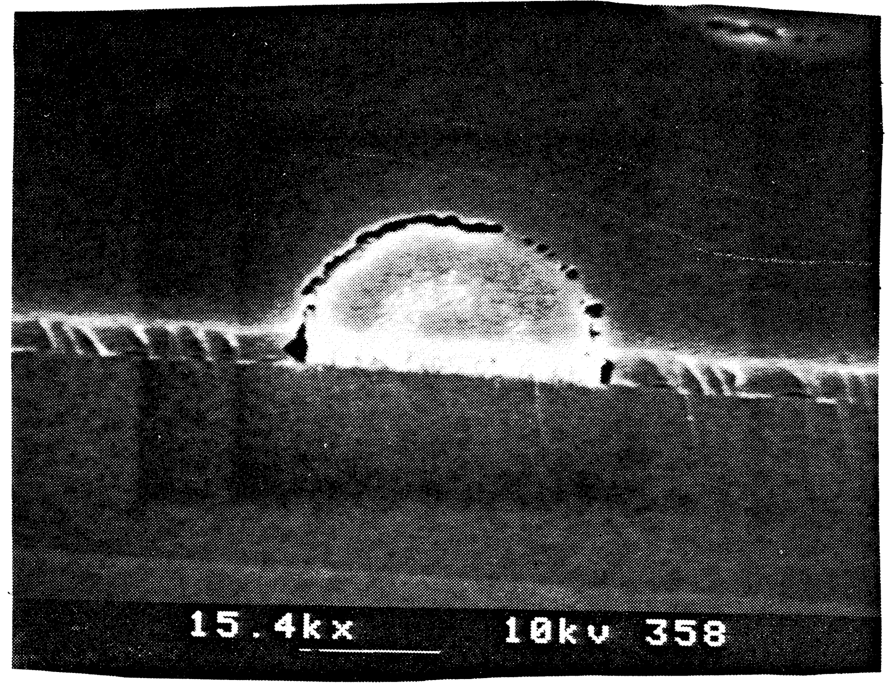

Figure 9. Trenches around the Nb counter electrode after a BOE etchback step.

to the Al_2O_3 trilayer tunnel barrier. An alternative insulator deposition technique for planarization which we are investigating is electron-cyclotron-resonance-chemical-vapor-deposition (ECR-CVD). Such systems are reportedly capable of rapid and uniform planarization of sub-micron features at low temperatures[24].

C. *Nb/Al(thick)–Al_2O_3/Nb* SNIS Elements

As the frequency of operation of an SIS mixer is increased into the submillimeter wavelength range, Josephson noise becomes a significant concern. However, because Josephson currents occur only between two superconductors, junctions consisting of an SIN (superconductor-insulator-normal metal) structure are free of Josephson noise. Chernin and Blundell, utilizing actual SIN I-V characteristics, have theoretically predicted good receiver

noise performance for SIN fundamental and subharmonic mixers at submillimeter wavelengths[25]. We propose to fabricate planar SNIS devices with integrated tuning elements composed of Nb/Al(thick)–Al_2O_3/Nb and NbCN structures (Fig. 10). These two SIN structures have $2\Delta/h$ cut off frequencies of 700 GHz and 1200 GHz respectively. The materials, as well as the interfaces between them, are quite similar to our present Nb/Al–Al_2O_3/Nb SIS devices.

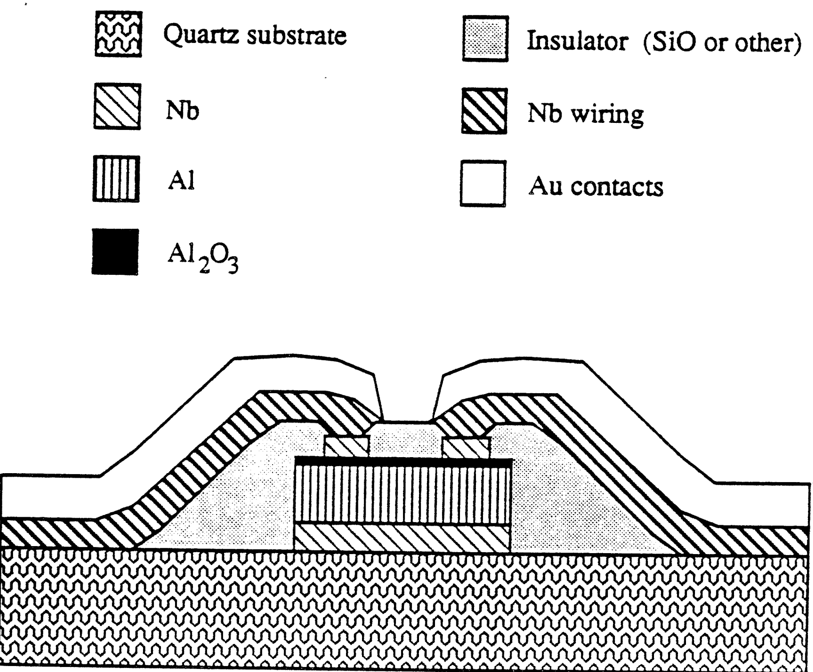

Figure 10. Cross section of Nb/Al(thick)–Al_2O_3/Nb structure

D. Direct Detection Results

The direct detector is an incoherent detector which can be utilized for continuum measurements. SIS direct detectors [26] do not require ^3He cooling as do the best Ge bolometers and therefore may be competitive for space applications. The theoretical response

of the dc tunneling current to radiation is given by the Tien-Gordon equation

$$I=\sum_{m=-\infty}^{m=\infty} J^2{}_m(\alpha)I(V_0 + mh\nu/e)$$

where $\alpha = \frac{eV_{rf}}{h\nu}$ [27]. This parameter can be used to give an estimate of the input power based on the equation

$$P=\frac{V_{rf}^2}{2R_D}$$

where R_D is the dynamic resistance [28]. The quantum limit for current responsivity (the amount of current produced by a given amount of incident radiation) is one electron per incident photon, which corresponds to a responsivity of 413 A/W at 585 GHz. Another parameter of interest is the noise equivalent power (NEP), the amount of power necessary for the signal be equal to the noise of the system. The value that we expect [26] is on the order of 10^{-15} W/$\sqrt{Hz}$, based on the leakage current of our junctions and the system bandwidth.

Nb/Al–Al_2O_3/Nb untuned junctions, described above, are used. The junctions are in series arrays of N = 2,4, and 6, and have a 90 degree integrated bow-tie antenna which is 1000 μm long. The bow-tie junction structure is placed on a copper mounting block behind a hemispherical quartz lens on an adjustable mount used to change the coupling of the radiation into the junction (Fig. 11). Free-standing metallic mesh bandpass filters which have a 10 per cent bandpass at the frequency of interest are placed in front of the lens [29]. One filter is at 4.2 K, and a dual filter is set at 77 K to block the room temperature radiation. The dual filters are offset from each other to block optical paths as well. The whole system is placed in an Infrared Laboratories HD 3-(8) dewar. In addition, we have external lenses to couple the radiation into the dewar. The radiation is provided by an Apollo far infrared laser system, Model 122.

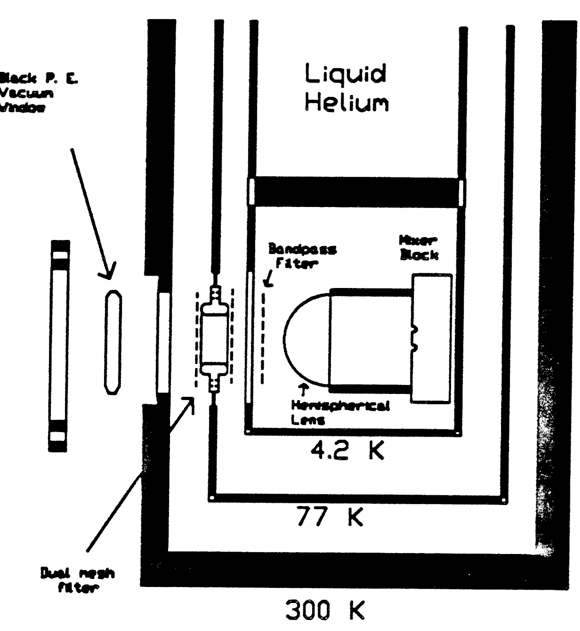

Figure 11. Schematic of the cryogenic dewar used for direct detection measurements.

The responsivity of these junctions has been measured for different power levels at 585 GHz and 763 GHz. Examples of the response at 585 GHz are shown for a two junction array with A = 1 μm^2 (Fig. 12a) and a six junction array with A = 2 μm^2 (Fig. 12b). An example of the response at 763 GHz taken for a six junction array is also shown (Fig. 12c). The measurements at 585 GHz show both quasiparticle and Josephson response. The Tien-Gordon equation was applied to the DC I-V curve and fitted to the experimental response curve in order to separate the two responses. As can be seen, the Tien-Gordon model works well above the gap at 585 GHz, but the Josephson effects interfere below the gap. This problem is particularly obvious in the six junction response ($\alpha = 0.66$) where a large Josephson step appears at about the half-gap. In the two junction array, the expected quasiparticle current, as predicted by the fit, was subtracted from the experimental curve, and the excess currents were found to follow qualitatively the expected power dependence of the Josephson response. We

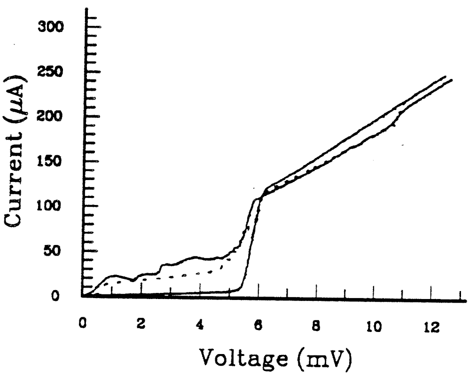

Figure 12a. D.C. I-V characteristic, experimental response, and fitted theoretical response (dashed) at 585 GHz with a two junction array.

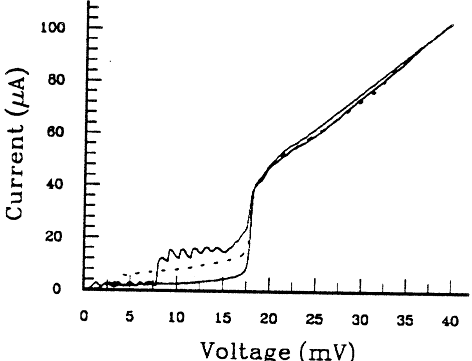

Figure 12b. D.C. I-V characteristic, experimental response, and fitted theoretical response (dashed) at 585 GHz with a six junction array.

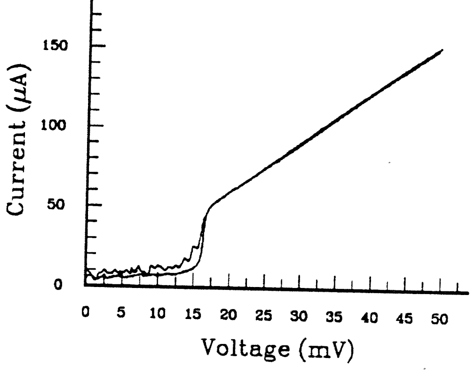

Figure 12c. D.C. I-V characteristic and experimental response at 763 GHz with a six junction array.

are currently extending our model to include the Josephson terms. Using the fitted value of $\alpha = 0.75$ and the theoretical dynamic resistance, the quasiparticle current response at 585 GHz was found to be 350 A/W, or $0.84(\hbar\omega/e)$. Our NEP measurements to date are not presented because they are amplifier-limited; future measurements will be made using low noise amplifiers.

IV. Summary

SIS mixer elements, based on the Nb/Al trilayer system, have given excellent results at millimeter wavelengths. Although other material systems and geometries (the NbN/MgO material system and the edge geometry in particular) appear attractive for submillimeter wavelengths, the Nb/Al trilayer system may prove to be a competitive technology. Our present research with the Nb trilayer system includes new fabrication techniques for sub-square-micron junction areas, SIS individually tuned and fixed tuned detector elements, and SIN structures. Direct detection experiments have been made at 585 GHz and 763 GHz with SIS junctions and a quasiparticle current response of $0.84(\hbar\omega/e)$ at 585 GHz was measured.

V. References

1. T.G. Phillips and D.P. Woody, Annu. Rev. Astron. Astrophys, 20, p. 285, 1982.
2. J. Ibruegger, K. Okuyama, R. Blundell, K. H. Gundlach, and E.J. Blum, Proc. of the 17th Int'l. Conf. on Low Temperature Physics, p.937, 1984.
3. D.W. Face, D.E. Prober, W.R. McGrath, and P.L. Richards, "High Quality tantalum superconducting tunnel junctions for microwave mixing in the quantum limit," Appl. Phys. Lett. 48 (16), p. 1098, 1986.
4. H. H. S. Javadi, W.R. McGrath, S.R. Cypher, B. Bumble, B.D. Hunt, and H.G. LeDuc, "Performance of SIS Mixers at 205 GHz Employing Submicron Nb and NbN Tunnel Junctions," Digest of the 15th Int'l. Conf. on Infrared and Millimeter Waves, 1990.
5. D.P. Woody and R.E. Miller, "Dual Channel 115 and 230 GHz SIS Receivers in Operation at the Owens Valley Radio Observatory," IEEE Trans. Magn., 25 (2), 1989.
6. L.R. D'Addario, "An SIS Mixer for 90-120 GHz with Gain and Wide Bandwidth," Int. J. Infrared and Millimeter Waves, 5(11), p.1419, 1984.
7. A.V. Raisanen, W.R. McGrath, P.L. Richards and F.L. Lloyd, "Broadband RF Match to a Millimeter-Wave SIS Quasi-Particle Mixer," IEEE Trans. Microwave Theory Tech., 33(12), p.1495, 1985.
8 A.R. Kerr, S.-K. Pan, and M.J. Feldman, "Integrated tuning elements for SIS mixers," Int. J. Infrared Millimeter Waves, 9(2), p.203, 1988. This paper was presented at the International Superconductivity Electronics Conference, Tokyo, Japan, 1987.
9. A.W. Lichtenberger, D.M. Lea, C. Li, F.L. Lloyd, R.J. Mattauch, M.J. Feldman, S.-K. Pan, and A.R. Kerr, "Fabrication of Micron Size Artificially Insulated $Nb/Al-Al_2O_3/Nb$ Junctions with a Trilevel Resist Liftoff Process," IEEE Trans. Magn., 27 (2), 1991.
10. A.R. Kerr and S.-K. Pan, "Some Recent Developments in the Design of SIS Mixers," Second International Symposium on Space Terahertz Technology, p.363, 1990.
11. D. Winkler, A.H. Worsham, N.G. Ugrass, D.E. Prober, N.R. Erikson and P.F. Goldsmith, "A 75-110 GHz SIS Mixer with Integrated Tuning and Coupled Gain,"Nonlinear Superconductive Electronics and Josephson Devices, 1991.
12. A.W. Lichtenberger, C.P. McClay, R.J. Mattauch, M.J. Feldman, S.K. Pan, and A.R. Kerr, "Fabrication of $Nb/Al-Al_2O_3/Nb$ Junctions with Extremely Low Leakage Currents," IEEE Trans. Magn. 25, p.1247, 1989.
13. D. Winkler and T. Claeson, J. Appl. Phys., 62, p.4482, 1987.
14. R.J. Mattauch, W.L. Bishop, and A.W. Lichtenberger, "Recent Results on: Surface-Channel Schottky, InGaAs Schottky, and Nb based SIS Mixer Element Research," First International Symposium on Space Terahertz Technology, p.273, March 1990.
15 S.-K. Pan and A.R. Kerr, National Radio Astronomy Observatory, private communication, January 1991.
16. A. Shoji, S. Kosaka, F. Shinoki, M. Aoyagi, and H. Hayakawa, "All Refractory Josephson Tunnel Junctions Fabricated By Reactive Ion Etching,"IEEE Trans. Magn. 19, p.827, 1983.

17. J. Inatani, "A Millimeter-wave Mixer with All-hard SIS Junctions", US-Japan Workshop on Josephson Junction Electronics, Hawaii, 1985.

18. H. Nakagawa, K. Nakaya, I. Hurosawa, S. Takada, and H. Hayakawa, "Nb/Al–oxide/Nb Tunnel Junctions for Josephson Integrated Circuits," Japn. J. of Appl. Phys., 25(1), p.L70, 1986.

19. H.G. LeDuc, J.A. Stern, S. Thakoor, and S. Khanna, "All Refractory NbN/MgO/ NbN Tunnel Junctions", IEEE Trans. Magn., 23, p.863, 1987.

20. J. Zmuidzinas, F. Sharifi, D.J. Van Harlingen, and K.Y. Lo, Proceedings of the International Symposium on Submillimeter and Millimeter Wavelengths Astronomy, Hawaii, 1988.

21. P. Feautrier, J. Blundell, M. Hanus, J.Y. Chenu, P. Encrenaz, and M. Carter, Low Noise 80-115 GHz Quasiparticle Mixer with Small Nb/Al-Oxide/Nb Tunnel Junctions," Int. J. Infrared Millimeter Waves, 11(2), p.189, 1990.

22. A.H. Worsham, D.E. Prober, J.H. Kang, J.X. Przybsyz, and M.J. Rooks, "High Quality Sub-Micron Trilayer Tunnel Junctions for a 100 GHz SIS Receiver," IEEE Trans. Magn. 27(2), 1991.

23. A.C. Hicks, "Development of an Edge Geometry and a New Trilayer Insulation Planarization Process for Small-area SIS Junctions," M.S. Thesis, 1990.

24. K. Machida and H. Oikawa, "SiO_2 Planarization Technology with Electron Cyclotron Resonance Plasma Deposition for Submicron Interconnections," J. Vac. Sci. Technol. B4(4), p.818, 1989.

25. L.M. Chernin and R. Blundell, "Harmonic Mixing in a Superconductor-Insulator-Normal Metal Tunnel Junction Receiver," J. Appl. Phys., 1991.

26. K.H. Gundlach, "Principles of Direct and Heterodyne Detection with SIS Junctions," in *Superconducting Electronics*, ed. by H. Weinstock and M. Nisenoff (Springer-Verlag, New York) pp.260-264, 1989.

27. P.K. Tien and J.P. Gordon, "Multiphoton Process Observed in the Interaction of Microwave Fields with the Tunneling Between Superconductor Films," Phys. Rev., 129, p.647, 1963.

28. J.R. Tucker and M.J. Feldman, "Quantum Detection at Millimeter Wavelengths," Rev. Mod. Phys., 57(4), pp.1055-1113, 1985.

29. J.E. Davis, "Bandpass Interference Filters for Very Far Infrared Astronomy," Infrared Phys., 20, pp.281-290, 1980.

A LOW NOISE 230 GHz HETERODYNE RECEIVER EMPLOYING .25μm^2 Area Nb/AlO$_x$/Nb TUNNEL JUNCTIONS.

J.W.Kooi[1], M.Chan[1], T.G.Phillips[1], B.Bumble[2] and H.G.LeDuc[2]

1- California Institute of Technology, Pasadena, CA 91125,

2- Center for Space Microelectronics Technology, Jet Propulsion Laboratory

Abstract

We report recent results for of a full height rectangular waveguide mixer with two tuning elements [1] and an integrated matching network. A .25μm^2 Nb/AlO$_x$/Nb superconducting insulating superconducting (SIS) tunnel junction was employed with ωRC $\approx$ 1.7 at 230 GHz. Detailed measurements of the receiver system noise have been made from 200-290 GHz with the junction at 4.2K. The lowest system noise temperature was recorded at 239 GHz, measuring 48 Kelvin DSB. Mixer noise and conversion loss have been calculated using the Shot noise method developed by Wengler and Woody [3]. System noise at 230 GHz has been evaluated both at 4.2K and 2.11K as a function of bias voltage, measuring 56K (DSB) and 47K (DSB) respectively. The 230 GHz receiver incorporates a one octave wide integrated low pass filter and matching network which transforms the pumped IF junction impedance to 50Ω over a wide range of impedances. It is believed that the receiver noise temperatures presented are the lowest yet reported for a 230 GHz receiver.

Introduction

The superconducting insulator superconducting (SIS) quasiparticle tunnel junction mixer has been shown to have great potential for producing heterodyne receivers approaching the quantum limit [2]. Feldman, [4] has shown that for slightly non ideal junctions using finite LO power the minimum noise temperature is controlled by the leakage current of the device. It will be seen that for the Nb/AlO_x/Nb

high density tunnel junctions tested the noise level is in theory raised by a mere 3.6 K above that given by the quantum noise limit. For waveguide mixers it is important to use small ωRC junctions with a normal state resistance in the order of 50-100 Ohm. This allows the junction to be efficiently coupled to the embedding circuit. Nb/AlO_x/Nb high current density junctions with ωRC of $\approx$ 1.7 have been tested from 202 to 290 GHz at 4.2 Kelvin. Typical system noise temperatures are 55K DSB from 200-250 GHz. At 265 GHz a waveguide resonance was evident which makes tuning the junction to the embedding impedance virtually impossible, degrading the receiver noise temperature to 278K DSB. To minimize the added IF noise contribution to the system it is essential that the local oscillator pumped junction impedance is properly matched to the 50 Ohm IF load.

For astronomical purposes it is highly desirable to have as wide an IF bandwidth as possible. This is especially true for extragalactic molecular line observations. In addition, it is desirable to provide a short to any out of band signals to prevent the junction from saturating [5]. To meet all these all criteria an integrated matching network was designed, resulting in IF efficiencies of 96% or better from 1.0 to 2.0 GHz making the use of IF isolators unnecessary.

$Nb/AlO_x/Nb$ Junction Fabrication

The Nb/AlO_x/Nb tunnel junctions were fabricated using a standard self-aligned lift-off trilayer process. The Nb/AlO_x/Nb trilayer was deposited in-situ in a high vacuum deposition system with a base pressure of $4 * 10^{-9}$ Torr, through a photoresist lift-off stencil (AZ5214) onto 0.004 inch thick quartz substrates. The trilayer remaining after lift-off formed the first half of the antenna/filter structure. The junction mesa was patterned using electron beam direct writing on a 1200$\mathring{A}$ thick PMMA followed by evaporation of $\approx$ 500$\mathring{A}$ chromium metal and subsequent lift-off. Contact regions of the trilayer are then protected with a photoresist stencil and the combined chromium/photoresist mask was used to etch the junction in a parallel plate reactive ion etcher (RIE).

The etch parameters were 62%CCl_2F_2 + 31%CF_4 + 7%O_2, 30 mTorr pressure, and .18 Watts/cm^2. The electrical isolation of the base electrode and subsequent wire layer are provided by thermal evaporation of 1500Å of SiO. The substrates were tilted and rotated during this operation. The chrome was lifted off using a commercial wet etch. The second half of the antenna was formed by a whole wafer deposition of Nb in the same vacuum system used for trilayer deposition and was patterned using RIE. Tunnel junctions with areas down to 0.25μm^2 were fabricated using this technique.

Wideband Matching Network

The system noise temperature is given by:

$$T_{sys} = T_{mix} + \left(\frac{T_{if}}{C_{loss} * \eta_{if}}\right)$$

To improve system noise temperature it is important to lower the IF contributed noise by improving the IF coupling efficiency (η_{if}) and lowering the IF noise temperature (T_{if}) and/or conversion loss (C_{loss}). IF coupling efficiency is improved by achieving a better match between the pumped junction impedance and the 50 Ohm IF load. Reducing losses before the cooled low noise amplifier lowers the IF noise temperature as can be seen from:

$$T_{if} = T_{e1} + \left(\frac{T_{e2}}{G_1}\right) + \left(\frac{T_{e3}}{G_1 * G_2}\right),$$

where Te1 is the added noise contribution before the first amplifier.

Lastly, mixer conversion loss is improved by reducing RF losses and achieving a better match between waveguide and junction impedance. For practical reasons the IF bandwidth was set to be one octave wide, from 1.0 to 2.0 GHz. As was observed earlier it is especially important to provide a short for out of band signals when using high current density junctions [4]. This prevents possible saturation problems.

The criteria for the integrated matching network are summed up below:

-To integrate a 5 pole Chebyshev low pass filter and match to a 50 Ohm IF load impedance in one design.

-To allow for junctions with normal state resistances of 50-100 Ohm, with a preferred value of 70-90 Ohm. The IF impedance is usually two and a half times the value of the normal state resistance under typical operating, so the matching network is centered at 160 Ohm, real.

-To achieve a flat in band response: 1.0 - 2.0 GHz

S11<-10dB for Rp 100-300 Ω

S11<-20dB for Rp 160 Ω

This eliminates the need for a cooled isolator and excess semi-rigid coaxial cabling, reducing losses.

-Out of band response: 2.0-22 GHz

S11>-.005 dB (Short)

It is important to present a short to out of band signals to avoid saturating the high current density sub-micron tunnel junctions. Chip capacitors have a parallel resonance (open) at approximately 10 GHz, making them impractical to use above this frequency.

-Small physical size to reduce losses and allow the matching network to be easily incorporated in the junction block. Quarter wave sections are too large at 1.5 GHz center frequency to be used.

In designing a microstrip low pass filter a large ratio of high and low impedances sections is critical. With the physical line width limited to about 0.25 mm it became clear that a small dielectric constant (ϵ_r) board was to be used. Furthermore it is highly desirable to use a temperature stable PC board with matched coefficients of expansion to Copper since the operating temperature is 4.2 Kelvin. RT/Duroid 6002 softboard with an ϵ_r of 2.94 was used. To achieve a wide rejection bandwidth we opted not to use chip capacitors but rather to use distributed capacitance on the board, which provides a high degree of rejection up to 22 GHz. A five pole Chebyshev low pass filter and transformer was used to achieve the criteria listed above. To present a true 160 Ω real impedance to the junction we accurately modeled the

RF Choke and included it in our Touchstone (EESOF) models. Figure 1 shows the physical layout, Figure 2 the equivalent electrical circuit. Figures 3 shows S11, the input reflection coefficient of the matching network as measured on a HP8510 network analyzer.

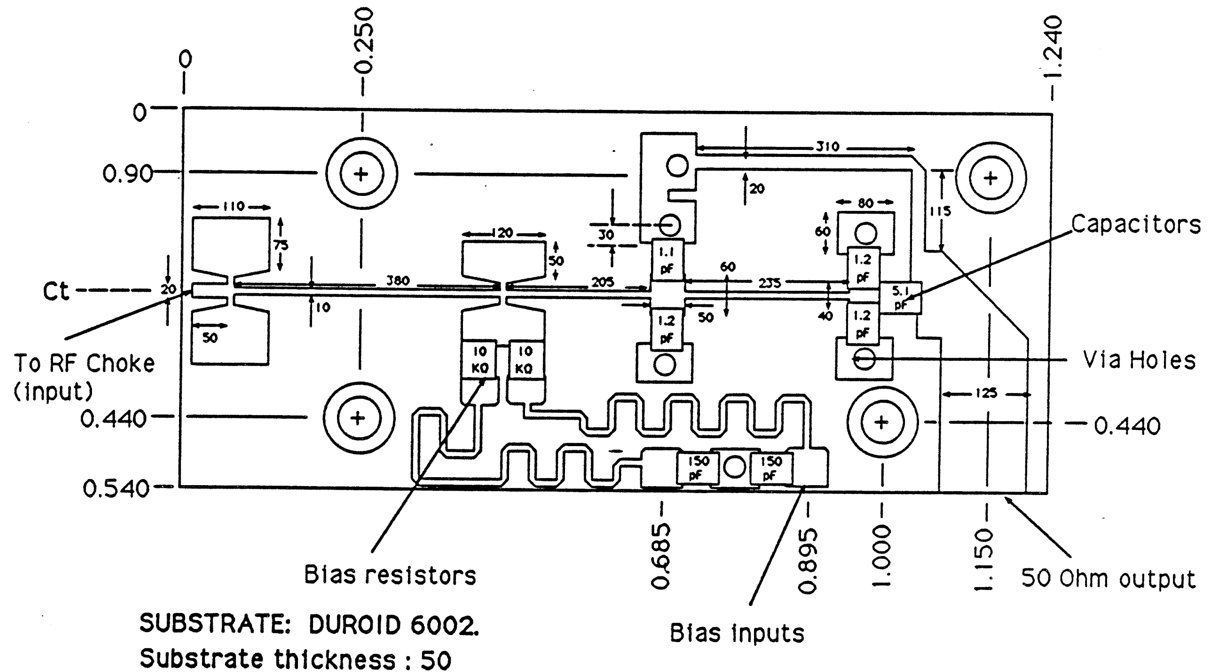

Figure 1. Layout wideband matching network.

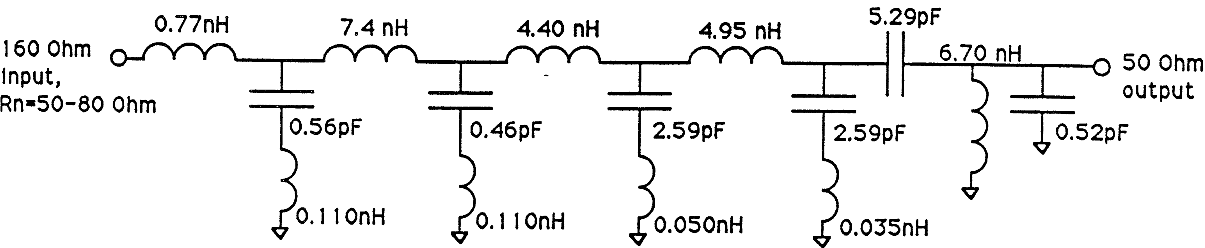

In band response (1.0 - 2.0 GHz) equivalent circuit:

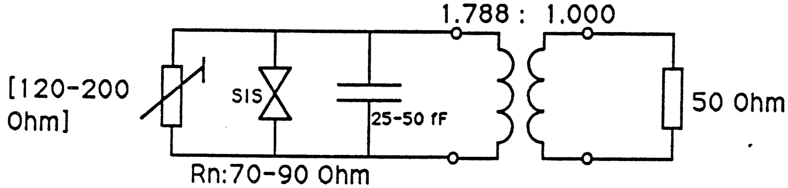

Figure 2. Equivalent electrical circuit.

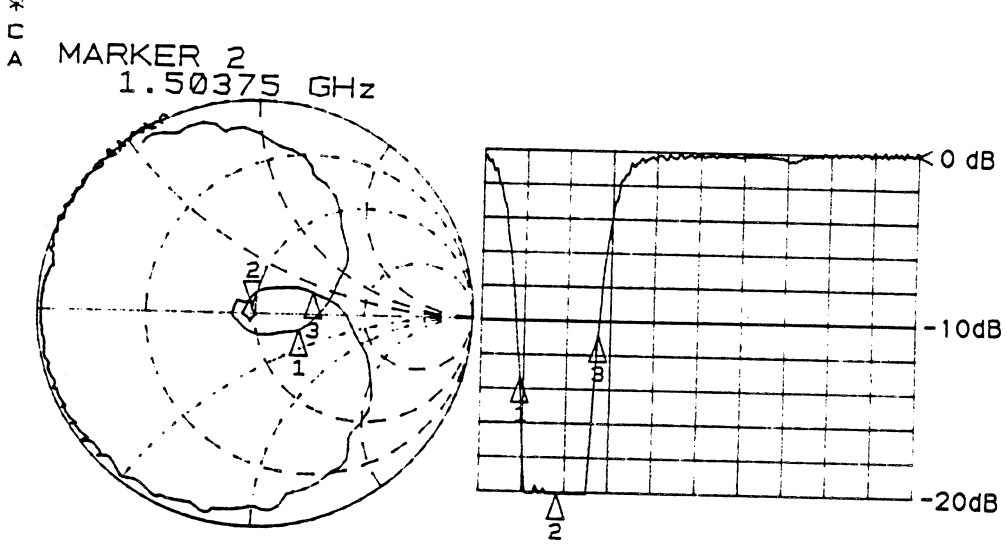

Figure 3. Input Reflection Coefficient (S11).

Measurements

Detailed measurements of receiver noise temperature (T_{sys}) were made from 202-290 GHz in 29 steps. The IF noise temperature (T_{if}), mixer noise temperature (T_{mix}) and conversion loss (C_{loss}) were all calculated using the 'Shot noise method' [2]. This method has to be modified to account for the different matching conditions in the normal state and pumped regions. One of the advantages of the integrated matching network is that the IF impedance presented to the junction is accurately known. The test setup is shown in Figure 4. The IF output of the 230 GHz mixer block was fed directly into the low noise amplifier. A 500 MHz LNA was used temporarily, to be replaced with a modified octave wide balanced HEMT amplifier centered at 1.5 GHz [6]. The IF spectral response for hot and cold loads was measured from 1.25-1.75 GHz, deviating less than 1 dB across the band. The LO is applied via a 0.5 mil Mylar beam splitter to the junction. During the tests the mixer was tuned for maximum noise output power, which is achieved when the junction is best matched to waveguide (low conversion loss).

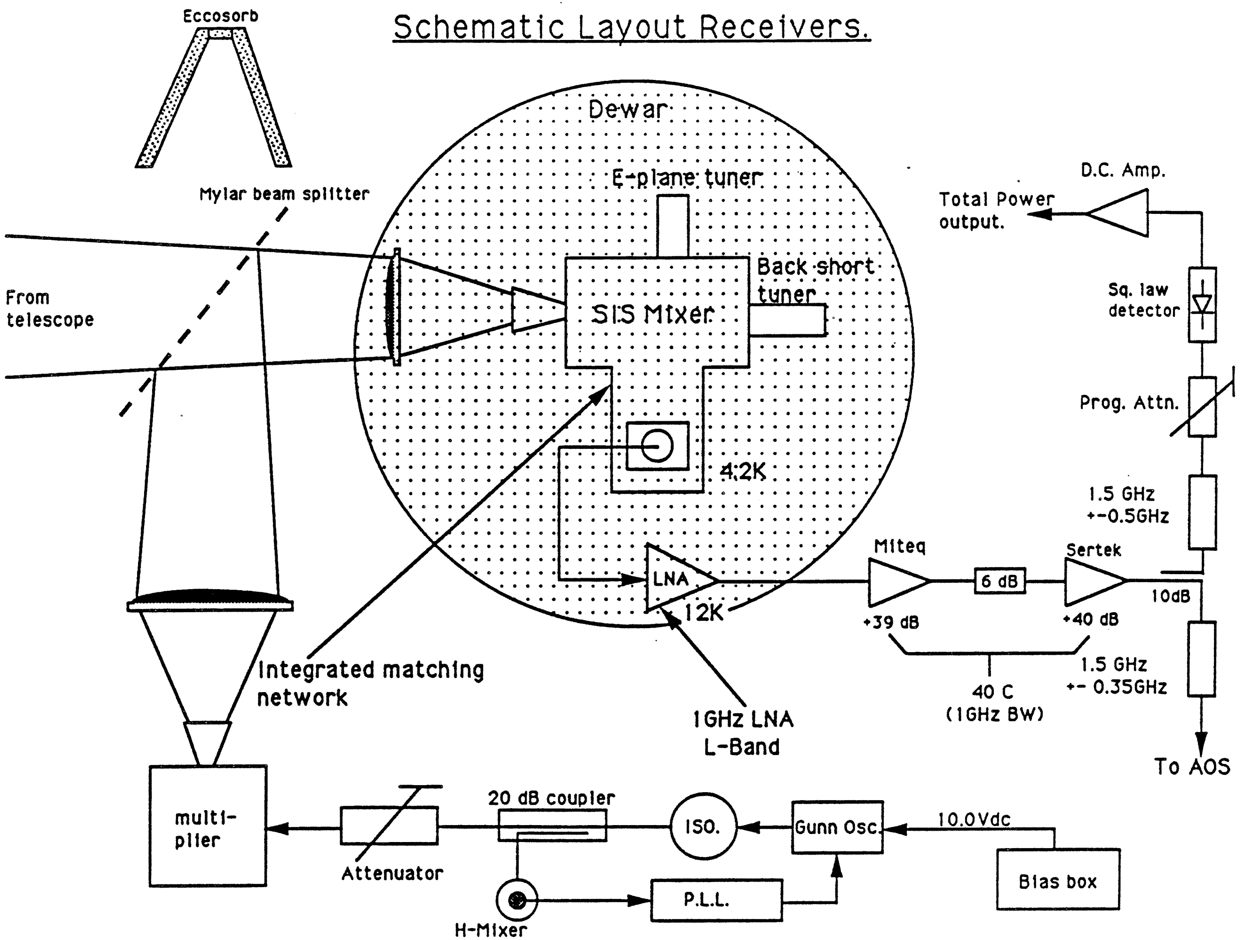

Figure 4. Schematic layout of the receiver.

The IF match generally remained good over a wide range of tuning conditions. The Y-factor measurement was independently verified using an HP 8562A Spectrum Analyzer, HP 436A Power meter and an HP 8472A Power detector. All measurements agreed within 5%. Data was also taken both at 4.2K and 2.11K with the same setup.

Results and discussion

Nb/AlO_x/Nb tunnel junctions with areas of .49μm^2, .33μm^2 and .25μm^2 and a ωRC product of 1.7 were mounted and tested in the receiver setup shown in figure 4. C_s for Niobium is taken to be 50fF/μm^2, however, there is reason to believe that it could be as large as 80fF/μm^2. If this is true the ωRC product

can be as high as 2.7 at 230 GHz. The best noise performance was clearly obtained with the $.25\mu m^2$ area junctions. This is expected as these junctions have the smallest shunt capacitance (12.5fF-20fF) and the largest normal state resistance (95Ω). This combination gives the best RF match while not significantly degrading the IF match (>96%).

The real part of the LO pumped IF impedance can be obtained from the slope of the I-V curve and is observed to be about $(2.5\text{-}3.0)R_n$ under normal operating conditions.

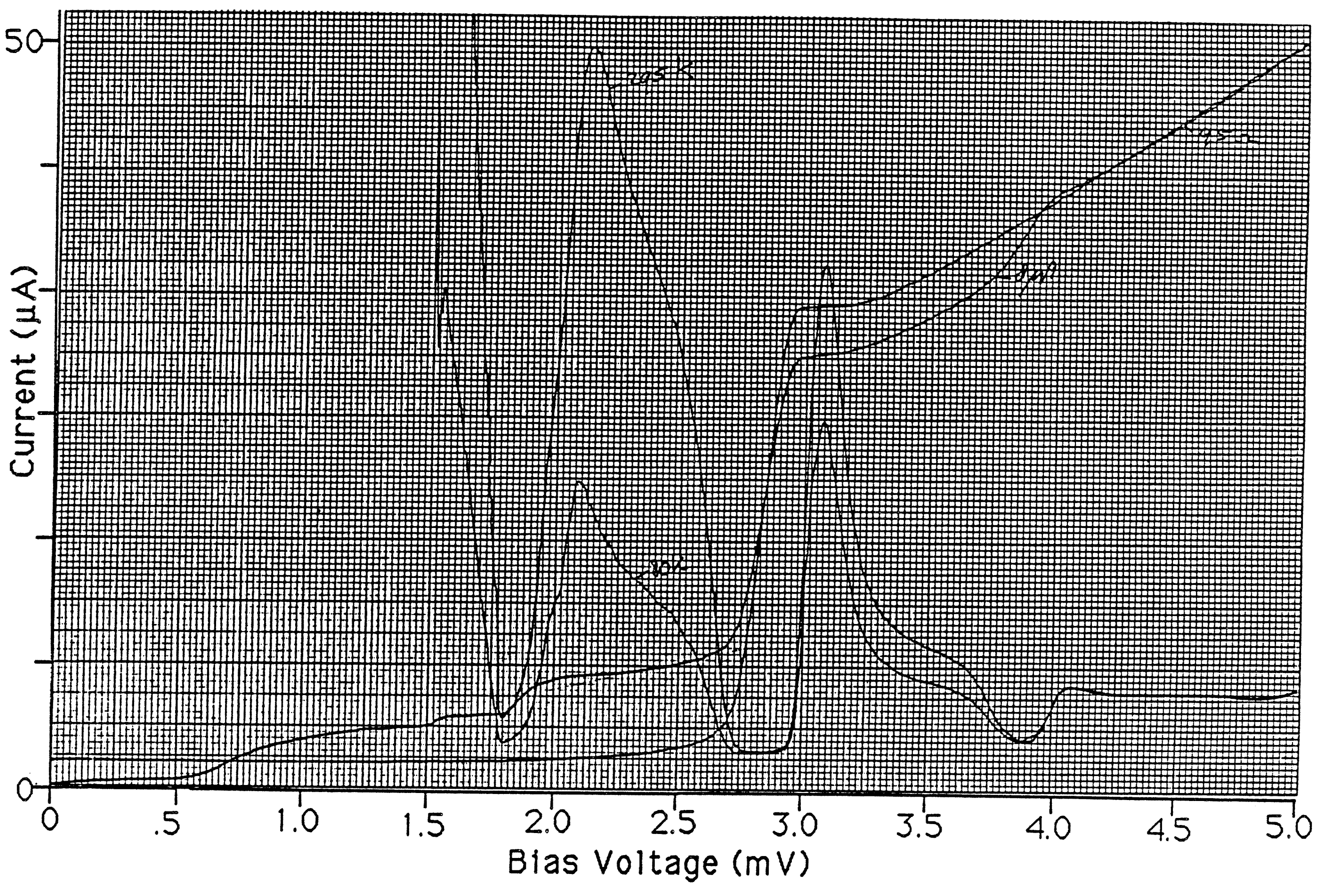

Figure 5. Nb/AlO$_x$/Nb I-V curve and IF response at 230 GHz.

Figure 5 shows the IV curve of a $.25\mu m^2$ area junction at 239 GHz and an operating temperature of 4.2 Kelvin. Four curves are shown: The unpumped and pumped I-V curves, and the hot load (295K) and cold load (80K) responses. The quasi-particle step ($h\nu/e$) at 239 GHz is .98 mV which can be easily verified from the pumped I-V curve. The typical bias voltage is Vgap minus half the photon step, ≈ 2.35 mV. The sub-gap leakage or dark current at this bias point is seen to be 2.7 μA. Figure (9) shows that the

typical operating condition to achieve maximum sensitivity is about 3 times the sub-gap leakage current at the proper bias point. This has been observed for Pb junctions as well. In this case the LO power on the junction was adjusted to register 8μA at 2.35 mV bias.

Figure 5 shows a Y-factor of about 2.70 at 239 GHz, corresponding to a system noise temperature of 48K DSB, which was the lowest value obtained at 4.2 kelvin. The IF noise contribution was calculated to be 10K giving a mixer noise temperature of 38K DSB. The first quasi-particle step shows up at (Vgap-hν/e) or 1.8 mV and the fourth Josephson step at 2mV, 4*($h\nu/2e$).

Feldman [3] has shown that for slightly non ideal junctions using finite LO power the minimum noise temperature is controlled by the leakage current of the junction at the bias point. Using Feldman's result we find, for the $.25\mu m^2$ junction tested that the theoretical device noise temperature has a value of 9.1K SSB or about 3.6K above the quantum noise limit.

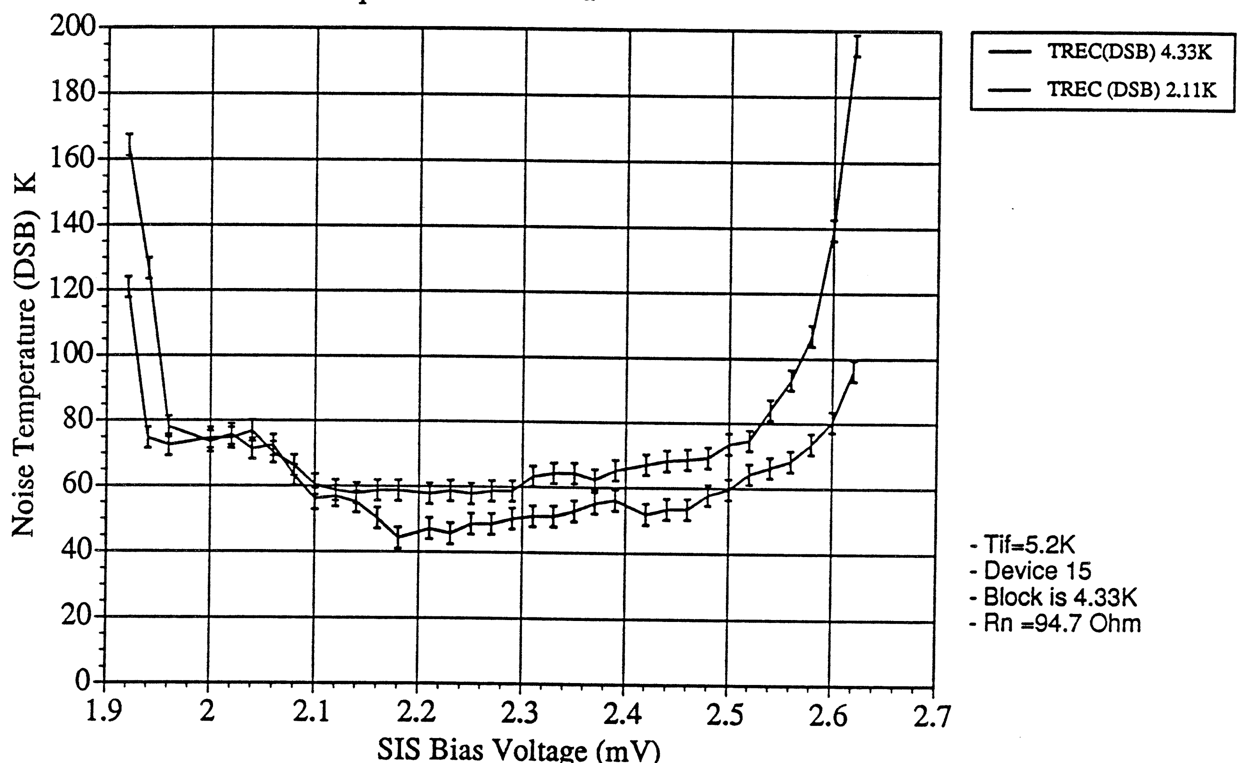

Figure 6. Receiver noise temperature at 230 GHz.

Cooling the junction to 2.11K shifted the gap voltage from 2.8mV to 2.95mV and decreased the sub-gap leakage current from 2.7μA to 2.0μA at 2.35 mV bias. Upon cooling the junction the receiver noise

temperature at 230 GHz decreased by 9K, to 47K DSB, and the conversion loss went down 26% from 3.5 dB to 2.6 dB. This is probably due to the reduction in leakage current and change in gap voltage. The shape of the I-V curve did not change significantly.

Figure 6 shows the receiver noise temperature at both 4.33 and 2.11 Kelvin. Note the change in gap voltage as the junction is cooled.

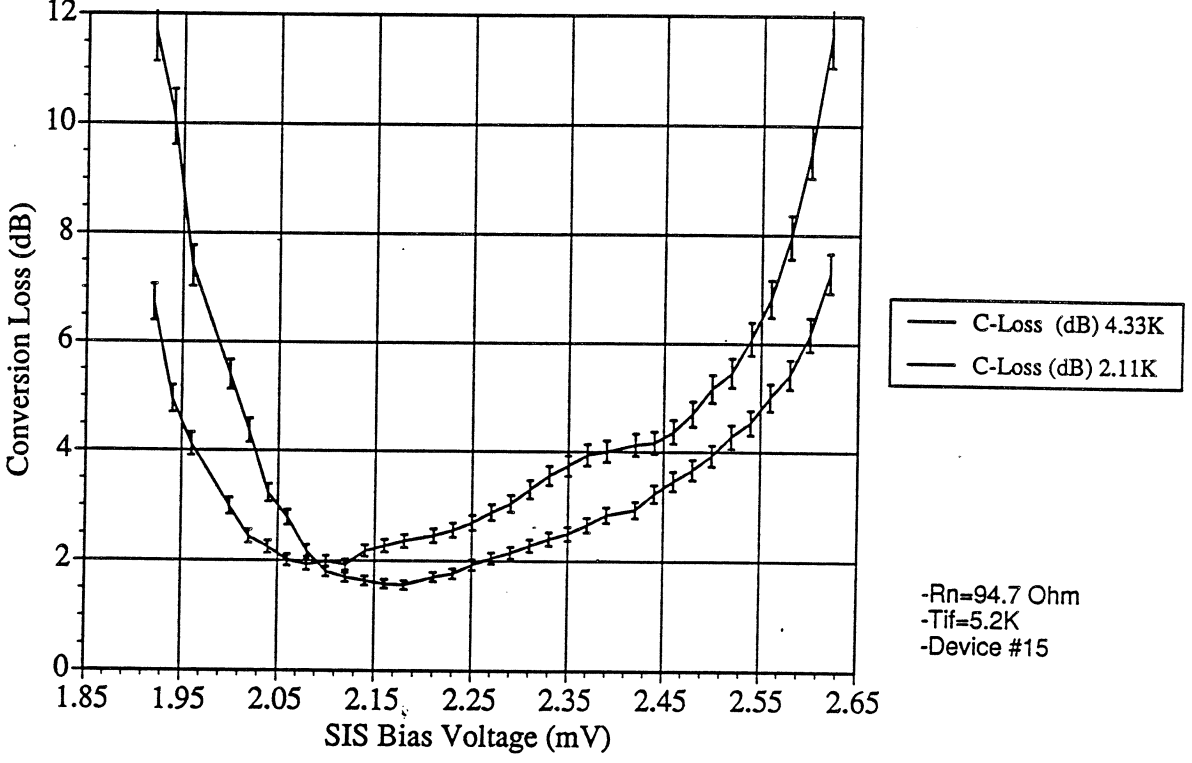

Figure 7. Mixer Conversion Loss at 230 GHz.

Figure 7 shows the conversion loss as a function of bias voltage measured both at 4.33 and 2.11 Kelvin. Note the sharp decrease in conversion loss at 2.35 mV bias as the curve shifts to the right due to a change in gap voltage. Figure 8 shows the receiver and mixer noise temperatures at 202 GHz. The difference in the curves is the IF noise contribution, about 10K. Figure 9 shows the receiver heterodyne response to LO power. Figure 10 shows the frequency response from 202 - 290 GHz for a $.25\mu m^2$ area junction, note the sharp rise in noise temperature at 265 GHz. The resonance was shown to be caused by the junction mount perturbing the waveguide, setting up undesirable modes [7]. This cross-mode coupling effectively changes the embedding impedance making a good RF match to the junction nearly impossible.

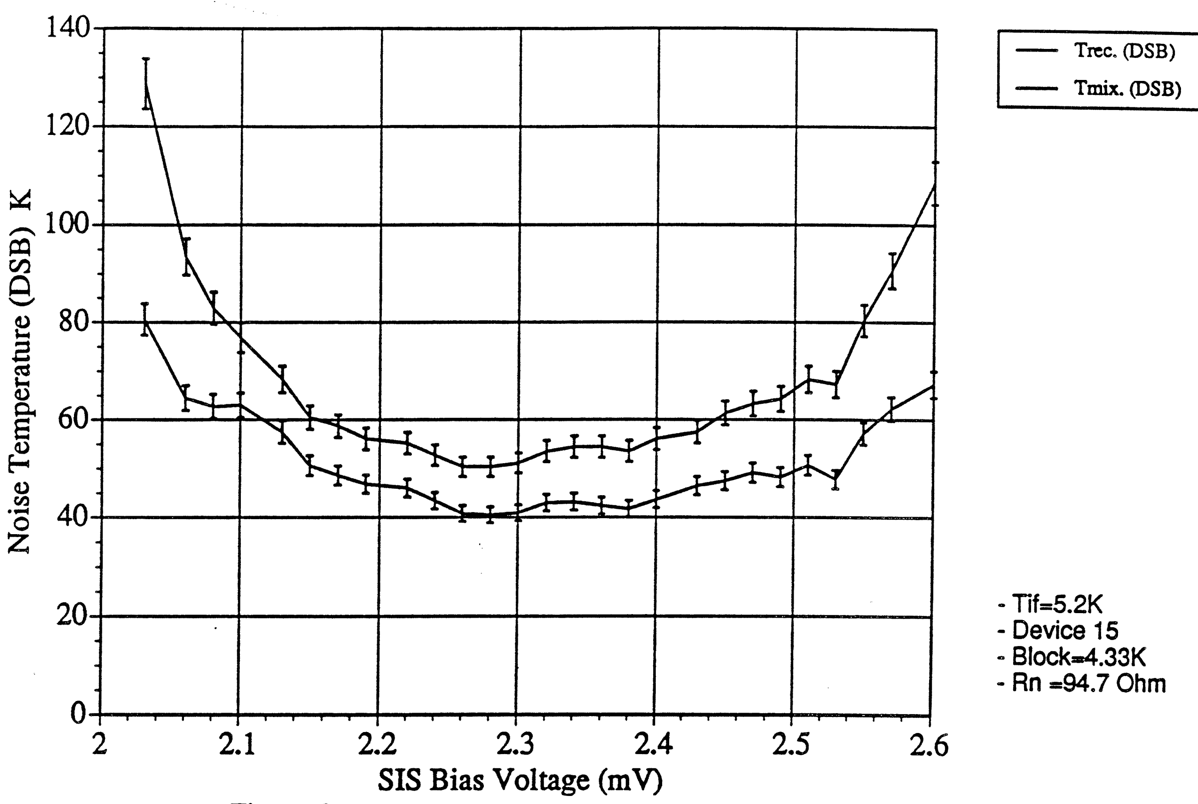

Figure 8. Receiver and Mixer noise temperature at 202 GHz.

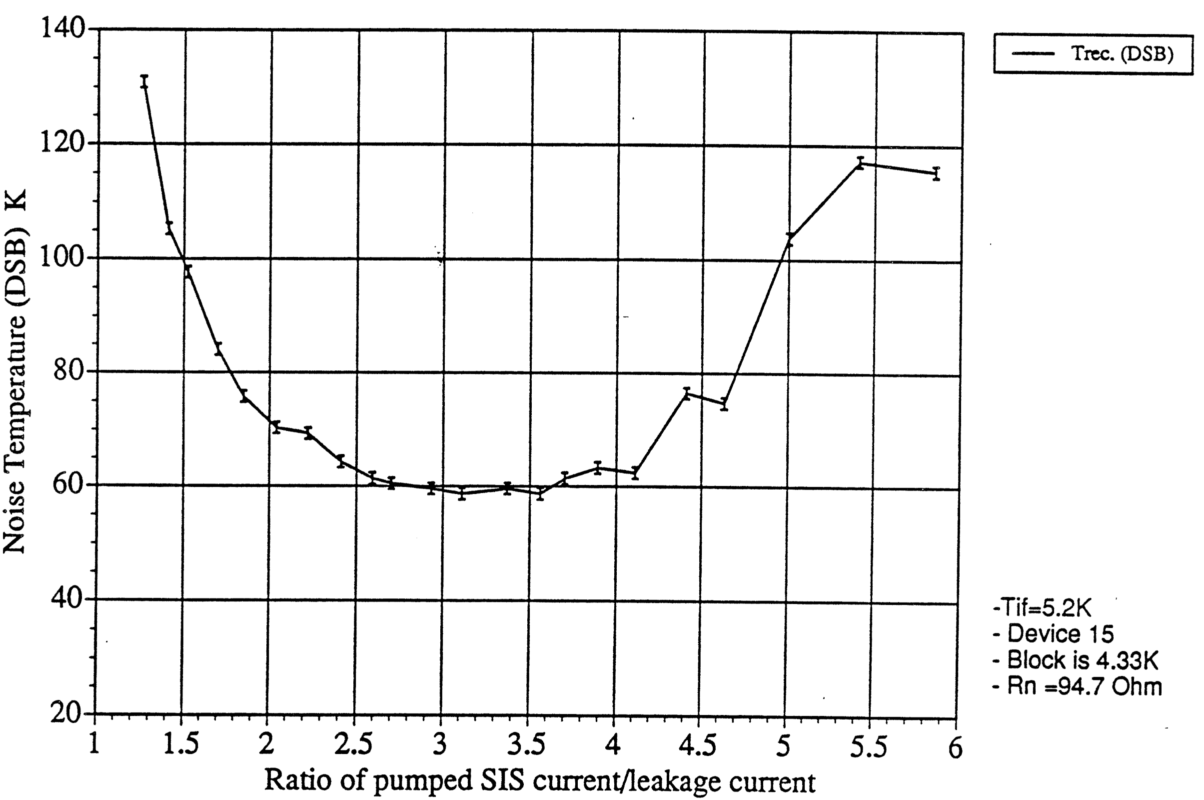

Figure 9. Receiver sensitivity as a function of LO power.

The junction was mounted in the center of the waveguide where computer models have shown the resonance to be the weakest. The resonance for Nb junctions appear stronger than their Pb counterparts perhaps in part due to a larger ωRC product than we expect. This would support the earlier argument that perhaps the C_s of Niobium is larger than the assumed 50fF/μm^2. Data from a physically similar .49μm^2 area junction with twice the shunt capacitance (25fF) shows a waveguide resonance at 250 GHz. The model predicts that the frequency where other modes are excited is solely dependent on the geometry of the junction mount and not in any way on the junction shunt capacitance. If this is true it would indicate that the change in resonant frequency seen is more a result of change in geometry rather than junction capacitance. This is an area that clearly needs more investigation. The conversion loss at the resonance increased to 11dB, confirming the inability to achieve a proper RF match under resonant conditions. Theoretical analysis shows that the resonance is pushed out of band when the waveguide height is reduced by 20%.

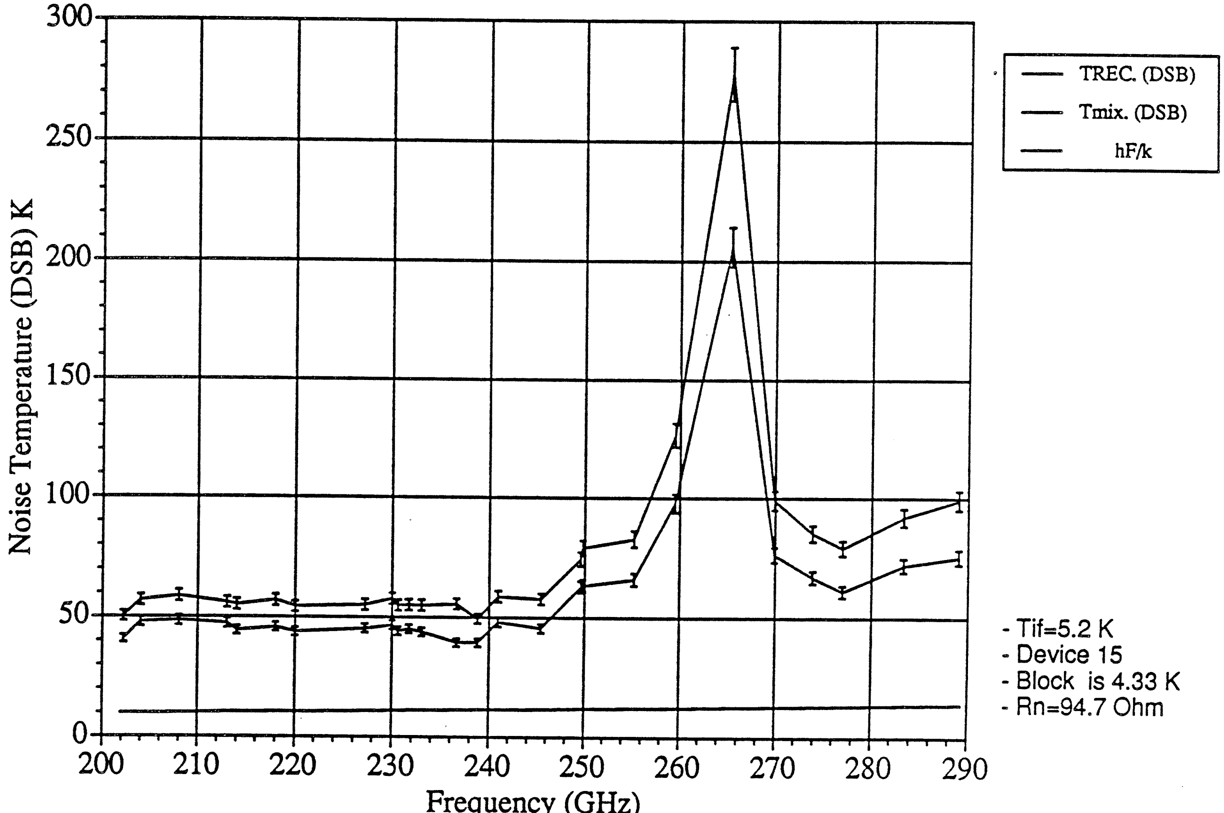

Figure 10. Frequency response of the 230 GHz waveguide Receiver.

Acknowledgments

We wish to thank Pat Schaffer for invaluable work on the receiver cryostat. Work at Caltech is supported in part by NASA grant# NAGW-107 and NSF grant# AST-9015755.

Summary

A 230 GHz SIS receiver with a wideband integrated matching network has been developed and tested using sub-micron Nb/AlO_x/Nb tunnel junctions. Detailed data has been taken from 202 to 290 GHz at 4.33 Kelvin. The receiver has a typical double sideband noise temperature of 56K from 200 GHz to 250 GHz. At 265 GHz the receiver noise temperature degraded to a 278K which is probably caused by cross-mode coupling due to the junction mount perturbing the waveguide. The lowest system noise temperature (48K DSB) and mixer noise temperature (38K DSB) were recorded at 239 GHz.

Data taken at 2.11 Kelvin and 230 GHz indicates that the mixer performance depends on the sub-gap leakage current of the junction. Conversion loss and mixer noise temperature decreased 26% and 16% respectively upon cooling the junction from 4.33 to 2.11 Kelvin.

Lastly, the importance of a proper IF match has been examined and experimentally verified.

References

1. B.N. Ellison and R.E. Miller, "A Low Noise 230 GHz SIS Receiver," Int. J. IR and mm Waves 8, 609-625, 1987

2. "Quantum Detection at Millimeter Wavelength", J.R. Tucker and M.J. Feldman, Rev. Mod. Phys. 57, 1055-1113, 1985

3. M.J. Wengler, D.P. Woody, R.E. Miller, T.G. Phillips, "A Low Noise Receiver for Millimeter and Submillimeter Wavelengths", Int. J. of IR and MM Waves, Vol 6, pp 697-706, 1985.

4. M.J. Feldman, "An Analytic Investigation of the Superconductor Quasiparticle Mixer in the

Low Power Limit", Accepted IEEE trans. Magn. Univ. of Rochester, Rochester NY 14627

5. L.R. D'Addario, "Saturation of the SIS Mixer by Out of Band Signals", IEEE, Microwave Theory and Techniques, Vol 36, No. 6, June 1988.

6. S. Padin, G. Ortiz. "A cooled 1-2 GHz balanced HEMT Amplifier." Accepted IEEE trans. MTT, 1991.

7. A Scale Mixer Model for SIS Waveguide receivers. T.H. Buttgenbach, T.D. Groesbeck, B. Ellison. Int J. of IR and MM waves, Vol. 11, No 1, 1990.

8. W.R. McGrath, J.A. Stern, H.H.S. Javadi, S.R. Cypher, B.D. Hunt, H.G. Leduc, "Performance of NbN Superconductive Tunnel Junctions as SIS mixers at 205 GHz. IEEE trans. Magn. 1991.

A 345 GHz waveguide mixer with two mechanical tuners using an array of four of Nb-Al-Al_2O_3-Nb SIS junctions .

C.E.Honingh#, M.M.T.M.Dierichs*, H.H.A.Schaeffer#, T.M.Klapwijk*, Th.de Graauw#

#Space Research Organization of the Netherlands, Landleven 12, 9700 AV Groningen, The Netherlands
*Department of Applied Physics and Materials Science Center, University of Groningen, Nijenborgh 18, 9747 AG Groningen, The Netherlands

Abstract

A waveguide mixer at 345 GHz, with both an E-plane tuner and a backshort as mechanical tuning elements is described. The guide has a two times reduced height and the tuners are contacting sliding shorts. As a detector we use an array of four Nb-Al-Al_2O_3-Nb SIS junctions in series. The area of one junction is $4\mu m^2$ and its normal state resistance is about 12 Ω, yielding at 345 GHz, $\omega RC \sim 5$.
The receiver noise temperature is below 550 K from 330 to 375 GHz with best results around 350 K measured with a hot and cold load calibration. The instantaneous bandwidth of the mixer is around 2 GHz. The performance of the receiver has been verified by measuring the gas emission line of CO.

Introduction

Our purpose is to build a sensitive receiver for astronomy applications. We study mixer performance at 345 GHz as a first step in building receivers for higher frequencies. Since space qualification is a long term goal of the project we focus on all-niobium junctions. They have proven to be very stable in time and have a reliable and reproducable performance. At 345 GHz no problems with the gap frequency of the material are expected. We find that a magnetic field is necessary to suppress the Josephson effect.

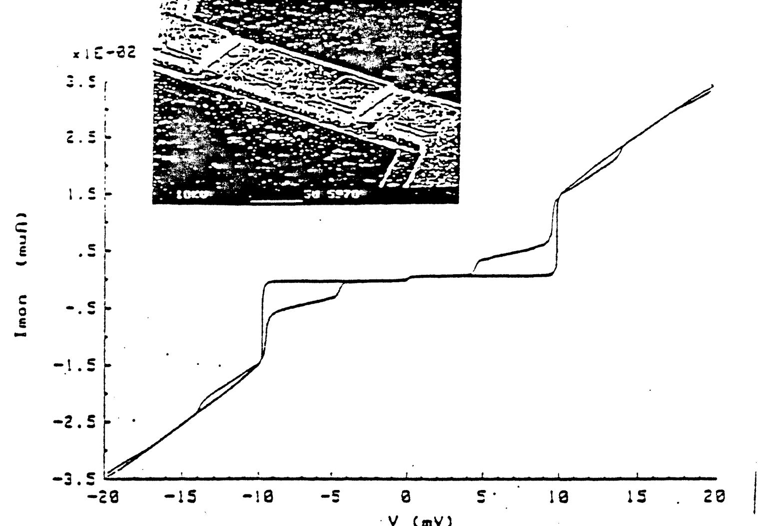

Figure 1a IV-characteristic of four Nb-Al_2O_3-Nb junctions in series. A magnetic field is applied. The pumped stepheight (345 GHz) shows the optimum mixer power level. The inset shows the actual array (SEM).

Design considerations

The junctions have areas of 2x2 μm^2 with a normal state resistance of 12 Ω. Taking 50 $fF/\mu m_2$ for the Al_2O_3

barrier this means that an impedance of (0.45 + 2.2j) Ω must be matched to the antenna.

To realize maximum tuning possibilities we chose a waveguide environment for the junctions. The best receivers built at lower frequencies used waveguides [1],[2]. At 345 GHZ waveguide technology is still possible and good mixer performance has been demonstrated using small area lead-junctions [3].

We use a two times reduced heigth waveguide (625 μm x 150 μm) to compromise between matching requirements and controlled fabrication. An additional advantage is that such a conservative design can still be scaled to higher frequencies. The waveguide is cut out in OFHC copper and so far not gold plated. Radiation is coupled into the waveguide with a diagonal horn [4] modified [5] for ease of fabrication . The distance between the E-plane tuner and the junctions is roughly half a guide wavelength. The substrate with the junctions lies symmetrically across the waveguide. The plane of the junctions is in parallel to the narrow wall of the waveguide. The substrate material is fused quartz and the dimensions are 2.5mm x 190 μm x 92 μm. The substrate channel is 220 μm x 200 μm.

With the two tuners the impedance of the junction can be matched to the waveguide. The quality of the tuners expressed in their VSWR should roughly be equal or less than the ratio of the waveguide impedance and the real part of the junction equivalent impedance. For one tuner this requires a VSWR of 250. It is reasonable to expect [6] a best VSWR of the order of 100. This means that with the given junction parameters an array of four junctions in series is sufficient.

An measured IV-curve of four junctions in series is given in Fig.1a. The inset shows the actual array. To minimize the effects of stress we applied an underlayer [7]. The Nb underlayer is 150 nm thick. The base and counter electrode are 50 nm thick, the Nb wiring layer is 700 nm and the Si insulating layer is 350 nm thick.

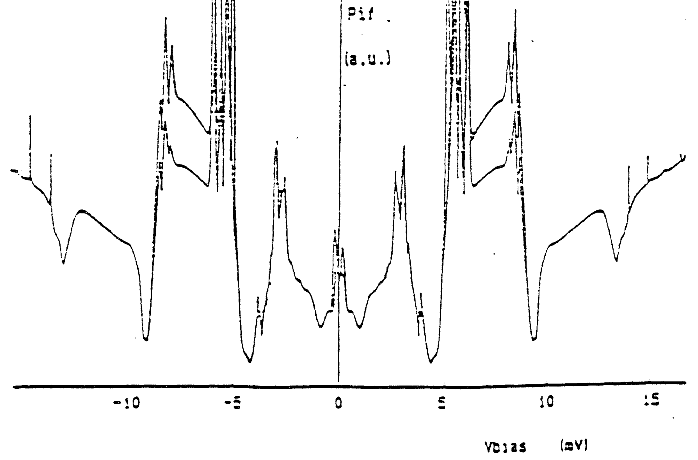

Figure 1b IF-output power as a function of bias voltage at a hot (upper) and cold load input of the mixer. The same magnetic field as in Fig. 1a is applied.

Measurements

The measurement set up is shown in Fig.2. The optimum pump power for various junctions is measured with a Golay cell. When the optimum pump power is low the noise temperature of the mixer is generally also low. The heigth of the quasiparticle step is roughly the same for all measured junctions at optimum pump power, an example is shown in Fig.1.

The noise temperature of the mixer is determined using a hot (300 K) and cold (80 K) load measurement. Results are summarized in Fig.3a.

For each frequency the optimum tuning point is used. The results are corrected for the beamsplitter transmission with 15 %.

As shown in Fig.2 we use a beamsplitter with a low transmission/reflection ratio, because the LO-source has not enough output power over the whole band.

From 330 GHz-375 GHz the noise temperature is below 550 DSB with best results around 350K.

The instantaneous bandwidth around 347 GHz is of the order of 2 GHz (Fig. 3b).

A plot of the IF-output as a function of bias voltage is given in Fig.1b. Because the four junctions of the array are not sufficiently identical the Josephson effect cannot be fully suppressed without reducing the gap of the niobium. The third minimum of the Fraunhofer dependency is used. For incomplete suppression of the Josephson effect the noise temperatures increase.

So far, no impedance transformer is used at the IF-frequency to match the junction to the 50 Ω IF-chain. The measured dynamic impedance of the junction is around 220 Ω.

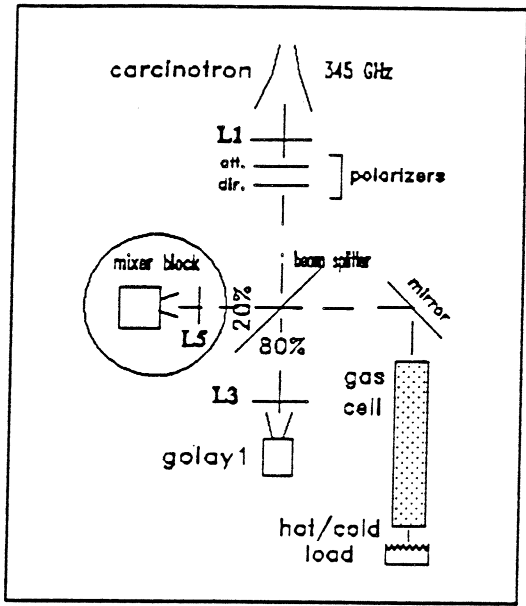

Figure 2 Schematic drawing of the measurment set-up. L1, L3 and L5 are HPD lenses. The beam splitter is made of 50 μm thick mylar foil.

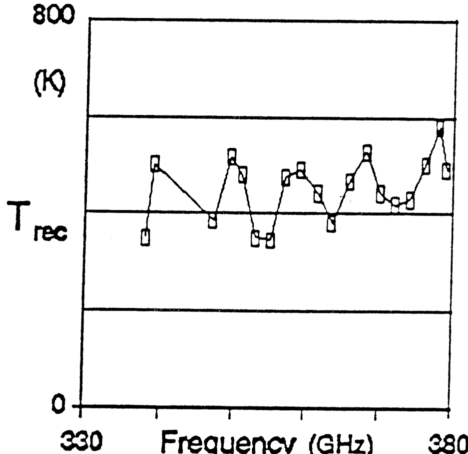

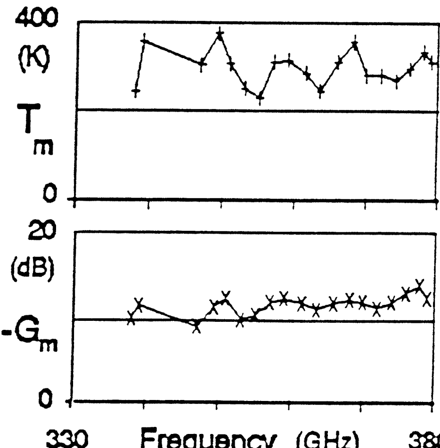

Figure 3a Receiver(T_{rec}) and mixer(T_m) noise temperature, and mixer conversion loss(G_m) obtained from a hot/cold load calibration. At each frequency the optimum tuning point of the mixer is used.

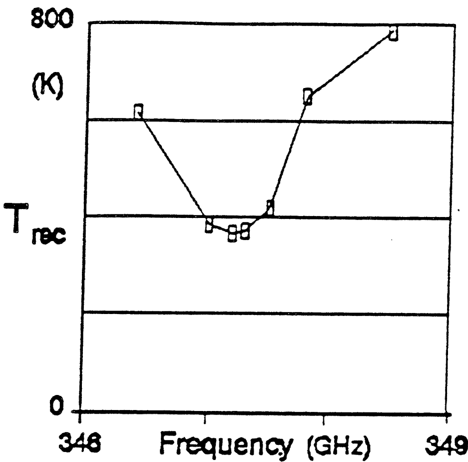

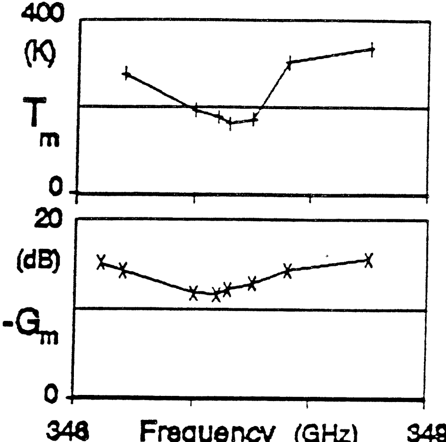

Figure 3b Receiver and mixer noise temperature, and mixer conversion gain as in Fig. 3a. The mixer is optimized at 347 GHz. At the other frequencies the tuning is not changed only the LO-power is adjusted.

The embedding impedance of the junction is analyzed with a 105x enlarged scale model (Fig.5). With a thin (D=1.25mm) coaxial cable the reflection of the mount is measured at the location of the junction. The impedance of the structure probing the waveguide with the two substrate channels shorted is given in Fig. 4A as a function of backshort position. Using the E-plane tuner the whole shaded region of impedances can be presented to the junction. The equivalent impedance of the four junctions in series (+) and its complex conjugate (x) are also indicated in Fig.4a. We ignored any possible induction in the interconnecting leads of the array.

The IF-filters are designed to form a short circuit at the waveguide wall. Without an E-plane tuner matching of the junction is impossible.

Future simpler designs of mixers at higher frequencies will preferably have only one mechanical tuning element. To anticipate on this development the length of the first section of the IF-filter is chosen to compensate the induction of the probe in the waveguide [8]. The resulting embedding impedance as a function of backshort position is given in Fig. 4b. First measurements [9] using a similar mixer with a single backshort done at the NFRA⁺ show receiver noise

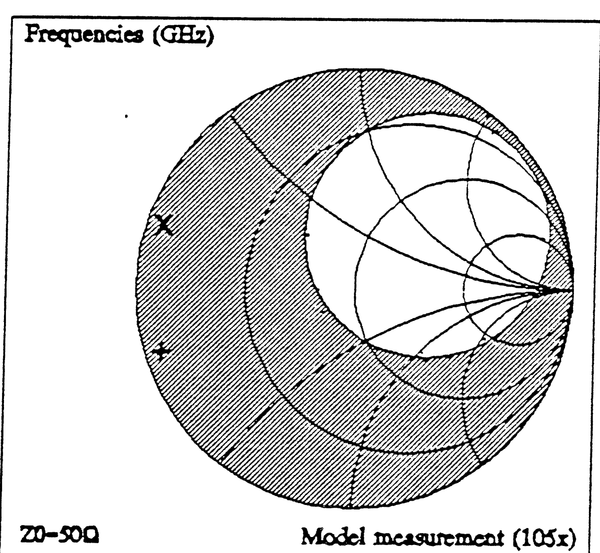

Figure 4a The circle shows the impedance of the probe in the waveguide as a function of backshort position. The angle of the probe is 70 deg., the substrate (εr=4) thickness is 6.5 mm.

temperatures of 300 K DSB. Similar designs without compensation of the inductance give in the same set up noise temperatures of 1000 K DSB.

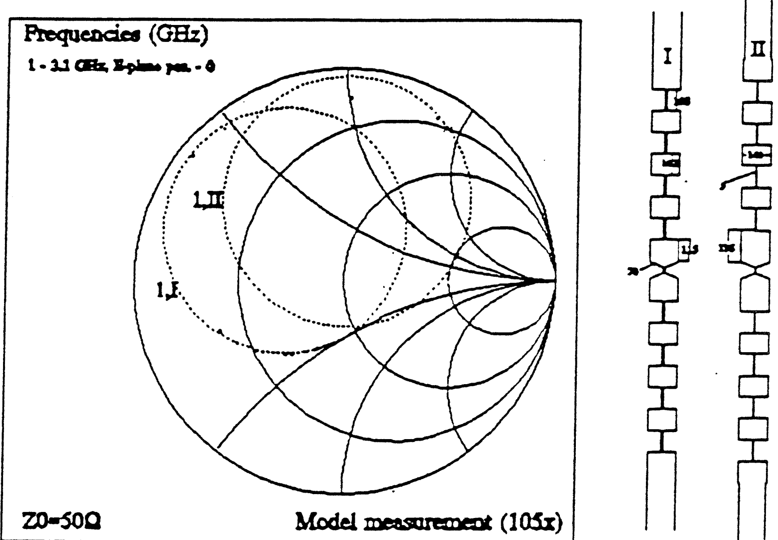

Figure 4b Effect of partly compensating the probe inductance by tuning the first section of the IF-filter. The dimensions in the corresponing filter drawings are in μm.

To verify the heterodyne response of the mixer we studied the emission line at 345.795 GHz of CO-molecules in a gas cell (Fig. 6).
At the IF-frequency we use an Acousto Optical Spectrometer (AOS) with 1025 diodes in a bandwidth of 100 MHz, with an integration time of 32 seconds. Before measuring the emission line the density of CO molecules is measured in absorption. This is done (Fig. 2) by directing the LO-signal through the cell and scanning the frequency.
Because of the narrow instantaneous bandwidth of the mixer the incoupling is optimized at the frequency of the molecular line. After optimization the LO is detuned by 1.4 GHz. A cold load is placed behind the cell while measuring emission.

Evaluation

The absolute value for the output power of the IF-amplifier at a hot (or a cold) load input of the mixer is given by :

$$P_{out} = kB((T_i + T_m)G_m G_{if} + T_{if} G_{if}) \quad (1)$$

where k is the Boltzmann constant, B is the bandwidth of the IF-system, T_i is the temperature of the load. T_m is the noise temperature of the mixer and G_m the conversion gain. With the known gain (G_{if} = 40 dB) and noise temperature (T_{if} = 7±3 K.) of the IF amplifier G_m and T_m are determined from two measurements with different T_i.
The absolute output power depends on the exact value of the pump level and on the suppression of the Josephson effect. Especially the suppression of the Josephson effect

may vary from one measurement to another causing a rather large uncertainty in the output power. The results of the calculations are given in Fig.3a and 3b.
When the geometrical capacitance of the junction array is added to the embedding impedance measured in the scale model the optimum impedance circle in Fig.4c results. The expected frequency dependence of the incoupling is also given. The expected instantaneous bandwidth would be about 1.5 GHz where the measured one (Fig. 3b) is about 2 GHz. This would point a reasonable good tuning and contradicts with the results on conversion gain.

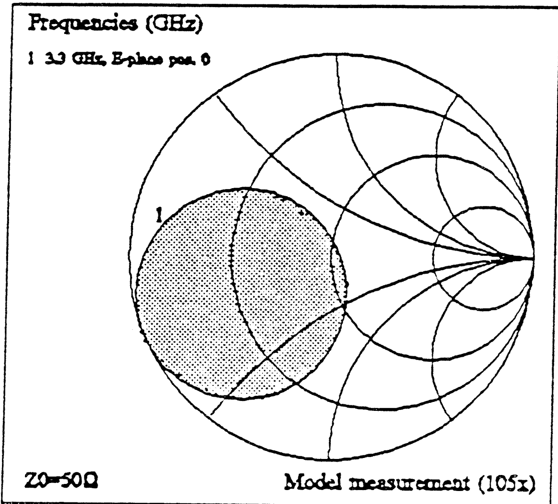

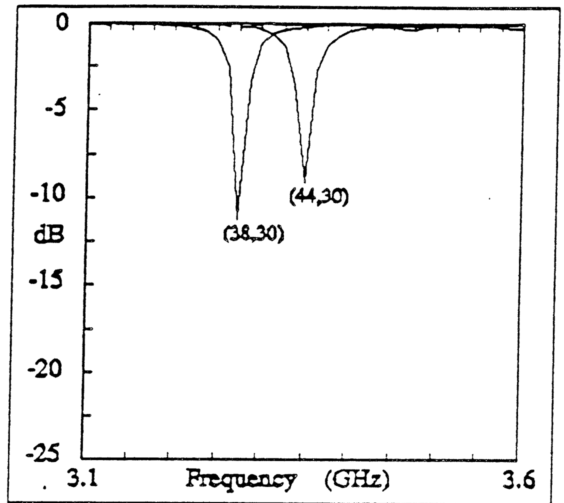

Figure 4c Resulting impedance and power reflection after adding 50 fF in parallel to the embedding impedance measured (to 50 Ω) in the scale model. The E-plane tuner is set at an optimum position.
The impedance is shown as a function of backshort position. The power reflection is given as a function of frequency at two different backshort settings.

The strength in degrees K of the molecular emission line of CO is calculated from 80*(1-A)+300*A, where A is the measured percentage of absorption (The gas in the cell is at room temperature). The strength of the emission line at the input of the mixer, corrected for 15 % beamsplitter loss, is 157 K, i.e. A=48%.
The vertical scale of the AOS is calibrated in degrees K by a hot and cold load measurement through the gas cell. The detected line strength for CO is 83 K.
From the difference in input and detected line strength a SSB noise temperature of 420 K is found.

Conclusions

Using a conventional waveguide design, a heterodyne mixer with an array of all -niobium junctions at 345 GHz is constructed.
Putting junctions in series seems to work without problems at 345 GHz.

The instantaneous bandwidth of the receiver is about 2 GHz. This means that the noise temperature of the mixer observed from the broadband hot/cold load calibration is closer to a SSB noise temperature than to a DSB one. The SSB noise temperature is about 420 K at 345 GHz verified by a gas emission line measurement of CO.
The instantaneous bandwidth compares roughly with the prediction from the scale model measurements.
There are preliminary indications that it is advantageous to compensate the inductance of the waveguide probe by the design of the IF filter. This also compares well with what can be predicted from scale model measurements.
The calculated conversion loss is much higher than might be expected from a SIS mixer which may be due to the quality of the backshorts.

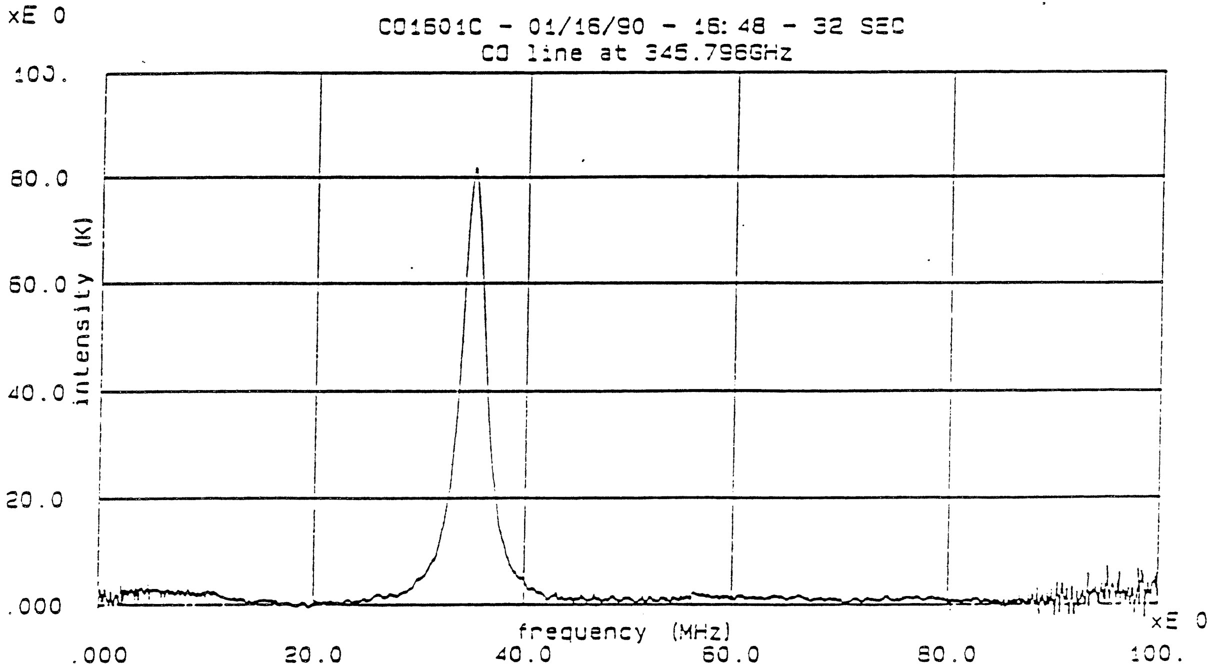

Figure 6 CO emission line at 345.795 GHz as measured with our receiver in the laboratory.

Acknowledgements

This work was supported by the European Space Agency under Contract No. 78908/88/NL/PB(Sc). Johan Wezelman, Gert de Lange, Herman v.d. Stadt and Bert Woestenburg(NFRA) are acknowledged for help with the measurements and valuable discussions.

+NFRA Netherlands Foundation for Research and Astronomy, Dwingeloo, Netherlands.

References

[1] A.R. Kerr, S.-K. Pan Int. J. Infr.& Mm waves, 11, p1169-1187, 1990
[2] R.Blundell, M.Carter, K.H. Gundlach Int. J. Infr.& Mm waves, 9, p361-370, 1988

[3] B.N Ellison, P.L.Schaffer, W.Schaal, D.Vail, R.E.Miller Int. J. Infr.& Mm waves, 10, p937-947, 1989
[4] A.W. Love Micrwave J. , 5, p117-122, 1962
[5] M.Carter IRAM, private communication, May 1990
[6] M.K. Brewer, A.V. Räisänen IEEE Trans. MTT-30, 5, p708-714, 1982
[7] H. Nakagawa, K. Nakaya, I. Kurosawa, S. Takada and H. Hayakawa: Jpn. J. Appl. Phys. 25 (1986) L70.
[8] C.E.Honingh unpublished results
[9] E. Woestenburg, NFRA , unpublished results.

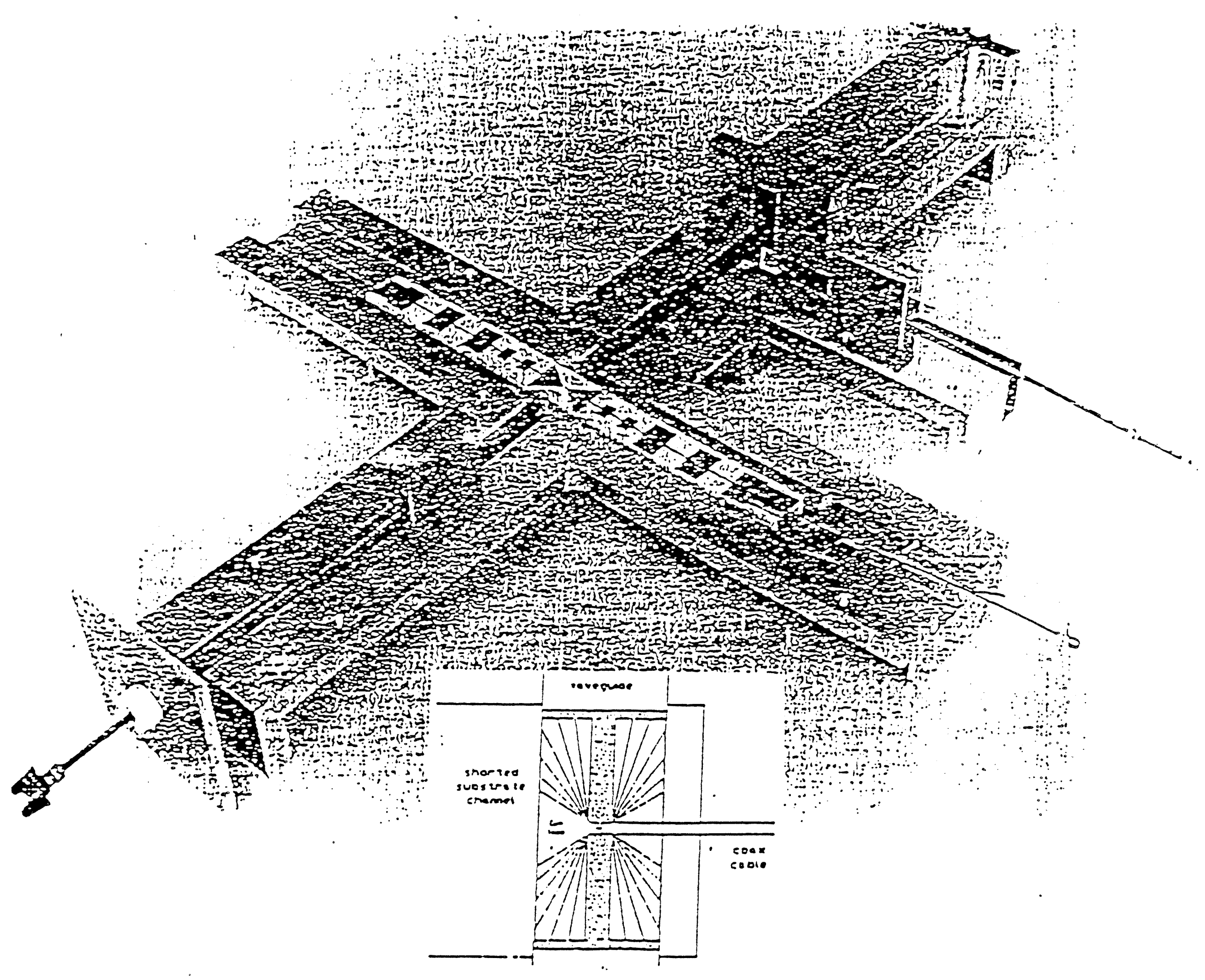

Figure 5 Photograph of the scale model. The coaxial cable is sitting at the right side of the substrate. The backshort is right behind the junction location and the E-plane tuner is constructed in the braod wall of the waveguide.
The inset shows the shows the probe in the waveguide as measured (see Fig. 4a) with different probe angles indicated. The substrate (hatched) has a diëlectric constant of 4 and is 6.5 mm thick.

Quasi-Optical Slot Antenna SIS Mixers

Jonas Zmuidzinas
Downs Laboratory of Physics, 320-47
California Institute of Technology, Pasadena CA 91125

and

H.G. LeDuc
Jet Propulsion Laboratory, 302-231
Pasadena, CA 91109

Abstract

The slot-antenna mixer is a new quasi-optical SIS mixer design which attempts to simultaneously solve the antenna pattern and impedance-matching problems to obtain highly efficient radiation coupling. The mixers have been fabricated by the authors at JPL's Microdevices Laboratory (MDL). The devices employ robust Nb/Al–oxide/Nb tunnel junctions, and have been tested at Caltech. A receiver noise temperature of 420 K (DSB) was measured at 500 GHz, which is the best yet reported for an SIS or Schottky mixer at this frequency. The design of this mixer is readily scalable to 1000 GHz with current fabrication capabilities. The design allows reasonable junction areas to be used, even at high frequencies, which can easily be fabricated using the Nb/Al-Oxide/Nb and NbN/MgO/NbN processes. For example, an 800 GHz mixer requires a single junction with an area of about 0.5 μm^2. The larger junction areas alleviate the effects of mixer saturation and allow strong suppression of the noise from the Josephson effect by the application of a magnetic field. The slot-antenna mixer should have a reasonable bandwidth, about 1.6:1, which would allow the 500–1000 GHz band to be covered with only 2-3 devices.

I. Introduction

Although mixers based on superconducting tunnel junctions (SIS mixers) are predicted to have sensitivities approaching the quantum limit at frequencies well into the submillimeter and perhaps as high as twice the gap frequency of the superconductor [1-3], the experimental realization of SIS mixers which operate at submillimeter wavelengths has remained difficult. There have been a number of reports in the literature in recent years (e.g. [4–6]) describing SIS mixers employing a variety of schemes to directly couple the radiation from a free–space beam into the tunnel junction. These designs use a system of lenses to focus the radiation onto a microantenna which is integrated on the same substrate on which the tunnel junction is fabricated. These quasi–optical designs avoid the problems associated with waveguides at short submillimeter wavelengths, and would make the fabrication of imaging mixer arrays a relatively straightforward task. However, in the past, the quasi–optical mixers generally did not couple the radiation into the tunnel junction as efficiently as waveguide designs (e.g. [7]). The two critical factors in this coupling are the antenna efficiency - that is, how well the antenna pattern matches the incoming radiation, both in amplitude <u>and</u> <u>phase</u> - and the impedance match between the tunnel junction and the antenna. The slot antenna mixer design is our first attempt at dealing with both of these issues in a design which is simple, robust, straightforward to fabricate, and relatively insensitive to fabrication tolerances.

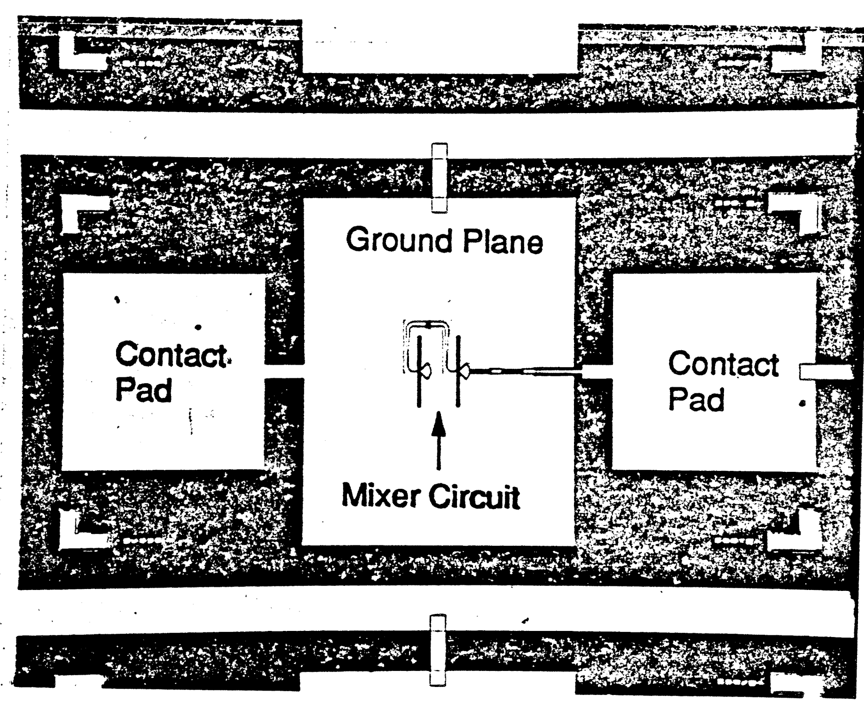

Figure 1a. Quasi-optical slot-antenna SIS mixer chip for 500 GHz.

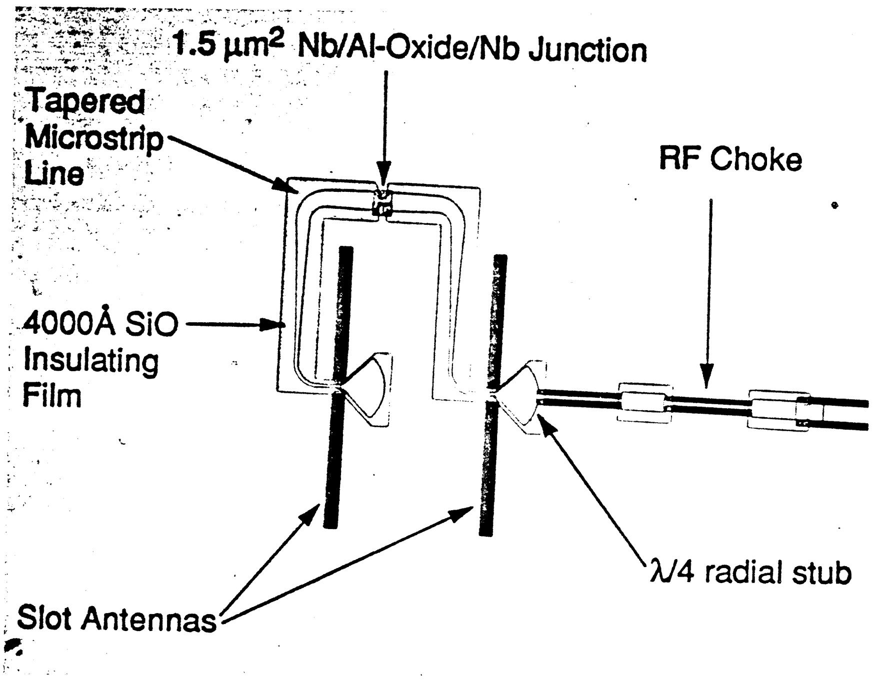

Figure 1b. Close-up view of slot-antenna mixer circuit.

II. Description of Mixer Design

Our mixer design consists of a twin-slot planar feed antenna, a Nb/Al-oxide/Nb or NbN/MgO/NbN SIS junction, and a tapered transmission line joining the junction to the two slot antennas (see Fig. 1). A hyperhemispherical lens is used to focus the incident radiation onto the twin-slot antenna (Fig. 2). A similar configuration for a quasi-optical Schottky mixer was described by Kerr, Siegel, and Mattauch [8]. The principal differences are that the Schottky design omitted the hyperhemispherical lens, used a quarter-wave section of transmission line for matching instead of a taper, and fed the two slots in series instead of in parallel.

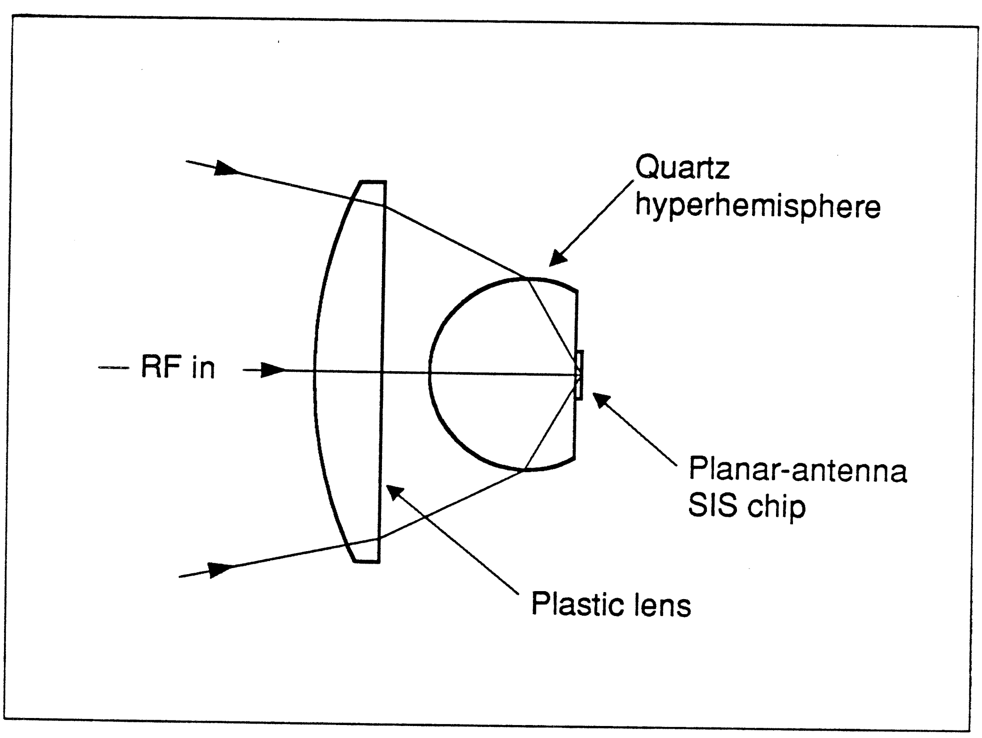

Figure 2. Slot antenna mixer optics.

A slot antenna on a semi-infinite dielectric substrate has a number of desirable properties. First of all, the antenna impedance is quite low and can be computed using a moment–method technique described by Kominami, Pozar, and Schaubert [9] which is essentially a numerical solution of Maxwell's equations. We have developed a program to perform this computation. The impedance as a function of frequency calculated for a single slot in the case of a crystal quartz substrate (ε_r = 4.53 on average) is shown in Fig. 3. In between two high-impedance resonances lies a broad region of low impedance. The impedance of a single slot antenna of length L = 0.47 λ (where λ is the free-space wavelength) and width W/L = 0.04 is Z_a = 35+j0 Ω. The antenna impedance bandwidth is quite broad. The frequency band over which the fractional power coupled from the antenna into a 35 Ω load is better than 50% is one octave. Detailed circuit simulations of the mixer indicate a 1.6:1 bandwidth for the mixer. We will be testing this prediction in the near future by using a newly–constructed fourier transform spectrometer (FTS) in our laboratory to measure the SIS direct-detection response in the manner of Hu *et al.* [10], as well as performing heterodyne tests over a range of frequencies.

Since the antenna impedance program also calculates the electric field distribution in the slot, the results of this program may be used to calculate rigorous antenna patterns. A contour plot of the resulting pattern radiated into the dielectric is shown in Fig. 4. The separation between the slots (S = 0.29 λ) was adjusted to produce a symmetric pattern with a half-power beam width of 47°. The main beam efficiency is calculated to be η_{MB} = 70%. The remaining power is radiated into small E-plane sidelobes (4%) and backwards into air (26%). The phase of the antenna pattern was also investigated. The antenna does have a small phase error, but fortunately this error causes a reduction in the coupling efficiency of only 2%. Aberrations in the focusing lenses can also produce phase errors in the antenna pattern of the overall receiver. The aberrations were calculated, and were also found to reduce the coupling efficiency by a negligible amount, < 2%. Finally, the polarization properties of the antenna are important. The twin-slot antenna has excellent polarization characteristics since it responds only to electric fields perpendicular to the slots.

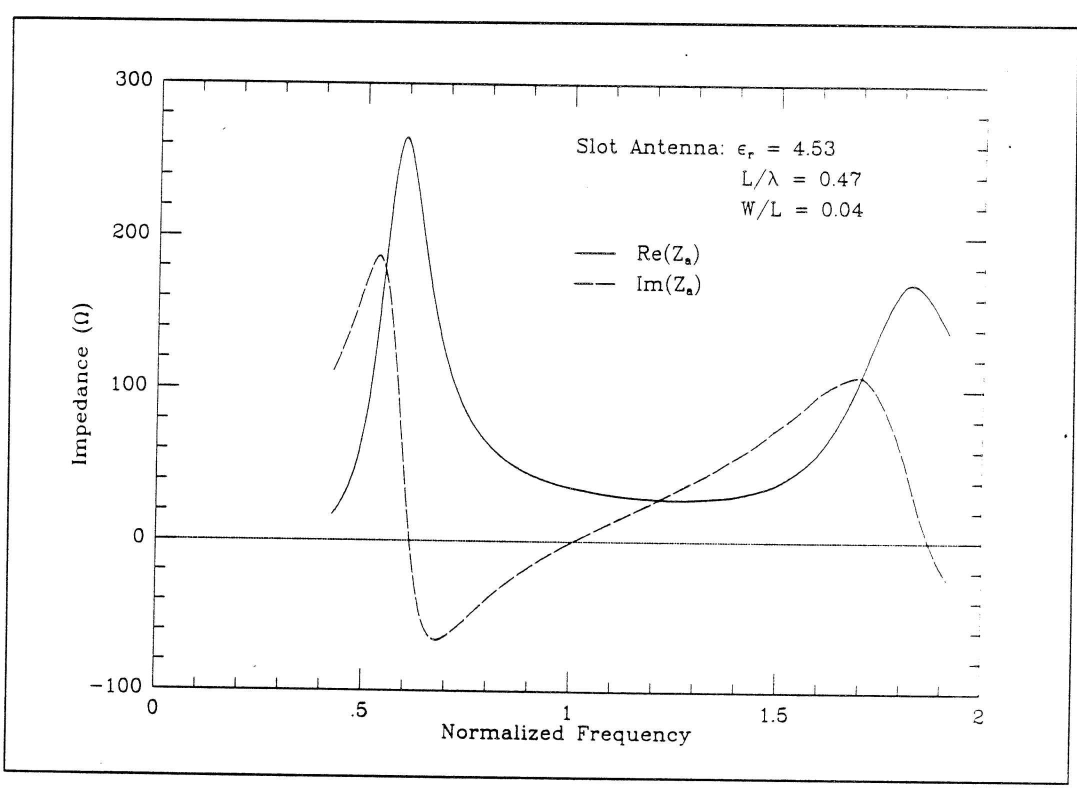

Figure 3. Slot antenna impedance as a function of frequency (on quartz).

The quartz hyperhemispherical lens serves two functions. First, it transforms the fairly broad beam of the twin-slot antenna (HPBW = 47°) to a narrower beam (HPBW = 22°). Second, it prevents power from being radiated into surface-wave modes as occurs when finite-thickness dielectric substrates are used. Essentially, the hyperhemisphere makes the dielectric substrate look semi-infinite. However, there is a reflection loss associated with the air-dielectric interface of the lens. For quartz, we calculate that the beam-averaged transmission through this interface is 86%, just a little lower than the transmission at normal incidence (87%). This loss can be almost completely eliminated by applying a quarter-wave anti-reflection coating on the hyperhemisphere.

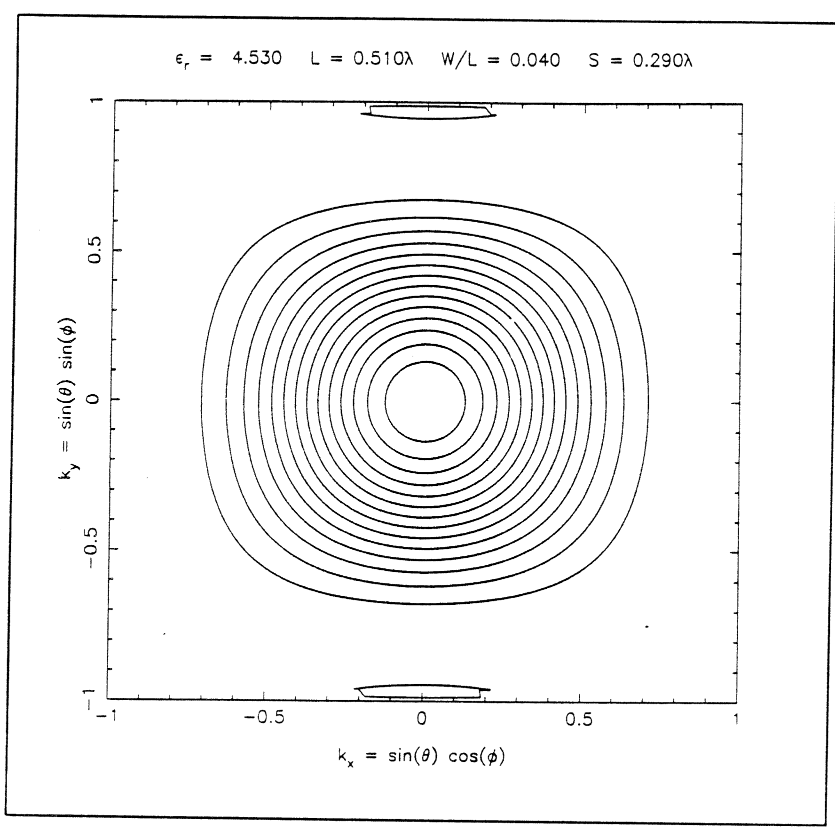

Figure 4. Power pattern of twin-slot antenna. Contours are linearly spaced, from 5 % to 95 % of the peak.

As compared to other submillimeter mixer designs, the slot-antenna mixer uses an SIS junction with a fairly large area. The junction area is scaled inversely with frequency, from ≈ 0.9 μm^2 at 500 GHz to ≈ 0.5 μm^2 at 800 GHz; the design rule is that $1/\omega C = 4\ \Omega$ (see below). These areas are calculated using a specific capacitance of C_s = 85 fF μm^{-2} [11], a value now believed to be appropriate for Nb/Al–Oxide/Nb junctions with current densities of ≈ 10 kA cm^{-2}. Unfortunately, the mixers were designed assuming a specific capacitance of C_s = 50 fF μm^{-2} appropriate for lower current density junctions, which leads to junction areas of 1.5 μm^2 at 500 GHz. The actual areas turned out to be ≈ 2.3 μm^2, because the mask design overcompensated for possible shrinkage in the junction dimensions during processing (see section III).

Larger–area junctions have a higher saturation power, require a smaller magnetic field to suppress the Josephson effect, are easier to fabricate, and are electrically more robust . The disadvantage is that a larger junction has a lower impedance, and the circuit design of the mixer must compensate for this. At 500 GHz, the reactance of the junction capacitance is $1/\omega C \approx 4\ \Omega$ for a high current density (≈ 10 kA cm^{-2}) 1 μm^2 Nb/Al-oxide/Nb junction. This is much lower than the normal–state resistance of the junction, and so the magnitude of the junction complex impedance is $|Z| \approx 1/\omega C$ to a good approximation. Our mixer design does not attempt to tune out the junction capacitance with an inductive shunt or an open–circuit transmission line stub. Rather, we transform the antenna impedance down to a level of $1/\omega C$, to obtain the best possible match to the junction under the constraint that the source resistance is required to be purely real. We have intentionally avoided using resonant circuits in this initial

design, because such circuits have tight dimensional tolerances and require good knowledge of the behavior of superconducting transmission lines at high frequencies. In our design a sacrifice is made in the coupling efficiency by not attempting to tune out the junction capacitance. The coupling efficiency due to this impedance mismatch is roughly

$$\eta = \frac{2}{1+\sqrt{1+Q^2}}$$

where Q is the $\omega R_N C$ product of the junction. For instance, if Q=3, this coupling efficiency is $\eta \approx 0.5$; the overall efficiency for coupling radiation into the junction (including the antenna efficiency) is estimated to be ≈ 0.3. In the future we will be experimenting with circuits which tune out the junction capacitance and eliminate this loss, at the expense of a narrower bandwidth.

To match the 35 Ω twin-slot antenna impedance to the $\approx 1\ \mu m^2$ SIS junction we use two tapered superconducting microstrip transmission lines. These lines are tapered from a characteristic impedance of 35 Ω at each slot to an impedance of 8 Ω at the junction. Since the two transmission lines feed the junction in parallel, the impedance seen by the junction is 4 Ω. The transmission lines do not disturb the slot antenna because the slot antenna has a ground plane everywhere except for the slot. The characteristics of the superconducting microstrip transmission lines used for the design of the mixer were calculated using an adaptation of the method described by Whitaker *et al.* [12], but since the design uses a tapered line, it is fairly insensitive to the actual phase velocity and characteristic impedance of the microstrip lines.

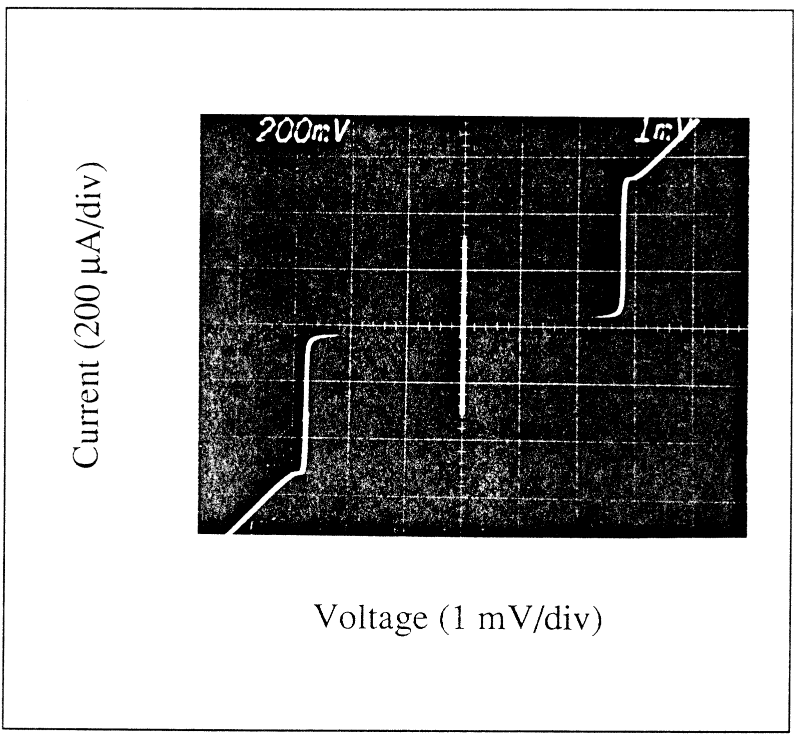

Figure 5. An I-V curve of a Nb/Al-Oxide/Nb junction in a slot-antenna mixer circuit.

III. Device Fabrication

The twin-slot mixers are fabricated at the Microdevices Laboratory at JPL. The mixers fabricated for testing at 500 GHz employed Nb/Al-Oxide/Nb tunnel junctions; mixers with NbN/MgO/NbN junctions will be fabricated in the near future for testing at 800 GHz. The mixers are manufactured using a four mask level fabrication process, which is similar to the planar NbN/MgO/NbN process described by LeDuc *et al.* [13]. In the first step, the Nb/Al–Oxide/Nb trilayer is sputtered on a substrate on which a lift–off stencil has been patterned using AZ 5214 photoresist in image–reversal mode. Most of the gross features of the mixer are defined in this step, including the slot antennas, the contact pads, and the ground plane. Following lift-off of the trilayer, reactive-ion etching (RIE) in a 63% CCl_2F_2, 31% CF_4, and 6% O_2 mixture at a pressure of 30 mT is used to define the junction, which is protected from the etch by AZ 5206 photoresist patterned in positive mode. Only the areas of the trilayer which are near the path of the transmission lines are exposed to the etch. After the etch but before the photoresist is removed, a 1500 Å layer of SiO is evaporated on the sample to isolate the junction and to provide a portion of the SiO needed for the transmission line dielectric. The evaporation is performed with the sample mounted on a rotating platform which is tilted at an angle with respect to the evaporation source. The combination of the tilt and rotation ensures good step coverage for the SiO film. The photoresist is then removed, exposing the junction area. Another layer of SiO, about 2500 to 3500 Å thick, is evaporated on the sample, this time through a lift–off mask patterned with AZ 5214 photoresist in image–reversal mode. The junction is protected by photoresist during this evaporation, of course. The total SiO thickness obtained in these two steps is 4000 – 5000 Å, which is the thickness needed for the microstrip transmission lines. After lift–off, a Nb wiring film is deposited on the entire substrate and patterned with RIE using an AZ 5214 photoresist mask. The microstrip lines are patterned in this step.

The fabrication results were quite good. The SIS junctions tested at 500 GHz had areas of $A \approx 2.3\ \mu m^2$, normal-state resistances of $R_N = 9\ \Omega$, current densities of $J_c \approx 10$ kA cm^{-2}, and $\omega R_N C \approx 4.6$. A typical I-V curve is shown in Fig. 5. The yield was high: 36 out of 37 devices tested had good I–V curves. The r.m.s. variation in the current step at the gap voltage was 4.5%, and the typical normal to subgap resistance ratio was $R_{sg}/R_N \approx 10$.

IV. Laboratory Results

Initial laboratory tests of the slot-antenna mixer at 500 GHz have been very encouraging. The local oscillator was a quintupled Gunn oscillator. The quintupler was obtained from Radiometer Physics (Peter Zimmerman) in West Germany [14]. The local oscillator was introduced into the signal path by using a 12% reflective mylar beamsplitter. With this arrangement, the mixer could be pumped with substantially more than the minimum LO power necessary for efficient mixing. The receiver sensitivity was measured with the standard hot/cold load Y–factor technique, using sheets of Eccosorb at room temperature (295 K) and dipped in liquid nitrogen (80 K). The IF was calibrated using the SIS junction shot noise as a variable temperature load. The measured I.F. power for the hot and cold loads as a function of voltage is shown in Fig. 6. This figure was obtained by suppressing the Josephson effect with a magnetic field. Structure is still visible in Fig. 6 in the vicinity of the second Shapiro step at 2 mV, but is suppressed to a remarkable degree compared to the case with no magnetic field. The application of the magnetic field allows low–noise mixing over a large fraction of the first photon step below the gap voltage. Without the field applied, reliable mixer operation could not be obtained. The results for the noise temperature are as

follows (SSB values are 2 x DSB) :

Receiver noise temperature (DSB)	T_{rec}	= 420 K
Conversion loss (DSB)	L_c	≈ 10 dB
IF Contribution	L_cT_{IF}	≈ 110 K
Mixer noise temperature (DSB)	T_m	≈ 240 K
(IF & beamsplitter contribution subtracted)		

These results give us confidence that with proper design, the application of a magnetic field will strongly suppress noise from the Josephson effect and will allow low-noise SIS mixing up to at least the gap frequency (700 GHz for Nb; ≈ 1400 GHz for NbN), and confirms previous experience with Pb–alloy SIS mixers at 500 GHz [15]. Excess noise produced by the Josephson effect has been thought to be a major limiting factor in the performance of SIS mixers at high frequencies [1,16]. While it is well known that a magnetic field applied to a junction suppresses the DC Josephson current, it has not been clear that a magnetic field would suppress high–frequency noise currents as well. Our results agree with the conclusions of Winkler, Claeson, and Rudner [17,18], who studied SIS mixing in Al tunnel junctions at frequencies (≈ 75 GHz) approaching the superconducting gap frequency of Al (≈ 90 GHz). These experiments indicated that magnetic fields would indeed allow the low–noise operation of SIS mixers close to the superconducting gap frequency.

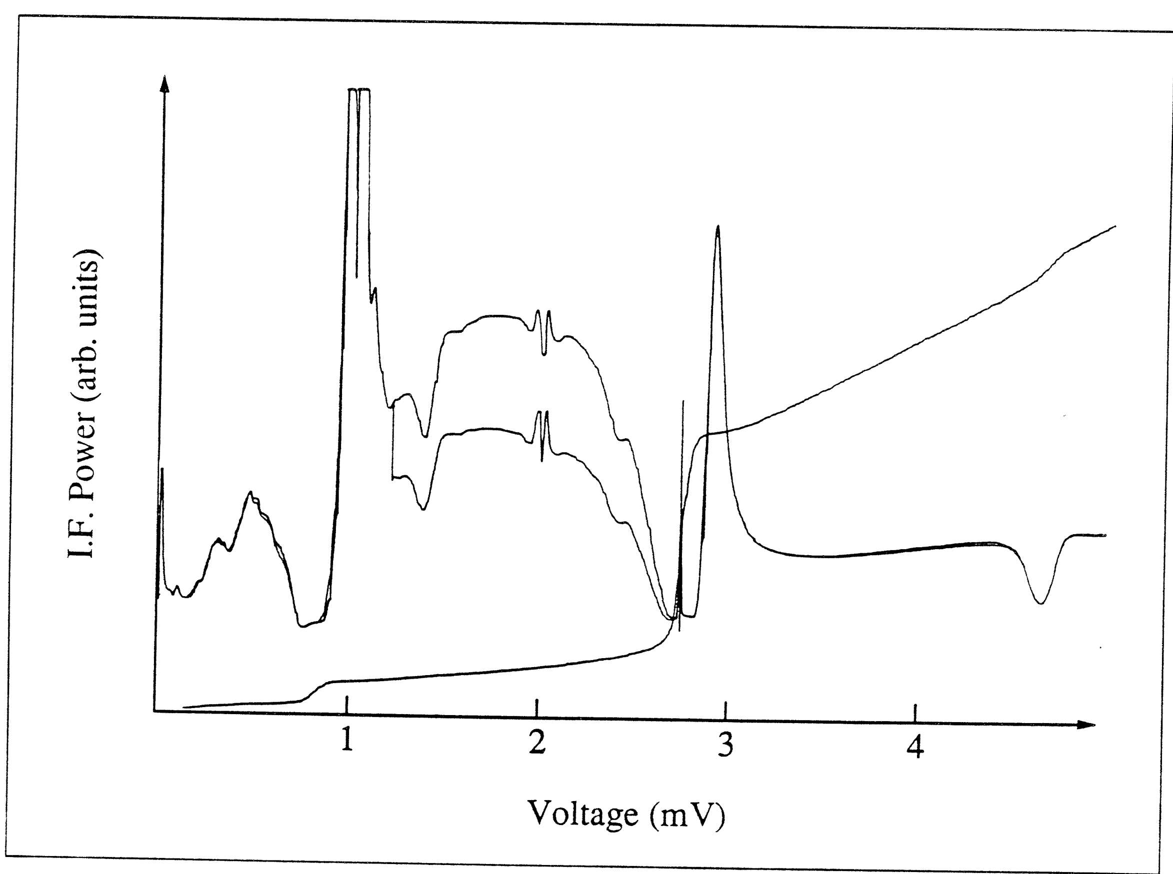

Figure 6. A measurement of the hot (295 K) and cold (80 K) load response of the twin-slot mixer at 500 GHz. The pumped I-V curve is also shown.

The mixer tests also show that there is room for improvement. The conversion loss is substantially higher than expected, and could be due to an impedance mismatch larger than calculated, excess loss in the microstrip transmission lines, or problems in the optical coupling. These will each be investigated. Also, the IF contribution to the system noise is larger than expected, and the cause of this needs to be located and corrected. In addition to these unknown factors, there are several parameters in the current design which are known not to be optimal. For instance, the junction area is too large by a factor of 2.5, the current density should be higher, the transmission line dimensions need to be adjusted, the lenses are not anti–reflection coated, and the beamsplitter reflectivity could be reduced. We therefore fully expect that a substantial improvement of the mixer sensitivity can be achieved, and that receiver noise temperatures at 500 GHz in the range 100–200 K (DSB) will be obtained. In the future, we also expect to measure the frequency response of the mixer by direct–detection experiments using a fourier–transform spectrometer as well as by heterodyne sensitivity measurements, to map the receiver beam pattern, and to measure the coupling efficiency of the receiver to a telescope.

Acknowledgement

We wish to thank T. Büttgenbach and J. Stern for helpful discussions. J. Z. is indebted to K.Y. Lo and T. G. Phillips for advice and encouragement, and to F. Sharifi and D. Van Harlingen for his introduction to superconducting device fabrication.

References

[1] J. R. Tucker and M. J. Feldman, "Quantum detection at millimeter wavelengths", *Rev. Mod. Phys.*, vol. 57, p. 1055, 1985.

[2] W. C. Danchi and E. C. Sutton, "Frequency dependence of quasiparticle mixers", *J. Appl. Phys.*, vol. 60, p. 3967, 1986.

[3] M. J. Wengler and D. P. Woody, "Quantum noise in heterodyne detection", *IEEE J. Quantum Electron.*, vol. 23, p. 613, 1987.

[4] M. Wengler, D. P. Woody, R. E. Miller, and T. G. Phillips, "A low noise receiver for millimeter and submillimeter wavelengths", *Int. J. Infrared and Millimeter Waves*, vol. 6, pp. 697-706, 1985.

[5] T. H. Büttgenbach, R. E. Miller, M. J. Wengler, D. M. Watson, and T. G. Phillips, "A broad-band low-noise SIS receiver for submillimeter astronomy", *IEEE Trans. Microwave Theory Tech.*, vol. MTT-36, pp. 1720-1726, Dec. 1985.

[6] X. Li, P. L. Richards, and F. L. Lloyd, "SIS quasiparticle mixers with bow-tie antennas", *Int'l J. IR & MM Waves*, vol. 9, p. 101, 1988.

[7] B. N. Ellison, P. L. Schaffer, W. Schaal, D. Vail, and R. E. Miller, "A 345 GHz SIS receiver for radio astronomy", *Int'l J. IR & MM Waves*, vol. 10, No. 8, 1989.

[8] Kerr, A.R., P.H. Siegel, and R.J. Mattauch, "A simple quasi-optical mixer for 100-120 GHz", *1977 IEEE MTT–S Int. Microwave Symp. Digest*, p. 96, 1977.

[9] M. Kominami, D.M. Pozar, and D.H. Schaubert, "Dipole and slot elements and arrays on semi-infinite substrates", *IEEE Trans. Antennas Propagat.*, vol. AP-29, p. 600, 1985.

[10] Q. Hu, C. A. Mears, P. L .Richards, F. L. Lloyd, "Measurement of integrated tuning elements for SIS mixers with a Fourier transform spectrometer", *Int'l J. IR & MM Waves*, vol. 9, p. 303, 1988.

[11] J. Stern, private communication, 1991.

[12] Whitaker, J.F., R. Sobolewski, D.R. Dykaar, T.Y. Hsiang, and G.A. Mourou, "Propagation model for ultrafast signals on superconducting dispersive striplines", *IEEE Trans. Microwave Theory Tech.*, vol. MTT-36, p. 277, 1988.

[13] LeDuc, H. G., J. A. Stern, S. Thakoor, and S. Khanna, "NbN/MgO/NbN SIS tunnel junctions for submillimeter wave mixers", *IEEE Trans. Magn.*, vol. MAG-23, 863, 1987.

[14] Radiometer Physics, Bergerwiesenstraße 15, 5309 Meckenheim, F.R.G.

[15] T. Büttgenbach, private communication, 1990.

[16] M. J. Feldman, "Theoretical considerations for THz SIS mixers", *Int'l J. IR & MM Waves*, vol. 8, No. 10, p. 1287, 1987.

[17] D. Winkler, T. Claeson, and S. Rudner, "Quasiparticle mixing close to the gap frequency in aluminum tunnel junctions", *IEEE Trans. Magn.*, vol. MAG-21, p. 896, 1985.

[18] D. Winkler, T. Claeson, and S. Rudner, in *SQUID '85*, edited by H. D. Hahlbohm and H. Lübbig (Walter de Gruyter & Co., Berlin 1985) p. 1005, 1985.

Millimeter-Wave Double-Dipole Antennas for High Efficiency Reflector Illumination

D.F. Filipovic, W.Y. Ali-Ahmad and G.M. Rebeiz

NASA/Center for Space Terahertz Technology
Electrical Engineering and Computer Science Department
University of Michigan
Ann Arbor, MI 48109-2122

An earlier version of this paper has been presented at the 15'th Intl. Conference of Infrared and Millimeter-Waves, Dec, 1990.

ABSTRACT

A double-dipole antenna integrated on a thin dielectric membrane and backed by a large ground plane is presented. The double-dipole design results in nearly equal E and H-plane patterns with a gain of 12-13 dB, a cross-polarization levels lower than -27 dB, and a main-beam efficiency of 90%. The input impedance is around 50Ω and will match well to a Schottky-diode or SIS detector. Pattern measurements at 234 GHz, 246 GHz and 258 GHz agree well with theory.The double-dipole antenna is a simple antenna to fabricate with a very low cross-polarization component, and is useful for millimeter and submillimeter-wave applications requiring a $\pm 5\%$ bandwidth.

I. INTRODUCTION

The use of thin dielectric membranes for millimeter-wave integrated-circuit antennas is now a well established technique for high-efficiency designs [1,2].The membranes are very thin compared to a free-space wavelength, and the antennas do not suffer from dielectric and substrate-mode losses. It is possible to integrate a radiating structure consisting of two dipole antennas on a dielectric membrane and backed by a ground plane that results in equal E and H-plane patterns and a very low cross-polarization component (Fig. 1). Double-dipole antennas have been previously investigated at millimeter-wave frequencies and have showed promise for high-efficiency applications [3,4]. The detector is integrated at the center of the coplanar stripline. A low-pass filter is used to isolate the IF/bias lines from the antenna. The double-dipole antenna is very simple to fabricate, and results in similar directivities to the integrated-horn antenna and with a high coupling efficiency to f/0.7-f/0.9 reflector systems.

II. DOUBLE-DIPOLE ANTENNA DESIGN

The antennas are integrated on a thin dielectric membrane and it is therefore possible to use free-space radiation techniques. The antennas have the same current distribution due to

the detector position and symmetry. For far-field pattern calculations, the antenna current distribution is given by the standing-wave current on an open-circuited transmission line. The method of images is used to account for the ground plane [4]. An optimization program was written to yield nearly equal E and H-plane patterns by changing the antenna lengths (l), the antenna spacing (d) and the membrane position from the ground plane (h). The dipole input impedance is found by assuming a more exact current distribution [5] and taking into account the mutual impedance effects between the antennas and their images. The dipole impedance is then transformed using transmission-line theory to the detector terminals. The double-dipole antenna input impedance is half the transformed impedance due to the parallel combination of the two dipoles. The coplanar-stripline characteristic impedance (Z_{cps}) is chosen to yield a final input impedance around 50Ω. It is possible to add a short coplanar stub along the transmission-line for impedance tuning considerations.

III. THEORETICAL AND EXPERIMENTAL RESULTS

A double-dipole antennas with parameters (l, d, h, Z_{cps}) of $(0.7\lambda, 0.55\lambda, 0.77\lambda, 300\Omega)$ was build for 246 GHz applications. The design yields nearly equal E, H and 45°-plane patterns with a 10-dB beamwidth of 78° and 70°, and a directivity of 11.7 dB, respectively. The measured input impedance on a 2 GHz microwave model is 50Ω for a ±5% bandwidth (Fig. 2). The measured patterns agree quite well with theory up to 45° (Fig. 3) where diffraction effects from the measurement set-up dominate (Fig. 4). The design indicates a sidelobe level lower than -13 dB and a -27 dB cross-polarization component in the 45°-plane. The sidelobe level could not be confirmed due to the measurement set-up, but a cross-polarization component less than -22 dB was measured at $30 - 35°$. Patterns measurements at $0.95f_0$ (234 GHz) and $1.05f_0$ (258 GHz) agree well with theory and result in symmetric patterns (Fig. 5). The slight dip of 1 dB at normal incidence at 254 GHz is not predicted by theory and could not be explained. The double-dipole antenna results in a theoretical coupling efficiency to a gaussian beam with $\theta_0 = 30°$ of 77%, 83%, and 84% at $0.95f_0$, f_0 and $1.05f_0$, respectively (Fig. 6). The measured electromagnetic coupling between two double- dipole antennas in the H-plane was lower than -20 dB (or -30 dB) for a center-to-center spacing of 1λ (or 1.5λ). The coupling in the E-plane was negligible for center-to-center spacing greater than 1.25λ. It is therefore possible to array the antennas for diffraction-limited imaging. We are now investigating the possible use of these antennas to high-gain submillimeter-wave reflector systems.

ACKNOWLEDGEMENTS

This work was supported by the NASA/Center for Space Terahertz Technology at the Univ. of Michigan.

REFERENCES

[1] G.M. Rebeiz, D P. Kasilingam, P.A. Stimson, Y. Guo and D.B. Rutledge, "Monolithic millimeter-wave two-dimensional horn imaging arrays," *IEEE Trans. Antennas Propag.*, vol. AP-28, pp. 1473-1482, Sept 1990.

[2] S.S. Gearhart, C.C. Ling and G.M. Rebeiz, " Integrated millimeter-wave corner- reflector antennas, " To appear in the July Issue of the *IEEE Trans. Antennas Propag.*, 1991.

[3] P.T. Parrish, T. Sollner, R.H. Mathews, H.R. Fetterman, C.D. Parker, P.E. Tannenwald and A.G. Cardiasmenos, "Printed dipole-Schottky diode millimeter-wave antenna array," *SPIE Millimeter-Wave Technology,* vol. 337, pp. 49-52, 1982.

[4] A. Skalare, " A dipole antenna feed for a dielectric lens surface," Internal report of the national Inst. for Space Research, P.O. Box 800, 9700 AV Groningen, The Netherlands, Jan. 1990.

[5] R.S. Elliott, *Antenna Theory and Design,* Prentice Hall, New York, Chapter 2 for patterns and Chapter 7 for impedances, 1981.

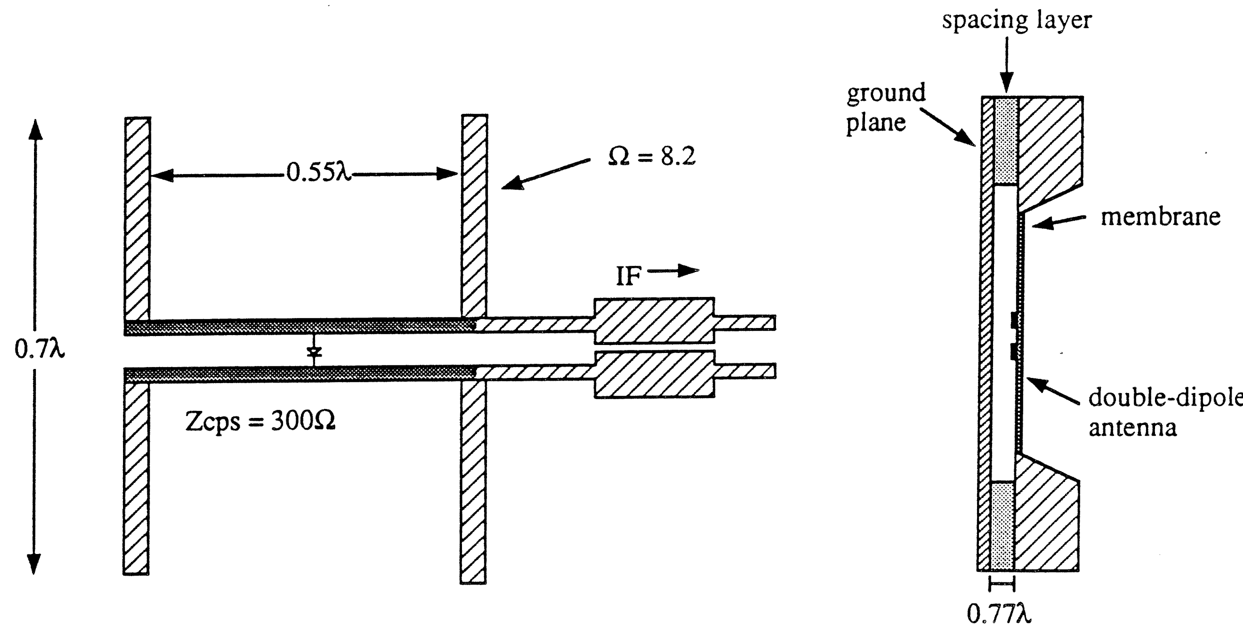

Figure 1: The double-dipole antenna on a thin-dielectric membrane and ba.·ked by a ground plane.

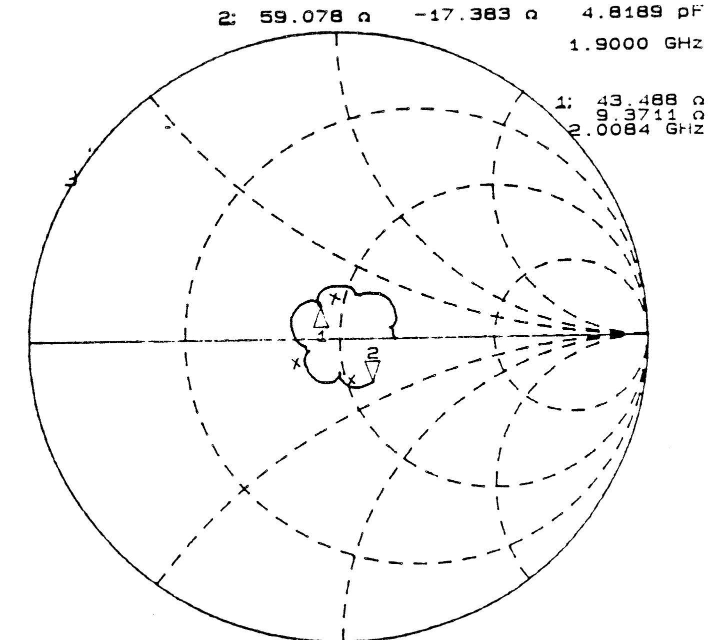

Figure 2: Measured input impedance of the double-dipole antenna at 2 GHz.

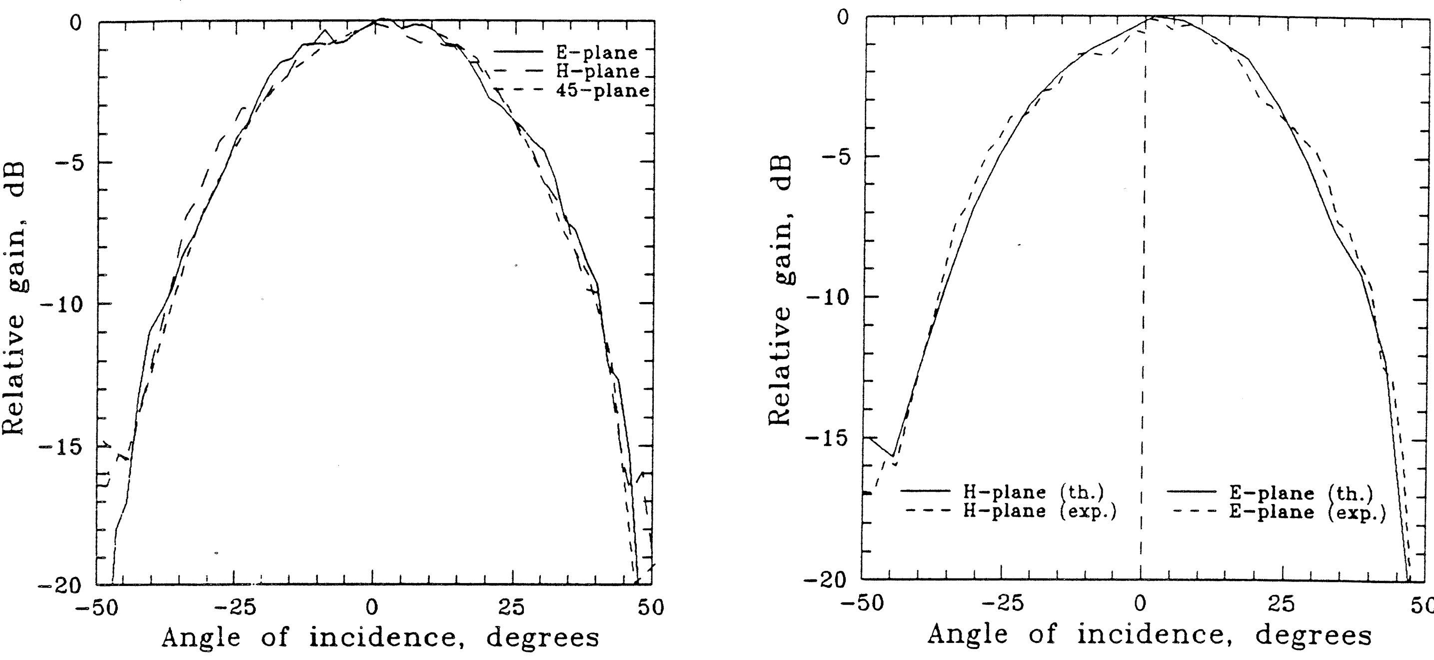

Figure 3: The measured E, H and 45° patterns at 246 GHz (left), and the comparison with theory for the E and H-plane patterns (right).

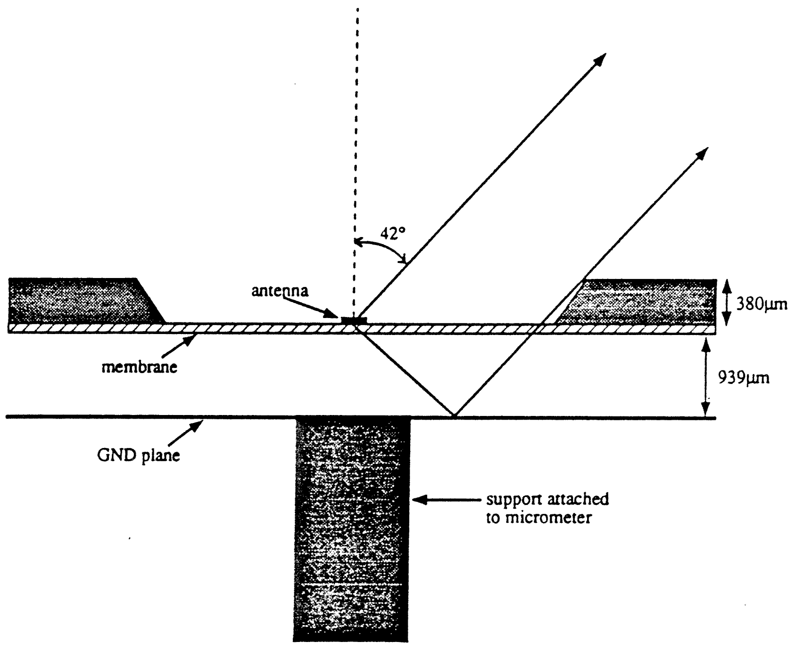

figure 4: The measurement set-up at 246 GHz. The finite size of the membrane introduces blockage and limits the measurement angle to ±40°.

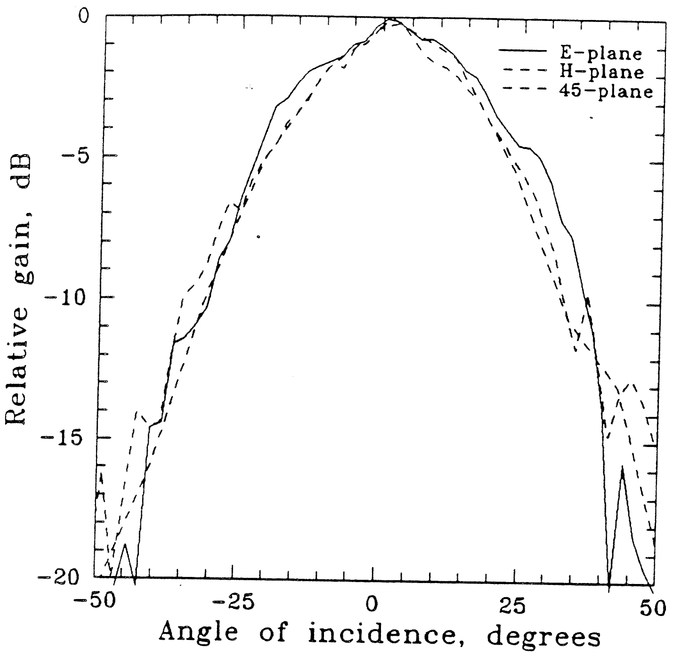

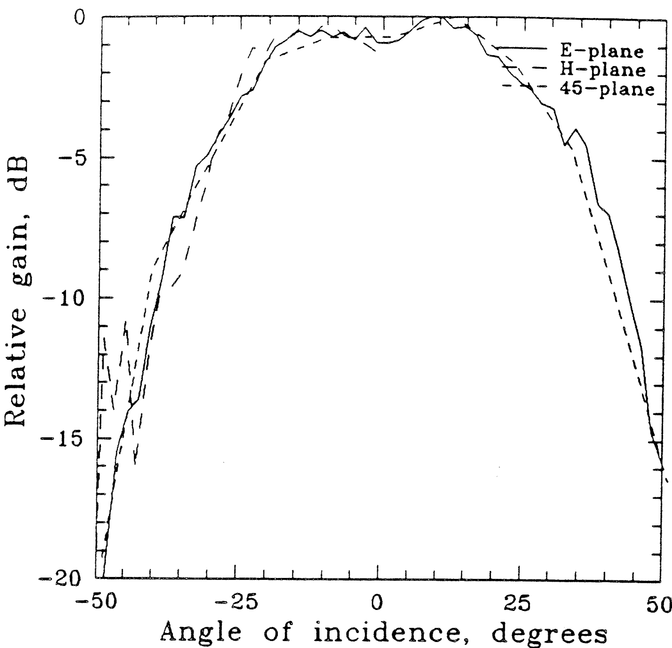

figure 5: The measured E, H and 45° patterns at $0.95f_0$ (234 GHz-left) and $1.05f_0$ (258 GHz-right).

Freq	Z_{ANT}	Gain	X-pol	ε_{mb} (-20dB)	$\varepsilon_{Gaus}(\theta_0=30°)$	$\varepsilon_{Gaus}(\theta_0=27°)$
$0.90\ f_0$	~ 50Ω	-	-	-	64.7%	66.5%
$0.95\ f_0$	~ 50Ω	11.8dB	-27dB	82%	77.4%	77.1%
f_0	~ 50Ω	11.7dB	-26dB	88%	83.4%	81.1%
$1.05\ f_0$	~ 50Ω	11.2dB	-25dB	91%	84.8%	80.9%
$1.10\ f_0$	~ 50Ω	-	-	-	82.7%	77.3%

figure 6: Calculated antenna parameters vs. frequency. ϵ_{mb} is defined as the main-beam efficiency till the -20 dB points and ϵ_{Gauss} is defined as the coupling efficiency to gaussian-beams of parameter θ_0.

SUBMILLIMETER BACKWARD-WAVE OSCILLATOR PROGRAM

N. Stankiewicz (LeRC)
L.R. Barnett (Analex Corp.)
J.A. Dayton, Jr. (LeRC)

SUBMILLIMETER BACKWARD-WAVE OSCILLATORS

OBJECTIVE

TO DEVELOP THE TECHNOLOGY FOR VOLTAGE TUNABLE LOCAL OSCILLATORS IN THE FREQUENCY RANGE 300-2000 GHz TO SUPPORT FUTURE NASA MISSIONS IN ASTROPHYSICS AND RADIO ASTRONOMY

SUBMILLIMETER BWO PROGRAM

PROGRAM STRUCTURE:

MIT LINCOLN LABORATORY: CIRCUIT ETCHING
(NOT FUNDED FY 1990)

UNIVERSITY OF UTAH: DESIGN AND TESTING
(TRANSFERRED TO LeRC FY 1989)

LeRC: OUTPUT COUPLER, GUN DESIGN

SUBMILLIMETER BACKWARD-WAVE OSCILLATORS

3 PROBLEMS:

1) FABRICATION TECHNIQUE FOR INTERDIGITAL LINE
   - HIGH IMPEDENCE CIRCUIT, HENCE
   - LOWER START CURRENT, AND
   - WIDER BANDWIDTH
   - LOWER BEAM VOLTAGE

2) HEAT TRANSFER PROBLEM
   - DIAMOND TYPE IIA HEAT SINK

3) LIFETIME PROBLEM
   - LONG LIFE CATHODE

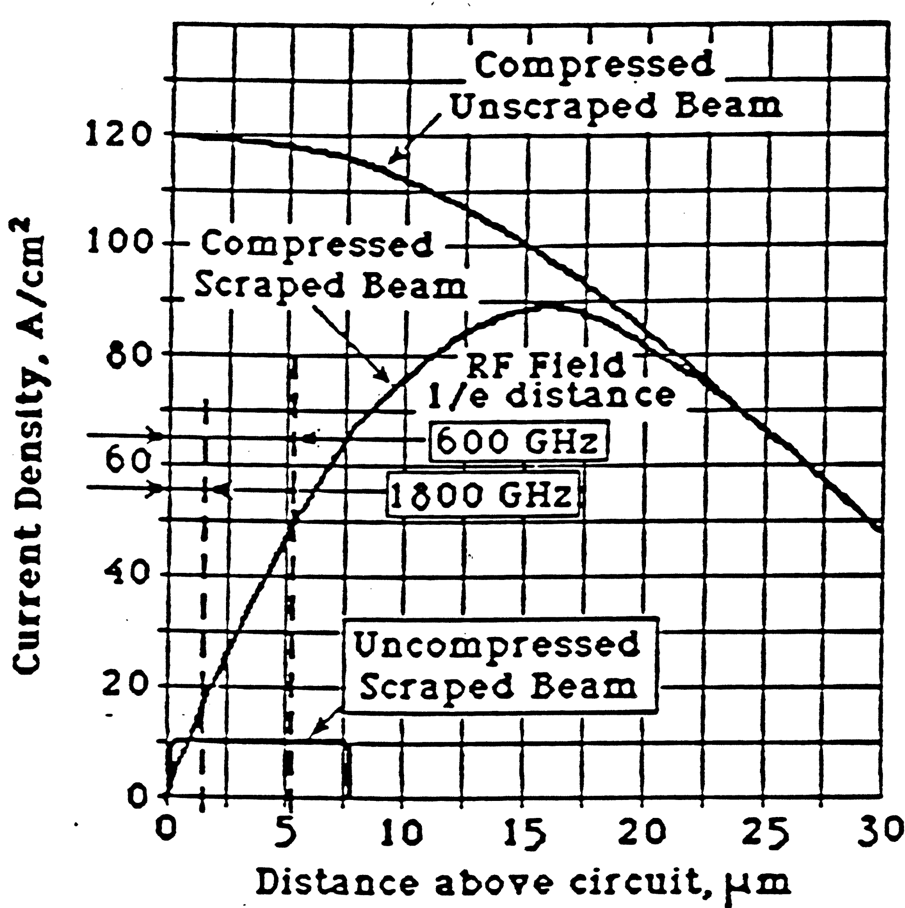

Fig. 2. Calculated beam current densities before and after circuit interception (scraped).

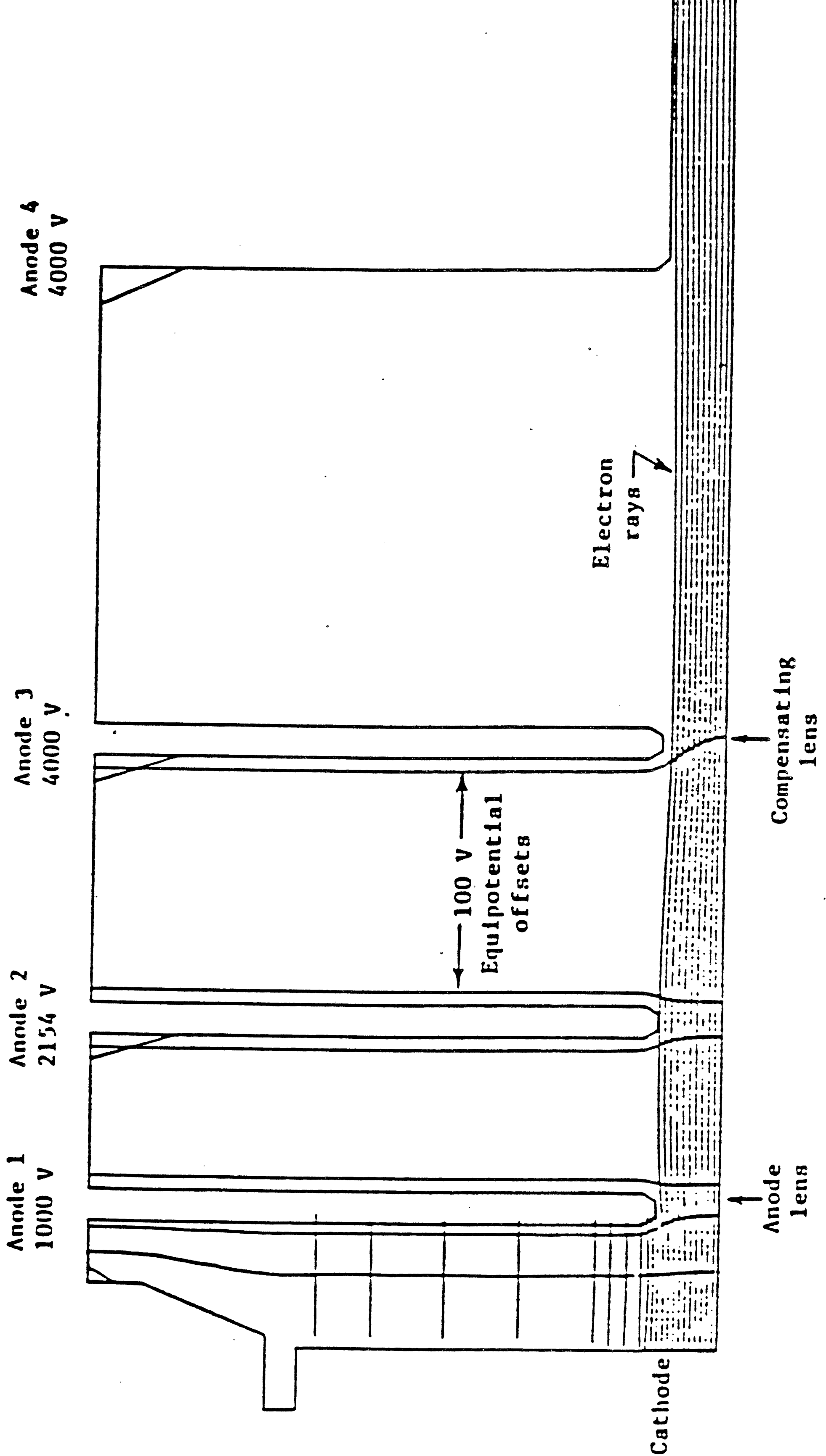

Fig. 7. The multielectrode lens compensated gun for the first experiment with calculated electron trajectories.

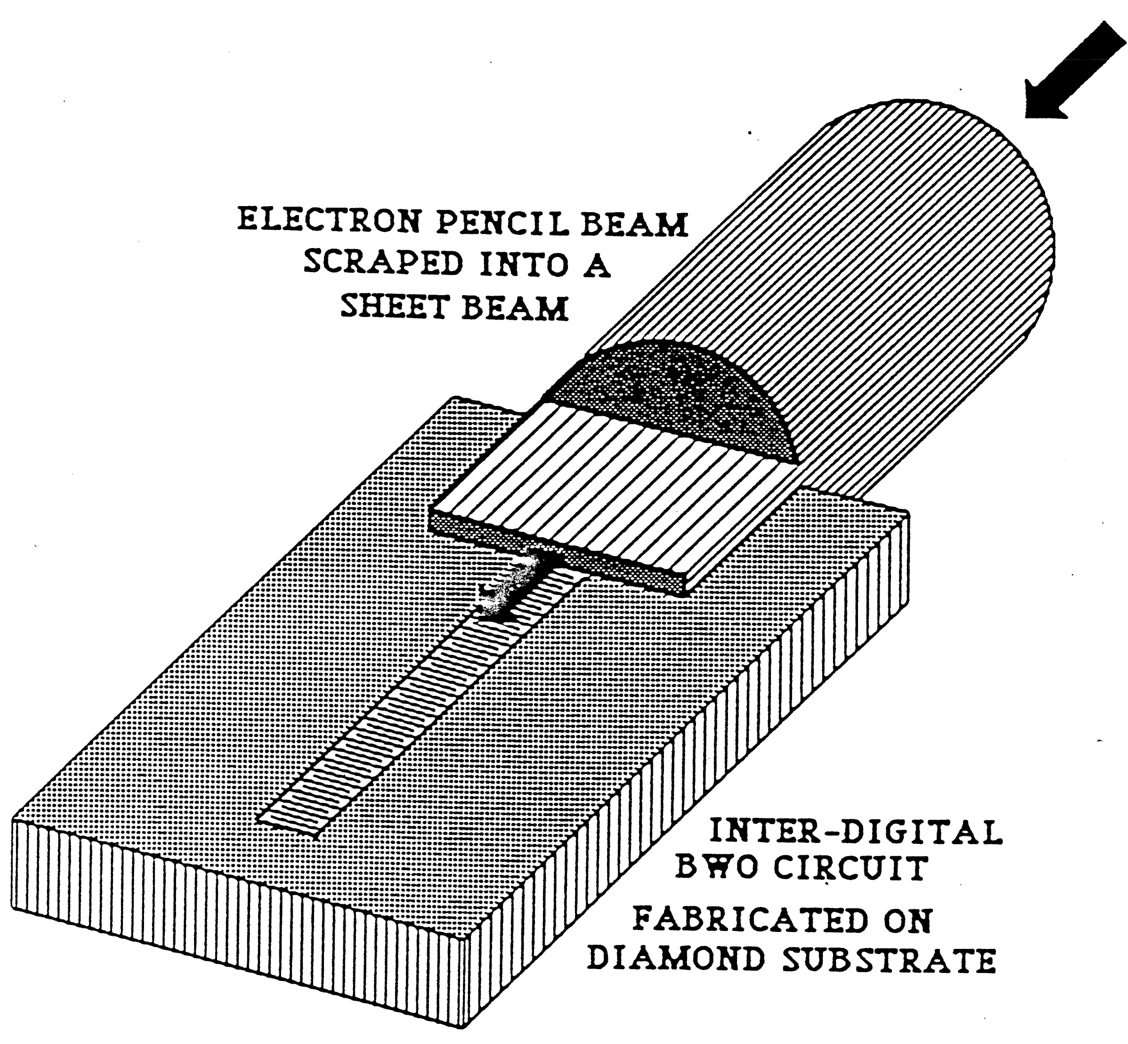

Fig. 1. Configuration of the electron beam with respect to the BWO circuit.

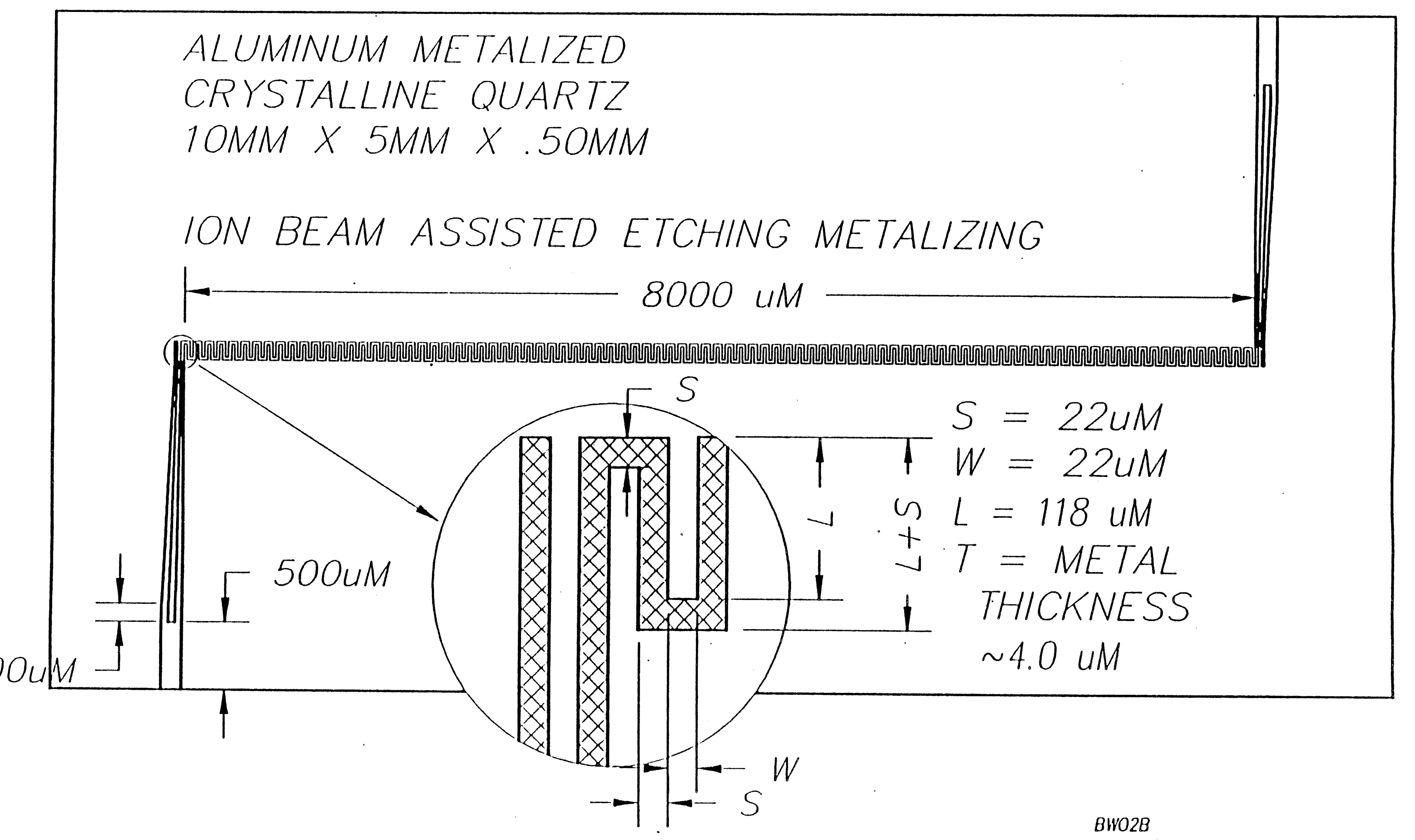

Fig. 14. Drawing of 200-250 GHJz backward-wave oscillator interdigital line as used to make circuits.

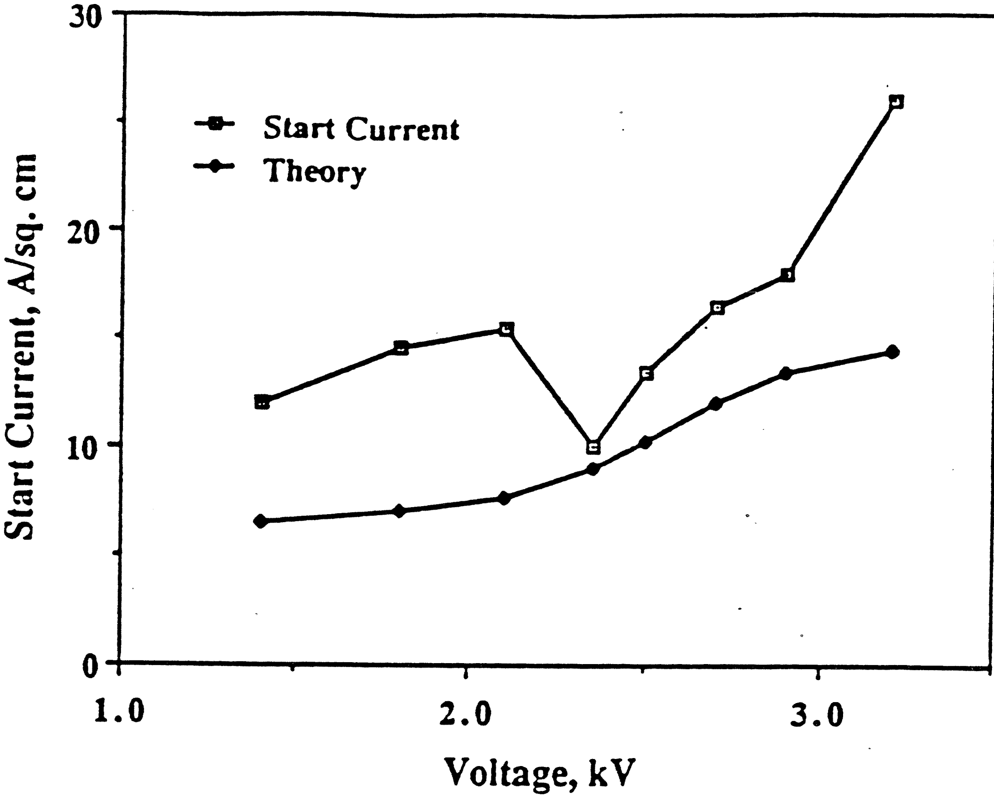

Fig. 19. Theoretical and experimental starting current for the aluminum metalized crystalline quartz circuit shown in Fig. 14.

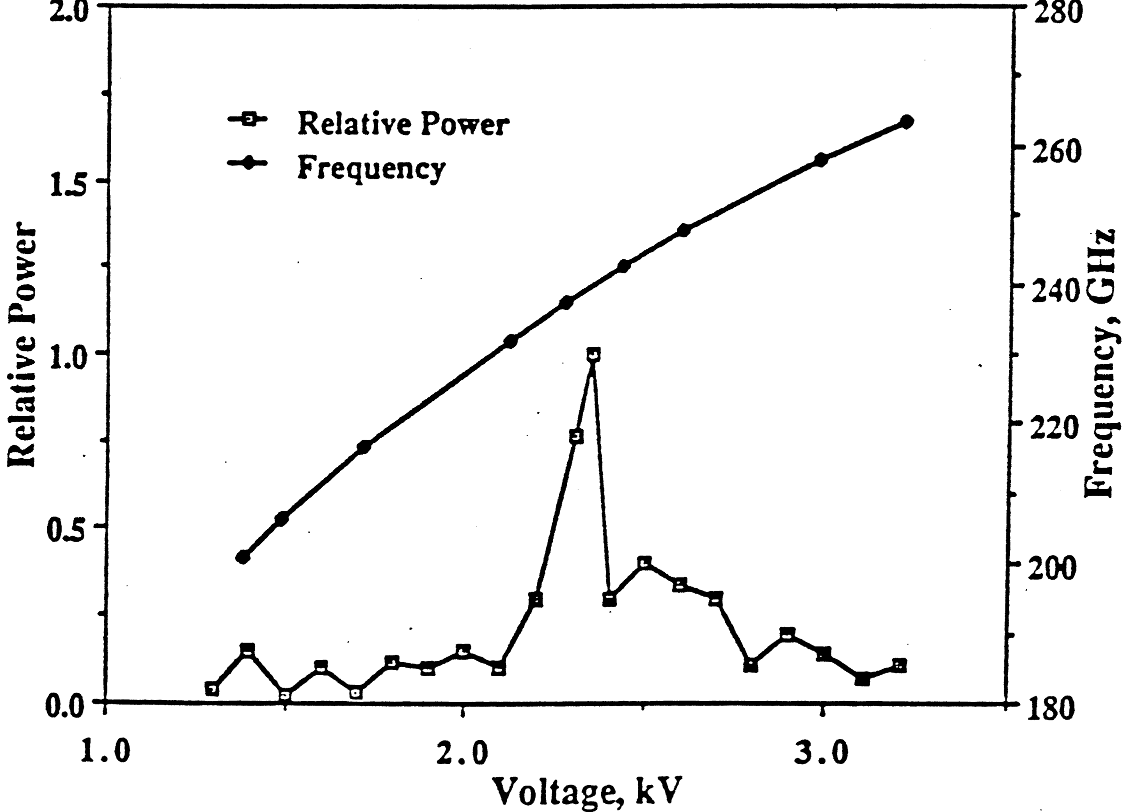

Fig. 20. Tuning curve and power output curve for the aluminum metalized crystalline quartz circuit shown in Fig. 14.

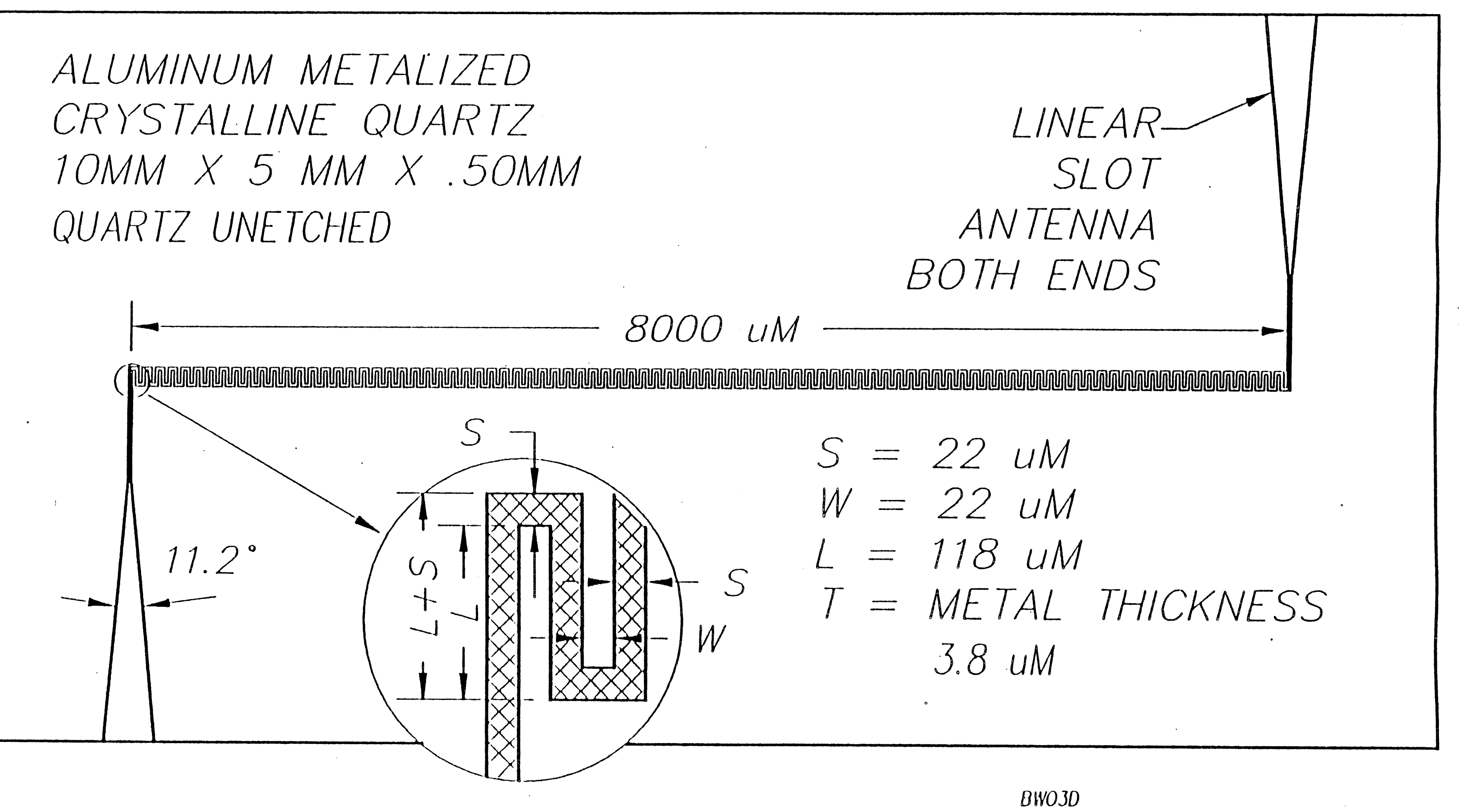

Fig. 23. Drawing of aluminum metalized crystalline quartz circuit with horn antenna for trying optical experiment.

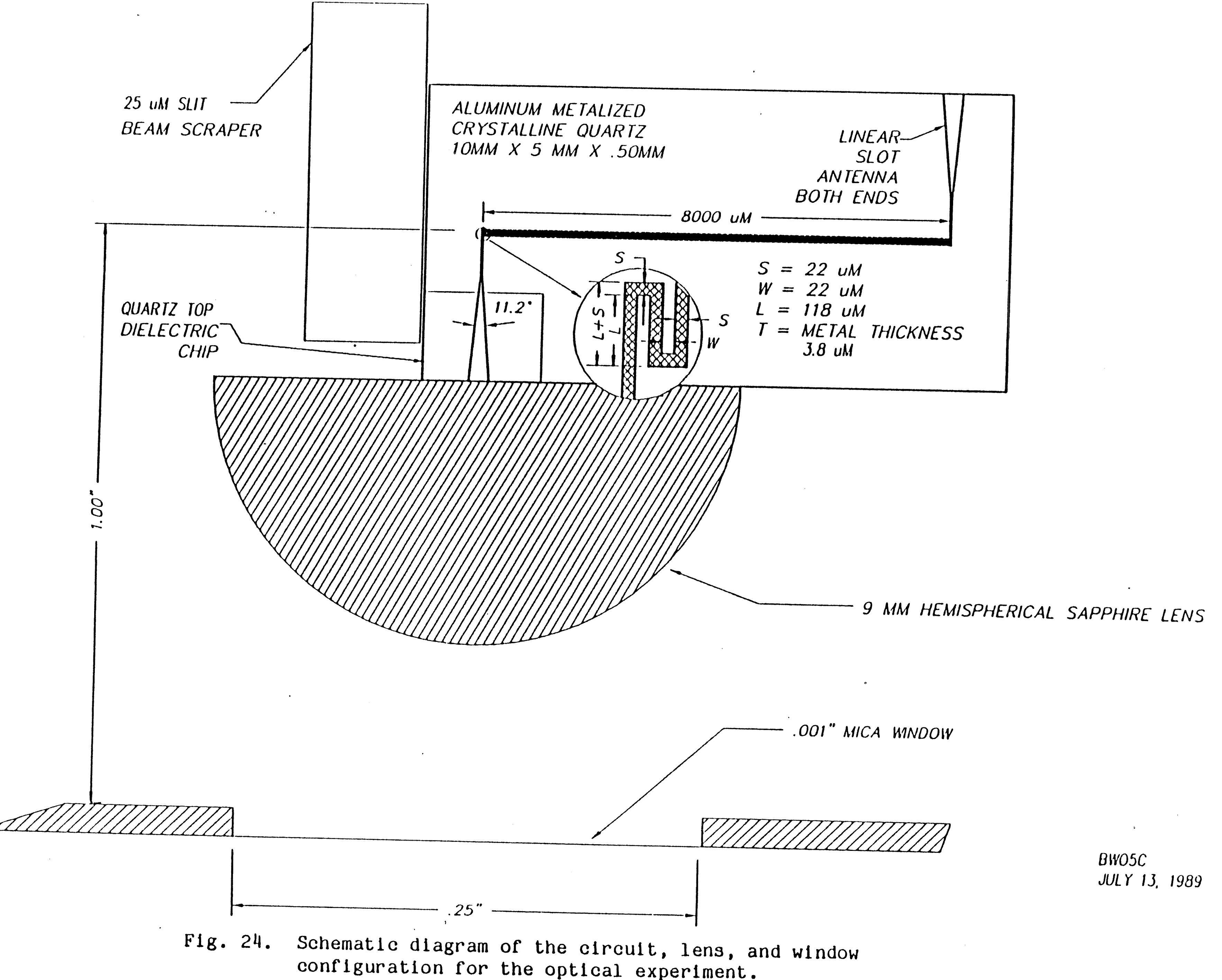

Fig. 24. Schematic diagram of the circuit, lens, and window configuration for the optical experiment.

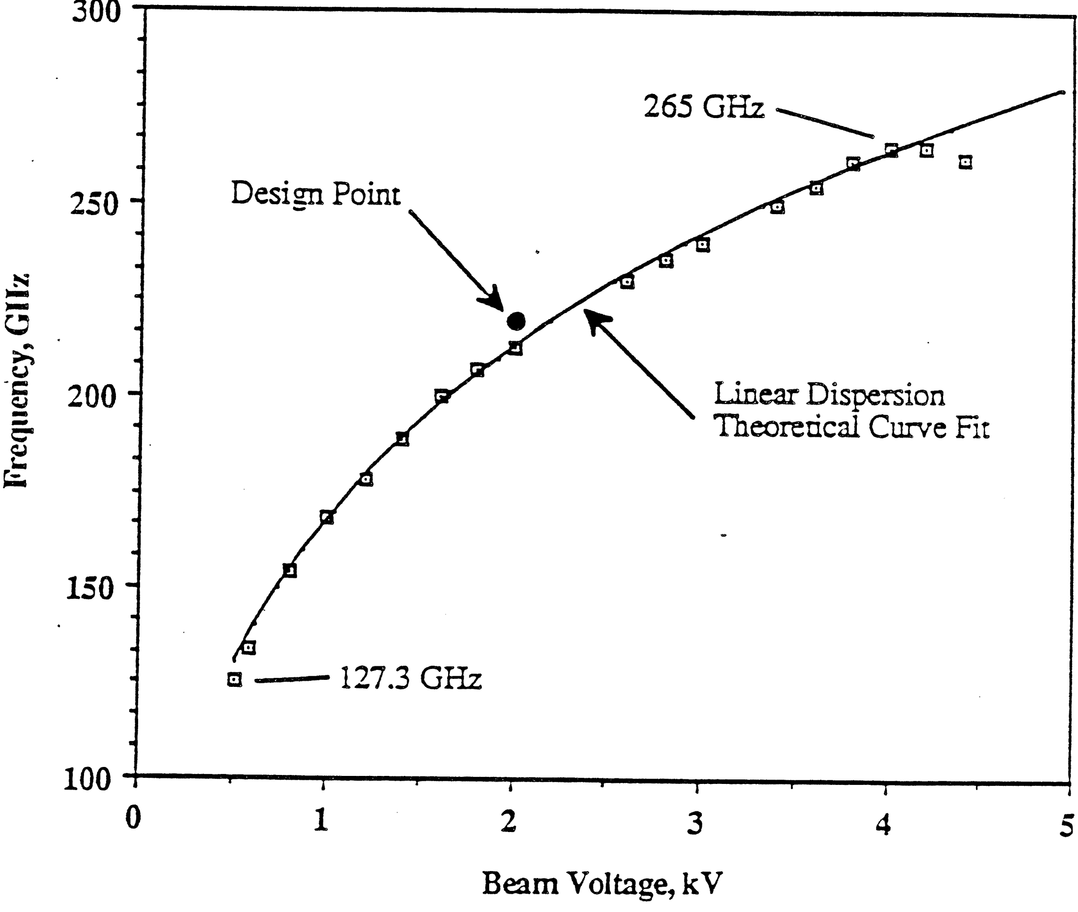

Fig 25. Quartz substrate BWO frequency versus beam voltage.

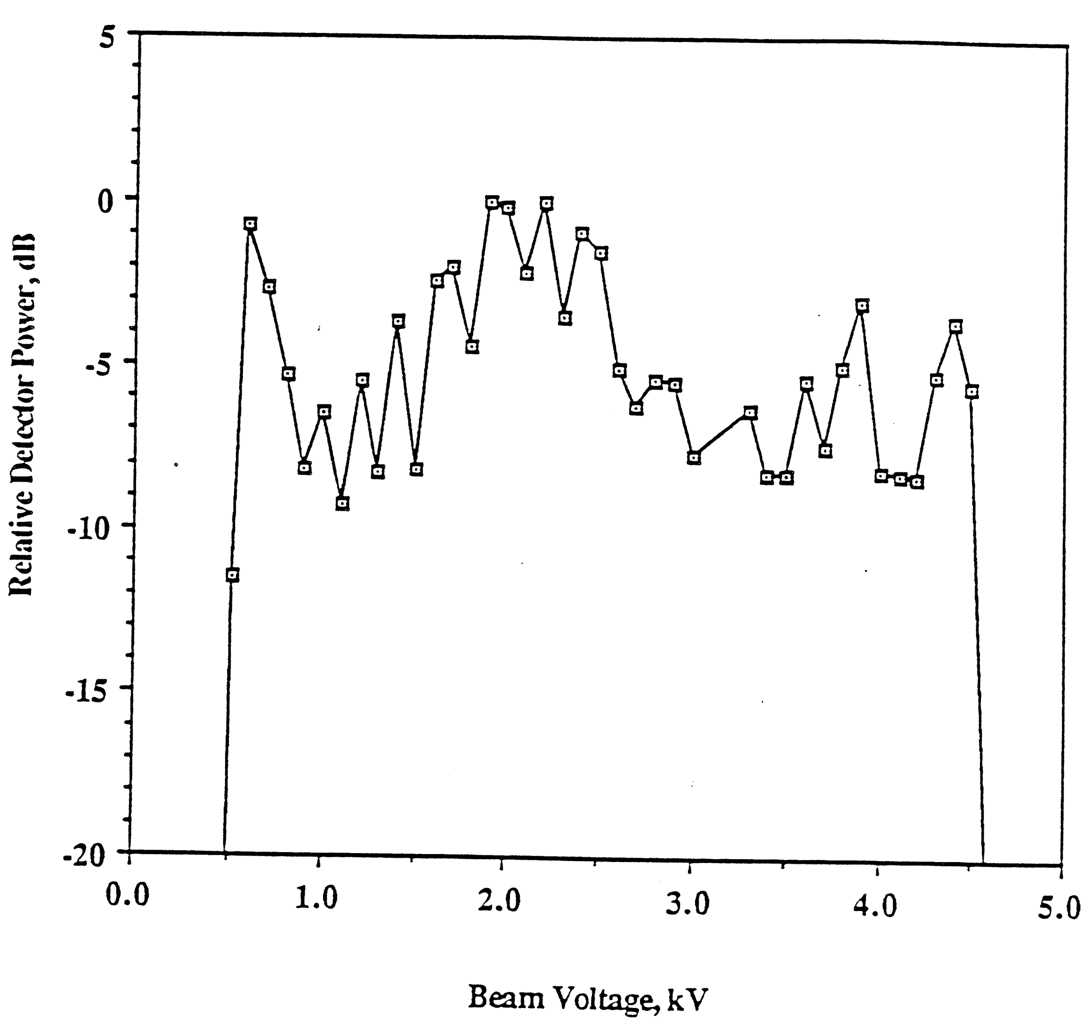

Fig..26. Quartz substrate BWO output.

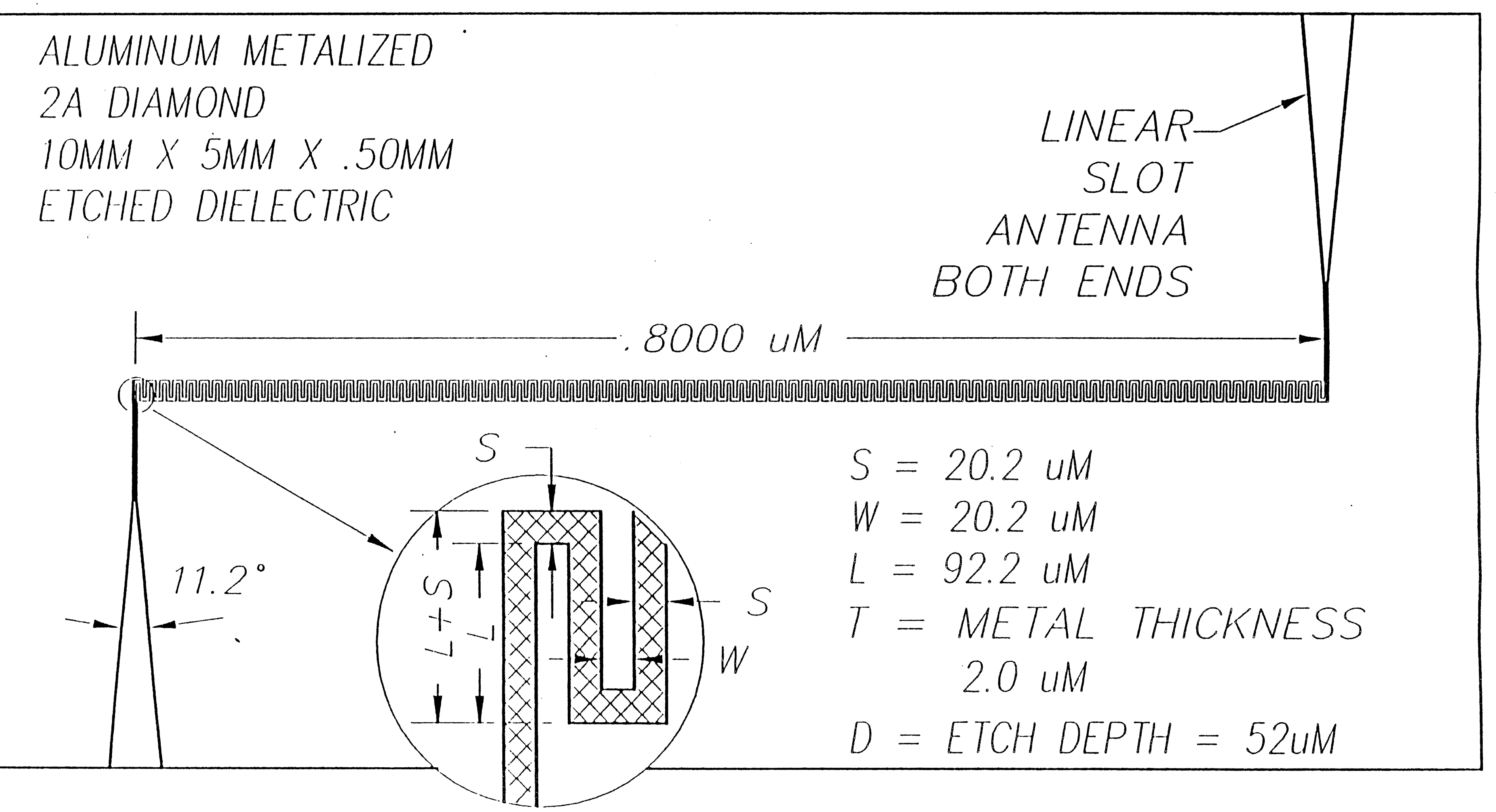

Fig. 27. Drawing of aluminum metalized etched diamond circuit with tapered slot antenna.

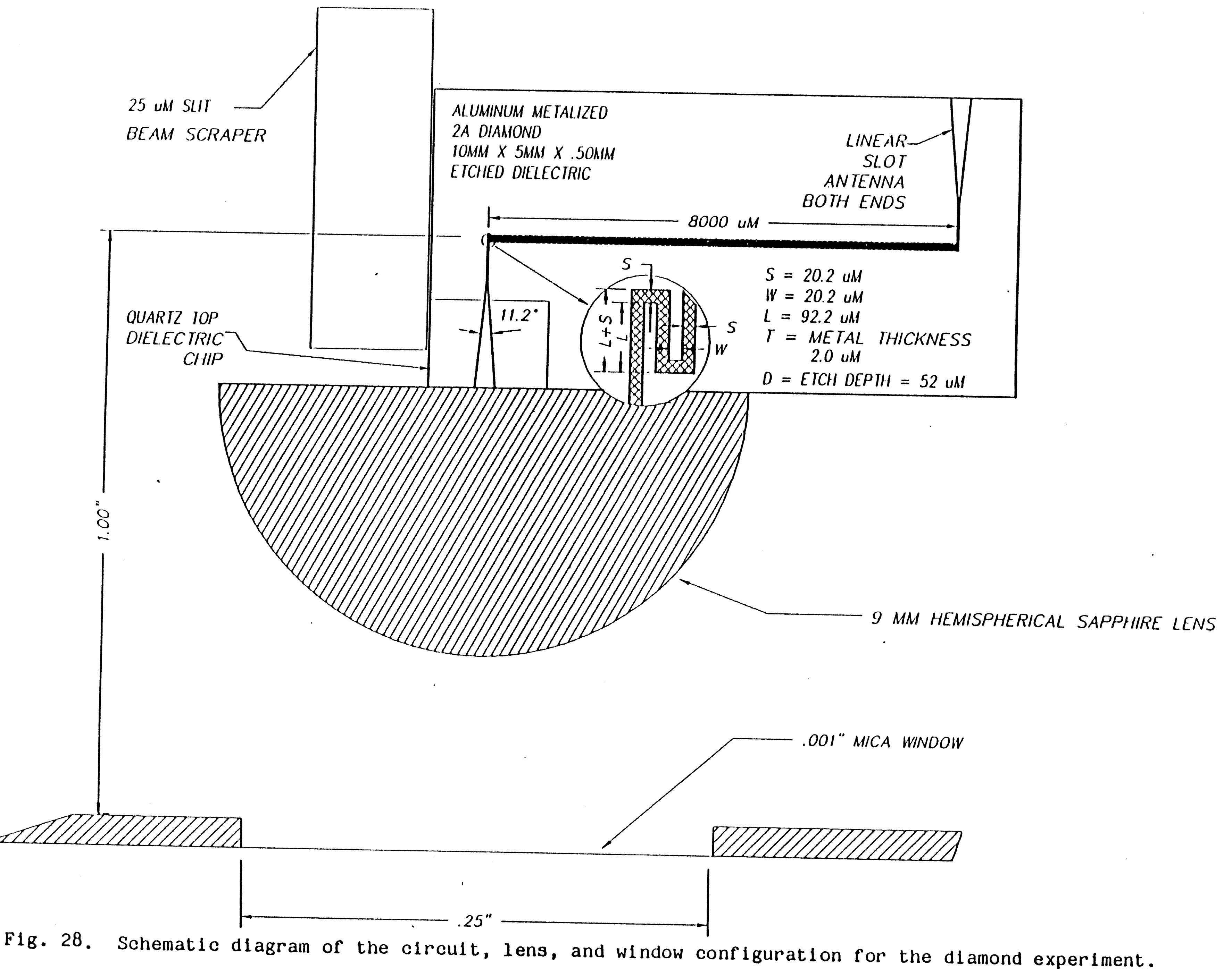

Fig. 28. Schematic diagram of the circuit, lens, and window configuration for the diamond experiment.

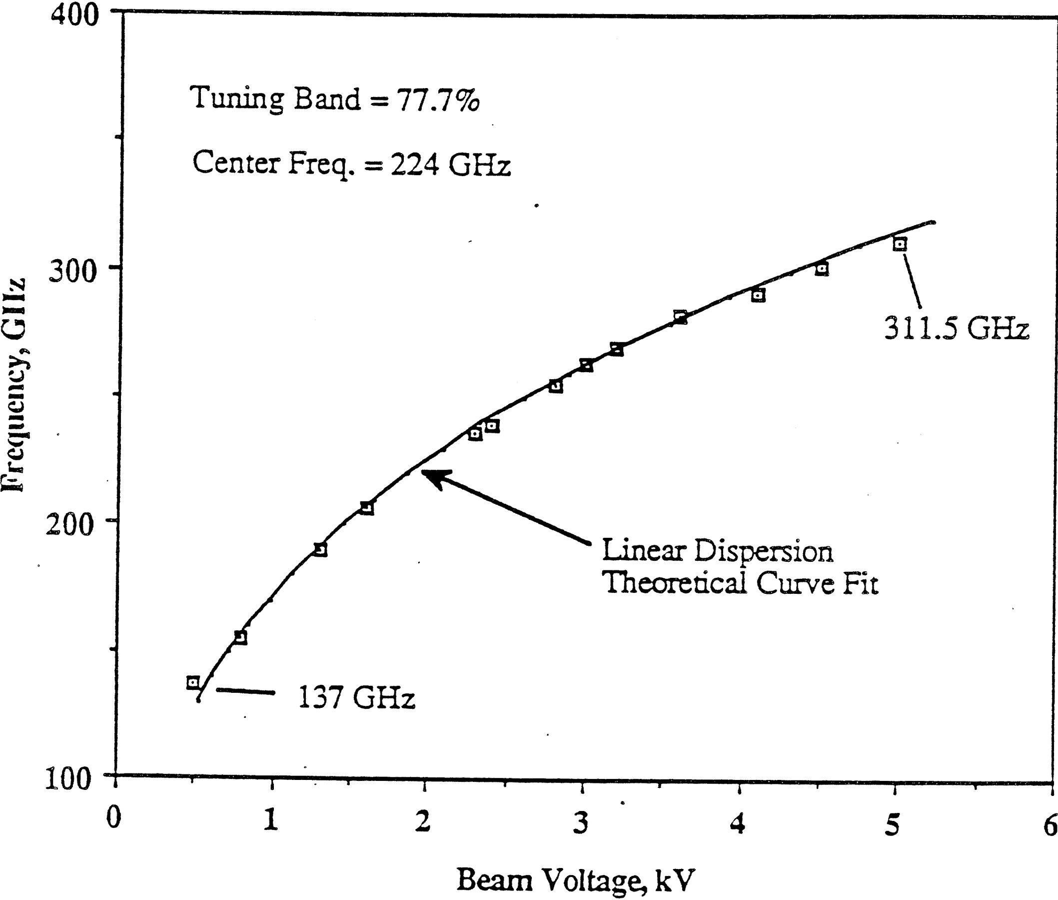

Fig. 29. Diamond substrate BWO tuning. Experimental frequency versus beam voltage.

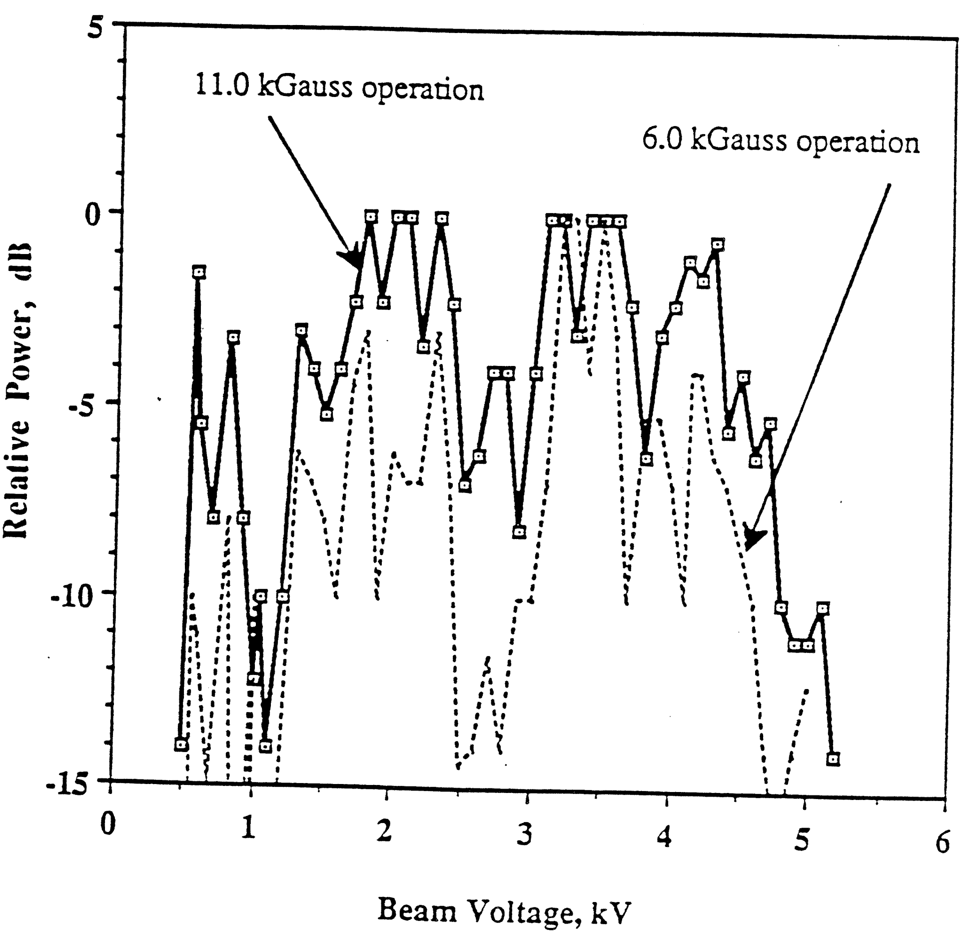

Fig. 30. Diamond substrate BWO. Relative power output versus voltage.

SUBMILLIMETER BWO PROGRAM

PROOF OF CONCEPTS RESULTS:

1) Al/QUARTZ SUBSTRATE
   COPLANER WAVEGUIDE/WAVEGUIDE
   200-265 GHz

2) Al/QUARTZ SUBSTRATE
   TAPERED SLOT LINE ANTENNA
   SAPPHIRE LENS
   127-265 GHz

3) Al/ETCHED DIAMOND SUBSTRATE
   137-312 GHz
   ESTIMATED POWER 1-10mW

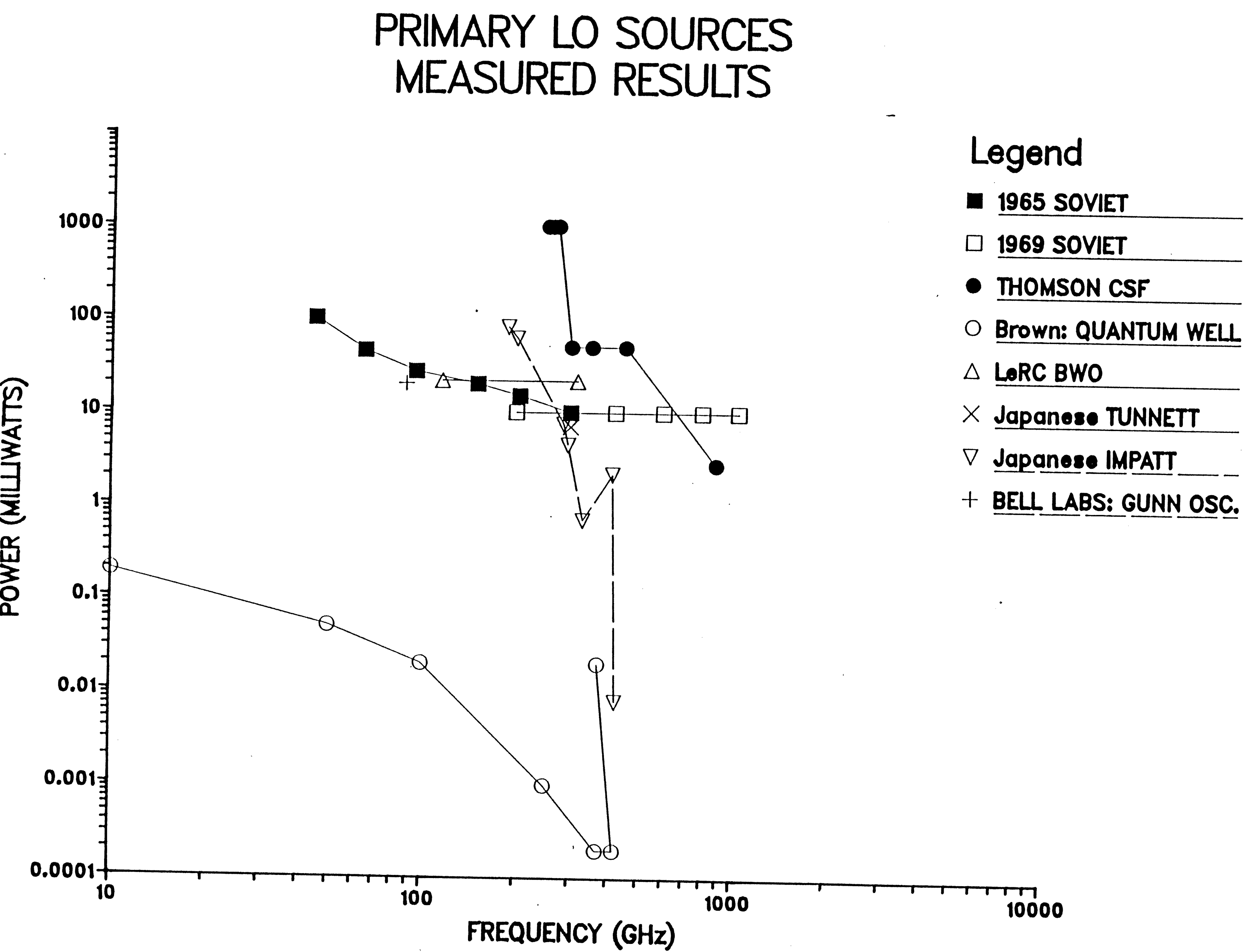
PRIMARY LO SOURCES
MEASURED RESULTS
Legend
1965 SOVIET
1969 SOVIET
THOMSON CSF
Brown: QUANTUM WELL
LeRC BWO
Japanese TUNNETT
Japanese IMPATT
BELL LABS: GUNN OSC.
POWER (MILLIWATTS)
1000
100
10
1
0.1
0.01
0.001
0.0001
10
100
1000
10000
FREQUENCY (GHz)

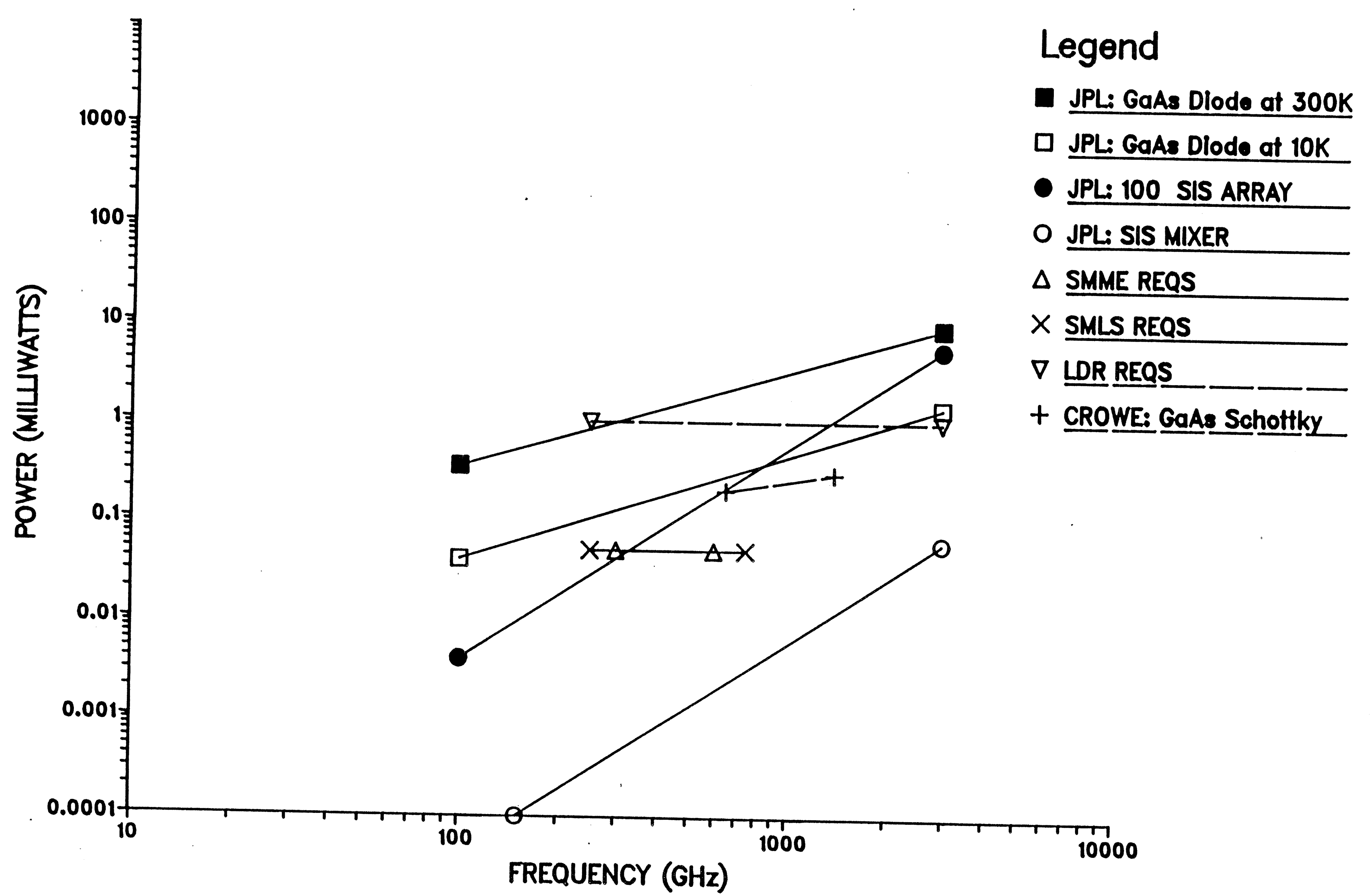
MINIMUM DETECTOR REQUIREMEMTS
Legend
JPL: GaAs Diode at 300K
JPL: GaAs Diode at 10K
JPL: 100 SIS ARRAY
JPL: SIS MIXER
SMME REQS
SMLS REQS
LDR REQS
CROWE: GaAs Schottky
POWER (MILLIWATTS)
1000
100
10
1
0.1
0.01
0.001
0.0001
10
100
1000
10000
FREQUENCY (GHz)

NASA
C-90-02787

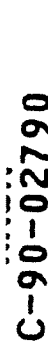
C-90-02790

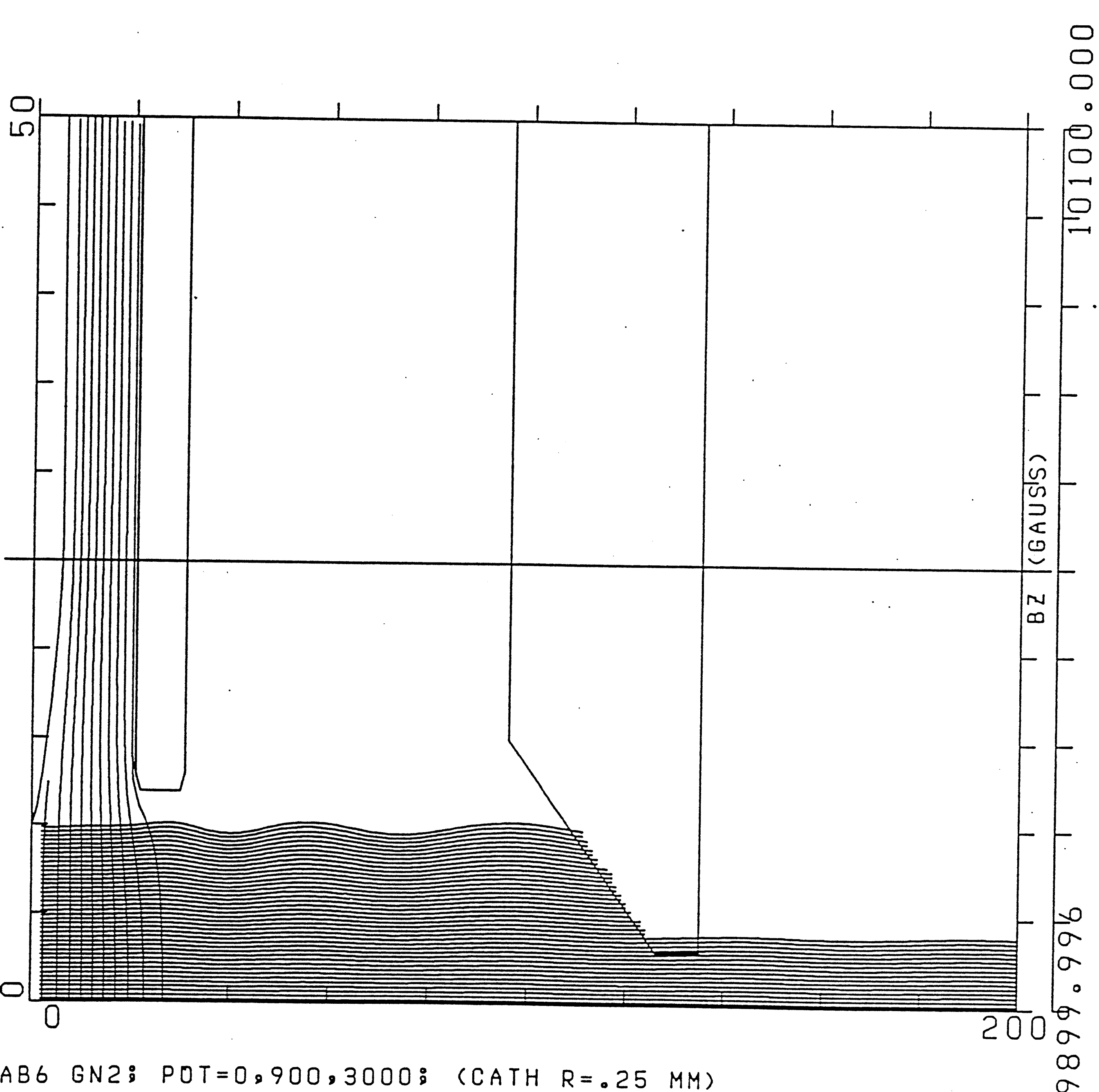

LAB6 GN2; POT=0,900,3000; (CATH R=.25 MM)

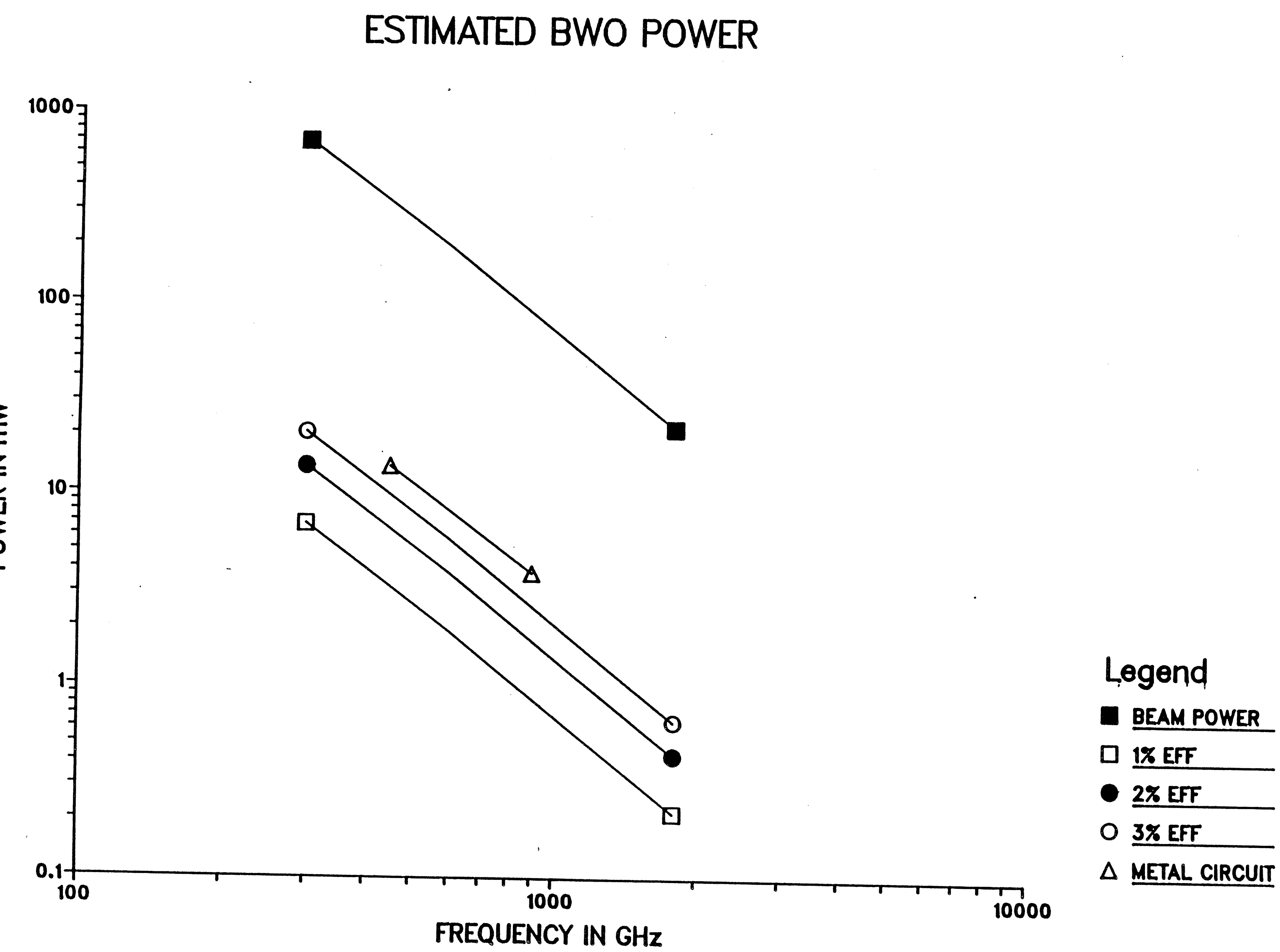
ESTIMATED BWO POWER
POWER IN mW
1000
100
10
1
0.1
FREQUENCY IN GHz
100
1000
10000
Legend
BEAM POWER
1% EFF
2% EFF
3% EFF
METAL CIRCUIT

SUBMILLIMETER BWO PROGRAM

BWO ADVANTAGES

- A PRIMARY SOURCE
- VOLTAGE TUNABLE
- STABLE PHASE LOCK CAPABILITY
- RELATIVE HIGH POWER AND EFFICIENCY
- SMALL PACKAGE
- BROAD BANDWIDTH
- MODEST INPUT POWER
- LONG LIFE CATHODE

SUBMILLIMETER BWO PROGRAM

FUTURE PLANS

- o WEDGE LaB_6 CATHODE
  - RIBBON BEAM
- o PARALLEL CIRCUITS
  - HIGHER OUTPUT POWER
  - IMPROVED EFFICIENCY
- o ALL METAL SLOW WAVE STRUCTURE
  - BULK CONDUCTIVITY
  - NO DIELECTRIC LOADING
  - 1 THz
- o MULTIPLE OUTPUT PORTS
  - IMPROVED OUTPUT COUPLERS
- o HIGH DUTY CYCLE OPERATION
  - IMPROVED POWER MEASUREMENTS

MILLIMETER WAVE RADIATION GENERATED BY OPTICAL MIXING IN FETs INTEGRATED WITH PRINTED CIRCUIT ANTENNAS

by

D.V. Plant, H.R. Fetterman, D.C. Scott, and D.C. Ni+
Department of Electrical Engineering
University of California, Los Angeles
Los Angeles, California 90024
(+ Present address: AT&T Bell Laboratories, Murray Hill, NJ 07974)

ABSTRACT

Millimeter wave radiation has been generated from FETs and HEMTs, integrated with printed circuit antennas, and illuminated with both pulsed and CW laser radiation. In the pulsed laser experiments, the repetitive picosecond (2.0 psec) excitation produced a millimeter wave radiation comb. Modulation of the millimeter waves was achieved by applying a swept RF signal to the transistor gate. Using this technique, tunable electrical sidebands were added to the optically generated carrier providing a method of transmitting information and doing high resolution spectroscopy. Using CW lasers, tunable millimeter wave radiation was generated by coherent mixing of the optical radiation in GaAs FETs integrated with printed circuit antennas. Employing a CW Kiton Red dye laser (600nm-640nm) and a frequency stabilized HeNe laser, this arrangement produced continuously tunable millimeter wave radiation optimized at 60 GHz. Planar twin dipole microstrip antennas with integrated FETs were used both to transmit and to receive the radiation. In a demonstration experiment, the millimeter wave radiation was propagated through narrow band quasi-optical Fabry-Perot filters and detected using heterodyne techniques.

I INTRODUCTION

Optical control of microwave and millimeter wave devices has attracted recent attention because of potential applications which involve both the advantages of optical interconnections and microwave propagation. Various control functions including gain control of amplifiers, oscillation tuning, locking and frequency modulation, switching, optical mixing, and optically induced negative photoconductivity have already been demonstrated[1-6]. In this paper, we report the generation and propagation of pulsed and continuous wave millimeter wave radiation using optical mixing in integrated GaAs FET printed circuit structures. In both cases, the optically generated and transmitted millimeter wave radiation was detected in real time with a highly sensitive FET antenna circuit using heterodyne detection techniques.

Previously, we demonstrated coherent mixing of optical radiation in FETs, HEMTs, and related three terminal devices[3]. This technique was then extended to 64 GHz using a GaAs FET integrated with a printed circuit antenna, which was designed to couple to millimeter wave frequencies[5]. This configuration permitted direct injection of a fundamental local oscillator and the optical radiation simultaneously to the device active region and demonstrated the mixing capability of these devices at high frequencies. In the series of experiments reported here, the active region of a GaAs FET antenna circuit is illuminated simultaneously by optical radiation from a CW dye laser and a frequency stabilized HeNe laser. The difference frequency between these optical signals radiates from the antenna and propagates in free space. It is then detected in a similar planar FET structure. This is the first report of the generation and free space propagation of millimeter wave radiation using optical mixing in these three terminal devices integrated with printed circuit antennas. The use of two FET antenna circuits further demonstrates the capabilities

of these circuits in an optically controlled transmitter and receiver system. Based on recent studies of optically controlled phased array antennas, this technique is well suited for applications in such systems[7].

II PULSED LASER EXCITATION

Initial experiments aimed at generating millimeter wave radiation were performed via pulsed laser excitation. A schematic representation of the experimental arrangement is illustrated in Figure 1. FETs (NEC/NE7100) and HEMTs (Rockwell International Science Center) were integrated on printed circuit RT/Duroid microstrip antennas. Identical twin dipole antennas with integrated devices were used both to transmit and to receive the radiation. However, in the case of the transmitter, the drain and source of the device were connected to the antenna, and in the case of the receiver, the gate and source were connected to the antenna. The full characterization of an integrated FET antenna circuit as a microwave gate mixer has been described previously, and results show the circuit has a conversion loss of approximately 6 dB when used as a heterodyne detector[8].

In the pulsed excitation experiments, the active region of the transmitting device was illuminated by 2.5 picosecond, 578nm optical pulses obtained from a synchronously pumped mode-locked Rhodamine 6G dye laser. The dye laser pump source was an actively mode-locked frequency doubled Nd:YAG laser operating at 76 MHz. The active region of the device was excited by 50 to 150 milliwatts of average power focused to 10 μm in diameter with a 5X lens. Using a sweep oscillator, a RF electrical modulation was applied to the transmitter gate. A reflex klystron, tunable from 55.5 GHz to 62.0 GHz, was used as a local oscillator for heterodyne detection of the radiation. Two teflon lenses with 25.4 mm focal lengths were placed between the transmitter and the receiver to create a collimated beam into which millimeter

wave filters were inserted. The detected output from the receiver was sent through various IF amplifiers (.75 - 2 GHz with a gain of 25 dB, and 6 - 18 GHz with a gain of 25 dB) and displayed in real time on a spectrum analyzer. A Hewlett Packard 9836 computer was used for data acquisition and processing.

The repetitive picosecond excitation produces a millimeter wave radiation comb whose signals are spaced at the laser mode-locking frequency (76 MHz). Because heterodyne detection is used, mixed signals which fall within the bandwidth of the IF amplifier from both the high and the low frequency side of the local oscillator will be detected. This is seen in Figure 2, where a spectrum analyzer trace of the detected radiation for a local oscillator frequency of 61.4 GHz is shown. This data was taken using the .75 - 2 GHz IF amplifier and the devices biased as follows: the transmitting FET with V_{ds} = 2.0V and V_{gs} = -3.0V, and the receiving FET with V_{ds} = 2.0V and V_{gs} = -0.6V. By tuning the local oscillator +/- 5.0 MHz the signals located in the upper sideband could be distinguished from those located in the lower sideband. In Figure 2, the larger amplitude signals are in the upper sideband (61.52 GHz - 63.02 GHz) and the lower amplitude signals are in the lower sideband (59.78 GHz-61.28 GHz). Using the various IF amplifiers, we measured the bandwidth of the radiation comb and found it extended from 45 GHz to 75 GHz. The average power in the millimeter wave beam was also measured using a slow response time liquid helium cooled silicon bolometer, and this measurement yielded an estimated power of >100 nanowatts.

Next, an electrical modulation was applied to the transmitter gate in addition to the dc bias, and this RF modulation produced tunable sidebands on the millimeter wave radiation. These sidebands could be used to completely fill in the transmission spectrum of a millimeter wave bandpass filter. In order to demonstrate this capability, we placed a Fabry-Perot interferometer with a narrow passband into the

millimeter wave beam. The filter consisted of two 50 lines/inch metal meshes mounted on optically flat retaining rings. Figure 3a is a spectrum analyzer trace of the transmission response of this filter without gate modulation. The filter both rejects the signals in the lower sideband (the lower amplitude signals in Figure 2) and filters the signals in the upper sideband that are out of the passband of the filter. Figure 3b is a spectrum analyzer trace of the filter after applying a swept electrical modulation to the transmitting FET gate. The filter is tuned to approximately 62.27 GHz and has a FWHM of approximately 250 MHz, which is in good agreement with the calculated finesse. This result demonstrates the high spectral resolution obtainable with this technique.

III CONTINUOUS WAVE LASER EXCITAION

A schematic representation of the continuous wave excitation experimental arrangement is illustrated in Figure 4. The transmitting FET was illuminated with light from a Kiton Red dye laser (600nm to 640nm, 400mW) and a frequency stabilized HeNe laser (632.8nm, 0.6 mW). The penetration depth of these lasers is about 0.3mm, which is of the same order as the thickness of the active region of the FET, and therefore sufficient to excite the GaAs active layer. The wavelength of the dye laser was locked to an external temperature stabilized Fabry-Perot reference cavity. The wavelength of the laser was monitored with both an optical wavemeter which had 0.001 nm resolution (<1.0 GHz), and an optical spectrum analyzer which had a 30 GHz free spectral range. The linewidth and stability of both lasers was typically less than 2 MHz. The beams were combined using a variable beam splitter which permitted changing the ratio of dye laser power to the HeNe laser power. In these experiments, the transmitting FET active region was excited by 20 to 80 milliwatts (25-100 kW/cm^2) from the dye laser and 0.15 to 0.36 milliwatts (200-450

W/cm^2) from the HeNe laser. Using a lens, the beams were focused to a spot size of 10μm in diameter. The klystron was used as a local oscillator for heterodyne detection of the radiation. The detected signal output from the receiving FET antenna circuit was sent through the .75 - 2 GHz IF amplifier and displayed on a spectrum analyzer. Again, two teflon lenses with 25.4 mm focal lengths were placed between the transmitter and the receiver to create a 10 cm long collimated beam into which millimeter wave filters were inserted. A Hewlett Packard 9836 computer was used for data acquisition and processing.

The optical excitation produces continuous wave, tunable, millimeter wave radiation which is optimized at 60 GHz due to the performance of the high gain antenna. A recording of a received signal at 60.25 GHz is shown in Figure 5. Here, the transmitting FET was illuminated by 80 mW from the dye laser and 0.15 mW from the HeNe laser. The local oscillator is tuned to 61.54 GHz and is irradiating the receiving FET antenna circuit with approximately 25 mW of power. For this data, the devices are biased as follows: the transmitting FET was biased with V_{ds} = 2.0V and V_{gs} = -2.0V, and the receiving FET was biased with V_{ds} = 2.0V and V_{gs} = -0.6V. In the case of the transmitter the device is biased below pinchoff (pinchoff voltage for this device at V_{ds} = 2.0 V is V_{gs} = -1.1 V), therefore photoexcited carriers via photoconduction mechanisms are responsible for generating the radiating laser difference frequency. For these FETs, previous studies show that the frequency response of the photoconduction mechanism is faster than that of the photovoltaic mechanism(9). The typical achievable signal to noise ratio for experimental conditions similar to those of Figure 5 was 30-35 dB. Based on the receiver conversion losses and the millimeter wave collecting optics, the power in the millimeter wave beam was estimated to be 1 nW. The polarization of the radiation

was measured and found to be linearly polarized as was expected from antenna design considerations.

In an effort to determine the lower limits at which the millimeter wave radiation could be generated, the ratio of the laser powers was varied. Although a complete study of the performance of the transmitting FET antenna circuit under various conditions of bias and illumination is necessary, preliminary results indicate that the mixing and re-radiation mechanisms require only modest levels of optical power. A S/N of 13dB was achievable with 20 mW of dye laser power and 0.38 mW of HeNe laser power. Conversely, saturation of the radiating signal strength was observed for dye laser powers in excess of 60 mW indicating a saturation of carriers in the active region of the transmitting device. Also, measurements of the radiating signal strength versus the orientation of the two lasers polarization showed that the optical mixing mechanism is optimized when the two beams are colinearly polarized. This result is critical with respect to the use of a fiber optic light delivery system. Using single mode, polarization preserving fiber in place of the lens, we successfully generated millimeter wave radiation using this light delivery system. Laser polarization orientation was controlled by placing a half wave plate in front of the fiber input tip. The output tip was brought to < 1 mm from the device active region and illuminated the device directly. Figure 7 is a typical recording of a received signal using fiber optic light delivery to pump the transmitting device/antenna circuit.

As a demonstration that we have tunable, narrow band millimeter wave radiation, we measured the response of the same tunable Fabry-Perot interferometer. The filter response was measured by tuning the dye laser and therefore, tuning the millimeter wave radiation through the pass band of the filter. The signal from the receiving FET was measured using a lock-in amplifier. The

lock-in reference channel was locked to the chopped HeNe laser. Figure 6 shows a recording of the response of the filter. The filter center frequency is at 60.65 GHz, and the full width at half maximum of the filter is 220 MHz. This is in good agreement with the calculated value.

IV CONCLUSIONS

Because the bandwidth of the radiation is limited primarily by the high gain antenna, future improvements to these techniques will include the use of broadband, high frequency antennas integrated with high speed three terminal devices. Devices with F_t's greater than 100 GHz are currently being investigated in this application. Cascading devices will provide optical mixing signal amplification prior to driving the antenna. Based on the preliminary study of the performance of the transmitting FET antenna circuit under varying conditions of illumination, our results indicate that low power, frequency stabilized, infrared semiconductor lasers could be used to replace the CW dye and HeNe lasers thus providing alternative compact light sources. Finally, this paper demonstrates the potential of converting millimeter wave signals on light directly into propagating millimeter wave radiation using planar FET structures. It should now be possible to make arrays of distributed sources using this technology.

V ACKNOWLEDGEMENTS

This work was supported by the Air Force Office of Scientific Research and the National Center for Integrated Photonics Technology. The authors would also like to thank Professor N. Luhmann, Jr. and M. Espiau of the Center for High Frequency Electronics for providing microwave components and test equipment, and Lenard

Shaw of the TRW Electronics and Technology division for providing high speed devices.

VI REFERENCES

1) A.J. Seeds and A.A.A. de Salles, "Optical control of microwave semiconductor devices," *IEEE Trans. Microwave Theory Tech.*, vol. **MTT-38**, pp. 577-585, 1990.

2) R. Simons, *Optical Control of Microwave Devices* (Artech House, Boston and London, 1990).

3) H. R. Fetterman, W.Y. Wu, and D. Ni., "Optical control of millimeter wave devices," Proc. *SPIE* , vol. **789**, pp. 50-53, 1987.

4) C.S. Chang, H.R. Fetterman, D. Ni, E. Sovero, B. Mathur, and W.J. Ho, "Negative photoconductivity in high electron mobility transistors," *Appl. Phys. Lett.*, vol. **51**, pp. 2233-2235, 1987.

5) D.C. Ni, H.R. Fetterman, and W. Chew, "Millimeter-Wave generation and characterization of a GaAs FET by optical mixing," *IEEE Trans. Microwave Theory Tech.*, vol. **MTT-38**, pp. 608-614, 1990.

6) P.R. Herczfeld (Guest Ed.), "Special Issue On Applications Of Lightwave Technology To Microwave Devices," *IEEE Trans. Microwave Theory Tech.*, **MTT-38**, 1990.

(7) G.J. Simonis, K.G. Purchase, "Optical generation, distribution, and control of microwaves using laser heterodyne," *IEEE Trans. Microwave Theory Tech.*, vol. **MTT-38**, pp. 667-669, 1990.

(8) W. Chew and H.R. Fetterman, "Printed circuit antennas with integrated FET detectors for millimeter-wave quasi-optics," *IEEE Trans. Microwave Theory Tech.*, vol. **MTT-37**, pp. 593-397, 1989.

(9) G.J. Papaionanou and J.R. Forrest, "On the photoresponse of GaAs MESFET's: Backgating and deep trap effects," *IEEE Trans. Electron. Devices*, vol. **ED-33**, pp. 373-378, 1986.

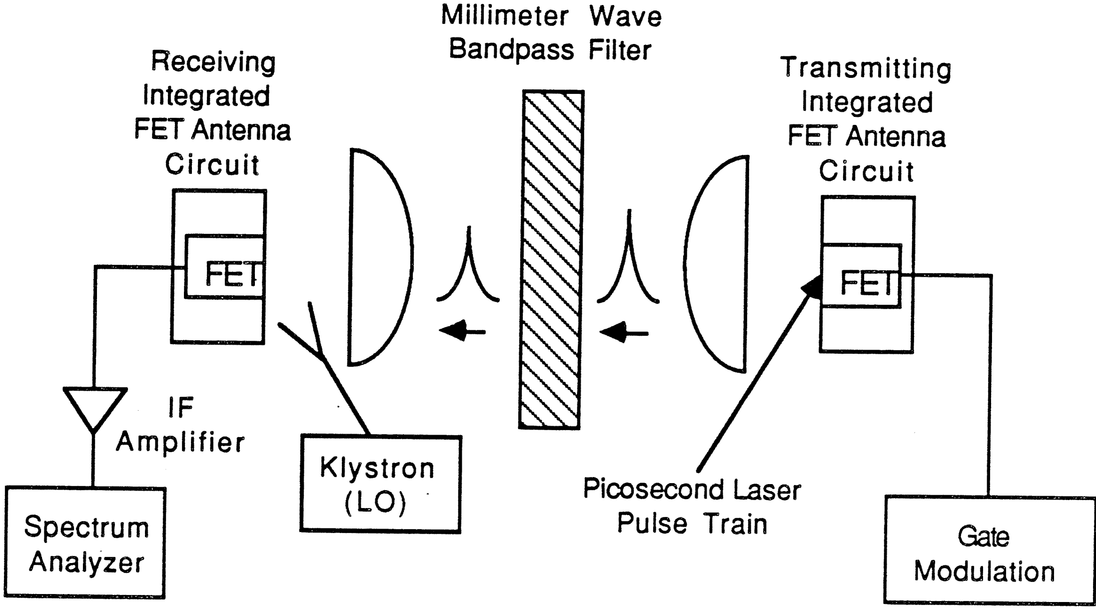

Figure 1: Schematic of the pulsed laser excitation experimental set-up.

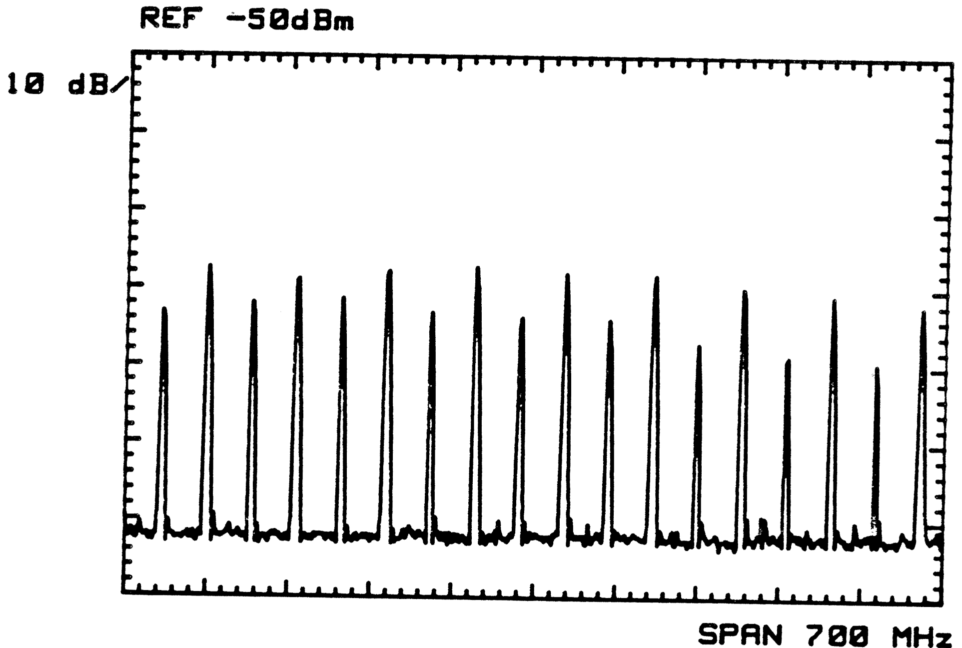

Figure 2: Millimeter wave radiation comb produced by optical excitation for a local oscillator frequency of 61.4 GHz. Signals located in the upper sideband are the larger amplitude signals, and signals located in the lower sideband are the lower amplitude signals.

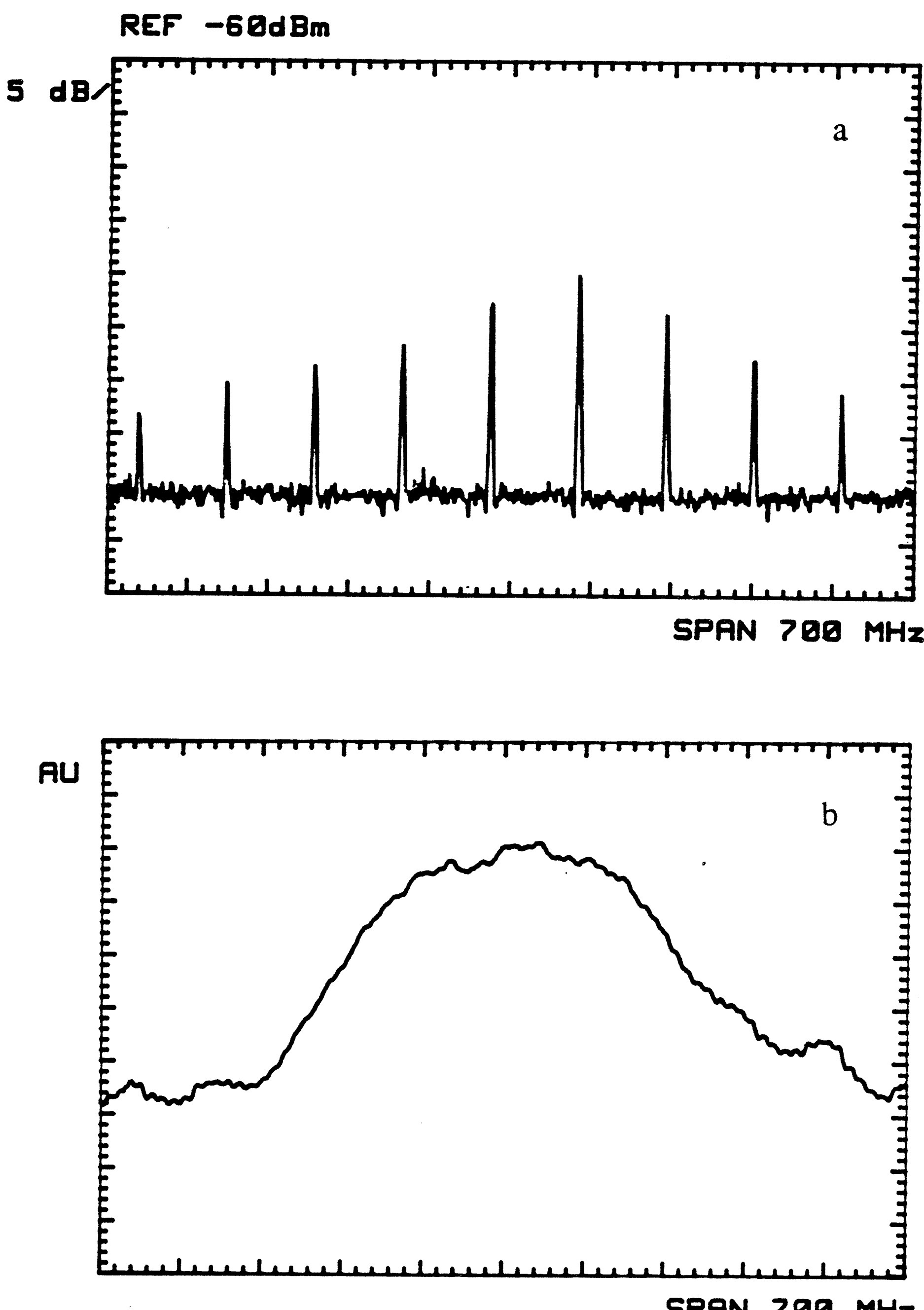

Figure 3: (a)Transmission response of a metal mesh Fabry-Perot interferometer without transmitter gate modulation. Tuned to 62.27 GHz, the filter rejects signals in the lower sideband and filters signals in the upper sideband (b)Transmission response of the same filter with a swept 0 dBm electrical modulation applied to the transmitting FET antenna circuit.

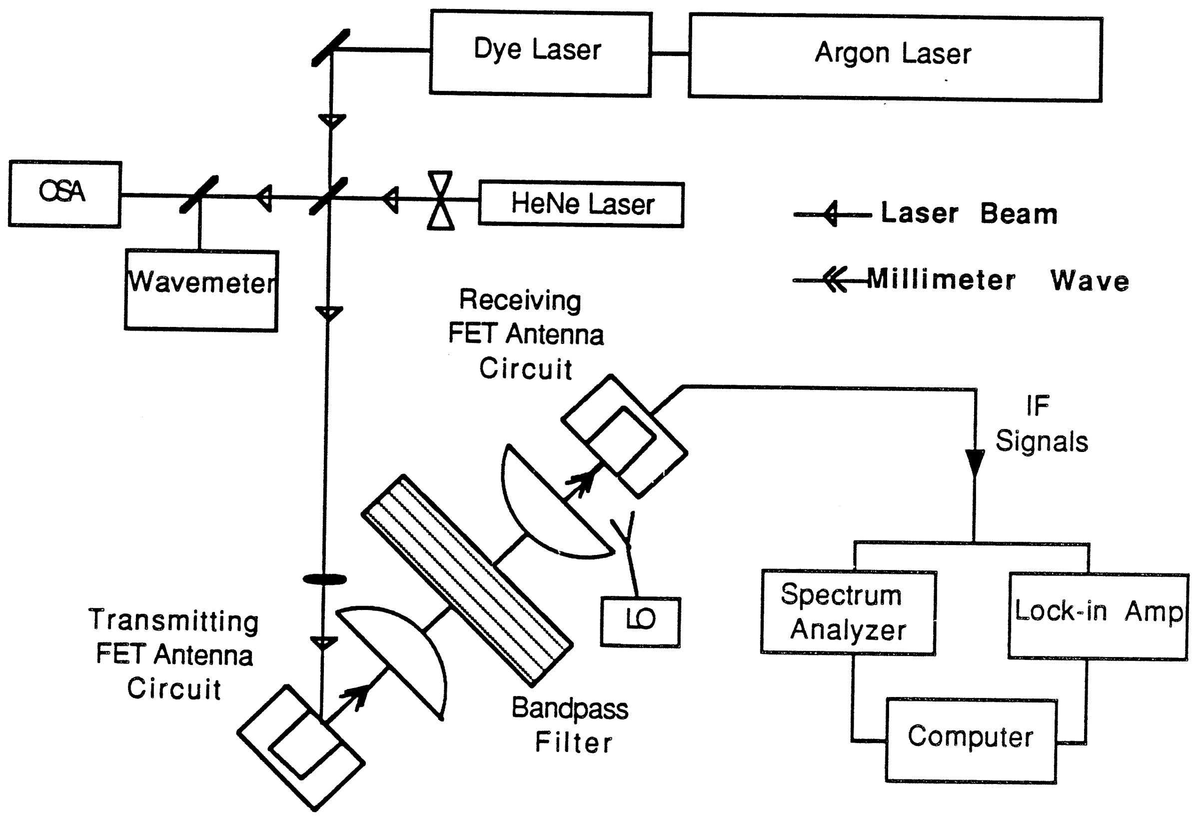

Figure 4: Schematic of the continuous wave excitation experimental set-up.

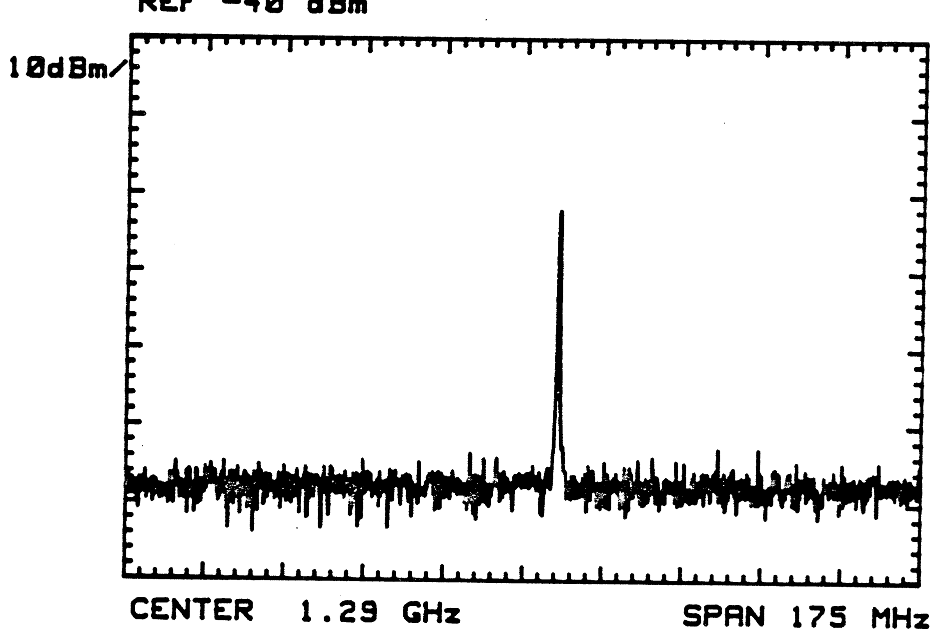

Figure 5: Recording of the received millimeter wave radiation at 60.25 GHz.

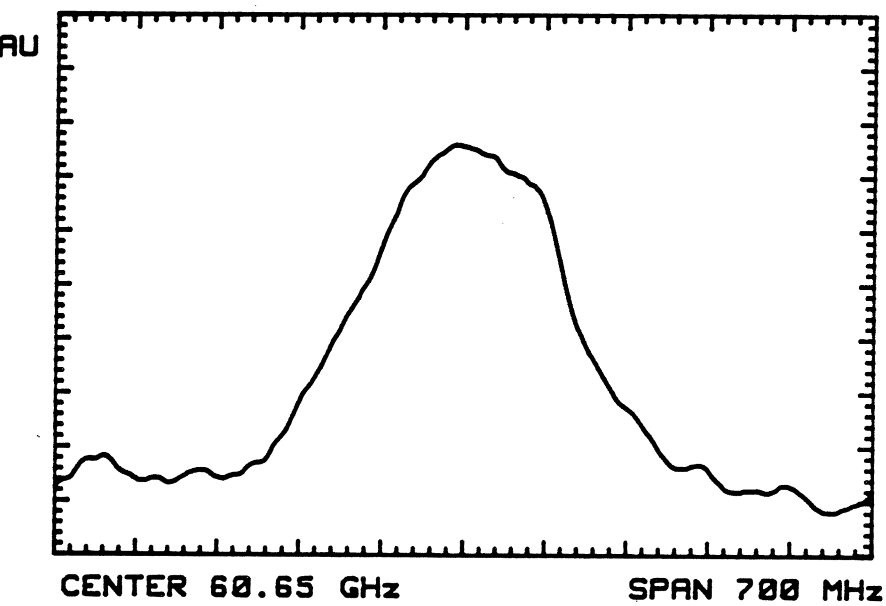

Figure 6: Transmission response of a metal mesh Fabry-Perot interferometer tuned to resonance at 60.65 GHz. Data was taken with a lock-in time constant of 1.0 second.

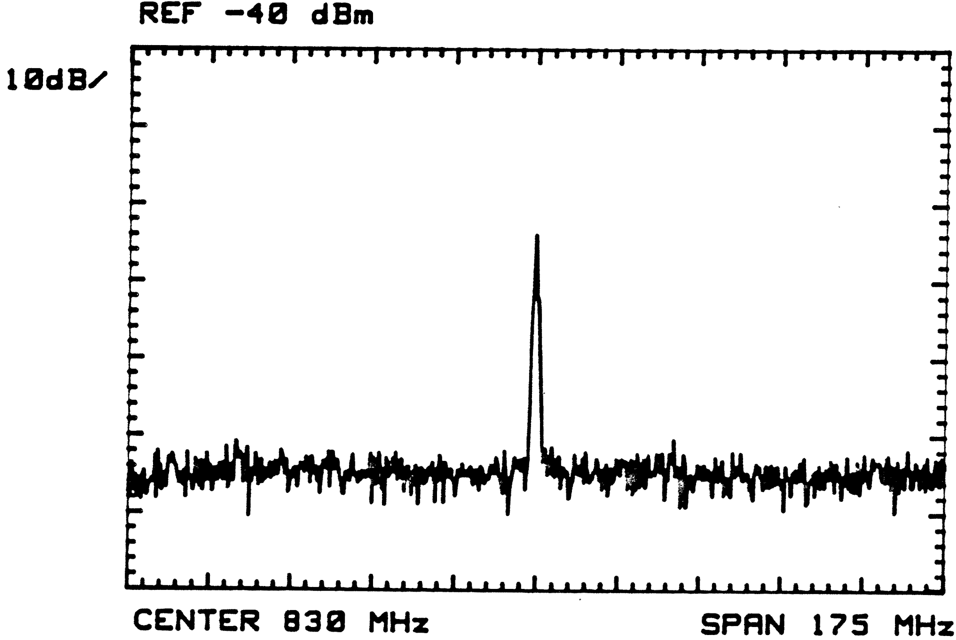

Figure 7: Recording of received millimeter wave radiation at 60.5 Ghz using fiber optic light delivery to pump device/antenna circuit.

Second International Symposium on
Space Terahertz Technology, February 26–28, 1991
Jet Propulsion Laboratory
California Institute of Technology
Pasadena, California

SLIDING BACKSHORTS FOR PLANAR CIRCUITS

Victor M. Lubecke,[1] William R. McGrath,[2] David B. Rutledge[1]

1. Division of Engineering and Applied Science, California Institute of Technology, Pasadena, CA 91125

2. Center for Space Microelectronics Technology, Jet Propulsion Laboratory, California Institute of Technology, Pasadena, CA 91109

Abstract — **The Superconductor-Insulator-Superconductor (SIS) tunnel junction is an extremely sensitive heterodyne detector at millimeter and submillimeter wavelengths. The large inherent capacitance associated with this device results in a substantial impedance mismatch with typical antennas and, therefore, requires a tuning circuit for optimum results. At frequencies where waveguide dimensions are realizable, impedance matching can be accomplished by embedding the detector in a waveguide circuit with adjustable waveguide backshorts. At higher frequencies, where waveguide dimensions become prohibitively small, a planar transmission line embedding circuit provides a reasonable alternative. Typically, such planar circuits offer no post-fabrication adjustability, resulting in demanding materials and design requirements. An adjustable planar embedding circuit based on coplanar transmission lines with movable non-contacting shorting elements has been developed. The shorting elements each consist of a thin metallic plate with an optimized arrangement of rectangular holes, placed along the insulated metallic transmission line to provide a periodic variation of the line impedance. A scale model (1–5 GHz) has shown that a large reflection coefficient, $|s_{11}| \geq -0.5\,\mathrm{dB}$, can be achieved with these sliding elements. A low frequency tuning circuit incorporating these shorting elements has been tested to demonstrate practical tuning ranges.**

I. Introduction

Low noise, high conversion efficiency, and low local oscillator power requirements have made the superconductor-insulator-superconducter (SIS) tunnel junction the mixer of choice for a wide range of millimeter and submillimeter wave heterodyne receiver applications [1,2]. However, SIS junctions have a large inherent capacitance which

results in an impedance mismatch when the detector is used with typical embedding circuits. It is therefore desirable to design a receiver which incorporates an adjustable impedance matching circuit to fully optimize the mixer.

SIS mixers with excellent performance have been demonstrated throughout the millimeter wave band using waveguide embedding circuits with one or two adjustable tuning elements [3,4]. At terahertz frequencies however, the very small physical dimensions of a waveguide become extremely difficult to fabricate accurately, and installing the SIS junction is a serious problem. If an array of mixers is desired, these difficulties are compounded. At this point, planar circuits are an attractive alternative. SIS junctions have a planar geometry and are readily integrated with planar transmission lines and antennas. Planar circuits, however, usually support tuning elements with only fixed dimensions. These are often in the form of open or short circuited tuning stubs. This lack of adjustability usually means that an effective circuit design requires an extremely well characterized SIS junction and substrate, as well as an extremely well controlled circuit fabrication process. This may not always be possible at these high frequencies [5,6].

An approach for a movable, non-contacting planar backshort which can be used to vary the electrical length of a coplanar strip transmission line tuning stub has been developed. This sliding circuit element allows for the design of an embedding circuit with a complex impedance that can be optimally adjusted to match the SIS device after the circuit has been fabricated.

II. The Planar Backshort

Placing a solid metallic plate across a coplanar strip transmission line, with a thin dielectric insulating layer in between, results in a reflection of RF power. Unfortunately, this reflection is not sufficient over any bandwidth for the plate to be used as a backshort in the design of a practical tuning circuit. This "sandwich" configuration does, however, result in a section of lower impedance transmission line. Quarter-wavelength sections of this line can be cascaded alternately with uncovered sections of "high" impedance line to create a series of impedance transformations which ultimately result in a very low impedance. When used as a backshort on a transmission line, this cascade produces an even larger reflection of RF power than the solid plate. We constructed and optimized such a planar backshort and it's geometry is illustrated in figure 1. It consists of a thin metal plate with rectangular holes of the proper dimension and spacing. A thin insulator keeps the plate from contacting the transmission line which reduces wear and allows the backshort to slide freely when pushed with a probe.

III. Model Measurements

We built a large scale model of the sliding backshort and measured the magnitude of the reflection coefficient with an HP 8510B network analyzer over a frequency range

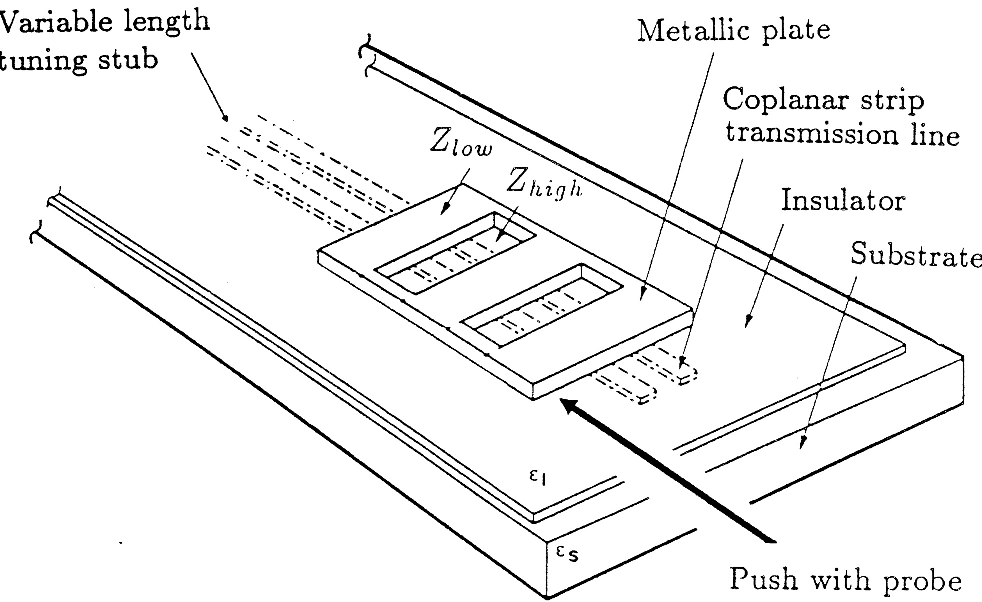

Figure 1. Design of sliding backshort on coplanar strip transmission line. The holes in the metal plate create a series of successive high and low impedance sections that produce a large reflection of RF power.

of 1 GHz to 5 GHz. This measurement required a transition between the coaxial input of the network analyzer and the coplanar line. Unfortunately, no standard transition with low VSWR is readily available. For this reason, we devised several distinct measurement techniques in order to obtain reliable results.

A natural choice of calibration technique for an HP8510B is the "Thru-Reflect-Line" (TRL) method which allows for measurements in nonstandard transmission media such as coplanar line. The transition between coaxial and coplanar line can, in principle, be accounted for in the calibration procedure. However, reproducible calibration standards in coplanar line are required. Reflections at connections between segments of coplanar line and uncertainties in the reflection standard lead to non-repeatable results and unacceptably high errors. As a result, this method was not pursued further.

Our second technique was a simple 1-port measurement of a circuit which employs a direct connection from coaxial to coplanar line. This measurement of $|s_{11}|$ was made over a 1.5 GHz to 2.5 GHz frequency range and figure 2(a) shows the test arrangement. The abrupt transition from coaxial line to coplanar line was formed at the edge of the stycast substrate with a flange mount SMA connector. The measurement was taken with the reference plane of the backshort adjusted to coincide with the SMA connector.

While this transition resulted in large unwanted reflections which increased the uncertainty of the measurement, the technique was useful because it allowed us to monitor the reflection coefficient for the backshort in real time as we optimized the dimensions of the backshort. The optimization was performed by systematically varying the

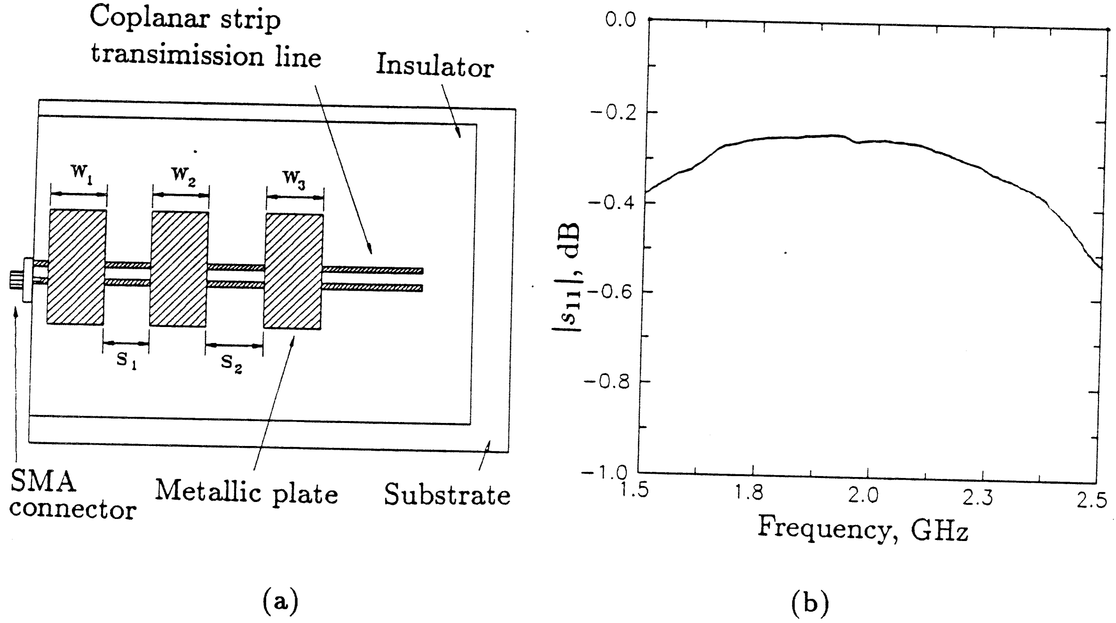

Figure 2. Test circuit used for optimization (a) and plot of reflection coefficient (b) for optimized sliding backshort at the SMA connector on 204-Ω transmission line.

length of the low and high impedance sections, the number of sections, the dimensions of the transmission line, and the thickness of the insulator in order to achieve the best reflection of RF power. Good performance was obtained for a coplanar transmission line with 2.1 mm wide copper strips, separated by a 5.2 mm gap and mounted on a 6 mm thick stycast substrate with a dielectric constant of 4. The characteristic impedance of this transmission line and its effective dielectric constant were determined to be 204 Ω and 2.3 respectively [7]. A 0.025 mm thick sheet of mylar was used to insulate the transmission line from the sliding shorting plate. This non-contacting, 76 mm wide, 6 mm thick aluminum shorting plate had two rectangular holes in it with dimensions and spacing of $w_1 = 24.3$ mm, $s_1 = 19.8$ mm, $w_2 = 24.3$ mm, $s_2 = 23.5$ mm, and $w_3 = 24.3$ mm. This resulted in uncovered high impedance sections, s_1 and s_2, and covered low impedance sections, w_1, w_2 and w_3, which were each approximately $\lambda_g/4$ long on the coplanar line.

A plot of $|s_{11}|$ versus frequency is shown in figure 2(b). This optimized planar backshort produced $|s_{11}|$ better than -0.3 dB over a 20% bandwidth. That is a reflection of more than 90% of the power in the incident wave. The center frequency was determined to be 2 GHz, which agrees exactly with the design frequency.

We noted that the front edge of the sliding metallic plate was very close to the discontinuity at the SMA connector and it may have interacted with fringing fields around the flange. In addition, the reflection coefficient decreased when the backshort was moved $\lambda_g/2$ from the SMA connector in order to reduce interactions with fringing fields. The error caused by this unwanted interference, along with the lack of a transmission measurement, motivated the design of a third measurement technique.

Figure 3 shows the system used for the third measurement technique. Here, the 204-Ω coplanar line was connected to the 50-Ω network analyzer inputs by means of two baluns of identical length. These baluns were made by gradually trimming the shield and teflon insulation from a semirigid, 3.5 mm wide coaxial line over approximately one wavelength at 2 GHz. This created a smooth transition to the coplanar line which minimized the power reflected at the connection. The return loss for these baluns is approximately –10 dB and the remaining undesired reflections from these transitions were gated out of the measurement using the low-pass time domain mode of the network analyzer. The frequency for this measurement was swept from 50 MHz to 20 GHz so that an accurate transformation between frequency and time could be made.

The full two-port scattering parameters for the system were measured under three different conditions. First, a reference measurement was made which would correspond to an ideal short. The baluns are identical in length and hence, the test model is symmetric about the midpoint of the coplanar line. Thus, the magnitude of the transmission measurement of this circuit with no short in place is equal to the reflection measurement with an ideal short at the midpoint. Reflection measurements for the sliding backshort were then made with the shorting plate arranged to reflect an incident wave from port 1 at the midpoint of the system and then, port 2. The values for $|s_{11}|$ from the first reflection measurement and $|s_{22}|$ from the second were normalized by dividing each by the values for $|s_{21}|$ and $|s_{12}|$ from the reference measurement, respectively. The two results were averaged to cancel the effect of any asymmetry in

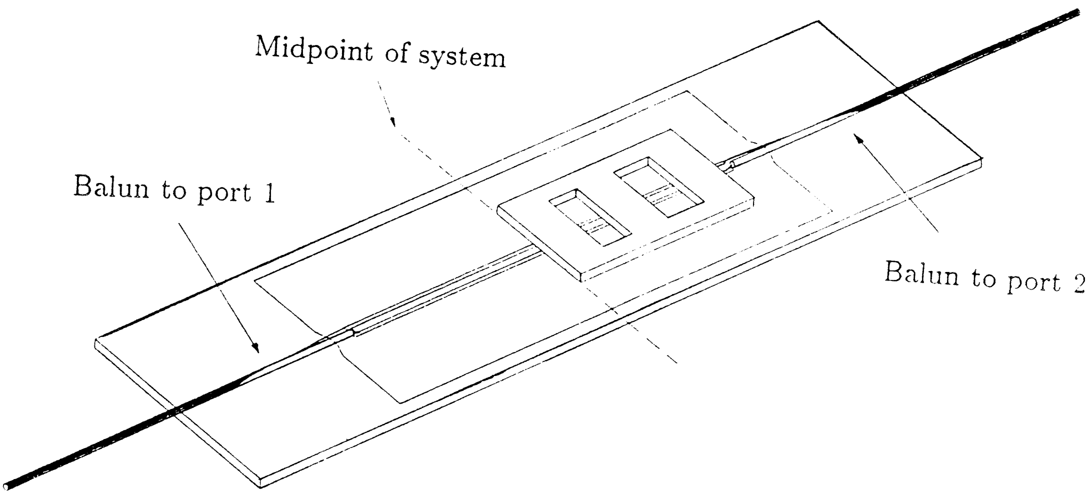

Figure 3. Test system used to measure two-port scattering parameters for sliding backshort. The coaxial line baluns are tapered to create a gradual transition between coaxial and coplanar line which reduces measurement uncertainty due to unwanted reflections at the transition.

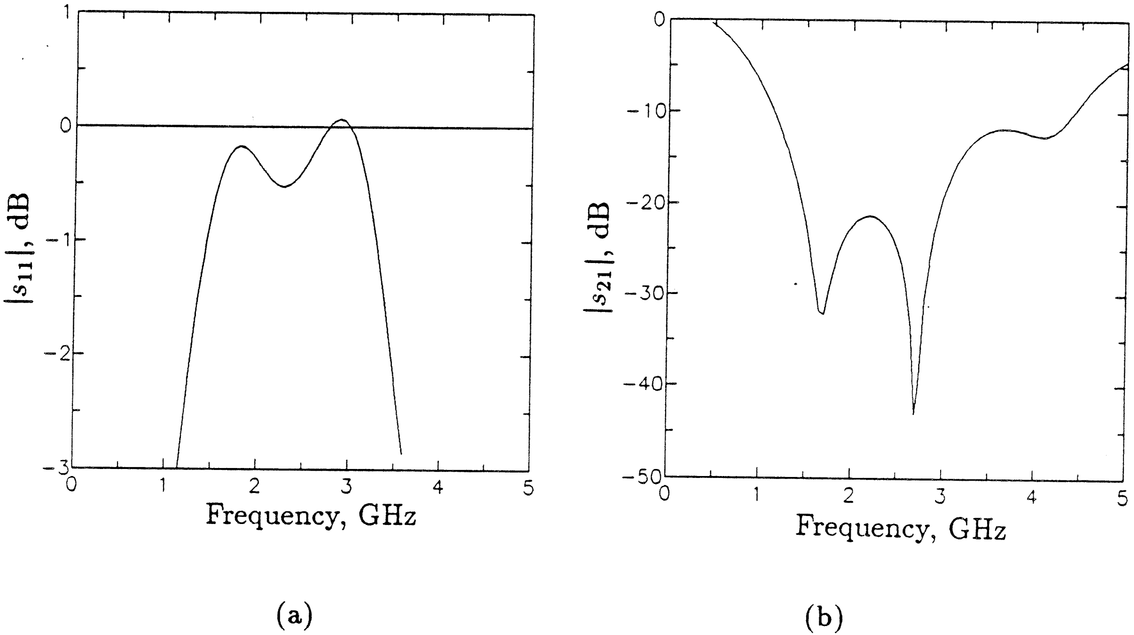

Figure 4. Plot of measured reflection coefficient (a) and transmission coefficient (b) for optimized sliding backshort. This measurement was made using baluns for transitions.

the system. Transmission measurements for the backshort were similarly normalized and averaged. The requirement of processing the measurement data, along with the large range of frequency, prohibited us form monitoring the 2 GHz reflection coefficient in real time for this measurement.

The results for the averaged, normalized $|s_{11}|$ and $|s_{21}|$ are shown in figure 4. The plot shows that $|s_{11}|$ was better than –0.5 dB over approximately an 80% bandwidth and the center frequency was slightly higher than 2 GHz. Over the peak located between 1.5 GHz and 2.5 GHz, $|s_{11}|$ is better than –0.3 dB over a 16% bandwidth and the center frequency is slightly lower than 2 GHz. This agrees well with the previous results shown in figure 2(b). Together, the plots of $|s_{11}|$ and $|s_{21}|$ appear to indicate that approximately 10% of the power for the incident wave is left unaccounted for, but the $\pm$ 0.2 dB uncertainty of our measurement is to large to verify this.

IV. Double Stub Tuner

In order to demonstrate the tuning range accessible in a planar circuit, we built a double-shunt stub tuner which incorporates two sliding backshorts. Figure 5(a) shows the equivalent circuit and figure 5(b) shows the circuit arrangement as measured. The characteristic impedance of the coplanar line is 90 Ω and the stub spacing is $\lambda_g/8$. A 90-Ω resistor was used to simulate a planar antenna impedance and a 3.5 mm wide semirigid coaxial probe was used to measure the range of impedance to which we could transform the resistor. The calibration reference plane for this measurement was set at end of the shield for the coaxial probe. Figure 6 is a Smith chart, normalized to

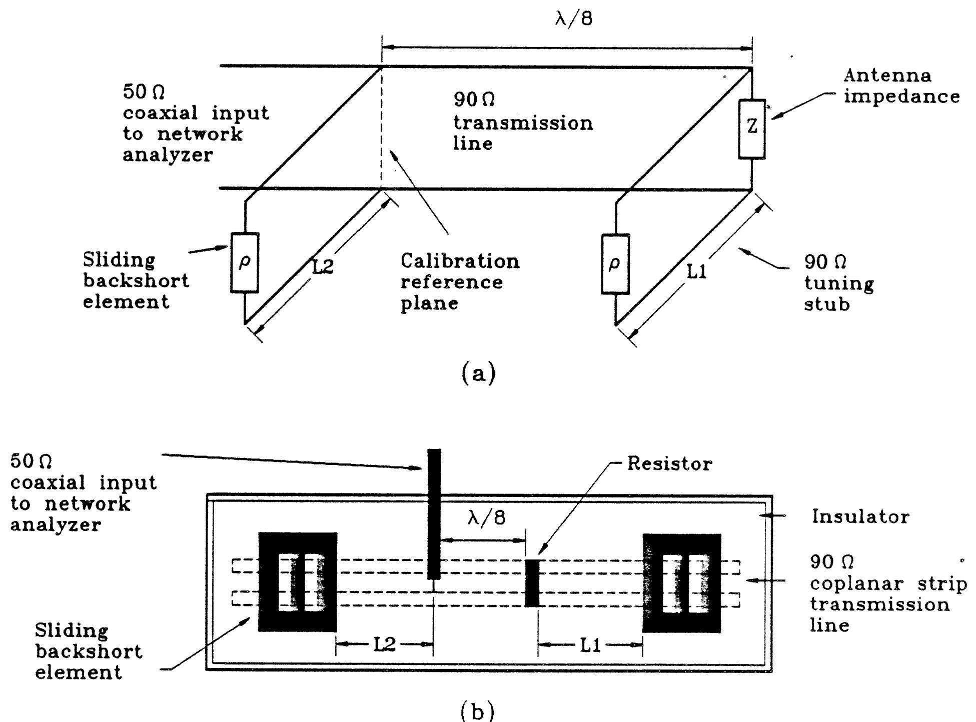

Figure 5. Schematic diagram for equivalent double-shunt stub tuner circuit (a) and circuit arrangement used for measurements (b).

the characteristic impedance of the line, which shows the accessible impedance region at 2 GHz. The overlap for the tuning region and the impedance region necessary for matching SIS devices implies that a circuit of this type might be useful for this purpose. Variations in the shape of this tuning region can be achieved by changing the spacing between the tuning stubs.

The solid and dashed boundary lines in figure 6 show a comparison between the measured impedance range of the double stub tuner and a computer simulation of the circuit using *Puff* [8], respectively. The simulation agrees well with the measured data. The reflection coefficient for the shorting element used in the computer model, a resistor, along with a phase shift at the probe tip to account for the calibration reference plane uncertainty, were fitted to match the measured Smith chart data. The resulting phase shift was 4 degrees and $|s_{11}|$ for the backshort model was –0.5 dB, which is slightly better than the –0.7 dB result that we measured for the same backshort by itself on a 90-Ω transmission line at 2 GHz.

V. Conclusion

We have demonstrated an approach for an adjustable planar backshort on coplanar strip transmission line. Results from a low-frequency model indicate that the backshort can be used to create tuning stubs whose electrical length can be varied after fabrication. This non-contacting backshort with cascaded high and low impedance sections should also work on slotline, coplanar waveguide and possibly microstrip line. By using advanced micro-machining techniques [9,10], it should be possible to create

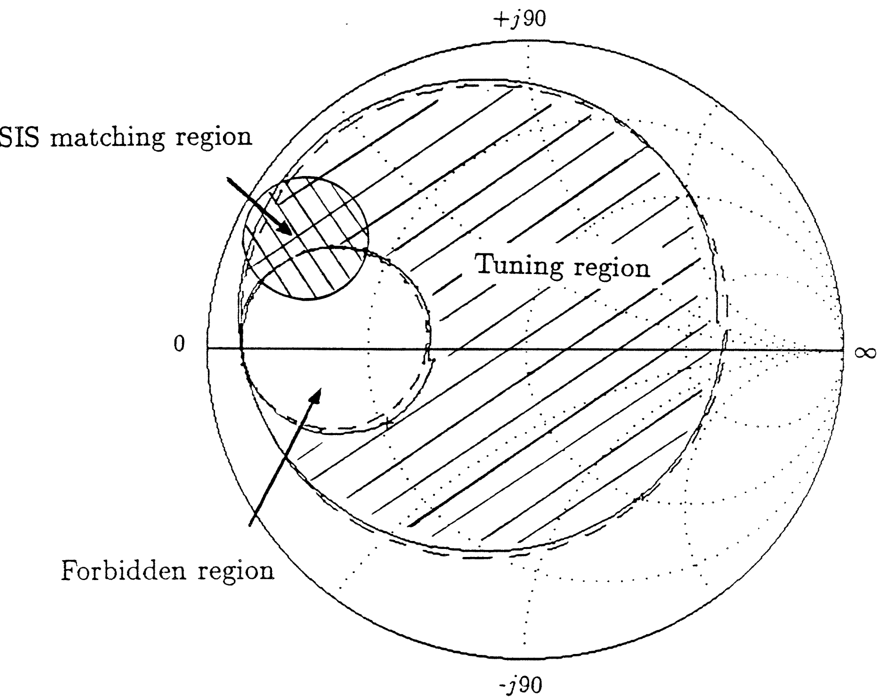

Figure 6. Smith chart showing measured (solid boundary) and fitted (dashed boundary) tuning region for double shunt stub tuner. The available tuning region covers the impedance region needed for matching to an SIS device.

adjustable impedance matching circuits at terahertz frequencies which would relax the design constraints for a wide range of integrated planar circuits.

VI. Acknowledgements

We wish to thank Y-C. Tai for his help in keeping the design viable for terahertz scaling through micro-machining techniques. We also wish to thank O. Borić, M. A. Frerking, E. Kollberg, K. Potter, P. Siegel, and T. Tolmunen for valuable discussions. This work was supported in part by the Jet Propulsion Laboratory, California Institute of Technology, under contract with the National Aeronautics and Space Administration and the Innovative Science and Technology Office of the Strategic Defense Initiative Organization.

References

[1] J.R Tucker and M.J. Feldman, "Quantum Detection at Millimeter Wavelengths," *Reviews of Modern Physics*, vol. 57, no. 4, pp. 1055-1113, October 1985.

[2] B.N. Ellison, P.L. Schaffer, W. Schaal, D.Vail, and R.E. Miller, "A 345 GHz SIS Receiver For Radio Astronomy," *International Journal of Infrared and Millimeter Waves*, vol. 10, no. 8, pp. 937-947, 1989.

[3] S-K. Pan, A.R. Kerr, M.J. Feldman, A.W. Kleinsasser, J.W. Stasiak, R.L. Sandstrom, and W.J. Gallagher,"An 85-116 GHz SIS Receiver Using Inductively Shunted

Edge Junctions," *IEEE Transactions on Microwave Theory and Techniques*, vol. 37, no. 3, pp. 580-592, March 1989.

[4] C.A. Mears, Q. Hu, P.L. Richards, A. H. Worsham, D.E. Prober, and A.V. Raisanen, "Quantum Limited Heterodyne Detection of Millimeter Waves Using Superconducting Tantalum Tunnel Junctions," *Applied Physics Letters*, vol. 57, no. 23, pp. 2487-2489, December 1990.

[5] Q. Hu, C A. Mears, P.L. Richards, and F.L. Lloyd, "MM Wave Quasioptical SIS Mixers," *IEEE Transactions on Magnetics*, vol. 25, no. 21, pp. 1380-1383, March 1989.

[6] W.R. McGrath, J.A. Stern, H.H.S. Javadi, S.R. Cypher, B.D. Hunt, and H.G. Le Duc, "Performance of NbN Superconducting Tunnel Junctions as SIS Mixers at 205 GHz," to Appear in *IEEE Transactions on Magnetics*, vol. 27, March 1991.

[7] Y.T. Lo, S.W. Lee, *Antenna Handbook*, Van Nostrand Reinhold Co., N. Y., p. 28-35, 1988.

[8] R. Compton, S.W. Wedge, D. Rutledge, *Puff: Computer Aided Design for Microwave Integrated Circuits*, (published at Caltech, Pasadena, California), 1990.

[9] L-S. Fan, Y-C. Tai, and R.S. Muller, "Integrated Movable Micromechanical Structures for Sensors and Actuators", *IEEE Transactions on Electron Devices*, vol. 35, no. 6, pp. 724-730, June 1988.

[10] M. Mehregany, K.J. Gabriel, and W.S.N. Trimmer, "Integrated Fabrication of Polysilicon Mechanisms," *IEEE Transactions on Electron Devices*, vol. 35, no. 6, pp. 719-723, June 1988.

Low-Loss Guiding Structures for THz Frequency Applications

A. G. Engel, Jr., T. E. van Deventer and Linda P. B. Katehi

NASA Center for Space Terahertz Technology
The University of Michigan

Abstract — The design and construction of low-loss monolithic transmission lines are critical to systems which require that THz-power be guided to the antenna front-end. This paper proposes two types of novel monolithic guiding structures, which are designed for the 0.4–2.0 THz and 0.1–0.4 THz ranges, respectively. Propagation in each of the waveguides is characterized by applying a mode-matching technique, and the structures are predicted to exhibit excellent power confinement and low losses. A modified integral equation method for the efficient and accurate analysis of three-dimensional structures such as power dividers, bends and stubs is also presented.

1 Introduction

Technology based on the frequency range of 0.1–2.0 THz offers narrow-beam, high-resolution antennas which are essential for intelligent computer control guidance, command systems for space applications, and sensors which operate in optically opaque media. Since these systems require that the generated THz-power be guided to the antenna front-end through complex feeding networks, the design and construction of low-loss monolithic transmission lines are critical.

There are two typical approaches for the design of these transmission lines. The first approach extends the use of planar conductors in well-established monolithic millimeter wave technology to higher frequencies. Planar circuit elements such as loads, transitions, junctions and lines perform quite well at frequencies up to 100 GHz, but ohmic and radiation losses become unacceptably high as the frequency increases further. The second approach extends optical techniques to lower frequencies. This approach is hindered by three factors. First, optical materials are usually incompatible with the semiconducting materials which are needed for active devices. Second, phenomena which dominate optical waves, such as nonlinear wave characteristics, are not present at terahertz frequencies. Finally, phenomena which are ignored at optical frequencies, such as radiation and electromagnetic coupling, are not negligible at terahertz frequencies.

A novel approach for the design of two types of monolithic guiding structures is presented in this paper. The two types are designed for specific frequencies in the 0.4–2.0 THz and 0.1–0.4 THz ranges, respectively. The development of these structures consists of two steps. The first step employs a well-known mode-matching technique to design and analyze propagation in two-dimensional structures. The second step considers the problem of circuit element design, and a modified integral equation technique is presented for the analysis of three-dimensional structures such as power dividers, bends and stubs.

2 Design

The design of the new waveguides is based on the millimeter wave dielectric waveguides which were extensively investigated for hybrid circuit applications in the 1970's and early 1980's. Examples of these waveguides include dielectric image guides [3], strip dielectric guides, insulated image guides, strip-slab guides [4], inverted strip dielectric guides [6], cladded image guides [5], and trapped image guides [7]. Like the mm-wave dielectric guides, the new waveguides are constructed from combinations of layers and ridges of various permittivities in order to provide a region wherein the propagating power is well-confined. However, whereas the widths of the mm-wave guides approach one guided wavelength in order to maximize field confinement, the dimensions of the new waveguides are on the order of a fraction of a guided wavelength, so that passive circuit elements such as inductors and couplers may be developed from these structures. In addition, the new waveguides are constructed from dielectric materials and structures which are available in monolithic technology so that the integration of active devices is possible. Also, the proposed structures may be applied as low-loss feeding networks and highly efficient radiating elements for arrays, since the physical size and dominant field component are similar to those of conventional microstrip.

The proposed structures consist of alternating layers of high and low permittivities (Figure 1). The abrupt changes in the permittivities in the x-direction are designed to optimize power confinement in the layer with the lowest permittivity. This layer, designated the *propagation layer*, is away from the ground plane, resulting in minimal ground plane conductor loss. A ridge or a semi-embedded strip provides power confinement in the y-direction. Two types of construction are proposed.

The first type of structure is suitable for the 0.4–2.0 THz region. The structures may be either ridged or semi-embedded and will be made of semiconducting materials grown on GaAs or InP substrates. The ridged structure is created by etching a layered wafer. The semi-embedded waveguide is fabricated by etching

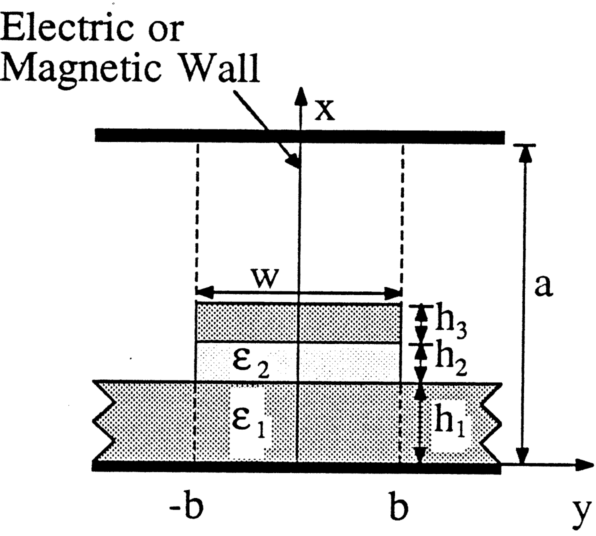

Figure 1: General structure for mode matching analysis.

a well of appropriate dimensions into a semiconducting substrate, filling the well with layers of intrinsic semiconducting materials using regrowth techniques, and etching again. In both the ridged and the semi-embedded structures, layers of 5–10 microns are required, and these layers can be grown by MOCVD.

As the frequency of operation decreases, thicker layers are required and the times required to grow the layers on the wafers become impractically large. Hence, a second type of waveguide is proposed for the sub-mm wave region (0.1–0.4 THz). This structure is constructed from a combination of semiconducting substrates and dielectric films; for example, a wafer of GaAs may be covered with a polyamide film, attached to another GaAs wafer with a thin epoxy glue, and etched to produce a ridged waveguide. The epoxy is expected to create a gap of approximately 1 micron, which would not affect the propagation characteristics. A similar structure could be created with silicon wafers and a quartz film; in this case, the wafers are attached with electrobonding.

In both cases, the waveguide construction fosters straightforward integrated circuit fabrication. Active devices may be fabricated on the substrates prior to the creation of the actual guiding structures. Transitions from the waveguides to the active devices could consist of very short lengths of microstrip near the devices. Passive structures may be created by fabricating the transmission lines in

the desired pattern on the substrate.

3 Characterization of Two-Dimensional Structures

The propagation constants γ $(= \alpha + j\beta)$ and fields of the proposed lines have been analyzed using a mode-matching method, similar to the ones employed in [1, 2, 3, 8, 9, 10]. The general structure, shown in Figure 1, is uniform in the z-direction. Along the y-axis, the structure is divided into sections at $y = \pm b$. Each section is divided into layers along the x-axis at $x = h_1$, $h_1 + h_2$ and $h_1 + h_2 + h_3$. Each layer is characterized by its permittivity ϵ; losses are accounted for with a complex permittivity $\epsilon = \epsilon_o \epsilon'(1.0 - j \tan \delta)$. The outer sections ($|y| > b$) extend to $y = \pm\infty$, and the ceiling is chosen to be far enough away from the guiding structure so as to not affect the guidance properties. Using symmetry, the structure can be simplified by adding either a magnetic or electric wall in the middle and only considering half of the structure.

Each section of the structure is a section of an inhomogeneous parallel plate waveguide, which supports TE_x and TM_x modes. The boundary conditions at $x = a_i$ determine the x-dependence of each mode in each section. Mode matching is utilized at $y = -b$, giving a matrix equation which relates the mode amplitudes in the section $y < -b$ to the mode amplitudes in the section $-b < y < 0$. A homogeneous system of equations results from the boundary conditions at $y = 0$. Values for the propagation constant are ascertained from zeros of the determinant of the system, and the homogeneous system may then be solved for the mode amplitudes.

The design parameters of an example of each type of guiding structure are given in Table 1 and the characterization of these structures is shown in Figures 2–7. The results were obtained using 18 TE_x and 18 TM_x modes in each section. The structures are designed specifically for 0.650 and 0.250 THz, respectively. Each structure has a GaAs substrate with a ground plane; the 0.650 THz waveguide consists of layers of AlAs and GaAs, and the 0.250 THz waveguide consists of layers of polyamide and GaAs. The dimensions of the propagation layers at the design frequencies are on the order of 1/10th of a guided wavelength $\lambda_g(= 2\pi/\beta)$.

Plots of the phase constant versus frequency for the dominant and first higher order modes of the 0.650 THz structure are shown in Figure 2. The dominant mode has no cut-off frequency, while the first higher order mode cuts off at approximately 1.250 THz. Similar results hold for the 0.250 THz structure (Figure 5), where the first higher order mode cuts off at 0.480 THz.

Both the dominant and first higher order modes are TM_z-like modes, with dominant electric field components in the x-direction. The dominant mode is very

0.650THz Waveguide	0.250THz Waveguide
$h_1 = 0.036\lambda_g$ (13μm)	$h_1 = 0.032\lambda_g$ (32μm)
$h_2 = 0.048\lambda_g$ (17μm)	$h_2 = 0.049\lambda_g$ (49μm)
$h_3 = 0.122\lambda_g$ (43μm)	$h_3 = 0.116\lambda_g$ (116μm)
$w = 0.064\lambda_g$ (23μm)	$w = 0.091\lambda_g$ (90μm)
$\epsilon_1 = 12.85\epsilon_o$ (GaAs)	$\epsilon_1 = 12.85\epsilon_o$ (GaAs)
$\epsilon_2 = 10.0\epsilon_o$ (AlAs)	$\epsilon_2 = 3.0\epsilon_o$ (polyamide)

Table 1: Parameters (as described in Figure 1) for waveguide design examples.

similar to a typical microstrip mode, so that the aforementioned coupling to active devices via short lengths of microstrip is easily achievable.

The power density of the dominant mode of each waveguide is extremely well-confined in the respective propagation layers (Figures 4 and 7). The power is better concentrated in the propagation layer in the latter example due to the larger contrasts between permittivities in adjacent layers. The power confinement is expected to lead to low radiation losses at discontinuities.

After including losses in the dielectric layers, the attenuation constant α of the dominant mode of each structure was calculated as a function of frequency (Figures 3 and 6). Approximate attenuation constant values for the two examples are 0.19 dB/λ_g (400 dB/m) at 0.650 THz and 0.05 dB/λ_g (18 dB/m) at 0.250 THz, respectively. When the lossless and lossy cases are compared, the phase constants β do not differ significantly. The attenuation of the waveguides is also contrasted with the attenuation of the conventional rectangular waveguide and microstrip. The rectangular waveguides were designed with center frequencies comparable to the design frequencies of the monolithic waveguide examples, and the attenuation of the rectangular waveguides from sidewall conductor losses was calculated in accordance with [11]. The microstrip attenuation from both conductor and dielectric losses was calculated using the technique described in [12]. Due to the impracticality of microstrip at 0.650 THz, the microstrip is shown only in com-

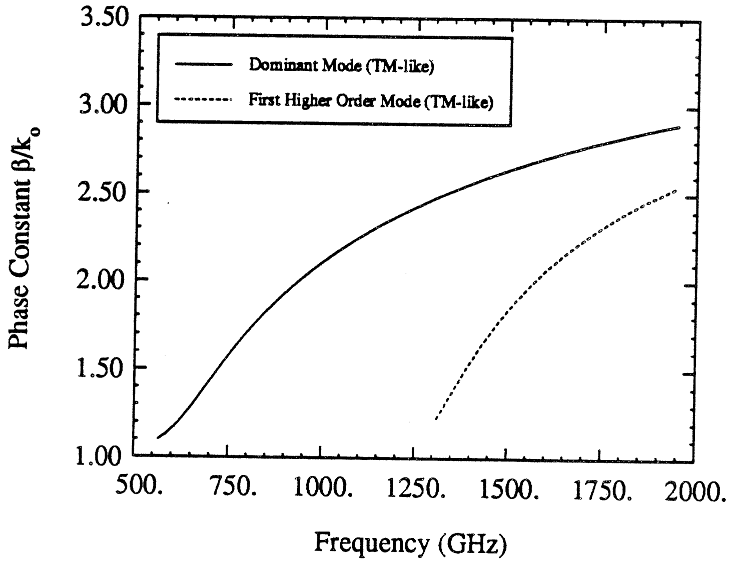

Figure 2: Phase constant of the 0.650 THz waveguide (Table 1).

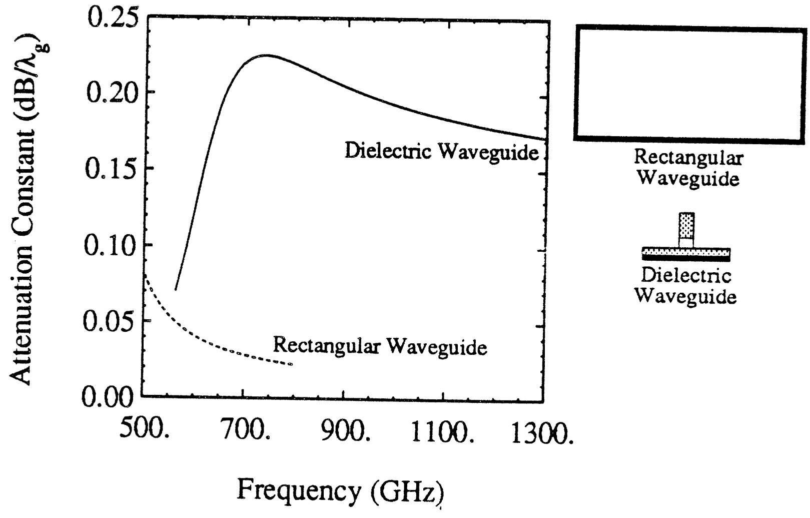

Figure 3: Attenuation constant of the 0.650 THz waveguide (Table 1, with $\epsilon_1 = 12.85(1.0 - j0.004)$ (GaAs) and $\epsilon_2 = 10.0(1.0 - j0.004)$ (AlAs)). Also shown is the attenuation of a 0.0367cm by 0.0184cm rectangular waveguide with gold sidewalls (conductivity = 4.1 x 10^5 S/cm). The two guiding structures are drawn in the same scale.

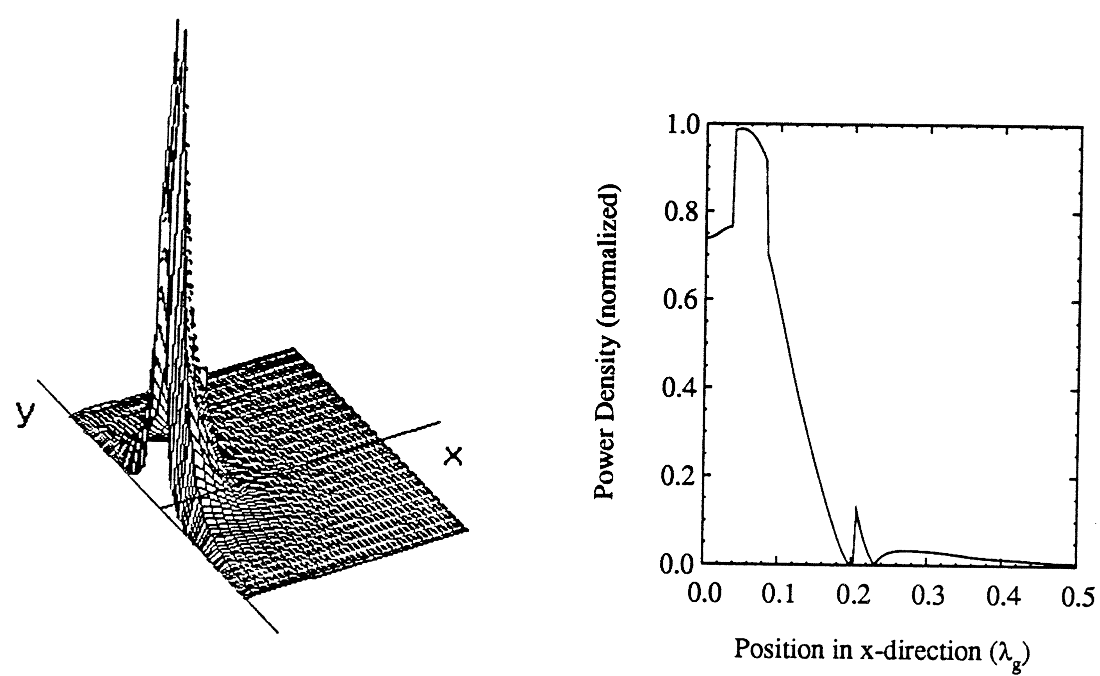

Figure 4: Power density in the 0.650 THz structure: At left, over the cross-section of the waveguide; at right, along the centerline of the waveguide.

parison to the 0.250 THz example. Although the new guiding structures do not have the extremely low attenuation exhibited by the rectangular waveguides, the new waveguides are smaller, and their monolithic nature allows for both easier construction of passive circuit elements (such as couplers, stubs, T-junctions, and inductors) and less arduous integration of active devices and device–waveguide transitions.

4 Characterization of Three-Dimensional Structures

The design of circuit elements requires a rigorous theoretical characterization of three-dimensional structures. Theoretical studies on geometrically simple optical and microwave dielectric waveguides have been presented in the past decade using approximate or numerical methods, such as the mode-matching technique described in the previous section. These methods have been exclusively applied to two-dimensional problems. Most of the existing numerical techniques perform a fine discretization of the cross-section introducing many unknowns and strong numerical instabilities. Consequently, an extension of these methods to three-dimensional problems introduces many practical limitations and requires special care [13].

Therefore, a novel method was developed to calculate the propagation characteristics of dielectric ridge structures in high frequency monolithic integrated

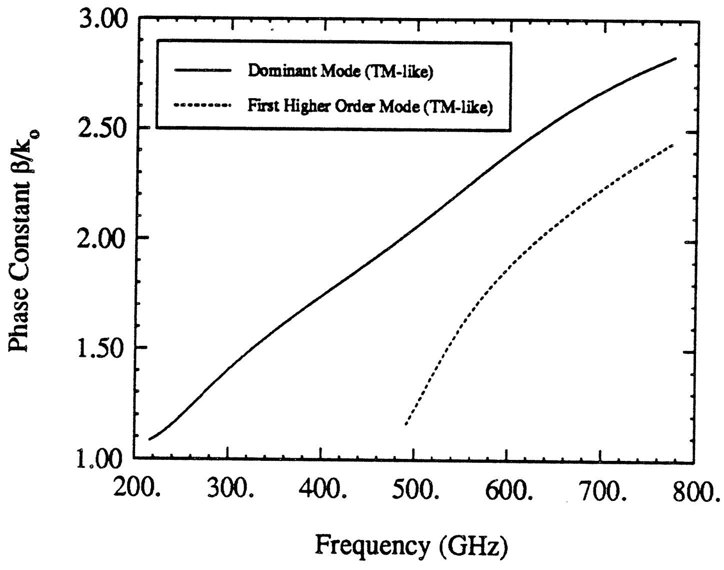

Figure 5: Phase constant of the 0.250 THz waveguide (Table 1).

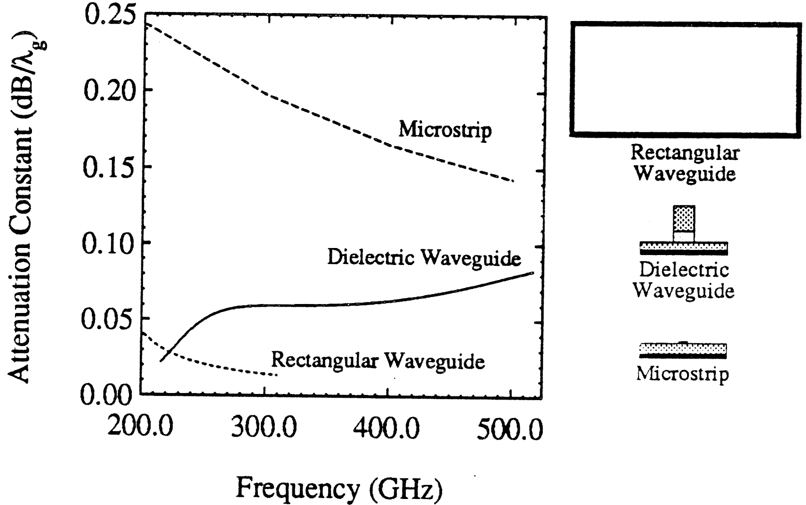

Figure 6: Attenuation constant of the 0.250 THz waveguide (Table 1, with $\epsilon_1 = 12.85(1.0 - j0.002)$ (GaAs) and $\epsilon_2 = 10.0(1.0 - j0.001)$ (polyamide)). Also shown is the attenuation of a 0.0955cm by 0.0478cm rectangular waveguide with gold sidewalls; and a 50Ω microstrip with substrate height = 100μm, strip width = 75μm, GaAs substrate ($\epsilon_r = 12.85(1.0 - j0.002)$), and strip conductivity = 3.33 x 10^5 S/cm. The three guiding structures are drawn in the same scale.

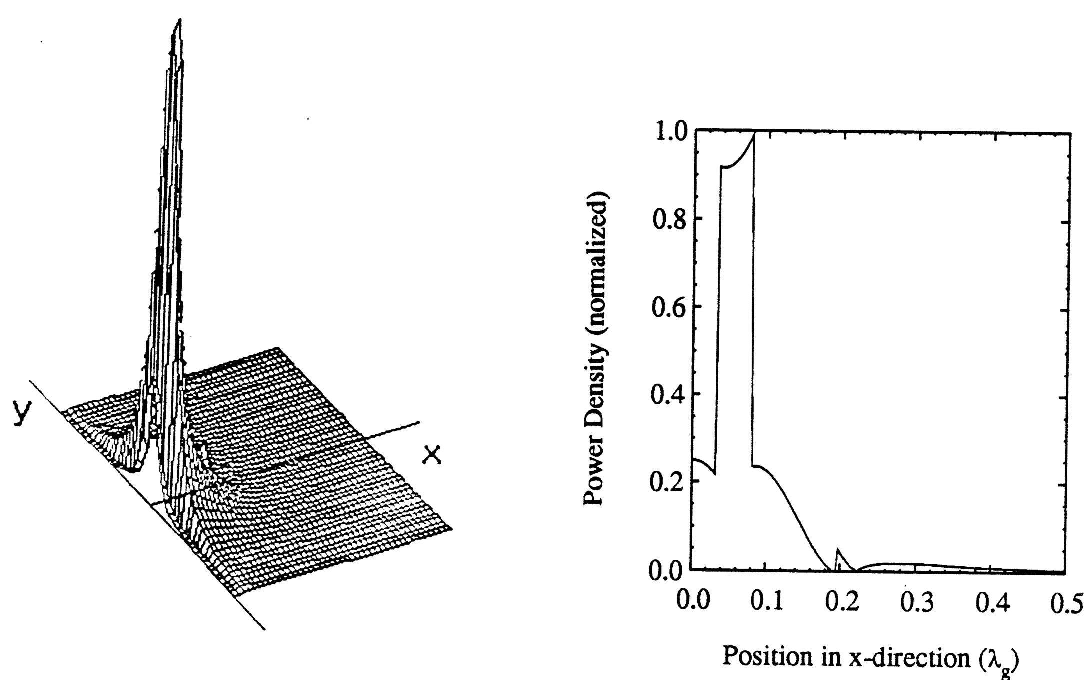

Figure 7: Power density in the 0.250 THz structure: At left, over the cross-section of the waveguide; at right, along the centerline of the waveguide.

circuits. The modified planar integral equation approach discussed here is a two-dimensional methodology which is rather unique in terms of combined accuracy and simplicity and has demonstrated excellent performance when applied to basic dielectric structures. The major advantage of this technique is that it can easily be extended to three dimensional problems without increasing the complexity of the solution.

For the sake of simplicity in the presentation of the technique and without loss of generality, we consider the dielectric structure shown in Figure 8 with non-magnetic materials and with the thickness $2h$ equal to a fraction of the dielectric wavelength and small compared to the strip width. Under these assumptions, the material of region (3) may be represented by an equivalent electric polarization current distribution occupying volume V_3. This volume polarization current is then replaced with an equivalent planar current sheet extending over the surface S_e. The equivalent surface current density radiates an electromagnetic field given by the well-known Pocklington integral equation involving the dyadic Green's function for the problem. In order to make the two boundary value problems presented in Figure 8 equivalent, the radiated field has to be identical to the original field on the surface S_3 surrounding volume V_3. Appropriate generalized boundary conditions are then enforced at the strip surfaces which provide a modified integral equation.

As a demonstration of the validity of the presented technique, the phase con-

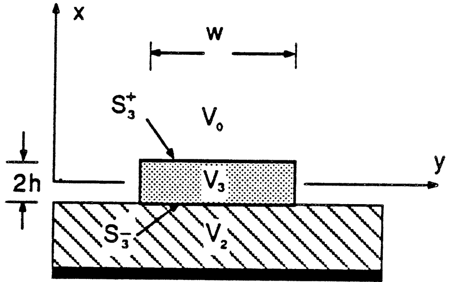

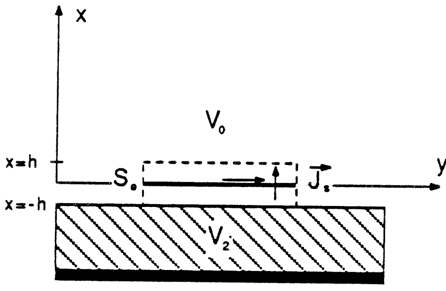

Figure 8: Equivalent polarization current.

stant of the dominant mode has been computed as a function of frequency and is shown in Figure 9. In this mode, the electric field component which is parallel to the dielectric interface (E_y) is a few orders of magnitude larger than the other two components. The theoretical results of this method show very good agreement with theoretical results derived from the classical 2-D modal analysis. As can be seen in Figure 9, the technique works very well even for electrically thick ridges ($w = 0.25\lambda_g$ at 120 GHz).

The planar integral equation technique can be further applied to study three-dimensional passive circuit elements such as power dividers, impedance transformers, bends and stubs. Such an extension is rather simple. With the replacement of the volume polarization current with an equivalent current of lower dimensionality, the original problem is simplified and can be treated as any other three-dimensional problem with unknown planar current densities. The development of this technique allows the design of novel monolithic circuits which can provide high performance at frequencies up to the terahertz region.

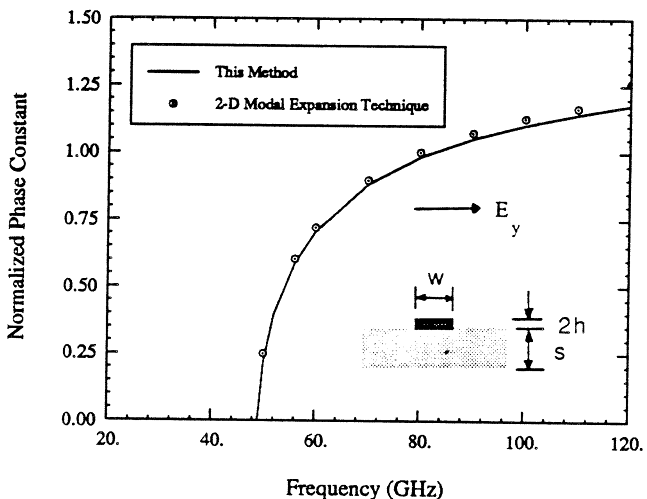

Figure 9: Comparison between the modified Green's function and the modal expansion method ($w = 0.5$ mm, $h = 62.5\ \mu$m, $s = 250\ \mu$m, $\epsilon_{strip} = 2$, $\epsilon_{substrate} = 12$).

5 Conclusion

Low-loss monolithic waveguides have been proposed for THz frequency applications and a modified planar integral equation approach has been developed for the analysis of monolithic structures using equivalent polarization currents. Future work in the development of these waveguides includes the optimization of the transmission lines. A wide range of designs is available; a different choice of materials, dimensions and layer arrangement could yield waveguides with better power confinement and lower losses than the examples which have been presented. In addition, three-dimensional structures will be characterized with the modified integral equation method. Experimental verification, beginning with large scale models and proceeding to actual structures, will also be performed. Eventually, the waveguides will be employed in THz monolithic circuits, such as low-loss an-

tenna feed networks.

Acknowledgements

This work was supported by the NASA Center for Space Terahertz Technology, and by the Army Research Office under the URI program, Contract No. DAAL03-87-K-0007.

References

[1] U. Crombach, "Analysis of Single and Coupled Rectangular Dielectric Waveguides," *IEEE Trans. Microwave Theory Tech.*, vol. MTT-29, pp. 870–4, September, 1981.

[2] R. Mittra, Y. Hou and V. Jamnejad, "Analysis of Open Dielectric Waveguides Using Mode-Matching Techniques and Variational Methods," *IEEE Trans. Microwave Theory Tech.*, vol. MTT-28, pp. 36–43, January, 1980.

[3] K. Solbach and I. Wolff, "The Electromagnetic Fields and The Phase Constants of Dielectric Image Lines," *IEEE Trans. Microwave Theory Tech.*, vol. MTT-26, pp. 266–74, April, 1978.

[4] W. V. McLevige, R. Mittra, and T. Itoh, "New Waveguide Structures for Millimeter-Wave and Optical Integrated Circuits," *IEEE Trans. Microwave Theory Tech.*, vol. MTT-23, pp. 788–94, October, 1975.

[5] K. Ogusu, "Numerical Analysis of the Rectangular Dielectric Waveguide and Its Modifications," *IEEE Trans. Microwave Theory Tech.*, vol. MTT-25, pp. 874–85, November, 1977.

[6] T. Itoh, "Inverted Strip Dielectric Waveguide for Millimeter-Wave Integrated Circuits," *IEEE Trans. Microwave Theory Tech.*, vol. MTT-24, pp. 821–7, November, 1980.

[7] T. Itoh and B. Adelseck, "Trapped Image Guide for Millimeter-Wave Circuits," *IEEE Trans. Microwave Theory Tech.*, vol. MTT-28, pp. 1433–6, December, 1980.

[8] R. Mittra and S. W. Lee, *Analytical Techniques in the Theory of Guided Waves.* New York: McGraw-Hill, 1961.

[9] S. Peng and A. A. Oliner, "Guidance and Leakage Properties of a Class of Open Dielectric Waveguides: Part I—Mathematical Formulations," *IEEE Trans. Microwave Theory Tech.*, vol. MTT-29, pp. 843–55, September, 1981.

[10] A. A. Oliner and S. Peng, "Guidance and Leakage Properties of a Class of Open Dielectric Waveguides: Part II—New Physical Effects," *IEEE Trans. Microwave Theory Tech.*, vol. MTT-29, pp. 855–69, September, 1981.

[11] C. A. Balanis, *Advanced Engineering Electromagnetics.* New York: John Wiley & Sons, 1989.

[12] T. E. van Deventer, P. B. Katehi, and A. Cangellaris, "An Integral Equation Method for the Evaluation of Conductor and Dielectric Losses in High Frequency Interconnects," *IEEE Trans. Microwave Theory Tech.*, vol. MTT-37, pp. 1964–72, December, 1989.

[13] B.J. Rubin, "Full-Wave Analysis of Waveguides involving Finite-Size Dielectric Regions," *IEEE MTT-International Symposium Digest*, Dallas, pp. 705-708, May 1990.

Improved Superconductive Mixer Coupling: Sub-millimeter Performance without Sub-micron Lithography

J. A. Carpenter, E. R. Arambula, E. B. Guillory, A. D. Smith

TRW Space & Technology Group

Redondo Beach, CA 90278

Abstract

Superconductor-Insulator-Superconductor (SIS) mixers stand as the most sensitive heterodyne detectors of millimeter and sub-millimeter wave radiation. Nevertheless, scientists attempting to apply SIS mixers to sub-millimeter wavelengths have been forced to cope with limited dynamic range, critical tuning of junction capacitance, and difficult lithographic requirements.

This paper describes a novel RF-coupling scheme, in which an on-chip impedance transformer matches large, low impedance junctions to the high impedance of waveguide and free space. By operating low impedance junctions, the system dynamic range improves by 15 dB, while junction tuning become significantly easier.

A 100 GHz demonstration of the transformer-matched SIS mixer has been built, and shows wide bandwidth and large (35 dB) dynamic range. Used as a direct detector, the SIS junction shows full quantum-limited response and wide (8 GHz at 91 GHz center frequency) instantaneous detection bandwidth.

Introduction

Superconductive (SIS) mixers have proven to be ideally suited to radioastronomical applications from microwave to submillimeter wavelengths. The extreme nonlinearity of the superconductive tunnel junction current-voltage characteristics gives rise to high conversion efficiency, sometimes in excess of 0 dB, with added mixer noise approaching the quantum limit, $T_M = hf/k_B$. In

addition, these devices require mere nanowatts of local oscillator (LO) power, a key advantage in the LO-starved submillimeter environment.

Despite their advantages over semiconductor mixers, SIS mixers have two drawbacks over semiconductor mixers - limited saturation power and large capacitance. While the power limitation is not a severe constraint for radioastronomy, in which both signals and background noise levels are quite small, saturation power and associated dynamic range are key considerations several terrestrial applications including communications and imaging.

Limited saturation power is a direct result from the quantum mechanical nature of SIS mixers. SIS mixing is essentially a photon-assisted tunneling activity. When biased within a photon voltage (hf/e) below the junction gap voltage (Δ/e), conservation of energy dictates that absorption of a millimeterwave photon can induce an electron to tunnel across the junction barrier. The conversion of millimeterwave energy to junction current defines the mixing process. Optimum mixer gain requires that the operating voltage be held within a narrow range on a photon-assisted tunneling step. As a result, the SIS mixer is an output voltage-limited device. The resultant input saturation power, P_{sig}, for a single junction mixer is given by[1]:

$$P_{sig} \leq (0.1\ hf/e)^2/GR_{Dyn}, \qquad (1)$$

where G is the mixer conversion efficiency, R_{Dyn} is the loaded output resistance of the mixer, f is the frequency, and h and e are the conventional physical constants. Experiments at Berkeley confirmed this theoretical prediction, with measured saturation of only 1.5 pW for a 36 GHz mixer with gain. Thus saturation power limits single junction SIS mixers to narrowband, small signal detection with quiet backgrounds.

At the same time that single junctions were first being developed, series arrays of junctions were being used both to increase the saturation power and also to ease lithographic requirements in mixer fabrication. By going to a series array of N identical junctions[2], the saturation power of the SIS mixer increases to[3]

$$P_{sig} \le N^2 (0.1\ hf/e)^2/GR_{Dyn}. \qquad (2)$$

This approach is illustrated in Table 1, line 1. In scaling the array, the total junction impedance is held fixed, and the individual junction resistances and areas are adjusted accordingly. Junction current density is held fixed.

Scaling to large arrays (with large saturation power) is complicated by junction capacitance. The relatively large capacitance of SIS junctions requires special care to efficiently couple power to the mixer elements. Researchers have attempted increasingly sophisticated technical approaches to avoid mixer saturation while maintaining the RF match necessary for maximum mixer sensitivity. Originally, mixer designs included single[4,5] or series-array[6] tunnel junctions(See Table 1, line 1.) These designs relied on external waveguide mechanical tuning elements, such as backshorts and tuning stubs, to inductively compensate for junction capacitance and other parasitic susceptances. This approach has achieved large gain and low noise, but only over a highly restricted bandwidth.

By adding an integrated tuning element, researchers were able to extend the instantaneous bandwidth while maintaining the gain and noise requirement necessary for sensitive mixing[7,8]. Table 1, line 2 diagrams this approach, with an array of junctions shown shunted by an on-chip tuning element such as an inductive stub. For millimeter wavelengths, the aggregate tuning approach limits the number of junctions in the array. Parasitic inductance along the series array of junctions, along the the capacitance of the individual junctions, gives rise to a LC resonance which prevents matching the waveguide signals.

Recently, workers have circumvented the LC resonance limitation by including a separate tuning structure at each mixer junction. This approach, shown in Table 1, line 3, can work up to much higher frequencies and much larger N than the other approaches. One difficulty in the separately tuned approach involves design tolerances. In order for the series bias current to produce identical operating voltage on each of the junctions, both the unpumped current-voltage characteristics and the rf embedding impedance must be identical for each of the junctions. The matching tolerance is

quite tight, especially for high gain mixers, which have large dynamic resistance at the mixer operating point.

A fourth coupling scheme has been proposed and demonstrated using parallel and series array feeds. By using RF pass and RF block components, the current paths for IF and RF radiation can be completely separated. The approach of Ermakov, et al. [9],

In this paper, we propose and report results from a different type of SIS array. We overcome both fabrication and electrical difficulties by integrating an RF-matching transformer directly on the SIS chip.

	Circuit schematic	Circuit description
1		Single or array of mixers with no integrated tuning element
2	B	Series array with aggregate tuning element
3	B B B	Series array with dedicated, integrated tuning
4	DC, IF LO, Sig	Rf series, IF parallel
5	Impedance-Matching Transformer B B	2-element tuned array with impedance matching transformer

Table 1. SIS mixer chip architectures

Mixer Chip Design

Our mixer design procedure began with the selection of a mounting fixture. Raisenen, et al., have thoroughly modeled[10] and tested a waveguide mount for millimeter wave mixing. The mixer elements sits in the E-field orientation across a full-height waveguide. A mechanically adjustable backshort provides for broadband impedance matching.

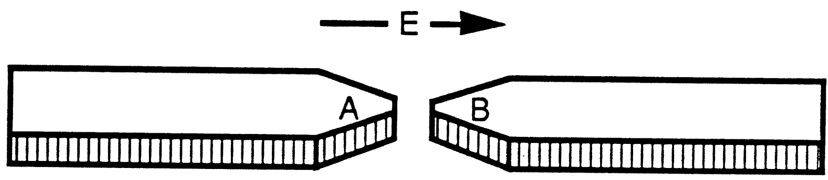

Figure 2. Electrode geometry. The E-field direction of the waveguide is shown.

The mixer element design must approximately match the impedance presented by the mixer block. Based upon the model measurements[9] a mixer element placed near the center of the waveguide and attached to RF-choked leads sees an embedding impedance of 60-100 Ω. Figure 2 shows the lead structure near the center of the waveguide. We maintained symmetry in our design, mirroring circuit patterns about the bisection plane.

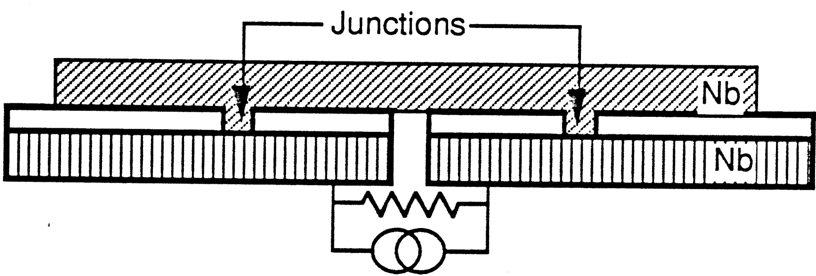

Figure 3. Mixer chip cross-sectional view. The lower niobium corresponds to the electrodes in Fig. 2. Dielectric layers are shown in white. Waveguide signals appear as the illustrated Norton equivalent across the electrodes.

We designed a microstrip transmission line transformer[11] to lower the source impedance seen by the mixer elements. The quarter wavelength transmission line extends from the electrode edge to the mixer junction, using the choke structure metallization as a groundplane. (See Fig. 3.) Each 8 Ω transmission line transforms the 30-50 Ω half-source impedance down to 1-2 Ω at the SIS tunnel junction.

A separate stub was added to tune out junction capacitance at the signal frequency. A series combination of high impedance line and quarter wavelength, open-ended low impedance line acted as a broadband, dc-blocking inductive element.

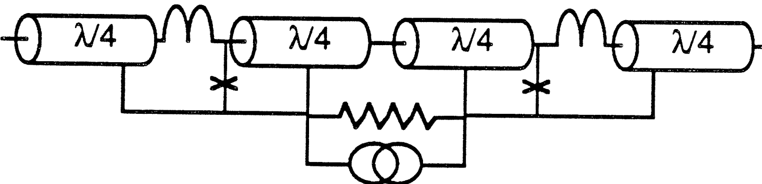

Figure 4. Electrical schematic of mixer chip. The central λ/4 microstrip transmission lines act as impedance transformers. The outside, open-ended λ/4 microstrip act as RF shorts. The inductors act to tune out junction capacitance at the signal frequency.

The transformer and susceptive matching network were implemented using the scheme shown in Fig. 4. All components, with the exception of the source and the junctions themselves, consisted of superconducting microstrip. The impedances of the microstrip were chosen to maximize mixer bandwidth. The quarterwave stubs were chosen as low impedance line, with short, high inductive microstrip directly connnecting to the junctions. We chose the impedance of the quarterwave transformers coupling the junctions to the antenna vertex to have impedances near the geometrical mean of the junction impedance and the antenna impedance.

The electric field distribribution is shown in Fig. 5. The tapered probe structure serves to concentrate the waveguide electric fields near the vertex. The vertex also serves as the launching point for microstrip modes propagating toward the tunnel junctions. Because the microstrip

fields tend to be highest near the vertex, while currents are large near the junctions.

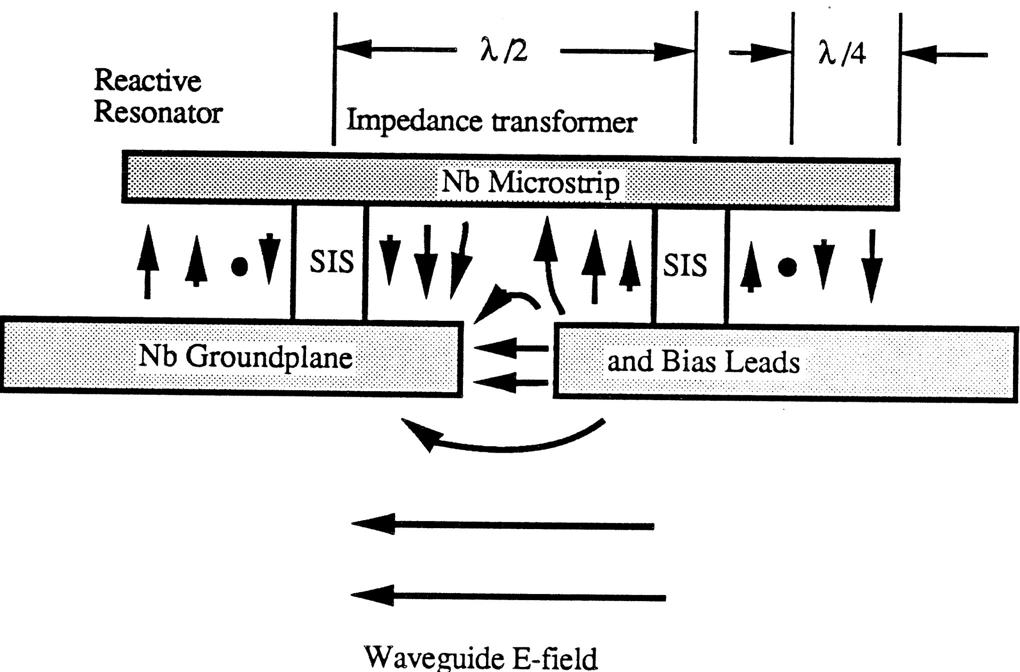

Figure 5. Electric fields for millimeterwave radiation. The vertex represents a high impedance point for the circuit, while the junction location is chosen as relatively low impedance.

Fabrication

The SIS mixers were prepared by depositing a trilayer structure of Nb/Al-AlO_x/Nb, onto a 5-mil quartz substrate. The base electrode of the trilayer (2000 Å), an aluminum layer, and the counter electrode (350 Å) were sputtered sequentially in a single vacuum chamber in an *in situ* process.[12] Immediately after the aluminum deposition, the samples were exposed to oxygen in a side-chamber of the deposition system in order to form the oxide tunneling barrier.

We fabricated the mixers using a 4-mask process. The junctions were defined by the selective niobium anodization process (SNAP)[13] with junction areas of 50 to 150 μm^2. These junction areas were considerably larger than the 1 - 10 μm^2 junction areas typical of SIS mixers. Isolation of each junction was achieved through a trilayer etch. In order to maintain tight tolerance of the

CF4 + 4% O2 plasma; the thin Al-AlOx layer was removed using a selective wet chemical etch. Finally, the Nb base electrode was removed again by RIE with the same plasma as the counter electrode. We patterned a layer of SiO on top of the junctions with a liftoff process. This mask allows a contact window for the final wiring. The wiring layer for the series connection of junctions and tuning structures was defined by a final RIE step.

SIS conversion efficiency and mixer noise depend strongly on the sub-gap leakage and abruptness of the current rise at $2\Delta/e$. The aluminum-based tunneling barrier plays a crucial role in determining the current-voltage characteristics of the SIS junctions. We therefore studied the aluminum thickness with the objective of optimizing junction characteristics essential for mixing.

In a series of experiments, we created a series of Nb/Al-AlO_x/Nb trilayers with aluminum thicknesses varying from 30 to 200 Å. A constant aluminum sputtering rate of 1 Å/sec was maintained with varying deposition times to achieve the range of aluminum thicknesses. We found the optimum aluminum layer thickness to be 50 Å. Thinner aluminum barriers produce leakier junctions. Thicker aluminum barriers reduced the abruptness of the $2\Delta/e$ current rise.

We also found good thermal contact to a thermal sink is essential. Trilayers with good thermal contact to the cooled wafer substrate holder displayed distinctly sharper current-voltage characteristics than those with poor contact. Device yield was improved through the use of heat sink paper, which minimizes substrate heating during deposition.

Results

The mixer chips were mounted in the E-field direction of the full-height waveguide mount. No special electrostatic handling requirements were needed to perform the experiment, and no junction burn-outs were observed during testing. We attribute this reliability to the ruggedness of niobium junctions and the large junction areas (>50 square microns) made possible by the transformer

approach. We observed 3 dB responsivity bandwidths up to 8 GHz. These rf bandwidths are within a factor of 2 of the fundamental bandwidth limit imposed by junction capacitance.

Our test procedure began with direct detection measurements. This allowed us to optimize the backshort position for best signal coupling and also to measure the rf bandwidth. The quantum limit for responsivity at 94 GHz is 2000 A/W if each photon enables one electron to flow across a junction. If two junction transits are required for current flow, as is the case in our N=2 geometry, the quantum limit reduces to 1000 A/W. The measured responsivities (see Fig. 5) were within experimental uncertainty of the latter quantum limit. The high responsivities observed indicate a good impedance match of the mixer circuit to the wave guide mount.

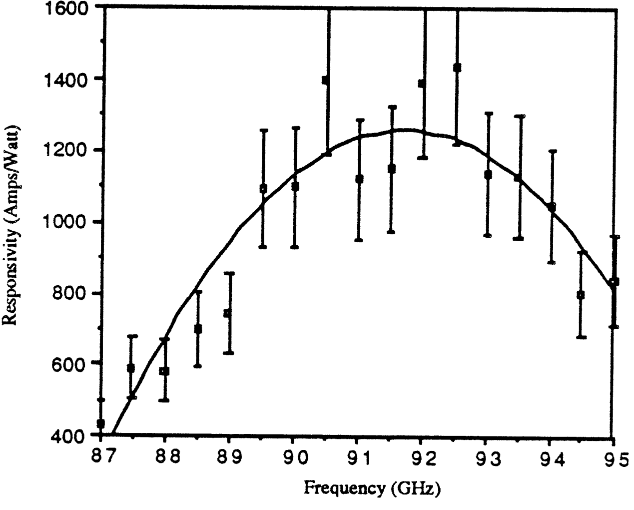

Figure 5. The measured responsivities of the mixer indicates good matching between the waveguide and the mixer.

When operated as a mixer, our devices showed excellent performance. We observed negative resistance which indicates infinite *available* gain. Actual coupled gain (power delivered to the IF amplifier normalized to signal input power at the mixer block) was measured to +13 $\pm$1 dB. Useful mixing over 0.7 GHz was observed. Plotted in Figure 6 is the LO response showing a mixer with +10 dB gain. We attribute the wide swings in conversion efficiency to reflections and standing waves in the cable leading from our mixer to our room temperature IF amplifier. Current test apparatus limitations have prevented us from making accurate receiver noise temperature measurements.

The mixer instantaneous bandwidth is significantly narrower than the corresponding direct detector bandwidth. The reason appears simply related to the basic operation of the SIS mixer. While the direct detector bandwidth is limited by an $R_{rf}C$ time, the mixer bandwidth is additionally limited by a IF bandwidth time constant of $R_{dc}C$. Since the dynamic resistance, R_{dc}, of the pumped junction is always significantly larger than the RF junction impedance, a stricter bandwidth limit will always appear for SIS junctions. This observation is consistent with our data.

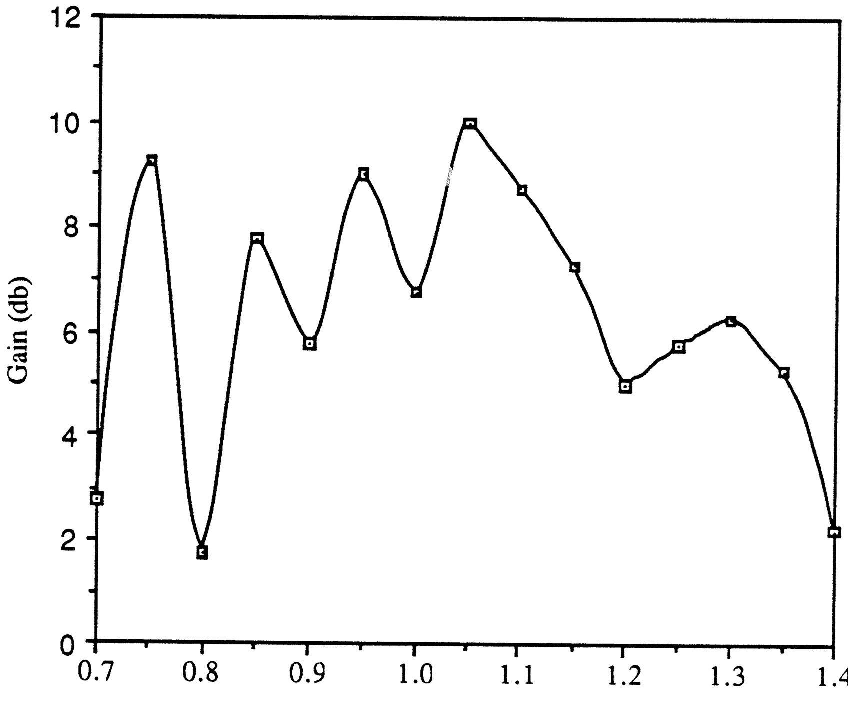

Figure 6. IF response showing mixer gain.

The power handling capacity of the transformer mixer is shown in Fig. 7. The particular mixer demonstrates over 30 dB of linear response, limited by our measurement capabilities. As shown the mixer is of low gain operating with -4 dB conversion efficiency. Nevertheless the enhancement in output power over conventional SIS mixers is apparent. Whereas conventional single junction 94 GHz mixers tend to saturate at -75 dBm output levels, our mixer delivered -55 dBm with no appreciable nonlinearity. Of the 20 dB power enhancement, we attribute 6 dB to the N=2 geometry, and 14 dB to impedance reduction.

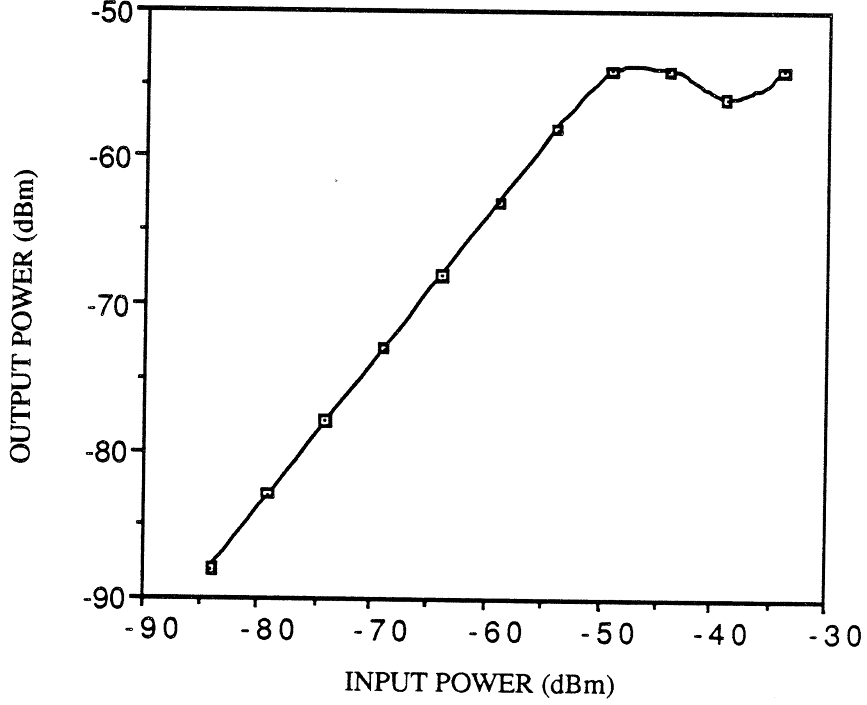

Figure 7. Saturation power of mixer with conversion gain.

Conclusions

We have developed a new type of SIS waveguide mixer circuit, using an integrated input transformer. The new circuit enhances the saturation power of the SIS mixer by 20 dB over

provides good rf match over wide bandwidths. In addition, the SIS mixer's large junction design reduces device burn-out and eases fabrication. The 20 dB increase in saturation power will allow the application of the mixer to communication and radar systems.

Acknowledgements

It is our pleasure to acknowledge important useful discussions with H. Chan, C. Jackson, W. R. McGrath and A. Silver. A. Raisanen supplied the mixer block design and T. Buttgenbach was responsible for the RF choke designs. M. J. Lewis and the TRW LTS foundry group were instrumental in mask production and wafer fabrication. Finally, summer hire R. Seed measured portions of the data.

References

1 A. D. Smith and P. L. Richards, "Analytic Solutions to Superconductor-Insulator-Superconductor Quantum Mixer Theory," J. Appl. Phys. 53, 3806-3812, 1982.

2 S. Rudner and T. Claeson, Appl. Phys. Lett. 34, 711 (1979).

3 S. Rudner and T. Claeson, Appl. Phys. Lett. 34, 711 (1979).

4 G. J. Dolan, T. G. Phillips, D. P. Woody, "Low-noise 115–GHz mixing in superconducting oxide-barrier tunnel junctions", Appl. Phys. Lett. 34, 347-349 (1979).

5 W. R. McGrath, P. L. Richards, A. D. Smith, H. van Kempen, R. A Batchelor, D. E. Prober, and P. Santhanam, Appl. Phys. Lett. 39, 655-658 (1981).

6 S. Rudner, M. J. Feldman, E. Kollberg, and T. Claeson, IEEE Trans. Magn. MAG-17, 690-693 (1981).

7 Q. Hu, C. A. Mears, P. L. Richards, and F. L. Lloyd, "Measurement of integrated tuning elements for SIS mixers with a Fourier transform spectrometer", Int. J. Infrared Millim. Waves 9, 303-320 (1988).

8 S.-K. Pan, A. R. Kerr, M. J. Feldman, A. W. Kleinsasser, J. Stasiak, R. L. Sandstrom, and W. J. Gallagher, "An SIS mixer for 85-116 GHz using inductively shunted edge-junctions",1988 IEEE MTT International Microwave Symposium Digest, 465-468 (1988).

9 An. B. Ermakov, V. P. Koshelets, S. A. Kovtonyuk, and S. V. Shitov, "Parallel Biased SIS-Arrays for MM Wave Mixers, to be published in ASC '90 proceedings.

10 A.V. Raisanen, W.R. McGrath, D.G. Crete, P.L. Richards, "Scaled Model Measurements of Embedding Impedances for SIS Waveguide Mixers", International Journal of Infrared and Millimeter Waves, Vol.6, No.12,1169-1189,1985.

11 V. Yu. Belitsky, I. L. Serpuchenko, M. A. Tarasov, and A. N. Vystavkin, "MM Waves Detection Using Integrated Structure with SIS Junction, Stripline Transformer and Spiral Antenna", Extended Abstracts of 1989 International Superconductivity Electronics Conference (ISEC '89), 179-182, (1989).

12 J. M. Murduck, J. Porter, W. Dozier, R. Sandell, J. Burch, J. Bulman, C. Dang, L. Lee, H. Chan, R. W. Simon, and A. H. Silver, "Niobium trilayer Process for Superconducting Circuits", IEEE Trans. Magn. MAG-25, 1139-1142, (1989).

13 H. Kroger, L. N. Smith, D. W. Jillie, "Selective Niobium Anodization Process for Fabricating Josephson Tunnel Junctions,", Appl. Phys. Lett. 39, 280-282, 1981.

D-band Vector Network Analyzer*

James Steimel Jr. and Jack East
Center for High Frequency Microelectronics
Dept. of Electrical Engineering and Computer Science
University of Michigan, Ann Arbor, Michigan

Abstract

This paper will describe the design, calibration, and performance of a 2 port vector network analyzer designed to operate between 140–160 GHz. Single frequency measurements can be made over this entire band. Signal level problems require broadband measurements is two ranges between 140 and 150 GHz and between 150 and 160 GHz. An external computer is used for the purpose of calculating the calibration coefficients of the network analyzer. The system can be calibrated to a systematic error of 1.5 dB with the limitations in the accuracy of the calibration due to loss in the system, limitations on the calibration standards, and reflections in the system. Problems in the calibration and software computer control will be described and several representative one port measurements results between 140 and 150 GHz will be presented.

1. Introduction

Vector measurement of devices and circuits is an important design and analysis tool at microwave frequencies. Direct probing of active devices on wafer and measurements on circuits using automatic vector network analyzers has reduced the time and greatly improved the accuracy of these measurements. Commercial systems are available from Hewlett Packard [1] and Wiltron [2] to 50 GHz for coaxial systems and to 110 GHz in waveguide. There are a variety of uses of these measurement systems at higher frequencies. Modern transistors have predicted unity current gain and

*This work was supported by the Army Research Office under contract DAAL-03-87-K-0007 (University Research Initiative Program).

power gain frequencies of several hundred GHz. However, these frequencies are based on extrapolated predictions based on measured data at lower frequencies. Recently Matloubian [3] published data that questioned the usual 6 dB per octave rolloff used in transistor frequency measurement. With higher frequency measurement systems available, S parameters could be obtained directly at higher frequencies. Transistor models could be confirmed, or more accurate models could be developed to improve device understanding and millimeter-wave circuit accuracy.

A second application of higher frequency vector measurement systems is the direct measurement of embedding circuits. Present millimeter wave mixer or harmonic multiplier circuits are usually designed as scale models, and measurements are obtained at lower freqüencies and scaled. With the aid of precise millimeter-wave standards, a variety of embedding circuit may be characterized. Each of the standards would be measured by the network analyzer, and the program used for calibration would calculate the de-embedding parameters. These parameters can also be used to characterize the embedding structure whether it is some waveguide to microstrip transition or an antenna array.

A third area of interest is in the physics of semiconductor materials. The frequency range above 100 GHz corresponds to typical scattering, momentum and energy relaxation time in semiconductor materials. These time constants can have a large effect on the terminal characteristics of devices above 100 GHz [4]. Direct measurement of the vector impedance of semiconductor samples over a range of frequencies would provide useful information about the basic properties and time constant of materials.

There are other network analyzer systems currently on the market which offer measurement to 110 GHz. Hewlett Packard offers test sets for its HP8510 network analyzer which allow measurements up to 110 GHz. A W band two port system would cost approximately $80K - $100K in additional to the cost of the basic network analyzer. The purpose of this paper is to describe a low cost two port frequency extender for an network analyzer for operation between 140 and 160 GHz. The design and operation of the extender is described in the next section. Calibration techniques and limitations

and some one port measurement results are discussed in section 3. A brief summary and proposed additional measurements are given in the last section.

2. Design

The D-band frequency extender uses frequency translation to allow measurements in the 140 - 160 GHz frequency range with an HP 8510 network analyzer and a HP 8515 test set. Most of the display functions of the 8510 system are used in the translated frequency range. The internal error correction can be used with error vectors obtained under external computer control. The extender is small enough to fit in front of an 8510 test set. The unit was fabricated by Millitech Corp. A block diagram of the measurement system is shown in figure 1. The extender is connected to the two measurement ports of the 8515 test set. This test set acts as an IF receiver, measuring ratios of reflected, transmitted and incident signals at frequencies between 6 and 26 GHz. The extender uses a mixer in each signal path for both up and down conversion. The mixers have a local oscillator frequency of 134 GHz. This is provided by a voltage tunable Gunn diode operating at 67 GHz and a doubler. A portion of the 67 GHz signal is sampled with a direction coupler and harmonic mixer and used to source lock the Gunn. The counter has an upper frequency limit of 100 GHz, preventing direct use of a 134 GHz source. The 134 GHz signal is split with a 3 Db hybrid and drives the two mixers through 10dB coupler couplers. The 134 GHz pump frequency mixes with the signal from the test set producing the 140 to 160 test signal. The 134 GHz local oscillator and the lower sideband image frequency are also present. Those frequencies are trapped inside the measurement system by high pass filters at the two test ports. The return signal from the measurement passes through system in the opposite direction, is mixed down to the 6–26 GHz frequency and returns to the 8510 test set. The image frequency will reflect off the high pass filter, and also appear as the same frequency as the test signal at the 8510 measurement port. The effect of the image frequency can be partially removed with careful calibration. The calibration procedure is described in the next section.

3. Calibration Procedure and Results

The 8510 network analyzer has internal software for error correction of measured data. Error correction involves measurements on known standards and calculation of error coefficients. The process is under internal software control in normal 8510 operation. Once these error coefficients are determined, error corrected data can be displayed. Typical waveguide standards are combinations of loads, shorts and offset shorts. A problem occurs with the D band system. The internal software uses a frequency dependent waveguide dispersion equation. Since the measurement frequency is shifted by 134 GHz, the resulting internal phase information is incorrect. To overcome this problem three D-band standards are measured and their uncorrected scattering parameters are uploaded to an IBM-XT computer using an IEEE-488 interface bus. A Pascal program was written which measures three standards: a matched load, a short, and an offset short. The error coefficients are calculated by the XT and downloaded back to the 8510 as a calibration set. Calibration problems, results and measured data are described in the next section.

The first attempt at one port calibration used a waveguide load, a flush short and an offset short. Since no calibration standards are commercially available above W band, the standards were machined internally. A resulting corrected measurement is shown in figure 2. There are two sources of error in this measurement. The first is the ripple in the data across frequency. Part of this ripple is due to a design problem with the system. In theory, the effect of the image frequency in the measurement system can be corrected by calibration. This is true over a narrow frequency range. However, there is a resonance in the system as the signal and image frequency sweep corresponding to multiple half wavelength distances between the mixer and the high pass filter at the image frequency. This effect was confirmed by changing the Gunn diode frequency by a small amount and noting a corresponding change in the resonance. A future design will have image trapped mixers. A second problem is the quality of the standards. The D band tunable load has a nominal return loss of approximately 25 Db. The waveguide offset short was machined out of a piece of brass and the guide had quarter

rounded corners limited by the end mill diameter. A second set of standards used a standard gain horn as a load. Although the nominal VSWR of the horn was higher than the load, the actual reflection coefficient was better. A tunable short was used for the short and offset short standards. A resulting corrected measurement is shown in figure 3. The ripple in the data is approximately 1.5 Db. Similar ripple information for HP waveguide systems is shown in figure 4 [the HP datapoints are from page 21 of reference 5]. The system was next used to measure some simple D band components. The return loss of a variable attenuator terminated with a short is shown in figure 5. For attenuation settings to approximately 10 - 15 Db, the return loss is the two way insertion loss of the attenuator. At higher attenuation levels, the return loss is limited by the input VSWR of the attenuator. Figure 6 shows the return loss of a standard gain horn radiating onto a metal plate at a distance of several inches.

4. Conclusions

The paper has discussed the design, calibration and performance of a vector network analyzer operating in D band. The system has a calibrated one port system ripple of 1.5 Db and a phase ripple of about 5 degrees. Preliminary results show that the system should be useful for device characterization, circuit measurements and a range of studies on semiconductor materials.

Acknowledgments: The initial design for this system was based on unpublished work and conversations with Dr. Dean Peterson. The unit was fabricated at Millitech Corp. with the help of Rich Chedester.

References

1. 1991 Hewlett Packard Test and Measurement Calalog

2. 1991 Wiltron Product Calatog

3. "Wide-Band Millimeter Wave Characterization of Sub-0.2 Micrometer Gate-Length AlInAs/GaInAs HEMT'S," by M. Matloubian, S.E. Rosenbaum, H.R. Fetterman and P.T. Greiling, *IEEE Microwave and Guided Wave Letters*, vol. 1, no. 2, i pp. 32–34, Feb., 1991.

4. "Current Saturation in Submillimeter Wave Varactors," by E. Kollberg, T. Tolmunen, M. Frerking and J. East, to be presented at this conference.

5. System manual for HP8510 A network analyzer system for R,Q,U,V and W bands

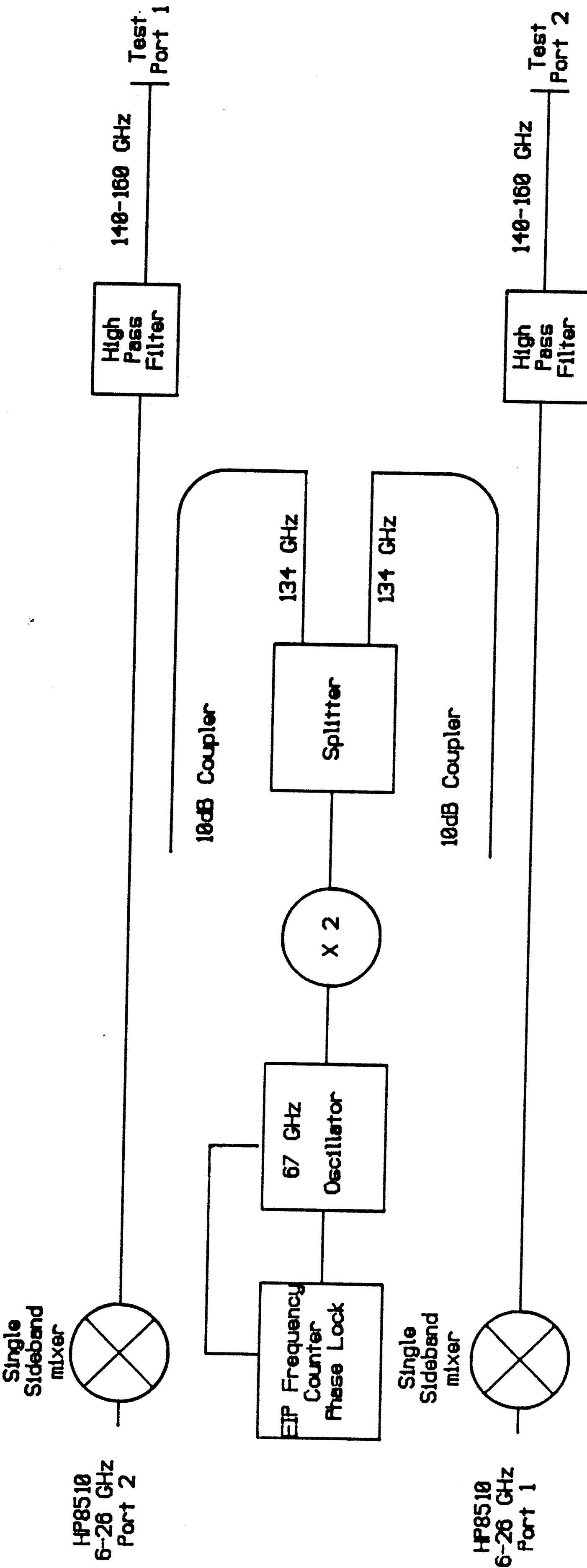

Figure 1. D-Band system Block Diagram

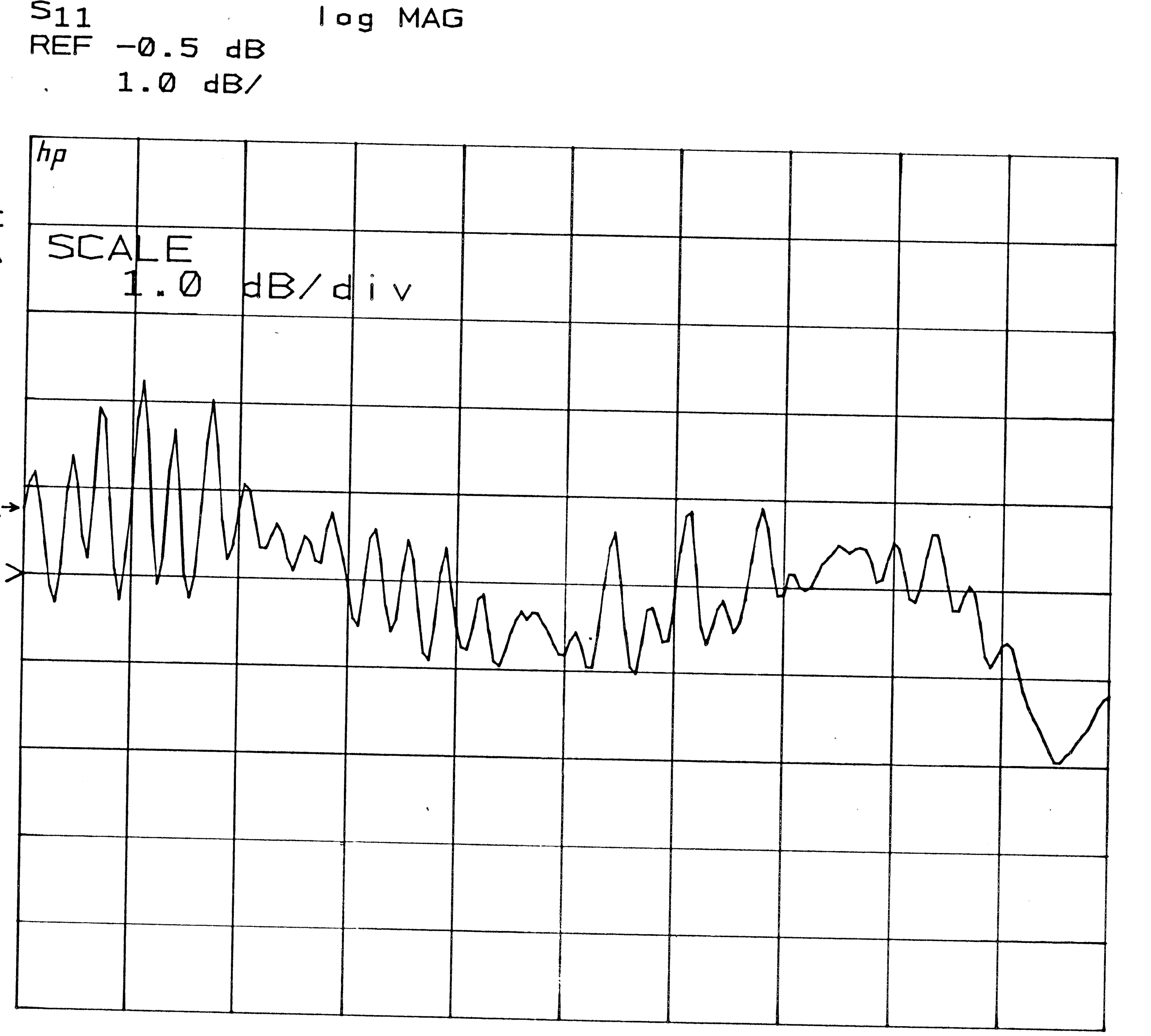

Figure 2. Phase and return loss of tunable waveguide short (140-150 GHz), cal set 1.

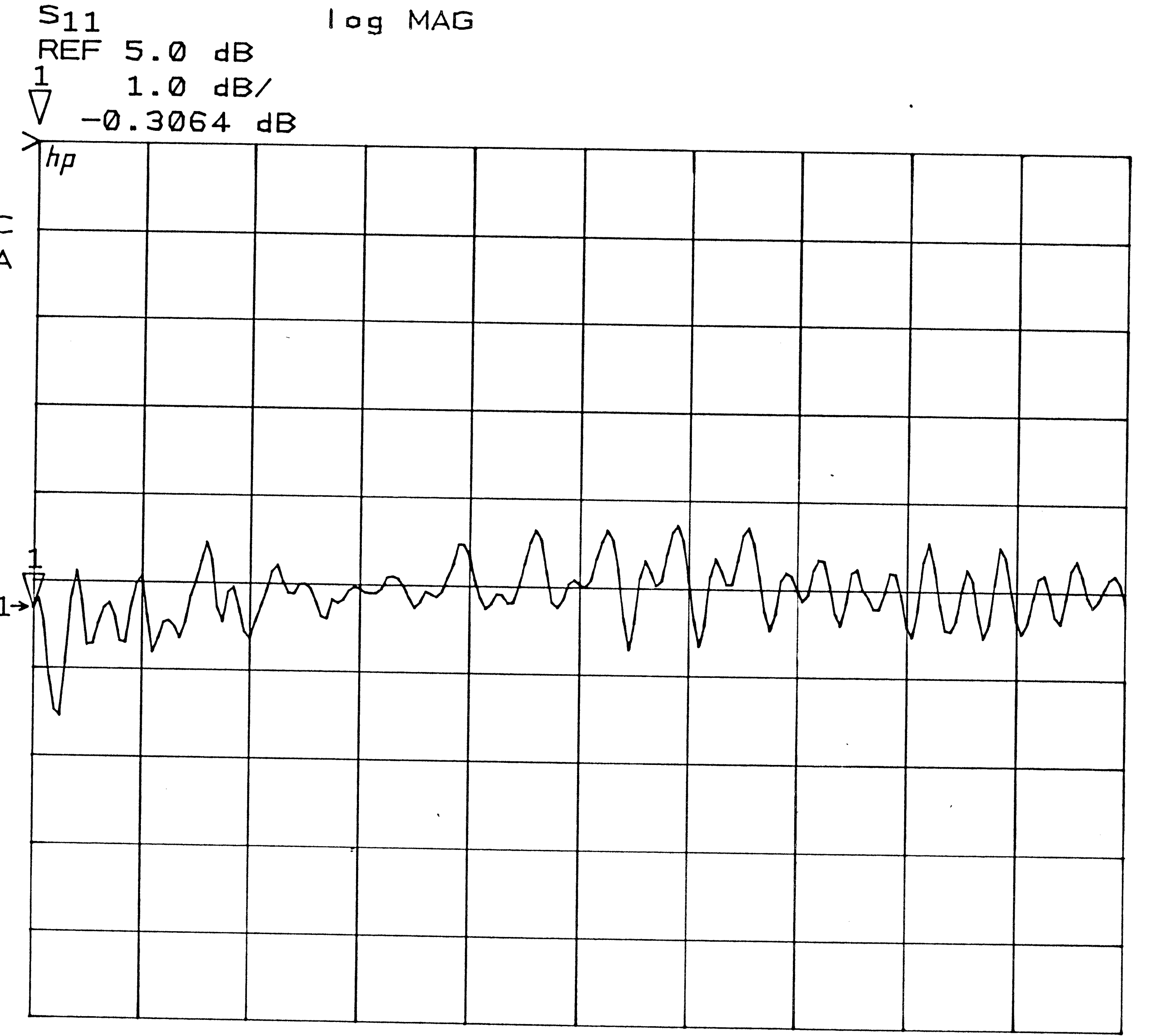

Figure 3. Phase and return loss of tunable waveguide short (140-150 GHz), cal set 1.

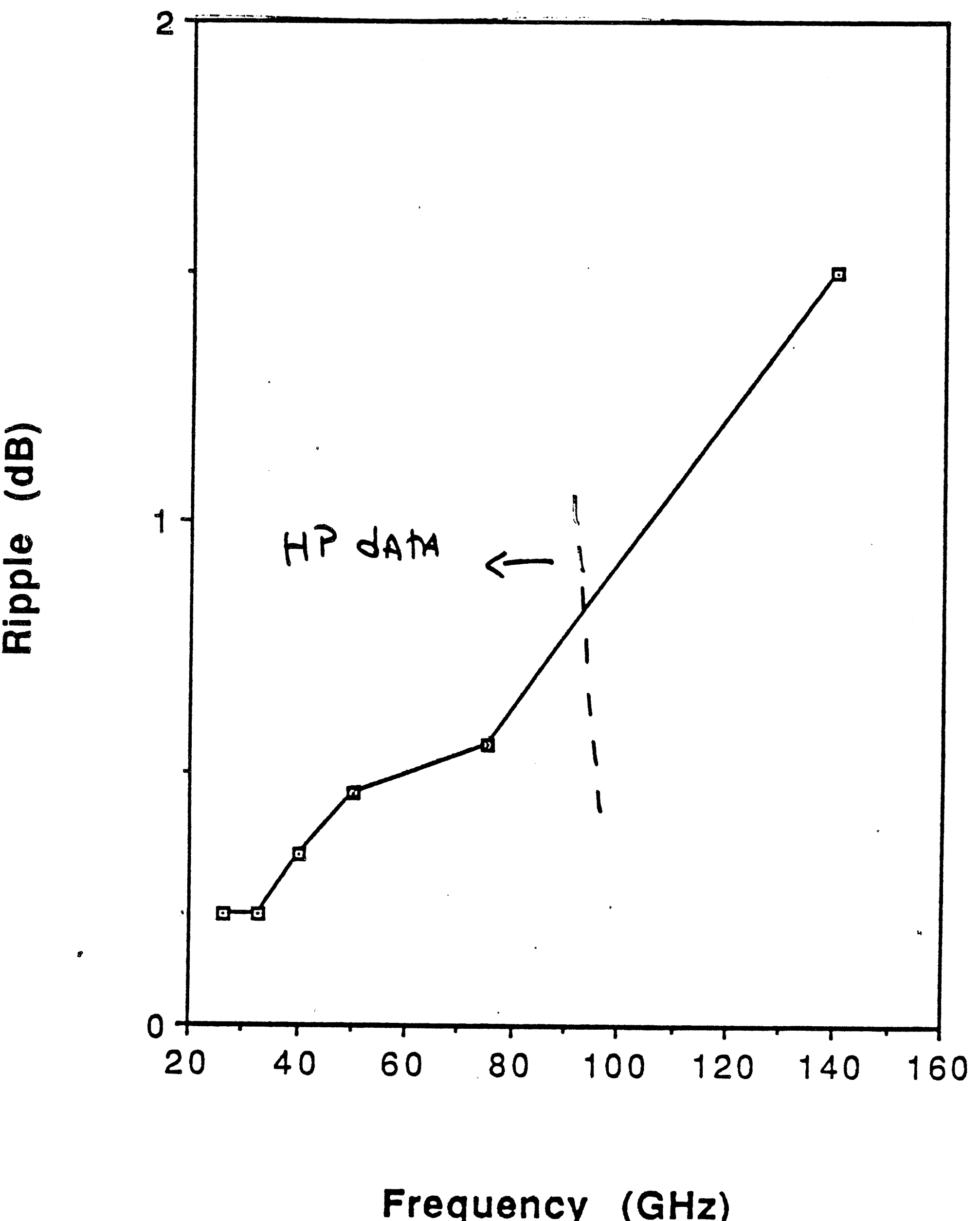

Figure 4. Overall system ripple comparison

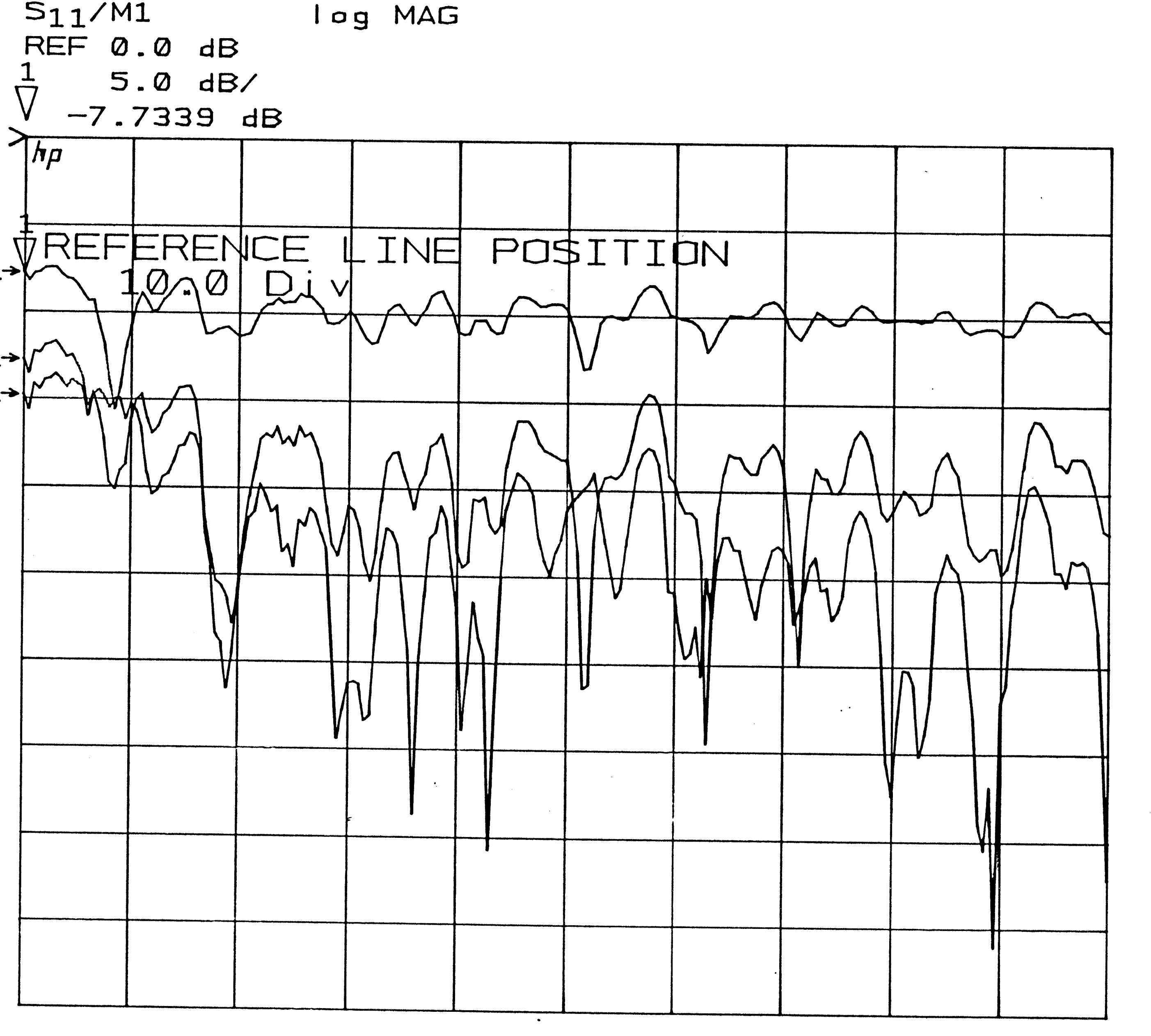

Figure 5. Return loss of a variable attenuator

S11 log MAG
REF -0.000 dB
10.0 dB/
-19.803 dB

START 6.000000000 GHz
STOP 16.000000000 GHz

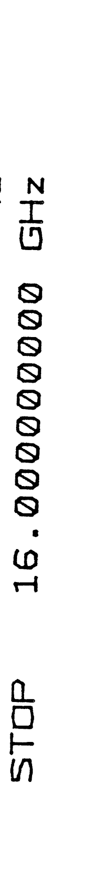

Figure 6. Return loss of a standard gain horn

TUNABLE HIGH FREQUENCY RADIATION SOURCE UTILIZING A RELATIVISTICALLY PROPAGATING IONIZATION FRONT

R. L. Savage Jr., C. Joshi, and W. B. Mori

Electrical Engineering and Physics Departments
University of California at Los Angeles

SUMMARY*

We have experimentally demonstrated a new type of tunable, high power radiation source capable of producing very short pulses. This technique utilizes a laser-produced ionization front which passes through a pulse of microwave radiation and in doing so causes the frequency of the radiation to upshift dramatically. By controlling the density of the plasma in the ionization front, we can continuously vary the degree of upshift. Source radiation at 35 GHz has been upshifted to more than 116 GHz.

The source radiation is provided by a pulsed magnetron that gives 300 nsec long, 10 kW peak power pulses at 35 GHz. This radiation is fed via rectangular waveguide through the side wall of a cylindrical copper cylinder that is closed by quartz windows at each end. The TE_{01} mode is excited and resonates in the cavity which is evacuated and filled with azulene vapor, which is chosen because it is easily ionized by ultraviolet radiation. A short (50 psec), intense (40 mJ) ultraviolet (266 nm) laser pulse is introduced through one of the quartz windows and propagates down the axis of the cavity. As the laser ionizes the azulene vapor, a sharp boundary is formed between the neutral gas and the newly created plasma. It is this boundary, which propagates at the group velocity of the laser radiation in the plasma-filled guide, that we refer to as an ionization front.

As the front propagates down the cavity, it encounter both the co-propagating and the counter-propagating radiation that make up the standing wave of source radiation in the cavity. Theory predicts that the frequencies of these two waves will

be upshifted by different amounts, but that in both cases the degree of upshift will be proportional to the plasma density in the front. This density is varied by adjusting the neutral azulene pressure in the cavity.

The upshifted radiation is detected by a series of diode detectors preceeded by sections of rectangular waveguides in various sizes that form a set of high-pass filters. A 1 Ghz bandwidth oscilloscope is used to display the upshifted radiation which appears in a single sub-nsec pulse. The detectors are rotated in the plane of the laser table about the output of the cavity in order to measure the antenna pattern of the radiation. This information is then used to estimate the amount of power in the upshifted pulses.

This proof-of-principle experiment has shown that the frequency of source radiation can be upshifted in a continuously tunable fashion to greater than a factor of three times the source frequency. The peak power in the upshifted pulses is more than half that of the source for 20 percent frequency upshift. The significant reduction in upshifted power detected at higher frequencies may be largely due to pump laser energy depletion along the cavity and the reduced response of the detection circuit as the duration of the pulses becomes shorter at higher frequencies. With slight modifications, this technique should be capable of producing short, high power pulses of radiation well into the terahertz frequency regime.

* A more detailed account of this work is published in Proceedings of the IEEE MTT-S International Microwave Symposium, June 11-14, 1991, Boston, Massachusetts, by the same authors under the title "Generaton of Highly Tunable Microwave Radiation Via a Relativistic Ionization Front."

Frequency Upshift in a resonant microwave cavity operating near cutoff. $V_g < C$

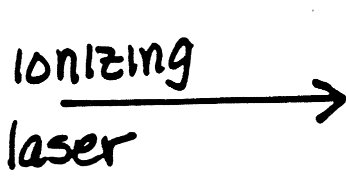

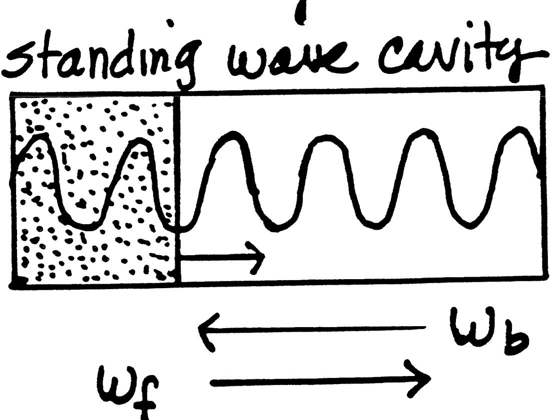

Theory:

$$\omega_{up_{b,f}} = \omega_0 \gamma^2 \left(1 \pm \beta \frac{v_g}{c}\right)\left[1 - \beta\left(1 - \frac{\omega_t^2}{\omega_0^2}\frac{1}{\gamma^2\left(1 \pm \beta \frac{v_g}{c}\right)^2}\right)^{1/2}\right]$$

$$\omega_t^2 = \omega_p^2 + \omega_c^2$$

Specific predictions:

1) large frequency upshifts $\quad \frac{\omega_{up}}{\omega_0} \propto n \quad \omega_{up_f} > \omega_{up_b}$

2) backward wave is reflected in the lab frame when $\omega_t > (1+\beta \frac{v_g}{c})\omega_0$ and leaves cavity in the forward direction

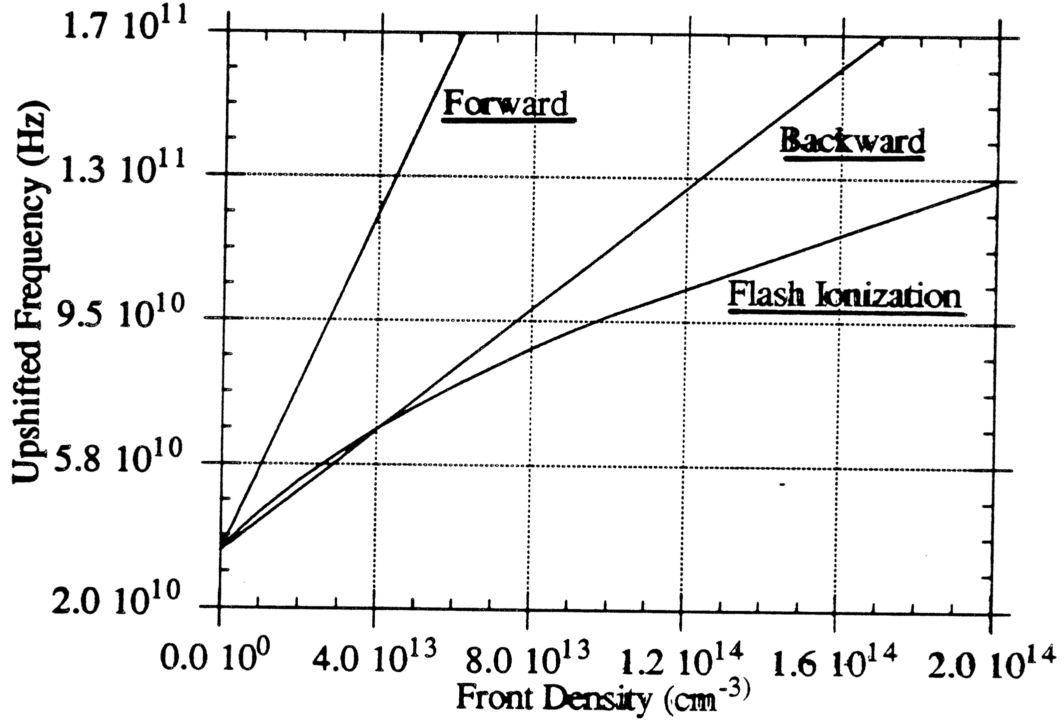

Flash ionization*: 1) $\omega_{up} = (\omega_o^2 + \omega_p^2)^{1/2} \propto \sqrt{n}$

2) $\omega_{up_f} = \omega_{up_b}$

* Wilks, Dawson, Mori PRL 61 1988

Joshi, etal IEEE Trans. Plasma Sci. 18 1990

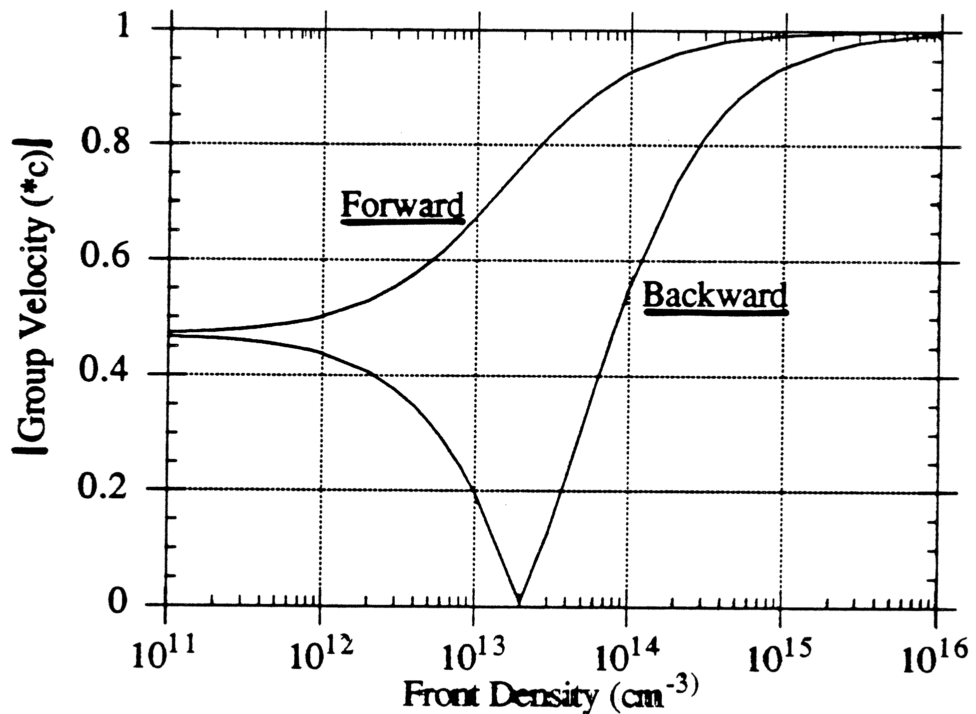
1
0.8
0.6
0.4
0.2
0
|Group Velocity (*c)|
Forward
Backward
10^{11}
10^{12}
10^{13}
10^{14}
10^{15}
10^{16}
Front Density (cm^{-3})

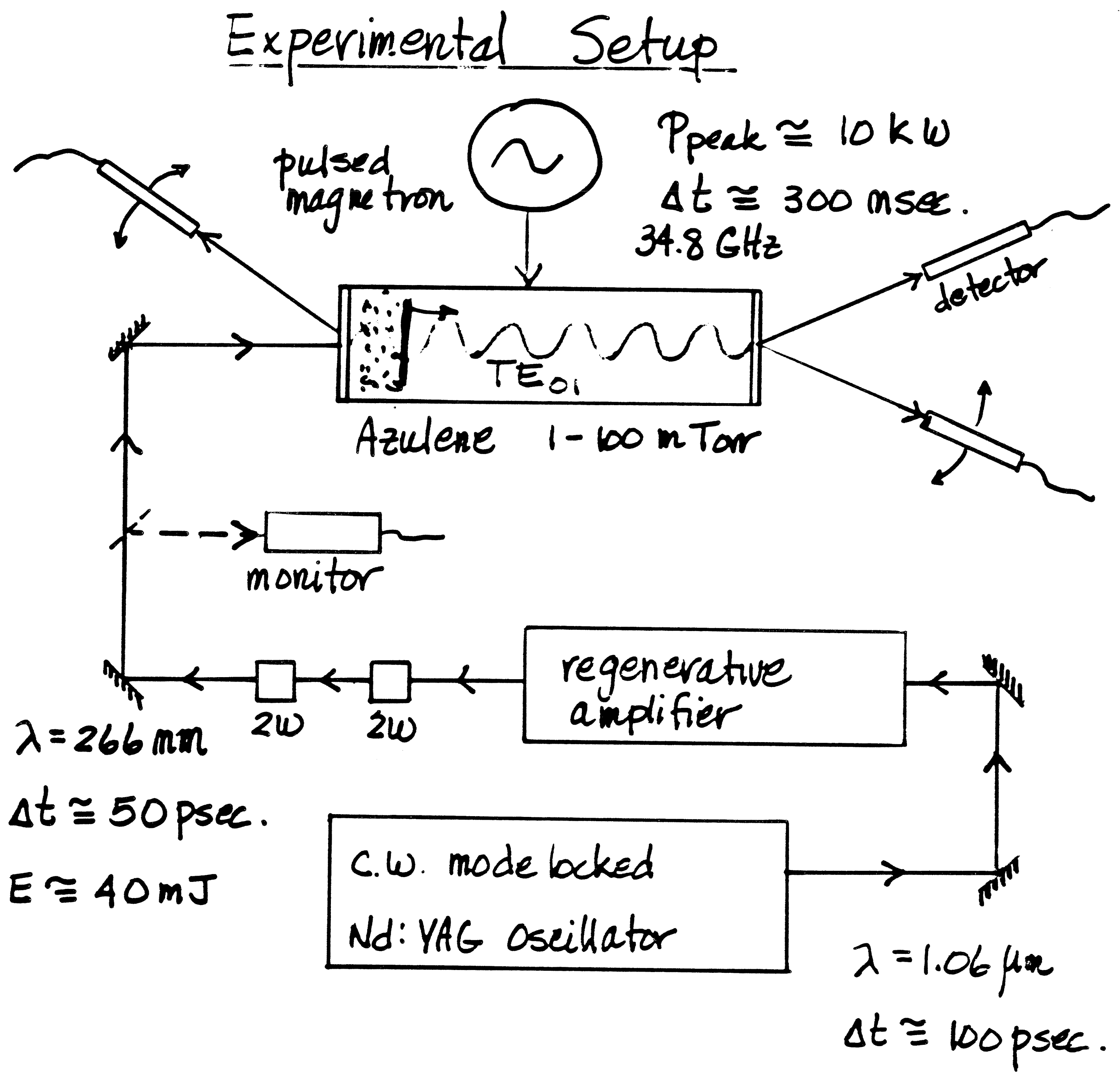

cavity length - 35 cm., diameter 1.2 cm

Vg - .47 c

wavelengths inside guide - 19

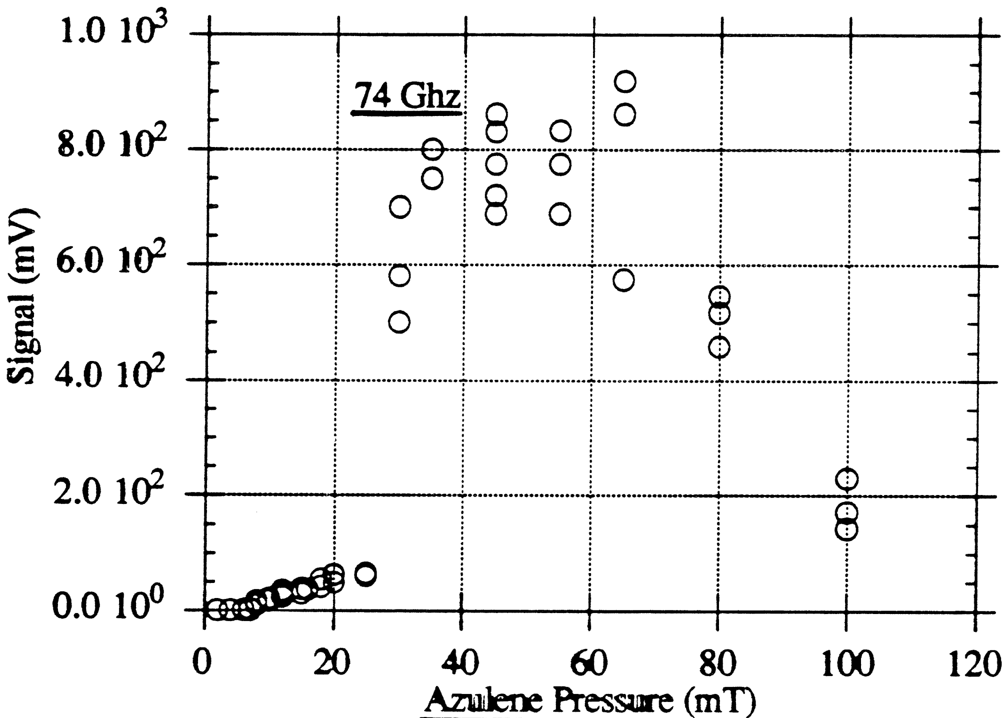
74 Ghz
1.0 10^3
8.0 10^2
6.0 10^2
4.0 10^2
2.0 10^2
0.0 10^0
Signal (mV)
0
20
40
60
80
100
120
Azulene Pressure (mT)

59 GHz channel - forward direction

Typical upshifted pulse

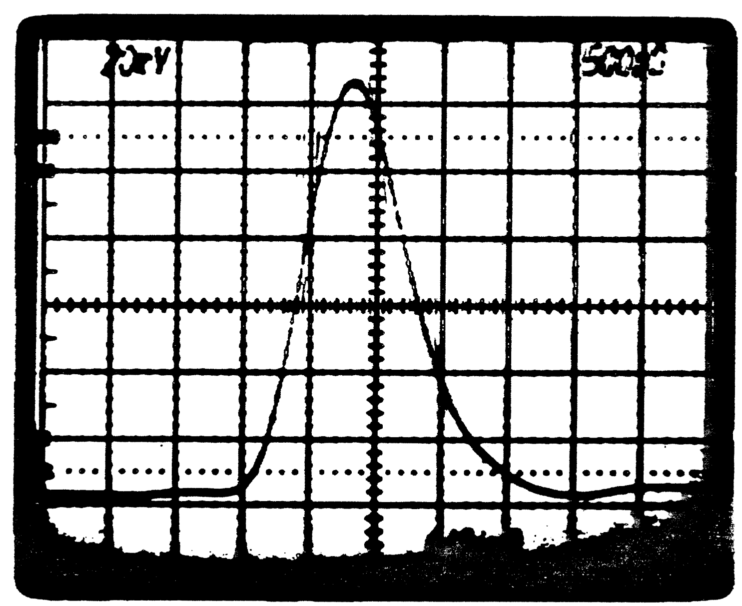

→| |← 500 psec.

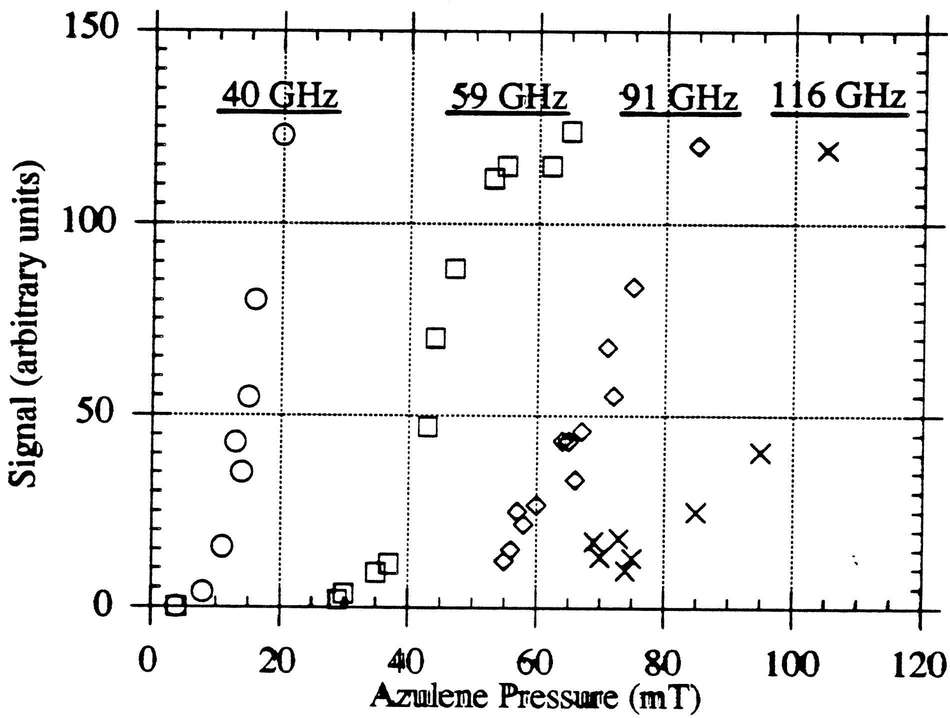

40 GHz
59 GHz
91 GHz
116 GHz
Signal (arbitrary units)
Azulene Pressure (mT)
150
100
50
0
0
20
40
60
80
100
120

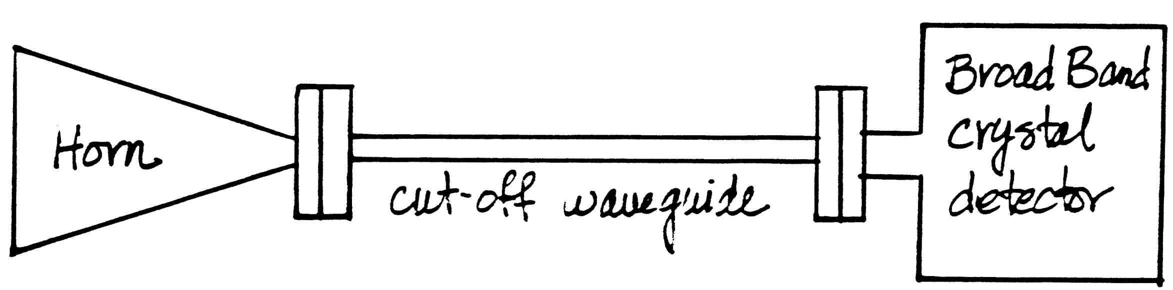

Horn
cut-off waveguide
Broad Band crystal detector

Source frequency detector 34.8 GHz

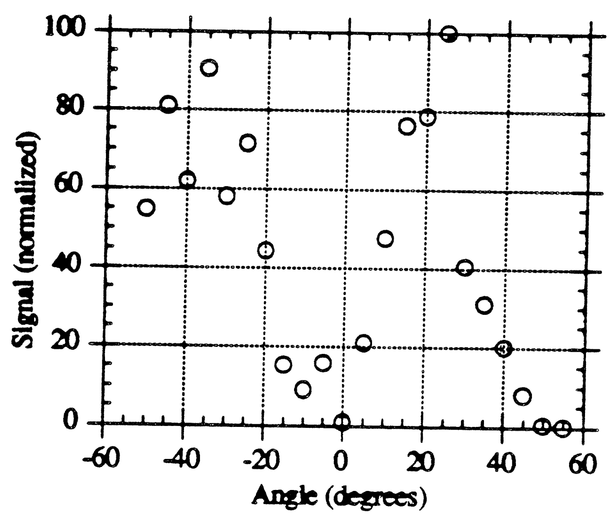

$P_{tot.} \approx 5.8$ kW

40 GHz detector channel

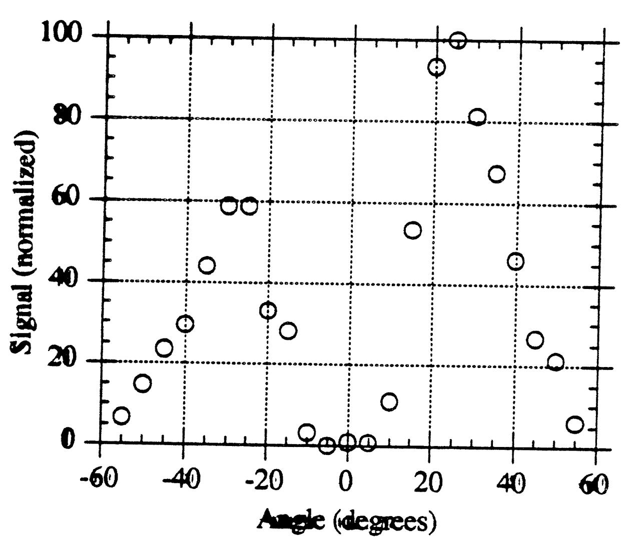

$P_{tot.} \approx 3.2$ kW

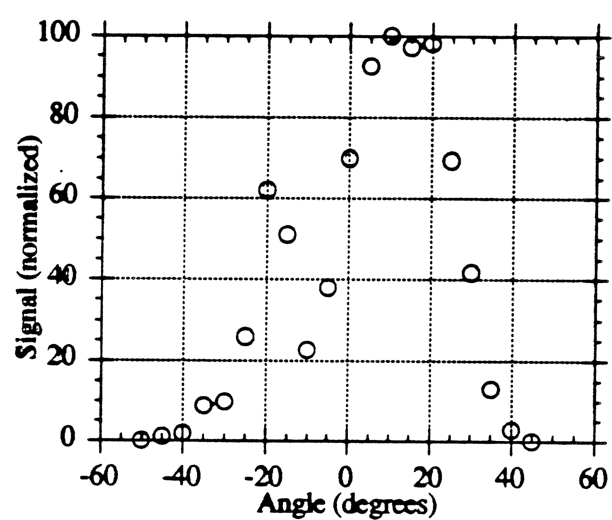

91 GHz
detector
channel

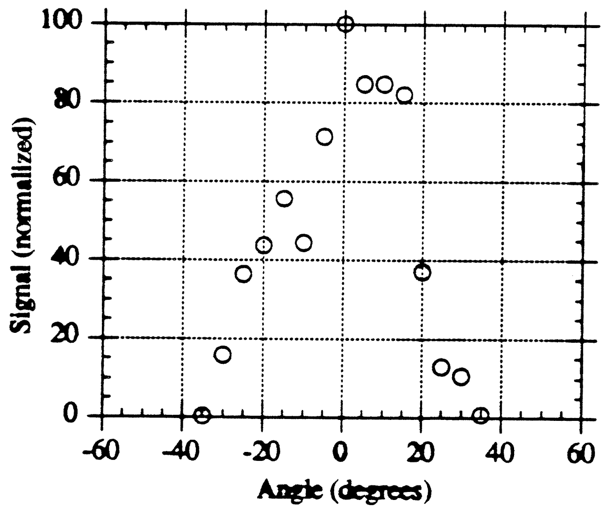

$P_{tot.} \approx 22\ W$

Summary

1) observed large frequency upshifts $\frac{\omega_{up}}{\omega_0} > 3$

2) upshifted radiation in both forward and backward directions

$\omega_{up_f} > \omega_{up_b}$ for a given front density

3) upshifted pulse widths less than 1 nsec

4) upshift scales roughly linearly with front density as predicted by relativistic ionization front theory

5) for $n = 5 \times 10^{14}\ cm^{-3}$, $\frac{\omega_f}{2\pi} = 1.1$ THz

Sub-Millimeterwave InP-Based High Electron Mobility Transistors

L.D. Nguyen, A.S. Brown, and L.E. Larson

Hughes Research Laboratories, Malibu, CA 90265

ABSTRACT

We report on a recent development of a 80 nm gatelength, InP-based Self-Aligned T-Gate High Electron Mobility Transistor (SAGHEMT) with an extrinsic current gain cutoff frequency (f_T) of 250 GHz. After subtracting a 10 fF gate pad capacitance, the intrinsic f_T of this device was estimated to be as high as 330 GHz. We believe that, with further scaling and optimization, the InP-based SAGHEMT holds great potentials as a planar, three-terminal semiconductor device at sub-millimeterwave frequencies.

INTRODUCTION

As the gatelength of a field-effect transistor (FET) approaches the nanometer regime, it becomes increasingly more difficult to improve the device speed by simply reducing the gate length. In this gate length regime, parasitic delays, such as drain delay (due to the extension of the drain depletion region) and capacitance charging time (gate pad and fringe), represent a large portion of the total delay and will ultimately limit the device extrinsic speed [1-3]. Evidences that support this claim are plenty and can be readily observed by plotting the f_T as a function of gate length. This is shown in Fig. 1 for a number of selected InP-based HEMTs fabricated in our laboratories [4, 5]. Due to parasitic delays, the rate of increase of f_T is significantly degraded as the gate length approaches the nanometer regime. In fact, we predict that a factor-of-2 reduction in gate length from the current 0.1 μm technology will only result in an approximately 50% increase in f_T.

Recently, however, a new, nanometer-scaled Self-Aligned Gate (SAG) process has been developed [5], in which the electron-beam-defined T-shaped gate serves as a shadow mask during

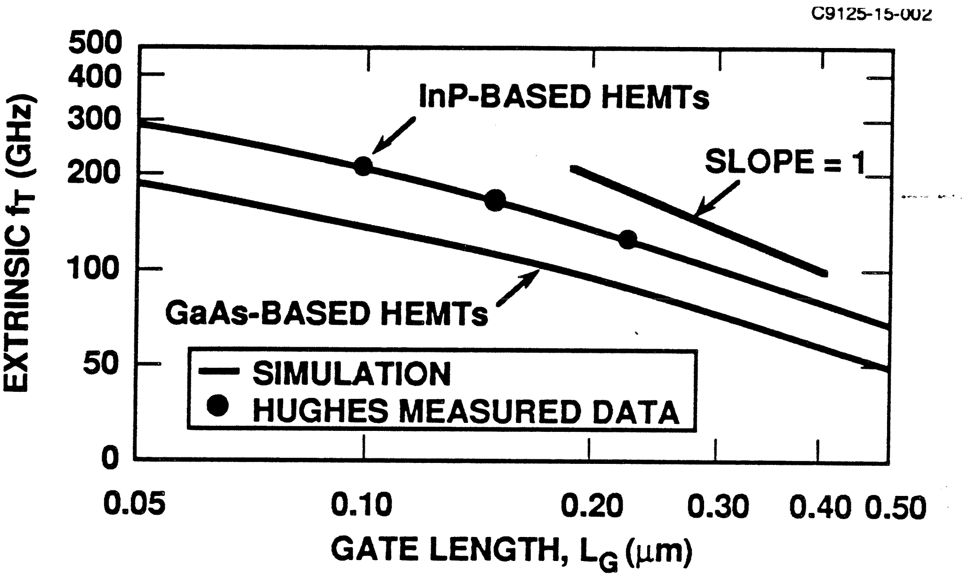

Fig. 1. Scaling of AlInAs/GaInAs HEMTs with gatelength. The effects of parasitics on f_T are evident at L_G <0.1 μm.

ohmic deposition, allowing the source and drain contacts to be "self-aligned" to the gate. This process has significantly reduced the device source and drain resistances, as well as the various parasitic delays associated with them [6]. Our recent work in this area and that of Mishra et al. have resulted in a record room-temperature f_T of 250 GHz for InP-based SAGHEMTs with gatelength between 80 and 120 nm [5, 7].

In the followings, we will present a characterization of the 80 nm gatelength InP-based SAGHEMT reported in Ref. [7], with particular emphasis on its potential scaling for sub-millimeterwave applications. With further optimization, we believe that it is possible to realize an ultrahigh performance InP-based SAGHEMT with 50 nm gatelength.

DEVICE FABRICATION

The process flow for the fabrication of our SAGHEMTs, as shown in Fig. 2, is identical to that in Ref. [4]. It typically consists of five major levels: (1) alignment marks, (2) device isolation, (3) T-gate definition by electron-beam lithography, recess, and metalization, (4) ohmic definition,

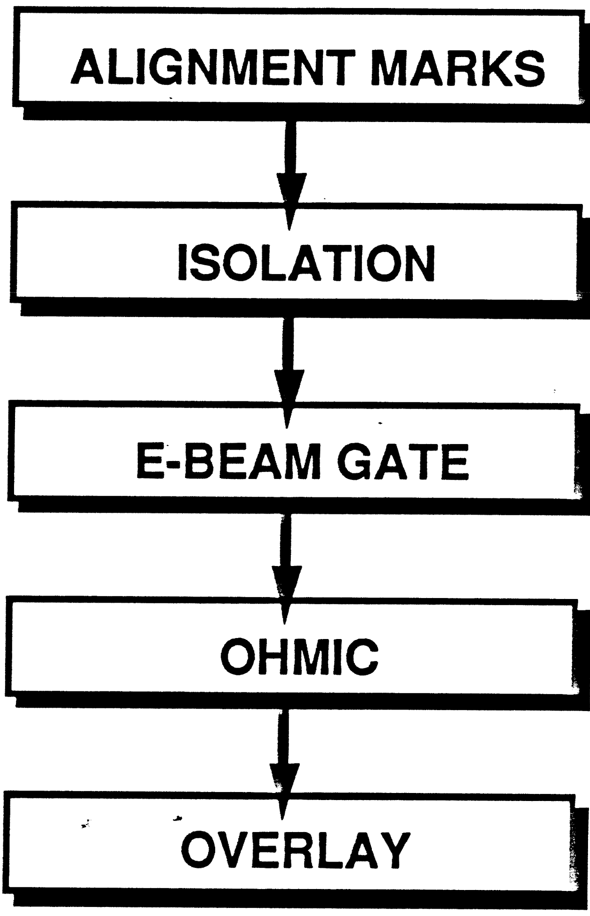

Fig. 2. Process flow for 80 nm SAGHEMTS.

metalization (with the T-gate serves as a shadow mask), and alloying, and (5) overlay metalization. In this self-aligned gate scheme, the ohmic level follows, rather than precedes, the gate level. Consequently, it is important that the ohmic alloying temperature not exceed some critical temperature beyond which the Schottky gate characteristic may be significantly degraded.

At the present time, we have routinely achieved a resolution of 80 nm for our T-gate process using a Phillips EBPG-4 electron-beam lithography system. This T-gate then serves as a shadow mask during ohmic deposition and effectively defines the source-drain contacts. A Scanning Electron Micrograph (SEM) of a typical SAGHEMT fabricated in this work is given in Fig. 3, which shows a gate length of approximately 80 nm and a source-drain spacing of 0.3 μm.

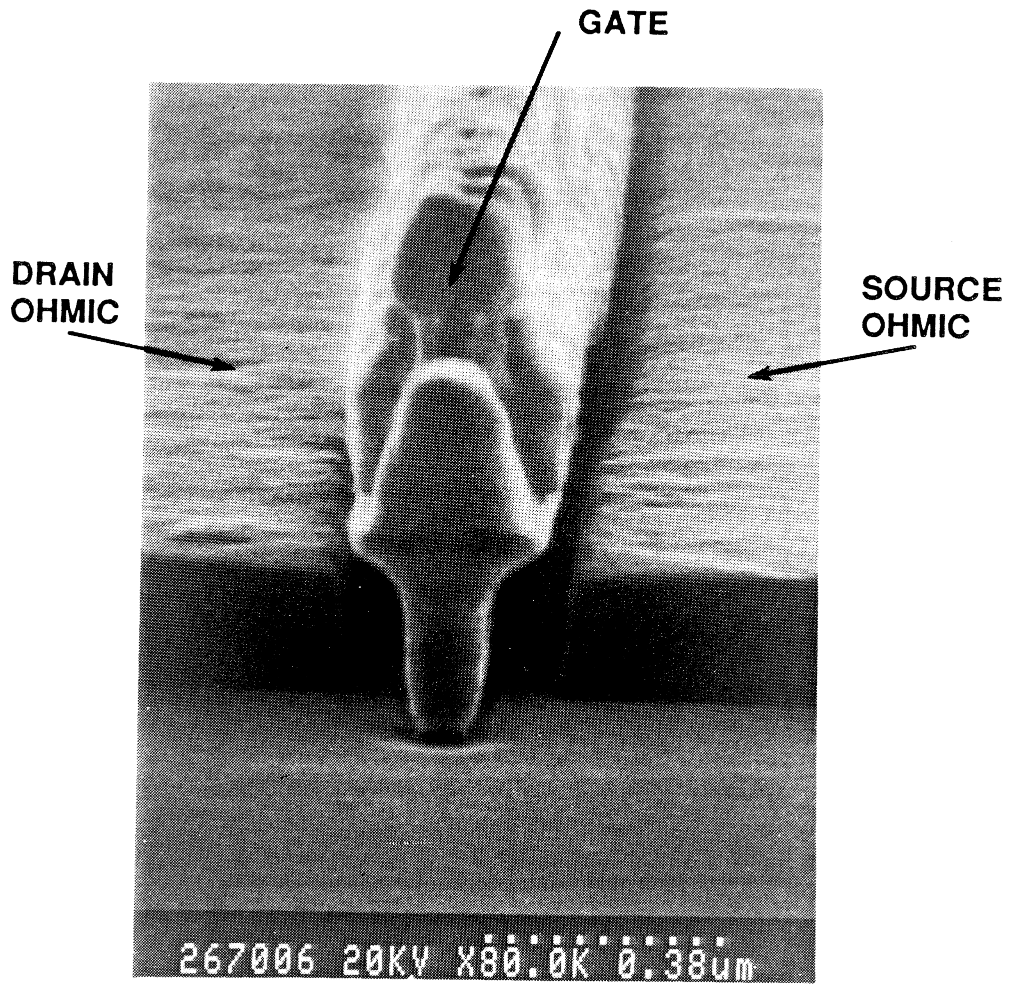

Fig. 3. SEM photograph of a 80 nm self-aligned HEMT with 0.3-μm source-drain spacing.

DEVICE RESULTS

We have successfully fabricated three (3) wafers with almost identical results using the above process. Typically, we have achieved a dc transconductance (g_m) of 950 to 1050 mS/mm for devices with a nominal threshold voltage (V_{th}) of - 0.5 V, and 1050 to 1150 mS/mm for those with a V_{th} of - 0.2 V.

The I-V characteristics of a typical 80-nm by 50-μm InP-based SAGHEMT with a g_m of 1050 mS/mm is given in Fig. 4. Despite the very short gatelength and source-drain spacing employed, the device exhibits excellent pinchoff characteristics and shows no apparent sign of "short channel" effects. As a result, we believe that further improvements can be obtained by reducing the gatelength to 50 nm.

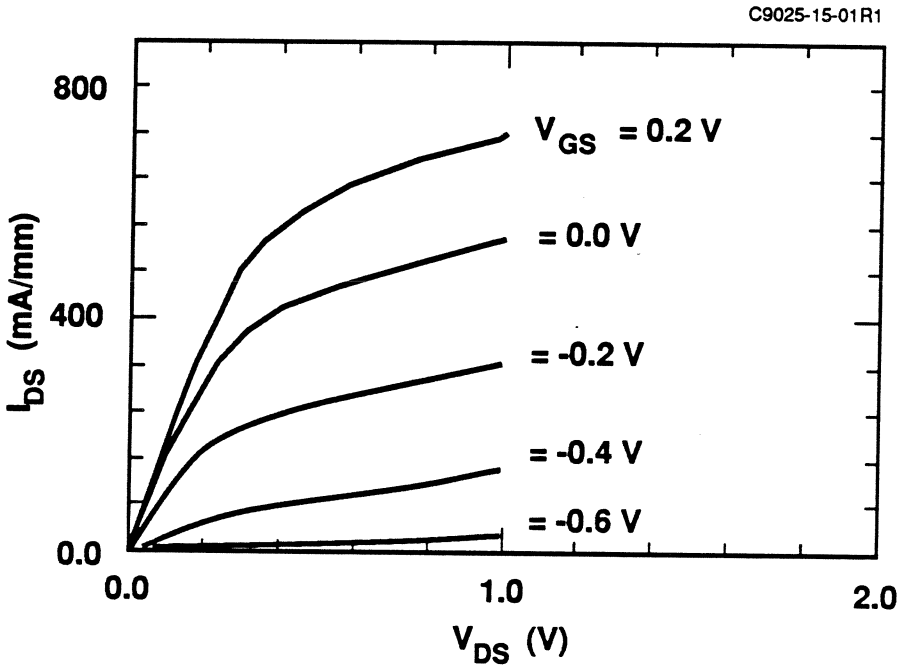

Fig. 4. I-V characteristics of a typical 80-nm by 50-μm AlInAs/GaInAs SAGHEMT.

As shown in Fig. 5, the extrapolation of the current gain versus frequency of a 80-nm by 50-μm SAGHEMT yields an extrinsic f_T of approximately 250 GHz. Without the presence of a 10 fF gate pad capacitance, the f_T (intrinsic) of the device was estimated to be as high as 330 GHz, which, we believe, is the highest value yet reported for any three-terminal semiconductor devices.

The potential scaling of our SAGHEMTs for sub-millimeterwave applications can be best examined with the aid of a small signal equivalent circuit model (see Fig. 6). Due to the very large gate periphery employed (e.g., 50 μm) and the presence of the gate pad capacitance, the power gain cutoff frequency (f_{max}) of our devices is currently limited to approximately 220 to 300 GHz. However, this limitation should be readily overcome by a simple scaling of gate width (W) since [8]

$$f_{max} = \frac{f_T}{\sqrt{4g_{ds}\left(R_s + R_i + R_g W^2 + \pi f_T L_s W\right) + 4\pi f_T C_{gd}\left(R_s + R_i + 2R_g W^2 + 2\pi f_T L_s W\right)}}$$

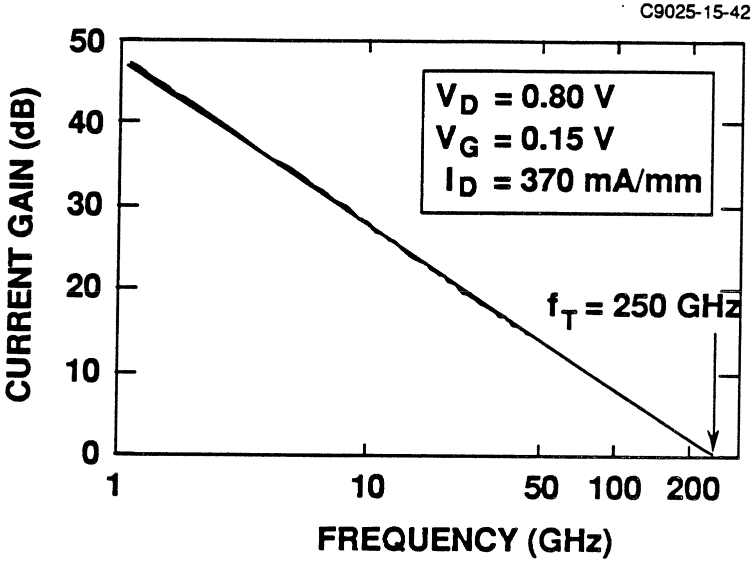

Fig. 5. Current gain versus frequency of a 80 nm by 50 µm AlInAs/GaInAs SAGHEMT (f_T = 250 GHz).

where f_T is the intrinsic value (ignoring the gate pad capacitance) and the various circuit elements are expressed in their respective units for a 1-mm-wide device. Thus, for the SAGHEMT presented in Fig. 6, f_T = 330 GHz, g_{ds} = 152 mS/mm, R_s = 0.11 Ω*mm, R_i = R_{gs} = 0.05 Ω*mm, R_g = 140 Ω/mm, C_{gd} = 0.1 pF/mm, and L_s = 6.0 pH. As shown in Fig. 7, our calculation suggests that a significant increase in f_{max} can be achieved with a smaller gate width device. In fact, an f_{max} in excess of 600 GHz has been estimated for a 10-µm-wide SAGHEMT, which clearly shows its great potentials as a planar, three-terminal semiconductor device for sub-millimeterwave applications.

We believe that even higher device performance can still be obtained with a further reduction in gate length and gate-to-channel separation. As shown in Fig. 8, we have simulated the dependence of the extrinsic f_T on gate length for an optimized InP-based SAGHEMT with a g_m of approximately 1400 mS/mm. At a gatelength of 50 nm, we predict an extrinsic f_T (including a 10 fF gate pad capacitance) approaching 400 GHz. This corresponds to an intrinsic f_T as high as 560 GHz and should result in significant improvements in device performance.

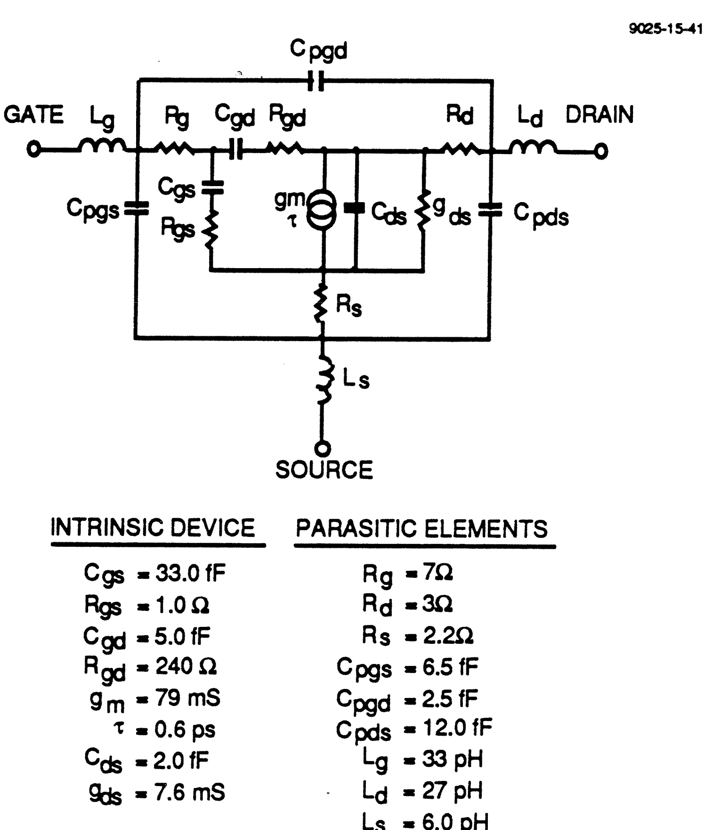

Fig. 6. An equivalent circuit model of a 80-nm by 50-μm AlInAs/GaInAs SAGHEMT.

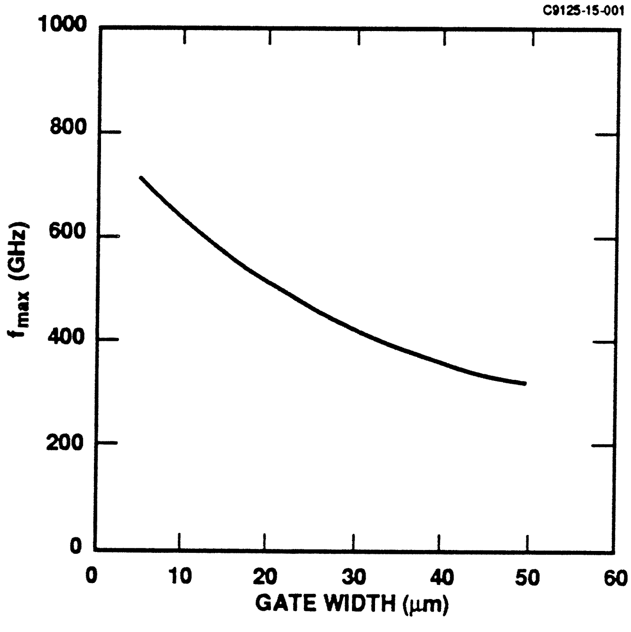

Fig. 7. Simulated results for F_{max} as a function of gate width.

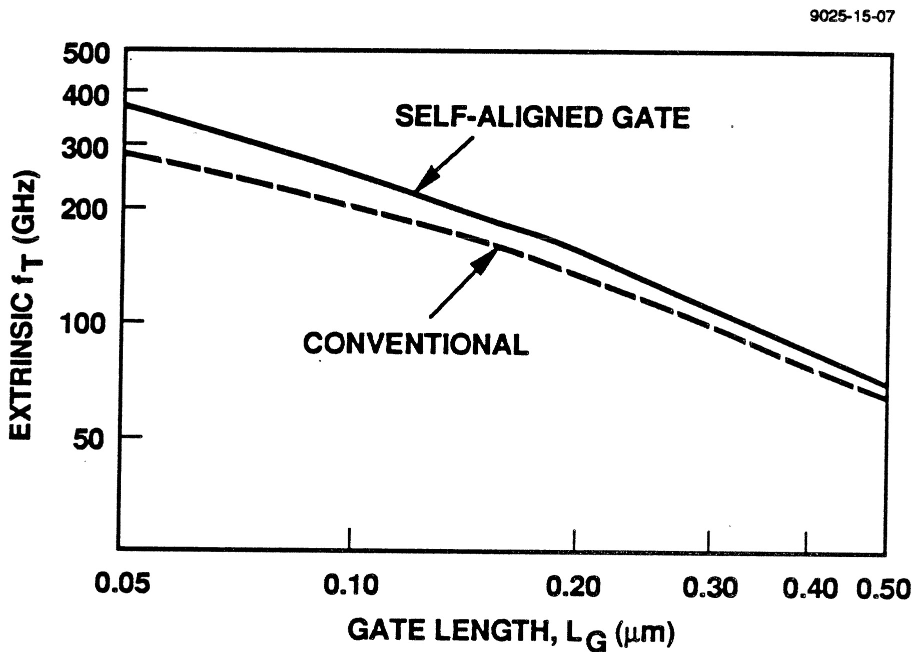

Fig. 8. Projected performance of self-aligned gate AlInAs/GaInAs HEMT in the early 1990s.

CONCLUSIONS

We have presented a characterization of a 80 nm gatelength InP-based SAGHEMT with good pinchoff characteristics and state-of-the-art f_T of 250 GHz. Our analysis indicates that it is possible to significantly improve the f_T by a further reduction of gate length, and the f_{max} by a simple scaling of gate width. We believe that, with further optimization, the InP-based SAGHEMT is an attractive candidate for sub-millimeterwave applications.

REFERENCES

[1] N. Moll, M.R. Hueschen, and A. Fischer-Colbrie, "Pulsed doped AlGaAs/InGaAs pseudomorphic MODFET's," IEEE Trans. Electron Devices, vol. 35, no. 7, Jul. 1988.

[2] L.D. Nguyen, P.J. Tasker, D.C. Radulescu, and L.F. Eastman, "Characterization of ultra-high-speed pseudomorphic AlGaAs/InGaAs (on GaAs) MODFET's," IEEE Trans. Electron Devices, vol. 36, no. 10, Oct. 1989

[3] L.D. Nguyen and P.J. Tasker, "Scaling issues for ultra-high-speed HEMTs," SPIE vol. 1288, High-Speed Electronics and Device Scaling, 1990

[4] U.K. Mishra, A.S. Brown, and S.E. Rosenbaum, "Dc and rf performance of 0.1 μm gate length $Al_{0.48}In_{0.52}As$-$Ga_{0.38}In_{0.62}As$ pseudomorphic HEMTs," in IEDM Tech. Dig., 1988

[5] U.K. Mishra, A.S. Brown, L.M. Jelloian, M. Thompson, L.D. Nguyen, and S.E. Rosenbaum, "Novel high performance self-aligned 0.15 μm long T-gate AlInAs/GaInAs HEMTs," in IEDM Tech. Dig., 1989

[6] P.J. Tasker and B. Hughes, "Importance of source and drain resistance to the maximum f_T of millimeter-wave MODFETs," IEEE Electron Device Lett., vol. 10, no. 7, Jul. 1989

[7] L.D. Nguyen, L.M. Jelloian, M. Thompson, and M. Lui, "Fabrication of a 80 nm self-aligned T-gate AlInAs/GaInAs HEMT," in IEDM Tech. Dig., 1990

[8] M. Fukuta et al., IEEE Trans. Electron Devices, ED-23, 1976

Wave-Coupled $LiNbO_3$ Electro-Optic Modulator for Microwave and Millimeter-Wave Modulation*

William B. Bridges and Finbar T. Sheehy
California Institute of Technology
and
James H. Schaffner
Hughes Research Laboratories

I. ABSTRACT

The phase velocity mismatch due to material dispersion in traveling-wave $LiNbO_3$ optical waveguide modulators may be greatly reduced by breaking the modulation transmission line into short segments and connecting each segment to its own surface antenna. The array of antennas is then illuminated by the modulation signal at an angle which produces a delay from antenna to antenna to match the optical waveguide's delay.

A phase modulator, 25 mm long with 5 dipole antenna/transmission-line elements, was operated from 4.3 to 13 GHz with a maximum phase modulation sensitivity of about 100 degrees/Watt$^{1/2}$. The optical wavelength was 633 nm. The expected variation of response with illumination angle was confirmed. A simple theory of antenna and transmission-line modulator behavior has been developed that matches the measured frequency response. This work was reported previously [1].

A second phase modulator, 18 mm long with 20 antenna/transmission-line elements, was operated at V-band and had a maximum phase modulation sensitivity of approximately 80 degrees/Watt$^{1/2}$. This showed that the modulator design can be scaled for mm-wave operation quite successfully.

A third modulator, using broad-band bow-tie antennas and designed for the range 60-100 GHz is being fabricated currently. The antenna array has provision for application of a dc bias voltage to the electrodes in order to bias a Mach-Zehnder optical amplitude modulator to the proper operating point.

---

* This work was supported by a grant from the Caltech President's Fund and a grant from Rome Air Development Center.

II. INTRODUCTION

Electro-optic modulators using $LiNbO_3$ have been demonstrated with modulation frequencies over 17 GHz and with modulation voltages less than 1 V [2,3]. Unfortunately there is a trade-off between sensitivity and bandwidth. While $LiNbO_3$ has a high electro-optic coefficient, it is also dispersive, having a much higher refractive index for microwave frequencies than for optical signals. The consequent mismatch of optical and microwave phase velocities limits the useful interaction length to about one-quarter free-space wavelength at the microwave frequency. If the modulator is long, for high sensitivity, then the maximum modulation frequency is low: if the modulation frequency is high then the modulator must be kept short, limiting sensitivity. We have demonstrated a new technique which overcomes this limitation and, as an added benefit, uses a waveguide to introduce the modulation signal. This latter feature may prove as important as the former for modulators operating in the millimeter wave range.

There have been previous approaches to overcoming the material dispersion limitation so as to achieve high modulation frequencies. Alferness et al.[4] have demonstrated a technique in which the modulation electrodes are divided into sections, each of which introduces a phase error of 180° between the optical and modulating signals. The sections are then connected together so as to correct the phase by 180°. In this way the average phase velocities of the two signals are kept equal. Some loss of sensitivity does occur because the electrode length which is required to introduce the 180° phase error is quite long.

Schaffner[5] has divided the electrodes into shorter sections to obtain greater sensitivity. The sections are connected by stub transmission lines that provide a phase delay of 360° minus the phase error introduced by each short electrode section. As in reference 4, the average phase velocity of the modulating signal is kept equal to that of the optical signal, but the shorter sections improve the sensitivity. However, as the sensitivity is increased by adding more sections, the bandwidth about the design frequency is decreased. This is also true of the Alferness method.

Our technique also divides the modulator into sections which limit the phase error per section. Now the individual sections are connected to surface antennas, as shown in Figure 1. The antennas are illuminated by a plane wave (the modulating signal) at an angle which provides the required phase-shift between modulator elements. Since the $LiNbO_3$ has a high value of ϵ_r the antennas are much more sensitive to radiation incident from inside the substrate than from outside [6]. The required angle of incidence for the plane-wave illumination is $\theta = \sin^{-1}(n_o/n_m)$ where n_o is the optical refractive index and n_m is the microwave refractive index of $LiNbO_3$. The addition of more modulator sections

does not affect the bandwidth in this case, as the bandwidth is simply that of a single modulator element.

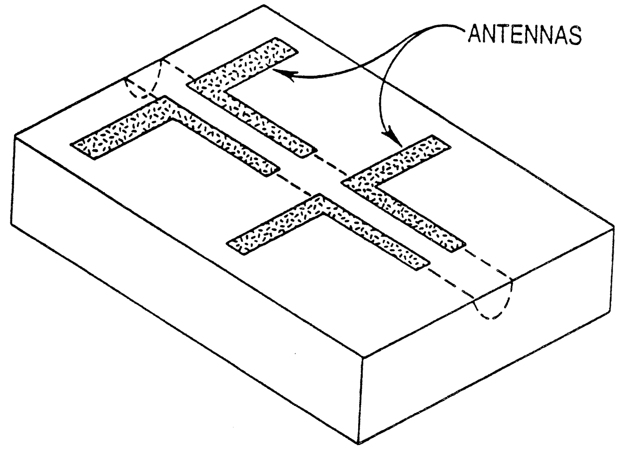

Figure 1. Schematic drawing of two dipole antennas and connected transmission line sections on the surface of a waveguide E-O modulator.

Since no physical connections are made to the antennas and the short modulating elements need not be terminated by matched loads (although they could be), no parasitic circuit elements (such as bond wires or connectors) are introduced which might limit the possibility of scaling to higher frequencies. The limits would be imposed by the size of the optical waveguide and by the absorbtion spectrum of the $LiNbO_3$ itself [7]. A modulator at 500 GHz should be quite practical (Figure 2). In addition, at these very high frequencies the attenuation per unit length in the modulating electrodes can be very high. In the antenna-coupled modulator the problem of attenuation of the modulating signal as it propagates from section to section does not exist, since the elements are driven "from the side", in parallel rather than in series. Since the number of modulator sections required would be large, the antenna-coupled modulator's bandwidth advantage becomes important also. In exchange for these advantages, we must develop efficient means for illuminating the modulator.

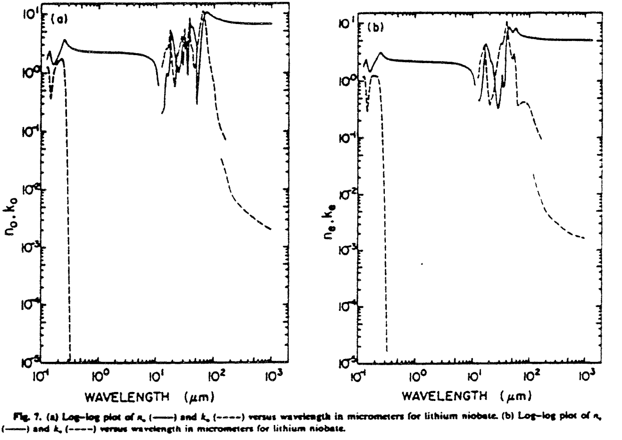

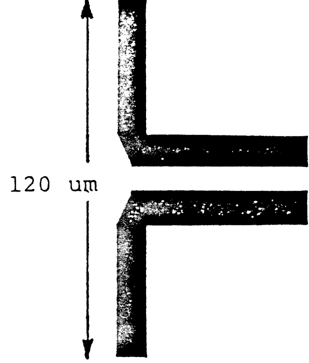

Figure 2. The absorbtion spectrum of $LiNbO_3$ and scaling of modulator elements show that a 500 GHz modulator is feasible.

III. X-BAND PROTOTYPE MODULATOR

Figure 3 shows the mask for an X-band prototype modulator. There are five antenna/modulator sections. The overall length is 25 mm. The antennas are "two half-waves in phase" dipoles, and the modulator sections are approximately a half-wave long at 12 GHz, based on an assumed effective microwave surface refractive index of 3.8 (i.e. the dielectric constant is taken as the mean of the dielectric constants of air and $LiNbO_3$). This electrode pattern was positioned over a straight section of optical waveguide to produce a phase modulator rather than a Mach-Zehnder amplitude modulator, but the same mask would also work if applied to one arm of a Mach-Zehnder. The 6μm optical waveguide was produced by in-diffusion of titanium.

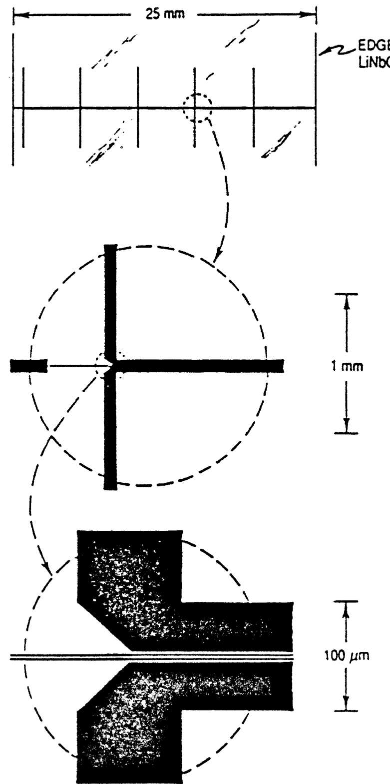

Figure 3. Photolithographic mask for 5 antenna-plus-transmission lines covering a 25 mm long optical waveguide. Magnified details are shown in the lower two drawings.

The microwave feed used to drive the modulator is shown in Figure 4. The $LiNbO_3$ substrate is attached to a wedge of Stycast ^{R} dielectric with ϵ_r=30, and the signal is matched into this material by two matching layers of intermediate dielectric constant. The wedge angle is 23° to match the microwave and optical phase velocities: a wedge is necessary because the critical angle is only 9°, making it impossible to couple into a flat substrate at any larger angle. The optical beam is coupled into and out of the optical waveguide using microscope objectives. Optical damage occurs in the guide at the 633 nm optical wavelength used, and optical power was limited because of this.

As was mentioned above, the pattern of an antenna on a dielectric substrate is directed more into the substrate than into the air. For ϵ_r=30 there is virtually no coupling on the air side. The pattern

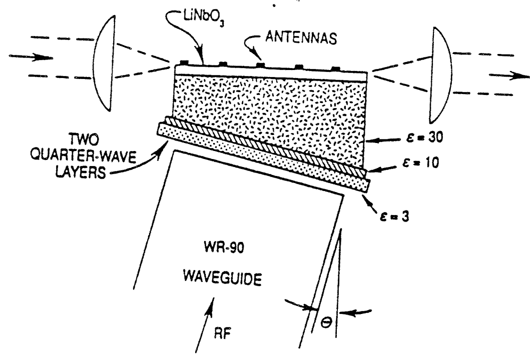

Figure 4. Schematic side view of an experimental modulator showing $LiNbO_3$ wafer with antennas, input and output lenses, wedged block of high dielectric constant material, matching layers, and microwave waveguide.

in the dielectric is also distorted by the presence of the interface. There is a peak response in the direction of the critical angle (here 9°). We used the theory of Enghetta et al. [4] to evaluate the pattern at the desired angle of 23°, and find that it is only about 0.5 dB down from the peak (Fig. 5).

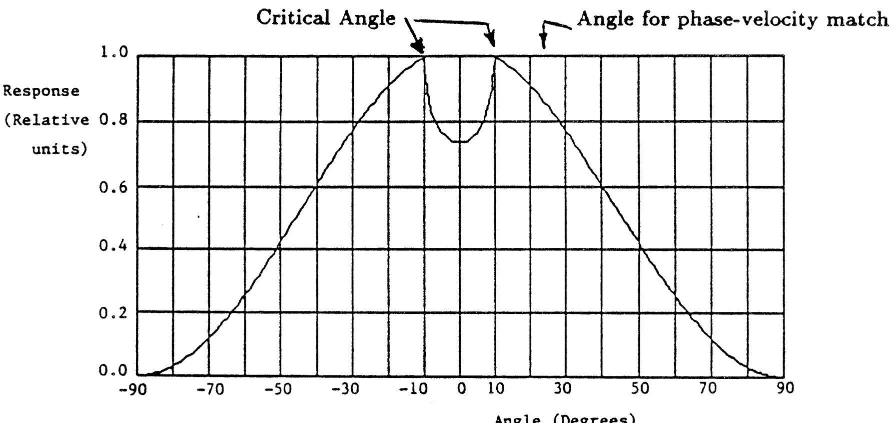

Figure 5. Antenna pattern of Dipole on $LiNbO_3$. (The cusp-like behavior at the critical angle is a real feature.)

The phase modulated signal cannot be detected using an amplitude detector. We used a scanning Fabry-Perot interferometer to show the existence of modulation sidebands and measure their amplitude. The phase deviation introduced by the modulator can be deduced from the amplitude of the sidebands relative to the carrier (for small phase deviation) from the formula [8]

$$\Delta\phi = 2\sqrt{\frac{P_{sideband}}{P_{carrier}}}$$

It is more usual to build an amplitude modulator and detect the signal directly, but the above method is simple and has the advantage that it works at much higher modulation frequencies, where a-m detectors are scarce. It has one notable disadvantage, however. The frequency spectrum is aliased by the scanning Fabry-Perot at frequency intervals equal to the free spectral range, so that sidebands which are an integral number of free spectral ranges off carrier are lost behind an aliased version of the carrier.

Figure 6 shows the modulator response as a function of frequency. The response is here defined as phase deviation normalized to the square root of the drive power, in units of "degrees per root Watt". This measure is linearly related to "degrees/radians per Volt", which is the common measurement when direct connections are made and voltage can be measured directly. There are no data points at 6, 8, 10 and 12 GHz due to the aliasing of the carrier at 2 GHz intervals making the sidebands invisible on the oscilloscope display. The graph shows straight-line interpolation between the data points.

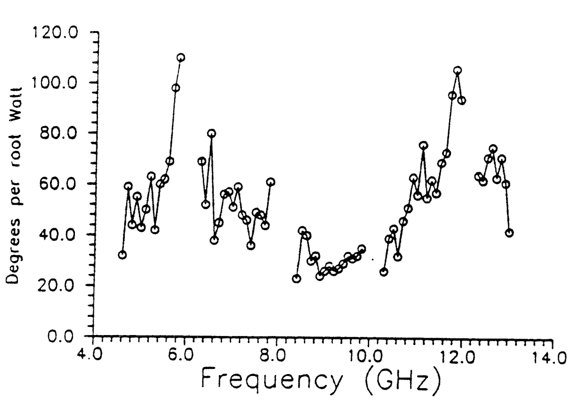

Figure 6. Frequency response of the experimental X-band modulator.

The modulator was operated with a number of different wedge angles to establish the effect of the illumination angle on performance. This may be modeled by considering the pattern of each antenna alone, the pattern of a phased array of such antennas (with the light in the optical waveguide doing the phasing), and the pattern of a phased array of antennas with unequal illumination. Figure 7 shows the patterns of arrays of 3, 4 and 5 equally illuminated antennas. We have included the smaller numbers of antennas because the antennas at either end of the modulator may be poorly illuminated. If a cosine distribution across the five antennas is assumed, the result is not unlike the 4-antenna case. Also plotted in Figure 7 is the average response over the 9-12 GHz band of the prototype modulator at each angle of incidence. The response peaks at about 23° as expected, confirming the phase-velocity-matching picture. The absence of the null in the experimental data is probably due to the multiple reflections inside the wedge.

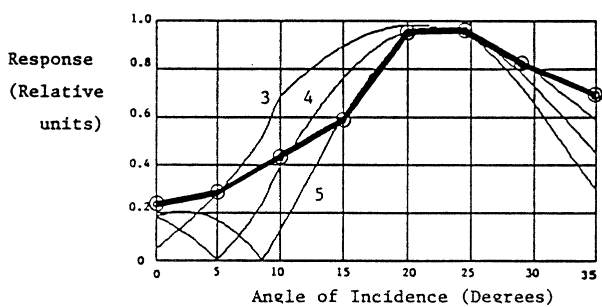

Figure 7. Effect of illumination angle on performance: theory for 3,4, and 5 antennas, and results from experimental modulator.

IV. V-BAND PROTOTYPE MODULATOR

A V-band phase modulator was designed based on scaling of the X-band prototype. The mask is shown in Figure 8. Essentially the design of each antenna/modulator element is based on a direct scaling of the original prototype, except that the electrode gap dimensions are fixed, and this fixes the lateral dimensions of the electrodes.

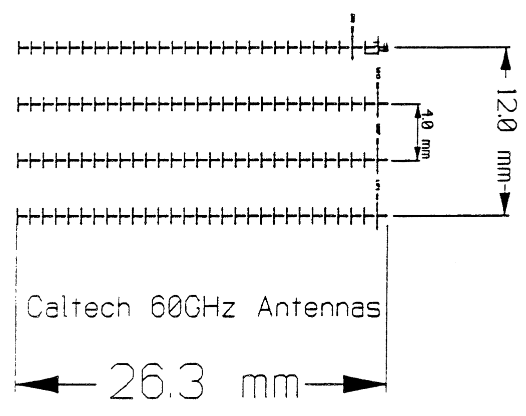

Figure 8. V-Band Modulator mask.

Since the mm-wave waveguide from which the modulating signal originates is now much smaller, while the antenna array is still long (more antennas), a different microwave feed is needed. The modulating signal is coupled from the waveguide into a tapered slab waveguide 1.5 mm thick. This tapered slab provides a means of expanding the wave to the dimensions of the antenna array, which was 1 x 18 mm. The power is matched into a slab of $LiNbO_3$ which is cut as a wedge to provide the correct angle of incidence for the modulating signal. The microwave feed is shown in Figure 9.

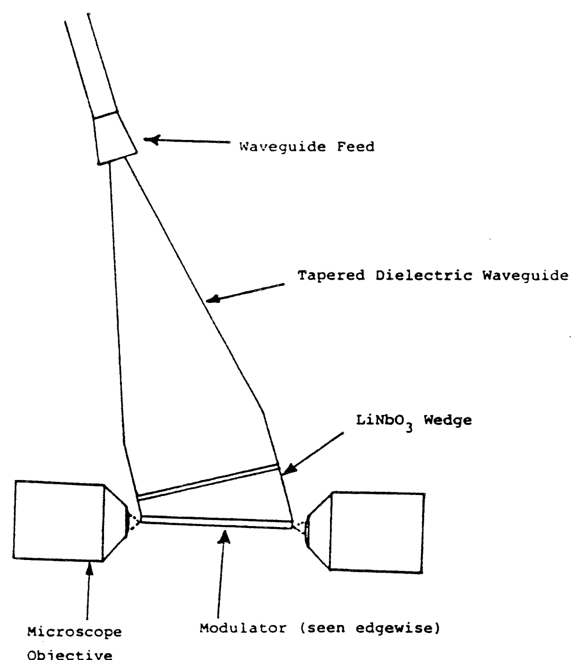

Figure 9. The V-band microwave feed.

The phase deviation was again measured using the scanning Fabry-Perot method, which works just as well with mm-wave as with microwave modulation. However we did not have complete confidence in the accuracy of our V-band power meter, and so can give only approximate results in terms of degrees of phase deviation per $Watt^{1/2}$. These results are shown in Figure 10.

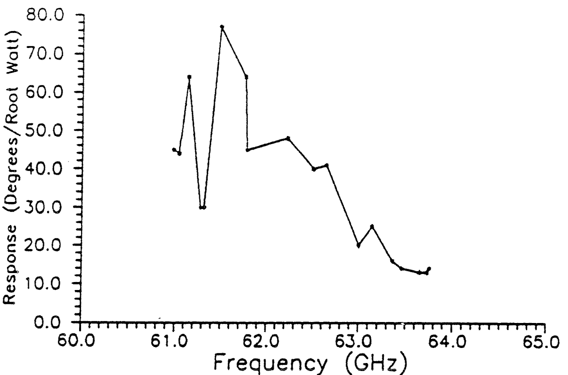

Figure 10. Frequency Response of the V-band prototype modulator.

V. DISCUSSION OF RESULTS

The structure of the frequency response arises from many sources: antenna and electrode resonance; reflections within the wedge; nonideal input matching layers; etc. However, we have found that the general shape of the X-band prototype modulator response is accounted for quite well by a model of the antenna/electrode impedance variations and the frequency response of the individual modulators. In this model the electrodes are treated as lossless transmission lines, open-circuit at the end; the antenna is treated as a lossy transmission line (the loss represents radiation effects); and the individual modulators have a frequency response basically determined by the well-known sinc-function response, except that there are two sinc terms, one for the forward-propagating wave at the modulation frequency and one for the wave reflected back from the open circuit at the end of the modulator electrodes.

The frequency response which is predicted by this simple model of impedances, modulator element frequency response and antenna gain is shown in Figure 11. It agrees remarkably well with the general shape of the experimentally determined response of the X-band prototype.

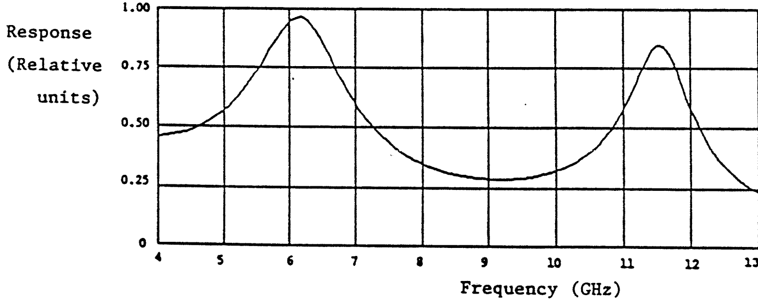

Figure 11. Frequency response predicted by simple model of antenna and electrode impedances, modulator element frequency response and antenna gain.

The peak around 12 GHz occurs when the modulator elements are a half wave long, at which point the antennas are approximately two half-wavelengths long. The antenna driving-point impedance and the modulator element input impedance are then both high. At 6 GHz there is another peak when the antenna is a half-wave long and the modulator element has a low input impedance. The lower-frequency peak also benefits from the increased modulator sensitivity at lower frequency - the modulator electrodes are electrically shorter and the sinc terms are nearer to unity. It was necessary to use WR 137 waveguide to measure this lower-frequency peak, so the microwave feed geometry was changed.

Peak response values exceed 100 degrees per $W^{1/2}$. This compares favorably with conventional microwave modulators (Erasme et al.[9] report a peak response of 131 degrees per $W^{1/2}$ for their phase-reversal travelling-wave modulator, operating at a wavelength of 1153 nm - note that sensitivity varies as $1/\lambda_{optical}$). This is only achieved over a narrow band, but is encouraging in a prototype. The narrow bandwidth results from the use of simple resonant elements. Other antenna designs with broadband elements will likely result in a flatter frequency response. Of course even here there is a region between the two peaks which is quite flat, but less sensitive by about 10 dB.

VI. FUTURE DEVELOPMENTS

To date we have demonstrated that the antenna-coupled modulator is capable of efficient mm-wave modulation of optical signals. However, the structure used had a relatively narrow bandwidth and was not ideally suited for use as part of a Mach-Zehnder amplitude-modulator structure. The Mach-Zehnder design requires a DC bias to ensure that the modulation drives the interferometer in its most linear (and most sensitive) regime. There is no good way to connect DC bias leads to the surface dipoles. A new modulator has been designed to overcome these two difficulties and is being fabricated at present. This new modulator uses bow-tie antennas in place of the dipoles. The bow-ties approximate frequency-independent structures, and this should allow much greater bandwidths. In addition the ends of the bow-ties interact only weakly with the radiation field and can be used as bias leads with little effect on RF performance. There is some sensitivity penalty associated with the use of these antennas, since the peaking of the response which was due to the dipole resonances is lost. The new modulator is designed to operate as a Mach-Zehnder amplitude modulator over the range 60-94 GHz. We also propose to demonstrate operation at 1.3 μm and/or 1.5 μm optical wavelengths.

The theory of antennas on dielectric substrates is not very well developed, although dipoles are well understood. Further developments in this area will be applicable to these modulators. Improved waveguide-to-antenna coupling is also desireable. Demonstrations at significantly higher modulation

frequencies would depend very much on the availability of mm-wave or sub-mm-wave power sources.

VII. ACKNOWLEDGEMENTS

The authors wish to acknowledge the technical support of Robert L. Joyce and Reynold E. Johnson in this work, and many valuable discussions with Robert W. Terhune.

VIII. REFERENCES

[1] William B. Bridges, F. T. Sheehy, and James H. Schaffner, "Velocity-Matched Electro-Optic Modulator," SPIE Vol. 1371 High Frequency Analog Fiber Optic Systems (1990) pp. 68-77, San Jose, California, September 1990

[2] G. E. Betts, L. M. Johnson, and C. H. Cox, III, "High-Sensitivity Lumped-Element Bandpass Modulators in $LiNbO_3$," IEEE J. Lightwave Tech., Vol. 7, pp 2078-2083, December 1989.

[3] C. M. Gee, G. D. Thurmond, and H. W. Yen, "17-GHz Bandwidth Electro-Optic Modulator," Appl. Phys. Lett., Vol. 43, pp 998-1000, December 1983.

[4] R. C. Alferness, S. K. Korotky, and E. A. J. Marcatili, "Velocity-Matching Techniques for Integrated Optic Traveling Wave Switch/Modulators," IEEE J. Quant. Electron., Vol. QE-20, pp 301-309, March 1984.

[5] J. H. Schaffner, "Analysis of a Millimeter Wave Integrated Electro-optic Modulator with a Periodic Electrode," Paper 13 at SPIE OE-LASE Conference 1217, Proceedings, pp 101-110, Los Angeles, Calif., January 16-17, 1990.

[6] N. Enghetta, C. H. Papas, and C. Elachi, "Radiation Patterns of Interfacial Dipole Antennas," Radio Science, Vol. 17, pp 1557-1566, Nov.-Dec. 1982.

[7] Handbook of Optical Constants of Solids, Edward D. Palik, Academic Press 1985

[8] See, for example, Reference Data for Radio Engineers, 5th Ed., Howard Sams, New York, 1968, Sec. 21-7.

[9] D. Erasme, D. A. Humphries, A. G. Roddie, and M. G. F. Wilson, "Design and Performance of Phase Reversal Traveling Wave Modulators," IEEE J. Lightwave Tech., Vol. 6, pp 933-936, June 1988.

A Planar Wideband Subharmonic Millimeter-Wave Receiver

B. K. Kormanyos, C.C. Ling and G.M. Rebeiz

NASA/Center for Space Terahertz Technology
Electrical Engineering and Computer Science Department
University of Michigan
Ann Arbor, MI 48109-2122

P.H. Ostdiek, W.L. Bishop and T.W. Crowe

Semiconductor Device Laboratory
Department of Electrical Engineering
University of Virginia
Charlottesville, VA 22903

The material presented below is intended as a review only and has already been published in the IEEE MTT-S Int. Microwave Symp. Digest, June 1991.

ABSTRACT

A wideband planar subharmonic mixer has been designed for millimeter-wave operation. The receiver consists of a back-to-back Schottky-diode pair integrated at the base of a wideband log-periodic antenna. The antenna is backed by a hyperhemispherical lens and tested at 178.5 GHz (and 140 GHz) with a 90 GHz (and 70 GHz) local oscillator. The results indicate a single-sideband conversion-loss of -12.8 dB without any RF or IF matching networks. The subharmonic monolithic approach results in an inexpensive wideband receiver and the design can be easily extended to receiver arrays.

I. INTRODUCTION

Millimeter-wave subharmonic mixers use an anti-parallel diode pair to generate a non-linear conductance waveform at twice the frequency of the applied LO signal [1,2]. Therefore, the required LO frequency is half that of the RF signal, and this offers unique advantages over fundamental single-ended mixers. Millimeter-wave subharmonic mixers require simpler filter-circuits designs and eliminate the use of potentially lossy quasi-optical diplexers. However, subharmonic mixing requires a well matched back-to-back diode pair for optimal performance. This is difficult to achieve at millimeter-wave frequencies with discrete devices, especially if the diodes are of the whisker-contacted type.

We have solved this problem and considerably simplified the receiver design by "integrating" a planar back-to-back GaAs Schottky-diodes at the apex of a wideband log-periodic antenna [3]. The log-periodic antenna catches both the RF and LO signals, and the LO signal

is injected quasi-optically using a simple dichroic filter (Fig. 1). The anti-parallel diodes are fabricated at the University of Virginia, and exhibit very low parasitic capacitances [4]. An optional matching network can be integrated at the antenna apex for better RF power transfer into the diode pair. The design results in an inexpensive monolithic receiver with potentially the same conversion-loss as single-ended waveguide mixers.

II. ANTENNA DESIGN AND MEASUREMENTS

The antenna is a wideband self-complementary log-periodic antenna with $\sigma = 0.5$ and $\tau = \sqrt{2}$ designed to cover the 30 GHz to 240 GHz band. The log-periodic antenna is placed on the back of a hyper-hemispherical lens to eliminate substrate modes and to yield a unidirectional pattern [5]. A polystyrene quarter-wave matching layer is used at the silicon-air interface to eliminate any reflected power from the lens. The antenna input impedance is 75Ω and is independent of frequency. Pattern measurement results show excellent E and H-plane patterns with a co-polarized directivity of 24.6 dB at 180 GHz (Fig. 2). It is important to note that the pattern enhancement is a result of the "Buettgenbach effect' which dictates that the antenna should be placed farther than the hyper-hemispherical focal point [6]. In our case, a position of 0.9mm behind the hyper-hemispherical focal point resulted in acceptable patterns at the LO frequency (90 GHz) and excellent patterns at the RF frequency (180 GHz)

III. DIODE DESIGN AND MEASUREMENTS

The anti-parallel diode chip was developed and fabricated at the University of Virginia for use in a 183 GHz waveguide receiver [4]. The chip is 250μm long, 125μm wide and approximately 50μm thick and was soldered on the antenna using a low-temperature process. A surface channel technology has been used to eliminate the conducing path between the anode and cathode pads. The parasitic capacitance can be further minimized by removing the semi-insulting GaAs substrate and replacing it with quartz. Furthermore, the quartz substrate can be easily removed after the chip is soldered in place by simply dissolving its adhesive [7]. The diode used in this research has a measured series resistance of 11Ω and a zero-bias capacitance of roughly 4 fF. The total parasitic capacitance for the quartz-diode is estimated at 3 fF, thereby yielding a figure-of-merit cutoff frequency of approximately 2 THz. The measured I-V curve for the diode pair after being mounted at the antenna terminals is shown in Fig. 3. The anodes are virtually identical with an ideality factor $n = 1.2$ and a turn on voltage of 0.7V at 1μA.

IV. MIXER MODELING AND MEASUREMENTS

A non-linear mixing program was written at the University of Michigan for the analysis of subharmonic mixers [8]. The program takes into account the asymmetrical I-V curve

of the back-to-back diodes. The higher-order terminating impedances are assumed to be resistive and equal to 75Ω in parallel with the parasitic capacitance of the diode. The analysis indicate that a conversion loss of 9.9dB is attainable at 180 GHz without an RF matching network. The corresponding RF and IF impedances are $26 - j30\Omega$ and 60Ω, respectively. It is possible to increase the conversion loss by 2 dB with an RF matching network at the expense of a narrowband design.

The single-sideband mixer performance was measured at 178.5 GHz (and 140 GHz) using a local oscillator at 90 GHz (and 70 GHz, respectively). The antenna directivity and substrate-lens dielectric losses (estimated at 0.5 dB) have been normalized out of the measurements. The directivity is measured by a full two- dimensional co- and cross-polarized scans of the antenna pattern. The conversion loss presented below (Fig. 4) is defined as the power measured at the IF port divided by the 178.5 GHz RF power available at the antenna terminals. It includes the RF and IF mismatch losses and the intrinsic conversion loss of the subharmonic mixer. A minimum conversion loss of 12.8 ± 0.5 dB was measured at 178.5 GHz with an estimated local oscillator power of 4.5 mW available at the antenna terminals. The minimum conversion loss at 140 GHz was 11.2 ± 0.5 dB with an estimated available LO power of 6 mW. The conversion loss could be further reduced by 2 dB with the addition of an RF matching network between the antenna and the mixer diodes. This will result in a double-sideband conversion loss of 6-7 dB at 140 GHz or 180 GHz, which is competitive with the best available waveguide mixers.

ACKNOWLEDGEMENTS

This work was supported by the NASA/Center for Space Terahertz Technology at the University of Michigan, and at the University of Virginia by NSF grant ECS-8913169, US-Army and Aerojet Electrosystems.

REFERENCES

[1] T.F. McMaster, M.V. Schneider, and W.Snell, Jr.,"Millimeter-wave receiver with subharmonic pump," *IEEE Trans. Microwave Theory Techn.*, vol. MTT-24, pp. 948-952, December 1976.

[2] E.R. Carlson, M.V. Schneider and T.F. McMaster, "Subharmonically pumped millimeter-wave mixers," *IEEE Trans. Microwave Theory Tech.*, vol. MTT-26, pp. 706-715, October 1978.

[3] R.H. Duhamel and D.E. Isbell, "Broadband logarithmically periodic antenna structure," *IRE National Convention Record*, Part I, pp. 119-128, 1957.

[4] P.H. Ostdiek, T.W. Crowe and I. Galin, "Integration of an anti-parallel pair of Schottky barrier diodes in millimeter-wave mixers," *15'th Int. Conf. Infrared Millimeter Waves*, Orlando, Florida, December 1990.

[5] D.B. Rutledge, D.P. Neikirk and D.P. Kasilingam, "Integrated-Circuit Antennas," *Infrared Millimeter Waves*, vol. 10, Chap. 1, K.J. Button, ed., Academic Press, New York, 1983.

[6] Thomas Buettgenbach, Dept. of Physics, Mathematics and Astronomy, California Institute of Technology, Pasadena, CA 91125.

[7] W. L. Bishop et. al., "A micron-thickness planar Schottky-diode chip for terahertz applications with theoretical minimum parasitic capacitance," *IEEE MTT-S Intl. Symp.*, pp. 1305-1308, Dallas, Texas, May 1990.

[8] A.R. Kerr, " Noise and loss in balanced and subharmonically pumped mixers: Part I-Theory," *IEEE Trans. Microwave Theory Tech.*, vol. MTT-27, No. 12, pp. 938-943, December 1978.

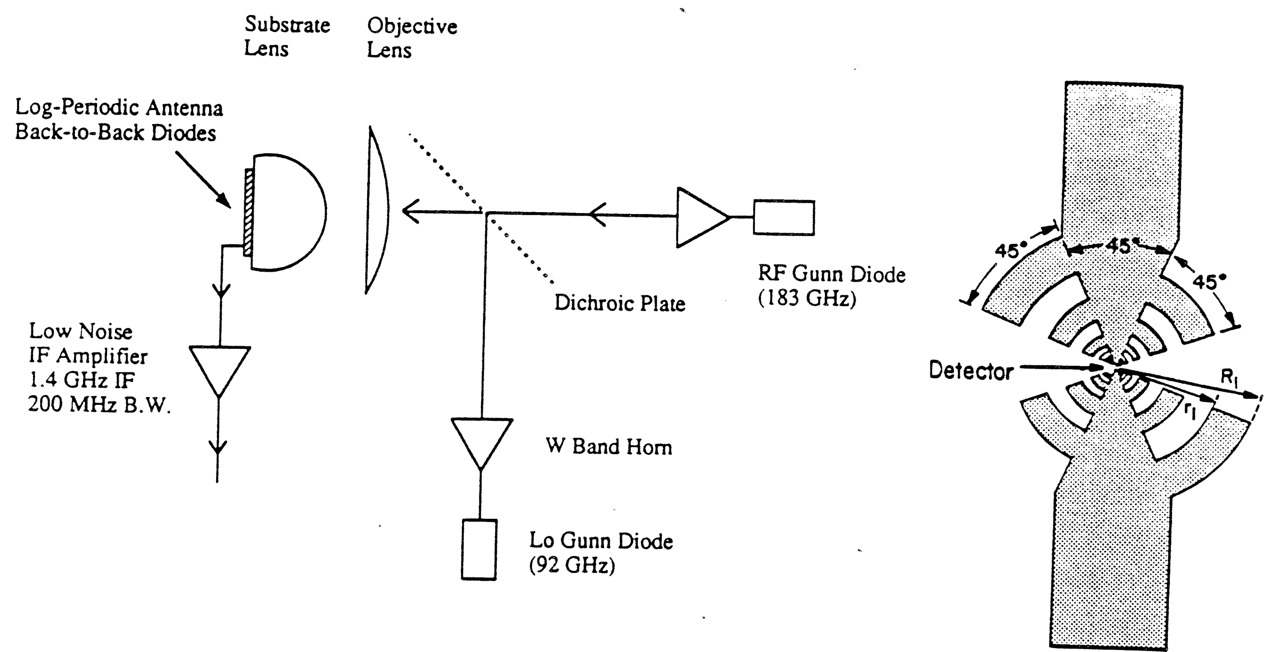

Figure 1: A quasi-optical subharmonic receiver with a dichroic plate for LO injection.

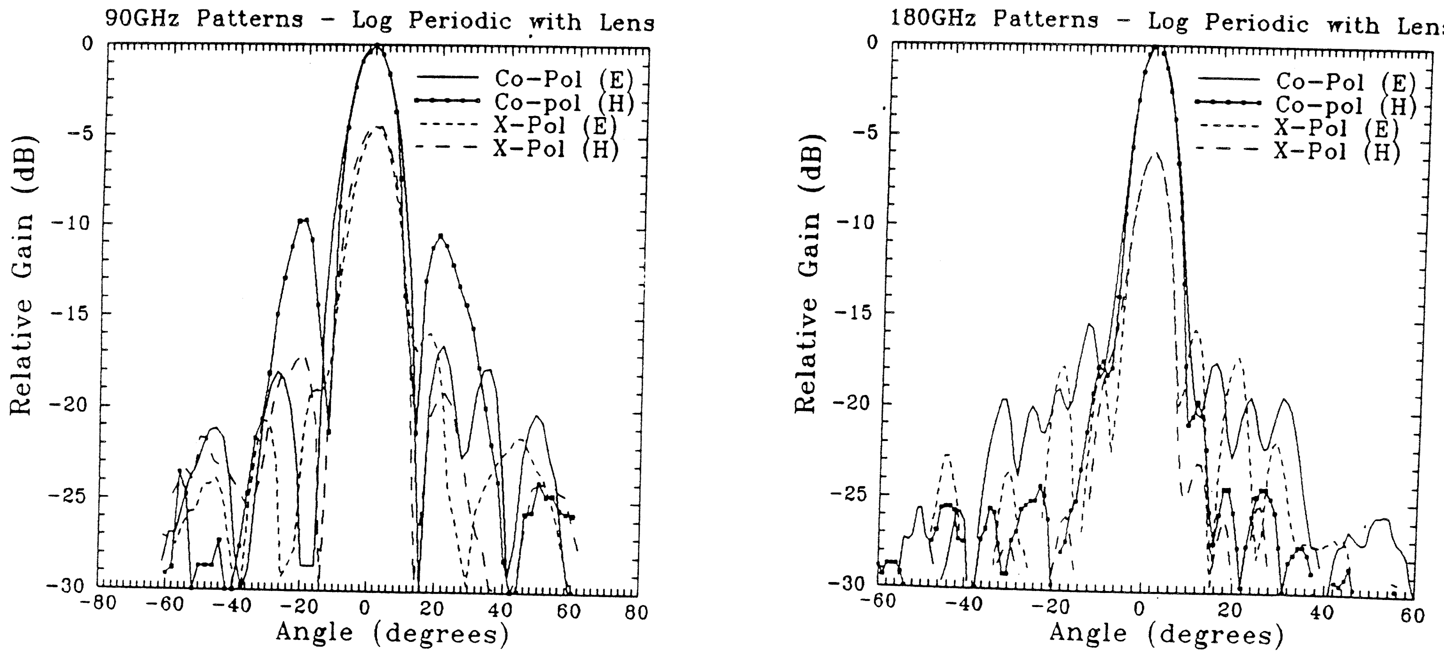

Figure 2: Measured antenna patterns at 90 GHz (left) and 180 GHz (right). The high cross-polarization component should not affect the coupling efficiency for radiometric applications but will reduce the quasi-optical local oscillator coupling by 1.5dB.

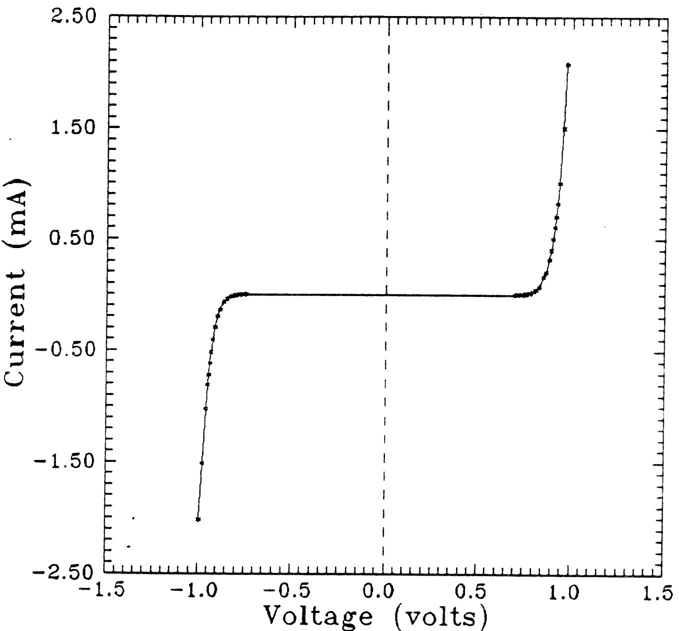

Figure 3: The measured dc I-V curve of the back-to-back Schottky diodes. The diode parameters are determined by least-square fitting of the equation $I = I_s \exp(V/nV_T - IR_s)$. The fitted parameters are $I_s = 7\text{x}10^{-17}$, $n = 1.2$ and $R_s = 11\Omega$.

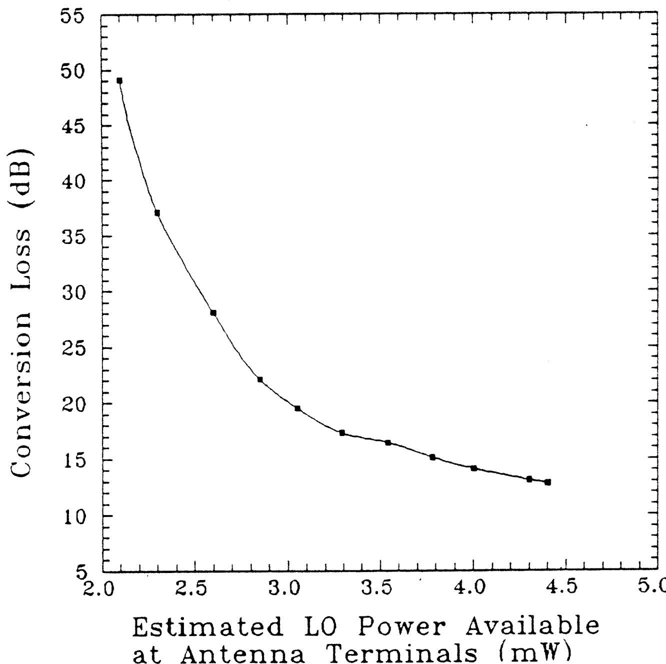

Figure 4: Measured subharmonic single-sideband conversion loss at 178.5 GHz with the antenna gain normalized out. The measured conversion loss is 12.8 ± 0.5 dB and can be reduced by 1-2 dB with a higher LO power.

380 GHz RECEIVER FRONT-END FOR THE BALLOON-BORNE RADIOASTRONOMICAL EXPERIMENT - PRONAOS -

O. Perrin, C. Robert, P. Feautrier,* P. Febvre, G. Beaudin, P. Encrenas,*
M. Gheudin, J. Lacroix,** G. Montignac**

Observatoire de Meudon, DEMIRM, 92195 Meudon Cedex, France
** Ecole Normale Supérieure de Paris, 24 rue Lhomond, 75005 Paris, France*
*** Observatoire de Bordeaux, 33270 Floirac, France*

ABSTRACT

A submillimeter balloon-born receiver, including a 380 GHz cryogenic Schottky diode mixer, with its LO source, followed by a 6 GHz HEMT IF amplifier, has been investigated. An SIS mixer with Nb/Al-Ox/Nb junctions should increase the sensitivity by a factor 2 or 3.

I. INTRODUCTION

To prepare future radioastronomical missions aboard satellites, a submillimeter balloon-borne spectrometer is being developed under the responsibility of the french Centre National d'Etudes Spatiales. This instrument will be used to simultaneously detect the 368 GHz O_2 and the 380 GHz H_2O lines in the interstellar medium. Observations in this part of the spectrum requires low atmospheric water vapor and molecular oxygen emission, so that the 2m telescope will fly under a 900 000 m^3 balloon at an altitude of $\approx$ 37 km.

2. SYSTEM DESCRIPTION

To calibrate this receiver (Fig. 1), the incoming beam is commuted between a hot load and a cold load by rotation of a flat mirror. Focusing of the beam is achieved by means of elliptical mirrors, and a Mach-Zender-type diplexer is used for LO injection to the mixer. The IF is centered at 5.85 GHz to allow simultaneous detection of the two molecular lines with only one receiver, so that both sidebands of the mixer contain a signal line. IF output is fed to a cryogenically cooled HEMT amplifier, further amplified by room-temperature amplifiers and then distributed to the Acousto Optical Spectrometer subsystem. The 374 GHz LO source consist of a phase locked 93.5 GHz Gunn oscillator. followed by two multipliers.

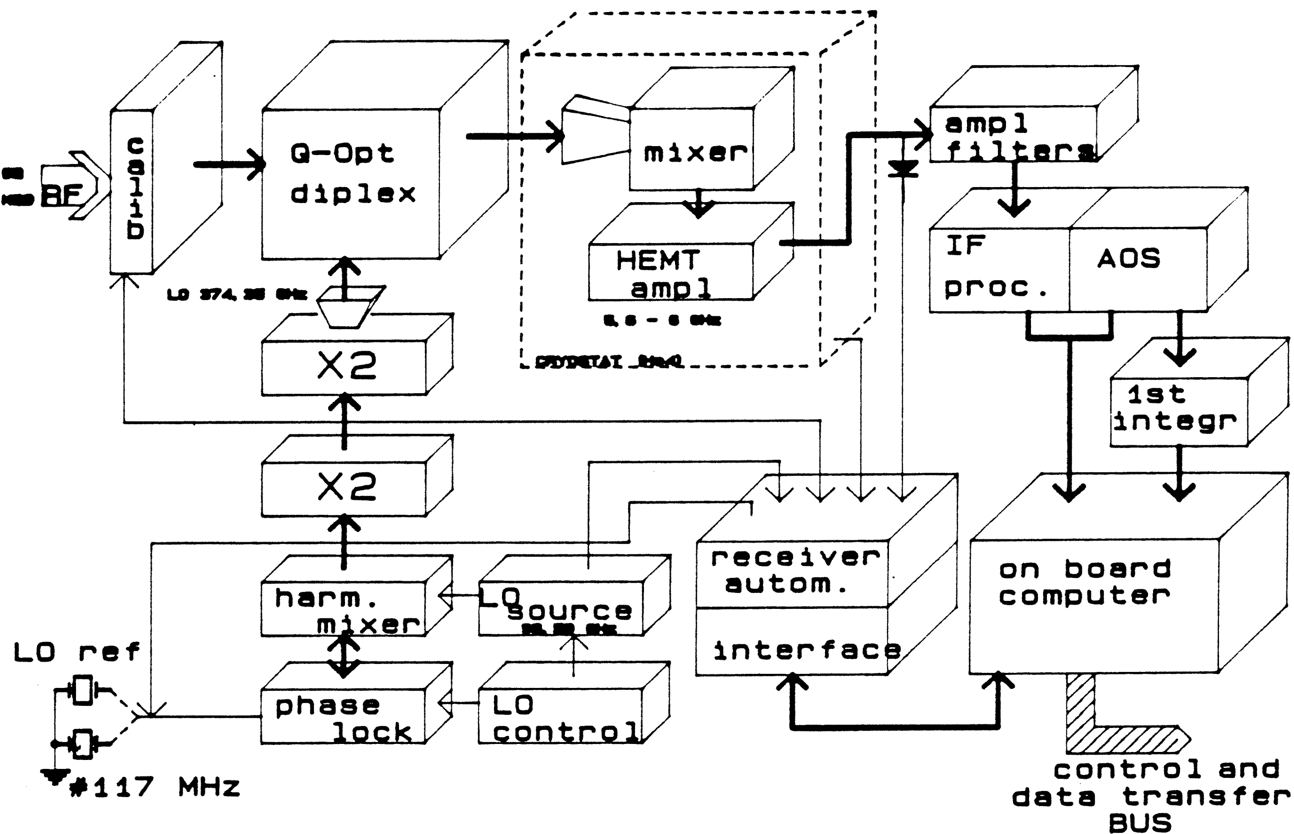

Fig 1 : In-bord recever schematic

3. SCHOTTKY MIXER DESIGN

3.1 - Diode choice

The first step in designing a submillimeter wavelength mixer is the choice of a GaAs Schottky barrier diode. The analysis given by T.W. Crowe and R.J. Mattauch[1] including time varying hot electron noise, reported receiver performance and experience of the laboratory in cryogenically cooled millimeter wavelength mixers, lead us to the choice of diodes with the following optimized parameters at 380 GHz : Cj(0) = 2.8 fF, Rs = 10 Ω at dc and Vo = $\eta kT/q$ = 29.5 mV at room temperature, and at 77 K : Rs = 29 Ω at dc and Vo = 12 mV.

3.2 - Optimum embedding impedances and driving conditions

The next task in the design procedure was to find out the optimum combination of embedding impedances seen by the diode. This was done by executing the original non-linear analysis program[2], modified to take into account time varying hot electron noise generated in the series resistance, because this noise mechanism cannot be neglected at submillimeter wavelength in an accurate mixer analysis (fig. 2). We assumed simplified embedding circuit which presents to the diode a will matched impedance at the IF port, the same impedance at both sidebands, high impedance at the second harmonic frequencies, and short-circuit at higher frequencies. This is likely to be a good approximation as it was found that sidebands beyond the second harmonic of the LO do not significantly affect the results. Moreover, with the chosen mixer mount, calculated impedances seen by the diode between 368 and 380 GHz differ by less than 10Ω, which was the accuracy of this analysis. This resulted in an optimum embedding impedance of 50 + j50Ω at both sidebands, with a 0,86 V diode bias voltage (100 μA) and a 400 μA rectified current, corresponding to a minimum mixer noise temperature, as can be seen in fig. 2. This figure also shows the effect of neglecting excess noise due to the hot electron mechanism and the correlation of its frequency components.

3.3 - Mixer mount characterization

The mixer is a single-ended fundamental waveguide mount, with a sliding finger-type contacting backshort to optimize coupling of the signals into the diode. The low value of optimum embedding impedance at sidebands lead us to choose a 0.7 x 0.12 mm reduced-height waveguide. The mixer mount includes a transition from rectangular waveguide to an integrated dual-mode Potter horn, as modified by Pickett[3], to minimize losses. The diode is contacted by a 8 µm diameter Phosphor-Bronze whisker, that has been etched. The IF is coupled out of the mixer by a section Chebychev microstrip filter, formed on a 75µm thick quartz substrate located in a 0,2 x 0,2 mm channel. This filter has been designed so that it presents a short-circuit or at least a very low impedance to the diode at the signal frequencies.

3.4 - Simplified equivalent circuit of the mixer structure

Fig. 3 illustrates a simplified equivalent circuit of the basic structure. A computer program was developed to calculate the values of Cgap and Lw from the formulae presented by R.L. Eisenhart and P.J. Khan[4]. As the whisker is bent in the practical mount, we used the approximate formula given by A.O. Lehto and A.V. Räisänen[5], which introduces a value of Lw depending upon whisker length. The low value of computed optimum embedding impedances results in a whisker as short as possible. Nevertheless, practical mount considerations lead us to use a 110 µm long whisker.

3.5 - Expected performances

The calculated impedances were then input in the mixer analysis program to find the optimum combination of mount parameter, such as whisker diameter and length, and performances of the mixer at room temperature. This resulted in the practical mount described here, with the following expected performances :

$(Tm)_{USB}$ = 1580 K, $(Tm)_{LSB}$ = 1600 K => $(Tm)_{DSB}$ = 795 K

$(Lm)_{USB}$ = 7.5 dB, $(Lm)_{LSB}$= 7.5 dB => $(Tm)_{DSB}$ = 4.5 dB

$Z_{FI} = 200\ \Omega$

3.6 - RF Measurements and results

Fig. 4 illustrates the DSB mixer noise temperature and conversion loss at various LO frequencies. Tuning of the backshort was optimized at 375 GHz only, resulting in Tm = 400 K and Lm = 0.7 dB. These performances have been obtained with 150 μA diode bias, and 500 μA rectified current, a driving condition not far from the one predicted by the non-linear analysis. Less than 200 μW of LO power was required to obtain the best noise temperature, which shows that a solid-state LO can be used to pump the mixer.

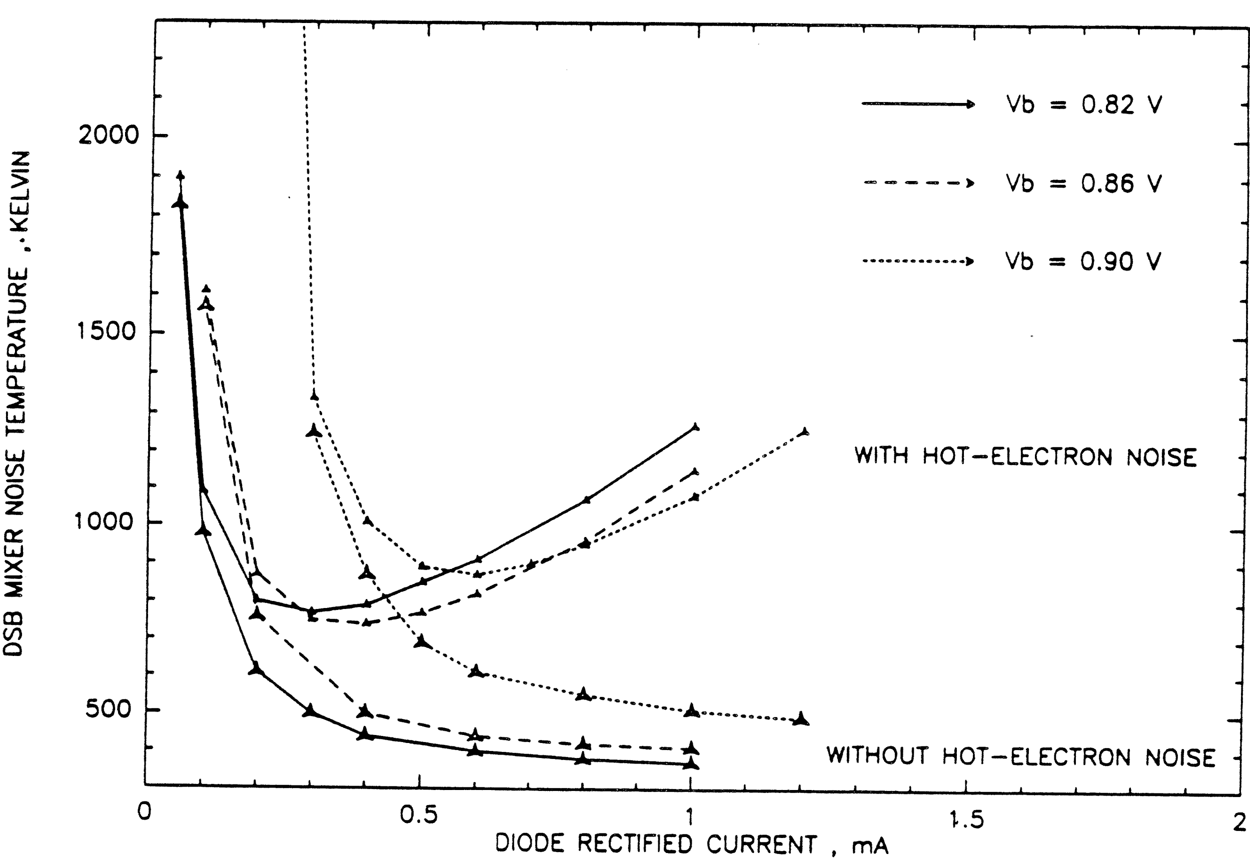

Fig. 2 : Computed minimum DSB mixer noise temperature versus P_{OL}, whith and without hot-electron noise.

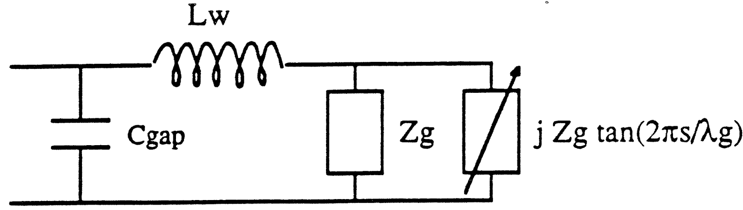

Fig. 3 : Simplified embedding network at fundamental frequency

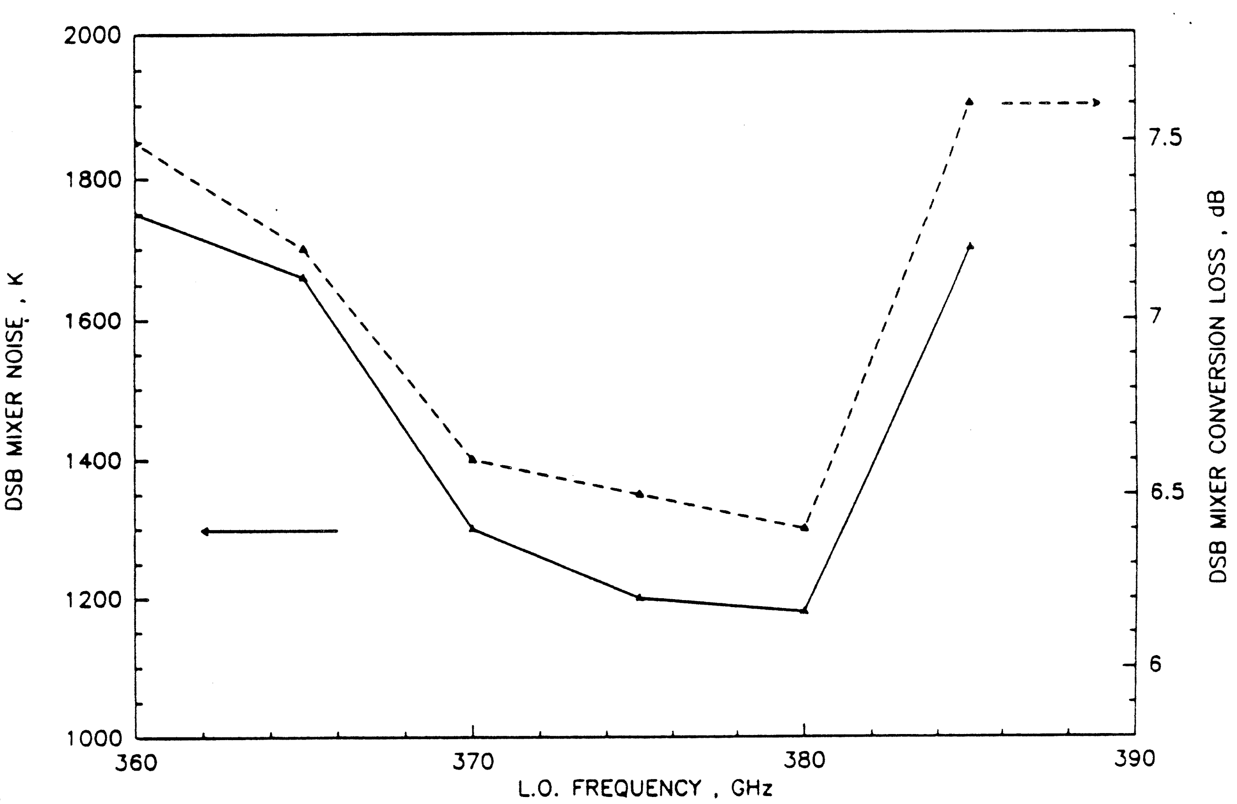

Fig. 4 : DSB mixer noise temperature and conversion loss, at various L.O. frequencies.

4. LOCAL OSCILLATOR

The 374 GHz LO source consists of a phase locked 93.5 GHz Gunn oscillator followed by two multipliers.

4.1 - Fundamental phase locked InP Gunn oscillator

Developed at the Bordeaux observatory : the fundamental InP Gunn is choice for its good performances on spectrum purity (Fig. 5a) large output power, wide band electrical tunning and reliability .

The good frequency stability≈ 10^{-8} is obtained by a classical phase-lock loop referenced to the thermaly stabilized quartz source (Fig. 5b).

Diode	Frequency (GHz)	Output power (mW)	Electrical tunning (MHz)	dF/dV (MHz/V)
Varian	93.575	40	< 200	500
Thomson	93.575	60	< 100	500
Marconi	93.575	50	> 200	600

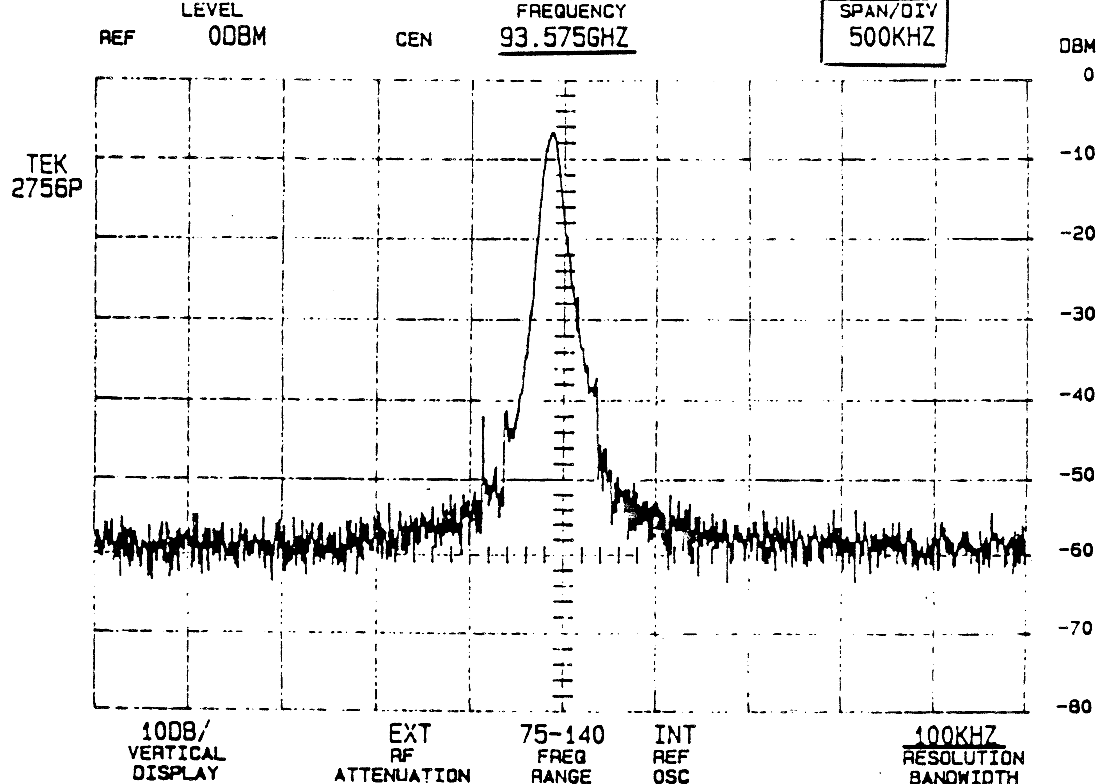

Fig. 5a : Free runing InP Gunn oscillator

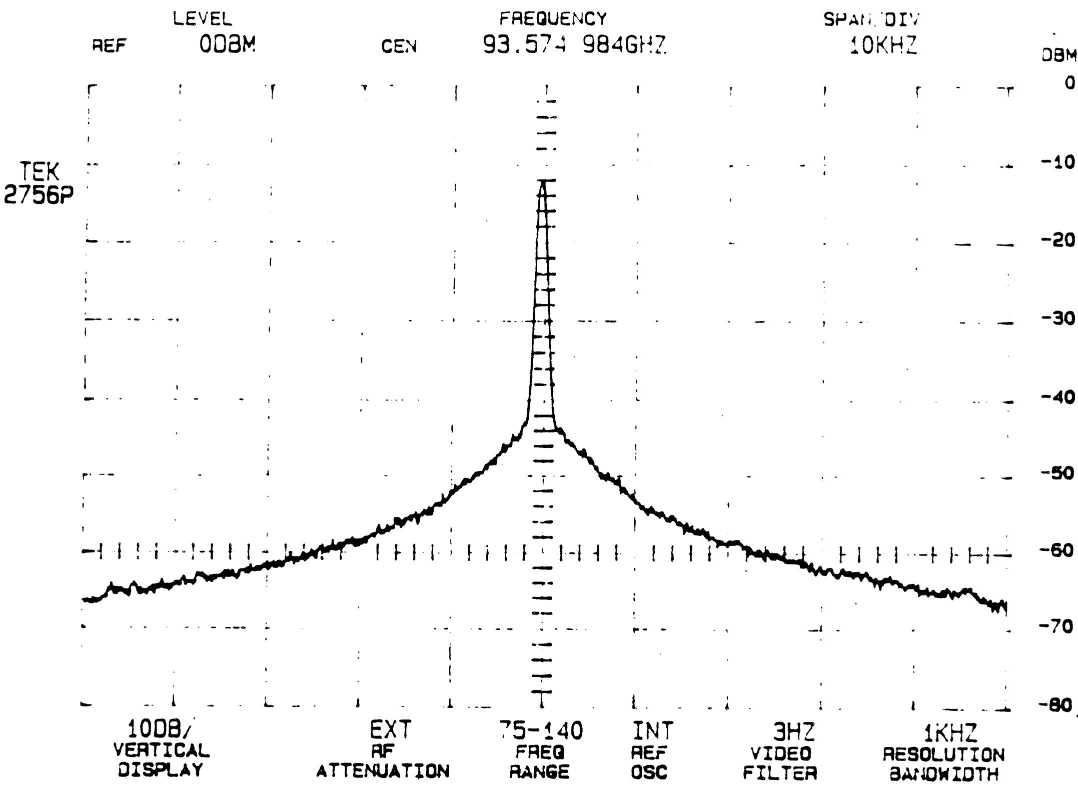

Fig. 5b : Phase-locked InP Gunn oscillator

4.2 - GaAs varactor multipliers

Two varactor doublers in serie are employed to obtain the LO power at 374 GHz.

The P. Siegel design has been used to make the **first 93,5/187 GHz doubler**. Varactor diodes from U. Va are tested and good result are obtained with the 5P8 batch (Fig. 6 a et b).

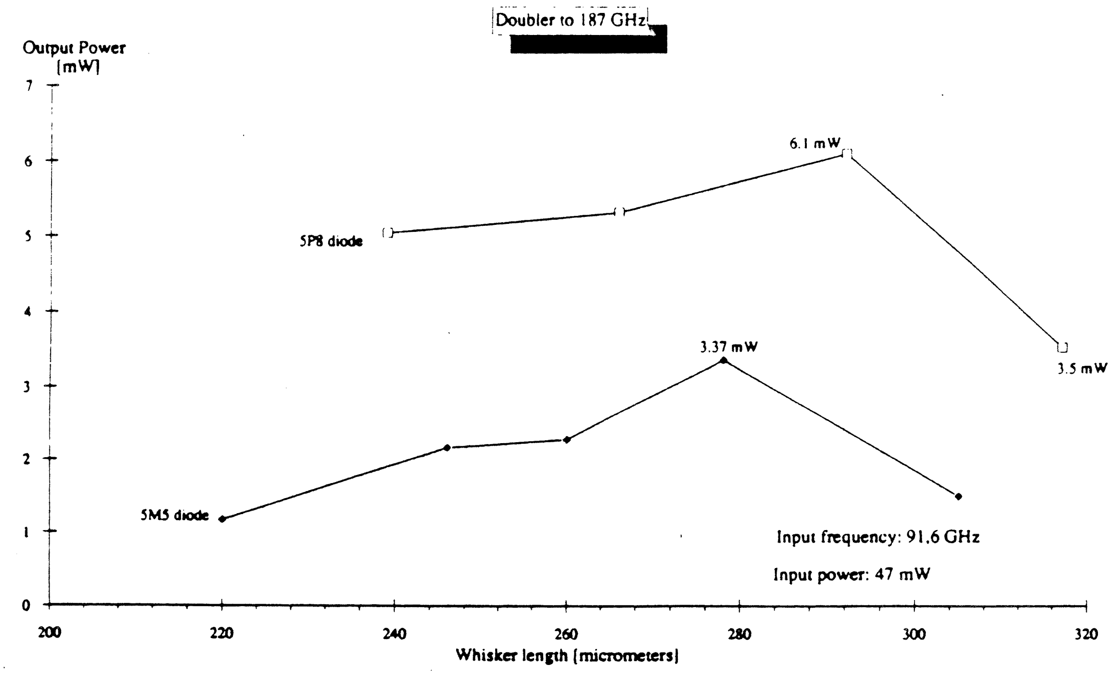

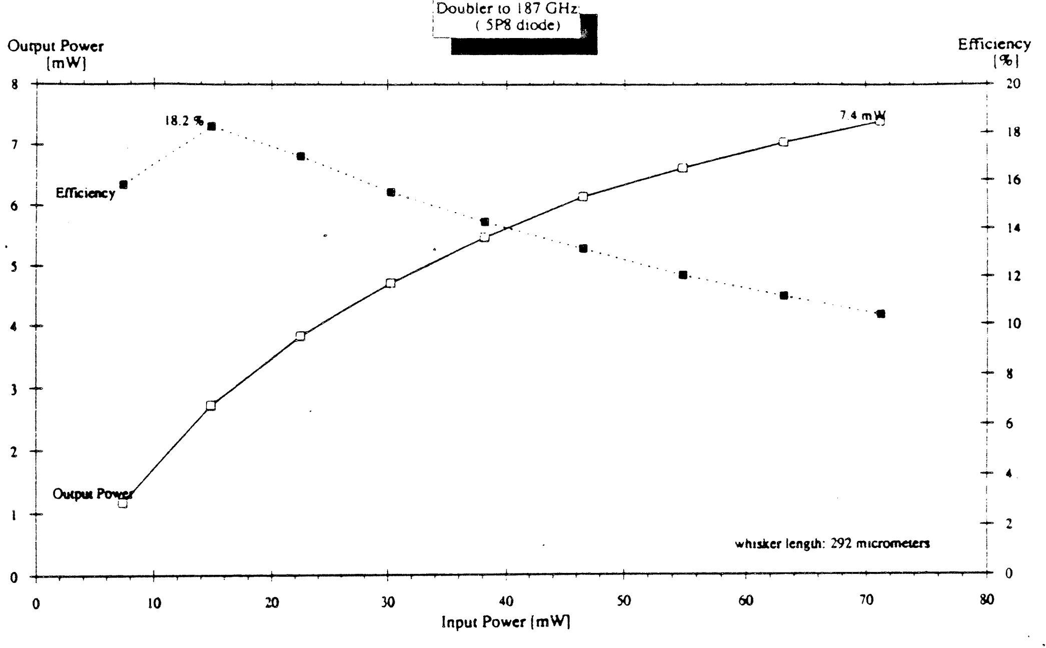

The **second 187/374 GHz doubler**, designed with an integrated horn (Fig. 7a) using U. Va varactor is under tests at this moment. The output power (Fig. 7b) is not quite powerful enough to drive a Schottky mixer ; but it is enough to pump an SIS junction.

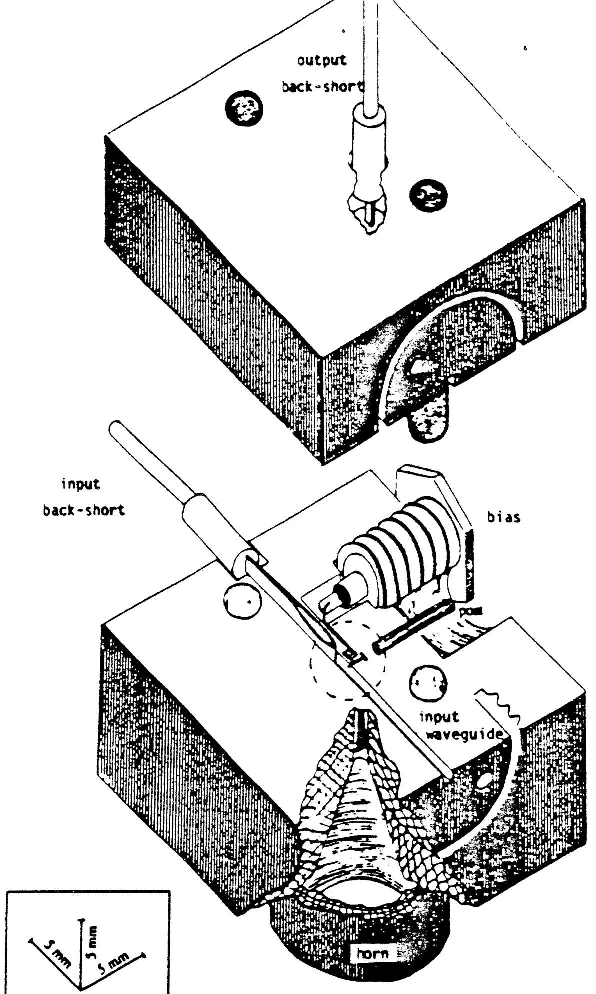

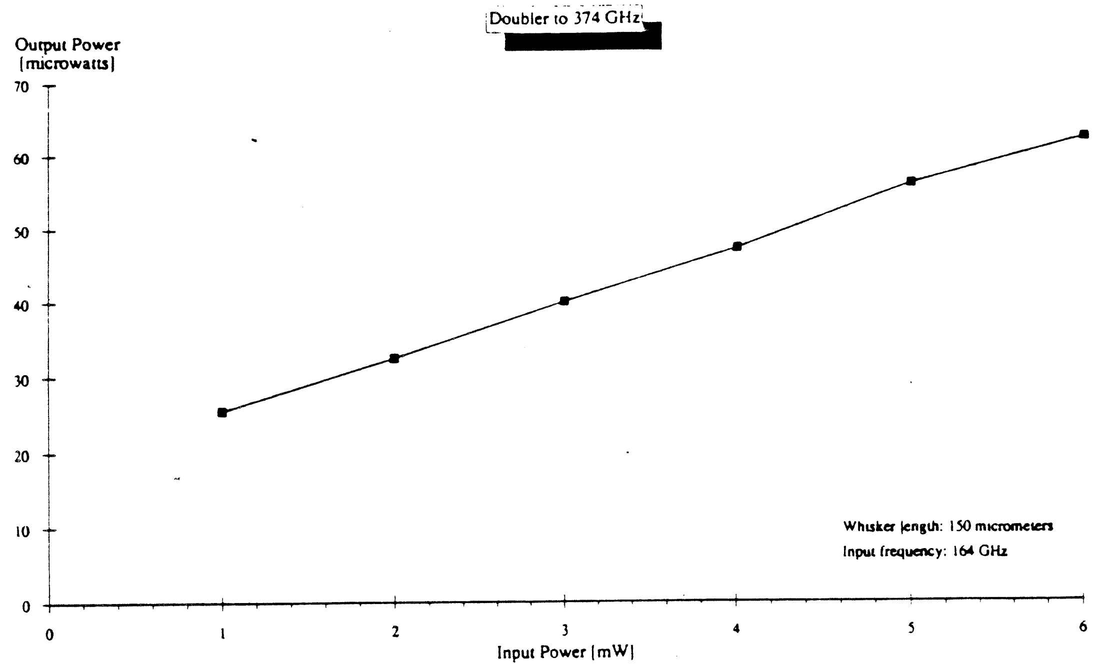

5. The 6 GHz HEMT LOW-NOISE COOLED AMPLIFIER

5.1 - Amplifier design and realization

The main aim in the design of the amplifier is to obtain a noise figure as small as possible at cryogenic temperature. Choice of transistors and of the technology of the transmission lines are two determining factors.

Amplifier gain shoud be ≥ 30 dB, so that the device includes 3 field-effect transistor stages : one HEMT (High Electron Mobility Transistor) and two conventional GaAs FET. The HEMT, which has the smallest noise figure, is at the front-end of the amplifier. After having tested several commercially available transistors, we have selected a Toshiba HEMT transistor S 8901 and two Mitsubishi FET transistors MGF 1412.

Fig. 8 illustrates the fonctional sub-assemblies of the amplifier :

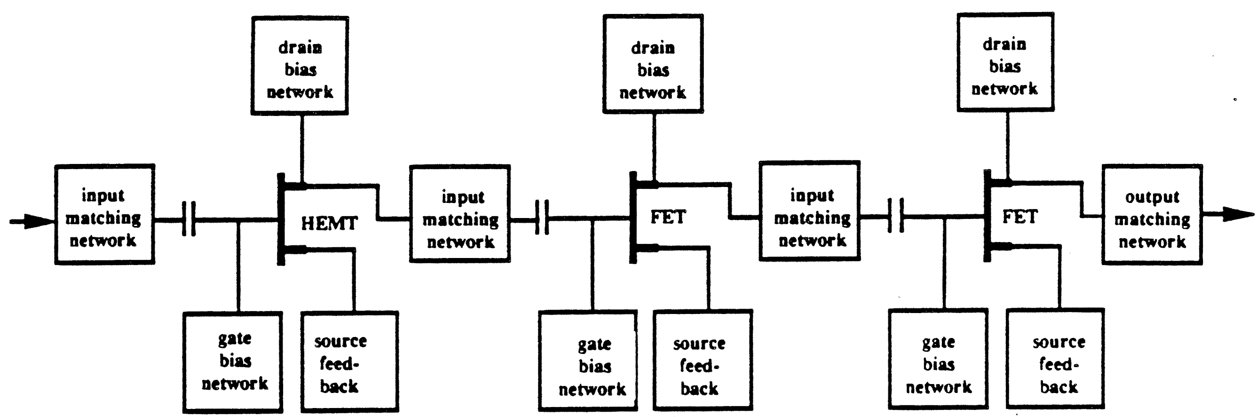

Fig. 8 : Synoptic scheme of the amplifier

The generator impedance of the transistor should be specified in order to obtain minimum noise. This optimum noise impedance is achieved by computer-aided matching lines[7]. The technology of coaxial line is chosen for its better performances at cryogenic temperatures. Indeed, it is based on the assembly of components which tolerates small contractions when the device is cooled down, thus avoiding to damage the bondings.

Matching networks mainly consist of quarter wave transformers, tunable on transmission lines[8]. Thus accurate tuning can offset the differences between transistors. Bias networks include conventional d.c. block, by-pass elements and Zener diodes to protect the transistors against surges. Source feed-backs allow low input reflexion simultaneously with the lowest noise ; they consist of a small source inductance whose connection to ground can be adjusted[9].

5.2 - Measurements and results

An important part of the study was devoted to the determination of the optimum operating temperature. In flight, the amplifier is located on a thermal screen, whose

conduction with the "4K stage" of a liquid helium increases as the amplifier temperature decreases. Thus, it is necessary to know the variation of the amplifier noise temperature as a function of the physical temperature, in order to choose the optimum screen temperature.

Gain and noise curves are presented in fig. 9 at room and cold temperatures. At a 27 K physical temperature, noise temperature is less than 21 K and gain flatness is $\pm$ 0.7 dB over the required bandwidth (5.6 - 6.1 GHz). The minimum noise temperature is 16K.

With the VSWR values ($\leq$ 1.5 at input and $\leq$ 1.3 at output), the use of our isolator is avoided. A small microstrip circuit has been realized to allow impedance matching between mixer output and amplifier input.

Noise temperature variation during the cooling is shown in Fig. 10. At the present time, we have chosen an operational temperature of 40 K as a trade-off between the weight of the cryostat and performances of the amplifier.

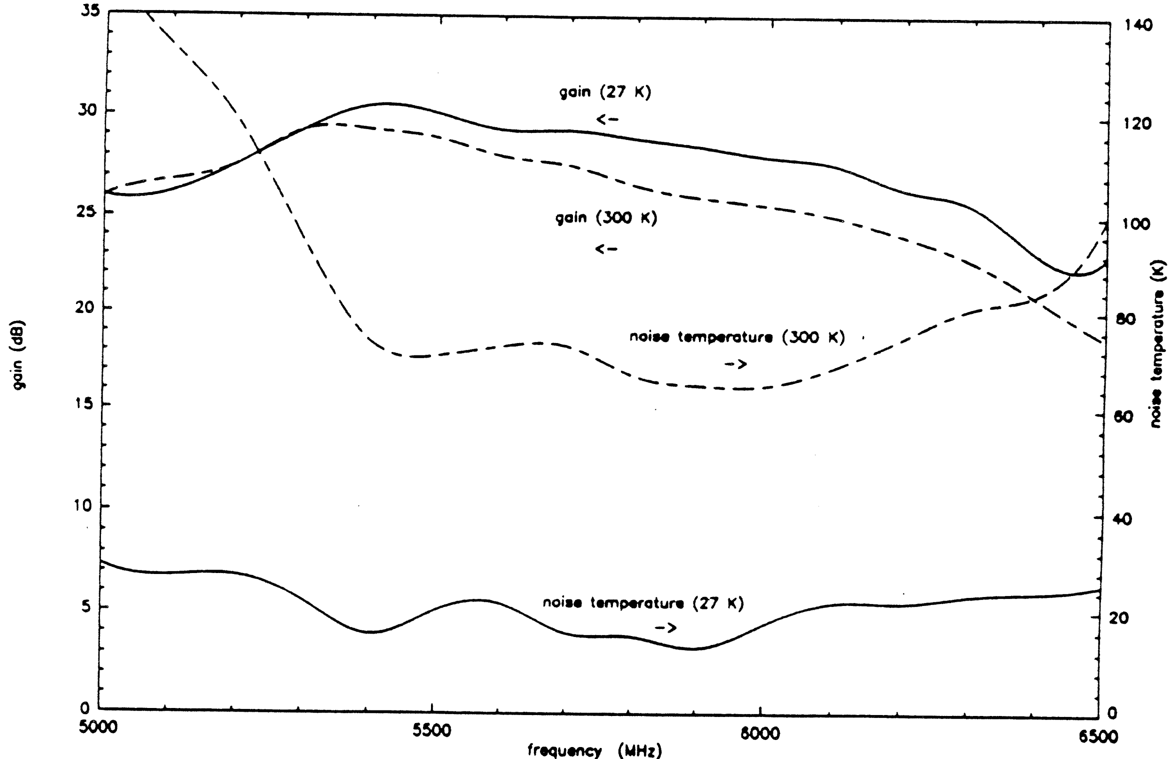

Fig. 9 : Measured characteristics of the amplifier

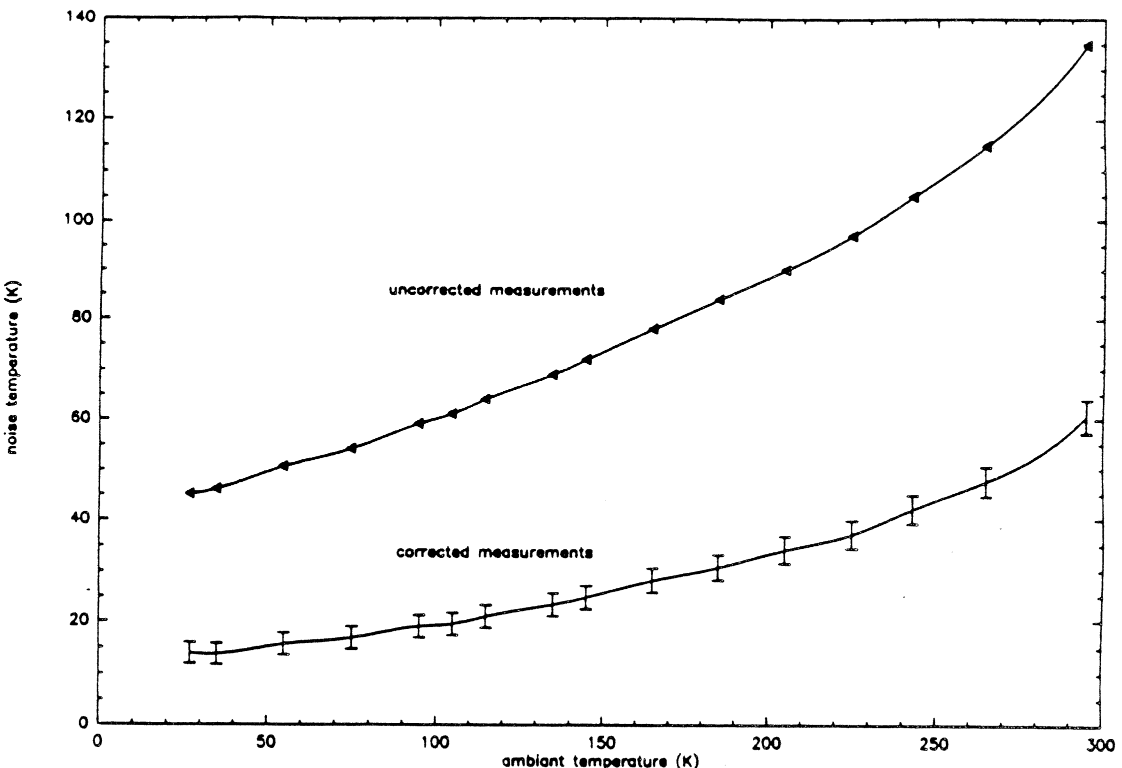

Fig. 10 : Noise temperature function of physical temperature

6. SIS Nb/Al-Ox/Nb JUNCTIONS

6.1 - Introduction

Difficulties in generating enough Local Oscillator (L.O.) power at high frequencies make SIS mixers very desirable for operation above 300 GHz. Their low LO power requirements and their low noise temperature are pushing many radioastronomy groups to develop SIS receivers in this frequency domain. While lead junctions have been widely used up to 760 GHz[10] their performance degrades with time which makes them especially difficult to use for space applications. Junctions made with a niobium or any niobium alloy film are mechanically very hard and very stable with respect to storage at room temperature and repeated thermal cyclings : we call them "all-refractory junctions". These characteristics have led these components to be used for very high speed integrated circuit technology[11,12].

The fabrication of rugged junctions using refractory materials like Nb/Al-Ox/Nb or NbN/MgOx/NbN is actively pursued by different groups as an alternative solution :

the specific properties of these types of junctions are very suitable for use in heterodyne receivers.

6.2 - Fabrication process of the tunnel junctions

We report the successful fabrication of small (2μm^2) arrays of Nb/Al-Ox/Nb junctions with excellent I/V characteristics resulting in low-noise receiver performance measured in the 80 - 115 GHz frequency range[19]. To obtain SIS mixers working at high frequencies (100 - 500 GHz), very small Nb/Al-Ox/Nb junctions (area ≤ 2 μm^2) are required. We have developed a fabrication process at the Ecole Normale Supérieure (Paris) with the collaboration of the Centre d'Etudes Nucléaires de Saclay (DPh-SRM, Ormes des merisiers) . Our process is based on "selective Niobium Etching Process (SNEP) first developed by Gurvitch et al [13,14] and improved by Yuda et al [15]. The main points are :

- deposition of the NB/Al-Ox/Nb sandwich without breaking the vacuun in order to obtain a good metal barrier interface.
- self-alignement insulation process in order to fabricate small junctions.
- definition of the junction area by Reactive Ion Etching (RIE).

The differents steps of this process are described on Fig. 11.

For radioastronomy applications, it is necessary to use fused quartz substrates ≤ 100 μm thick) and to deposit stress-free films to obtain junction areas under 4 μm[16,17]. We succeeded in realizing all Niobium junctions down to 4 μm^2 (Fig. 12). Contrary to lead junction fabrication processes, our method leads to a high rate of successful junctions made on a single wafer (about 70%) with similar characteristics (josephson current, normal resistance). For operation at 100 GHz, we fabricated an array of 4 tunnel junctions in series which corresponded to an effective area of 1 μm^2. The I/V characteristic is shown in Fig. 13. The normal resistance R_N of this array is 206 Ω. The sharpness of this curve is excellent : the leakage current is below 2 μA at 4.2 K and

unmeasurable at 2.5 K with this sensitivy. Moreover, this characteristic did not change over six months at room temperature.

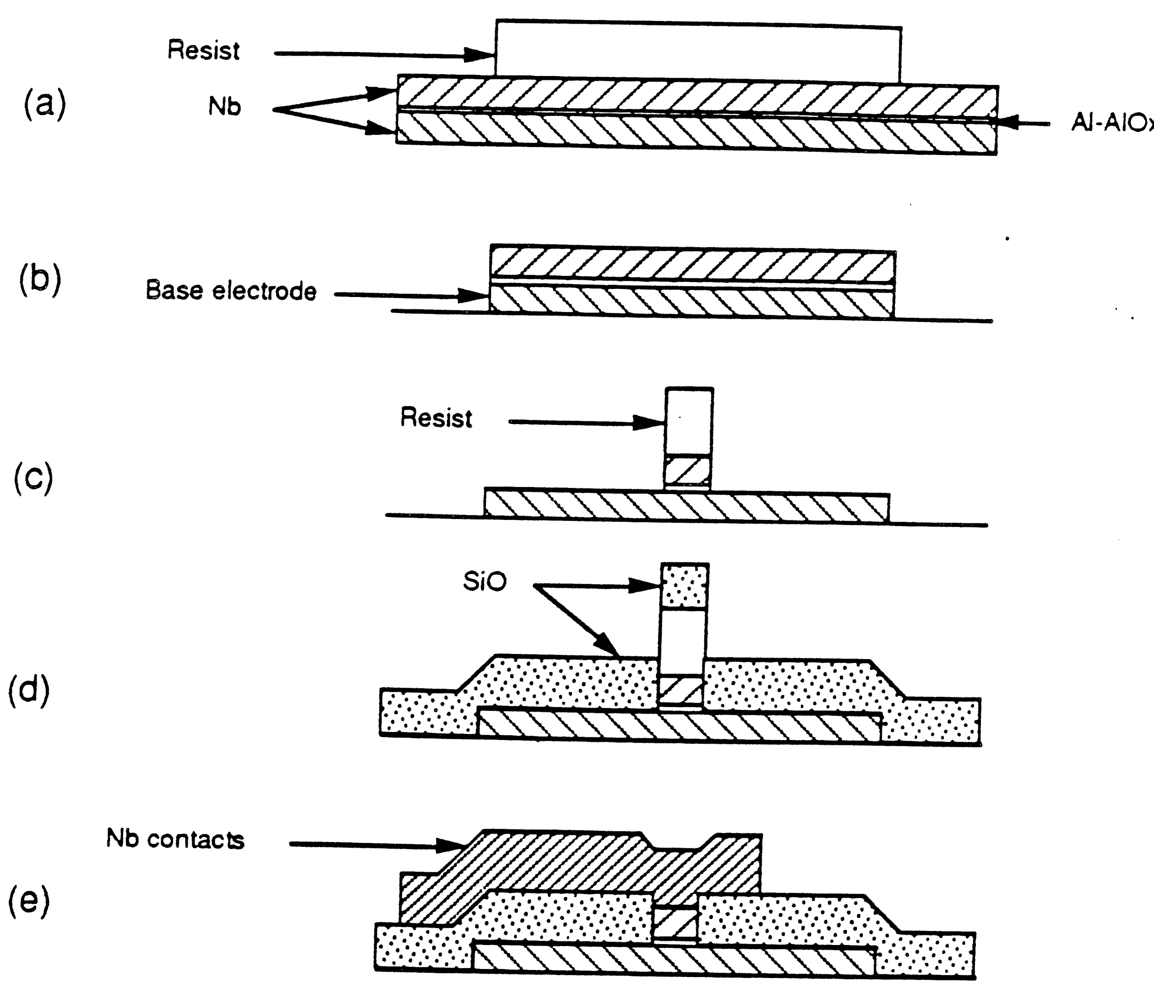

Fig. 11 : Fabrication process of NB/Al-AlOx/Nb junctions (a) Nb/Al-AlOx/Nb deposition. Definition of the base electrode by photolithography. (b) Trilayer etching. (c) Upper electrode etching. (d) self aligned depostion of a SIO insulating layer. (e) Nb interconnection layer.

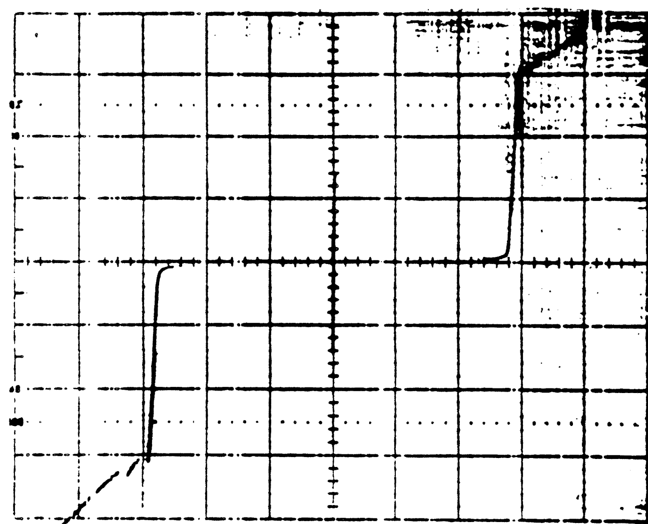

Fig. 12 : TRI 38 # 3

20μA/div

2mV/diV

$S_{eff} = 2\mu m^2; R_N = 103\ \Omega;$

$R_{300K} = 140\ \Omega$

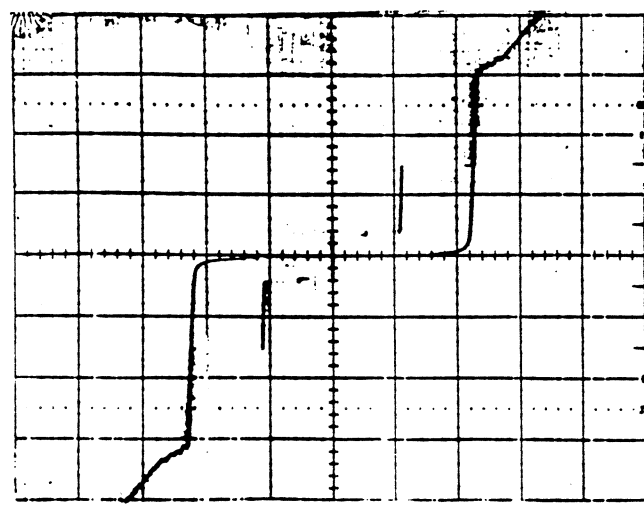

Fig. 13 : TRI 38 # 1

20μA/div

5mV/diV

$S_{eff} = 1\mu m^2; R_N = 206\ \Omega;$

$R_{300K} = 230\ \Omega$

The "knee" structure after the gap voltage is a consequence of a proximity effect[18]. This effect can be reduced by decreasing the aluminium thickness of the trilayer. We note that the Josephson currents of the two junctions in series are equal within the measurement uncertainties. This criterion is fundamental for mixer applications.

The 2 µm square junctions are very stable to repeated thermal cyclings between room and liquid He temperature. This is an important improvement compared with lead-alloy junctions.

7. CONCLUSIONS

A 380 GHz Schottky diode mixer was analysed theoretically, designed, constructed and tested over à 25 GHz bandwidth. time varying hot-electron noise has been taken into account, resulting in a more accurate analysis. Theoretical simulation showed that is may be possible to obtain 4.5 dB DSB conversion loss, and 800 K mixer noise temperature. However, these performances require reduced bandwidth and lossless waveguide mount, which is far from a pratical mount at 380 GHz. Experimentally, we obtained minimum conversion loss and noise : Lm = 6.5 dB and Tm = 1200 K, at 375-380 GHz. The main reason to the difference between theoretical and experimental results may be losses of the waveguide mount, as 1.8 dB surface resistance losses lead to almost the same performances. The rest of the difference can be explained with slightly different diode parameters, and excess noise due to the use of a carcinotron as the LO, or overlooked mechanisms such as intervalley scattering and trap induced noise[6]. The next step will be to cool the mixer down to cryogenic temperature. However, these first experimental results confirm the possibility of using such a mixer in a submillimeter balloon-born spectrometer for radioastronomical observations.

The 374 GHz phase-locked LO source has been made with an InP fundamental Gunn oscillator at 93,5 GHz followed by two GaAs varactor doublers. This subsystem is under tests but it gives enough power to drive an SIS mixer.

An HEMT IF amplifier has been specifically designed for cryogenic applications, it meets fully the specifications and will be used in connexion with a submillimeter mixer. The contribution of the amplifier to the system noise is about 20%. Next improvements is to smooth the gain and noise curves over the band of interest.

SIS Nb/Al-Ox/Nb junctions with small areas have been sucessfully fabricated, implemented and characterized in a receiver system working in the 3 mm wave frequency range[19]. A very important fact is that the Nb junctions proved very stable with repeated thermal cyclings betwen room and liquide He temperature. This is an important improvement compared to Pb junctions. The Nb/Al-Ox/Nb junctions do constitute a very promising mixing element for space applications. Many improvements on the fabrication process are in view in order to reach 1 μm^2per junction and to operate up to 400 GHz for the balloon borne experiment : study of etching profiles, utilization of an electron beam lithography, and development of other fabrication processes.

Acknoledgments : This work has been made with the technical contribution of A. Deschamps, C. Gac, F. Gadéa, A. Germont, P. Landry, G. Ruffié (DEMIRM) ; S. Lebourg, J. Morin, P. Vola (SERT-Obs Meudon) ; V. Thévenet, F. Gex (DASGAL-Obs de Paris) ; M. Bois, M. Hanus, M.C. Lemonnier, J.C. Pernot (ENS-Paris) ; M. Chauvet (Obs, Bordeaux) and J. Narbonne, G. Pons (CESR, Toulouse).

8. REFERENCES

1 - Crowe T.W., Mattauch R.J. : "Analysis and optimization of millimeter and submillimeter wavelength mixer diodes", IEEE-MTT, vol. MTT-35, feb. 1987

2 - Siegel P.H., Kerr A.R., Hwang W. : "Topics in the optimization of millimeter-wave", NASA technical paper 2287, 1984

3 - Pickett H.M., Hardy J.C., Farhoomand J. : "Characterization of a dual-mode horn for submillimeter wavelengths", IEEE-MTT, vol. MTT-32, aug. 1984.

4 - Eisenhart R.L., Khan P.J. : "Theoretical and experimental analysis of a waveguide mounting structure", IEE-MTT, vol. MTT-19, aug. 1971.

5 - Lehto A.O., Räisänen A.V. : "Embedding impedance of a millimeter wave Schottky mixer : scaled model measurements and computer simulations", Int. J. of IR. and MM. Waves, vol. 4, n)4, 1983.

6 - Hegazi G.M., Jelenski A., Yngvesson K.S. : "Limitations of microwave and millimeter-wave mixers due to excess noise", IEEE-MTT, vol. MTT-33, dec. 1985.

7 - Pospierszalski M.W. : "Modeling of noise parameters of FET's and MODFET's and their frequency dependence, IEEE trans MTT, vol. 37, sept. 1989.

8 - Tomassetti G., Weinreb S., Wellington K. : "Low noise, 10.7 GHz, cooled, GASFET amplifier", NRAO Electronics Division Internal Report n°222, nov. 1981.

9 - Weinreb S. : "Low noise cooled GASFET amplifiers, IEEE trans. MTT, vol. 28, oct 1980.

10 - Buttgenbach T.H., Miller R.E., Wengler M.J., Watson D.M. and Phillips T.G. : IEEE trans. MTT, vol. MTT-36, pp 1720-1726, 1988.

11 - 12 - Hoko H., Imarura T., Hasuo S. : "Vertically integrated josephson integrated circuits with stacked Nb/Al-Ox/Nb junctions", Tech. Digest of international Electron devices meeting, Washington, DC, pp 385-388, 1987.

13 - Gurvitch M., Washington M.A., Huggings H.A., Rowell T.M. , IEE Trans Magn. MAG-19, 791 , 1983.

14 - Gurvitch M., Washington M.A., Huggings H.A., Appl. Phys. Lett. 42, 472, 1983

15 - Yuda M., Kuroda K., Nakamo J., Jap Journ. of Appl. Phys., vol. 26, n°3, march 1987.

16 - Wu C.T., Thin Solid Films, 64, 1979, pp 103-110

17 - Kuroda K., Yuda M., J. Appl. Phys. 63(7), April 1988.

18 - Morohashi S., Haquio S., J. Appl. Phys., Vol 61, pp 4835-4849, may 1987.

19 - Feautrier P., Blondel J., Hanus M., Chenu J.Y., Encrenaz P., Carter M. : "Low noise 80-115 GHz quasi-particule mixer with small Nb/Al-Ox/Nb tunnel junctions", International Journal of Infrared and Millimeter waves, vol. 11, n°2, 1990.

SUBMILLIMETER RECEIVER DEVELOPMENT AT THE UNIVERSITY OF COLOGNE

J.Hernichel, F.Lewen, K.Matthes, M.Klumb
T.Rose, G.Winnewisser, P.Zimmermann

I. Physikalisches Institut
Universität zu Köln
Zülpicher Straße 77
D-5000 Köln 41
Germany

Abstract

A 345 GHz radio-astronomy receiver was developed at the I. Physik. Institut of the university of Cologne and optimized for observations of the CO 3→2 line. The GaAs Schottky mixer and HEMT-amplifier are cooled to 20 K. The DSB noise temperature measured at the telescope is in the range of 350-380 K. A quasi-optical mirror arrangement focuses the sky and local oscillator radiation through a Potter horn into the mixer. For diplexing we use a folded Fabry-Perot. In order to optimize the observing mode, the stability was analyzed through the Allan variance method adopted in Cologne for this purpose using a 1 GHz bandwidth acousto-optical spectrometer (AOS) built in Cologne. The results of the Allan plots showed that the complete system could be operated in total power mode with integration times up to 100 seconds per duty cycle. Baseline ripples were analyzed in detail by simulated spectra with the AOS and were reduced by insertion of tilted vacuum windows and installing a phase shifter in the signal path.

A 460 GHz "bread board" receiver was tested in the lab. The final receiver should be finished in fall 1991 so that the first observing run will be in winter 1991/92.

Introduction

Astronomical observations at wavelengths below 1 mm require accurately figured telescopes located on very dry sites. These requirements are well satisfied by the Cologne radio telescope located on the Gornergrat near Zermatt, Switzerland (KOSMA, Kölner Observatorium für Submillimeter Astronomie). The site has excellent weather conditions in winter time: in the period mid-November to mid-March the precipitable water vapor is below 1 mm for about 20% of the time. The 3 m telescope is a Cassegrain antenna with an altitude-azimuth mount and a surface accuracy on manufacture of 30 μm rms. Since December 1988 the telescope has been equipped with a GaAs Schottky mixer receiver operating around 345.8 GHz. With a spatial resolution of about 80" it is ideally suited for mapping large areas of molecular clouds. The submillimeter Schottky receivers presently developed are steps of a large program aiming at a Schottky receiver at 650 GHz with solid-state LO source for future airborne and space applications.

The 345 GHz Receiver

As a first step into the submillimeter range we have developed a 345 GHz Schottky-Receiver [1]. Based on the experiences of two winter sessions at the observatory we modified the optics and designed a new system for the winter 1990/91 observing period. We use a foldet Fabry-Perot resonator (FPR) instead of a Martin-Puplett Interferometer (MPI). Measurements have shown that the transmission at the band-pass edge (±300 MHz) is 90% for the MPI compared to 98% for the FPR. This will give a better signal-to-noise ratio at the band edge. Transmission loss through the diplexer is 0.5 dB. A block diagram of the receiver is shown in figure 1. The quasi optical design incorporates elliptical of-axis mirrors. The mirror diameters are three times the 1/e beam radius, resulting in power loss of less than 20 dB. The new mirrors are corrected for phase errors [5] and were produced on the NC-milling machine in our institute. The power loss through the optics is in the range of 0.9–1.1 dB. For calibration purposes the signal input port can be switched to a cold load (40 K) and a hot load (300 K) by a load-select mirror. For decoupling the mixer block from vibrations of the cold-head, we located the mixer on a fiberglass support at the dewar bottom. To cool down the mixer we connect it via flexible copper cable with the 18 K-stage. Local oscillator power is provided by a 115 GHz Gunn oscillator (PLL stabilized) followed by a varactor tripler which was developed at the University of Cologne. The Gunn oscillator is a GaAs type with 40 mW output power. The multiplier uses a University of Virginia Schottky

diode of type 6P4. The multiplier produces an output power of 3.2 mW (8% efficiency) [8]. The mixer uses a single diode, is fundamentally pumped and the IF section is coaxial. The 2I1-150 diode (Univ. of Virginia) has C_0=4.5 fF, R_s=13.5 Ω and U_{br}=8.0 V. The bandwidth of the HEMT-amplifier is 800 MHz at 1.4 GHz midfrequency; its noise temperature is ≃10 K [3]. The system noise temperature measured at the telescope is 350-380 K (DSB) compared to 500-550 K with the "old" version optics.

We did baseline ripple measurements by using a phase shifter. The idea is to shift standing waves periodically by $\lambda/2$ so that the averaged baseline ripple disappears. In our case the phaseshifter consists of a 0.21 mm half teflon disk, rotating with 20 Hz. Figure 2 shows that the power amplitude reduction is on the order of factor 2–3. In order to optimize the observing mode we had to get information about the system stability. With the knowledge of the statistical behavior of the complete sytem, (source , front end and back end) we could decide if the RMS noise decreases like white noise with longer integration time, in relation to the radiometer formula. This was analysed through the Allan variance method [6] adopted in Cologne, using a 1 GHz bandwidth acoustooptical spectrometer (AOS) built in Cologne. The program allows to show the collected data of two AOS–channels as the normalized count difference (NCD) between them. It indicates the noise evaluation versus time (figure 3). The result of the Allan plots (figure 4) shows that the complete sytem stability allows to operate in total power mode with an integration times up to 100 seconds per duty cycle [2]. Baseline ripples were analyzed in detail by simulated spectra with the AOS and were reduced by insertion of tilted vacuum windows and location of the cold load at the Brewster angle, to avoid standing waves in the optical path.

Beam pattern measurements have been made for the mixer (modified Potter horn, figure 5), the whole system, and the receiver integrated at the telescope. We measured a 1/e opening angle of the Potter horn Θ_{0m}=10.5° compared to the calculated value Θ_{0c}=10.3°. The measured receiver beam has Θ_{0m}=8.0°-8.6° compared to the calculated value Θ_{0c}=8.2°.

The 460 GHz Receiver

The next step to higher frequencies is the 460 GHz receiver. First heterodyne measurements were made in the lab. A block diagram of this receiver is shown in figure 6. The signal path is P1,E1,P2, diplexer, P3, E4 into the mixer. The LO-path is E2, diplexer, P3, E4, mixer ("E" stands for elliptical, and "P" for plane mirror). The hot load and a flat mirror for the cold load (E3) are motor driven. The LO is a InPh Gunn oscillator; 45 mW at 114.7 GHz, followed by a varactor quadrupler using a Univ. of Virginia Schottky diode 2T2; R_s=12Ω, C_j=5 fF. The multiplier output power is 800 μW (efficiency=1.8%). The mixer is a Schottky waveguide mixer with a 1T6 diode (R_s=20 Ω, C_{j0}=0.35 fF). The uncooled mixer conversion loss and noise temperature were measured [4]: T_m=1700 K L_m=6.8 dB. The overall uncooled system temperature is T_s=3500 K (DSB). One of the next steps will be to optimize the mixer IF-matching. The final cooled receiver should be ready for a CO 4→3 observing run in fall 1991.

Conclusion

We have designed and built a cryogenically cooled 345 GHz receiver which has been installed on the 3 m KOSMA telescope to observe CO 3→2 in the interstellar medium. The cooled mixer is a GaAs Schottky diode mounted in a waveguide structure. Local oscillator injection is by quasi-optical Fabry-Perot ring resonator. The noise temperature measured at the telescope is 350-380 K (DSB). We have designed and built a 460 GHz test system. The uncooled noise temperature is 3500 K (DSB). The final receiver (cooled version) will be installed in the telescope in the winter of 1991/92.

Acknowledgements

The receiver development presented here was funded by the Bundesminister für Forschung und Technologie (BMFT), and partly by the Deutsche Forschungsgemeinschaft (DFG) through grant SFB-301.

References

[1] HERNICHEL, J.: *Aufbau und Inbetriebnahme des 345 GHz Empfängers für das Kölner 3 m-Radioteleskop*, Diplom Thesis, Univ. Cologne (1989).

[2] KLUMB, M.: *Untersuchung der Grenzempfindlichkeit eines radioastronomischen Empfangssystems*, Diplom Thesis, Univ. Cologne (1990).

[3] LEWEN, F.: *Aufbau und Optimierung eines HEMT-ZF-Verstärkers*, Diplom Thesis, Univ. Cologne (1990).

[4] MATTHES, K.: *Aufbau eines 460 GHz-Empfangssystems*, Diplom Thesis, Univ. Cologne (1990).

[5] ROSE, T.: *Aufbau eines SIS-Empfangssytem mit quasioptischem Mischer*, Diplom Thesis, Univ. Cologne (1989).

[6] SCHIEDER, R.: *Characterisation and Measurement of System Stability* Proceedings of SPIE. Vol. 598, pp. 189-192 (1985).

[7] WINNEWISSER, G., ZIMMERMANN, P., HERNICHEL, J., MILLER, M., SCHIEDER, R., UNGERECHTS, H.: *CO submillimeter observations from Gornergrat*, Astron. Astophys. 230,248-251 (1990).

[8] ZIMMERMANN, P.: *490 GHz solid state source with varactor quintupler*, Proceedings of 13th International Conference on Infrared and Millimeter Waves (1988).

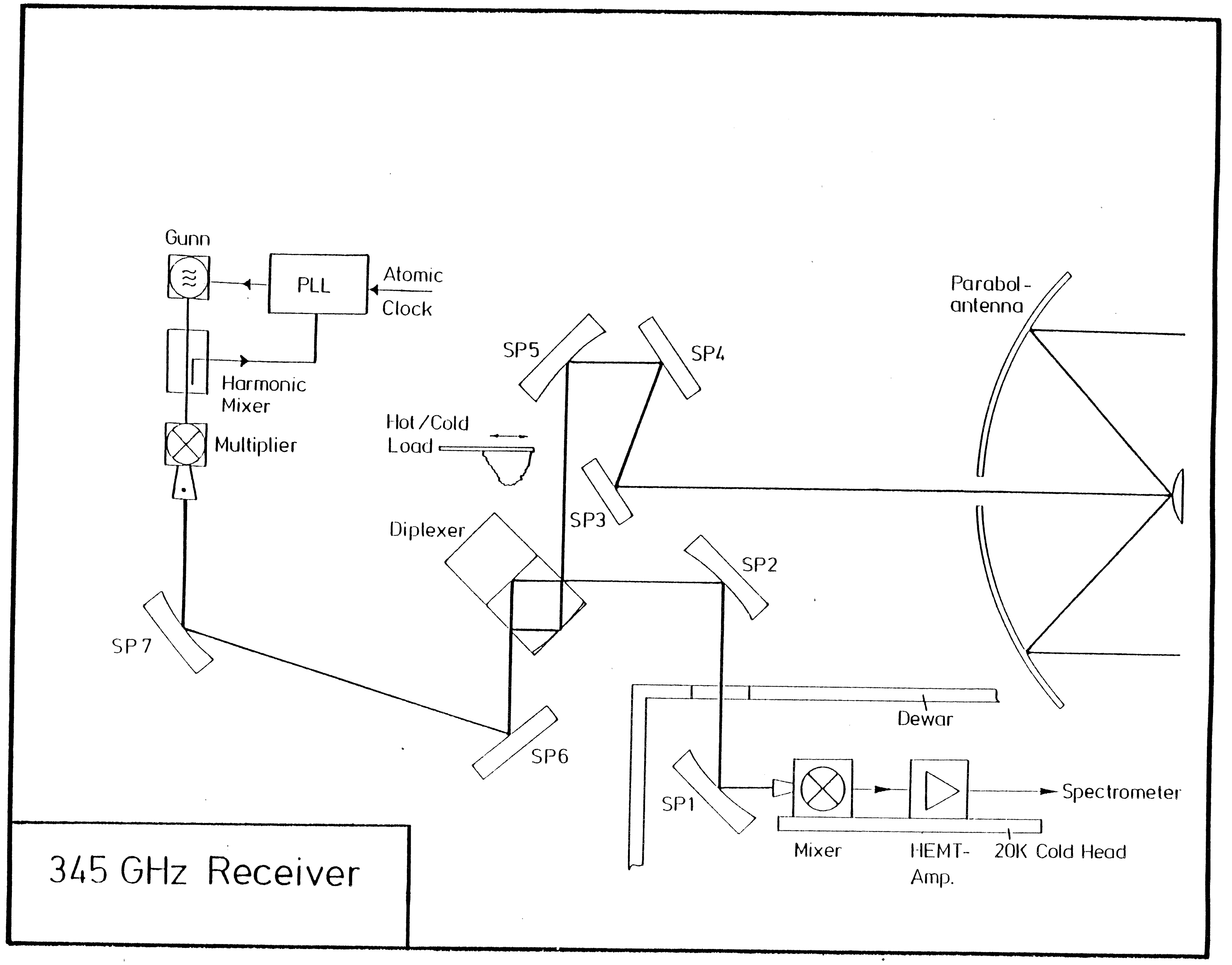
Gunn
PLL
Atomic
Clock
Harmonic
Mixer
Multiplier
Hot/Cold
Load
SP5
SP4
SP3
Diplexer
SP2
SP7
SP6
SP1
Parabol-
antenna
Dewar
Mixer
HEMT-
Amp.
20K Cold Head
Spectrometer
345 GHz Receiver

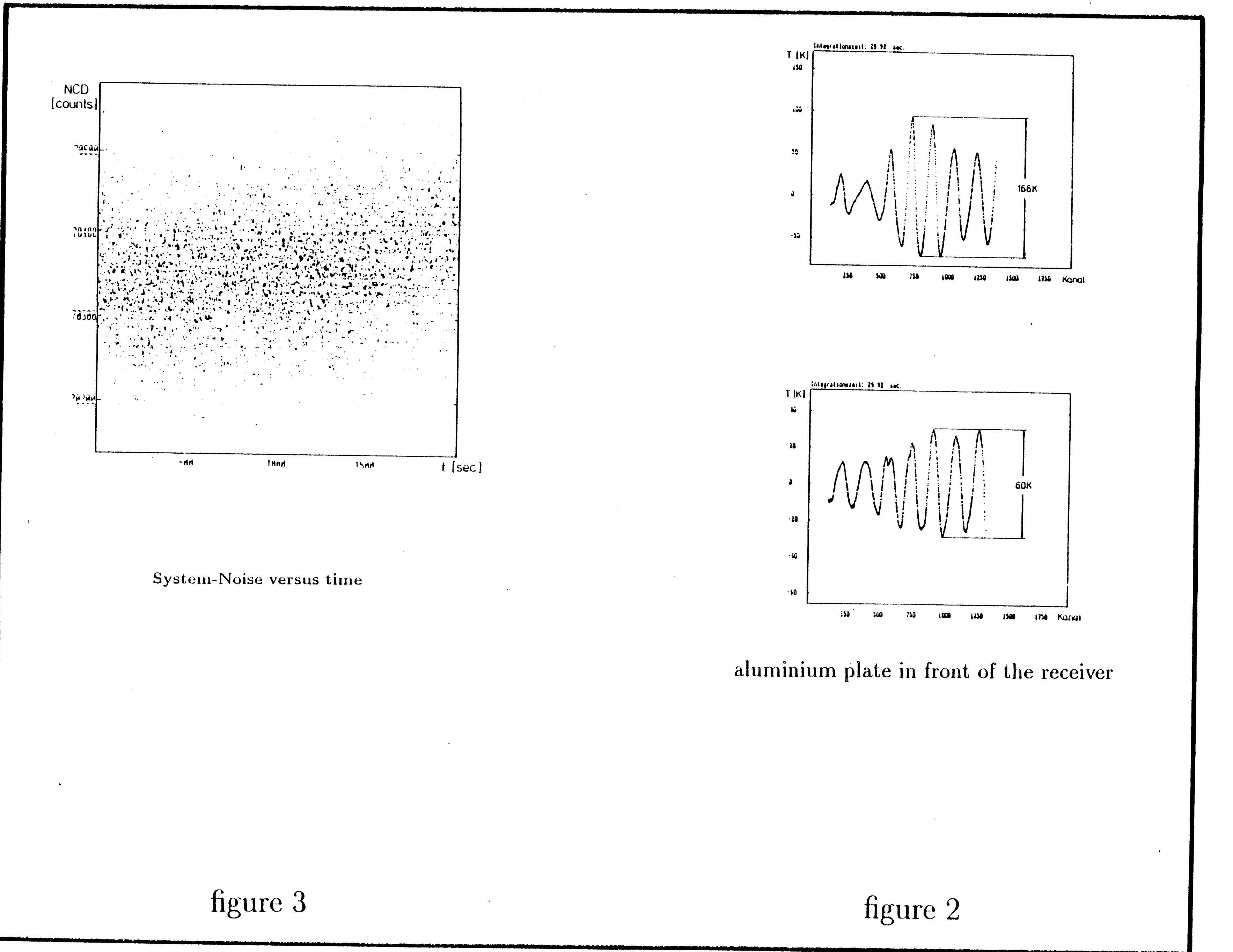

System-Noise versus time

aluminium plate in front of the receiver

figure 3

figure 2

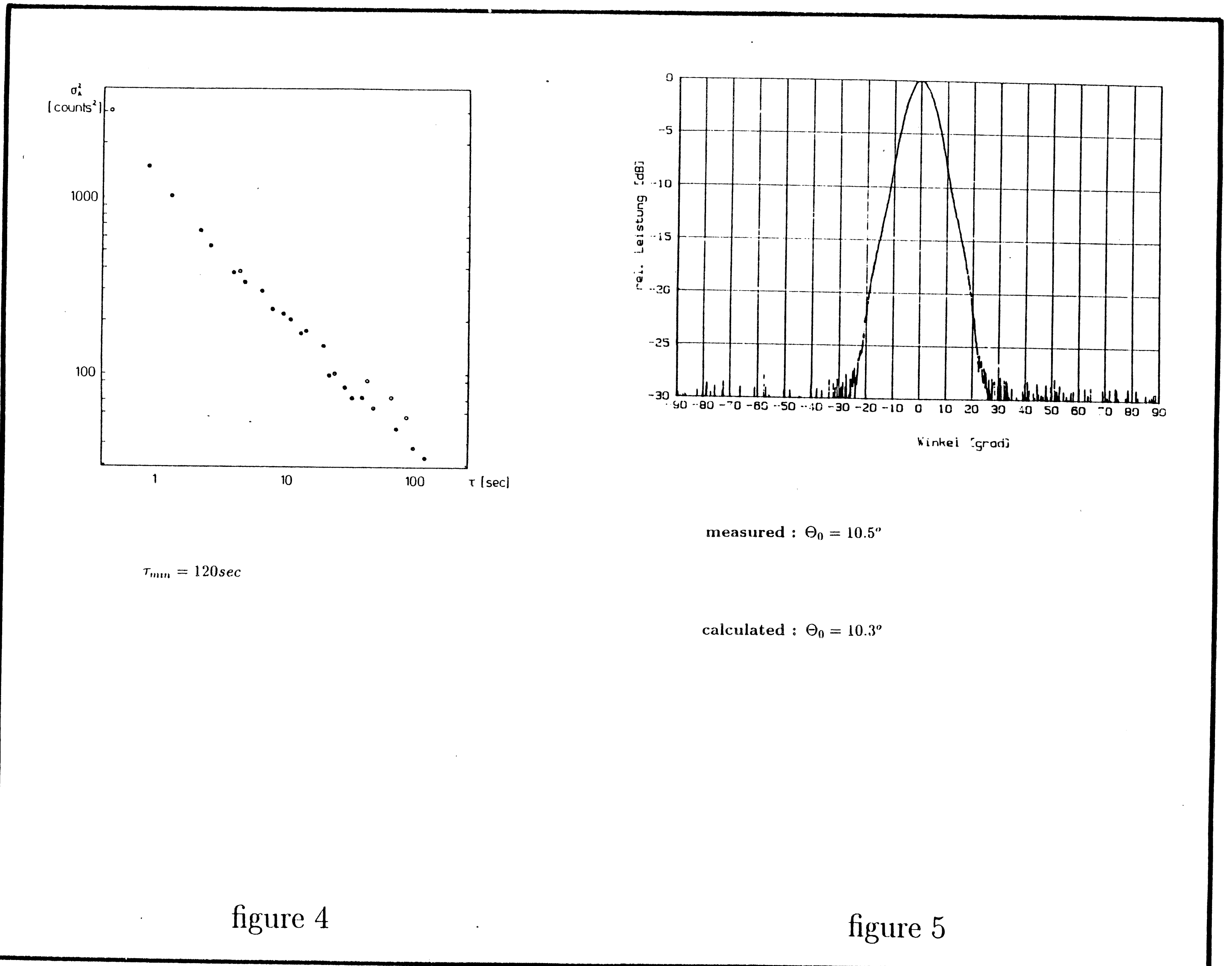

figure 4

figure 5

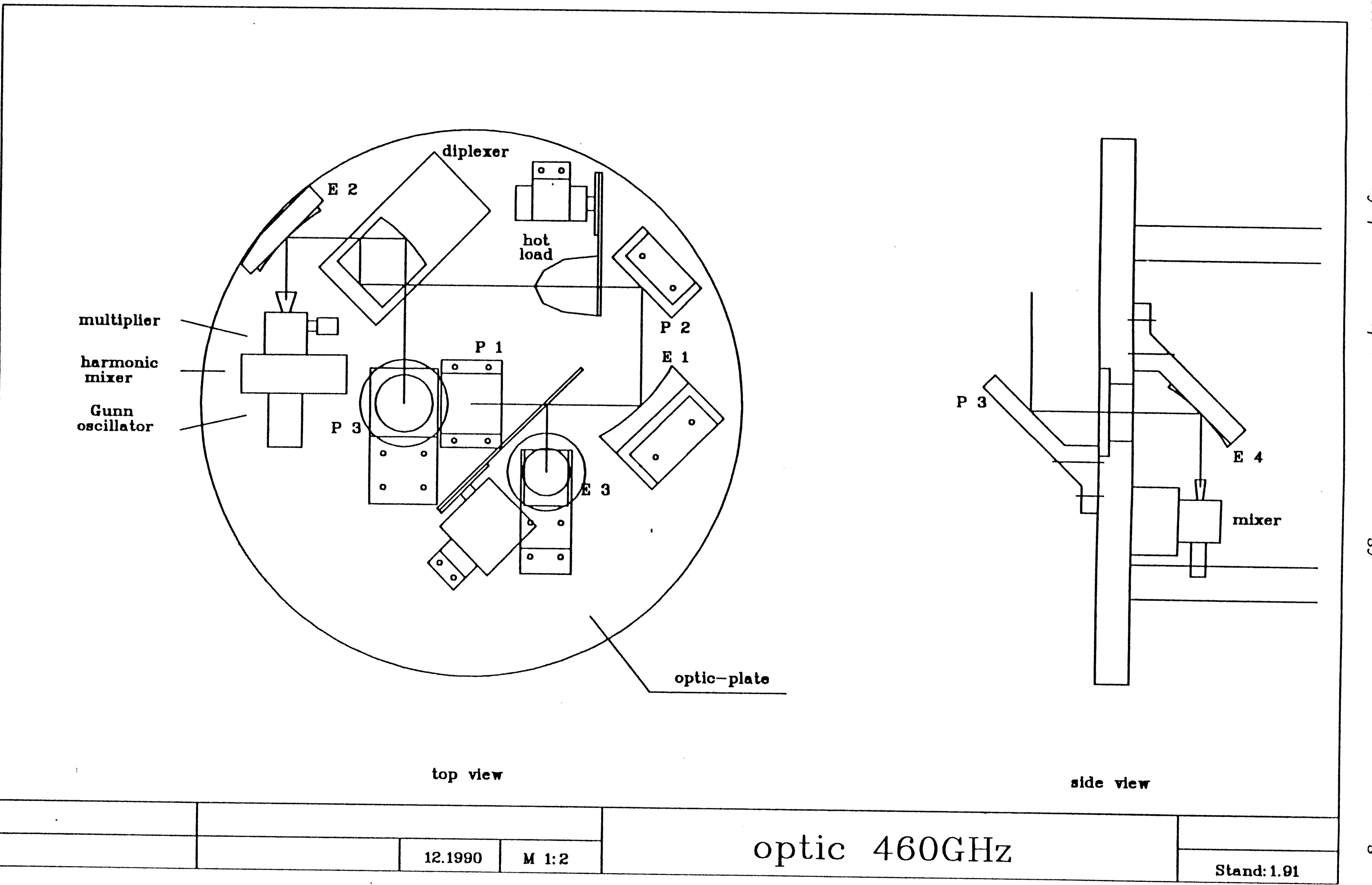

figure 6

A WATER VAPOUR AND TEMPERATURE ATMOSPHERIC VERTICAL SOUNDER BETWEEN 110 AND 190 GHz : OBSERVING CAMPAIGNS IN PROSPECT.

Abba* P., Beaudin G., Deschamps A., Encrenaz P., Gheudin M., Jégou J.R., Prigent C., Ruffié G., Thomas** G.

Département de Radioastronomie Millimétrique - DEMIRM
Observatoire de Meudon 92190 MEUDON, FRANCE

ABSTRACT

Today meteorologists are interested in the ability to obtain atmospheric data even under predominantly cloudy conditions. This points to the use of a microwave instrument on a geostationary satellite. The french National Space Agency (CNES) is supporting a development of a 10 channels millimeter-wave vertical sounder in the 110 - 190 GHz range. Sounding five channels around the 118 GHz O_2 line gives a temperature profile of the atmosphere up to 25 km. For the water vapour retrieval from 2-3 km to 8-10 km, three channels analyse the H_2O line at 183 GHz. Two "window channels" (110 and 150 GHz) correct the 118 and 183 GHz measurements from the surface contamination. The receiver is described, with special emphasis on the quasi-optical filtering techniques and superheterodyne reception.

The purpose of flying this receiver is twofold:

- transfering the millimeter-wave technology from University laboratory to the industry (Meudon Observatory to Matra) and therefore testing the space technological reliability.
- flying on an airborne and validating the atmospheric parameters retrieving schemes at these frequencies for future satellite missions.

1 - INTRODUCTION

Since the operational success of the Microwave Sounding Unit (MSU - on board the american meteorological satellites TIROS-NOAA), the microwave technology advances have now made possible the use of higher frequencies in space, soon providing the meteorological community with

* Now in Alcatel-Espace, Toulouse, France.

** CNES - Centre National d'Etudes Spatiales, Toulouse, France.

an "all weather" sounding capability of the temperature and water vapour profiles in the atmosphere (Figure 1).

Missons	Frequencies			Orbite	Resolution
	Temperature sounding	Humidity sounding	Window channel		
AMSU-A AMSU-B (NOAA) AMSUB-E (EUMETSAT)	11 channels between 52 and 58 GHz	3 channels around 183 GHz	23.8 , 31.4 50.3 , 89.0 157 GHz	polar	from 15 to 50 km nadir
METEOSAT 2de generation	5 channels around 118 GHz	3 channels around 183 GHz	110 - 150 GHz	geostationnary	from 50 to 100 km nadir
SSMT SSMT/2 (DMSP)	6 channels between 53 and 60 GHz	3 channels around 183 GHz	90 - 150 GHz	polar	from 40 to 180 km nadir

Figure 1 : future meteorological radiometric missions aboard satellites.

To prepare these future meteorological radiometric missions aboard satellites, a 10 channels radiometer between 110 and 190 GHz has been developed under the responsability of the french Centre National d'Etudes Spatiales (CNES) and with Matra Espace technical support.

The breadboard characteristics are derived from the European Space Agency (ESA) Meteosat 2nd Generation millimeter-wave project specifications [1]. Sounding five DSB (Double Side Band) channels around the 118 GHz O_2 line give a temperature profile of the atmosphere up to 25 km. For the water vapour retrieval from 2-3 km to 8-10 km, three DSB channels analyse the H_2O line at 183 GHz. Two "window channels " (110 and 150 GHz) correct the 118 and 183 GHz measurements from the surface contamination. Double orthogonal polarization measurements are available to analyse the polarized surface contribution.

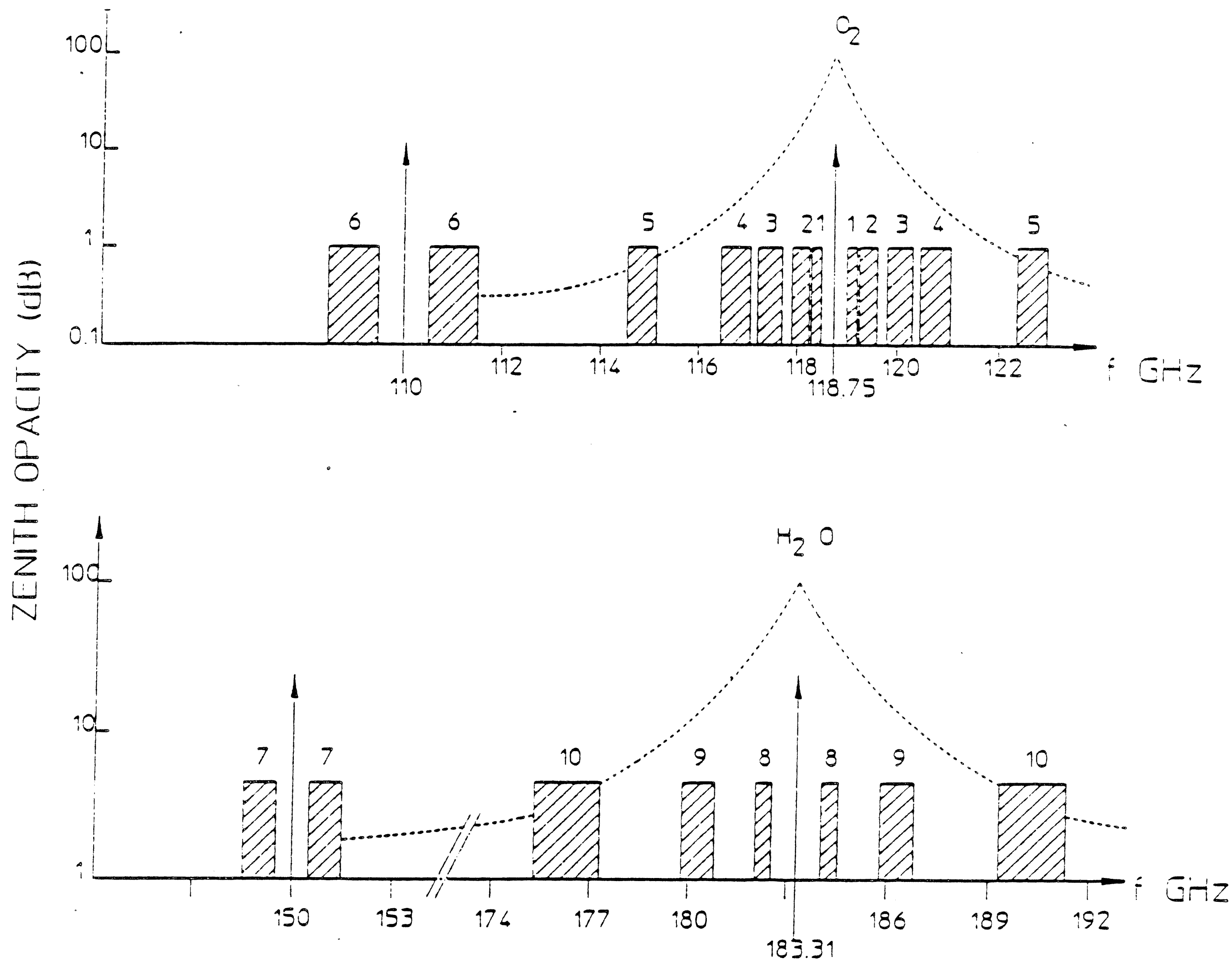

Channel	Centre Frequency (GHz)	Bandwidth (MHz)	Sensitivity (K)
1	118.75 +/- 0.33	200	0.4
2	118.75 +/- 0.65	350	0.25
3	118.75 +/- 1.30	500	0.25
4	118.75 +/- 2.00	600	0.25
5	118.75 +/- 3.90	600	0.25
6	110	1000	0.25
7	150	1000	0.25
8	183.31 +/- 1.000	500	0.5
9	183.31 +/- 3.000	1000	0.5
10	183.31 +/- 7.000	2000	0.5

Figure 2: channel presentation with required sensitivity.

2 - RECEIVER DESIGN

Above 100 GHz, quasi-optical free-space propagation of the signal is adopted, waveguides being to lossy [2]. For a convenient separation of the 110 and 118 GHz channels, we propose a double input beam system. The half-power beamwidths are 4.5 degrees, compatible with sounding from a plane without additive antenna.

The two initial beams are then divided into four (O_2, H_2O and two "window channels") using quasi-optical filtering. Next each band is driven to a low-noise mixer for superheterodyne reception.

Each band is finally analysed. By demultiplexing the mixer outputs, the 118 and 183 GHz bands are separated into different channels.

To calibrate this total power receiver, the incoming beam is commuted to a hot load (300 K) and cold load (77 K), by rotation of a flat mirror.

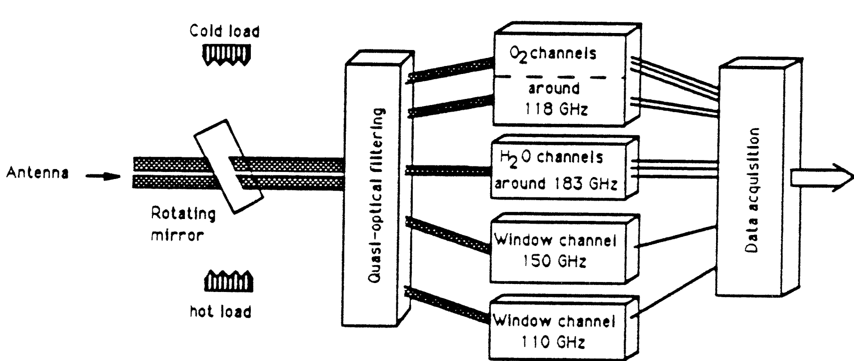

Figure 3: receiver general block-diagram.

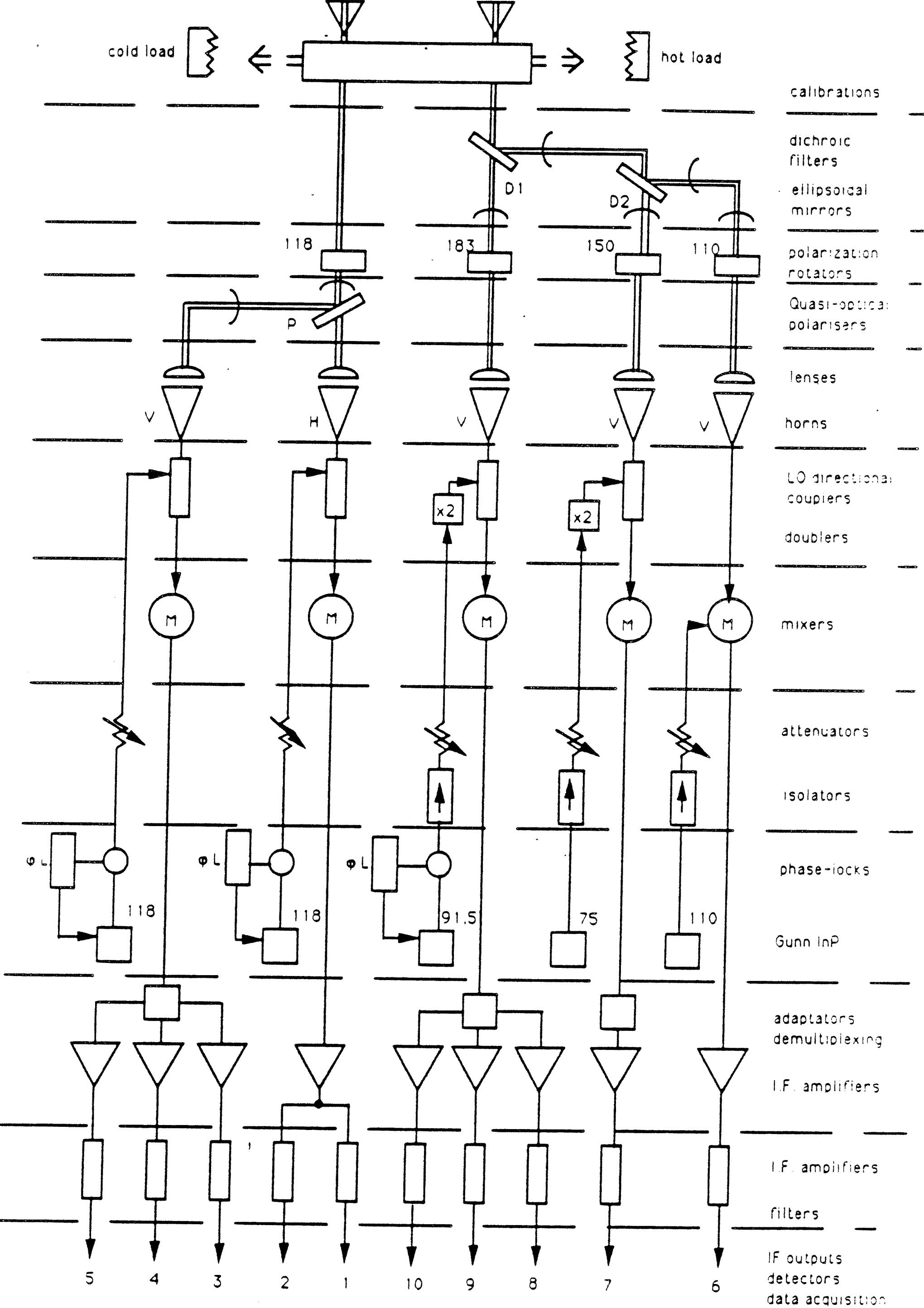

Figure 4 : breadboard schematic configuration.

Following is a complete breadboard description including quasi-optical and millimeter-wave techniques.

3 - QUASI-OPTICAL FILTERING AND INJECTION

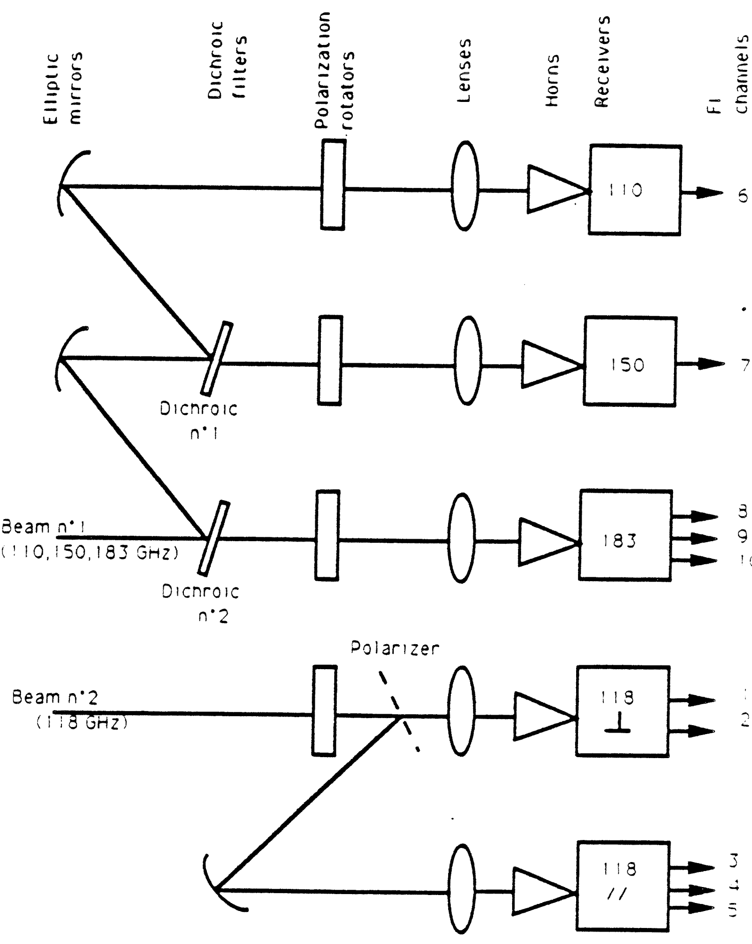

Figure 5 : quasi-optical synoptic.

The double input beam system is composed as follows: one part of the beam is analyzed at 118 GHz, the other part being dedicated to the other channels. The 110, 150 and 183 GHz are separated by two dichroic filters. For each beam, a polarization rotator enables alternative measurements of two orthogonal polarizations of the signal. To achieve proper separation of five IF channels around 118 GHz, the beam is splitted in two by a quasi-optical **polarizer**. Then corrugated lenses focus the beams down to the horns.

The dichroic filters consist of aluminium plates regularly drilled. An electromagnetic description was proposed considering the incident and reflected scattering field as a plane wave superposition with a 15° incident beam angle. Each hole behaves like a circular waveguide propagating the TE_{11} mode. The hole location and diameter and the plate thickness are determined in

order to minimize the transmission losses: the 110 and 150 GHz are separated with 0.5 dB losses at 110 GHz and 15 dB rejection at 150 GHz [3].

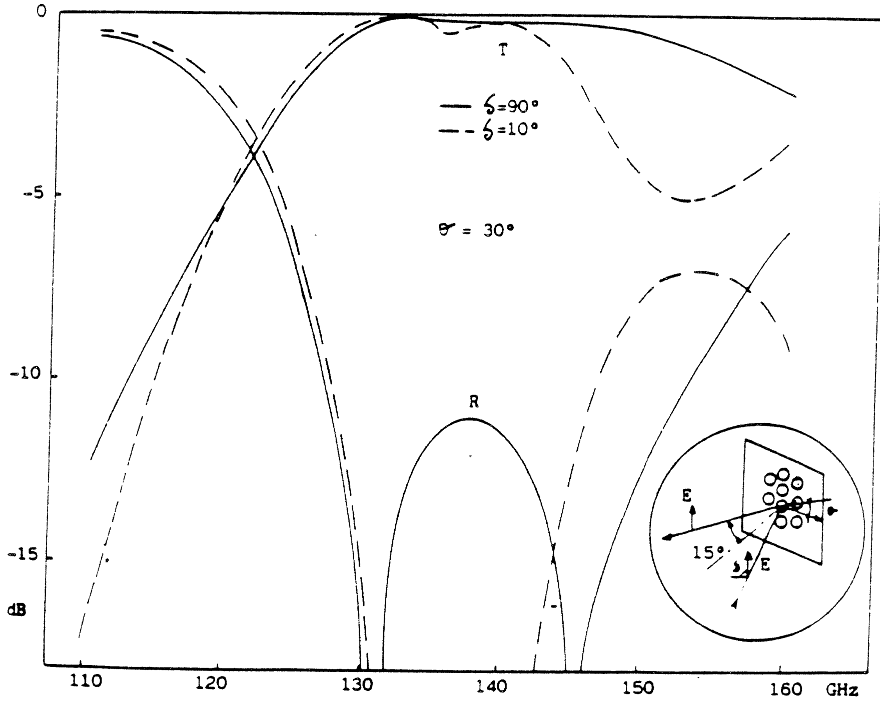

Figure 6 : transmission and reflection dichroic filter response.

The polarization rotators: oxygen and water vapour atmospheric emission is not polarized. On the contrary, ground or cloud reflected radiation is polarized which affects the window channels 6 - 7 and the edges (5 - 10). Polarization orientation depends on the reflecting surface roughness and on the incidence angle. For this reason the receiver includes a dual linear polarization capability (V and H) obtained with polarization rotators in front of each fixed horn-mixer assembly. They are simply composed of a grid of parallel brass wires (i.e. a polarizer) and of a metallic plate, placed a quarter of a wavelength behind the grid. When the wires are vertically oriented, the vertical component of the incident wave is reflected and detected; when the wires are $\pi/4$ oriented, the horizontal component of the wave is rotated to the vertical direction by the device and therefore detected by the fixed receiver. The plate-to-grid distance is adjusted with a high precision. The device is mounted on a rotating motor with two fixed positions [4].

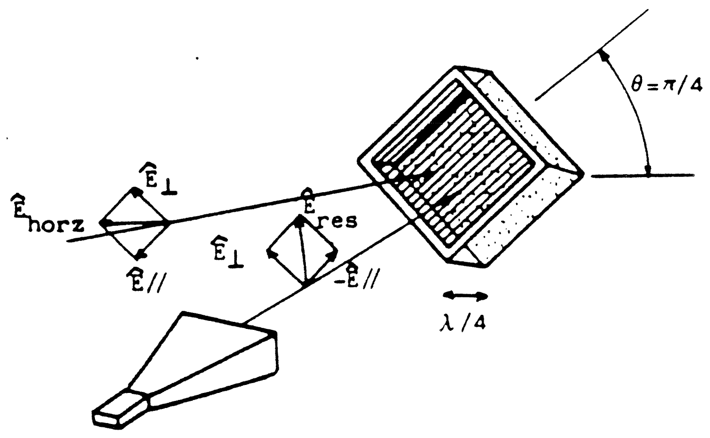

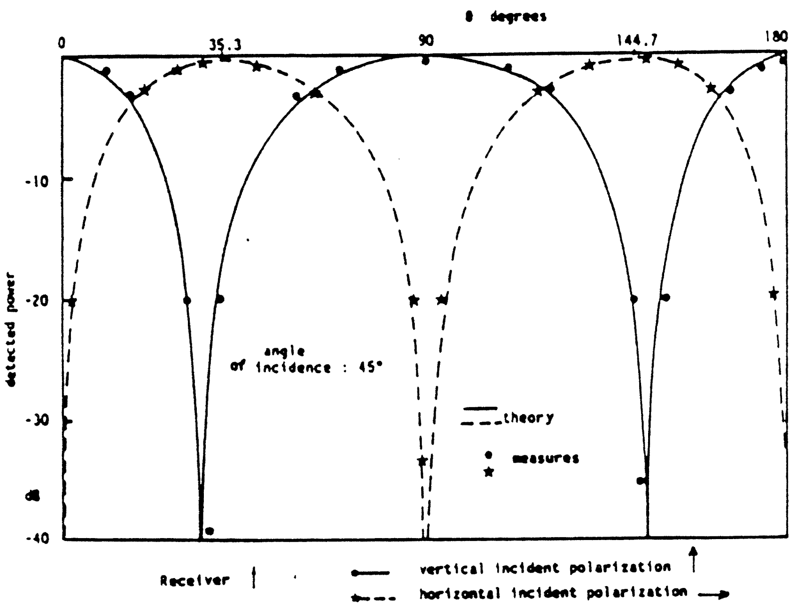

Figure 7 : polarization rotator design and performances.

The lenses: in each channel, a biconvex corrugated lens focuses the gaussian beam down to the horn phase center. The lens diameter is chosen at least four times the waist size to minimize diffraction losses. Corrugated teflon is used for its low reflection and transmission losses.

The horns: for a good operation of the quasi-optical devices, the propagating beams have to be highly gaussian and symetric. Corrugated horns are preferred to Potter's horns for their higher bandwidth (9% bandwidth is required around 183 GHz) [2], [5].

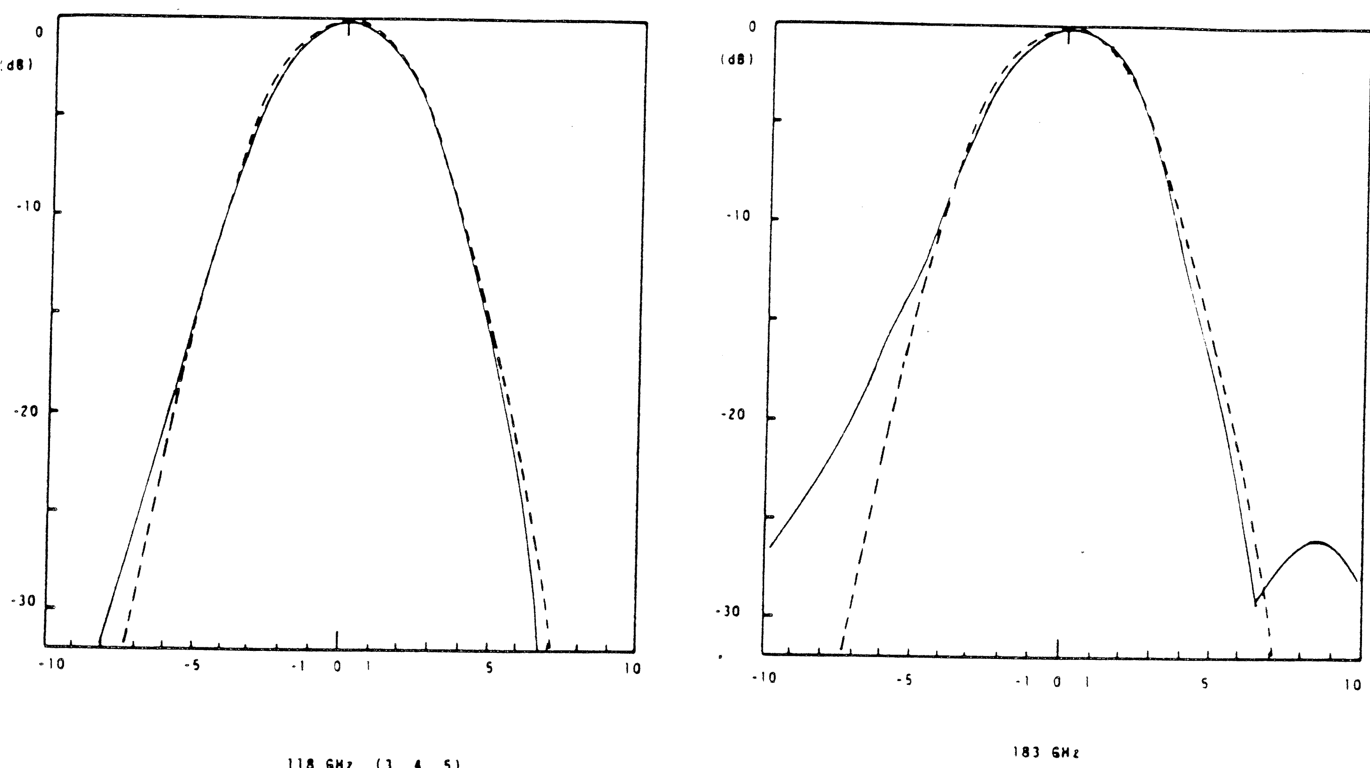

Figure 8: beam pattern of a 118 and 183 GHz channel.

4 - SUPERHETERODYNE LOW NOISE TECHNIQUE

The reception technique is that used in a radiotelescope superheterodyne receiver [6] working in the millimeter-wave field of the spectrum: each signal collected by a horn is delivered to a low-noise mixer for IF (Intermediate Frequency) conversion and then amplified for detection.

The local oscillators and multipliers: the local oscillators (LO) were developed in Bordeaux Observatory. InP Gunn diodes were preferred to GaAs Gunn diodes for working in fundamental mode beyond 100 GHz. They provide less power than Impatt diodes but their noise performances are much better. Thus, at 150 GHz and 183 GHz, frequency doublers are required.

The LO sources capabilities are: 70 mW at 75 GHz, 35 mW at 91.5 GHz, 10 mW at 110 GHz and 8 mW at 118 GHz.

The multiplier efficiencies are respectively 20 % and 8 % for the 75-150 GHz and 91.5-183 GHz doublers.

For stability sake local oscillators are phase-locked at 118 and 91.5 GHz.

The mixers [7], [8]: we have a good experience in low-noise single-ended mixers and we selected them, using honey-comb GaAs Schottky diodes provided by the University of Virginia - USA. The DSB measured performances in figure 9 are given at 1 GHz IF with 500 MHz bandwidth. Directional couplers are used for LO signals injection. Even at 183 GHz, such a solution is possible thanks to the high power available from the InP Gunn oscillator and despite the inherent waveguide-coupler losses.

F_{LO} (GHz)	118	150	183
T_M (K)	500	600	750
L_M (dB)	4.5	6.2	6.2
P_{LO}^* (µW)	400	250	150

* P_{LO} designates the LO access mixer input power. The LO sources are combined with a 10 dB directional coupler.

Figure 9 : whisker-contacted diode mixer performances (DSB).

Because of the output mismatch, the performances of a single-ended mixer can significantly decrease when working on a IF very wide bandwidth. However, in the case of a meteorological instrument, the noise temperature performances are not as drastic as in a radiotelescope. It can be interesting to consider an other mixer technology than whisker-contacted diodes. Increasing progress in semiconductor components make the beam lead or planar Schottky diodes an attractive solution: their structure enables an easy and reliable balanced mounting compared with whisker-contacted diode, reducing the IF impedance and thus making the matching easier. A two beam lead diode balanced mixer was studied, thanks to a complete nonlinear and linear analysis based on the harmonic balance method [7], [8]. A computer program was developed for conversion loss prediction [9]. Our approach includes the beam lead diode electric scheme and the balanced configuration with respect to the external circuit depending on the harmonics and sideband frequencies parity. Each access of the mixer was investigated in order to provide an accurate embedding impedance network describing the linear external circuit. This yields to discuss the electomagnetic description of millimeter-wave circuits. The DSB measured performances are given in figure 10:

F_{LO} (GHz)	P_{LO}^{*} (mW)	IF (GHz)	L_M (dB)	T_M (K)
90	6	0.2 - 2**	3	300
110	6	0.2 - 2**	6	900
118	10	1 - 2	7.5	1050

* The crossbar configuration enables a direct LO signal injection.

** The test set-up includes three low noise amplifiers (NF = 1.3 dB) to cover the IF bandwidth.

Figure 10 : beam lead diode balanced mixer performances (DSB).

At the present time, the substitution of the single-ended whisker-contacted diode mixer can not be considered at 118 GHz. Some investigations should be lead with planar diodes (University of Virginia - USA).

At 110 GHz, the performances are comparable with those measured on the Alpha beam lead diode balanced mixer firstly selected for channel 6 (L_M = 6.2 dB, T_M = 1000 K).

Our mixer is already working on the Portos radiometer 90 GHz channel (CNES - Matra), and could be used on the AMSUB-E radiometer 89 GHz channel (ESA - Matra).

A subharmonical whisker-contacted diode balanced mixer is being studied at 183 GHz in collaboration with Matra Espace and MS2I. Such a solution will avoid the use of a doubler combined with a single-ended mixer. In addition to that, the balanced configuration will make the IF matching easier: this is a critical point for the channels 8, 9 and 10.

The IF demultiplexing and amplification: at each mixer output, demultiplexing and matching circuits for IF channels are realized in microstrip technology.

Cascaded low-noise IF amplifiers (around 1 dB noise figure and 30 dB gain) deliver a -20 dBm power level necessary for the tunnel diode detectors. Predetection bandwidths are determined by an accurate filtering of each channel.

A digitalizer is used to convert the detector output voltage into a frequency. Data are recorded by a specific 16 bits-counter board slotted in a AT Personal Computer. A 18 bits precision is obtained thanks to software data processing.

5 - PERFORMANCES

The quasi-optical losses are detailed in figure 11. For each channel, the receiver noise-temperature was measured many times, using a hot-cold load method. At each step an additional quasi-optical element was included, forming then a different receiver. The losses are deducted from two "successive receiver" measurements, considering the quasi-optical element to be characterized as an ideal attenuator at room temperature. The radiometer perfomances are gathered in figure 12.

Channel	FLO (GHz)	Lens	Polarizer	elliptical mirror	Polarization rotator	Dichroic 183/150	filter 150/110	Total quasi optical loss
1	118.75	0.25	T 0.35	0.1	0.1	-		0.8
2	118.75	0.25	T 0.35	0.1	0.1	-		0.80
3	118.75	0.23	R 0.2	0.1	0.12	-		0.65
4	118.75	0.2	R 0.1	0.1	0.13	-		0.53
5	118.75	0.26	R 0.1	0.1	0.12	-		0.58
6	110	0.25	-	0.12	0.1	R 0.1	R 0.18	0.75
7	150	0.38	-	0.1	0.24	R 0.11	T 0.55	1.38
8	183.31	0.25	-	0.1	0.38	T 0.54		1.27
9	183.31	0.33	-	0.15	0.38	T 0.54		1.4
10	183.31	-	-	-	-			

Figure 11 : quasi-optical losses (dB).

Channel	F (GHz)	IF (GHz)	T_R* (K)	T_R** (K)	ΔT*** (K)	ΔT (K) esa
1	118.75	0.23 - 0.43	1710	2180	0.47	0.4
2	118.75	0.475 - 0.825	1430	1800	0.3	0.25
3	118.75	1.05 - 1.55	2875	3390	0.46	0.25
4	118.75	1.7 - 2.3	1350	1580	0.2	0.25
5	118.75	3.6 - 4.2	2750	3250	0.4	0.25
6	110	0.05 - 1	1350	1670	0.16	0.25
7	150	1 - 2	2900	4250	0.4	0.25
8	183.31	0.75 - 1.25	2350	3090	0.42	0.5
9	183.31	2.5 - 3.5	3500	4760	0.46	0.5
10	183.31	6 - 8	—	—	—	0.5

* receiver temperature (excluding quasi-optical losses).

** total receiver temperature (including quasi-optical losses).

*** integration time is 110 ms.

Figure 12 : radiometer performances.

6 - OBSERVATION CAMPAIGNS

Related to the technological radiometric developments in our laboratory, we have been working on a direct radiative transfer model adapted to frequencies up to 200 GHz [10]. In order to validate this model and to prepare the retrieving schemes of the atmospheric parameters from satellite observations, we propose confrontation with radiometric observations.

Ground-based preparatory observations.

The meteorological station in Trappes (France) provides in situ measurements of atmospheric pressure, temperature and humidity, up to 35 km, every 12 hours. From observations in the less opaque radiometer channels, we will analyse the gazeous atmospheric continuum, still very controversal above 100 GHz.

Airborne campaigns.

The group is already involved in a joint English-French flying campaign for the analysis of 89 and 157 GHz atmospheric window-channels: the Microwave Airborne Radiometer and Scanning System (MARSS) has been developed by the BMO (British Meteorological Office) and the LMD (Laboratoire de Météorologie Dynamique).

The purpose of flying the 110-118-150-183 GHz receiver on a plane would be twofold:

- testing the space technology reliability.

- studying the radiative transfer in the atmosphere and the surface properties at frequencies corresponding to future satellite missions. At these millimeter wavelengths, the observations are sparse. Efforts have to be made to validate the retrieving schemes of the atmospheric parameters from spaceborne sounding at these frequencies.

7 - CONCLUSION

The sounder is at the moment under test. The first improvements will concern the IF mixer output matching which is at the present time a critical point, especially for channels 3, 5, 7 and 10. On one hand the microstrip demultiplexer combined with single-ended whisker-contacted diode mixer, and on the other hand the beam lead diode balanced mixer and the subharmonical balanced mixer will be thorougly studied in order to determine the best choice.

The double input beam system was adopted because of the difficulty to separate accurately the 110 and 118 GHz signals. A single input beam configuration could be selected by switching the "window channel" 6 (110 GHz) down to 100 GHz.

The breadboard should be used for ground-based observations in the middle of 1991. The first airborne campaign is planned for the year after. In order to better approach satellite conditions, we also envisage a stratospheric balloon or airplane fly.

Acknowledgment : this work was made with the technical support of F. Gadéa, S. Lebourg, J. Morin, G. Rérat (Meudon Observatory), M. Chauvet, J. Lacroix, G. Montignac (Bordeaux Observatory) and the collaboration of C. Letrou (INT-Evry), S. Toutain (ENSTBr-Brest), M. Chaubet (CNES-Toulouse), Matra Espace (Toulouse-Vélizy), MS2I (Montigny).

REFERENCES

[1] A. Chedin, D. Pick, R. Rizzi, "Second Generation Meteosat", Ravenna Workshop on the Operational Instruments, Summary Report, 3-5 nov. 1986.

[2] P. F. Goldsmith, "Quasi-optical techniques at millimeter and submillimeter wavelengths", in Infrared and Millimeter Waves, vol. 6: Systems and Components, K.J. Button (ed.), Academic Press, New York, pp. 277-343, 1982.

[3] C. Letrou, "Conception de diplexeurs dichroîques dans le domaine millimétrique", 6es Journées Nationales Microondes, pp. 64-65, Montpellier, France, juin 1989.

[4] C. Prigent, P. Abba, M. Gheudin, "A quasi-optical polarization rotator", International Journal of Infrared and Millimeter Waves, vol. 9, n° 5, pp. 477-490, may 1988.

[5] P. D. Potter, "A new horn antenna with suppressed sidelobes and equal beamwidths", Microwave J., vol. 6, pp. 71-78, 1963.

[6] J. D. Kraus, "Radio Astronomy", 2nd edition, Cygnus-Quasar Books, Powell, Ohio, 1986.

[7] D. N. Held, A. R. Kerr, "Conversion loss and noise of microwave and millimeter-wave mixers: Part 1-Theory, Part 2-Experiment", IEEE Trans. Microwave Theory Tech., vol. MTT-26, pp. 49-61, feb. 1978.

[8] P. H. Siegel, A. R. Kerr, W. Hwang, "Topics in the optimization of millimeter-wave mixers", NASA Technical Paper 2287, 1984.

[9] J. R. Jégou, J. M. Goutoule, G. Beaudin, G. Ruffié, S. Toutain, "Harmonic balance method for conversion loss prediction of a millimeter-wave crossbar balanced mixer", 20th European microwave conference, proceedings Vol. 1, pp. 157-161, Budapest , dec. 1990.

[10] C. Prigent, P. Abba, N. A. Scott, S. Stringer, "A synthetic atmospheric millimeter-wave propagation model for future meteorological radiometric missions", in IGARSS'88 (1988 International Geoscience And Remote Sensing Symposium), Remote sensing : moving towards the 21st century, 12-16 September 1988, Edinburgh, UK, vol. II, esa SP-284, IEEE 88CH2497-6, pp. 953-956, aug.. 1988.